UNIVERSIDADE DA BEIRA INTERIOR
Ciências

Biosynthesis, purification and delivery of minicircle DNA for gene therapy

Vítor Manuel Abreu Gaspar

Tese para obtenção do Grau de Doutor em
Bioquímica
(3º ciclo de estudos)

Orientador: Prof. Doutora Fani Pereira de Sousa
Co-orientador: Prof. Doutor Ilídio Joaquim Sobreira Correia
Co-orientador: Prof. Doutora Chantal Pichon

Covilhã, outubro de 2015

Dedicatory

To my family, to my girlfriend and her (my) family

"Let us, then, be up and doing,
With a heart for any fate.
Still achieving, still pursuing,
Learn to labor and to wait."

Henry Wadsworth Longfellow

The development of this Doctoral thesis was supported by the Portuguese Foundation for Science and Technology (FCT) through an individual PhD fellowship (SFRH/BD/80402/2011), granted under the program QREN - POPH Type 4.1 – Advanced Training, co-funded by the European Social Fund and by national funds from the MCTES.

Acknowledgments

This research was only made possible with the contribute of numerous persons that with their know-how, talent, and immense will to advance scientific knowledge have inspired me to pursue new avenues and helped develop the work presented throughout this PhD thesis.

In particular, I would first like to acknowledge my supervisors Prof. Dr. Fani Sousa, Prof. Dr. Ilídio Correia and Professor Dr. Chantal Pichon for their immense expertise, critical thinking, scientific guidance, invaluable support at all times, and especially, when difficulties crossed our path. I am also grateful to my supervisors for always trusting, listening and encouraging me when new ideas appeared. Overall, it has been an enormous privilege to work and evolve as a person and as a scientist under their supervision over the past years.

I wish, as well, to acknowledge Professor Dr. João Queiroz for giving me the opportunity to do research in the Biotechnology and Biomolecular Sciences group back in 2009. Moreover, I would also like to show my appreciation for his continuous support, expertise, and for always having an important word of advice.

I would like to acknowledge University of Beira Interior, in particular the Health Sciences Faculty and the Health Sciences Research Centre, as well as the Centre de Biophysique Moléculaire of University of Orleans, France, for providing all the facilities and equipment to develop these studies.

Moreover, I would like to acknowledge all the persons from Health Sciences Research Centre to whom I contacted during my PhD. Especially, I would like to express my appreciation to all my group colleagues and very good friends. Likewise, I would kindly like to acknowledge all technicians, researchers and professors from the Centre de Biophysique Moléculaire for receiving me so well at the lab, for always being very helpful in everything and for kindly sharing their extensive scientific expertise with me.

I am also deeply grateful to my friends and my family for always being supportive and for all their love and advices. From my heart I would like to thank you Sofia for the invaluable moments we spend together, for your love and indescribable support, and foremost for supporting the dreams we share.

List of scientific publications

Scientific articles published in peer-reviewed international journals included in this Doctoral thesis

I. **Sensitive Detection of Peptide - Minicircle DNA Interactions by Surface Plasmon Resonance**
Gaspar, V.M., Cruz, C., Queiroz, J.A., Pichon, C., Correia, I.J., Sousa, F.
Analytical Chemistry, 2013, 85 (4):2304-2315
DOI: 10.1021/ac303288x
(I.F. upon submission = 5.695; Current I.F. (2015 citation reports) = 5.636; Q1 and TOP 10 (Chemistry, Analytical (4/74))).

II. **Biofunctionalized Nanoparticles with pH-responsive and Cell Penetrating Blocks for Gene Delivery**
Gaspar, V.M., Marques, J.G., Sousa, F., Louro, R.O., Queiroz, J.A., Correia, I.J.
Nanotechnology, 2013, 24 (27):275101
DOI: 10.1088/0957-4484/24/27/275101
(I.F. upon submission = 3.842; Current I.F. (2015 citation reports) = 3.821; Q1 (Materials Science, Multidisciplinary (40/259)); Q1 (Physics, Applied (20/143)); Q2 (Nanoscience and Nanotechnology (25/79))).

III. **Improved Minicircle DNA Biosynthesis for Gene Therapy Applications**
Gaspar, V.M., Maia, C.J., Queiroz, J.A., Pichon, C., Correia I.J., Sousa F.
Human Gene Therapy Methods, 2014, 25 (2):93-105
DOI: 10.1089/hgtb.2013.020
(I.F. upon submission = 4.019; Current I.F. (2015 citation reports) = 2.436; Q2 (Biotechnology & Applied Microbiology (65/162)); Q3 (Genetics & Heredity (88/167)); Q3 (Medicine, Research & Experimental (63/123))).

IV. **Poly(2-ethyl-2-oxazoline)-PLA-g-PEI Amphiphilic Triblock Micelles for Co-delivery of Minicircle DNA and Chemotherapeutics**
Gaspar, V.M., Gonçalves, C., de Melo-Diogo, D., Costa, E.C., Queiroz, J.A., Pichon, C., Sousa F., Correia, I.J.
Journal of Controlled Release, 2014, 189:90-104
DOI: 10.1016/j.jconrel.2014.06.040
(I.F. upon submission = 7.261; Current I.F. (2015 citation reports) = 7.705; Q1 and TOP 10 (Pharmacology and Pharmacy (10/254)); Q1 (Chemistry Multidisciplinary (17/157))).

V. **Folate-Targeted Multifunctional Amino Acid-Chitosan Nanoparticles for Improved Cancer Therapy**
Gaspar, V.M., Costa, E.C., Queiroz, J.A., Pichon, C., Sousa F., Correia, I.J.
Pharmaceutical Research, 2015, 32 (2):562-577
DOI: 10.1007/s11095-014-1486-0
(I.F. upon submission = 3.952; Current I.F. (2015 citation reports) = 3.420; Q1 (Pharmacology and Pharmacy (63/254)); Q1 (Chemistry Multidisciplinary (39/157))).

VI. **Minicircle DNA Vectors for Gene Therapy: Advances and Applications**
Gaspar, V.M., de Melo-Diogo, D., Costa, E.C., Moreira, A.F., Queiroz, J.A., Pichon, C., Correia I.J., Sousa F.
Expert Opinion on Biological Therapy, 2015, 15 (3):353-379
DOI: 10.1517/14712598.2015.996544
(I.F. upon submission = 3.653; Current I.F. (2015 citation reports) = 3.743; Q1 (Medicine Research and Experimental (28/123)); Q1 (Biotechnology & Applied Microbiology (30/162))).

VII. **Gas-generating TPGS-PLGA Microspheres Loaded with Nanoparticles (NIMPS) for Co-delivery of Minicircle DNA and Antitumoral Drugs**
Gaspar, V.M., Moreira, A.F., Costa, E.C., Queiroz, J.A., Sousa, F., Pichon, C., Correia, I.J.
Colloids and Surfaces B: Biointerfaces, 2015, 134:287-294
DOI: 10.1016/j.colsurfb.2015.07.004
(I.F. upon submission = 4.287; Current I.F. (2015 citation reports) = 4.152; Q1 (Biophysics (16/73)); Q1 (Chemistry, Physical (34/139)); Q1 (Materials Science, Biomaterials (8/33))).

VIII. **Bioreducible Poly(2-ethyl-2-oxazoline)-PLA-PEI-SS Triblock Copolymer Micelles for Co-delivery of DNA minicircles and Doxorubicin**
Gaspar, V.M., Baril, P., Costa, E.C., de Melo-Diogo, D., Foucher, F., Queiroz, J.A., Sousa, F., Pichon, C., Correia, I.J.
Journal of Controlled Release, 2015, 213:175-191
DOI: 10.1016/j.jconrel.2015.07.011
(I.F. upon submission = 7.261; Current I.F. (2015 citation reports) = 7.705; Q1 and TOP 10 (Pharmacology and Pharmacy (10/254)); Q1 (Chemistry Multidisciplinary (17/157))).

Book chapters in peer reviewed scientific books published by international publishers included in this Doctoral thesis

I. **Multifunctional Nanocarriers for Co-delivery of Nucleic Acids and Chemotherapeutics to Cancer Cells**
Gaspar, V.M., Moreira, A.F., de Melo-Diogo, D., Costa, E.C., Queiroz, J.A., Sousa, F., Pichon, C., Correia, I.J.
Year: 2015
Publisher: Elsevier
Book Title: Nanobiomaterials of Medical Imaging – Volume VIII
Book Series: Applications of Nanobiomaterials (Multi-Volume SET I-XI)
Series Editor: Alexandru Mihai Grumezescu
Publication status: Accepted for publication.

Scientific articles published in peer-reviewed international journals not included in this Doctoral thesis

I. **Nanoparticle Mediated Delivery of Pure P53 Supercoiled Plasmid DNA for Gene Therapy**
Gaspar, V.M., Correia, I.J., Sousa, A., Silva, F., Paquete, C.M., Queiroz, J.A., Sousa, F.
Journal of Controlled Release, 2011, 156 (2):212-222
DOI: 10.1016/j.jconrel.2011.08.007
(I.F. upon submission = 7.261; Current I.F. (2015 citation reports) = 7.705; Q1 and TOP 10 (Pharmacology and Pharmacy (10/254)); Q1 (Chemistry Multidisciplinary (17/157))).

II. **Formulation of Chitosan-TPP-pDNA Nanocapsules for Gene Therapy Applications**
Gaspar, V.M., Sousa, F., Queiroz, J.A., Correia, I.J.
Nanotechnology, 2011, 22 (1):015101
DOI: 10.1088/0957-4484/22/1/015101
(I.F. upon submission = 3.842; Current I.F. (2015 citation reports) = 3.821; Q1 (Materials Science, Multidisciplinary (40/259)); Q1 (Physics, Applied (20/143)); Q2 (Nanoscience and Nanotechnology (25/79))).

III. **Evaluation of Nanoparticle Uptake in Co-culture Cancer Models**
Costa, E.C., **Gaspar, V.M.**, Marques, J.G., Coutinho, P., Correia, I.J.
Plos One, 2013, 8 (7):e70072
DOI: 10.1371/journal.pone.0070072
(I.F. upon submission = 3.730; Current I.F. (2015 citation reports) = 3.234; Q1 and TOP 10 (Multidisciplinary Sciences (8/56))).

IV. **Microencapsulated Chitosan-Dextran Sulfate Nanoparticles for Controlled Delivery of Bioactive Molecules and Cells in Bone Regeneration**
Valente, J.*, **Gaspar, V.M.***, Antunes, B., Coutinho, P., Correia, I.J.
Polymer, 2013, 54 (1):5-15
DOI: 10.1016/j.polymer.2012.10.032
(I.F. upon submission = 3.379; Current I.F. (2015 citation reports) = 3.562; Q1 (Polymer science (16/82))).*Co-first authors.

V. **Bioactive Polymeric-Ceramic Hybrid 3D Scaffold for Application in Bone Tissue Regeneration**

Torres, A.L., **Gaspar, V.M.**, Serra, I.R., Diogo, G.S., Fradique R., Silva, A.P., Correia, I.J.

Materials Science & Engineering C - Materials for Biological Applications, 2014, 33 (7):4460-4469

DOI: 10.1016/j.msec.2013.07.003

(I.F. upon submission = 2.404; Current I.F. (2014 citation reports) = 3.088; Q3 (Materials Science, Biomaterials (17/33))).

VI. **Synthesis and Characterization of Micelles as Carriers of Non-steroidal Anti-inflammatory Drugs (NSAID) for Application in Breast Cancer Therapy**

Marques, J.G., **Gaspar, V.M.**, Costa, E.C., Paquete, C.M., Correia, I.J.

Colloids and Surfaces B Biointerfaces, 2014, 113:375-383

DOI: 10.1016/j.colsurfb.2013.09.037

(I.F. upon submission = 4.287; Current I.F. (2015 citation reports) = 4.152; Q1 (Biophysics (16/73)); Q1 (Chemistry, Physical (34/139)); Q1 (Materials Science, Biomaterials (8/33))).

VII. **Manufacture of ß-TCP/Alginate Scaffolds Through a Fab@Home Model for Application in Bone Tissue Engineering**

Diogo, G.S., **Gaspar, V.M.**, Serra, I.R., Fradique, R., Correia, I.J.

Biofabrication, 2014, 6:025001

DOI: 10.1088/1758-5082/6/2/025001

(I.F. upon submission= 3.705; I.F. (2015 citation report) = 4.289; Q1 and TOP 10 (Materials Science, Biomaterials (7/33)); Q1 and TOP 10 (Engineering, Biomedical (7/76))).

VIII. **Co-delivery of Sildenafil (Viagra®) and Crizotinib for Synergistic and Improved Antitumoral Therapy**

Marques, J.G., **Gaspar V.M.**, Markl, D., Costa, E.C., Gallardo, E., Correia, I.J.

Pharmaceutical Research, 2014, 31 (9):2516-2528

DOI: 10.1007/s11095-014-1347-x

(I.F. upon submission = 3.952; Current I.F. (2015 citation reports) = 3.420; Q1 (Pharmacology and Pharmacy (63/254)); Q1 (Chemistry Multidisciplinary (39/157))).

IX. **Optimization of Liquid Overlay Technique to Formulate Heterogenic 3D Co-cultures Models**

Costa, E.C., **Gaspar, V.M.**, Coutinho, P., Correia, I.J.

Biotechnology & Bioengineering, 2014, 111 (8):1672-1685

DOI: 10.1002/bit.25210

(I.F. upon submission = 3.648; Current I.F. (2015 citation reports) = 4.126; Q1 (Multidisciplinary Sciences (24/162))).

X. **Combinatorial Delivery of Crizotinib-Palbociclib-Sildenafil Using TPGS-PLA Micelles for Improved Cancer Treatment**

de Melo-Diogo, D., **Gaspar, V.M.**, Costa, E.C., Moreira, A.F., Oppolzer, D., Gallardo, E., Correia, I.J.

European Journal of Pharmaceutics and Biopharmaceutics, 2014, 88 (3):718-729

DOI: 10.1016/j.ejpb.2014.09.013

(I.F. upon submission = 3.826; Current I.F. (2015 citation reports) = 3.383; Q1 (Pharmacology and Pharmacy (64/254))).

XI. **Preparation of End-capped pH-sensitive Mesoporous Silica Nanocarriers for On-demand Drug Delivery**

Moreira, A.F., **Gaspar, V.M.**, Costa, E.C., de Melo-Diogo, D., Machado, P., Paquete, C.M., Correia, I.J.

European Journal of Pharmaceutics and Biopharmaceutics, 2014, 88 (3):1012-1025

DOI: 10.1016/j.ejpb.2014.09.002

(I.F. upon submission = 3.826; Current I.F. (2015 citation reports) = 3.383; Q1 (Pharmacology and Pharmacy (64/254))).

XII. **Chitosan/Arginine-Chitosan Polymer Blends for Assembly of Nanofibrous Membranes for Wound Regeneration**

Antunes, B.P., Moreira, A.F., **Gaspar, V.M.**, Correia, I.J.

Carbohydrate Polymers, 2015, 130:104-112

DOI: 10.1016/j.carbpol.2015.04.072

(I.F. upon submission = 3.916; Current I.F. (2015 citation reports) = 4.074; Q1 and TOP 10 (Chemistry Applied (4/70); Q1 and TOP 10 (Chemistry Organic (10/57)); Q1 and TOP 10 (Polymer Science (9/82))).

List of scientific communications

Oral scientific communications related to this Doctoral thesis

I. **Gaspar, V.M.**, Sousa, F., Louro, R.O., Queiroz, J.A., Correia, I.J., "Cell Internalizing and pH-responsive Nanoparticles for Improved Delivery of DNA Biopharmaceuticals", presented in IV Symposium of Pharmacy - 1st International Symposium of Pharmacy Biotechnology and Pharmacy, Polytechnic Institute of Guarda (IPG), July 6th, 2012, Guarda, Portugal.

II. **Gaspar, V.M.**, Sousa, F., Louro, R.O., Queiroz, J.A., Correia, I.J., "Biofunctionalized Nanoparticles for Improved Delivery of Biopharmaceuticals", presented in VII Annual CICS Symposium, University of Beira Interior (UBI), July 3rd, 2012, Covilhã, Portugal.

III. **Gaspar, V.M.**, Marques, J.M., Sousa, F., Louro, R.O., Queiroz, J.A., Correia, I.J., "Characterization of Nanomedicines Uptake and Intracellular Trafficking in Cancer Cells", presented in VI Symposium on Technology and Health, Polytechnic Institute of Guarda (IPG), May 3rd, 2013, Guarda, Portugal.

IV. **Gaspar, V.M.**, Louro, R.O., Queiroz, J.A., Pichon, C., Sousa, F., Correia, I.J., "Delivery of DNA Biopharmaceuticals by Nonviral Nanoparticulated Carriers", presented in MICROBIOTEC13, University of Aveiro (UA), December 6th to 8th, 2013, Aveiro, Portugal.

V. **Gaspar, V.M.**, Cruz, C., Maia, C.J., Queiroz, J.A., Pichon C., Correia I.J., Sousa, F., "Screening of Novel Ligands to Purify Biosynthesized Minicircle DNA for Therapeutic Applications", presented in IX CICS Symposium, University of Beira Interior (UBI) June 30th to July 1st, 2014, Covilhã, Portugal.

VI. **Gaspar, V.M.**, Costa, E.C., Louro, R.O., Queiroz, J.A., Pichon, C., Sousa, F., Correia, I.J., "Nanomaterials for Delivery of Biomolecules with Application in Cancer Therapy", presented in V National Conference of Biomedical Sciences, University of Beira Interior (UBI), March 13th to 15th, 2014, Covilhã, Portugal.

VII. **Gaspar, V.M.**, Gonçalves, C., de Melo-Diogo, D., Costa, E.C., Queiroz, J.A., Pichon, C., Sousa, F., Correia, I.J., "Simultaneous Delivery of Drugs and Genes by Multi-block Polymeric Nanomicelles for Synergistic Cancer Therapy", presented in Nanoscience and Nanotechnology International Conference - NanoPT, February 11th to 13th, 2015, Porto, Portugal.

Invited oral scientific communications

I. **Gaspar, V.M.,** Correia, I.J., Queiroz, J.A., Sousa, F., "Development of a New Gene Delivery Vehicle for Future Application in Cancer Therapy", presented in Transboudary Forum in Biotechnology - INESPO (Innovation Network Spain-Portugal), University of Beira Interior (UBI), October 25th, 2013, Covilhã, Portugal.

II. **Gaspar, V.M.,** Costa, E.C., Marques, J.G., Louro, R.O., Queiroz, J.A., Pichon, C., Sousa, F., and Correia, I.J., "Development of Nanosystems for Delivery of Bioactive Molecules with Application in Cancer Therapy", presented in Clinical Sessions of the Hospital of Cova da Beira (HCB), May 22nd, 2014, Covilhã, Portugal.

III. **Gaspar, V.M.**, Gonçalves, C., de Melo-Diogo, D., Costa, E.C., Queiroz, J.A., Pichon, C., Sousa, F., Correia, I.J., "Polymeric Nanocarriers for Delivery of Multiple Bioactive Molecules to Breast Cancer Cells", presented in Biochemistry Symposium, University of Beira Interior (UBI), May 6th to 7th, 2015, Covilhã, Portugal.

Oral scientific communications unrelated to this Doctoral thesis

I. **Gaspar, V.M.**, Sousa, F., Queiroz, J.A., Correia, I.J., "Development of a New Drug Delivery System for Application in Cancer Gene Therapy", presented in II National Conference of Biomedical Sciences, University of Beira Interior (UBI), March 3rd to 5th, 2011, Covilhã, Portugal.

II. **Gaspar, V.M.**, Sousa, A., Silva, F., Correia, I.J., Queiroz, J.A., Sousa, F., "Encapsulation of P53 Supercoiled pDNA in Chitosan Nanoparticles", presented in Conferences of Chemistry and Biochemistry, University of Beira Interior (UBI), May 16th and 17th, 2012, Covilhã, Portugal.

III. **Gaspar, V.M.**, Correia, I.J., Sousa A., Silva, F., Queiroz, J.A., Sousa, F., "Nanoparticle Mediated Delivery of Pure P53 Plasmid DNA for Cancer Therapy", presented in Oncology Congress, University of Beira Interior (UBI), January 6th, 2012, Covilhã, Portugal.

Poster presentations related to this Doctoral thesis

I. **Gaspar, V.M.**, Sousa, F., Louro, R.O., Queiroz, J.A., Correia, I.J., "Imaging Cell Uptake and Intracellular Trafficking of Nanomedicines by Confocal Microscopy", presented in Bioimaging 2012 - 1st International Symposium in Applied Bioimaging Bridging Development and Application, September 19th to 21st, 2012, Porto, Portugal.

II. **Gaspar, V.M.**, Sousa, F., Louro, R.O., Queiroz, J.A., Correia, I.J., "Cell internalizing and pH-responsive Chitosan Nanoparticles for Improved Delivery of DNA Biopharmaceuticals", presented in 13th Trends in Nanotechnology International Conference, September 10th to 14th, 2012, Madrid, Spain.

III. **Gaspar, V.M.**, Costa, E., Marques, J.G., Queiroz, J.A., Pichon, C., Sousa, F, Correia, I.J., "Evaluation of Targeted Gene Delivery to Cancer Cells Trough High Throughput Fluorescence Microscopy", presented in 1st POLARIS Workshop International Conference, October 7th to 9th, 2013, Porto, Portugal.

IV. **Gaspar, V.M.**, Marques, J.G., Sousa, F., Louro, R.O., Queiroz, J.A., Correia, I.J., "Characterization of Chitosan Nanoparticles Uptake and Intracellular Trafficking in Cancer Cells", presented in 11th International Conference of the European Chitin Society, May 5th to 8th, 2013, Porto, Portugal.

V. **Gaspar, V.M.**, Marques, J.G., Sousa, F., Louro, R.O., Queiroz, J.A., Correia, I.J., "Amino Acids as Functionalization Materials for Nanoparticulated Delivery Systems", presented in NanoPT - Nanoscience and Nanotechnology International Conference, February 13th to 15th, 2013, Porto, Portugal.

VI. **Gaspar, V.M.**, Costa, E.C., Queiroz, J.A., Pichon, C., Sousa, F., Correia, I.J., "Evaluation of Targeted Gene Delivery to Cancer Cells Trough High Throughput Fluorescence Microscopy", presented in Biannual Meeting of the Portuguese Society of Materials (SPM), May 4th, 2014, Covilhã, Portugal.

Poster presentations unrelated to this Doctoral thesis

I. **Gaspar, V.M.**, Sousa, F., Queiroz, J.A., Correia, I.J., "Development of Chitosan Nanocapsules for Cancer Gene Therapy Applications", presented in XVIII International Conference on Bioencapsulation, October 1st and 2nd, 2011, Porto, Portugal.

II. **Gaspar, V.M.**, Correia, I.J., Sousa, A., Queiroz, J.A., Sousa, F., "Purification and Nanoparticle Mediated Delivery of P53 Supercoiled Plasmid DNA for Cancer Gene Therapy", presented in Affinity Congress, June 16th to 19th, 2011, Tavira, Portugal.

III. **Gaspar, V.M.**, Correia, I.J., Sousa, A., Silva, F., Paquete, C.M., Queiroz, J.A., Sousa, F., "Development of Chitosan Nanoparticles Loaded with Purified Supercoiled Plasmid DNA Biopharmaceuticals for Cancer Gene Therapy", presented in 3rd Congress of the Portuguese Society of Pharmaceutical Sciences / 9th Portuguese-Spanish Conference on Controlled Drug Delivery - New Trends in Pharmaceutical Sciences, October 13th to 15th, 2012, Porto, Portugal.

IV. Marques, J.G., **Gaspar, V.M.**, Costa, E.C., Paquete, C.M., Correia, I.J., "Development of Micelles as Carriers of Non-steroidal Anti-inflammatory Drugs (NSAID) for Application in Breast Cancer Therapy", presented in VIII Annual CICS Symposium, University of Beira Interior (UBI), July 1st and 2nd, 2012, Covilhã, Portugal.

V. Costa, E.C., **Gaspar, V.M.**, Marques, J.G., Coutinho, P., Correia, I.J., "Mimicking Breast Cancer Microenvironment with *In Vitro* Co-culture Models", presented in VI Symposium of Technology and Health, Polytechnic Institute of Guarda (IPG), May 3rd, 2013, Guarda, Portugal.

VI. Oppolzer, D., Marques, J.G., Diogo, D., **Gaspar, V.M.**, Gallardo, E., Correia, I.J., "Simultaneous Determination of Sildenafil and Crizotinib using HPLC-DAD", presented in 8th National Meeting of Chromatography, December 2nd, 2013, Covilhã, Portugal.

VII. Moreira, A.F., **Gaspar, V.M.**, Costa, E.C., de Melo-Diogo, D., Machado, P., Paquete, C.M., Correia, I.J., "Synthesis and Characterization of MCM-41 type Silica Nanoparticles by a Stöber Modified Method", presented in Bienal Meeting of the Portuguese Materials Society (SPM), May 4th, 2014, Covilhã, Portugal.

VIII. Costa, E.C., **Gaspar, V.M.**, de Melo-Diogo, D., Moreira, A.F., Marques, J.G., Coutinho, P., Correia, I.J., "Co-cultures for Nanoparticles Uptake Analysis", presented in IX Annual CICS Symposium, University of Beira Interior (UBI), June 30th and July 1st, 2014, Covilhã, Portugal.

IX. Marques, J.G., **Gaspar, V.M.**, Markl, D., Costa, E.C., de Melo-Diogo, D., Moreira, A.F., Gallardo, E., Correia, I.J., "Co-delivery of a Dual Drug Combination in Polymeric Nanovehicles for Improved Anticancer Therapy", presented in IX Annual CICS Symposium, University of Beira Interior (UBI), June 30th and July 1st, 2014, Covilhã, Portugal.

X. Costa, E.C., **Gaspar, V.M.**, de Melo-Diogo, D., Moreira, A.F., Marques, J.G., Coutinho, P., Correia, I.J., "Evaluation of nanoparticles uptake in breast cancer co-cultures", presented in Biannual Meeting of the Portuguese Materials Society (SPM), May 4th, 2014, Covilhã, Portugal.

XI. Moreira, A.F., **Gaspar, V.M.**, Costa, E.C., de Melo-Diogo, D., Machado, P., Paquete, C.M., Correia, I.J., "Synthesis and characterization of MCM-41 type silica nanoparticles by a Stöber modified method", presented in Biannual Meeting of the Portuguese Materials Society (SPM), May 4th, 2014, Covilhã, Portugal.

XII. Moreira, A.F., **Gaspar, V.M.**, Costa, E.C., de Melo-Diogo, D., Machado, P., Paquete, C.M., Correia, I.J., "Development of Mesoporous Silica Nanoparticles for Drug Delivery to Cancer Cells", presented in IX Annual CICS Symposium, University of Beira Interior (UBI), June 30th to July 1st, 2014, Covilhã, Portugal.

XIII. Costa, E.C., **Gaspar, V.M.**, de Melo-Diogo, D., Moreira, A.F., Marques, J.G., Coutinho, P., Correia, I.J., "Optimization of Liquid Overlay Technique (LOT) to produce 3D Breast and Cervical Co-Culture Models", presented in VIII National Symposium in Technology and Health, Polytechnic Institute of Guarda (IPG), April 17th, 2015, Guarda, Portugal.

XIV. Moreira, A.F., **Gaspar, V.M.**, Costa, E.C., de Melo-Diogo, D., Machado, P., Paquete, C.M., Correia, I.J., "Calcium carbonate coated nanoparticles for pH-responsive drug co-delivery to prostate cancer cells", presented in VIII National Symposium in Technology and Health, Polytechnic Institute of Guarda (IPG), April 17th, 2015, Guarda, Portugal.

XV. de Melo-Diogo, D., **Gaspar, V.M.**, Costa, E.C., Moreira, A.F., Oppolzer, D., Gallardo, E., Correia, I.J., "Triple-drug co-delivery by TPGS-PLA micelles for lung cancer therapy", presented in VIII National Symposium in Technology and Health, Polytechnic Institute of Guarda (IPG), April 17th, 2015, Guarda, Portugal.

Awards related to this Doctoral thesis

I. Oral presentation of the work entitled "Cell Internalizing and pH-responsive Nanoparticles for Improved Delivery of DNA Biopharmaceuticals", presented in IV Pharmacy Symposium. Awarded by Polytechnic Institute of Guarda (IPG), 2012, Guarda, Portugal.

II. Poster presentation of the work entitled "Cell internalizing and pH-responsive Chitosan Nanoparticles for Improved Delivery of DNA Biopharmaceuticals", presented in 13th Trends in Nanotechnology International Conference. Awarded by Phantoms Foundation, 2012, Madrid, Spain.

III. Oral presentation of the work entitled "Biofunctionalized Nanoparticles for Improved Delivery of Biopharmaceuticals", presented in VII Annual CICS Symposium. Awarded by CICS-UBI – Health Sciences Research Centre, University of Beira Interior (UBI), 2012, Covilhã, Portugal.

IV. Oral presentation of the work entitled "Characterization of Nanomedicines Uptake and Intracellular Trafficking in Cancer Cells", presented in VI Symposium on Technology and Health. Awarded by Polytechnic Institute of Guarda (IPG), 2013, Guarda, Portugal.

V. Lengthy talk of the work entitled "Screening of Novel Ligands to Purify Biosynthesized Minicircle DNA for Therapeutic Applications", presented in XI CICS Symposium. Awarded by CICS-UBI – Health Sciences Research Centre, University of Beira Interior (UBI), 2014, Covilhã, Portugal.

Resumo alargado

A prevalência de um grande número de doenças que atualmente afetam o bem-estar da população ou que são responsáveis por elevadas taxas de mortalidade, constitui um dos maiores desafios que a sociedade enfrenta na atualidade. Por forma a restituir a qualidade de vida aos pacientes e melhorar a saúde da população em geral, têm sido realizados vários esforços no sentido de acelerar o desenvolvimento de novas abordagens terapêuticas que possam ser aplicadas no tratamento de patologias particularmente complexas ou incuráveis, como é o caso do cancro. Atualmente, os tratamentos que são administrados a pacientes diagnosticados com neoplasias malignas apenas permitem obter uma pequena melhoria ao nível das taxas de sobrevivência e um curto incremento do tempo de vida sem ocorrer a reincidência do tumor. Por outro lado, é importante salientar, que mesmo estas pequenas melhorias acarretam efeitos secundários severos que agravam o estado de saúde dos pacientes durante o tratamento oncológico. Esta realidade reforça a necessidade urgente de explorar novas abordagens terapêuticas, que possam ser mais eficientes e menos tóxicas para o organismo.

Entre as várias terapias que presentemente se encontram em desenvolvimento para tratamento do cancro, a terapia génica baseada na administração de biofármacos constituídos por ácidos nucleicos, nomeadamente ADN não viral, tem revelado um grande potencial a nível terapêutico. De facto, contrariamente aos agentes anticancerígenos utilizados em meio clínico, os biofármacos de ADN podem conter simultaneamente informação genética que bloqueie a proliferação celular desregulada, ou que induza a morte das células cancerígenas sem que os tecidos saudáveis sejam afetados. Além destas caraterísticas únicas, os grandes desenvolvimentos observados nas últimas décadas na produção de biofármacos de ADN, e o facto de estes serem aprovados pelas agências reguladoras europeias e norte americanas (Agência Europeia do Medicamento (EMA) e a Administração de Alimentos e Medicamentos dos Estados Unidos da América (US-FDA), respetivamente), reforçam o potencial de aplicação clínica da tecnologia do ADN não viral. Neste contexto, o ADN plasmídico (pADN) permanece como o vetor mais utilizado para terapia génica. No entanto, apesar das potencialidades do pADN, a sua utilização a nível clínico encontra-se limitada pela sua baixa eficácia e rápida degradação *in vivo*. Tendo em conta estes problemas, novas abordagens têm sido desenvolvidas para incrementar a utilização do ADN não viral como um biofármaco eficaz. Os vetores de ADN minicircular (mcADN) são uma das alternativas que recentemente começou a ser explorada para terapia génica. Estes vetores são entidades episssomais geradas durante o crescimento bacteriano e que contêm apenas o transgene de interesse e o promotor necessário à sua transcrição do em células eucarióticas. Ao contrário do pADN, estas entidades não contêm a sequência de ácidos nucleicos necessária para amplificação bacteriana. A remoção desta informação genética supérflua origina, por sua vez, um aumento significativo da atividade biológica do mcADN. Na sua essência, a tecnologia do mcADN é baseada na recombinação

intramolecular de vetores plasmídicos especialmente desenhados para gerar mcADN e mini plasmídeos que contêm as sequências bacterianas indesejáveis. Posteriormente os vetores plasmídicos remanescentes (plasmídeos parentais e mini-plasmídeos) são parcialmente eliminados por ação de nucleases, durante o crescimento bacteriano. Este mecanismo complexo foi apenas recentemente descrito e muitos dos seus parâmetros permanecem ainda por investigar. A otimização deste bioprocesso assume assim um papel fulcral do ponto de vista da produção e aplicação terapêutica, uma vez que vários fatores podem afetar a quantidade e a pureza dos biofármacos produzidos.

Para além da necessidade de explorar de forma mais aprofundada a tecnologia do mcADN, é também importante melhorar o seu modo de administração, uma vez que este parâmetro permanece como um dos principais fatores que restringe a aplicação dos biofármacos de ADN em meio clínico. O desenvolvimento de novas formulações farmacêuticas que permitam explorar e inovar a administração do material genético exógeno, pode assim ter um tremendo impacto no tratamento do cancro ou de outras doenças.

Tendo em conta este contexto, este doutoramento teve como objetivo otimizar os parâmetros de biossíntese do mcADN, desenvolver e testar novos ligandos que permitam a sua purificação de acordo com as normas internacionais, e ainda produzir novos transportadores poliméricos que permitam efetuar a entrega destes vetores *in vitro* e *in vivo*. Como um ponto adicional a este estudo integrativo, foi também explorada a formulação de micro e nanoveículos com capacidade de responder a estímulos biológicos e que simultaneamente permitam a entrega de novas combinações de mcADN e fármacos anticancerígenos.

Inicialmente, procedeu-se ao estudo dos parâmetros associados ao processo de produção do mcADN, nomeadamente através da avaliação e manipulação da replicação dos plasmídeos parentais (PP) numa estirpe da bactéria *Escherichia coli* modificada geneticamente (ZYCY10P3S2T). Durante estes estudos, investigou-se se a manipulação da temperatura de crescimento das culturas bacterianas poderia ter um impacto positivo ao nível da quantidade de mcADN produzido em fases posteriores do processo, uma vez que, um maior número de espécies parentais estaria disponível para dar origem ao mcADN. Os resultados obtidos indicaram que um aumento da temperatura de crescimento de 37 °C para 42 °C originava uma maior quantidade de vetores PP por biomassa. Neste estudo, foi também efetuada uma monitorização da conversão de PP em mcADN e mini plasmídeos durante o crescimento bacteriano. Esta monitorização permitiu estabelecer pontos-chave, durante a fase de conversão de PP para mcADN, em que a produção e a pureza das preparações do mcADN era máxima. Estes resultados constituem um importante ponto de partida para a criação de um protocolo de produção que assegure máxima produtividade, pureza, e qualidade destes biofármacos.

Após a otimização dos parâmetros de produção do mcADN foi seguidamente estudada a utilização de di-péptidos de L-arginina para efetuar o isolamento e purificação do mcADN. Estes novos ligandos são particularmente interessantes para as aplicações acima descritas, pois mimetizam as interações bioespecíficas que ocorrem naturalmente entre os aminoácidos e o ADN *in vivo*. Como prova de conceito, amostras de PP e mcADN foram injetadas em chips microfluídicos contendo os di-péptidos de arginina imobilizados quimicamente. Durante estes ensaios, foi utilizada a técnica de ressonância de plasmões de superfície que permitiu analisar de forma mais exata as interações estabelecidas entre os analitos de ADN e os ligandos imobilizados. Os resultados obtidos, revelaram que a formação, ou a quebra das interações analito-ligando, depende da temperatura e do tipo de solução tampão que é colocada na superfície do chip, antes, e durante, a injeção das amostras de ADN. Este perfil de ligação-eluição sob condições específicas comprovou a potencial utilização destes ligandos para o isolamento ou purificação de biofármacos de mcADN.

Além dos estudos anteriores, foram também desenvolvidos novos nanotransportadores para efetuar a entrega de ADN exógeno às células alvo. Numa fase inicial, foi efetuada a modificação do quitosano através de ligações química com diferentes aminoácidos, nomeadamente a L-arginina e a L-histidina, com o intuito de melhorar as caraterísticas físico-químicas do biopolímero e a sua capacidade de entregar material genético a células cancerígenas. O quitosano foi funcionalizado através da utilização de carbodiimida/sucinimida para promover a conjugação química entre o C-terminal dos aminoácidos e as aminas ($-NH_2$) primárias da cadeia polimérica. O sucesso da funcionalização do polímero foi verificado por espectroscopia de ressonância magnética nuclear de protão (2D ^{1}H RMN) e por espectroscopia de infravermelho com transformada de Fourier (FTIR), que demonstraram a existência de um novo material biologicamente ativo, isto é, com carater responsivo ao pH e com carga positiva à sua superfície. Estas caraterísticas foram utilizadas para produzir nanopartículas através de interações electroestáticas que são naturalmente estabelecidas entre os vetores plasmídicos modelo e a cadeia polimérica catiónica. Estudos *in vitro* em que foram usadas células tumorais demonstraram que as nanopartículas biofuncionais contendo ADN plasmídico possuíam uma maior capacidade de internalização e também uma maior eficácia de transfeção, quando comparadas com nanopartículas apenas formadas por quitosano não modificado.

Com o objetivo de aumentar a seletividade destes nanotransportadores para as células alvo, num estudo subsequente, o quitosano-histidina-arginina foi modificado com cadeias de maleimida-poli(etileno glicol)-ácido fólico (MAL-PEG-FA) através da reação entre grupos tiol e o grupo maleimida do polímero MAL-PEG-FA. Esta abordagem, não só permitiu ligar eficazmente o polímero PEG, que confere uma maior estabilidade no ambiente biológico, mas também permitiu ligar quimicamente as pequenas moléculas de FA que são reconhecidas pelo recetor folato geralmente sobre-expresso na superfície das células tumorais.

A seletividade destes sistemas de entrega direcionada foi avaliada *in vitro* em modelos de co-culturas 2D formados por células tumorais que sobre-expressam o recetor folato e por fibroblastos da pele. A internalização das nanopartículas nas células cancerígenas foi estudada por microscopia confocal e citometria de fluxo, tendo os resultados revelado que os nanotransportadores são seletivamente internalizados nas células tumorais. Neste estudo, foi ainda avaliada a internalização destes nanossistemas em aglomerados tridimensionais de células cancerígenas (esferoides 3D). Os resultados obtidos demonstraram que as nanopartículas funcionalizadas com PEG-FA tinham a capacidade de penetrar nestes modelos de tumores sólidos e de promover a expressão de um gene modelo. Para completar estes estudos, as nanopartículas foram ainda utilizadas para efetuar a entrega de ADN plasmídico contendo o gene supressor de tumores p53 a esferoides de células tumorais. Após a entrega do material genético verificou-se que ocorreu uma diminuição do tamanho dos esferoides, o que permitiu verificar a utilização desta tecnologia para transferência de genes de forma seletiva às células tumorais.

Posteriormente, foi explorada a possibilidade de utilizar nanoveículos poliméricos para co-entrega de fármacos anticancerígenos e biofármacos de mcADN. Este estudo baseou-se no facto de que a entrega simultânea de múltiplas moléculas bioativas pode trazer benefícios em termos de eficiência terapêutica. Para concretizar este conceito de co-entrega, foram produzidos novos nanomateriais poliméricos, uma vez que as nanopartículas de quitosano necessitavam de modificações químicas complexas para terem capacidade de encapsular fármacos e condensar ácidos nucleicos simultaneamente. Para sintetizar os novos nanomateriais, foi utilizada a técnica de polimerização por abertura do anel do L-ácido lático para promover a formação de um copolímero de dois blocos composto pelo material hidrofílico poli(2-etil-2-oxazolina) e pelo material hidrofóbico poli(L-ácido lático) (PEOz-PLA). Após ter sido verificada a formação deste nanomaterial, o grupo hidroxilo deste copolímero foi ativado e conjugado quimicamente com polietilenimina linear (PEI) para formar um copolímero contendo três componentes (PEOz-PLA-g-PEI) e com caráter anfifílico e catiónico. Estes nanomateriais foram produzidos de uma forma orientada para a sua aplicação, tendo por base a necessidade de assegurar a biocompatibilidade, atividade biológica e também as caraterísticas físico-químicas para incorporar fármacos e genes num único nanotransportador. De forma a promover a formação de nanoveículos, os copolímeros foram dispersados em soluções aquosas e irradiados com ultrassons. Este procedimento originou a formação espontânea de nanomicelas com uma arquitetura núcleo-concha e com uma carga positiva na sua superfície. Por outro lado, como demonstrado pelos ensaios realizados por electroforese em gel de agarose, as micelas pré-formadas foram capazes de complexar, através de interações eletrostáticas, os vetores de mcADN carregados negativamente. A administração de micelas PEOz-PLA-g-PEI/mcADN em modelos *in vivo* de tumores da mama demonstrou que estes transportadores asseguram uma expressão eficaz do transgene incluído no mcADN. Adicionalmente, o conceito de co-entrega de fármacos anticancerígenos (Doxorubicina) e mcADN foi comprovado através da incorporação

simultânea destas moléculas bioativas nas micelas. Estudos efetuados através de microscopia confocal e de ensaios metabólicos não radioativos indicaram que os nanoveículos contendo fármacos e ácidos nucleicos possuem uma grande eficácia de internalização e desencadeiam a morte celular das células tumorais devido à ação do composto anticancerígeno.

Após ter sido demonstrado o potencial desta múltipla administração, foi investigada a possibilidade de produzir veículos para co-entrega que tivessem a capacidade de responder a estímulos biológicos. A produção destes transportadores responsivos a estímulos biológicos teve por base o conceito de que esta propriedade poderia melhorar o controlo da libertação das moléculas bioativas no local alvo e no tempo desejado. Para concretizar a produção destes nanomateriais "inteligentes", foram testadas duas abordagens diferentes com os nanoveículos produzidos anteriormente: (i) nanopartículas poliméricas compostas por quitosano modificado com aminoácidos e (ii) nanomicelas poliméricas compostas por PEOz-PLA-g-PEI.

Num primeiro estudo, foram produzidas pelo método de dupla emulsão agua-óleo-água (W/O/W) com difusão e evaporação do solvente, microesferas biodegradáveis compostas por poli(D,L-ácido láctico-co-glicólico)-álcool polivinílico-D-α-tocoferol-PEG sucinato. Nas microesferas foi incorporado bicarbonato de sódio ($NaHCO_3$), o fármaco doxorubicina e também nanopartículas de quitosano-histidina-arginina/mcADN para promover a co-entrega de moléculas bioativas. A incorporação do bicarbonato de sódio conferiu às microesferas um caráter responsivo ao pH visto que este composto origina a formação de dióxido de carbono (CO_2) em meio ácido, similar ao encontrado nos tumores sólidos *in vivo*. O gás formado originou, por sua vez, a destruição da parede das microesferas tal como se comprovou por microscopia eletrónica de varrimento. Esta destruição das micropartículas promoveu a libertação das nanopartículas de mcADN e também do agente anticancerígeno doxorubicina. Os resultados obtidos por microscopia confocal confirmaram não só a incorporação das nanopartículas dentro das microesferas, como também permitiram visualizar a internalização destes veículos nas células tumorais do colo do útero e ainda a expressão do gene contido no mcADN. Adicionalmente, os ensaios de citotoxicidade realizados em modelos *in vitro* de células cultivadas em 2D, revelaram que os micro-nanoveículos híbridos promovem mais morte celular quando comparados com a ação do fármaco livre ou das microesferas contendo apenas doxorubicina.

Num segundo estudo, o bloco catiónico do copolímero PEOz-PLA-g-PEI foi modificado quimicamente com ligações dissulfeto (S-S) para promover a libertação do mcADN de uma forma responsiva às condições de redução-oxidação (redox) das ligações S-S no espaço intracelular. Esta propriedade permite a libertação dos ácidos nucleicos tanto no citoplasma como no núcleo e promove uma libertação mais controlada do mcADN no interior da célula. Neste estudo foi também utilizada a tecnologia dos di-péptidos de L-arginina para isolar a isoforma superenrolada do mcADN.

De forma a promover o isolamento desta isoforma do mcADN por cromatografia de afinidade os di-péptidos foram imobilizados quimicamente em colunas monolíticas. O mcADN superenrolado recuperado foi depois condensado por interações eletrostáticas estabelecidas com o novo copolímero PEOz-PLA-g-PEI-SS. Esta interação originou a formação de nanomicelas bioresponsivas contendo os ácidos nucleicos minicirculares. A administração destes nanoveículos a esferoides 3D comprovou um aumento da expressão génica quando comparado com as nanomicelas não responsivas a estímulos redox. Adicionalmente, procedeu-se também à administração das nanomicelas PEOz-PLA-g-PEI-SS contendo doxorubicina e mcADN em modelos animais. Nestes ensaios verificou-se que estes sistemas promovem uma redução do volume dos tumores ao longo do tempo.

Em termos globais, a investigação efetuada durante este doutoramento permitiu identificar novos parâmetros e aperfeiçoar o processo de produção de mcADN. Posteriormente, foram também testados novos ligandos peptídicos que foram utilizados no isolamento da isoforma superenrolada do mcADN. Estes resultados são importantes num contexto laboratorial e também relevantes para a futura aplicação da tecnologia do mcADN à larga escala. Além destes avanços, a avaliação pré-clínica dos nanoveículos desenvolvidos ao longo deste doutoramento, demonstrou que a utilização de diferentes polímeros bioativos, juntamente com o caráter responsivo, tem um efeito positivo ao nível da performance biológica destes sistemas de entrega. Tendo em conta que nos estudos efetuados, os minicírculos expressaram genes modelo, pode antecipar-se que a inclusão de um, ou vários, genes anticancerígenos irá potenciar o impacto terapêutico destes vetores. Assim sendo, e em forma de análise final, de entre todos os nanotransportadores desenvolvidos, as micelas de PEOz-PLA-g-PEI-SS demonstraram uma maior eficácia na expressão génica quando comparados com os outros sistemas desenvolvidos para co-entrega. Além destes resultados promissores obtidos *in vitro*, a ação destes sistemas foi também validada *in vivo*, uma vez que foi comprovada a co-entrega eficaz de mcADN e de doxorubicina aos tumores implantados em modelos animais. Estes resultados revelam assim o enorme potencial das micelas de PEOz-PLA-g-PEI-SS para futura aplicação médica tanto ao nível do tratamento do cancro, como possivelmente de outras patologias que beneficiem da co-entrega de várias moléculas bioativas.

Palavras-chave

ADN minicircular, Biossíntese, Cancro, Terapia génica, Transportadores poliméricos.

Abstract

The prevalence of numerous diseases which are currently responsible for high mortality rates or that affect people well-being is one of the major challenges faced by nowadays society. To improve general health and population quality of life, tremendous efforts have been focused on speeding up the discovery of innovative pharmaceutics for treatment of particularly complex and incurable pathologies such as cancer. Currently, the generally applied anticancer treatments result only in a slight increase in patient survival rates and additional lifetime without disease recurrence. However, these improvements are often short-lived and are associated with severe systemic toxicity that debilitates patients health during treatment. This fact demonstrates the ineffectiveness and reduced safety of clinically administered therapies, and above all, emphasizes the urging necessity to discover more efficient approaches that can promote a better therapeutic outcome with fewer side-effects.

From the numerous anticancer treatments currently under development, those based on nonviral gene transfer with nucleic acid-based pharmaceuticals have a great therapeutic potential since they are currently approved for human use by United States Food and Drug Administration (US-FDA) and European Medidicines Agency (EMA) regulatory agencies, can be produced at industrial scale and are highly versatile. In fact, unlike standard cytotoxic drugs, the original structure of DNA biopharmaceuticals can be precisely engineered to encode multiple, tumor suppressor genes which may simultaneously affect cancer cells proliferation, or induce their destruction without direct damage to healthy tissues. In this context, plasmid DNA (pDNA) gene expression cassettes remain the gold standard biopharmaceuticals for gene therapy. However, despite being a promising tool, the widespread use of standard plasmid vectors is restricted by their short-term activity *in vivo*. Therefore, to realize the full potential of this therapeutic approach other alternatives for transgene expression in humans must be explored. In this context, a recently upgraded technology based on the use of minimalistic gene expression cassettes devoid of the bacterial backbone, so-termed DNA minicircles, has shown to provide the required biological efficiency. Due to the fact that this is a relatively new technology the parameters of mcDNA production in prokaryotic organisms have not yet been correctly explored. The optimization of this bioprocess assumes a critical importance from a manufacture and therapeutic point of view, since various factors may affect the productivity, final stability and purity of mcDNA preparations. A part from these necessary improvements, mcDNA gene transfer to diseased tissues also remains as one the most rate limiting steps in the translation of these therapies from bench-to-bedside, being necessary as well to improve the currently existing technologies for DNA transfer to eukaryotic cells.

Taking this background into account, the main hypothesis of this work was to explore and optimize mcDNA biosynthesis, to screen ligands for purification of these vectors and develop biocompatible polymeric nanocarriers for minicircle gene delivery to different *in vitro* and *in vivo* cancer models. As an additional remark to this integrative study, the synthesis of stimuli-responsive delivery systems for co-administration of mcDNA-drug combinations to cancer cells was also investigated.

Bioprocess optimization was initially performed by studying and manipulating the amplification of template parental plasmids (PP) in an *Escherichia coli* strain (ZYCY10P3S2T) genetically modified to produce mcDNA from plasmid templates with high efficiency. During these experiments it was hypothesized that the manipulation of bacterial growth temperature could provide important improvements in the quantity of mcDNA produced in later stages of the process. The obtained results indicated that an increase in bacterial growth temperature maximized the amount of template plasmids per biomass. In addition to this enhancement, a real-time monitoring of the PP–to-mcDNA intramolecular recombination process revealed that the time of mcDNA recovery significantly affects both the final yield and also the presence of residual PP and mini-plasmid (mP) species in minicircle preparations. These important findings demonstrate that maximum productivity and pharmaceutical-grade minicircle batches were obtained at specific time points during the induction phase.

Having established optimal bioprocess parameters, the use of novel L-arginine dipeptide ligands for mcDNA biopharmaceuticals isolation or purification was investigated. These dipeptide ligands are particularly interesting as they take advantage of biomimetic interactions that are naturally established between amino acids and DNA *in vivo*. As a proof-of-concept, mcDNA vectors and PP template plasmids were injected into microfluidic chips containing chemically immobilized dipeptides. The sensitive screening obtained by surface plasmon resonance indicated that by manipulating temperature conditions and buffer type, different ligand-analyte interactions could be established. This dynamic binding-elution profile of mcDNA and PP species, under specific conditions, indicated these peptides could possibly be employed in the development of a platform for biopharmaceuticals isolation or purification.

Alongside with these studies, the development of biocompatible nanosized gene delivery systems based on amino acid modified chitosan was explored. For this purpose L-histidine and L-arginine amino acids were selected for chitosan backbone functionalization through a two-step chemical modification. In this study it was proposed that amino acid biocompatible moieties could improve the polymer physicochemical structure and its capacity to condense and deliver genetic material to cancer cells. The chemical modification of chitosan with both amino acid moieties through zero-length crosslinkers was successful and resulted in the development of a novel biofunctionalized material with pH-responsive character and positive charge. These characteristics allowed the formulation of DNA-nanocarriers through attractive electrostatic interactions with model pDNA vectors, under mild conditions. These nanoparticles

achieved an improved cellular uptake and higher transgene expression efficiency in cancer cells when compared to their non-modified counterparts. As a further attempt to improve the selectivity of these delivery systems towards target cancer cells, in a subsequent study, the hybrid polymer was chemically grafted with poly(ethylene glycol)-folic acid blocks via Michael type thiol-maleimide coupling. This chemical grafting promoted a selective inclusion of folic acid cell targeting moieties into amino acid modified chitosan. The targeting specificity of the formulated DNA-loaded multifunctional carriers was confirmed in *in vitro* 2D co-culture models comprised by folic acid positive cancer cells and normal human fibroblasts. In addition, the results obtained in 3D multicellular spheroids indicated that the targeted particles penetrated into these *in vitro* models of solid tumors and accomplished significant transgene expression. A time-course, high-throughput analysis, performed after nanocarriers containing the p53 tumor suppressor DNA were administered, revealed a reduction in spheroids volume along time, thereby supporting the possible use of this technology for cell-selective gene transfer.

From this standpoint, it was hypothesized that polymeric delivery systems could also be used for simultaneous co-delivery of chemotherapeutic drugs and DNA biopharmaceuticals. It was anticipated that such combinatorial approach could provide a superior anticancer effect and contribute for the development of more efficient treatments. To materialize this challenging concept, beyond-state-of-the-art triblock copolymers were chemically synthesized since biofunctional chitosan nanocarriers required complex chemical modifications to co-encapsulate mcDNA and drugs. The new synthetic nanomaterials for co-delivery were produced in an application-oriented, safe-by-design, approach that took into account the necessity to assure materials biocompatibility, biological performance and also the physicochemical properties required for simultaneous encapsulation of drug and genes in a single nanocarrier. The obtained results demonstrate that the triblock copolymers self-assembled into nanosized biocompatible micelles with core-shell structure in aqueous environment and condensed mcDNA vectors with high efficacy. *In vivo* administration of mcDNA-loaded micelleplexes to solid tumors also originated significant transgene expression, which shows the therapeutic potential of this delivery system. The co-delivery concept was also demonstrated with the simultaneous encapsulation of an anticancer drug (Doxorubicin), and mcDNA, in the micellar carriers. As revealed by confocal microscopy and metabolic assays, the dual-loaded micelleplexes presented significant cellular uptake and cytotoxic activity in cancer cells when compared to free drug.

After demonstrating the potential associated with drug-gene co-delivery, the formulation of stimuli-sensitive co-delivery systems was investigated. The production of carriers with dynamic response to precise biological cues was expected to provide a new level of therapeutic efficiency since the release of bioactive molecules could be controlled in a spatiotemporal mode. To explore the manufacture of such “smart” nanomaterials two different approaches based on the formerly developed nanocarriers were explored.

In a first study, mcDNA-loaded biofunctionalized chitosan nanocarriers were encapsulated in gas-generating poly(D,L-lactic-co-glycolic acid) (PLGA) biodegradable microspheres, previously loaded with an antitumoral drug and sodium bicarbonate. The assembled nanoparticle-in-microsphere hybrid systems were capable of generating carbon dioxide (CO_2) bubbles in acidic environment due to bicarbonate presence. In turn, this gas production originated a rapid disassemble of microspheres shell, and consequent contents release. *In vitro*, the dual-loaded hybrid carrier demonstrated a higher cytotoxicity in cancer cells when compared to that of free drugs or single drug-loaded microspheres. In addition to this platform, in a second study the cationic block of the triblock copolymers was modified with disulfide linkages to allow a redox-responsive release of mcDNA vectors in intracellular compartments poly(2-ethyl-2-oxazoline)-poly(L-lactic acid)-g-polyethylenimine-disulfide (PEOz-PLA-g-PEI-SS). In this study an affinity chromatography monolith disk immobilized with previously investigated L-arginine dipeptide ligands was used to isolate mcDNA supercoiled isoform. The evaluation of bioreducible micelles in 3D *in vitro* models and orthotopic *in vivo* tumors indicated that this system has improved transgene expression efficacy and promotes tumor regression when it is used for co-delivery of Doxorubicin and mcDNA.

Overall, the research performed throughout this Doctoral thesis described improvements in mcDNA production process and led to the discovery of potential ligands for the isolation of its supercoiled isoform. The original results obtained during this work provide an important body of knowledge in the applicability of the mcDNA technology at a larger scale. Furthermore, the pre-clinical evaluation performed on newly developed nanomedicines demonstrated that grafting multifunctional moieties, or imprinting a stimuli-sensitive character to nanocarriers has a positive effect on their biological performance. It is important to mention that the future inclusion of one or more tumor suppressor genes in mcDNA vectors may contribute to potentiate their therapeutic effect. In this context, and as a concluding remark, the particularly promising results obtained with the administration of PEOz-PLA-g-PEI-SS dual-loaded and stimuli-sensitive micelles demonstrated that these systems enclose an outstanding potential for medical applications in a foreseeable future.

Keywords

Biosynthesis, Cancer, Gene therapy, Minicircle DNA, Polymeric carriers.

Thesis Overview

This Doctoral thesis is organized in 4 main sections containing a total of 12 chapters. The first section discloses the general and specific aims established for the development of this thesis and provides a comprehensive literature review related to mcDNA technology, as well as to the use of multifunctional micro and nanocarriers for delivery of bioactive molecules. This section is based on a published review article and a book chapter accepted for publication. The second and third sections present the results obtained during this Doctoral work, being comprised by a total of 7 original research articles published in international peer reviewed journals. The fourth section outlines the concluding remarks of this Doctoral thesis, as well as the future perspectives regarding the applicability of the technologies developed throughout this work. In detail the different sections are organized as follows:

Section I – Introduction

Chapter 1 describes in detail the general and specific aims established for this Doctoral thesis.

Chapter 2 contextualizes the key concept underlying mcDNA gene expression vectors and the different methodologies for minicircles biosynthesis in recombinant bacteria. Alongside, different regulatory demands for human administration and the use of mcDNA in cancer gene therapy applications are highlighted.

Chapter 3 reviews the various classes of technologies employed in mcDNA gene transfer to eukaryotic cells, their intrinsic advantages and limitations. In addition, the major extracellular and intracellular barriers to nonviral gene delivery are also focused, since these remain as one of the major limitations towards clinical application.

Chapter 4 comprises a concise overview of multifunctional nanocarriers characteristics and state-of-the-art nanomaterials used for formulation of nanosized systems for co-delivery.

Section II – Minicircle biosynthesis and evaluation of peptide ligands

Chapter 5 and 6 presents the studies and results obtained for mcDNA biosynthesis optimization and for the evaluation of novel peptide ligands for these nucleic acids recognition. In this section the articles published in peer reviewed international journals are organized in the following order:

Chapter 5 – Improved Minicircle DNA Biosynthesis for Gene Therapy Applications.

Chapter 6 – Sensitive Detection of Peptide - Minicircle DNA Interactions by Surface Plasmon Resonance.

Section III – Formulation of multifunctional delivery systems

Chapter 7 to 11 consists of the studies and results obtained for the formulation of different polymeric carriers for delivery of bioactive molecules. In this section the articles published in peer reviewed international journals are organized in the following order:

Chapter 7 - Biofunctionalized Nanoparticles with pH-responsive and Cell Penetrating Blocks for Gene Delivery.

Chapter 8 - Folate-Targeted Multifunctional Amino Acid-Chitosan Nanoparticles for Improved Cancer Therapy.

Chapter 9 - Poly(2-ethyl-2-oxazoline)-PLA-g-PEI Amphiphilic Triblock Micelles for Co-delivery of Minicircle DNA and Chemotherapeutics.

Chapter 10 - Gas-generating TPGS-PLGA Microspheres Loaded with Nanoparticles (NIMPS) for Co-delivery of Minicircle DNA and Antitumoral Drugs.

Chapter 11 - Bioreducible Poly(2-ethyl-2-oxazoline)-PLA-PEI-SS Triblock Copolymer Micelles for Co-delivery of DNA and Doxorubicin.

Section IV – General Conclusions and Future Perspectives

Chapter 12 summarizes the main conclusions of the Doctoral thesis and also encloses a key discussion on the translational challenges associated with DNA minicircles and the synthesized polymeric delivery systems for single and co-delivery. Future perspectives on key topics that may be further explored in the foreseeable future are also highlighted.

Index

Chapter 9

Chapter 10

Chapter 11

Section IV

Chapter 12

List of Figures

List of Tables

List of Acronyms

AFM	Atomic Force Microscopy
ALK	Anaplastic Lymphoma Kinase
ALL	Acute Lymphoblastic Leukemia
AMPs	Advanced Medicinal Products
Antibodies	Antibodies
APCs	Antigen Presenting Cells
ASCL1	Achaete-Scute Complex-Like 1 Protein
ATRA	All-Trans-Retinoic Acid
bac-ORI	Bacterial Origin of Replication
BCA	Bicinchoninic Acid Assay
Bcl-2	B-cell lymphoma-2
bPEI	Branched Polyethylenimine
CD44	Cluster of Differentiation 44
CD47	Cluster of Differentiation 47
CdSe QDs	Cadmium-Selenide Quantum Dots
cGMP	Current Good Manufacturing Practices
CMC	Chemistry, Manufacturing, and Control
CMV	Cytomegalovirus
CO_2	Carbon Dioxide
COOH	Carboxyl
CpG ODN	Cytosine-Phosphodiester-Guanine Oligodeoxynucleotide
CPPs	Cell penetrating peptides
Cre	Causes Recombination
cRGD	Cyclic RGD
CsCl	Cesium chloride
CTCs	Circulating Tumor Cells
DCChol	3ß-[N-(N',N'-dimethylaminoethane)-carbamoyl]cholesterol
DDAB	Dimethyldioctadecyl-ammonium Bromide
DNA	Deoxyribonucleic Acid
DNAse	Deoxyribonuclease
Dox	Doxorubicin
DPPC	1,2-dipalmitoyl-sn-glycero-3-phosphocholine
DSPE–mPEG2000	1,2-distearoyl-sn-glycero-3-phosphoethanolamine-N-methoxy poly(ethylene glycol)
E. coli	*Escherichia coli*
EBV	Epstein- Barr Virus
EMA	European Medidicines Agency
EPR	Enhanced Permeability and Retention Effect
Er/YAG	Erbium-doped Yttrium Aluminum Garnet
fAbs	Antibody Fragments
gDNA	Genomic DNA
GLP	Good Laboratory Practice
GO	Graphene Oxide
GOI	Gene of Interest
HA	Hyaluronic acid

h-AAT	Human α-1 antitrypsin
HGT	Horizontal Gene Transfer
HIF1-α	Hypoxia-inducible factor 1-alpha
HMSNs	Hollow Mesoporous Silica Nanoparticles
HPLC	High-Performance Liquid Chromatography
HPLC-ESI	HPLC coupled to Electrospray Ionization Mass Spectrometry
HQG	High-Quality Grade
IFN-γ	Interferon-gamma
INDs	Investigational New Drug Applications
Int	Integrase
iPSCs	Induced Pluripotent Stem Cells
iRGD	Cysteine - Arginine - Glycine – Aspartic Acid - Lysine - Glycine - Proline – Aspartic Acid – Cysteine (CRGDKGPDC)
Kbp	Kilo Base Pairs
LAL	Limulus Amebocyte Lysate
LCST	Lower Critical Solution Temperature
LPNs	Lipid-polymer Hybrid Nanocarriers
MAL-PEG-FA	Maleimide-Poly(ethylene glycol)-Folic Acid
mcDNA	Minicircle DNA
MCF-7/ADR	Doxorubicin-resistant Breast Cancer Cells
MDR	Multi Drug Resistance
miRNA	Micro RNA
MMP-9	Matrix Metalloproteinase-9
mP	Mini-plasmids
mPEG	Methoxy Poly (ethylene glycol)
MRI	Magnetic Resonance Imaging
mRNA	Messenger RNA
MSNs	Mesoporous Silica Nanoparticles
mTERT	Mouse Telomerase Reverse Transcriptase
MTG	Methyl Thioglycolate
MVP	Major Vault Protein
MW	Molecular Weight
$NaHCO_3$	Sodium Bicarbonate
NGR	Cysteine - Asparagine - Glycine - Arginine - Cysteine - Glycine (CNGRCG)
NH_2	Amine
NIR	Near Infra-red
NLS	Nuclear Localization Sequence
OH	Hydroxyl
oriP-CMV	Epstein-Barr Gene Promoter Linked to Cytomegalovirus
ORT	Operator-repressor Titration
PAMAM	Poly amidoamine
PBLA	Poly(ß-benzyl L-aspartate)
PCL	Poly (ε-caprolactone)
PDMAEMA	Poly(2-(dimethylamino)ethyl methacrylate)
pDNA	Plasmid Deoxyribonucleic Acid
PEG	Poly(ethylene glycol)
PEG-PLL-PLLeu	Poly(ethylene glycol)-b-Poly(L-lysine)-b-Poly(L-leucine)
PEI	Polyethylenimine
PEI-PEG	Polyethylenimine-Poly(ethylene glycol)

PEOz	Poly(2-ethyl-2-oxazoline)
PEOz-PLA	Poly(2-ethyl-2-oxazoline)-Poly(L-lactic acid)
PEOz-PLA-g-PEI-SS	Poly(2-ethyl-2-oxazoline)-Poly(L-lactic acid)-g-Polyethylenimine-Disulfide
P-gp	P-glycoprotein
PHEMA	Poly(2-hydroxyethyl methacrylate)
pHPMA	Poly(N-(2-hydroxypropyl) methacrylamide)
PLA	Poly(L-lactic acid)
PLGA	Poly(D,L-lactic-co-glycolic acid)
Plk1	Polo-like Kinase 1
PLL	Poly(L-lysine)
polyA	Polyadenylation
PP	Parental Plasmids
PPEEA	PEG-PCL-poly(2-aminoethylethylene phosphate)
PSS	Poly(sodium 4-styrenesulfonates)
PTT	Photothermal Therapy
qRT-PCR	Quantitative Real-Time Polymerase Chain Reaction
RBPS	Recombination-Based Plasmid Separation
RES	Reticuloendothelial System
RGD	Arginine-Glycine-Aspartate
RGD4C	Lysine-Alanine-Cysteine-Aspartic Acid-Cysteine-Arginine-Glycine-Aspartic Acid-Cysteine-Phenylalanine-Cysteine-Glycine (KACDCRGDCFCG)
shRNA	Short Hairpin Ribonucleic Acid
siRNA	Small Interfering RNA
STAB1	Special AT-rich Sequence Binding Protein 1
TAT	Glycine – Arginine – Lysine – Lysine – Arginine – Arginine - Glutamine-Arginine – Arginine – Arginine – Proline – Glutamine (GRKKRRQRRRPQ)
tBMA	Ter-butyl methacrylate
TGA	Thioglycolic Acid
T-MEND	Tetra-lamellar Multi-functional Envelope-type Nano Device
TRAIL	TNF-related apoptosis-inducing ligand
US	United States
US-FDA	United States Food and Drug Administration
WHO	World Health Organization
φC31-*int*	φC31 Integrase

Section I

Global Aims and Introduction

CHAPTER 1

1. Global Aims

Minicircle technology encloses a remarkable potential for therapeutic applications in humans due to its recognized safety and prolonged activity. Taking advantage of this potential and using it in combination with nanodevices capable of DNA delivery may provide the possibility to develop mcDNA-based treatments for diseases that are currently considered incurable, such as cancer.

In this context, the global aim of this Doctoral work comprises the biosynthesis, purification and delivery of mcDNA vectors either as stand-alone biopharmaceuticals, or in combination with small anticancer drugs. The information gathered from this integrative study is envisioned to positively impact the various stages of biopharmaceuticals manufacture, recovery, and nanocarriers-mediated administration to human cells. In the present thesis a particular emphasis is given to the development of polymeric gene delivery systems in an attempt to bridge the gap that limits effective DNA administration via nanovehicles. Alongside, the production of nanomaterials for co-delivery of mcDNA and small drugs was explored with the aim to take advantage of the therapeutic potential enclosed by combinatorial cancer therapies. According to these main aims, this Doctoral work was developed by following a systematic approach that involved different studies with well-defined objectives:

I. Characterize and explore minicircles generation in recombinant bacteria that enclose the φC31/I-SceI conversion system

Specific aim: Investigate the effect of growth conditions in the amplification of template parental vectors in ZYCY10P3S2T genetically modified bacteria and study the parental-to-minicircle dynamic recombination process in order to establish an optimal recovery stage.

II. Study the potential of dipeptide ligands for binding and recovery of mcDNA biopharmaceuticals

Specific aim: Test innovative dipeptide ligands comprised by arginine, histidine, or their combinations thereof, and quantify ligand-analyte binding affinity through highly sensitive surface plasmon resonance analysis under specific binding-elution conditions (e.g., temperature, pH and ionic strength).

III. Evaluate the potential for chitosan amino acid conjugates to be used for DNA delivery to cancer cells

Specific aim: Assess the influence of chitosan amino acid biofunctionalization in the physicochemical properties, biocompatibility, and biological performance under conditions that reproduce the biological environment. Also, determine the required chemical modifications to molecularly graft cell targeting moieties in biofunctionalized chitosan and evaluate the differences in selectivity towards cancer cells.

IV. Produce nanosized micellar carriers with suitable characteristics for co-delivery

Specific aim: Synthesize biocompatible, amphiphilic triblock copolymers with suitable physicochemical characteristics to allow the co-loading of drug-gene combinations. Also, characterize the physicochemical properties of the resulting carriers, the simultaneous administration of these bioactive molecules to cancer cells and the overall biological performance.

V. Synthesize multifunctional carriers with stimuli-responsive properties and capacity for co-delivery of drug-gene combinations

Specific aim: Test different approaches for production of nanocarriers with redox-responsive properties, or microcarriers with pH responsive character and with specific design for drug-gene co-delivery to cancer cells. In addition, investigate the responsiveness of the systems to biological stimuli, their biocompatibility and gene transfer/cytotoxic efficacy.

CHAPTER 2

This chapter is based on the publication entitled: Minicircle DNA vectors for Gene Therapy: Advances and Applications, *Human Gene Therapy Methods*, 2014, 25 (2):93-105.

2. Minicircle DNA technology for nonviral gene therapy

2.1. Gene therapy concept

The concept of using nonviral nucleic acid-based biopharmaceuticals as advanced medicinal products (AMPs) is attracting an ever-growing interest due to their unmatched safety and extraordinary potential to create breakthrough treatments for incurable diseases with worldwide prevalence [1]. An applicability that is further highlighted by the significant body of evidence continuously emerging from various scientific reports and ongoing clinical trials, documenting the relevance of using genes, based on double-stranded DNA or RNA (e.g., small interfering RNA (siRNA), short hairpin RNA (shRNA) and messenger RNA (mRNA)), as active AMPs to ultimately accomplish a therapeutic effect [2]. This enabling technology provides the foundation for developing numerous treatment strategies spanning from the manufacture of advanced DNA vaccines, to the generation of induced pluripotent stem cells (iPSCs), or to the expression of therapeutic transgenes, a modality of biological treatment, termed gene therapy [3].

Gene therapy is a particularly interesting methodology that takes advantage on the administration of exogenous nucleic acids to pathological cells as a tool to correct the function of a defective gene or manipulate cellular gene expression patterns to restore homeostasis [2]. In this context, the use of DNA biopharmaceuticals is very attractive for gene therapy because the therapeutic transgenes of interest are generated by the cell transcriptional machinery [4]. Moreover, as recently demonstrated by Kang and Bae, the versatility of DNA vectors allows them to be used for example in shRNA production [5]. In this strategy, the shRNA intracellular levels are also under tight control of the host cells metabolism [5]. This is a critical parameter, since an over-dose of anti-sense oligonucleotides has shown to induce severe hepatotoxicity following silencing of human α-1 antitrypsin (h-AAT) liver enzyme in transgenic mice [6]. Currently, different classes of vectors are available for promoting therapeutic transgene delivery and expression in eukaryotic cells including virus, plasmids, cosmids and artificial chromosomes [7]. Among these, bacterial plasmid DNA (pDNA) remains a promising biomolecule for gene transfer, with several studies and clinical trials currently in progress worldwide [8]. This choice is commonly supported by the relative safety of pDNA in comparison with viral-based vectors, because there is a nearly zero risk of genetic material integration into the host genome [3]. To be produced in recombinant bacteria and also express their therapeutic gene of interest (GOI), the pDNA backbone includes a bacterial origin of replication (bac-ORI), an antibiotic resistance gene (e.g., Kanamycin) to avoid the propagation of plasmid-free bacteria, and finally a transcription unit containing an eukaryotic promoter, the GOI and a polyadenylation (polyA) sequence to increase GOI expression and nuclease resistance (Figure 1 B) [3]. In the cell nucleus, pDNA is typically maintained as an episomal entity that is physically detached and independently replicated from host chromosomal DNA [9]. Even with this exceptional benefit, the translation of standard pDNA biopharmaceuticals from bench-to-

bedside remains highly compromised by their relatively low expression levels and transient character [3, 10].

In this context, in recent times, different strategies are trying to overcome these issues by unraveling the potential of a generation of small plasmid cassettes, so-termed minicircle DNA (mcDNA) [10, 11]. Minicircles are classified as nonviral, episomal, covalently closed circular gene expression vectors, generally biosynthesized in recombinant bacteria that consist in minimalistic backbones with potential to meet the clinical requirements for safe and long-lasting gene expression (Figure 1 A) [12]. From an historical perspective, these constructs were initially reported by Cameron and Schleef, in a patent filled in 1995, and that remains currently active [13]. In this invention, minicircles are originally defined as an enabling technology for gene transfer into mammalian cells and are claimed to be comprised by an unique array of characteristics that include: (i) an inherent supercoiled topological isoform; (ii) the lack of any bac-ORI; (iii) the absence of any sequence coding for antibiotic resistance; (iv) the existence of a therapeutic transgene whose expression is controlled by a mammalian promoter; and (v) the existence of a specific sequence attributed to the site of recombination where the precursor parental plasmid (PP) yields the minicircle (Figure 1 B) [13].

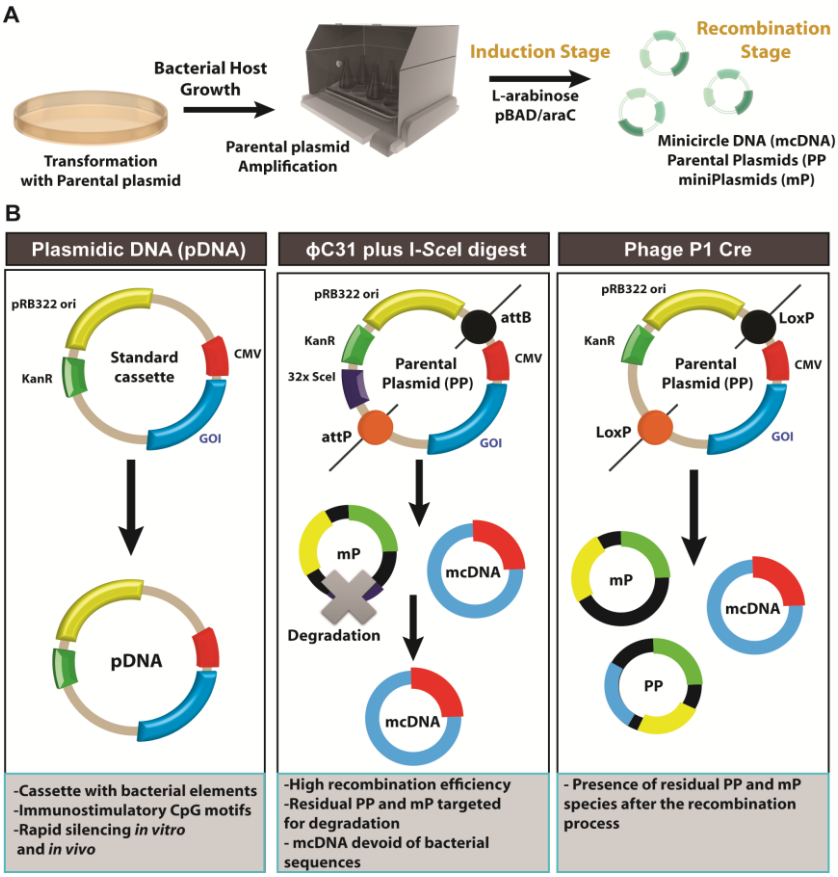

Figure 1. Schematics of the bioprocess for generation of mcDNA vectors. A.) Overview of mcDNA production process from recombinant bacterial hosts. B.) Summary of different technologies for mcDNA generation. The λ-*Int* and *ParA* resolvase systems are not represented since they have *attP*/*attB* hybrid sites, similarly to the φC31/I-SceI technology.

Recently, this technology has been remarkably upgraded with the developments reported by Kay and co-workers who concentrate mostly on the use of a genetically modified recombinant *Escherichia coli* (*E. coli*) strain which generates mcDNA vectors by *in vivo* site-specific recombination. This strategy allows the removal of surplus PP species and mini-plasmids (mP) that result from the recombination process [11]. Considering that both template and mP vectors enclose the bac-ORI sequence and antibiotic resistance markers, their subsequent elimination by homing endonucleases during bacterial amplification is a valuable improvement in comparison with other technologies [11]. The removal of all the sequences required for vector propagation in bacteria, including the bac-ORI and antibiotic resistance genes, is in fact the rationale underlying the initial development of mcDNA cassettes [14]. There are several reasons for removing the prokaryotic resistance marker genes from nonviral vectors, the most important being their possible integration into host cells genome and their potential for horizontal gene transfer (HGT) to human microbiota [15, 16]. HGT assumes further significance in light of reports that emphasize the role of host-microbe interactions in the onset of several diseases such as inflammatory bowel disease or multiple sclerosis [17]. It is important to emphasize that not only minicircles achieve enhanced gene transfer efficiency with the elimination of undesired antibiotic resistance sequences. Other vectors, for example the plasmid based on Operator-repressor titration (ORT) technology, or the mini-intronic plasmid enclosing RNA/OUT antisense RNA technology for bacterial selection, have similarly taken benefit of antibiotic free backbone [15]. The exclusion of bac-ORI sequences from minicircles really sets this technology apart from the previously cited vectors, and also contributes for their gene transfer efficiency. Such is evidenced by the positive influence of bac-ORI elimination in the levels and duration of mcDNA biopharmaceuticals expression *in vivo*, as observed by Chen and co-workers [18]. Furthermore, the elimination of these unnecessary sequences also reduces the overall mcDNA backbone size.

Vector size has shown to be directly associated with the levels and extent of transgene expression in mammalian cells [19, 20]. Up to now, it has been reported that a larger construct size is detrimental for nucleic acid transfer efficiency, with a substantial decrease in expression being observed at approximately 6 kilo base pairs (kbp) [15]. This reduced efficiency as a function of size is mainly attributed to the limited free diffusion of bigger vectors through the cell cytoplasm [21]. Regarding this parameter, the administration of a minimalistic 2.9 kbp minicircle in quiescent cells originated a 77-fold increase in gene expression, when compared to that of a plasmid vector with more than 52 kbp in size [15]. From the present standpoint, it is clearly noticeable that mcDNA technology is an efficient tool to develop innovative nucleic-acid-based medicines. However, it also becomes evident that an optimal conversion from template PP into mcDNA biopharmaceuticals is critical to obtain pure preparations, and that further modifications to vector structure, or its delivery through specialized nanocarriers must be addressed in order to fulfill the motivation of using mcDNA in clinical applications [1].

Recent strategies to improve clinical-grade mcDNA production, and to increase transgene expression efficiency are detailed in the following section of this thesis.

2.2. McDNA biosynthesis in recombinant organisms

The widespread use of clinical-grade mcDNA biopharmaceuticals is remarkably challenging from a manufacturing point of view since the conversion of template PPs into mcDNA is a relatively complex process. This PP-mcDNA conversion initially involves an external induction of bacteria to activate the expression of genes coding for the recombination machinery (induction stage). This process is followed by the precise action of site-specific recombinases that start minicircle biosynthesis (recombination stage) (Figure 1) [11]. Interestingly, this multistep procedure occurs during the course of continuous bacterial amplification [1]. Throughout this dynamic production process, different species are generated: (i) the mcDNA of interest, as well as residual plasmids containing bacterial elements like (ii) PP precursors, and (iii) mP species [11]. These species are all present at a given time point after the induction phase, regardless of the methodology used for mcDNA production [22]. The presence of residual PP and mP vectors is highly disadvantageous as these vectors are contaminants of the final mcDNA preparation and need to be removed before administration to the host due to biosafety concerns [11]. Prior to the induction stage, mcDNA precursor plasmids are generally amplified in gram-negative *E. coli* bacteria during fermentation [23, 24]), because this recombinant organism presents unique characteristics including relatively fast growth kinetics, high population density and a high ratio of growth/nutrient consumption [25]. Recombinant technology based on prokaryotic bacteria is economically attractive due to its relative low cost and the significant number of pDNA vector copies produced in a single batch [25]. However, the so-termed metabolic burden that naturally occurs during *E. coli* amplification influences both the maintenance of plasmid replication in culture, as well as its structural stability [8]. Then, this is a critical parameter that has a negative effect in vector yield and consequently on the amount of PP template available for mcDNA generation [1]. Optimizing this bioprocess is therefore a requirement for the production of mcDNA at an industrial scale, and some reports have recently started addressing this issue [1, 25]. Following PP amplification, the induction stage is stimulated by the addition of an inductor (e.g., L-arabinose) that promotes the expression of the cellular machinery responsible for the conversion of PP templates to mcDNA [11, 26, 27]. This is a critical bioprocess parameter since the minicircle production system has shown to be exceptionally influenced by the concentration of L-arabinose and the time-point upon which bacterial cultures are induced [1, 11, 22]. Actually, a significant decrease in mcDNA yield has been reported when the induction stage was started at the middle of the exponential bacterial growth phase, contrariwise to the higher yield obtained once induction was performed at the end of this period [1]. At the onset of induction, all the elements necessary for conversion of PP precursors into minicircles are being actively expressed and immediately start to generate the biopharmaceuticals of interest recombination stage. Site-specific recombination is particularly a well-established methodology [28, 29]), and constitutes the underlying principle for mcDNA generation from its parental

templates [11]. This method enables the excision, integration or exchange of exact DNA segments (30 to 40 bp, or longer), which are specific hybrid anchoring sites (e.g., *attB and attP*) for site-specific recombinases, bacteriophage enzymes that mediate the exchange reaction in these substrates [29]. Once recombinases recognize and bind to the hybrid sites in PP templates, strand exchange/re-assemble is promoted, with both mcDNA and mP vectors being generated. Each of the resulting vectors contains two new hybrid sites (e.g., *attR* and *attL*), respectively [1]. Interestingly, this genetic engineering tool is exceptionally precise and conservative. Such is evidenced by the fact that in the course of DNA strands excision/re-assemble, the resulting mcDNA and mP share the nucleotides of their PP precursors. In addition, all mcDNA sequences of interest (GOI, eukaryotic promoter and polyA) are preserved throughout the entire conversion process [1, 28]. These valuable features contribute for the robustness of PP to mcDNA recombination and most importantly, influence the final yield of minicircle biopharmaceuticals. The integrases that mediate site-specific recombination can be classified in two major families: (i) serine and (ii) tyrosine recombinases due to their different recombination properties [28] and both have been equally used for the production of DNA minicircles from precursor plasmids. In the following sections, a focus will be given to the most relevant phage integrases employed so far for minicircle generation.

2.2.1. Phage I integrase

Phage I integrase (*Int*) is a tyrosine recombinase that catalyzes conservative recombination [30]. *Int* intrinsic function is to execute integration of the lambda (λ) phage genome into its target host [29]. On the other hand, to exert its activity phage λ-*Int* requires accessory, host-encoded proteins, to bind to its *att* hybrid sites, a rather limiting parameter that increases bioprocess variability [29, 30]. The λ-*Int* system is not only a useful genetic engineering tool for chromosomal integration of transgenes particularly in *E. coli* but also finds application in synthetic biology, as evidenced by the broadly used Gateway™ cloning technology (Life Technologies Ltd, California) [31]. Although the application of the *Int* system in the manipulation of human cells genome has encountered several obstacles, recently a mutated λ-*Int* derivative has shown potential for a sophisticated application in the engineering of mammalian artificial chromosomes for modification of multipotent stem cells [29, 32].

Concerning mcDNA production, the λ-*Int* system was the first method used to generate these biopharmaceuticals. It was disclosed in a patent with priority date of February 1995, filled by Cameron and Schleef (EP 0815214; United States (US) Patents 6 143 530, and 6 492 164) [33]. Later, Darquet and co-workers employed λ-*Int* to produce mcDNA encoding the luciferase (Luc) reporter gene. In this study, λ-*Int* recombinase was expressed endogenously by the *E. coli* strain, with the template plasmid cassette bearing the hybrid *attP*/*attB* inserts flanking the mammalian expression unit [29]. However, the intrinsic toxicity of the λ-*Int* system in bacterial host originated low yields of PP-mcDNA recombination (from 40 to 70 %). Consequently, a significant amount of unconverted PP templates contaminated the final preparation [14, 29].

Recently, advances in λ-*Int* mediated mcDNA production have been described by Zechiedrich and co-workers in a US patent accepted in May 2014 [34]. In this noteworthy invention, the λ system is disclosed in such context to generate so-termed supercoiled MiniVectors™ comprising shRNA, micro RNA (miRNA) or a GOI from PPs containing the hybrid *att* sites (*E. coli* strain LZ54). These minimalistic constructs are in all features similar to mcDNA, lacking the entire bacterial replication unit. However, it is stated in patent description that these cassettes have an upper size limit up to approximately 1.1 kbp [34]. Nevertheless, the presence of residual plasmid contaminants in the final preparations will require further attention before the development of a new therapy based on the λ-*Int* system and MiniVectors™. Interestingly, a small size exhibited relevant influence in the biological performance of such biopharmaceuticals, being demonstrated by Zechiedrich and colleagues that MiniVectors™ are not only resistant to incubation in 100 % serum during 48 h, but also achieve a remarkable 30-fold higher gene silencing than standard pDNA in difficult-to-transfect human non-Hodgkin's Ki-positive large cell lymphoma line (K299) [34]. From a therapeutic perspective, these are encouraging preliminary results but which ought to be further validated in a clinical scenario.

2.2.2. Phage P1 *Cre* recombinase

The Phage P1 'causes recombination' (*Cre*) tyrosine *Int* was initially described by Austin and co-workers in 1981, and unlike λ-*Int*, it catalyzes a bi-directional, site-specific recombination once it binds to its *loxP* hybrid sites (34-bp) (Figure 1 B) [29, 35]. During the last decades, *Cre* recombinase has been widely employed as an *in vivo* genetic engineering tool for the establishment of knockout animal models [36], or for the modification of mammalian cell lines genomic DNA [37]. However, the application of the *Cre-loxP* system in the production of minicircle vectors was only possible with the insertion of a mutated hybrid site containing an additional 8 bp central spacer that inhibits bi-directionality [27, 29]. Assuring a unidirectional recombination is crucial in minicircles manufacture because mcDNA and mP species could be recombined to yield their parental template or mixed concatamers. The use of *Cre-Int* unidirectional system for mcDNA manufacture was initially described by a patent filed by Bigger and co-workers (US application 11/249929) [13]. For this purpose, one *loxP* half-site was mutated, whereas the corresponding remained wild-type. After recombination the resulting hybrid site is no longer active and unidirectionality is guaranteed [13]. Despite being an elegant strategy, the yield of conversion from PP to mcDNA was not absolute, with residual plasmids being present in the final batch. The existence of contaminants severely compromises the clinical applicability of these biopharmaceuticals since a deleterious immunologic response from the host may be elicited [1]. Due to this significant issue, Bigger and colleagues disclosed an additional approach which combined the use of a restriction endonuclease to digest both PP and mP after recombination, followed by a laborious purification using cesium chloride (CsCl)-ethidium bromide density centrifugation [13, 14]. Although this strategy increased the overall yield of minicircles, it is a suboptimal set up that involves high cost, low yield and poor scalability from a manufacturing and pharmaceutical perspective. Such drawbacks render *Cre-*

mediated recombination a less attractive choice in comparison with the more advanced methods currently available.

2.2.3. *ParA* resolvase

ParA is a serine recombinase of the resolvase/invertase family of enzymes and catalyzes an irreversible, conservative, site specific intramolecular recombination upon binding to a target supercoiled plasmid containing two identical hybrid binding sites (133 bp) belonging to the multimer resolution system (MRS) [38]. *ParA* resolvase has been broadly applied in genetic engineering of both prokaryotic and eukaryotic hosts, with various reports evidencing its particular use for the production of genetically modified plant cells [39, 40]. This system is also very suitable for minicircles production in bacterial hosts because *ParA* resolvase is highly efficient in mediating these recombination events during bacterial amplification [38]. For mcDNA production, the *ParA* gene is inserted in the bacterial genome under the control of the *pBAD/AraC* L-arabinose inducible system [41, 42]). This unique control system has key features that include: (i) an *AraC*-mediated repression of *ParA* resolvase transcription in the absence of the sugar arabinose; and (ii) the expression of the recombinase by the *araBAD* operon, which is stimulated in the presence of L-arabinose [26, 38]. It is important to emphasize that the *BAD* promoter has shown residual expression during bacterial amplification, a limiting factor for minicircles production [26]. The rationale for using *pBAD/AraC* during minicircles production is established on the possibility to dynamically modulate *ParA* expression with L-arabinose addition/glucose depletion during bacterial cultivations. In this context, to produce highly pure minicircles, Mayrhofer and co-workers conceived a straightforward methodology that takes advantage of *ParA* resolvase to mediate the intramolecular recombination of parental templates into mcDNA in *E. coli* K12 strain followed by affinity chromatography purification of mcDNA crude preparations [43]. Using this 'Recombination-Based Plasmid Separation' (RBPS) technology Mayrhofer accomplished a PP-mcDNA recombination efficiency higher than 99.5 %, a remarkable enzymatic activity that contributes for the applicability of this system in large-scale production [43]. In addition to the catalytic activity of *ParA* resolvase, its molecular fraction to PP templates also markedly influences mcDNA overall yield and a high stoichiometric *ParA/PP* ratio is crucial to achieve maximum efficiency [38, 43]. After recombination, the mcDNA of interest was purified with high yield by removing residual PP and mP recombination products through affinity chromatography based on the biorecognition between LacI/lactose operon sites present in mcDNA cassette [43]. This technology was recently upgraded in a patent issued to Mayrhofer and co-workers which discloses the use of *ParA* resolvase in combination with mcDNA immobilization in the cell wall of bacterial hosts as an alternative purification during bacterial culture [44]. In this invention, the MC4100 *E. coli* strain was selected for minicircle generation since arabinose expression/repression system is under higher endogenous control. From a reasonable viewpoint, it becomes clear that in comparison with the former recombination systems (*Cre* and λ-*Int*), the RBPS-technology is a more promising platform for the manufacture and purification of clinical-grade mcDNA biopharmaceuticals at large-scale.

2.2.4. φC31-integrase/I-SceI homing endonuclease system

The Streptomyces bacteriophage φC31 integrase (φC31-*int*) is a serine recombinase that mediates unidirectional recombination events between its *attP*/*attB* binding sites (~ 40 bp) (Figure 1 B) through catalytic and DNA-binding domains, which control the entire process [29]. Unlike other recombinases, φC31-*int* neither requires supercoiled topoisoforms in its substrates, nor the assistance of supplementary host factors as in the case of λ-*Int* [45]. The relative simplicity of φC31-*int* has encouraged its extensive use in advanced therapeutic applications that span from site-specific integration of pDNA transgenes in liver, lung or neuronal cells for robust and long-term gene expression, up to the production of iPSCs [45]. To date, these studies have been performed only in a preclinical set up and the question does remain on whether chromosomal instability or severe immunological responses may occur after gene transfer to a human host [45]. Such probability is not a concern when episomal minicircles are administered. The φC31-*int* system has also been exploited for high-throughput production of mcDNA in recombinant bacteria [22]. Chen and co-workers, have developed a φC31-*int* mediated technology to produce mcDNA in suitable quantities for systemic administration in mouse liver [46]. As reported, the PP-mcDNA recombination was nearly complete, with > 97 % template species being converted to the biopharmaceuticals of interest. In this system, the φC31-*int* was allocated in the PP under tight control of the inducible *pBAD*/*AraC* promoter [46]. Despite achieving more than three-fold higher expression of h-AAT transgene in comparison with standard pDNA. However, the removal of residual mP and PP from minicircle formulations was still performed by using an expensive, laborious and low-yield methodology based on CsCl ultracentrifugation and restriction enzymes for degradation of bac-ORI plasmids [46]. Therefore, to avoid these rate-limiting steps, later Chen and co-workers, described a technology that greatly improved the production procedure by taking advantage of I-SceI homing endonucleases, which eliminated both mP and PP species (Figure 1 B) [22]. Exceptionally, these dynamic events were all stimulated with a one-step input of L-arabinose (Figure 1 A), since both the φC31-*int* and I-SceI were placed under control of the same *BAD* promoter. This well-designed bioprocess achieved 9-fold higher production yield than the original protocol. Just as importantly, this approach sustained the preparation of mcDNA with 97 % purity [22]. More recently, Kay and co-workers, further improved this one-step minicircle production technology by engineering a genetically modified *E. coli* strain (ZYCY10P3S2T), which produced high quality mcDNA batches with ten-fold fewer contaminating plasmids (0.4 - 1.5 % residuals) [11]. Moreover, a 3 to 5-fold higher yield of minicircles was attained in a cost-effective and simple over-night bacterial culture.

Overall, a critical analysis of all these technologies suggests that further manipulation and monitoring of the numerous process parameters is fundamental to produce mcDNA in suitable amounts for the emergent demand of DNA biopharmaceuticals. Gathering such knowledge will only be possible with the use of analytical tools that provide real-time in-line monitoring throughout this dynamic manufacturing process (e.g., flow cytometry, atomic force microscopy

capillary gel electrophoresis, microfluidic-based separation or quantitative real-time polymerase chain reaction (qRT-PCR) [8,33]). An exact follow-up is also vital to assure that the genetic material is produced with purity and high quality to comply with the current regulatory demands for administration of biopharmaceuticals to human hosts.

2.3. Regulatory demands for minicircle biopharmaceuticals preparations

The development and validation of minicircle-based therapeutic products comprises various stages: (i) bioprocess engineering; (ii) pre-clinical laboratorial research with *in vitro* and *in vivo* studies; (iii) clinical trials, and finally, (iv) large-scale manufacture for clinical use [47, 48]. All these phases are subjected to strict guidelines issued by regulatory agencies (e.g., US-FDA and EMA, Table 1), with the aim to guarantee the quality, efficiency and safety of the biopharmaceuticals for human administration [48]. According to the anticipated mcDNA application different regulations are applied. The first of these guiding principles is defined as good laboratory practice (GLP) and outlines the basic requirements for *in vitro* and *in vivo* laboratorial research [47]. The main principle underlying GLPs is the standardization of pre-clinical assays to ensure data quality, integrity and reproducibility (described in detail in the European directives 2004/9-10/EC). Failure to follow these guidelines can lead to suspension of product development [47]. GLP quality standards are mainly adequate for pharmaceutical applications that involve the administration of high-quality grade (HQG) mcDNA for gene delivery or gene expression studies in cell lines and animal models [48]. To guarantee that biopharmaceuticals are totally safe for direct gene transfer to humans (e.g., DNA vaccines, DNA-loaded medical devices), clinical trials have to comply with good clinical practice as stated by EMA [49]. Moreover, the manufacturing process itself must conform to the so-termed current good manufacturing practices (cGMP), an extra set of guidelines that regulates all parameters associated with nucleic acids production (e.g., quality control, upstream contaminants, standard operating procedures, batch-to-batch reproducibility [48]). As an endpoint, HQG mcDNA preparation must be devoid of contaminants that could induce any deleterious immunologic response from the host (Table 1). In this context, the recent advances focused on the elimination of contaminant mP and PP species during bacterial growth may provide more pure preparations after the mcDNA biosynthesis process [1, 11]. It is important to underline that currently there is a growing commercial interest in mcDNA vector construction, which is available as cGMP compliant and can be used for preclinical and clinical investigations. There are commercial vendors that presently provide on-demand mcDNA formulations with cGMP-grade quality (Table 2).

Table 1. Summary of the parameters to be considered for preparations of mcDNA biopharmaceuticals. Some parameters have strict guidelines although others have yet to be addressed by regulatory agencies such as the presence of parental (PP) or mini-plasmid (mP) species.

Impurities from Bacterial Host				
Product Parameters	**Requirements**	**Quantitative/Qualitative Tests**	**Possible Biological Response**	**Regulatory Guidelines/Guidance Documentation**
Endotoxins/Pyrogenicity	< 10 Endotoxin units/mg plasmid	Limulus amebocyte lysate (LAL) Rabbit pyrogen test	Severe immunologic response that may include fever, inflammation or anaphylaxis	US-FDA - Considerations for Plasmid DNA Vaccines for Infectious Disease Indications [50]
RNA	Undetectable (<1 %)	Agarose Gel Electrophoresis		
Proteins	Undetectable (<1 %)	Bicinchoninic Acid Assay (BCA)		
Genomic DNA (gDNA)	< 0.01 µg/µg plasmid (<1 %)	qRT-PCR Southern blot		
Parental Plasmids (PP)	Not defined (Undetectable levels anticipated to be beneficial)	Agarose and Capillary Gel Electrophoresis qRT-PCR (with specific primers [1])	Horizontal gene transfer Severe immunologic response due to presence of bacterial backbone	Legislation not yet available from regulatory agencies
Mini-plasmid (mP)				

Table 1. Continued.

DNA preparations				
Product Parameters	**Requirements**	**Quantitative/Qualitative Tests**	**Possible Biological Response**	**Regulatory Guidelines/Guidance Documentation**
Identity	Confirm construct identity	Restriction Enzyme Digestion Agarose Gel Electrophoresis Transformation Efficiency Complete Vector Sequencing	Horizontal gene transfer Severe immunologic response due to presence of bacterial backbone Non-specific organ cytotoxicity due to off-target expression of exogenous gene of interest	US-FDA - Considerations for Plasmid DNA Vaccines for Infectious Disease Indications [50]
Topological isoform (linear, relaxed, denaturated)	<5 % present in final preparation	Agarose Electrophoresis Atomic Force Microscopy (AFM) imaging [51]	Possible reduction in transgene expression potency	
Covalently closed circular DNA	> 97 % supercoiled in final preparation	Agarose and Capillary Gel Electrophoresis Analytical Chromatography [52] AFM imaging [51]	Improved transgene expression efficiency after *in vitro* administration [53]	
Sterility	Undetectable microorganisms	Gram staining Growth assays	Localized or systemic immune-pathological reaction	US-FDA - Content and Review of Chemistry, Manufacturing, and Control (CMC) Information for Human Gene Therapy Investigational New Drug Applications (INDs) [54]

Table 1. Continued.

Impurities from process				
Product Parameters	**Requirements**	**Quantitative/Qualitative Tests**	**Possible Biological Response**	**Regulatory Guidelines/Guidance Documentation**
Organic solvents	Undetectable levels are beneficial (Acceptable levels subject to approval from regulatory agencies)	Gas Chromatography [55]	Carcinogenic effects (Class 1) Irreversible cytotoxicity (e.g., neurotoxicity or teratogenicity) (Class 2) [56]	US-FDA - Guidance for Industry, Q3C Impurities: Residual Solvents [57]
Selection antibiotics	Total removal is recommended (Acceptable levels subject to approval from regulatory agencies)	High-performance Liquid Chromatography coupled to Electrospray Ionization Mass Spectrometry (HPLC-ESI) [58]	Potential hypersensitivity reactions, especially to β-lactam antibiotics Endogenous bacteria antibiotic resistance Associated problems can be overcome with selection-free systems (RNA-OUT, pFAR)	US-FDA - Guidance for Human Somatic Cell Therapy and Gene Therapy [59]

Table 2. Summary of the existing companies that presently provide mcDNA vector preparations.

Company Description	Production system	mcDNA preparation	Type of purification	Customization	Ref.
System Biosciences®	φC31/ I-SceI recombinase system in ZYCY10P3S2T *E.coli* strain	Endotoxin free preparations MC-Fection™ transfection reagent provided to confirm vector efficiency	Minicircle producing kit that allows the removal of genomic DNA and parental templates contamination with the use of Minicircle-safe deoxyribonuclease (DNAse) and restriction enzymes	Customized DNA vectors can be provided on demand	[11]
Plasmid Factory®	Patented Technology (non-disclosed)	cGMP grade quality mcDNA provided in McBox® containing the mcDNA of interest and a pDNA for transfection comparison	Chromatographic purification which originates pure preparations	Customized DNA vectors can be provided on demand	[60]

2.4. McDNA for cancer gene therapy

Nowadays cancer remains one of the most difficult to treat and predominant diseases that affects mankind. According to the World Health Organization (WHO) cancer has been responsible for more than 8.2 million deaths in 2012, and it is projected that this global incidence will duplicate within the next 20 years [61]. In line with this upsurge, it is predicted that in the USA alone, over 1.65 million new cases will be diagnosed during 2015 [62]. These alarming statistics expose the urgent necessity to actively pursue the discovery of ground-breaking treatments that can have a realistic impact in patient survival and quality of life [63]. Currently, the existing therapeutic modalities for cancer treatment are typically based on invasive surgery to remove tumor tissue and on the administration of radio or chemotherapy [61]. Although significant advances have been recently accomplished in the development of more effective radiotherapy apparatus for treatment of localized tumors (reviewed in detail by Baskar and co-workers [64]), the possibility of permanent damage of reproductive organs, or creation of secondary tumors due to radiation exposure is still a major issue. Hence, the administration of chemotherapeutics continues to be the gold standard treatment for patients diagnosed with early stage, late stage or non-localized, metastatic cancers [65, 66]. Adjuvant chemotherapy has been administered in conjugation with radiotherapy as a strategy to improve the therapeutic outcome, but only minor improvements in patients life expectancy have been obtained. The simultaneous use of both treatments is not a completely feasible alternative due to intolerable side effects.

Essentially, chemotherapy is based on the administration of drugs that are able to trigger cancer cells apoptosis (cytotoxic activity) or control cell proliferation by targeting important cell cycle checkpoints (cytostatic activity) [67]. However, due to inherent physicochemical characteristics, anticancer agents have some issues that are eventually responsible for a reduced clinical efficacy. One of these limitations is the poor water solubility of the majority of natural or chemical molecules with antitumoral activity. This characteristic affects drugs pharmacokinetic profile and hinders their delivery through the generally used administration routes (e.g., oral, intravenous, intradermal, inhalation [68]). Anticancer agents also exhibit insufficient penetration and diffusion in the tumor interstitium, a critical aspect, since malignant cells are therefore exposed to different quantities of drug depending on their location in the diseased tissue [69]. In addition, the lack of selectivity of chemotherapeutics towards cancer cells results in severe damage to healthy organs [70]. These harmful side effects are one the most important limitations of anticancer drugs, and largely restrict their maximum tolerated dosage, as well as their frequency of administration [61]. Due to this narrow therapeutic window and significant tissue partition, antineoplastic agents have poor bioavailability at the target tumor site, which results in poor therapeutic efficacy.

In the past decade nonviral DNA-based gene therapy has arisen as a promising modality for cancer therapy in addition to chemotherapeutics. Since it can eliminate specific disease hallmarks, both at a genomic or transcriptional levels, in a considerably safer mode when

compared to its viral-based counterparts [71]. This treatment is based on the administration of exogenous nucleic acid biopharmaceuticals into malignant cells via various delivery platforms with the aim to control, suppress, or enhance a cellular function that ultimately culminates in cell death or senescence [71-73]. As such, nonviral cancer gene therapy generally targets different abnormalities including those related to: (i) cell proliferation and apoptosis pathways; (ii) DNA repair mechanisms and (iii) MDR proteins expression and function [74]. Recent studies have also extended the therapeutic targets of nonviral nucleic acids by showing their potential to be used for development of vaccines which stimulate immune system cells (e.g., T lymphocytes or antigen presenting cells (APCs) like dendritic cells) to specifically recognize and destroy neoplastic cells a treatment modality so-termed Cancer Immunotherapy [75, 76].

Up until now, however, the widespread translation of mcDNA nonviral cancer gene therapies from bench-to-bedside has yet to be fulfilled [77]. This fact is mainly correlated with DNA biopharmaceuticals difficulty in maintaining sufficiently high protein levels and in assuring the expression of exogenous genes during prolonged periods of time [60]. This transient expression has been recently improved with the development of advanced nonviral gene expression cassettes such as mcDNA, which have demonstrated long-term expression and improved safety as emphasized in the former sections [11, 71]. The motivation of applying mcDNA in cancer therapy is established mostly on using these vectors as a more effective approach to: (i) restore the expression of tumor suppressor genes [53]; (ii) silence oncogenic proteins [78]; (iii) sensitize immune cells to recognize and attack malignant cells; or (iv) induce the expression of molecules with antitumoral activity [79]. As an example, Zhao and co-workers, used liposome-assisted (Lipofectamine 2000®) transfection of Karpas299 cells with a MiniVector™ DNA encoding for anaplastic lymphoma kinase (ALK) shRNA for cancer therapy, a strategy that caused a significant silencing (25 %) of this oncoprotein [78]. As a result of ALK silencing, cancer cells growth was inhibited by 40 %. More importantly, the PP-ALK-shRNA original vector only induced an ALK silencing of ~ 1 % with transfected cells showing a similar proliferative activity as untreated cancer cells [78]. These findings evidence the improved therapeutic effect of mcDNA-shRNA delivery in difficult-to-transfect cancer cells when compared to its plasmid counterpart. On a different approach, Wu and colleagues studied the therapeutic effect of an mcDNA cassette encoding Interferon-gamma (IFN-γ) for antitumoral gene therapy for human nasopharyngeal carcinoma [79]. In comparison to p2fC31-IFN-γ parental templates, minicircle-IFN-γ elicited 19 to 102-fold higher IFN expression levels in different cells lines *in vitro* (e.g., HEK293 cells and NIH 3T3 fibroblasts). This remarkable expression efficiency also resulted in reduced relative cell growth rates when mcDNA-IFN-γ was administered to nasopharyngeal carcinoma cell lines, via Lipofectamine 2000® liposomes, thus demonstrating its therapeutic potential. In a similar report, liposome-minicircles encoding IFN-γ but under the control of different promoters, cytomegalovirus (CMV), and *oriP* (Epstein-Barr gene promoter linked to CMV), were administered to evaluate a possible increase in the therapeutic effect [80]. The rationale underlying the use of *oriP*-CMV in this study is the concept that nasopharyngeal carcinoma cells contain Epstein- Barr virus (EBV) genome and a cell-specific expression of IFN-γ can be obtained

[80]. *In vitro* data revealed that mcDNA-*oriP*-IFN-γ vectors achieved a selective transgene expression in EBV-positive cell line and are significantly less cytotoxic to normal, or EBV-negative cancer cells. Curiously, *in vivo* administration of minicircle-liposome nanocarriers to nude mice bearing nasopharyngeal carcinoma xenografts resulted in a significant increase in survival.

At this point, it is however important to emphasize that the administration of mcDNA biopharmaceuticals, radiation, or anticancer agents as a stand-alone therapy, has proven to be insufficient to completely eradicate malignant cells or obtain full cancer ablation without recurrence. This event occurs due to the fact that cancer cells acquire a multi-drug resistant phenotype by over-expressing drug efflux transporters following first line treatment with chemotherapeutics. Similarly, following treatment with DNA biopharmaceuticals, cancer cells can also reprogram intracellular signaling pathways in order to counteract the impact of the expression of exogenous tumor suppressor genes. This multi-resistant phenotype of cancer cells and their ability to adapt to deleterious conditions thus demands the discovery of novel approaches that can overcome such phenomena.

To overcome these issues, novel treatments based on the combination of different bioactive molecules, i.e., combination therapy, can overcome the limitations of single treatments by using not one, but multiple therapeutics [61]. The first evidence of combinatorial therapies applicability in humans was described in the seminal report of Frei and co-workers in 1965. In this study a group of anticancer agents were administered to patients with acute lymphoblastic leukemia (ALL). This strategy resulted in a long-term remission period of ALL patients [81]. Since that time and up to now, several other anticancer drug-drug combinations have been investigated, and emerging evidence from pre-clinical and clinical trials has, in some cases, corroborated the anticipated therapeutic improvements [66, 82]. Yet, in various types of cancer the cytotoxicity of more potent drug combinations and their pharmacokinetic/ pharmacodynamic properties, are issues that continue to affect the therapeutic outcome and patient survival. In order to change this reality, recent studies are exploring the co-delivery of antitumoral agents along with nucleic acids, in an attempt to develop less toxic and more effective treatments.

Nucleic acids-drug co-delivery is particularly promising as a treatment modality for cancer because various disease hallmarks including cancers cells multi-drug resistance, invasion/metastasis and resistance to apoptosis, can all be targeted at once as means to achieve a more powerful therapeutic effect [83]. The main rationale for drug-nucleic acid combination therapy is the simultaneous administration of different anticancer agents along with mcDNA biopharmaceuticals, so as to promote an additive or synergistic outcome. Synergism occurs when the effect of the administered bioactive molecules is higher than the sum of their separate use [84, 85]. A synergistic effect is highly desirable in combinatorial therapy since a smaller dose of drug-genes would be sufficient to promote an antitumoral effect

to a similar extent. Such outcome can be obtained with both drug-drug or drug-nucleic acids administration [66]. Following drug-nucleic acid co-delivery to target cells, the main objective is to take advantage of anticancer drugs activity and of the cell replication machinery to express the therapeutic transgene of interest that will further contribute to the therapeutic effect [86]. This is a particularly encouraging technology as precise nucleotide sequences can be designed to target specific genes to which a drug or macromolecule has not yet been discovered to affect, the so-termed non-druggable targets [61]. While it is envisioned that these combination therapies could be administered in humans, *per se*, the administration of drugs and naked mcDNA biopharmaceuticals for example via intravenous injection is difficult due to drugs poor water solubility, rapid clearance and tissue partition as previously described. Adding to this, minicircles are highly instable in serum and have a negligible cellular uptake due to their inability to cross the extracellular membrane. Owing to these limitations, in the last decade an enormous focus has been given to the development of delivery systems that can protect, transport and deliver into the target site, different bioactive molecules or their varied combinations.

In the upcoming chapter a particular focus is given to the technologies and delivery systems available for administration of mcDNA biopharmaceuticals. Moreover, due to the importance of biological barriers to mcDNA administration *in vivo* an outline of these major hurdles is also provided.

CHAPTER 3

This chapter is based on the publication entitled: Minicircle DNA vectors for gene therapy: advances and applications, *Human Gene Therapy Methods*, 2014, 25 (2):93-105.

3. Technologies for mcDNA biopharmaceuticals gene transfer

The use of mcDNA biopharmaceuticals in patients must rely on proficient gene transfer technologies that can protect the genetic material and ultimately promote its delivery into the target tissues and the intracellular site of action. Currently, a plethora of physical and chemical methodologies have been developed for exogenous DNA transfer to diseased cells (Figure 2). However, the optimal gene transfer technology has yet to be developed.

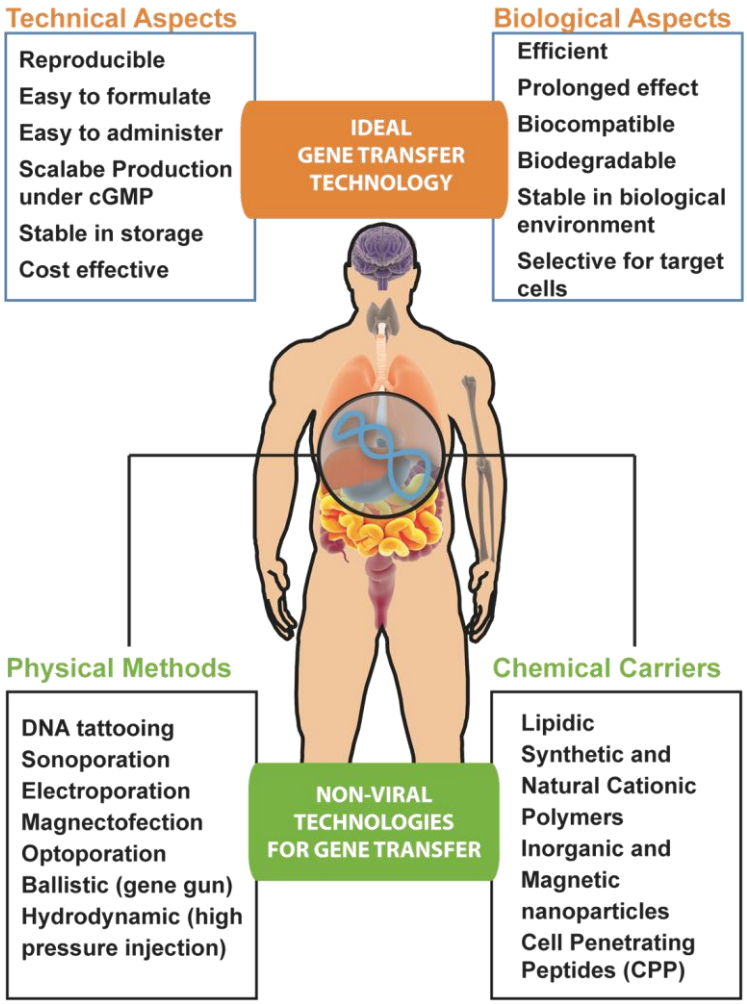

Figure 2. Schematics of the concept of an ideal gene transfer technology and summary of the currently existing nonviral methods to promote gene transfer.

In this context, in the past few decades, a significant effort has been given to the active development of various types of gene transfer technologies including cationic nanosized delivery systems which are particularly valuable for mcDNA delivery due to its inherent negative charge. Moreover, it is also important to emphasize that despite the major advances regarding the design of different nucleic acids delivery systems (Table 3), few reports have explored the delivery of mcDNA biopharmaceuticals via nanocarriers so far.

Table 3. Summary of the currently available gene transfer technologies.

Chemical carriers					
Gene Transfer Technologies	**Mechanism of Gene Transfer**	**Advantages**	**Disadvantages**	**Perspectives for optimal gene transfer**	**Ref.**
Synthetic cationic polymers (Polyplexes)	Condensation of genetic material by counter ion electrostatic interactions between negatively charged nucleic acids and positively charged chemical groups in the condensing agents The DNA-loaded nanocarriers are internalized in target cells via various cellular uptake pathways In the case of micellar carriers direct translocation trough the plasma membrane can take place	Ratiometric control over amine content and polymer molecular weight Structurally versatile (linear, branched, star-shaped) Narrow molecular weight (MW) distribution	Possible presence of contaminants from chemical synthesis Possible scalability issues Relatively instable in biological environment (protein corona) Low nuclear uptake Charge-dependent toxicity	The inclusion of stealth hydrophilic polymers can improve biological performance by reducing unspecific interactions with blood components Possibility to include stimuli responsive linkages (pH, redox, temperature, light) to promote controlled DNA release Shielding of the positive charge with negative moieties can improve therapeutic effectiveness The inclusion of cell targeting moieties can improve selectivity towards cancer cells. However, the inclusion of targeting elements can modify the biocompatibility and nanocarriers biological performance	[2, 87]
Natural cationic polymers (Polyplexes)		Higher MW polydispersity in comparison to synthetic carriers Biodegradable Scalable Cost-effective	Unstable in biological environment (protein corona) Relatively low cellular uptake and endosomal release Low nuclear uptake Charge dependent toxicity Low cell selectivity after systemic administration		

Table 3. Continued.

Chemical carriers					
Gene Transfer Technologies	**Mechanism of Gene Transfer**	**Advantages**	**Disadvantages**	**Perspectives for optimal gene transfer**	**Ref.**
Lipidic nanoparticles (Lipoplexes)	Condensation of genetic material by counter ion electrostatic interactions between negatively charged nucleic acids and positively charged lipids In the case lipid carriers direct fusion with the plasma membrane and subsequent release of DNA content also can take place	Easy to formulate and with controllable size Formulation versatility Scalable	Charge and structure dependent toxicity Low cell selectivity (non-targeted formulations) Possible instability in biological environment (aggregation with serum) Accelerated blood clearance Generation of inflammatory or anti-inflammatory responses	The inclusion of stealth hydrophilic polymers can improve biological performance by reducing unspecific interactions with blood components Use of negatively charged lipids can improve therapeutic effectiveness by reducing cationic net charge The inclusion of cell targeting moieties can improve selectivity towards cancer cells. However, the inclusion of targeting elements can modify biocompatibility and nanocarriers biological performance	[2, 87]
Lipid-Polymer hybrid carriers (Lipopolyplexes)		Addition of polymer moieties can improve therapeutic efficiency and DNA condensation			

Table 3. Continued.

Chemical carriers					
Gene Transfer Technologies	**Mechanism of Gene Transfer**	**Advantages**	**Disadvantages**	**Perspectives for optimal gene transfer**	**Ref.**
Inorganic nanoparticles	Electrostatic interaction with DNA Chemically dependent DNA condensation Encapsulation of DNA in porous/mesoporous nanostructures Cellular uptake and DNA delivery is promoted via general cellular uptake pathways	Relative ease of assembly Chemical, thermal and physical stability Possible conjugation with polymers or lipids and other biomolecules Can be used for theranostic applications	Toxicity and possible long term effects of particle accumulation in tissues (Acute or chronic toxicity) Possible issues of environmental pollution	Grafting inorganic nanoparticles into polymers, lipids and other biomolecules (e.g., antibodies oligonucleotides) can improve their therapeutic efficacy Surface functionalization with stealth polymers can improve blood compatibility and circulation time Precise control over the hydrodynamic size of the nanocarriers will have a positive impact in their efficacy	[88-90]

Table 3. Continued.

Chemical carriers					
Gene Transfer Technologies	**Mechanism of Gene Transfer**	**Advantages**	**Disadvantages**	**Perspectives for optimal gene transfer**	**Ref.**
Cell penetrating peptides (CPPs)	Mainly electrostatic interaction between positively charged peptide chemical groups and nucleic acids The molecular mechanism of CPP-DNA cell uptake is dependent of the nature of the CPP (cationic, amphipathic, hydrophobic). From this standpoint it has been described that CPPs can achieve cellular uptake via direct membrane translocation and via generally used cellular uptake pathways	Efficient cellular uptake Efficient endosomal release Relatively low cytotoxicity Chemical versatility for conjugation with other nanocarriers Low immunogenicity	Relatively low specificity toward target cells or tissues Possible instability in biological environment after systemic administration of CPP-DNA conjugates	Formulation of CPP- polymer CPP-lipid hybrids can improve gene transfer efficiency. Optimization of the physicochemical parameters of the final carriers will influence their therapeutic potential and need to be optimized The study of uptake mechanisms of each CPP formulation will contribute to evaluate their cell selectivity Optimization of the inclusion of Nuclear Localization Sequences (NLS) can significantly enhance transfer efficiency	[114-116]

Table 3. Continued.

Physical Methods					
Gene Transfer Technologies	**Mechanism of Gene Transfer**	**Advantages**	**Disadvantages**	**Perspectives for optimal gene transfer**	**Ref.**
Electroporation	Application of an electric field for "cell poration" (i.e., reversible permeabilization of the extracellular membrane), which then allows uptake of genetic material through electrophoresis Electroporation has been performed up-to-date in the skin, muscle, tumors	Efficient naked DNA transfer Cost-effective Minor inflammation in the site of application	Moderately invasive and requires surgery to access deep organs Relative low number of transfected cells in a single procedure Currents must be precisely controlled for the clinical setting, possible cell death Electrodes in contact with patient	Size and number of pores created must be optimized to achieve a compromise between efficiency and cytotoxicity. Safer and more portable electrode designs can pave the way for implantable devices that promote the controlled delivery of DNA Pre-treatment of target tissue with permeability enhancers can improve gene expression	[33, 117-119]
Sonoporation	Sonoporation employs ultrasound to transiently induce defects in the plasma membrane of the cell and thus promote cellular uptake of the desired genetic material, (e.g., naked DNA)	Non-invasive in comparison to electroporation Instant cell recovery from permeabilization after exposure Envisioned to be used in various therapies including diabetes, skeletal muscle disease, cardiac diseases, cancer (melanoma, prostate)	Several parameters to optimize and control Temperature increases in target tissues (frequency and energy dependent) Extensive mechanic forces can cause cell disruption and death	The use of gas-loaded microbubbles enhances gene delivery by increasing DNA bioavailability in target site Inclusion of targeting moieties and manufacture of optimal colloidal formulations that protect/encapsulate DNA and release it in a stimuli- responsive mode may contribute for optimal gene transfer, especially following systemic administration	[119-121]

Table 3. Continued.

Physical Methods					
Gene Transfer Technologies	**Mechanism of Gene Transfer**	**Advantages**	**Disadvantages**	**Perspectives for optimal gene transfer**	**Ref.**
Magnetofection	Takes advantage of DNA encapsulation in magnetic nanoparticles modified to be cationic (e.g., with lipids or polymers) Particles are guided to the target location by an external magnetic field and gene transfer is mediated by cell entry pathways	Externally controlled via external magnetic field Can be used for Theranostics Localized delivery Efficient and less invasive when compared with electroporation	Toxicity and stability problems associated with magnetic nanoparticles aggregation Non-specific cytotoxicity Excretion and biodegradability issues	The use of dynamic magnetic fields can improve magnetic-mediated gene therapy Optimizations in particle size, shape, targeting and stability will positively influence response to the external magnetic field, improve biocompatibility and selectivity Optimization in external control over particle *in vivo* fate can improve specificity	[118, 120, 122]
Optoporation (Laser-assisted)	Based on the use of laser irradiation to induce the formation of transient pores in the extracellular membrane. This pore formation allows naked DNA to enter the cells	Local delivery Possibility of penetration in deep tissue regions	Narrow delivery window between irradiation and DNA administration Induction of local inflammation Possible changes in skin architecture (skin damage)	Can be conjugated with black carbon nanoparticles for generation of photoacoustic energy Hand-held devices with Erbium-doped Yttrium Aluminum Garnet (Er/YAG) lasers has shown promise human use and further tests must be performed	[118-120]

Table 3. Continued.

Physical Methods					
Gene Transfer Technologies	**Mechanism of Gene Transfer**	**Advantages**	**Disadvantages**	**Perspectives for optimal gene transfer**	**Ref.**
Hydrodynamic injection	Consists in the bolus intravenous injection of a significant volume of a DNA containing solution that induces transitory membrane destabilization in hepatocytes and promotes gene delivery	Highly efficient and simple to perform No major tissue damage in animal models Suitable for hepatic gene transfer	High total injection volume Limited in gene transfer of poorly accessible locations (e.g., brain)	Image-guided and computer-controlled hydrodynamic injection can pave the way for application in humans Lower injection volumes may contribute for clinical application	[120, 123]
Microneedles	Devices with structurally defined arrays of micrometer sized needles that penetrate skin (*stratum corneum*) and deliver genes by micro channels. Microneedles can be solid, hollow, coated and dissolvable DNA cellular uptake is mediated by cationic polymers/lipids in coated microneedles (layer-by-layer). Alternatively, DNA uptake can be promoted by DNA-polycation direct delivery in the microchannels created by solid microneedles	Pain-free technology Biocompatible Minimally invasive Localized delivery Efficient for gene transfer Possibility for scaled up production Precise manufacture conditions	Limited usage in deep organs Possible risk of infection must be studied for each device No *in situ* quantification or visual confirmation of delivered dose	The design of dissolving microneedles can promote the release of genetic material in an extended time frame and promote prolonged gene expression Conjugation with other delivery systems by immobilization in needles matrix can further improve therapeutic efficacy	[119, 124-126]

3.1. Major biological barriers underlying gene transfer with nanocarriers

Prior to fulfilling their anticipated therapeutic effect in diseased tissues, mcDNA vectors must initially overcome numerous extracellular and intracellular barriers that vary according to the selected administration route (e.g., intravenous, intradermal, oral, cytoplasmic) or gene delivery platform [2]. These barriers severely affect gene transfer efficiency and must be fully understood in order to exploit the full potential of gene delivery systems to treat human disease [91]. Presently, intravenous injection is the most commonly used route of administration for nanocarriers designed for cancer therapy due to tumors leaky vasculature which promotes passive accumulation of nanocarriers [105].

In general, after systemic administration, the major extracellular barriers to the delivery of genetic material include to tumor tissues include: (i) the existence of DNA degrading nucleases (*in vitro* - present in culture medium supplemented with serum; *in vivo* - present mainly in the blood stream and cytoplasm); (ii) the pharmacokinetic/pharmacodynamic profile of naked or encapsulated nucleic acids (e.g., blood clearance, bioavailability); (iii) non-specific uptake by the reticuloendothelial system (RES); (iv) extravasation from the blood stream into target tissues; and (v) the negatively charged extracellular membrane [92] (Figure 3).

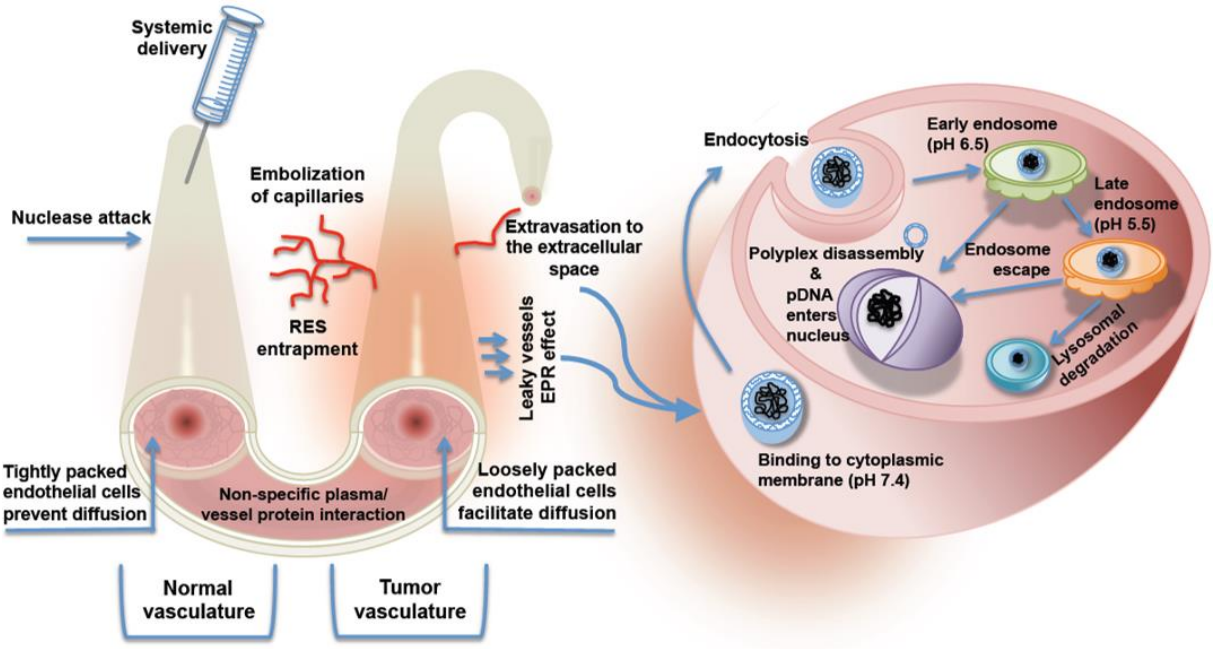

Figure 3. Overview of the major extracellular and intracellular barriers to DNA biopharmaceuticals delivery via intravenous administration (Adapted from McCrudden and co-workers [93]).

Following, translocation into the intracellular compartment via the different cellular uptake mechanisms [94, 95], the transgenes continue the route towards their final target and need to escape from degradative lysosomal vesicles, diffuse through the cytoplasm, transpose the nuclear envelope and finally establish contact with the replication machinery localized within

the nucleus [96]. Considering this multipart journey, it is clear that several parameters are limiting elements in the final levels and duration of transgene expression [97, 98]. This step-wise delivery process is thus highly complex and has been decisive in the limited number of mcDNA-based pharmaceuticals currently approved for patients treatment. On the other hand, these challenges have also contributed for an exponential progress in engineered delivery systems with adapted characteristics to overcome such barriers [99]. In the following sub-chapters, the obstacles encountered during systemic circulation, translocation of the plasma membrane in target cells and uptake into the nuclear compartment will be focused.

3.1.1. *In vivo* barriers to nonviral gene delivery - systemic circulation and tissue extravasation

In vivo gene delivery with nonviral nanoparticulate carrier via systemic administration is a highly challenging task [91]. Once injected into blood circulation, DNA-loaded nanocarriers need to evade tissue partition (e.g., liver, spleen), glomerular filtration in the kidneys (size threshold < 5 nm), and unspecific uptake by the reticuloendothelial system (RES) which is ultimately responsible for particles rapid clearance and poor bioavailability in tumor tissues. Moreover, the complex set of proteins that is found in the blood stream is another parameter that limits nanoparticle mediated delivery because it has been described that a complex protein corona forms in the surface of nanocarriers immediately after contact with biological fluids, thus changing its original chemical entity and triggering a biological response (Figure 4) [100].

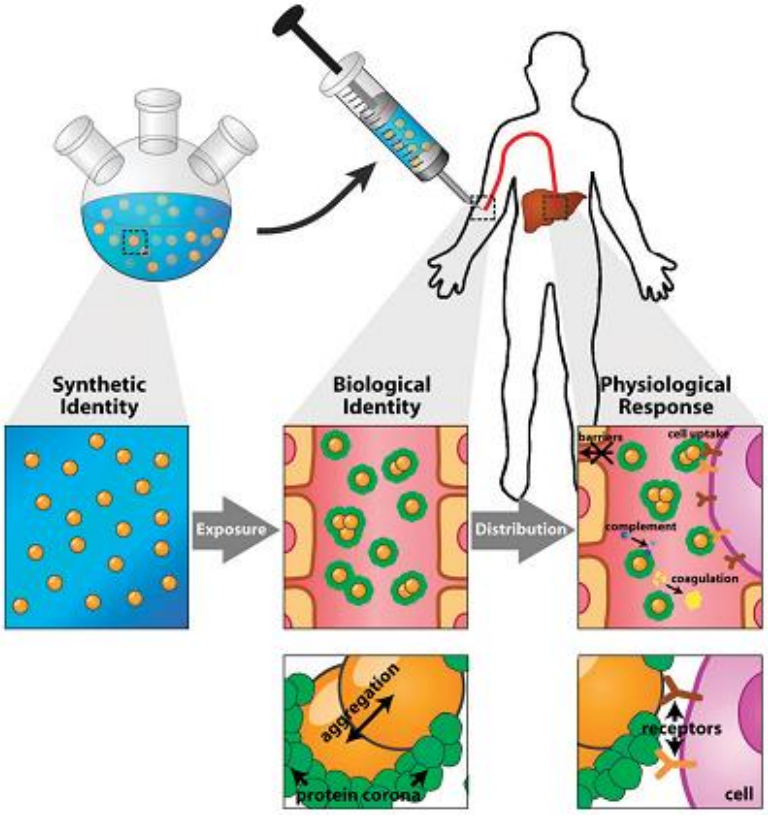

Figure 4. Modifications to nanocarriers identity (physicochemical properties) upon contact with biological fluids after intravenous injection. (Adapted from Walkey and co-workers [101]).

To overcome these physiological barriers, various reports describe the use of hydrophilic polymers, namely PEG, as a strategy to minimize phagocytosis by RES and the formation of a nanoparticle-protein corona [91]. However, recent issues regarding the use of PEGylated nanocarriers, namely the potential immunogenicity and accelerated blood clearance of PEG-based liposomes, have evidenced the necessity to exploit novel hydrophilic polymers [102]. Recent advances in this topic involve the use of minimalistic 'self-peptides' as new options to minimize phagocytic clearance and increase blood circulation time. This concept developed by Rodriguez and co-workers is based on the rationale that phagocytes avoid clearing of the body's own cells [103]. This biological marker is the cluster of differentiation 47 (CD47) membrane protein and the inclusion of computer designed CD47-peptide mimics in particles surface has minimized macrophage-mediated phagocytosis and increased bioavailability in A549-derived tumors [103]. Despite these novel strategies bring forth significant advances for the systemic delivery of DNA-loaded nanocarriers, the extravasation from circulation is yet another rate-limiting parameter in successful gene delivery. In fact, the endothelium monolayer constitutes a significant barrier to nanoparticles extravasation into tissues [104], being responsible for a markedly decrease in the dose delivered to diseased tissues [104]. To exceed this obstacle, various alternatives based on the use of the enhanced permeability and retention effect (EPR) [105], or on the use of vasculature-targeted nanocarriers, are being developed. The latter is particularly interesting since both an active recognition of the diseased vasculature and an increase in bioavailability can be attained. Using this approach, Schleich and co-workers developed αVβ3 integrin-targeted poly(D,L-lactic-co-glycolic acid)-iron oxide-paclitaxel nanocarriers via Arginine-Glycine-Aspartate (RGD) peptide conjugation into nanocarriers surface. This design promoted an improved accumulation in tumor tissues [106] in comparison with non-targeted systems. Interestingly, this initial targeting was further enhanced by the use of magnetic resonance imaging (MRI), which led to an additional increase in the amount of tumor-localized nanocarriers. This particular example emphasizes that in the future, the combination of various strategies can prove to be beneficial for achieving higher levels of transgene expression and ultimately for improving the therapeutic outcome.

3.1.2. Translocation of the plasma membrane – nanocarriers cellular uptake

Following extravasation into diseased tissues, the plasma membrane also constitutes a major rate-limiting barrier to gene transfer. The translocation of exogenous DNA into the intracellular compartment is crucial to achieve successful expression of therapeutic transgenes. Currently, it is well accepted that chemical carriers are internalized either via the various cell uptake pathways or by other mechanisms associated with the carrier type (e.g., cell penetrating peptides) (Table 4). The ability of DNA-loaded delivery systems to transpose the plasma membrane is mainly dependent on the interactions established with target cells at the nano-bio interface [107]. Several parameters, including, nanoparticles size [108], shape [108], surface charge [109] or type of targeting ligand play a critical role in promoting or hindering

cellular uptake of non-targeted/targeted nanocarriers, both *in vitro,* and *in vivo,* via a preferential uptake pathway (Figure 5).

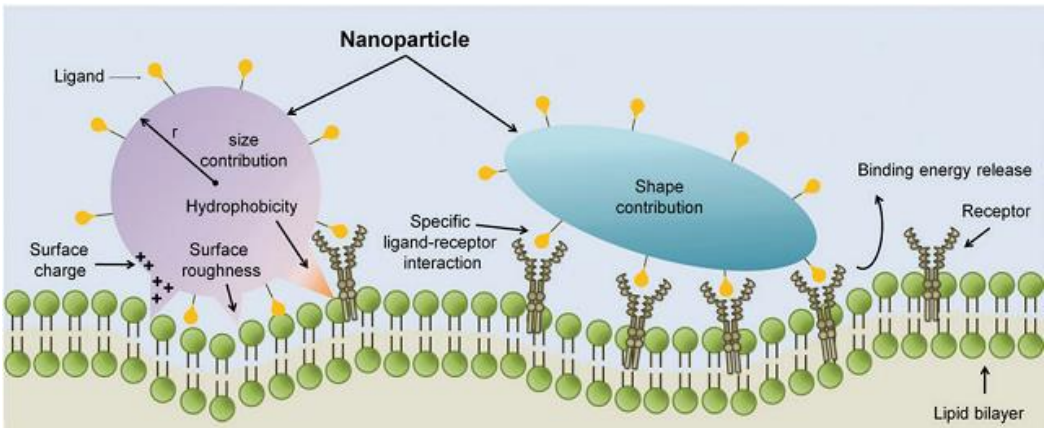

Factors that govern the nanoparticle internalization

Promotive factors	Resistive factors
Specific binding : Ligand-receptor affinity, ligand density	Stretching and elasticity of cell membrane
Nonspecific binding: hydrophobicity, surface roughness, surface charge	Thermal fluctuation of cell membrane
Optimum particle size and shape contribution	Receptor diffusion on the binding front
Free energy at contact size	Hydrophobic exclusion of polar surface by surface membrane
Energy dependent membrane and cytoskeleton components (*e.g.* energy required to form clathrin vesicle and promote membrane ruffling)	Stretching of receptor ligand-bonds, bond elasticity,

Figure 5. Parameters involved in the nanoparticle internalization process. (Adapted from Setyawati and co-workers [110]).

This parameter assumes further importance since a deficient cell uptake can compromise the overall transgene expression efficiency in diseased cells. Efforts have been made to overcome these issues by using cell targeted nanocarriers. In this context, Ge and co-workers recently reported the formulation of polyplex micelles for pDNA with tethered cyclic RGD (cRGD) moieties in the particle surface as means to achieve cell selectivity and increase cellular uptake *in vivo* [111].

3.1.3. Nuclear uptake

The nuclear import of DNA-loaded nonviral nanocarriers or naked DNA gene expression vectors is considered as a key limiting barrier of the entire process of gene transfer especially in non-dividing cells [96]. Naked DNA vectors are generally transported to the intra-nuclear compartment via activity of importins (karyopherins), that are proteins which recognize a nuclear localization sequence (NLS) in the nonviral gene expression cassette (e.g., the SV40 Large T-antigen NLS sequence). Although this process seems straightforward, it is not as efficient as that mediated by some viral vectors [112], a fact that accounts for the lower transgene expression efficiency of episomal nonviral vectors. Various efforts have been put forward to improve the nuclear uptake of such expression cassettes these include: (i) the conjugation to NLS-containing peptides; (ii) formulation of DNA complexes with nuclear

proteins; (iii) addition of small molecule ligands (e.g., dexamethasone, all-trans-retinoic acid (ATRA)); and (iv) inclusion of nuclear-targeting sequences in DNA vectors [96, 113]. Using the latter strategy, Breuzard and co-workers have developed a pDNA vector with a KB optimized insert (3NF) to promote NF-KB mediated nuclear import. The obtained results demonstrate a remarkable five-fold higher copy number of pDNA bearing two 3NF sequences upstream and downstream of the coding gene (p3NF-luc-3NF vector) in the nucleus of HeLa cells when compared to non-targeted pDNA [97]. Regardless of KB being inserted in pDNA, this approach is also suitable for mcDNA vectors and presents fewer issues and costs in comparison with peptide inclusion. Apart from this, other advances in the nuclear uptake of DNA-loaded nanocarriers have been reported recently. In an elegant approach, Akita and co-workers developed a Tetra-lamellar Multi-functional Envelope-type Nano Device (T-MEND) composed of a polycation-DNA core coated with various fusogenic lipids [114]. This unique architecture allowed the delivery of protamine-DNA complexes directly to the nuclear compartment by fusion of the multilamelar vesicles directly with the nuclear membrane [114]. As reported, this direct fusogenic delivery system required two additional lipid layers for transposition of the outer and inner nuclear membrane. As an end result, this delivery system promoted a significant gene expression in non-dividing cells. These examples provide important insights regarding the modulation of exogenous DNA nuclear uptake and the importance of achieving nuclear localization of these biopharmaceuticals.

CHAPTER 4

This chapter is based on the book chapter entitled: Multifunctional Nanocarriers for Co-delivery of Nucleic Acids and Chemotherapeutics to Cancer Cells, accepted for publication.

4. Multifunctional nanocarriers for nucleic acids delivery and drug-nucleic acids co-delivery

The design of nanomaterials for nucleic acids-drugs co-delivery is remarkably challenging due to the inherent physicochemical differences of these bioactive molecules. From the numerous types of materials available for biomedical applications, too few have demonstrated the necessary chemical, physical and biological versatility to accomplish simultaneous drug-gene encapsulation and complexation.

To overcome this lack of appropriate materials, the scientific community has focused during the last decades on the development of precisely designed and multifunctional nanomaterials for co-delivery applications. For this purpose various types of chemical modifications with macromolecules, as well as different conjugations of materials, or the synthesis of novel co-polymers, have all been explored. The concept of multifunctional particles is focused herein as conceptual classification similar to that proposed by Agrawal and co-workers, but adapted to nucleic acids-drug co-delivery [115]. Essentially, multifunctionality is the term that describes the various levels of modifications/characteristics that can be imprinted in a single nanocarrier projected for delivery of bioactive molecules to eukaryotic cells (Figure 6).

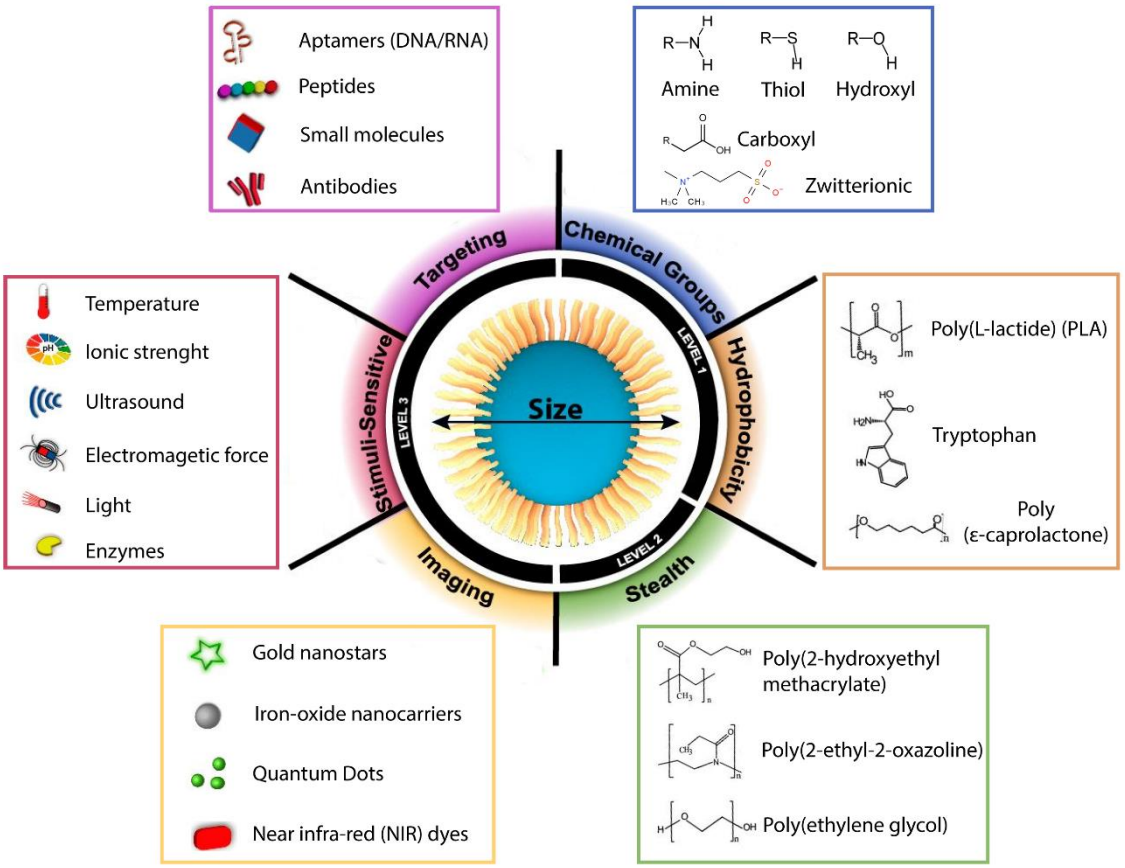

Figure 6. Schematic representation of required physicochemical properties and various levels of multifunctional characteristics that can be imprinted in a single nanoparticle designed for co-delivery of drug-gene combinations. Hydrophobicity, and cationic charge are particularly important to promote drug encapsulation and gene complexation, respectively.

The first level of multifunctionality is correlated with the formulation of nanomaterials with properties that promote complexation of nucleic acids such as positive charge. This level also comprises the physicochemical properties required for simultaneous encapsulation of nucleic acids and antitumoral drugs (e.g., hydrophobic small molecules) [83]. The second level involves the simple modification of nanocarriers surface properties with non-fouling polymers (resistant to protein adsorption), or macromolecules, that ultimately improve blood circulation time and reduce opsonization by phagocytic cells of RES (e.g., macrophages, splenocytes (spleen), kupffer cells (liver)). The third, and more complex level of multifunctionality, includes the introduction of stimuli-responsive properties that allow nanocarriers to react to particular biological/external cues and release their therapeutics in a controlled mode. Also, this level comprises the introduction of one or multiple cell targeting moieties, and the inclusion of drugs-imaging probes for both targeted therapy and imaging - Theranostics. Despite their diversified nature, and these different levels, all the delivery systems must share fundamental properties to deliver nucleic acids or co-deliver different drug-gene combinations. Such features, types of materials used for formulation of delivery systems and their advantages/disadvantages are summarized in Table 4.

Table 4. Summary of the design considerations for gene and drug-gene co-delivery systems.

Nanocarriers design	Technical approach	Parameters to be optimized	Advantages	Disadvantages	Materials
Stealth properties imprinted in nanocarriers	Immobilization of hydrophilic polymers (e.g., PEG) on nanocarriers surface, creating an hydrophilic shell Immobilization of minimalistic "self" peptides to inhibit phagocytosis by the RES system (e.g., hCD47 analogue peptide) [103]	Hydrophilic polymers molecular weight/non-fouling properties Structural organization (linear or branched) Chemical groups (pendant or terminal) Detachable or non-detachable shell Surface density	Confers stability in biological fluids [116] Increases nanocarriers blood circulation by minimizing opsonisation Limits the formation of a protein corona [101] Protects DNA and drugs from enzymatic degradation [102] Hydrophilic shell formed with biocompatible polymers improves nanocarriers biocompatibility (particularly in inorganic delivery systems) [117] Novel classes of hydrophilic polymers are overcoming the issues of previously used materials (PEG) [118] The use of minimal "self" peptides minimizes immune system responses [103] Hydrophilic polymers can be used as anchors for cell targeting moieties in nanocarriers exterior surface [119]	Some PEG-based nanocarriers exhibit accelerated blood clearance phenomena after multiple administrations [120] Hydrophilic shell has shown to limit gene expression due to lower nanocarriers cellular uptake, reduces drug release and transfection (so-termed PEG dilemma) [121, 122]	PEG [123] Poly(2-ethyl-2-Oxazoline) (PEOz) [124] Poly(N-(2-hydroxypropyl) methacrylamide) (pHPMA) [125] Poly(2-hydroxyethyl methacrylate)(PHEMA) [126] Poly (carboxybetaine) [127] Dextran [128]

Table 4. Continued.

Nanocarriers design	Technical approach	Parameters to be optimized	Advantages	Disadvantages	Materials
Nucleic acid condensation or entrapment in nanocarriers	Cationic chemical groups included in nanocarriers structure to establish electrostatic interactions with negatively charged nucleic acids (RNA and DNA) Important differences in the overall surface charge between DNA biomolecules and RNA (less amount of negative charges due to smaller size) must be taken into account since they influence condensation efficiency and particles overall size Nucleic acids can also be loaded in nanocarriers porous structures, aqueous core (e.g., liposomes), or barrel-like structures via host-guest interactions (e.g., Polyrotaxanes) [129]	Localization of the cationic groups in the nanocarriers structure Cationic moieties spatial distribution (linear, hyperbranched, ramified dendrimers) Density of cationic groups in the nanocarriers before and after nucleic acids complexation Polycations molecular weight when cationic polymers are used pKa of cationic groups and protonation in the range of tumor acidic pH /physiological pH Pore size and presence of amine groups influences DNA/RNA entrapment efficiency [130]	Cationic moieties condense negatively charged nucleic acids under mild, or physiological conditions, with high efficiency [131] Effective nucleic acids condensation protects genetic material from endonuclease-mediated degradation [131] Cationic moieties can confer endosomal/lysosomal release of nanocarriers [132] Therapeutics release from nanoparticles can be promoted by events that destabilize nanoparticles cationic zone (counter ions) Nanocarriers pores or aqueous core provide the perfect reservoir for nucleic acids entrapment [133, 134] Nanocarriers pores protect nucleic acids when capped with other macromolecules/polymers [135]	Excessive cationic charge promotes significant *in vitro* and *in vivo* toxicity [136, 137] Excessive cationic charge may affect nucleic acids release and the onset of gene expression/silencing Excess cationic charge may lead to interaction with blood components and haemolysis Excess cationic charge in nanocarriers may lead to the formation of a hard protein corona that changes the physicochemical profile of the nanocarriers	Polyethylenimine (PEI) [138] Poly(2-(dimethylamino) ethyl methacrylate) (PDMAEMA) [139] Chitosan [140] Poly (amidoamine) (PAMAM) dendrimers [141] Poly(L-lysine) (PLL) [123] Mesoporous silica [135]

Table 4. Continued.

Nanocarriers design	Technical approach	Parameters to be optimized	Advantages	Disadvantages	Materials
Encapsulation of small molecule drugs with anticancer activity	Hydrophobic moieties included in nanocarriers structure to establish hydrophobic interactions with poorly water soluble chemotherapeutics Nanocarriers containing porous structure that entraps small molecules (e.g., silica nanocarriers mesopores), suitable for encapsulation of hydrophobic and hydrophilic anticancer compounds Drug encapsulation mediated by supra-molecular host-guest interactions (non-covalent stereoelectronic arrangement, hydrogen bonding or π-π stacking (e.g., observed with cyclodextrin, caliraxene or graphene oxide) [142-144] Covalent linkage of drugs with chemical moieties in nanomaterials structure (e.g., Polymer-drug conjugates) [145]	Method of encapsulation (e.g., water-oil-water (w/o/w) emulsification, solvent evaporation-film hydration, nanoprecipitation, microfluidic-assisted) Amount of drug encapsulated and its correlation with therapeutic dosage in humans Molecular weight of the hydrophobic chain in hydrophobic polymers and crystallinity of the hydrophobic chain (Polymeric nanocarriers) [146] Lipid bilayer rigidity, lipophilic chain size and type (Liposomal nanocarriers) [147] Characteristics inherent to nanoparticles pores such as diameter and overall charge Hydrophobicity or hydrophilicity of the small molecules to be loaded in the nanocarriers Release profile and strategies to reduce burst release	Improves the *in vivo* biodistribution and bioavailability of anticancer drugs Reduces the drug dosage needed to obtain a similar or higher effect to that of free drugs [148] Reduces deleterious side effect of cytotoxic drugs in healthy tissues (Tissue partition) [149] May reduce the Multi Drug Resistance (MDR) phenomenon depending on the MDR-1 inhibition capacity of the nanomaterials that comprise the delivery system (e.g., tocopherol-PEG succinate) [85] Covalent linkage to nanocarriers reduces residual drug release in circulation	Burst release of small molecule drugs in biological environment if the conjugation of materials in the delivery system or its physicochemical properties are not optimal to promote controlled release [150] In nanocarriers with covalently bound drugs without stimuli-responsive linkages a complete release may not be obtained limiting the amount of delivered drug	Poly (ε-caprolactone) (PCL) Poly (L-lactic acid) (PLA) [151] Ter-butyl methacrylate (tBMA) [152] Mesoporous silica [153] Cyclodextrin Graphene oxide (GO)

Table 4. Continued.

Nanocarriers design	Technical approach	Parameters to be optimized	Advantages	Disadvantages	Materials
Targeting ligands	Nanoparticles surface decoration with ligands that endow selectivity towards target cancer cells Various classes of ligands available: • Antibodies (Ab)/ Antibody fragments (fAbs) • Small molecules (e.g., Folic acid, Anisamide, biotin, etc.) • Peptides/Proteins (e.g., Transferrin) Carbohydrate ligands allow selectivity for particular types of cancer cells (e.g., galactose), for targeting to liver cancer cells or Hyaluronic acid for targeting CD44 receptor over-expressed in malignant cells	Density of ligands in nanocarriers surface Chemical bonds or layer-by-layer deposition of ligands in particles surface Spatial orientation of the ligands and its ligand-receptor interactions at the nano-bio interface Selectivity and binding affinity towards target receptor Confirmation of the over-expression of therapeutic target in cancer cells	Targeting ligand decorated nanocarriers can improve therapeutics accumulation in the tumor site and also in cancer cells, thus improving the therapeutic effect Some targeting agents (e.g., antibodies, peptides) also present antitumoral properties Vasculature and tumor penetrating targeting peptides can provide a double targeting to the tumor microenvironment (CRGDKGPDC (iRGD) and CNGRCG (NGR) peptides [154]	Targeted nanocarriers may display a protein corona even if they have non-fouling polymers since the inclusion of the targeting moiety can alter the properties of the delivery system [155] Targeted nanocarriers uptake route can end-up in endosomes/lysosomes that may lead to therapeutics degradation if nanocarriers are unable to promote lysosomal release Generally low tumor penetration Relative inefficacy or available ligands to target metastatic niches and circulating tumor cells (CTCs) [156] Complexity and economic cost of including targeting moieties can impair widespread clinical translation	Folic acid [157] Anisamide [158] Transferrin [159] cRGD [160] Trastuzumab (Herceptin®) [161] Hyaluronic acid [162]

Table 4. Continued.

Nanocarriers design	Technical approach	Parameters to be optimized	Advantages	Disadvantages	Materials
Stimuli responsiveness	Nanocarriers for co-delivery can be engineered to release their nucleic acids and drugs in the target site via response to biological stimuli Stimuli employed strategies to promote on-demand cargo release include those based on: • pH • redox potentials (thiol-disulfide exchange) • temperature • enzymatic degradation • light • ultrasound • magnetic energy Responsiveness can be inherent to nanoparticles structural components or imprinted through additional components such as coatings or incorporation gas-forming agents	In the design of redox-sensitive nanocarriers the different redox pools in the human body should be considered In the design of pH responsive systems the pKa of the stimuli-responsive groups should be chosen according to the environmental pH of the tumor microenvironment or the lysosomal compartments In the design of temperature responsive delivery systems, ideally, the payload should be released at temperatures above 37 °C (Lower critical solution temperature (LCST) above body temperature) [163]	Redox responsive nanocarriers take advantage of the redox potentials of intracellular compartments pH sensitive systems allow drug release in the acidic tumor microenvironment or in lysosomal acidic compartments [131] Enzyme responsive nanocarriers can take advantage of overexpressed enzymes in the tumor microenvironment (e.g., Matrix Metalloproteinase-9 (MMP-9)) [164]	Ultrasound responsive systems should be designed to be biological effective in a temperature range that does not damage exposed tissues Light penetrating capacity across tissues should be considered whenever designing light-responsive nanocarriers	Poly(N-isopropylacrylamide) (PNIPAM) [165] Graphene oxide [166] Inorganic $CaCO_3$ coatings [148]

Table 4. Continued.

Nanocarriers design	Technical approach	Parameters to be optimized	Advantages	Disadvantages	Materials
Medical Imaging	Nanocarriers can be used in medical imaging to identify the tumour/metastasis and study nanocarriers biodistribution Imaging capacity can be inherent to the nanoparticles as for example in: • gold nanoparticles or gold nanoclusters • magnetic nanoparticles • Quantum dots Imaging capacity can also be endowed through different strategies such as inclusion of different imaging agents: • Near infra-red (NIR) dyes • Radioactive compounds • Magnetic resonance imaging (MRI) contrast agents (Gadolinium)	Biocompatibility of the imaging conjugates or imaging loaded nanocarriers must be ensured Effective loading of imaging agents in nanocarriers must be optimized to achieve the best signal-to-noise ratio	Allows simultaneous therapy and imaging of during treatment Allows the detection of residual tumor masses/cells after the treatment has been applied one or more times	Certain quantum dots formulations present toxicity [167] Quantum dots tumor distribution may be heterogeneous [168] Gadolinium-based MRI agents may cause nephrogenic systemic fibrosis [169] Gold nanoclusters complexes may induce acute or prolonged toxicity [170]	Cadmium-Selenide quantum dots (CdSe QDs) [171] Iron oxides (FeO_4) [172] NIR dye - Dy677 [173] Gold nanoparticles [174]

4.1. Materials for assembly of multifunctional nanocarriers designed to co-deliver drug-gene combinations

4.1.1. Inorganic nanomaterials

4.1.1.1. Gold

Gold nanoparticles are attractive candidates to efficiently deliver different bioactive molecules to the desired target. They possess unique chemical and physical characteristics often required for therapeutics delivery [175]. In fact, the gold core of nanoparticles is inert and hydrophobic drugs can be loaded in this system via hydrophobic interactions [176]. The fabrication processes currently described in the literature (e.g., heat-induced, gold salts reduction) allow the manufacture of monodisperse particles with different shapes and tuneable size (from 1 to 150 nm) [175, 176]. Moreover, due to the chemical versatility of gold, the surface of gold nanocarriers can be readily functionalized through thiol linkages, conferring them a high versatility [177]. Also, gold nanoparticles can absorb light in the near infra-red region, which gives them an intrinsic capacity to be applied in theranostic applications or photothermal therapy (PTT) [177]. For drug-gene co-delivery applications, the incorporation of bioactive molecules in gold nanoparticles can be accomplished using two primary strategies, covalent attachment and supramolecular assembly [175, 176, 178]. In the first, the bioactive molecules can be attached onto the gold nanoparticles surface *via* thiol linkages [179]. This approach confers a redox-responsive release of the payload, through a thiol-disulfide exchange or spatial exchange between the gold nanoparticle and intracellular glutathione [180]. On the other side, the supramolecular assembly of gold nanocarriers can provide the establishment of non-covalent interactions between gold nanoparticles and their cargo [180]. These non-covalent interactions include electrostatic forces between nucleic acids negatively charged groups and the positively charged gold surface [181]. Also, gold nanocarriers can be employed in the loading of small chemotherapeutic molecules by adding suitable hydrophobic moieties or polymers to gold nanocarriers surface [180].

The use of gold nanocarriers for co-delivery applications was reported by Xiau and co-workers, which developed multifunctional gold nanorods to simultaneously deliver to neuroendocrine cancer cells the anticancer drug doxorubicin and siRNA directed to silence the achaete-scute complex-like 1 protein (ASCL1) [182]. This co-delivery system also contained the octreotide targeting ligand in order to direct the nanocarriers towards cancer cells that overexpress somatostatin receptors. In order to promote the loading of these two different molecules, methyl thioglycolate (MTG) and thioglycolic acid (TGA) were first conjugated onto gold nanorods surface via thiol coupling. Subsequently, doxorubicin was conjugated onto gold nanorods surface MTG linker *via* the pH sensitive hydrazone bond. siRNA was complexed onto cationic polyarginine segments previously conjugated with TGA linker.

This multifunctional delivery system exhibited an efficient gene silencing and a significant anti-proliferative activity [182].

4.1.1.2. Silica

Mesoporous silica nanoparticles (MSNs) are highly versatile delivery platforms because they present a large surface area and pore volume, tunable pore size, shape and straightforward surface functionalization via chemical modification (e.g., amine coupling, thiol coupling) [183]. Furthermore, silica-based nanocarriers are highly resistant to heat, acidic and basic pH, mechanical stress and hydrolysis induced degradation, properties which render them suitable candidates for drug and nucleic acid delivery [184]. Bioactive molecules incorporation into the silica matrix can occur via adsorption into MSNs pores, chemical linkage in pores, or surface grafting [183, 184]. The incorporation of bioactive molecules into the silica matrix is the most commonly used methodology to load therapeutics in these nanocarriers. The biomolecules can be adsorbed into MSNs pores due to hydrophobic or electrostatic interactions with negatively charged MSNs inner surface [148]. The extent of adsorption can be modulated by introducing functional groups (amine, thiol, etc.) in silica nanocarriers pores, or surface to create additional interactions [183]. Furthermore, MSNs surface can be functionalized to allow bioactive molecules or polymers adsorption, such versatility opens the possibility to add cell targeting molecules [185]. By taking advantage of this nanomaterial as a template Zhu and co-workers prepared ferromagnetic hollow mesoporous silica nanoparticles (HMSNs) coated with poly(L-lysine) (PLL) with the objective to co-deliver drugs and nucleic acids [186]. Fluorescein and cytosine-phosphodiester-guanine oligodeoxynucleotide (CpG ODN) were used as the model hydrophobic molecule and as the model nucleic acids, respectively. Fluorescein was internalized into the hollow HMSNs internal core via hydrogen bonding. The, CpG ODN was electrostatically incorporated into PLL the cationic external layer. The resulting system presented sizes in the range of 400 nm and positive zeta potential (+ 8.4 mV). In addition, the system was assembled via layer-by-layer to allow α-chymotrypsin-mediated release of the drug and gene payloads. In addition these HMSNs nanocarriers also combine the conjugation of enzyme-responsive release with the possibility for magnetic targeting to the desired site via externally applied magnetic fields.

In another approach, Meng and co-workers developed polyethylenimine-poly(ethylene glycol) (PEI-PEG) coated MSNs to simultaneously deliver doxorubicin and P-glycoprotein (P-gp) targeted siRNA to human breast cancer xenografts [187]. In this approach, doxorubicin was adsorbed into silica mesopores and siRNA was condensed in the PEI layer via electrostatic interaction. The initial screening tests confirmed the synergistic effect of the doxorubicin/siRNA combination in drug resistant human breast cancer cells. Moreover, the intravenous delivery to multidrug resistant MCF-7 tumors resulted in an enhanced inhibition of tumor growth when compared to free doxorubicin or the carrier loaded with either drug or siRNA alone. Interestingly, a heterogeneous P-gp knockdown was observed in the tumor volume. This

resulted in a higher accumulation of Dox in cells with lower P-gp expression. Similarly, Ma and co-workers developed folic acid targeted HMSNs coated with PEI to co-deliver doxorubicin and B-cell lymphoma (Bcl-2) siRNA to cancer cells [188]. The anticancer drug was encapsulated in the hollow internal core and the PEI external layer allowed the siRNA binding through electrostatic interactions. The *in vitro* studies conducted in cancer cells with low and high expression of the folic acid receptor, MCF-7 and HeLa respectively, showed preferential accumulation, via folic acid receptor mediated endocytosis, in HeLa cells. Furthermore, the combinatorial delivery efficiently silenced the Bcl-2 expression in HeLa cells, which enhanced the doxorubicin cytotoxic effect.

4.1.1.3. Carbon

Carbon based nanomaterials are comprised by low dimensional sp^2 carbon and exhibit unique physicochemical properties [189]. Between the different carbon based materials, graphene has gained a significant interest for application in biomedical applications such as drug delivery. Graphene is an atom thick monolayer of carbon atoms arranged in a two dimensional honeycomb structure [190]. Graphene oxide (GO), an oxidized derivative of graphene, has been widely used due to its facile synthesis, high water solubility, colloidal stability, high surface-to-volume ratio, high drug loading capacity and NIR emission, as well as, potential to be used for PTT [190]. The incorporation of bioactive molecules in these structures can be accomplished by π−π stacking interactions between the carbon rings of graphene oxide and the bioactive molecule aromatic rings, by hydrophobic interactions or chemical linkage [191]. Using this nanomaterial, Hu and co-workers developed a nanoscale GO delivery system, which was modified with folate conjugated trimethyl chitosan to simultaneously load doxorubicin and pDNA [192]. The resulting system exhibited a size of 112 nm, was positively charged (+30.9 mV), and was efficiently internalized via folate receptor mediated endocytosis. Furthermore, chitosan modified GO efficiently loaded both doxorubicin and pDNA. Doxorubicin was incorporated into the system via π−π stacking interactions between the drug and GO sheets. In addition, pDNA was condensed into the system via electrostatic interaction with the positively charged chitosan polymer backbone. In a similar approach, Zhi and co-workers developed a GO based nanocomplex for co-delivery of doxorubicin and miR-21 targeted siRNA to drug resistant breast cancer cells [193]. During the design of the multifunctional delivery system, PEI and poly(sodium 4-styrenesulfonates) (PSS) were adsorbed to graphene oxide by a layer-by-layer method. The loading of the anticancer drug was once again promoted by π−π stacking interactions between the drug aromatic rings and GO. The loading of miR-21-siRNA nucleotides was promoted via electrostatic complexation with the PEI layer in a similar way to the previous example. The results showed that the produced carrier was capable to efficiently silence miR-21 and enhance drug accumulation in doxorubicin-resistant breast cancer cells. This improved accumulation and drug-gene co-delivery resulted in an enhanced therapeutic effect.

In another report using GO-based materials, Yang and co-workers developed a PAMAM dendrimer and gadolinium functionalized GO multifunctional carriers for combinatorial delivery to human glioblastoma (U87) cells. This multifunctional delivery system was comprised by epirubicin (antitumoral drug), Let-7g-miRNA, and gadolinium for MRI imaging [194]. The gadolinium and the PAMAM dendrimer were chemically conjugated with graphene originating a nanosized system (150 nm) with a highly positive surface charge (+ 50 mV). The subsequent drug and miRNA loading occurred by a step-wise electrostatic interaction, the initial adsorption of Let-7g miRNA onto the graphene based system led to a switch on the surface charge from positive to negative values(- 18 mV). Afterwards, the adsorption of positively charged epirubicin resulted in a second charge reversal to positive values (+33 mV). This co-delivery approach resulted in an enhanced cytotoxicity to human glioblastoma U87 cell line. Furthermore, *in vivo* monitoring via MRI revealed that the carriers crossed the blood-brain barrier with the assistance of focused ultrasound and allowed the quantification of drug/miRNA delivered in real-time [194].

4.1.2. Lipid based nanomaterials

4.1.2.1. Liposomes

Liposomes were the first delivery system approved by the EMA and US-FDA for cancer treatment [195]. Liposomes can present diverse structures and compositions, but in general these systems are closed spherical vesicles comprised by a membrane-like lipid bilayer and an aqueous core compartment [196]. Such vesicles can be organized in single or multiple concentric bilayers [196]. Moreover, natural or synthetic lipids can be used to originate the lipidic bilayers [197]. This inner aqueous core and lipid external bilayer organization makes liposomes suitable to simultaneously transport drugs and genes [198]. The bioactive molecules can be accommodated in the aqueous nucleus, inside the lipidic bilayer or conjugated/adsorbed in liposomes surface [198].

By taking advantage of these materials Qu and co-workers formulated a liposome-based system to promote the co-delivery of Bcl-2 siRNA and docetaxel to lung cancer models [199]. The liposomal carriers were comprised by 1,2-dipalmitoyl-sn-glycero-3-phosphocholine (DPPC), 1,2-distearoyl-sn-glycero-3-phosphoethanolamine-N-methoxy poly(ethylene glycol) (DSPE–mPEG 2000), cholesterol and dimethyldioctadecyl-ammonium bromide (DOAB). Docetaxel was incorporated within the lipidic bilayer and siRNA was complexed in the cationic liposomal surface provided by DSPE. The resulting dual-loaded nanocarriers (~165 nm, + 13mV), presented a sustained payload release and were capable to efficiently inhibit human lung cancer A549 and H226 cell lines proliferation. Moreover, *in vivo* studies in A549 tumor xenograft models showed that combinatorial drug-gene delivery reduced the tumor volume significantly, with injected mice presenting a survival rate of 100 % at 21 days following injection [199].

In another report, Zhang and co-workers developed a pH-responsive liposomal system to simultaneously deliver antagomir-10b (mir-10b) and Paclitaxel for the treatment of murine metastatic mammary tumor models [200]. The liposomal carriers were comprised by DSPE-PEG_{2000}-[D]-H_6L_9. The histidine-lysine peptide ([D] -H_6L_9) is a pH responsive antimicrobial peptide and was tethered into the surface of liposomes. In this system, paclitaxel was incorporated in the interior of the lipidic bilayer and the antagomir-10b was complexed with liposome cationic surface. *In vitro* experiments revealed that the protonation of [D]-H_6L_9 in acidic pH helped the endosomal escape and promoted the release of drug and gene payloads. Moreover, *in vitro* and *in vivo* studies confirmed the silencing of mir-10b, which in combination with paclitaxel efficiently delayed tumor growth and impaired the formation of metastatic niches. Also using liposomes, Peng and co-workers developed multifunctional thermosensitive-magnetic-cationic liposomes loaded with doxorubicin and shRNA for silencing of "special AT-rich sequence binding protein 1" (SATB1), as a nanocarrier for gastric cancer treatment [201]. Cholesterol, 1,2-Dipalmitoyl-sn-glycero-3-phosphocholine (DPPC), 3ß-[N-(N',N'-dimethylaminoethane)-carbamoyl] cholesterol (DCChol) and DOAB were used to produce thermosensitive liposomes. Magnetic fluid, Fe_3O_4, was encapsulated with ammonium sulphate buffer. Subsequently, doxorubicin was encapsulated by using the ammonium sulphate gradient method. Finally, the pGFP-SATB1-shRNA plasmid vector was incorporated in the liposome due to electrostatic interactions between the cationic lipids and plasmid DNA. The developed system showed a more pronounced drug release at 42 ºC in comparison to that obtained at 37 ºC. Also, the studies revealed that the developed liposomes improved the delivery efficiency due to magnetic field guidance. The combinatorial delivery promoted an inhibition of gastric cancers cell growth *in vitro* and in gastric cancer xenografts *in vivo*, when compared to single delivery.

4.1.2.2. Lipid-polymer hybrids

Lipid-polymer hybrid nanocarriers (LPNs) have been developed to address the limitations of polymeric nanoparticles and liposomes [202]. Commonly, LPNs structure is comprised by a polymer core a lipid envelope and an external lipid-PEG layer [203]. These three components imprint in LPNs characteristics of polymeric nanoparticles and of liposomes simultaneously [202]. The polymer core confers to the particle a high structural integrity, stability during storage and is the main reservoir to encapsulate bioactive molecules [202].The lipid envelope and the lipid-PEG layer are responsible for LPNs high biocompatibility and bioavailability. These lipids also function as a barrier that minimizes residual cargo leakage, enabling a more sustained release profile [203]. The incorporation of bioactive molecules in lipid-polymers hybrids can occur by conjugation with the polymer or lipid-based layers [203]. This conjugation can occur before or after layers formation by electrostatic, hydrophobic, or covalent interactions [202, 203]. Alternatively, the bioactive molecules can also be adsorbed or tethered in the external face of the lipid envelop [202].

Taking advantage of these hybrid systems, Zhao and co-workers developed a lipid-polymer carrier for a combinatorial delivery of siRNA for hypoxia-inducible factor 1-alpha (HIF1-α) and gemcitabine, in order to eliminate pancreatic cancer cells [204]. The produced nanocarriers were comprised by a cationic block co-polymer core of mPEG-PLGA/PVA/PLL and a PEGylated lipid bilayer shell containing lecithin, DSPE-mPEG-2000, and cholesterol. The incorporation of bioactive molecules (both drug and siRNA) occurred prior to lipid layer formation. Gemcitabine was encapsulated into co-polymers hydrophilic core, while the negatively charged siRNA was adsorbed in the PLL layer. The PEGylated lipid shell that encapsulated gemcitabine-siRNA nanocarriers decreased drug leakage and siRNA degradation, and at the same time, increased the circulation time in the bloodstream. The *in vitro* and *in vivo* assays showed that the lipid-polymer hybrid system efficiently suppressed HIF1-α expression, which in turn originated an enhanced antitumoral effect. In particular, the *in vivo* assays showed that the tumor volume growth during time was greatly reduced. Moreover, it was also observed an enhanced capacity to inhibit tumor metastasis in an orthotropic tumor model of pancreatic cancer.

4.1.3. Natural and semi-synthetic nanomaterials

4.1.3.1. Chitosan

Chitosan is a semi-synthetic material obtained by deacetylation of chitin and is comprised by D-glucosamine and N-acetyl-D-glucosamine monomers linked through β (1,4) glycosidic bonds. This semi-synthetic polymer is biocompatible, relatively hydrophilic, biodegradable and non-immunogenic [205]. Moreover, it also possesses anti-microbial activity and offers easy functionalization or modification through its hydroxyl (-OH) and amine (-NH2) functional groups [205, 206]. Due to these characteristics chitosan-based materials have been extensively investigated to produce microspheres and nanoparticles for delivery of numerous bioactive agents including: (i) drugs [207]; (ii) peptides [208]; (iii) enzymes [209]; (iv) proteins [210]; (v) nucleic acids [53]; and (vi) antigens [211]. For gene delivery applications chitosan is generally used to condense nucleic acids via electrostatic interactions between its amine residues and the negatively charged phosphate groups of nucleic acids [131]. To encapsulate poorly-soluble compounds (e.g., chemotherapeutics), hydrophobic interactions between chitosan-based materials and the compound of interest must be established. To accomplish this encapsulation chitosan is generally modified with hydrophobic moieties (Deoxycholic acid [207]) or other polymers that may confer an amphiphilic character to the final material [212]. The simultaneous encapsulation of nucleic acids and chemotherapeutics in chitosan-based nanoparticles is generally performed in a two-step process. Initially, chitosan-nanocarriers loaded with chemotherapeutics are formulated through hydrophobic interactions. Next, drug loaded chitosan nanoparticles are complexed with nucleic acids via electrostatic interactions. To aid in the formulation and stabilization of chitosan-based nanocarriers the polymer chains can be further cross-linked either through covalent linkage or counterion molecules [213]. Moreover, other molecules can also be conjugated to chitosan to increase its transfection

efficiency (e.g., PEI [214]), selectivity towards cancer cells (e.g., folic acid [215]), or blood circulation time (e.g., PEG [216]).

By taking advantage of this material, Bao and co-workers developed chitosan-based nanoparticles for the co-delivery of candesartan and p53-wt plasmid DNA for anti-angiogenesis cancer therapy [214]. For this purpose the authors modified chitosan backbone with a branched polyethylenimine (bPEI)-candesartan conjugate. The rationale behind this modification was to increase chitosan nanoparticles transfection efficiency, buffering capacity and selectivity towards pancreatic cancer cells. *In vitro* studies confirmed the endosomal escaping capacity of the developed nanoparticles. *In vivo*, the co-delivery of candesartan and the wild type tumor suppressor p53 in chitosan-based nanoparticles promoted the highest reduction in tumor volume and the highest inhibition of angiogenesis in pancreatic tumor-bearing mice. Finally, the inclusion of candesartan was also a valuable addition in what concerns cell selectivity, since its inclusion increased the accumulation of the chitosan-based particles in the tumor. In another approach, Wei and co-workers modified chitosan with glycidyltrimethylammonium chloride to synthesize N-[(2-hydroxy-3-trimethylammonium) propyl] chitosan chloride [217]. This novel derivate was then used to formulate nanoparticles for co-delivery of siRNA for mouse telomerase reverse transcriptase (mTERT) and paclitaxel. This modification promoted an increase in chitosan nanoparticles transfection efficiency and oral bioavailability. The authors also verified that chitosan-based nanoparticles had an endosomal escaping capacity, a factor which is highly important for the overall therapeutic effect. *In vivo* it was verified that the co-delivery of both therapeutics by chitosan-based nanoparticles promoted the highest: (i) downregulation of mTERT, (ii) reduction of telomerase activity, and (iii) accumulation of siRNA and paclitaxel in the tumor. The co-delivery of siRNA mTERT and paclitaxel through chitosan-modified nanoparticles promoted the highest antitumoral effect in comparison to single therapy.

4.1.3.2. Alginate

Alginate is a natural anionic polysaccharide comprised by alternating repeated residues of D-mannuronate and L-guluronate joined with ß(1,4) linkages [218]. This natural polymer is biocompatible, biodegradable, non-immunogenic and presents mucoadhesive properties [219]. Alginate can be easily modified through its carboxyl (-COOH) and hydroxyl (-OH) functional groups. These characteristics account for the widespread use of alginate-based materials for nanoparticles assembly [220]. The first mechanism for particles formulation is based on the complexation of negatively charged alginate and nucleic acids with polycations (e.g., chitosan, PEI) by electrostatic interactions [221]. Alginate-based nanoparticles for gene delivery can be also be prepared through ionic crosslinking between alginate and divalent ions (e.g., Ca^{2+}, Mg^{2+}) [222]. By using this biomaterial, Caffagi and co-workers formulated cisplatin-loaded alginate nanocarriers *via* polyelectrolyte condensation by using chitosan as the cationic moiety [223]. For the co-delivery of drug and genes to tumor cells, Zhao and co-workers recently optimized

the assembly of alginate/calcium carbonate hybrid nanoparticles [224]. In a subsequent work the same group employed the optimized system for the co-delivery of p53-expressing pDNA and doxorubicin [225]. It was observed that the simultaneous delivery of both therapeutic agents would promote a higher anti-proliferative effect in comparison to the delivery of a single therapeutic agent.

4.1.3.2. Dextran

Dextran is a polysaccharide comprised by D-glucopyranose repeating units linked through glycosidic linkages [226]. Dextran is biocompatible, biodegradable, presents anti-thrombotic and anti-inflammatory properties [227]. Dextran functional hydroxyl groups (-OH) offer an easy anchoring point for chemical conjugation with other materials. As an example, dextran can be modified with hydrophobic moieties in order to form dextran-based amphiphiles. These amphiphilic derivates can then encapsulate poorly water soluble chemotherapeutics through hydrophobic interactions and self-assemble into nanocarriers in aqueous solution [228]. Using this approach, Anitha and co-workers developed curcumin loaded nanoparticles through polyelectrolyte complexation between negatively charged dextran-sulfate and positively charged chitosan [229]. For gene delivery purposes, dextran based gene delivery systems can be formulated through electrostatic interactions between dextran-polycation chemical conjugates/mixtures and nucleic acids. Using this simple strategy, Jiang and co-workers, formulated nanoparticles for nucleic acid delivery using dextran-PEI and dextran-spermine conjugates, respectively [230]. In the context of multifunctional carriers for co-delivery, Sun and co-workers prepared Dextran-based nanoparticles for the co-administration of a drug-gene combination [231]. Such was possible through the chemical conjugation of PEI and doxorubicin into dextran, followed by complexation of this hybrid polymer with pDNA. *In vitro* results demonstrated that these nanoparticles promoted exogenous gene expression, as well as, cytotoxicity in cancer cells.

4.1.3.3. Hyaluronic acid (hyaluronan)

Hyaluronic acid (HA) is a natural, anionic, linear, polysaccharide composed by alternating units of β(1,4) linked D-glucuronic acid and β(1,3) N-acetyl-D-glucosamine [232]. Hyaluronic acid is described as being biocompatible, biodegradable and non-immunogenic [232, 233], as well as being present in various tissues where it participates in different signaling cascades through interaction with its cluster of differentiation 44 (CD44) receptor [234]. The signaling cascade occurs when HA binds to a CD44 variant (CD44v), a CD44 isoform that is constitutively activated and has high affinity to this polysaccharide [234, 235]. CD44v is over-expressed by cancer cells and therefore targeting this receptor using HA is a promising strategy do direct nanocarriers to cancer cells [235]. The potential of HA for targeting cancer cells and the ease of chemical modification through its chemical groups (-OH and -COOH) contribute to its widespread use in the formulation of nanocarriers for cancer therapy. Hyaluronan based nanoparticles for gene delivery can be prepared through polyelectrolyte complexation [236, 237]. The nanoparticle

assembly is mainly mediated by electrostatic interactions between negatively charged components (hyaluronic acid and nucleic acids) plus polycations (e.g., chitosan, PEI). Alternatively, hyaluronic acid can be covalently modified with polycations to formulate nanocarriers for gene delivery [238]. Hyaluronic acid can also be used in the formulation of drug delivery systems. For this end, hyaluronic acid based drug-loaded nanoparticles can be prepared by polyelectrolyte complexation [239]. Alternatively, hyaluronan can be covalently modified with hydrophobic moieties to form self-assembled nanocarriers capable of drug loading [240].

Taking the former properties into account, Deng and co-workers investigated the use of HA for co-delivery by formulating HA-chitosan nanoparticles for encapsulation of doxorubicin and miR-34a [162]. *In vitro* results demonstrated that HA-based nanocarriers significantly enhanced doxorubicin and miR-34a accumulation in cancer cells. Moreover, nanocarriers mediated delivery of miR-34a biopharmaceuticals resulted in a down-regulation of Bcl-2 anti-apoptotic protein expression, thus indicating a successful delivery and release of therapeutic miRNA. The *in vitro* co-delivery of this drug-gene combination also resulted in an improved cytotoxicity towards cancer cells and decreased cancer cells migration. Furthermore, *in vivo* results showed that the dual loaded hyaluronan-based nanocarriers accomplish the highest antitumoral effect in comparison to single loaded formulations. Such promising results corroborate the use of this biopolymer for targeted co-delivery of drug-gene combinations. In addition, Han and co-workers modified hyaluronan with a PAMAM dendrimer (Generation 5) to promote drug-nucleic acids co-delivery [241]. This modified polymer was then used to formulate nanocarriers loaded with doxorubicin and Major Vault Protein (MVP) siRNA. The results obtained in this study indicate that the co-delivery of therapeutics promoted a higher drug accumulation in the nucleus of doxorubicin-resistant breast cancer cells (MCF-7/ADR). It was also verified that co-delivery sensitized drug resistant cancer cells to the action of doxorubicin and promoted a higher cytotoxic effect. Preliminary *in vivo* results demonstrated that HA-PAMAM nanoparticles could enhance doxorubicin accumulation in the tumor site and increase anticancer drug bioavailability as well.

4.1.3.4. Cyclodextrins

Cyclodextrins are semi-natural cyclic oligosaccharides comprised by D-glucopyranose units linked through α(1,4) glycosidic bonds [242]. This cyclic compound is biocompatible, non-toxic, non-immunogenic and can be chemically modified through its hydroxyl groups (-OH) [242]. Cyclodextrins have a unique “barrel”-like structure comprised by a hydrophilic outer surface and an hydrophobic inner cavity [243]. This inner cavity can accommodate some molecules such as chemotherapeutics, polymers and small molecules through the so-termed host-guest interactions [244]. For these reasons cyclodextrins have been widely used for the formulation of supramolecular delivery systems [245].

Cyclodextrin-based nanoparticles for gene delivery can be prepared by using negatively charged cyclodextrin derivatives or by using cationic modified cyclodextrins. In this context, Teijeiro-Osorio and co-workers, developed negatively charged cyclodextrin derivatives (sulfobutyl ether-ß-cyclodextrin and carboximethyl-ß-cyclodextrin) in combination with a polycation and an ionic crosslinker to prepare nanoparticles for gene delivery [246]. Alternatively, cyclodextrins can be covalently modified with polycations for the formulation of gene delivery systems through electrostatic interactions [247]. For drug delivery purposes, cyclodextrin-based drug delivery systems are prepared using modified cyclodextrin polymers or through host guest interactions. Regarding the use of this material for co-delivery, Zhang and co-workers prepared nanoparticles through the host-guest interaction between a ß-cyclodextrin-cationic polymer (bPEI) conjugate (host) and a hydrophobic polymer, poly(ß-benzyl L-aspartate) (PBLA), containing benzyl groups (guest) [248]. These supramolecular core-shell nanoassemblies were capable of encapsulating poorly water-soluble drugs (dexamethasone) through hydrophobic interactions between the drug and the hydrophobic barrel core. In addition, this report also showed the capacity of these supramolecular nanocarriers to complex pDNA through interactions with the cationic nanoparticle shell. In a different approach Fan and co-workers formulated nanocarriers based on the assembly of PEI-cyclodextrin conjugate (host) with adamantane-doxorubicin conjugate (guest) [249]. Nucleic acids were further complexed in this system through electrostatic attraction with adamantine residues, resulting in a nanoplatform for the co-delivery of doxorubicin and a plasmid encoding for TNF-related apoptosis-inducing ligand (TRAIL) protein. *In vitro* it was demonstrated that nanoparticles increased TRAIL protein expression and that the co-delivery of both therapeutics promoted the highest cytotoxicity in cancer cells. Nanocarriers-mediated co-delivery of doxorubicin and pTRAIL to *in vivo* tumors resulted in the highest antitumoral effect in comparison to single administration of the bioactive molecules., Hu and co-workers, using a similar cyclodextrin-based system but for the co-delivery of adamantine-Paclitaxel and plasmid encoding to survivin shRNA, demonstrated *in vitro* that the co-delivery of those therapeutics yielded the highest decrease in survivin and Bcl-2 expression [250]. Cytotoxic assays revealed that the co-delivery of the drug-gene combination mediated by the nanodelivery system promoted a higher cytotoxic effect. Additional antitumoral assays *in vivo* also demonstrated that the co-delivery of paclitaxel and plasmid encoding survivin shRNA promotes the highest reduction in tumor growth and weight.

4.1.3.5. Polyamino acids

Polyamino acid-based nanocarriers are generally comprised by a conjugation of polyamino acids with different properties and depending on the hydrophobicity/hydrophilicity of its constituents they can originate nanosized micelles, vesicles or solid nanoparticles [251]. Polyamino-acids such as poly(glutamic acid), poly(aspartic acid) or PLL have been widely used because of their biodegradability, biocompatibility and wide number of side functional groups (-OH, -NH_2) [252, 253]. The loading of different bioactive molecules in the polyamino acid based carriers can be promoted by hydrophobic or electrostatic interactions, hydrogen bonds, ion

coordination or by direct chemical grafting (e.g., polymer drug-conjugates) [252]. The possibility to create a wide range of interactions supports the encapsulation of both hydrophobic and/or hydrophilic compounds with high efficiency [251, 252]. Using this class of materials Zheng and co-workers produced cationic micelles comprised by a triblock copolymer of poly(ethylene glycol)-b-poly(L-lysine)-b-poly(L-leucine) (PEG-PLL-PLLeu) to simultaneously deliver docetaxel and Bcl-2 siRNA to MCF-7 human breast cancer cells [123]. Docetaxel was encapsulated in PLLeu hydrophobic core, and siRNA complexed with the PLL cationic layer, whilst PEG conferred a stealth character to the system. The performed *in vitro* assays showed that these micelles were capable of being internalized by MCF-7 cells and deliver both docetaxel and siRNA. Such resulted in the reduction of Bcl-2 expression and in an improved cytotoxic effect. Moreover, *in vivo* studies performed in MCF-7 xenograft tumor models revealed that this combinatorial therapy promoted a decrease in Bcl-2 expression and reduced tumor volume along time. Alternatively, Liu and colleagues employed a T7 peptide targeted PLL-dendrigraft modified with glutamic acid to deliver both doxorubicin and pORF-hTRAIL to glioma cell models [254]. Dox was loaded on the surface of the poly(L-lysine) dendrigraft using the glutamic acid as a pH sensitive linker, on the other side pORF-hTRAIL was encapsulated in the core of the dendrigraft. The *in vitro* and *in vivo* data showed that T7 affinity to transferrin receptors enhanced the cellular internalization and tumor accumulation. The obtained results demonstrate that when compared with stand-alone therapy with doxorubicin or TRAIL, the drug/pORF-hTRAIL combinatorial therapy achieved a significantly improved therapeutic effect, which was corroborated by the delayed tumor progression and prolonged survival time of tumor-bearing mice.

4.1.4. Synthetic nanomaterials

4.1.4.1. Poly (ε-caprolactone)

Poly (ε-caprolactone) (PCL) is an aliphatic, semi-crystalline, polyester composed by repeating units of hexanoate [255]. This material is biocompatible, biodegradable and presents good mechanical properties [256], having a broad application in tissue engineering. PCL can be conjugated with different materials via direct chemical linkage through hydroxyl groups (-OH), or by chain-growth polymerization. This versatility allows to imprint new physicochemical properties in this material (e.g., amphiphilicity, stimuli-responsiveness) and widens its applications, thus making it one of the most explored materials also for nanomedicine [256].

For the particular formulation of nanocarriers PCL is usually modified with hydrophilic polymers forming amphiphilic bock copolymers that, under specific conditions, self-assemble into nano-sized systems. Amongst the hydrophilic polymers that can be explored, those that are “stealth”-like and/or cationic have gathered attention due to the advantageous properties that they confer. Xin and co-workers synthetized PCL-based nanoparticles for drug delivery by using a combination of methoxy poly(ethylene glycol) (mPEG) modified PCL (PEG-PCL) [257]. During nanoparticle preparation by O/W emulsion/solvent evaporation, the drug loading was promoted

by hydrophobic interactions between the nanocarriers PCL hydrophobic core and the poorly soluble anticancer drug paclitaxel.

PCL based nanocarriers can also be used for nucleic acids delivery, yet to effectively perform this function additional modifications are required. For this purpose, PCL is commonly conjugated with cationic polymers/small molecules and with "stealth"-like polymers that confer both the necessary chemical groups for nucleic acids condensation and the non-fouling properties required for systemic *in vivo* administration. Moreover, this hydrophobic block also improves the overall biological performance of the gene delivery system as it may shield the residual positive charge of the system. Lin and co-workers formulated PCL-based gene delivery nanoparticles using a triblock copolymer of mPEG, PCL and PDMAEMA [258]. Other PCL-based triblock copolymers with similar functions such as mPEG-PCL-PEI [259] or PHEMA-PDMAEMA-PCL have also been employed for the same purpose [260].

For the co-delivery of drugs and genes, PCL-based nanoparticles are frequently prepared using PCL triblock copolymers similar to those formerly described [261, 262]. Shi and co-workers prepared PCL-based nanoparticles for the co-delivery of doxorubicin and survivin T34A (dominant negative mutant) pDNA using mPEG–PCL–PEI triblock copolymer [261]. *In vitro* results demonstrated that the delivery of doxorubicin and pDNA promotes an enhanced therapeutic effect. *In vivo* assays showed that the co-delivery of both pharmaceuticals achieves the highest reduction in tumor growth and the highest reduction in metastatic nodules. In another report, Sun and co-workers formulated nanoparticles for the co-delivery of paclitaxel and polo-like kinase 1 (Plk1) siRNA using PEG-PCL-poly(2-aminoethylethylene phosphate) (PPEEA) triblock copolymer [262]. *In vitro* data corroborated the concept that PPEEA triblock nanocarriers mediated co-delivery of both pharmaceuticals, enhances their accumulation in cancer cells and elicits the highest cytotoxicity in comparison to administration of single therapeutics. *In vivo* studies revealed that the dual loaded nanocarriers accumulate in tumor tissues, and that the dual-loaded drug-nucleic acids are effectively delivered to tumor cells. The anticancer effect of drug-siRNA co-delivery nanocarriers was superior when compared to that of the separate administration of each therapeutic either in nanoparticles, or as free agents, thus supporting the added benefit of simultaneous delivery. Xiong and co-workers employed the mixed micelle concept to formulate dual targeted PCL-based nanoparticles to co-deliver doxorubicin and P-gp siRNA for drug resistant breast cancer therapy [173]. For this purpose they synthetized a PEG-PCL based co-polymer in which the PCL segment had a pendant group for further modification. This polymer was then modified with a short-cationic segment to provide a site for siRNA complexation or conjugated with doxorubicin by using a pH sensitive linker. Moreover, the hydrophilic segment of PEG-PCL-cationic PEG-PCL-DOX polymers was further modified with cell penetrating peptide GRKKRRQRRRPQ (TAT) and doubly cyclized α5β3 integrin targeting peptide KACDCRGDCFCG (RGD4C), respectively. *In vitro* it was verified that the dual targeted nanoparticles promoted the highest intracellular accumulation of doxorubicin and siRNA.

Moreover, through fluorescent imaging it was observed that the dual targeted nanoparticles containing those therapeutics mediated the highest intracellular uptake and nuclear accumulation of doxorubicin. Accordingly, the cytotoxicity promoted by the dual targeted co-delivery micelles in drug-resistant cells was the highest.

4.1.4.2. Polymers of Lactic acid and Lactic-co-glycolic acid

Poly(lactic acid) (PLA) and poly(D,L-lactic-co-glycolic acid) (PLGA) are synthetic polymers composed by repeating units of lactic acid and lactic/glycolic acid, respectively. These polymers are biocompatible and biodegradable [263]. Numerous biomedical solutions containing PLA and PLGA are approved by US-FDA and EMA [264, 265], therefore confirming the potential and benefits of these polyesters for biomedical applications.

Lactide-based materials are one of the most employed to formulate nanoparticles for drug delivery. For this purpose the most common strategy is to modify PLA and PLGA with hydrophilic polymers such as PEG-derivatives [85, 266, 267], forming amphiphilic diblock co-polymers that assemble into nanosized carriers in aqueous solution. During the assembly process PLA/PLGA-based nanoparticles hydrophobic core encapsulates poorly-soluble anticancer drugs. Triblock copolymers containing lactide-based polymers are also used to prepared nanoparticles for drug delivery [268-270]. Alternatively drugs can also be conjugated to lactide-based amphiphilic materials to prepare nanoparticles for drug delivery [150, 271].

Lactide-based nanoparticles can also be employed in gene delivery. For this purpose lactide-based nanoparticles containing a hybrid matrix composed by PLA (or PLGA) and polycations such as PEI, chitosan or PDMAEMA can be used to formulate gene delivery systems [272, 273]. Similar to other types of nanoparticles, in these conjugates nucleic acids encapsulation is also mediated by electrostatic interactions. Alternatively, lactide-based polymers can be conjugated with polycations to produce cationic amphiphiles capable of delivering genes [274-276]. Moreover, other hydrophilic polymers can be included in polycation-lactide based materials to produce nanoparticles for gene delivery [277-279]. Lactide-based drug-gene co-delivery systems can be prepared using nanoparticles that contain hydrophobic and cationic moieties [139, 280, 281]. In this context, Quian and co-workers reported the dual-loading of miR-21 inhibitor and doxorubicin in star-branched PLA-b-PDMAEMA copolymers for treatment of glioma. The resulting micellar carriers were less toxic than PEI 25 kDa, promoted lysosomal release and promoted a higher accumulation of doxorubicin in the nucleus of LN299 glioma cells in 2D *in vitro* cultures. Moreover, *in vivo* data obtained from glioma tumor-bearing mice revealed that dual delivery of doxorubicin/miR-21 elicited the highest reduction in tumor volume [139].

References

1. Gaspar, V.M., Maia, C.J., Queiroz, J.A., Pichon, C., Correia, I.J., and Sousa, F., *Improved Minicircle DNA Biosynthesis for Gene Therapy Applications.* Human Gene Therapy Methods, 2014. **25**(2): p. 93-105.
2. Yin, H., Kanasty, R.L., Eltoukhy, A.A., Vegas, A.J., Dorkin, J.R., and Anderson, D.G., *Non-viral vectors for gene-based therapy.* Nature Reviews Genetics, 2014. **15**(8): p. 541-555.
3. Gill, D.R., Pringle, I.A., and Hyde, S.C., *Progress and Prospects: The design and production of plasmid vectors.* Gene Therapy, 2009. **16**(2): p. 165-171.
4. Scholz, C. and Wagner, E., *Therapeutic plasmid DNA versus siRNA delivery: Common and different tasks for synthetic carriers.* Journal of Controlled Release, 2012. **161**(2): p. 554-565.
5. Chang Kang, H. and Bae, Y.H., *Co-delivery of small interfering RNA and plasmid DNA using a polymeric vector incorporating endosomolytic oligomeric sulfonamide.* Biomaterials, 2011. **32**(21): p. 4914-4924.
6. Grimm, D., Streetz, K.L., Jopling, C.L., Storm, T.A., Pandey, K., Davis, C.R., Marion, P., Salazar, F., and Kay, M.A., *Fatality in mice due to oversaturation of cellular microRNA/short hairpin RNA pathways.* Nature, 2006. **441**(7092): p. 537-541.
7. Kouprina, N., Tomilin, A.N., Masumoto, H., Earnshaw, W.C., and Larionov, V., *Human artificial chromosome-based gene delivery vectors for biomedicine and biotechnology.* Expert Opinion on Drug Delivery, 2014. **11**(4): p. 517-535.
8. Silva, F., Queiroz, J.A., and Domingues, F.C., *Evaluating metabolic stress and plasmid stability in plasmid DNA production by Escherichia coli.* Biotechnology Advances, 2012. **30**(3): p. 691-708.
9. Sherman, D., *Advanced Textbook on Gene Transfer, Gene Therapy and Genetic Pharmacology: Principles, Delivery and Pharmacological and Biomedical Applications of Nucleotide-based Therapies.* 2014. Imperial College Press.
10. Osborn, M.J., McElmurry, R.T., Lees, C.J., DeFeo, A.P., Chen, Z.-Y., Kay, M.A., Naldini, L., Freeman, G., Tolar, J., and Blazar, B.R., *Minicircle DNA-based gene therapy coupled with immune modulation permits long-term expression of a-L-Iduronidase in mice with Mucopolysaccharidosis Type I.* Molecular Therapy, 2011. **19**(3): p. 450-460.
11. Kay, M.A., He, C.Y., and Chen, Z.Y., *A robust system for production of minicircle DNA vectors.* Nature Biotechnology, 2010. **28**(12): p. 1287–1289.
12. Maniar, L.E.G., Maniar, J.M., Chen, Z.-Y., Lu, J., Fire, A.Z., and Kay, M.A., *Minicircle DNA vectors achieve sustained expression reflected by active chromatin and transcriptional level.* Molecular Therapy, 2013. **21**(1): p. 131-138.
13. Grund, M. and Schleef, M., *Minicircle Patents: A Short IP Overview of Optimizing Nonviral DNA Vectors.* Minicircle and Miniplasmid DNA Vectors: The Future of Nonviral and Viral Gene Transfer. 2013. Wiley-Blackwell. p. 1-6.
14. Darquet, A., Cameron, B., Wils, P., Scherman, D., and Crouzet, J., *A new DNA vehicle for nonviral gene delivery: supercoiled minicircle.* Gene Therapy, 1997. **4**(12): p. 1341.
15. Oliveira, P.H. and Mairhofer, J., *Marker-free plasmids for biotechnological applications – implications and perspectives.* Trends in Biotechnology, 2013. **31**(9): p. 539-547.
16. Jostins, L., Ripke, S., Weersma, R.K., Duerr, R.H., McGovern, D.P., Hui, K.Y., Lee, J.C., Philip Schumm, L., Sharma, Y., Anderson, C.A., Essers, J., Mitrovic, M., Ning, K., Cleynen, I., Theatre, E., Spain, S.L., Raychaudhuri, S., Goyette, P., Wei, Z., Abraham, C., Achkar, J.-P., Ahmad, T., Amininejad, L., Ananthakrishnan, A.N., Andersen, V., Andrews, J.M., Baidoo, L., Balschun, T., Bampton, P.A., Bitton, A., Boucher, G., Brand, S., Buning, C., Cohain, A., Cichon, S., D/'Amato, M., De Jong, D., Devaney, K.L., Dubinsky, M., Edwards, C., Ellinghaus, D., Ferguson, L.R., Franchimont, D., Fransen, K., Gearry, R., Georges, M., Gieger, C., Glas, J., Haritunians, T., Hart, A., Hawkey, C., Hedl, M., Hu, X., Karlsen, T.H., Kupcinskas, L., Kugathasan, S., Latiano, A., Laukens, D., Lawrance, I.C., Lees, C.W., Louis, E., Mahy, G., Mansfield, J., Morgan, A.R., Mowat, C., Newman, W., Palmieri, O., Ponsioen, C.Y., Potocnik, U., Prescott, N.J., Regueiro, M., Rotter, J.I., Russell, R.K., Sanderson, J.D., Sans, M., Satsangi, J., Schreiber, S., Simms, L.A., Sventoraityte, J., Targan, S.R., Taylor, K.D., Tremelling, M., Verspaget, H.W., De Vos, M., Wijmenga, C., Wilson, D.C., Winkelmann, J., Xavier, R.J., Zeissig, S., Zhang, B., Zhang, C.K., Zhao, H., Silverberg, M.S., Annese, V., Hakonarson, H., Brant, S.R., Radford-Smith, G., Mathew, C.G., Rioux, J.D., Schadt, E.E., Daly, M.J., Franke, A., Parkes, M., Vermeire, S., Barrett, J.C. and Cho, J.H., *Host-microbe interactions have shaped the genetic architecture of inflammatory bowel disease.* Nature, 2012. **491**(7422): p. 119-124.
17. Berer, K., Mues, M., Koutrolos, M., Rasbi, Z.A., Boziki, M., Johner, C., Wekerle, H., and Krishnamoorthy, G., *Commensal microbiota and myelin autoantigen cooperate to trigger autoimmune demyelination.* Nature, 2011. **479**(7374): p. 538-541.
18. Chen, Z.Y., Riu, E., He, C.Y., Xu, H., and Kay, M.A., *Silencing of episomal transgene expression in liver by plasmid bacterial backbone DNA is independent of CpG methylation.* Molecular Therapy, 2008. **16**(3): p. 548-556.

19. Kreiss, P., Mailhe, P., Scherman, D., Pitard, B., Cameron, B., Rangara, R., Aguerre-Charriol, O., Airiau, M., and Crouzet, J., *Plasmid DNA size does not affect the physicochemical properties of lipoplexes but modulates gene transfer efficiency*. Nucleic Acids Research, 1999. **27**(19): p. 3792-3798.
20. Ribeiro, S., Mairhofer, J., Madeira, C., Diogo, M.M., Lobato da Silva, C., Monteiro, G., Grabherr, R., and Cabral, J.M., *Plasmid DNA size does affect nonviral gene delivery efficiency in stem cells*. Cellular Reprogramming, 2012. **14**(2): p. 130-137.
21. Lukacs, G.L., Haggie, P., Seksek, O., Lechardeur, D., Freedman, N., and Verkman, A.S., *Size-dependent DNA mobility in cytoplasm and nucleus*. Journal of Biological Chemistry, 2000. **275**(3): p. 1625-1629.
22. Chen, Z., He, C., and Kay, M., *Improved production and purification of minicircle DNA vector free of plasmid bacterial sequences and capable of persistent transgene expression in vivo*. Human Gene Therapy, 2005. **16**(1): p. 126-131.
23. Tejeda-Mansir, A. and Montesinos, R.M., *Upstream processing of plasmid DNA for vaccine and gene therapy applications*. Recent Patents on Biotechnology, 2008. **2**(3): p. 156-172.
24. Urthaler, J., Schuchnigg, H., Garidel, P., and Huber, H., *Industrial Manufacturing of Plasmid-DNA Products for Gene Vaccination and Therapy*, in *Gene Vaccines*. 2012, Springer Vienna. p. 311-330.
25. Carnes, A.E., Luke, J.M., Vincent, J.M., Schukar, A., Anderson, S., Hodgson, C.P., and Williams, J.A., *Plasmid DNA fermentation strain and process-specific effects on vector yield, quality, and transgene expression*. Biotechnology and Bioengineering, 2011. **108**(2): p. 354-363.
26. Simcikova, M., Prather, K.L., Prazeres, D.M., and Monteiro, G.A., *On the dual effect of glucose during production of pBAD/AraC-based minicircles*. Vaccine, 2014. **32**(24): p. 2843-2846.
27. Bigger, B.W., Tolmachov, O., Collombet, J.-M., Fragkos, M., Palaszewski, I., and Coutelle, C., *An araC-controlled bacterial Cre expression system to produce DNA minicircle vectors for nuclear and mitochondrial gene therapy*. Journal of Biological Chemistry, 2001. **276**(25): p. 23018-23027.
28. Groth, A.C. and Calos, M.P., *Phage integrases: biology and applications*. Journal of Molecular Biology, 2004. **335**(3): p. 667-678.
29. Nafissi, N. and Slavcev, R., *Bacteriophage recombination systems and biotechnical applications*. Applied Microbiology and Biotechnology, 2014. **98**(7): p. 2841-2851.
30. Cassell, G.D. and Segall, A.M., *Mechanism of Inhibition of site-specific recombination by the Holliday Junction-trapping peptide WKHYNY: Insights into Phage λ Integrase-mediated strand exchange*. Journal of Molecular Biology, 2003. **327**(2): p. 413-429.
31. Fogg, P.C.M., Colloms, S., Rosser, S., Stark, M., and Smith, M.C.M., *New applications for phage integrases*. Journal of Molecular Biology, 2014. **426**(15): p. 2703-2716.
32. Katona, R., Vanderbyl, S., and Perez, C., *Mammalian Artificial Chromosomes and clinical applications for genetic modification of stem cells: An overview*, in *mammalian chromosome engineering*, G. Hadlaczky, Editor. 2011, Humana Press. p. 199-216.
33. Schleef, M., *Minicircle and Miniplasmid DNA Vectors: The Future of Non-viral and Viral Gene Transfer*. 2013. John Wiley & Sons.
34. Zechiedrich, E.L., Fogg, J., Catanese, D.J., Bakkalbasi, E., and Gilbert, B.E., *Supercoiled minivectors for gene therapy applications*. 2014, Baylor College of Medicine, US patent application 8729044 B2.
35. Austin, S., Ziese, M., and Sternberg, N., *A novel role for site-specific recombination in maintenance of bacterial replicons*. Cell, 1981. **25**(3): p. 729-736.
36. Marecki, J.C., Parajuli, N., Crow, J.P., and MacMillan-Crow, L.A., *The use of the Cre/loxP system to study oxidative stress in tissue-specific manganese superoxide dismutase knockout models*. Antioxidants & Redox Signaling, 2014. **20**(10): p. 1655-1670.
37. Economides, A.N., Valenzuela, D.M., Davis, S., and Yancopoulos, G., *Methods of modifying genes in eukaryotic cells*. 2014, US Patent 20,140,155,689.
38. Mayrhofer, P. and Iro, M., *Minicircle-DNA*, in *Gene Vaccines*, J. Thalhamer, R. Weiss, and S. Scheiblhofer, Editors. 2012, Springer Vienna. p. 297-310.
39. Moon, H.S., Abercrombie, L.L., Eda, S., Blanvillain, R., Thomson, J.G., Ow, D.W., and Stewart Jr, C., *Transgene excision in pollen using a codon optimized serine resolvase CinH-RS2 site-specific recombination system*. Plant Molecular Biology, 2011. **75**(6): p. 621-631.
40. Lombardo, L., *Genetic use restriction technologies: a review*. Plant Biotechnology Journal, 2014.
41. Lee, N., Wilcox, G., Gielow, W., Arnold, J., Cleary, P., and Englesberg, E., *In vitro activation of the transcription of araBAD operon by araC activator*. Proceedings of the National Academy of Sciences, 1974. **71**(3): p. 634-638.
42. Khlebnikov, A., Datsenko, K.A., Skaug, T., Wanner, B.L., and Keasling, J.D., *Homogeneous expression of the PBAD promoter in Escherichia coli by constitutive expression of the low-affinity high-capacity AraE transporter*. Microbiology, 2001. **147**(12): p. 3241-3247.
43. Mayrhofer, P., Blaesen, M., Schleef, M., and Jechlinger, W., *Minicircle-DNA production by site specific recombination and protein-DNA interaction chromatography*. The Journal of Gene Medicine, 2008. **10**(11): p. 1253-1269.

44. Mayrhofer, P., Jechlinger, W., and Lubitz, W., *Minicircle vector production*. 2014, US Patent 8,647,863.
45. L Chavez, C. and P Calos, M., *Therapeutic applications of the PhiC31 integrase system*. Current Gene Therapy, 2011. **11**(5): p. 375-381.
46. Chen, Z.-Y., He, C.-Y., Ehrhardt, A., and Kay, M.A., *Minicircle DNA vectors devoid of bacterial dna result in persistent and high-level transgene expression in vivo*. Molecular Therapy, 2003. **8**(3): p. 495-500.
47. Prazeres, D.M.F., *Good Manufacturing Practice and Validation*, in *Plasmid Biopharmaceuticals: Basics, Applications, and Manufacturing*. 2011. p. 327-355.
48. Schmeer, M. and Schleef, M., *Pharmaceutical Grade Large-Scale Plasmid DNA Manufacturing Process*, in *DNA Vaccines*, M. Rinaldi, D. Fioretti, and S. Iurescia, Editors. 2014, Springer New York. p. 219-240.
49. E.M.A., *Guideline on follow-up of patients administered with gene therapy medicinal products*. 2009. p. 12.
50. U.S. Food and Drug Administration., *Guidance for industry: considerations for plasmid DNA vaccines for infectious disease indications*. Rockville, MD, 2005.
51. Stenler, S., Wiklander, O.P., Badal-Tejedor, M., Turunen, J., Nordin, J.Z., Hallengärd, D., Wahren, B., Andaloussi, S.E., Rutland, M.W., and Smith, C.E., *Micro-minicircle gene therapy: Implications of size on fermentation, complexation, shearing resistance, and expression*. Molecular Therapy—Nucleic Acids, 2014. **3**(1): p. e140.
52. Mota, É., Sousa, Â., Černigoj, U., Queiroz, J.A., Tomaz, C.T., and Sousa, F., *Rapid quantification of supercoiled plasmid deoxyribonucleic acid using a monolithic ion exchanger*. Journal of Chromatography A, 2013. **1291**(0): p. 114-121.
53. Gaspar, V.M., Correia, I.J., Sousa, Â., Silva, F., Paquete, C.M., Queiroz, J.A., and Sousa, F., *Nanoparticle mediated delivery of pure P53 supercoiled plasmid dna for gene therapy*. Journal of Controlled Release, 2011. **156**(2): p. 212–222.
54. U.S. Food and Drug Administration - *Guidance for FDA Reviewers and Sponsors: Content and Review of Chemistry, Manufacturing, and Control (CMC) Information for Human Somatic Cell Therapy Investigational New Drug Applications (INDs)*. Center for Biologics Evaluation and Research, Rockville, MD, 2008.
55. B'Hymer, C., *Residual solvent testing: a review of gas-chromatographic and alternative techniques*. Pharmaceutical Research, 2003. **20**(3): p. 337-344.
56. Grodowska, K. and Parczewski, A., *Organic solvents in the pharmaceutical industry*. Acta Poloniae Pharmaceutica – Drug Research 2010. **67**(3): p. 3-12.
57. U.S. Food and Drug Administration - *Guidance for Industry, Q3C Impurities: Residual Solvents*. Center for Biologics Evaluation and Research, Rockville, MD, 1997.
58. Gao, P., Munir, M., and Xagoraraki, I., *Correlation of tetracycline and sulfonamide antibiotics with corresponding resistance genes and resistant bacteria in a conventional municipal wastewater treatment plant*. Science of The Total Environment, 2012. **421–422**: p. 173-183.
59. U.S. Food and Drug Administration - *Guidance for Industry: Guidance for Human Somatic Cell Therapy and Gene Therapy*. Center for Biologics Evaluation and Research, Rockville, MD, 2014.
60. Kobelt, D., Schleef, M., Schmeer, M., Aumann, J., Schlag, P.M., and Walther, W., *Performance of high quality minicircle dna for in vitro and in vivo gene transfer*. Molecular Biotechnology, 2013. **53**(1): p. 80-89.
61. Gandhi, N.S., Tekade, R.K., and Chougule, M.B., *Nanocarrier mediated delivery of siRNA/miRNA in combination with chemotherapeutic agents for cancer therapy: Current progress and advances*. Journal of Controlled Release, 2014. **194**: p. 238-256.
62. Siegel, R.L., Miller, K.D., and Jemal, A., *Cancer statistics, 2015*. CA: A Cancer Journal for Clinicians, 2015. **65**(1): p. 5-29.
63. del Burgo, L.S., Pedraz, J., and Orive, G., *Advanced nanovehicles for cancer management*. Drug Discovery Today, 2014. **19**(10): p. 1659-1670.
64. Baskar, R., Lee, K.A., Yeo, R., and Yeoh, K.-W., *Cancer and radiation therapy: current advances and future directions*. International Journal of Medical Sciences, 2012. **9**(3): p. 193-199.
65. Baxevanis, C.N., Perez, S.A., and Papamichail, M., *Combinatorial treatments including vaccines, chemotherapy and monoclonal antibodies for cancer therapy*. Cancer Immunol Immunother, 2009. **58**(3): p. 317-324.
66. Mignani, S.M., Bryszewska, M., Klajnert-Maculewicz, B., Zablocka, M., and Majoral, J.-P., *Advances in combination therapies based on nanoparticles for efficacious cancer treatment: an analytic report*. Biomacromolecules, 2015. **16**(1): p. 1-27.
67. Spoerri, L., Oo, Z.Y., Larsen, J.E., Haass, N.K., Gabrielli, B., and Pavey, S., *Cell Cycle Checkpoint and DNA Damage Response Defects as Anticancer Targets: From Molecular Mechanisms to Therapeutic Opportunities*, in *Stress Response Pathways in Cancer*. 2015, Springer. p. 29-49.
68. Creixell, M. and Peppas, N.A., *Co-delivery of siRNA and therapeutic agents using nanocarriers to overcome cancer resistance*. Nano Today, 2012. **7**(4): p. 367-379.
69. Minchinton, A.I. and Tannock, I.F., *Drug penetration in solid tumours*. Nature Reviews Cancer, 2006. **6**(8): p. 583-592.

70. Markovsky, E., Baabur-Cohen, H., Eldar-Boock, A., Omer, L., Tiram, G., Ferber, S., Ofek, P., Polyak, D., Scomparin, A., and Satchi-Fainaro, R., *Administration, distribution, metabolism and elimination of polymer therapeutics.* Journal of Controlled Release, 2012. **161**(2): p. 446-460.
71. Gaspar, V., Melo-Diogo, D.d., Costa, E., Moreira, A., Queiroz, J., Pichon, C., Correia, I., and Sousa, F., *Minicircle DNA vectors for gene therapy: advances and applications.* Expert Opinion on Biological Therapy, 2015. **15**(3): p. 353-379.
72. Brenner, M. and Hung, M.-C., *Cancer Gene Therapy by Viral and Non-viral Vectors*. 2014: John Wiley & Sons.
73. Howard, K.A., *RNA interference from biology to therapeutics*. 2012: Springer Science & Business Media.
74. Navarro, G., Pan, J., and Torchilin, V.P., *Micelle-like nanoparticles as carriers for DNA and siRNA.* Molecular Pharmaceutics, 2015. **12**(2): p. 301-313.
75. Rosenberg, S.A., Yang, J.C., and Restifo, N.P., *Cancer immunotherapy: moving beyond current vaccines.* Nature medicine, 2004. **10**(9): p. 909-915.
76. de la Fuente, M., Langer, R., and Alonso, M., *Nanotechnology Approaches for Cancer Immunotherapy and Immunomodulation*, in *Nano-Oncologicals*. 2014. Springer International Publishing. p. 215-242.
77. Ronald, J.A., Chuang, H.-Y., Dragulescu-Andrasi, A., Hori, S.S., and Gambhir, S.S., Detecting cancers through tumor-activatable minicircles that lead to a detectable blood biomarker. Proceedings of the National Academy of Sciences, 2015. **112**(10): p. 3068-3073.
78. Zhao, N., Fogg, J.M., Zechiedrich, L., and Zu, Y., *Transfection of shRNA-encoding Minivector DNA of a few hundred base pairs to regulate gene expression in lymphoma cells.* Gene Therapy, 2011. **18**(3): p. 220-224.
79. Wu, J., Xiao, X., Zhao, P., Xue, G., Zhu, Y., Zhu, X., Zheng, L., Zeng, Y., and Huang, W., *Minicircle-IFNγ induces antiproliferative and antitumoral effects in human nasopharyngeal carcinoma.* Clinical Cancer Research, 2006. **12**(15): p. 4702-4713.
80. Zuo, Y., Wu, J., Xu, Z., Yang, S., Yan, H., Tan, L., Meng, X., Ying, X., Liu, R., Kang, T., and Huang, W., *Minicircle-oriP-IFNγ: A novel targeted gene therapeutic system for EBV positive human nasopharyngeal carcinoma.* PLoS ONE, 2011. **6**(5): p. e19407.
81. Frei 3rd, E., Karon, M., Levin, R.H., Freireich, E.J., Taylor, R.J., Hananian, J., Selawry, O., Holland, J.F., Hoogstraten, B., and Wolman, I.J., *The effectiveness of combinations of antileukemic agents in inducing and maintaining remission in children with acute leukemia.* Blood, 1965. **26**(5): p. 642.
82. Chabner, B.A. and Roberts, T.G., *Chemotherapy and the war on cancer.* Nature Reviews Cancer, 2005. **5**(1): p. 65-72.
83. Li, J., Wang, Y., Zhu, Y., and Oupický, D., *Recent advances in delivery of drug–nucleic acid combinations for cancer treatment.* Journal of Controlled Release, 2013. **172**(2): p. 589-600.
84. Tallarida, R.J., *Drug synergism and dose-effect data analysis*. 2000: CRC Press.
85. de Melo-Diogo, D., Gaspar, V.M., Costa, E.C., Moreira, A.F., Oppolzer, D., Gallardo, E., and Correia, I.J., *Combinatorial delivery of Crizotinib–Palbociclib–Sildenafil using TPGS-PLA micelles for improved cancer treatment.* European Journal of Pharmaceutics and Biopharmaceutics, 2014. **88**(3): p. 718-729.
86. Jhaveri, A., Deshpande, P., and Torchilin, V., *Stimuli-sensitive nanopreparations for combination cancer therapy.* Journal of Controlled Release, 2014. **190**: p. 352-370.
87. Miyata, K., Nishiyama, N., and Kataoka, K., *Rational design of smart supramolecular assemblies for gene delivery: chemical challenges in the creation of artificial viruses.* Chemical Society Reviews, 2012. **41**(7): p. 2562-2574.
88. Tonga, G.Y., Moyano, D.F., Kim, C.S., and Rotello, V.M., *Inorganic nanoparticles for therapeutic delivery: Trials, tribulations and promise.* Current Opinion in Colloid & Interface Science, 2014. **19**(2): p.49-55.
89. Kango, S., Kalia, S., Celli, A., Njuguna, J., Habibi, Y., and Kumar, R., *Surface modification of inorganic nanoparticles for development of organic–inorganic nanocomposites—A review.* Progress in Polymer Science, 2013. **38**(8): p. 1232-1261.
90. Nam, J., Won, N., Bang, J., Jin, H., Park, J., Jung, S., Jung, S., Park, Y., and Kim, S., *Surface engineering of inorganic nanoparticles for imaging and therapy.* Advanced Drug Delivery Reviews, 2013. **65**(5): p. 622-648.
91. Chrastina, A., Massey, K.A., and Schnitzer, J.E., *Overcoming in vivo barriers to targeted nanodelivery.* Wiley Interdisciplinary Reviews: Nanomedicine and Nanobiotechnology, 2011. **3**(4): p. 421-437.
92. Mitragotri, S., Burke, P.A., and Langer, R., *Overcoming the challenges in administering biopharmaceuticals: formulation and delivery strategies.* Nature Reviews Drug Discovery, 2014. **13**(9): p. 655-672.
93. McCrudden, C.M. and McCarthy, H.O., *Cancer gene therapy–key biological concepts in the design of multifunctional non-viral delivery systems.* Gene Therapy-Tools and Potential Applications, 2013. InTech press. p. 81-84.

94. Iversen, T.-G., Skotland, T., and Sandvig, K., *Endocytosis and intracellular transport of nanoparticles: present knowledge and need for future studies.* Nano Today, 2011. **6**(2): p. 176-185.
95. Yameen, B., Choi, W.I., Vilos, C., Swami, A., Shi, J., and Farokhzad, O.C., *Insight into nanoparticle cellular uptake and intracellular targeting.* Journal of Controlled Release, 2014. **190**: p. 485-499.
96. Lam, A. and Dean, D., *Progress and prospects: nuclear import of nonviral vectors.* Gene Therapy, 2010. **17**(4): p. 439-447.
97. Breuzard, G., Tertil, M., Goncalves, C., Cheradame, H., Geguan, P., Pichon, C., and Midoux, P., *Nuclear delivery of NF {kappa} B-assisted DNA/polymer complexes: plasmid DNA quantitation by confocal laser scanning microscopy and evidence of nuclear polyplexes by FRET imaging.* Nucleic Acids Research, 2008. **36**(12): p. e71.
98. Gonçalves, C., Ardourel, M.-Y., Decoville, M., Breuzard, G., Midoux, P., Hartmann, B., and Pichon, C., *An optimized extended DNA kappa B site that enhances plasmid DNA nuclear import and gene expression.* The Journal of Gene Medicine, 2009. **11**(5): p. 401-411.
99. Blanco, E., Shen, H., and Ferrari, M., Principles of nanoparticle design for overcoming biological barriers to drug delivery. Nat Biotech, 2015. **33**(9): p. 941-951.
100. Monopoli, M.P., Walczyk, D., Campbell, A., Elia, G., Lynch, I., Baldelli Bombelli, F., and Dawson, K.A., *Physical− chemical aspects of protein corona: relevance to in vitro and in vivo biological impacts of nanoparticles.* Journal of the American Chemical Society, 2011. **133**(8): p. 2525-2534.
101. Walkey, C.D. and Chan, W.C., *Understanding and controlling the interaction of nanomaterials with proteins in a physiological environment.* Chemical Society Reviews, 2012. **41**(7): p. 2780-2799.
102. Knop, K., Hoogenboom, R., Fischer, D., and Schubert, U.S., *Poly (ethylene glycol) in drug delivery: pros and cons as well as potential alternatives.* Angewandte Chemie International Edition, 2010. **49**(36): p. 6288-6308.
103. Rodriguez, P.L., Harada, T., Christian, D.A., Pantano, D.A., Tsai, R.K., and Discher, D.E., *Minimal" Self" peptides that inhibit phagocytic clearance and enhance delivery of nanoparticles.* Science, 2013. **339**(6122): p. 971-975.
104. Barua, S. and Mitragotri, S., *Challenges associated with penetration of nanoparticles across cell and tissue barriers: A review of current status and future prospects.* Nano Today, 2014. **9**(2): p. 223-243.
105. Maeda, H., Nakamura, H., and Fang, J., *The EPR effect for macromolecular drug delivery to solid tumors: improvement of tumor uptake, lowering of systemic toxicity, and distinct tumor imaging in vivo.* Advanced drug delivery reviews, 2013. **65**(1): p. 71-79.
106. Schleich, N., Po, C., Jacobs, D., Ucakar, B., Gallez, B., Danhier, F., and Préat, V., *Comparison of active, passive and magnetic targeting to tumors of multifunctional paclitaxel/SPIO-loaded nanoparticles for tumor imaging and therapy.* Journal of Controlled Release, 2014. **194**: p. 82-91.
107. Nel, A.E., Mädler, L., Velegol, D., Xia, T., Hoek, E.M., Somasundaran, P., Klaessig, F., Castranova, V., and Thompson, M., *Understanding biophysicochemical interactions at the nano-bio interface.* Nature materials, 2009. **8**(7): p. 543-557.
108. Black, K.C., Wang, Y., Luehmann, H.P., Cai, X., Xing, W., Pang, B., Zhao, Y., Cutler, C.S., Wang, L.V., and Liu, Y., *Radioactive 198Au-Doped Nanostructures with Different Shapes for in vivo Analyses of Their Biodistribution, Tumor Uptake, and Intratumoral Distribution.* ACS Nano, 2014. **8**(5): p. 4385-4394.
109. Chung, T.-H., Wu, S.-H., Yao, M., Lu, C.-W., Lin, Y.-S., Hung, Y., Mou, C.-Y., Chen, Y.-C., and Huang, D.-M., *The effect of surface charge on the uptake and biological function of mesoporous silica nanoparticles in 3T3-L1 cells and human mesenchymal stem cells.* Biomaterials, 2007. **28**(19): p. 2959-2966.
110. Setyawati, M.I., Tay, C.Y., Docter, D., Stauber, R.H., and Leong, D.T., *Understanding and exploiting nanoparticles' intimacy with the blood vessel and blood.* Chemical Society Reviews, 2015. **in press**.
111. Ge, Z., Chen, Q., Osada, K., Liu, X., Tockary, T.A., Uchida, S., Dirisala, A., Ishii, T., Nomoto, T., and Toh, K., *Targeted gene delivery by polyplex micelles with crowded PEG palisade and cRGD moiety for systemic treatment of pancreatic tumors.* Biomaterials, 2014. **35**(10): p. 3416-3426.
112. Au, S., Wu, W., and Panté, N., *Baculovirus Nuclear Import: Open, Nuclear Pore Complex (NPC) Sesame.* Viruses, 2013. **5**(7): p. 1885-1900.
113. van Gaal, E.V., Oosting, R.S., van Eijk, R., Bakowska, M., Feyen, D., Kok, R.J., Hennink, W.E., Crommelin, D.J., and Mastrobattista, E., *DNA nuclear targeting sequences for non-viral gene delivery.* Pharmaceutical research, 2011. **28**(7): p. 1707-1722.
114. Akita, H., Kudo, A., Minoura, A., Yamaguti, M., Khalil, I.A., Moriguchi, R., Masuda, T., Danev, R., Nagayama, K., Kogure, K., and Harashima, H., *Multi-layered nanoparticles for penetrating the endosome and nuclear membrane via a step-wise membrane fusion process.* Biomaterials, 2009. **30**(15): p. 2940-2949.

115. Agrawal, A.K., Urimi, D., and Jain, S., *Multifunctional Polymeric Nano-Carriers in Targeted Drug Delivery*, in *Targeted Drug Delivery: Concepts and Design*. 2015. Springer. p. 461-500.
116. Pozzi, D., Colapicchioni, V., Caracciolo, G., Piovesana, S., Capriotti, A.L., Palchetti, S., De Grossi, S., Riccioli, A., Amenitsch, H., and Laganà, A., *Effect of polyethyleneglycol (PEG) chain length on the bio-nano-interactions between PEGylated lipid nanoparticles and biological fluids: from nanostructure to uptake in cancer cells.* Nanoscale, 2014. **6**(5): p. 2782-2792.
117. Karakoti, A.S., Das, S., Thevuthasan, S., and Seal, S., *PEGylated inorganic nanoparticles.* Angewandte Chemie International Edition, 2011. **50**(9): p. 1980-1994.
118. Barz, M., Luxenhofer, R., Zentel, R., and Vicent, M.J., *Overcoming the PEG-addiction: well-defined alternatives to PEG, from structure-property relationships to better defined therapeutics.* Polymer Chemistry, 2011. **2**(9): p. 1900-1918.
119. Ge, Z., Chen, Q., Osada, K., Liu, X., Tockary, T.A., Uchida, S., Dirisala, A., Ishii, T., Nomoto, T., Toh, K., Matsumoto, Y., Oba, M., Kano, M.R., Itaka, K., and Kataoka, K., Targeted gene delivery by polyplex micelles with crowded PEG palisade and cRGD moiety for systemic treatment of pancreatic tumors. Biomaterials, 2014. **35**(10): p. 3416-3426.
120. Yang, W., Liu, S., Bai, T., Keefe, A.J., Zhang, L., Ella-Menye, J.-R., Li, Y., and Jiang, S., *Poly (carboxybetaine) nanomaterials enable long circulation and prevent polymer-specific antibody production.* Nano Today, 2014. **9**(1): p. 10-16.
121. Romberg, B., Hennink, W., and Storm, G., *Sheddable Coatings for Long-Circulating Nanoparticles.* Pharmaceutical Research, 2008. **25**(1): p. 55-71.
122. Noga, M., Edinger, D., Kläger, R., Wegner, S.V., Spatz, J.P., Wagner, E., Winter, G., and Besheer, A., *The effect of molar mass and degree of hydroxyethylation on the controlled shielding and deshielding of hydroxyethyl starch-coated polyplexes.* Biomaterials, 2013. **34**(10): p. 2530-2538.
123. Zheng, C., Zheng, M., Gong, P., Deng, J., Yi, H., Zhang, P., Zhang, Y., Liu, P., Ma, Y., and Cai, L., *Polypeptide cationic micelles mediated co-delivery of docetaxel and siRNA for synergistic tumor therapy.* Biomaterials, 2013. **34**(13): p. 3431-3438.
124. Gaspar, V.M., Baril, P., Costa, E.C., de Melo-Diogo, D., Foucher, F., Queiroz, J.A., Sousa, F., Pichon, C., and Correia, I.J., Bioreducible poly (2-ethyl-2-oxazoline)–PLA–PEI-SS triblock copolymer micelles for co-delivery of DNA minicircles and Doxorubicin. Journal of Controlled Release, 2015. 213: p. 175-191.
125. Liu, T., Li, X., Qian, Y., Hu, X., and Liu, S., *Multifunctional pH-Disintegrable micellar nanoparticles of asymmetrically functionalized β-cyclodextrin-based star copolymer covalently conjugated with doxorubicin and DOTA-Gd moieties.* Biomaterials, 2012. **33**(8): p. 2521-2531.
126. Lowe, S., O'Brien-Simpson, N.M., Connal, L.A., Antibiofouling polymer interfaces: poly (ethylene glycol) and other promising candidates. Polymer Chemistry, 2015. **6**(2): p. 198-212.
127. Yang, W., Zhang, L., Wang, S., White, A.D., and Jiang, S., *Functionalizable and ultra stable nanoparticles coated with zwitterionic poly(carboxybetaine) in undiluted blood serum.* Biomaterials, 2009. **30**(29): p. 5617-5621.
128. Toman, P., Lien, C.-F., Ahmad, Z., Dietrich, S., Smith, J.R., An, Q., Molnár, É., Pilkington, G.J., Górecki, D.C., Tsibouklis, J., and Barbu, E., Nanoparticles of alkylglyceryl-dextran-graft-poly(lactic acid) for drug delivery to the brain: Preparation and *in vitro* investigation. Acta Biomaterialia, 2015. **23**: p. 250-262.
129. Yamada, Y., Nomura, T., Harashima, H., Yamashita, A., and Yui, N., *Post-nuclear gene delivery events for transgene expression by biocleavable polyrotaxanes.* Biomaterials, 2012. **33**(15): p. 3952-3958.
130. Kim, M.-H., Na, H.-K., Kim, Y.-K., Ryoo, S.-R., Cho, H.S., Lee, K.E., Jeon, H., Ryoo, R., and Min, D.-H., *Facile Synthesis of Monodispersed Mesoporous Silica Nanoparticles with Ultralarge Pores and Their Application in Gene Delivery.* ACS Nano, 2011. **5**(5): p. 3568-3576.
131. Gaspar, V., Marques, J., Sousa, F., Louro, R., Queiroz, J., and Correia, I., *Biofunctionalized nanoparticles with pH-responsive and cell penetrating blocks for gene delivery.* Nanotechnology, 2013. **24**(27): p. 275101.
132. Gaspar, V.M., Gonçalves, C., de Melo-Diogo, D., Costa, E.C., Queiroz, J.A., Pichon, C., Sousa, F., and Correia, I.J., *Poly(2-ethyl-2-oxazoline)-PLA-g-PEI amphiphilic triblock micelles for co-delivery of minicircle DNA and chemotherapeutics.* Journal of Controlled Release, 2014. **189**: p. 90-104.
133. Gao, F., Botella, P., Corma, A., Blesa, J., and Dong, L., *Monodispersed Mesoporous Silica Nanoparticles with Very Large Pores for Enhanced Adsorption and Release of DNA.* The Journal of Physical Chemistry B, 2009. **113**(6): p. 1796-1804.
134. Mendonça, L.S., Firmino, F., Moreira, J.N., Pedroso de Lima, M.C., and Simões, S., *Transferrin receptor-targeted liposomes encapsulating anti-BCR-ABL siRNA or asODN for chronic myeloid leukemia treatment.* Bioconjugate Chemistry, 2009. **21**(1): p. 157-168.
135. Li, X., Xie, Q.R., Zhang, J., Xia, W., and Gu, H., *The packaging of siRNA within the mesoporous structure of silica nanoparticles.* Biomaterials, 2011. **32**(35): p. 9546-9556.
136. Moghimi, S.M., Symonds, P., Murray, J.C., Hunter, A.C., Debska, G., and Szewczyk, A., *A two-stage poly (ethylenimine)-mediated cytotoxicity: implications for gene transfer/therapy.* Molecular Therapy, 2005. **11**(6): p. 990-995.

137. Lv, H., Zhang, S., Wang, B., Cui, S., and Yan, J., *Toxicity of cationic lipids and cationic polymers in gene delivery.* Journal of Controlled Release, 2006. **114**(1): p. 100-109.
138. Ganas, C., Weiß, A., Nazarenus, M., Rösler, S., Kissel, T., Rivera_Gil, P., and Parak, W.J., Biodegradable capsules as non-viral vectors for *in vitro* delivery of PEI/siRNA polyplexes for efficient gene silencing. Journal of Controlled Release, 2014. **196**: p. 132-138.
139. Qian, X., Long, L., Shi, Z., Liu, C., Qiu, M., Sheng, J., Pu, P., Yuan, X., Ren, Y., and Kang, C., *Star-branched amphiphilic PLA-b-PDMAEMA copolymers for co-delivery of miR-21 inhibitor and doxorubicin to treat glioma.* Biomaterials, 2014. **35**(7): p. 2322-2335.
140. Jean, M., Alameh, M., De Jesus, D., Thibault, M., Lavertu, M., Darras, V., Nelea, M., Buschmann, M.D., and Merzouki, A., Chitosan-based therapeutic nanoparticles for combination gene therapy and gene silencing of *in vitro* cell lines relevant to type 2 diabetes. European Journal of Pharmaceutical Sciences, 2012. 45(1): p. 138-149.
141. Mastorakos, P., Kambhampati, S.P., Mishra, M.K., Wu, T., Song, E., Hanes, J., and Kannan, R.M., Hydroxyl PAMAM dendrimer-based gene vectors for transgene delivery to human retinal pigment epithelial cells. Nanoscale, 2015. **7**(9): p. 3845-3856.
142. Zhang, J. and Ma, P.X., *Host-guest interactions mediated nano-assemblies using cyclodextrin-containing hydrophilic polymers and their biomedical applications.* Nano Today, 2010. **5**(4): p. 337-350.
143. Huang, X., *Delivery of Paclitaxel Using PEGylated Graphene Oxide as a Nanocarrier.* ACS Applied Materials & Interfaces, 2015. **7**(2): p. 1355-1363.
144. Yu, G., Jie, K., and Huang, F., *Supramolecular Amphiphiles Based on Host–Guest Molecular Recognition Motifs.* Chemical Reviews, 2015.
145. Delplace, V., Couvreur, P., and Nicolas, J., *Recent trends in the design of anticancer polymer prodrug nanocarriers.* Polymer Chemistry, 2014. **5**(5): p. 1529-1544.
146. Shuai, X., Ai, H., Nasongkla, N., Kim, S., and Gao, J., *Micellar carriers based on block copolymers of poly (ε-caprolactone) and poly (ethylene glycol) for doxorubicin delivery.* Journal of Controlled Release, 2004. **98**(3): p. 415-426.
147. Kulkarni, S.B., Betageri, G.V., and Singh, M., *Factors affecting microencapsulation of drugs in liposomes.* Journal of Microencapsulation, 1995. **12**(3): p. 229-246.
148. Li, J., Lyv, Z., Li, Y., Liu, H., Wang, J., Zhan, W., Chen, H., Chen, H., and Li, X., A theranostic prodrug delivery system based on Pt(IV) conjugated nano-graphene oxide with synergistic effect to enhance the therapeutic efficacy of Pt drug. Biomaterials, 2015. **51**: p. 12-21.
149. Maksimenko, A., Dosio, F., Mougin, J., Ferrero, A., Wack, S., Reddy, L.H., Weyn, A.-A., Lepeltier, E., Bourgaux, C., and Stella, B., *A unique squalenoylated and nonpegylated doxorubicin nanomedicine with systemic long-circulating properties and anticancer activity.* Proceedings of the National Academy of Sciences, 2014. **111**(2): p. E217-E226.
150. Yoo, H.S. and Park, T.G., *Biodegradable polymeric micelles composed of doxorubicin conjugated PLGA-PEG block copolymer.* Journal of Controlled Release, 2001. **70**(1–2): p. 63-70.
151. Ma, C., Pan, P., Shan, G., Bao, Y., Fujita, M., and Maeda, M., *Core-Shell Structure, Biodegradation, and Drug Release Behavior of Poly (lactic acid)/Poly (ethylene glycol) Block Copolymer Micelles Tuned by Macromolecular Stereostructure.* Langmuir, 2015. **31**(4): p. 1527-1536.
152. Forbes, D.C. and Peppas, N.A., *Polycationic Nanoparticles for siRNA Delivery: Comparing ARGET ATRP and UV-Initiated Formulations.* ACS Nano, 2014. **8**(3): p. 2908-2917.
153. Moreira, A.F., Gaspar, V.M., Costa, E.C., de Melo-Diogo, D., Machado, P., Paquete, C.M., and Correia, I.J., *Preparation of end-capped pH-sensitive mesoporous silica nanocarriers for on-demand drug delivery.* European Journal of Pharmaceutics and Biopharmaceutics, 2014. **88**(3): p. 1012-1025.
154. Dai, W., Fan, Y., Zhang, H., Wang, X., Zhang, Q., and Wang, X., *A comprehensive study of iRGD-modified liposomes with improved chemotherapeutic efficacy on B16 melanoma.* Drug Delivery, 2015. **22**(1): p. 10-20.
155. Salvati, A., Pitek, A.S., Monopoli, M.P., Prapainop, K., Bombelli, F.B., Hristov, D.R., Kelly, P.M., Aberg, C., Mahon, E., and Dawson, K.A., *Transferrin-functionalized nanoparticles lose their targeting capabilities when a biomolecule corona adsorbs on the surface.* Nature Nanotechnology, 2013. **8**(2): p. 137-143.
156. Lammers, T., Kiessling, F., Hennink, W.E., and Storm, G., *Drug targeting to tumors: Principles, pitfalls and (pre-) clinical progress.* Journal of Controlled Release, 2012. **161**(2): p. 175-187.
157. Liao, R., Yi, S., Liu, M., Jin, W., and Yang, B., Folic-Acid-Targeted Self-Assembling Supramolecular Carrier for Gene Delivery. ChemBioChem, 2015. **16**(11): p. 1622-1628.
158. Guo, J., Ogier, J.R., Desgranges, S., Darcy, R., and Caitriona, O., *Anisamide-targeted cyclodextrin nanoparticles for siRNA delivery to prostate tumours in mice.* Biomaterials, 2012. **33**(31): p. 7775-7784.
159. Zhao, C., Liu, X., Liu, J., Yang, Z., Rong, X., Li, M., Liang, X., and Wu, Y., *Transferrin conjugated poly(γ-glutamicacid-maleimide-co-l-lactide)-1,2-dipalmitoylsn-glycero-3-phosphoethanolamine copolymer nanoparticles for targeting drug delivery.* Colloids and Surfaces B: Biointerfaces, 2014. **123**: p. 787-796.

160. Yang, X., Hong, H., Grailer, J.J., Rowland, I.J., Javadi, A., Hurley, S.A., Xiao, Y., Yang, Y., Zhang, Y., Nickles, R.J., Cai, W., Steeber, D.A., and Gong, S., *cRGD-functionalized, DOX-conjugated, and 64Cu-labeled superparamagnetic iron oxide nanoparticles for targeted anticancer drug delivery and PET/MR imaging.* Biomaterials, 2011. **32**(17): p. 4151-4160.
161. Mi, Y., Zhao, J., and Feng, S.-S., *Targeted co-delivery of docetaxel, cisplatin and herceptin by vitamin E TPGS-cisplatin prodrug nanoparticles for multimodality treatment of cancer.* Journal of Controlled Release, 2013. **169**(3): p. 185-192.
162. Deng, X., Cao, M., Zhang, J., Hu, K., Yin, Z., Zhou, Z., Xiao, X., Yang, Y., Sheng, W., Wu, Y., and Zeng, Y., *Hyaluronic acid-chitosan nanoparticles for co-delivery of MiR-34a and doxorubicin in therapy against triple negative breast cancer.* Biomaterials, 2014. **35**(14): p. 4333-4344.
163. Ganta, S., Devalapally, H., Shahiwala, A., and Amiji, M., *A review of stimuli-responsive nanocarriers for drug and gene delivery.* Journal of Controlled Release, 2008. **126**(3): p. 187-204.
164. MacEwan, S.R., Callahan, D.J., and Chilkoti, A., *Stimulus-responsive macromolecules and nanoparticles for cancer drug delivery.* Nanomedicine, 2010. **5**(5): p. 793-806.
165. Purushotham, S., Chang, P.E., Rumpel, H., Kee, I.H., Ng, R.T., Chow, P.K., Tan, C.K., and Ramanujan, R.V., *Thermoresponsive core-shell magnetic nanoparticles for combined modalities of cancer therapy.* Nanotechnology, 2009. **20**(30): p. 305101.
166. Matteini, P., Tatini, F., Cavigli, L., Ottaviano, S., Ghini, G., and Pini, R., *Graphene as a photothermal switch for controlled drug release.* Nanoscale, 2014. **6**(14): p. 7947-7953.
167. Byers, R.J. and Hitchman, E.R., *Quantum Dots Brighten Biological Imaging.* Progress in Histochemistry and Cytochemistry, 2011. **45**(4): p. 201-237.
168. Tavares, A.J., Chong, L., Petryayeva, E., Algar, W.R., and Krull, U.J., *Quantum dots as contrast agents for in vivo tumor imaging: progress and issues.* Analytical and bioanalytical chemistry, 2011. **399**(7): p. 2331-2342.
169. Perazella, M.A., *Current status of gadolinium toxicity in patients with kidney disease.* Clinical Journal of the American Society of Nephrology, 2009. **4**(2): p. 461-469.
170. Zhang, X.-D., Wu, D., Shen, X., Liu, P.-X., Fan, F.-Y., and Fan, S.-J., *In vivo renal clearance, biodistribution, toxicity of gold nanoclusters.* Biomaterials, 2012. **33**(18): p. 4628-4638.
171. Pan, J. and Feng, S.-S., *Targeting and imaging cancer cells by Folate-decorated, quantum dots (QDs)- loaded nanoparticles of biodegradable polymers.* Biomaterials, 2009. **30**(6): p. 1176-1183.
172. Yu, M.K., Jeong, Y.Y., Park, J., Park, S., Kim, J.W., Min, J.J., Kim, K., and Jon, S., *Drug-Loaded superparamagnetic iron oxide nanoparticles for combined cancer imaging and therapy in vivo.* Angewandte Chemie International Edition, 2008. **47**(29): p. 5362-5365.
173. Xiong, X.-B. and Lavasanifar, A., *Traceable multifunctional micellar nanocarriers for cancer-targeted co-delivery of MDR-1 siRNA and doxorubicin.* ACS nano, 2011. **5**(6): p. 5202-5213.
174. Kim, D., Jeong, Y.Y., and Jon, S., *A Drug-Loaded Aptamer−Gold nanoparticle bioconjugate for combined ct imaging and therapy of prostate cancer.* ACS Nano, 2010. **4**(7): p. 3689-3696.
175. Duncan, B., Kim, C., and Rotello, V.M., *Gold nanoparticle platforms as drug and biomacromolecule delivery systems.* Journal of controlled release : official journal of the Controlled Release Society, 2010. **148**(1): p. 122-7.
176. Vigderman, L. and Zubarev, E.R., *Therapeutic platforms based on gold nanoparticles and their covalent conjugates with drug molecules.* Advanced Drug Delivery Reviews, 2013. **65**(5): p. 663-676.
177. Dreaden, E.C., Alkilany, A.M., Huang, X., Murphy, C.J., and El-Sayed, M.A., *The golden age: gold nanoparticles for biomedicine.* Chemical Society Reviews, 2012. **41**(7): p. 2740-2779.
178. Pissuwan, D., Niidome, T., and Cortie, M.B., *The forthcoming applications of gold nanoparticles in drug and gene delivery systems.* Journal of Controlled Release, 2011. **149**(1): p. 65-71.
179. Wang, F., Wang, Y.-C., Dou, S., Xiong, M.-H., Sun, T.-M., and Wang, J., *Doxorubicin-tethered responsive gold nanoparticles facilitate intracellular drug delivery for overcoming multidrug resistance in cancer cells.* ACS nano, 2011. **5**(5): p. 3679-92.
180. Rana, S., Bajaj, A., Mout, R., and Rotello, V.M., *Monolayer coated gold nanoparticles for delivery applications.* Advanced drug delivery reviews, 2012. **64**(2): p. 200-216.
181. Ghosh, R., Singh, L.C., Shohet, J.M., and Gunaratne, P.H., *A gold nanoparticle platform for the delivery of functional microRNAs into cancer cells.* Biomaterials, 2013. **34**(3): p. 807-816.
182. Xiao, Y., Jaskula-Sztul, R., Javadi, A., Xu, W., Eide, J., Dammalapati, A., Kunnimalaiyaan, M., Chen, H., and Gong, S., *Co-delivery of doxorubicin and siRNA using octreotide-conjugated gold nanorods for targeted neuroendocrine cancer therapy.* Nanoscale, 2012. **4**(22): p. 7185-7193.
183. Mamaeva, V., Sahlgren, C., and Linden, M., *Mesoporous silica nanoparticles in medicine-Recent advances.* Advanced Drug Delivery Reviews, 2013. **65**(5): p. 689-702.
184. Slowing, I.I., Vivero-Escoto, J.L., Wu, C.W., and Lin, V.S.Y., *Mesoporous silica nanoparticles as controlled release drug delivery and gene transfection carriers.* Advanced Drug Delivery Reviews, 2008. **60**(11): p. 1278-1288.
185. Bhakta, G., Sharma, R.K., Gupta, N., Cool, S., Nurcombe, V., and Maitra, A., *Multifunctional silica nanoparticles with potentials of imaging and gene delivery.* Nanomedicine-Nanotechnology Biology and Medicine, 2011. **7**(4): p. 472-479.

186. Zhu, Y.F., Meng, W.J., Gao, H., and Hanagata, N., *Hollow mesoporous silica/Poly(L-lysine) particles for codelivery of drug and gene with enzyme-triggered release property.* Journal of Physical Chemistry C, 2011. **115**(28): p. 13630-13636.
187. Meng, H., Mai, W.X., Zhang, H.Y., Xue, M., Xia, T., Lin, S.J., Wang, X., Zhao, Y., Ji, Z.X., Zink, J.I., and Nel, A.E., *Codelivery of an optimal drug/siRNA combination using mesoporous silica nanoparticles to overcome drug resistance in breast cancer in vitro and in vivo.* ACS Nano, 2013. **7**(2): p. 994-1005.
188. Ma, X., Zhao, Y., Ng, K.W., and Zhao, Y.L., *Integrated hollow mesoporous silica nanoparticles for target drug/siRNA co-delivery.* Chemistry-A European Journal, 2013. **19**(46): p. 15593-15603.
189. Liu, Z., Robinson, J.T., Tabakman, S.M., Yang, K., and Dai, H.J., *Carbon materials for drug delivery & cancer therapy.* Materials Today, 2011. **14**(7-8): p. 316-323.
190. Zhang, Y., Nayak, T.R., Hong, H., and Cai, W.B., *Graphene: a versatile nanoplatform for biomedical applications.* Nanoscale, 2012. **4**(13): p. 3833-3842.
191. Goenka, S., Sant, V., and Sant, S., *Graphene-based nanomaterials for drug delivery and tissue engineering.* Journal of Controlled Release, 2014. **173**: p. 75-88.
192. Hu, H.L., Tang, C., and Yin, C.H., *Folate conjugated trimethyl chitosan/graphene oxide nanocomplexes as potential carriers for drug and gene delivery.* Materials Letters, 2014. **125**: p. 82-85.
193. Zhi, F., Dong, H.F., Jia, X.F., Guo, W.J., Lu, H.T., Yang, Y.L., Ju, H.X., Zhang, X.J., and Hu, Y.Q., *Functionalized graphene oxide mediated adriamycin delivery and miR-21 gene silencing to overcome tumor multidrug resistance in vitro.* PLoS ONE, 2013. **8**(3): p. e60034.
194. Yang, H.W., Huang, C.Y., Chih-Wen, L., Liu, H.L., Huang, C.W., Liao, S.S., Chen, P.Y., Lu, Y.J., Wei, K.C., and Ma, C.C.M., *Gadolinium-functionalized nanographene oxide for combined drug and microRNA delivery and magnetic resonance imaging.* Biomaterials, 2014. **35**(24): p. 6534-6542.
195. Wang, M. and Thanou, M., *Targeting nanoparticles to cancer.* Pharmacological Research, 2010. **62**(2): p. 90-99.
196. Al-Jamal, W.T. and Kostarelos, K., *Liposomes: From a clinically established drug delivery system to a nanoparticle platform for theranostic nanomedicine.* Accounts of Chemical Research, 2011. **44**(10): p. 1094-1104.
197. Zhang, H.B., Wang, G.J., and Yang, H.A., *Drug delivery systems for differential release in combination therapy.* Expert Opinion on Drug Delivery, 2011. **8**(2): p. 171-190.
198. Allen, T.M. and Cullis, P.R., *Liposomal drug delivery systems: From concept to clinical applications.* Advanced Drug Delivery Reviews, 2013. **65**(1): p. 36-48.
199. Qu, M.H., Zeng, R.F., Fang, S., Dai, Q.S., Li, H.P., and Long, J.T., *Liposome-based co-delivery of siRNA and docetaxel for the synergistic treatment of lung cancer.* International Journal of Pharmaceutics, 2014. **474**(1-2): p. 112-122.
200. Zhang, Q.Y., Ran, R., Zhang, L., Liu, Y.Y., Mei, L., Zhang, Z.R., Gao, H.L., and He, Q., *Simultaneous delivery of therapeutic antagomirs with paclitaxel for the management of metastatic tumors by a pH-responsive anti-microbial peptide-mediated liposomal delivery system.* Journal of Controlled Release, 2015. **197**: p. 208-218.
201. Peng, Z., Wang, C.X., Fang, E.H., Lu, X.M., Wang, G.B., and Tong, Q., *Co-delivery of doxorubicin and SATB1 shRNA by thermosensitive magnetic cationic liposomes for gastric cancer therapy.* PLoS ONE, 2014. **9**(3): p. e92924.
202. Hadinoto, K., Sundaresan, A., and Cheow, W.S., *Lipid-polymer hybrid nanoparticles as a new generation therapeutic delivery platform: A review.* European Journal of Pharmaceutics and Biopharmaceutics, 2013. **85**(3, Part A): p. 427-443.
203. Mandal, B., Bhattacharjee, H., Mittal, N., Sah, H., Balabathula, P., Thoma, L.A., and Wood, G.C., *Core-shell-type lipid-polymer hybrid nanoparticles as a drug delivery platform.* Nanomedicine: Nanotechnology, Biology and Medicine, 2013. **9**(4): p. 474-491.
204. Zhao, X., Li, F., Li, Y., Wang, H., Ren, H., Chen, J., Nie, G., and Hao, J., *Co-delivery of HIF1a siRNA and gemcitabine via biocompatible lipid-polymer hybrid nanoparticles for effective treatment of pancreatic cancer.* Biomaterials, 2015. **46**: p. 13-25.
205. Kim, I.-Y., Seo, S.-J., Moon, H.-S., Yoo, M.-K., Park, I.-Y., Kim, B.-C., and Cho, C.-S., *Chitosan and its derivatives for tissue engineering applications.* Biotechnology Advances, 2008. **26**(1): p. 1-21.
206. Alves, N. and Mano, J., *Chitosan derivatives obtained by chemical modifications for biomedical and environmental applications.* International Journal of Biological Macromolecules, 2008. **43**(5): p. 401-414.
207. Marques, J.G., Gaspar, V.M., Costa, E., Paquete, C.M., and Correia, I.J., *Synthesis and characterization of micelles as carriers of non-steroidal anti-inflammatory drugs (NSAID) for application in breast cancer therapy.* Colloids and Surfaces B: Biointerfaces, 2014. **113**: p. 375-383.
208. Lalatsa, A., Garrett, N., Ferrarelli, T., Moger, J., Schatzlein, A., and Uchegbu, I., *Delivery of peptides to the blood and brain after oral uptake of quaternary ammonium palmitoyl glycol chitosan nanoparticles.* Molecular Pharmaceutics, 2012. **9**(6): p. 1764-1774.

209. Jose, S., Fangueiro, J., Smitha, J., Cinu, T., Chacko, A., Premaletha, K., and Souto, E., *Cross-linked chitosan microspheres for oral delivery of insulin: Taguchi design and in vivo testing.* Colloids and Surfaces B: Biointerfaces, 2012. **92**: p. 175-179.
210. Valente, J., Gaspar, V., Antunes, B., Countinho, P., and Correia, I., *Microencapsulated chitosan-dextran sulfate nanoparticles for controled delivery of bioactive molecules and cells in bone regeneration.* Polymer, 2013. **54**(1): p. 5-15.
211. Subbiah, R., Ramalingam, P., Ramasundaram, S., Park, K., Ramasamy, M.K., and Choi, K.J., *N, N, N-Trimethyl chitosan nanoparticles for controlled intranasal delivery of HBV surface antigen.* Carbohydrate polymers, 2012. **89**(4): p. 1289-1297.
212. Yang, Y., Wang, S., Wang, Y., Wang, X., Wang, Q., and Chen, M., *Advances in self-assembled chitosan nanomaterials for drug delivery.* Biotechnology Advances, 2014. **32**(7): p. 1301-1316.
213. Gaspar, V., Sousa, F., Queiroz, J., and Correia, I., *Formulation of chitosan-TPP-pDNA nanocapsules for gene therapy applications.* Nanotechnology, 2011. **22**(1): p. 015101.
214. Bao, X., Wang, W., Wang, C., Wang, Y., Zhou, J., Ding, Y., Wang, X., and Jin, Y., *A chitosan-graft-PEI-candesartan conjugate for targeted co-delivery of drug and gene in anti-angiogenesis cancer therapy.* Biomaterials, 2014. **35**(29): p. 8450-8466.
215. Gaspar, V., Costa, E., Queiroz, J., Pichon, C., Sousa, F., and Correia, I., *Folate-targeted multifunctional amino acid-chitosan nanoparticles for improved cancer therapy.* Pharmaceutical Research, 2015. **32**(2): p. 562-577.
216. Najafabadi, A.H., Abdouss, M., and Faghihi, S., *Synthesis and evaluation of PEG-O-chitosan nanoparticles for delivery of poor water soluble drugs: Ibuprofen.* Materials Science and Engineering: C, 2014. **41**: p. 91-99.
217. Wei, W., Lv, P.-P., Chen, X.-M., Yue, Z.-G., Fu, Q., Liu, S.-Y., Yue, H., and Ma, G.-H., *Codelivery of mTERT siRNA and paclitaxel by chitosan-based nanoparticles promoted synergistic tumor suppression.* Biomaterials, 2013. **34**(15): p. 3912-3923.
218. Lee, K.Y. and Mooney, D.J., *Alginate: properties and biomedical applications.* Progress in Polymer Science, 2012. **37**(1): p. 106-126.
219. George, M. and Abraham, T.E., *Polyionic hydrocolloids for the intestinal delivery of protein drugs: alginate and chitosan—a review.* Journal of Controlled Release, 2006. **114**(1): p. 1-14.
220. Gazori, T., Haririan, I., Fouladdel, S., Namazi, A., Nomani, A., and Azizi, E., *Inhibition of EGFR expression with chitosan/alginate nanoparticles encapsulating antisense oligonucleotides in T47D cell line using RT-PCR and immunocytochemistry.* Carbohydrate Polymers, 2010. **80**(4): p. 1042-1047.
221. Patnaik, S., Aggarwal, A., Nimesh, S., Goel, A., Ganguli, M., Saini, N., Singh, Y., and Gupta, K., *PEI-alginate nanocomposites as efficient in vitro gene transfection agents.* Journal of Controlled Release, 2006. **114**(3): p. 398-409.
222. You, J.O. and Peng, C.A. *Calcium-alginate nanoparticles formed by reverse microemulsion as gene carriers. Macromolecular Symposia.* 2005. Wiley Online Library.
223. Cafaggi, S., Russo, E., Stefani, R., Leardi, R., Caviglioli, G., Parodi, B., Bignardi, G., De Totero, D., Aiello, C., and Viale, M., *Preparation and evaluation of nanoparticles made of chitosan or N-trimethyl chitosan and a cisplatin-alginate complex.* Journal of Controlled Release, 2007. **121**(1): p. 110-123.
224. Zhao, D., Zhuo, R.-X., and Cheng, S.-X., *Alginate modified nanostructured calcium carbonate with enhanced delivery efficiency for gene and drug delivery.* Molecular BioSystems, 2012. **8**(3): p. 753-759.
225. Zhao, D., Liu, C.-J., Zhuo, R.-X., and Cheng, S.-X., *Alginate/$CaCO_3$ hybrid nanoparticles for efficient codelivery of antitumor gene and drug.* Molecular pharmaceutics, 2012. **9**(10): p. 2887-2893.
226. Varshosaz, J., *Dextran conjugates in drug delivery.* Expert Opinion on Drug Delivery, 2012. **9**(5): p. 509-523.
227. Sun, G. and Mao, J.J., *Engineering dextran-based scaffolds for drug delivery and tissue repair.* Nanomedicine, 2012. **7**(11): p. 1771-1784.
228. Sun, H., Guo, B., Li, X., Cheng, R., Meng, F., Liu, H., and Zhong, Z., *Shell-sheddable micelles based on dextran-SS-poly (ε-caprolactone) diblock copolymer for efficient intracellular release of doxorubicin.* Biomacromolecules, 2010. **11**(4): p. 848-854.
229. Anitha, A., Deepagan, V., Rani, V.D., Menon, D., Nair, S., and Jayakumar, R., *Preparation, characterization, in vitro drug release and biological studies of curcumin loaded dextran sulphate-chitosan nanoparticles.* Carbohydrate Polymers, 2011. **84**(3): p. 1158-1164.
230. Jiang, D. and Salem, A.K., *Optimized dextran-polyethylenimine conjugates are efficient non-viral vectors with reduced cytotoxicity when used in serum containing environments.* International Journal of Pharmaceutics, 2012. **427**(1): p. 71-79.
231. Sun, K., Wang, J., Zhang, J., Hua, M., Liu, C., and Chen, T., *Dextran-g-PEI nanoparticles as a carrier for co-delivery of adriamycin and plasmid into osteosarcoma cells.* International Journal of Biological Macromolecules, 2011. **49**(2): p. 173-180.

232. Dicker, K.T., Gurski, L.A., Pradhan-Bhatt, S., Witt, R.L., Farach-Carson, M.C., and Jia, X., *Hyaluronan: a simple polysaccharide with diverse biological functions.* Acta Biomaterialia, 2014. **10**(4): p. 1558-1570.
233. Arpicco, S., Milla, P., Stella, B., and Dosio, F., *Hyaluronic acid conjugates as vectors for the active targeting of drugs, genes and nanocomposites in cancer treatment.* Molecules, 2014. **19**(3): p. 3193-3230.
234. Skandalis, S.S., Gialeli, C., Theocharis, A.D., and Karamanos, N.K., *Advances and Advantages of Nanomedicine in the Pharmacological Targeting of Hyaluronan-CD44 Interactions and Signaling in Cancer.* Hyaluronan Signaling and Turnover, 2014. **123**: p. 277-317.
235. Misra, S., Heldin, P., Hascall, V.C., Karamanos, N.K., Skandalis, S.S., Markwald, R.R., and Ghatak, S., *Hyaluronan-CD44 interactions as potential targets for cancer therapy.* FEBS Journal, 2011. **278**(9): p. 1429-1443.
236. Duceppe, N. and Tabrizian, M., *Factors influencing the transfection efficiency of ultra low molecular weight chitosan/hyaluronic acid nanoparticles.* Biomaterials, 2009. **30**(13): p. 2625-2631.
237. Raviña, M., Cubillo, E., Olmeda, D., Novoa-Carballal, R., Fernandez-Megia, E., Riguera, R., Sánchez, A., Cano, A., and Alonso, M.J., *Hyaluronic acid/chitosan-g-poly(ethylene glycol) nanoparticles for gene therapy: an application for pDNA and siRNA delivery.* Pharmaceutical Research, 2010. **27**(12): p. 2544-2555.
238. Ganesh, S., Iyer, A.K., Morrissey, D.V., and Amiji, M.M., *Hyaluronic acid based self-assembling nanosystems for CD44 target mediated siRNA delivery to solid tumors.* Biomaterials, 2013. **34**(13): p. 3489-3502.
239. Ghasemi, Z., Dinarvand, R., Mottaghitalab, F., Esfandyari-Manesh, M., Sayari, E., and Atyabi, F., *Aptamer decorated hyaluronan/chitosan nanoparticles for targeted delivery of 5-fluorouracil to MUC1 overexpressing adenocarcinomas.* Carbohydrate Polymers, 2015. **121**: p. 190-198.
240. Huang, J., Zhang, H., Yu, Y., Chen, Y., Wang, D., Zhang, G., Zhou, G., Liu, J., Sun, Z., and Sun, D., *Biodegradable self-assembled nanoparticles of poly (D, L-lactide-co-glycolide)/hyaluronic acid block copolymers for target delivery of docetaxel to breast cancer.* Biomaterials, 2014. **35**(1): p. 550-566.
241. Han, M., Lv, Q., Tang, X.J., Hu, Y.L., Xu, D.H., Li, F.Z., Liang, W.Q., and Gao, J.Q., *Overcoming drug resistance of MCF-7/ADR cells by altering intracellular distribution of doxorubicin via MVP knockdown with a novel siRNA polyamidoamine-hyaluronic acid complex.* Journal of Controlled Release, 2012. **163**(2): p. 136-44.
242. Mellet, C.O., Fernández, J.M.G., and Benito, J.M., *Cyclodextrin-based gene delivery systems.* Chemical Society Reviews, 2011. **40**(3): p. 1586-1608.
243. Zhou, J. and Ritter, H., *Cyclodextrin functionalized polymers as drug delivery systems.* Polymer Chemistry, 2010. **1**(10): p. 1552-1559.
244. Hu, Q.-D., Tang, G.-P., and Chu, P.K., *Cyclodextrin-based host-guest supramolecular nanoparticles for delivery: From design to applications.* Accounts of Chemical Research, 2014. **47**(7): p. 2017-2025.
245. Zhang, J. and Ma, P.X., *Cyclodextrin-based supramolecular systems for drug delivery: recent progress and future perspective.* Advanced Drug Delivery Reviews, 2013. **65**(9): p. 1215-1233.
246. Teijeiro-Osorio, D., Remuñán-López, C., and Alonso, M.J., *Chitosan/cyclodextrin nanoparticles can efficiently transfect the airway epithelium in vitro.* European Journal of Pharmaceutics and Biopharmaceutics, 2009. **71**(2): p. 257-263.
247. Yang, C., Li, H., Goh, S.H., and Li, J., *Cationic star polymers consisting of a-cyclodextrin core and oligoethylenimine arms as nonviral gene delivery vectors.* Biomaterials, 2007. **28**(21): p. 3245-3254.
248. Zhang, J., Sun, H., and Ma, P.X., *Host– guest interaction mediated polymeric assemblies: multifunctional nanoparticles for drug and gene delivery.* ACS Nano, 2010. **4**(2): p. 1049-1059.
249. Gao, H., Qian, J., Cao, S., Yang, Z., Pang, Z., Pan, S., Fan, L., Xi, Z., Jiang, X., and Zhang, Q., *Precise glioma targeting of and penetration by aptamer and peptide dual-functioned nanoparticles.* Biomaterials, 2012. **33**(20): p. 5115-23.
250. Hu, Q., Li, W., Hu, X., Hu, Q., Shen, J., Jin, X., Zhou, J., Tang, G., and Chu, P.K., *Synergistic treatment of ovarian cancer by co-delivery of survivin shRNA and paclitaxel via supramolecular micellar assembly.* Biomaterials, 2012. **33**(27): p. 6580-6591.
251. Lalatsa, A., Schatzlein, A.G., Mazza, M., Thi, B.H.L., and Uchegbu, I.F., *Amphiphilic poly(L-amino acids) - New materials for drug delivery.* Journal of Controlled Release, 2012. **161**(2): p. 523-536.
252. Xu, H., Yao, Q., Cai, C., Gou, J., Zhang, Y., Zhong, H., and Tang, X., *Amphiphilic poly(amino acid) based micelles applied to drug delivery: The in vitro and in vivo challenges and the corresponding potential strategies.* Journal of Controlled Release, 2015. **199**: p. 84-97.
253. Gonzalo, T., Lollo, G., Garcia-Fuentes, M., Torres, D., Correa, J., Riguera, R., Fernandez-Megia, E., Calvo, P., Aviles, P., Guillen, M.J., and Alonso, M.J., *A new potential nano-oncological therapy based on polyamino acid nanocapsules.* Journal of Controlled Release, 2013. **169**(1-2): p. 10-16.

254. Pan, L., He, Q., Liu, J., Chen, Y., Ma, M., Zhang, L., and Shi, J., *Nuclear-targeted drug delivery of TAT peptide-conjugated monodisperse mesoporous silica nanoparticles.* Journal of the American Chemical Society, 2012. **134**(13): p. 5722-5.
255. Labet, M. and Thielemans, W., *Synthesis of polycaprolactone: a review.* Chemical Society Reviews, 2009. **38**(12): p. 3484-3504.
256. Dash, T.K. and Konkimalla, V.B., *Poly-ε-caprolactone based formulations for drug delivery and tissue engineering: A review.* Journal of Controlled Release, 2012. **158**(1): p. 15-33.
257. Xin, H., Jiang, X., Gu, J., Sha, X., Chen, L., Law, K., Chen, Y., Wang, X., Jiang, Y., and Fang, X., *Angiopep-conjugated poly(ethylene glycol)-co-poly(ε-caprolactone) nanoparticles as dual-targeting drug delivery system for brain glioma.* Biomaterials, 2011. **32**(18): p. 4293-4305.
258. Lin, D., Jiang, Q., Cheng, Q., Huang, Y., Huang, P., Han, S., Guo, S., Liang, Z., and Dong, A., *Polycation-detachable nanoparticles self-assembled from mPEG-PCL-g-SS-PDMAEMA for in vitro and in vivo siRNA delivery.* Acta Biomaterialia, 2013. **9**(8): p. 7746-7757.
259. Liu, Y., Samsonova, O., Sproat, B., Merkel, O., and Kissel, T., *Biophysical characterization of hyper-branched polyethylenimine-graft- polycaprolactone-block-mono-methoxyl-poly(ethylene glycol) copolymers (hy-PEI-PCL-mPEG) for siRNA delivery.* Journal of Controlled Release, 2011. **153**(3): p. 262-268.
260. Han, S., Wan, H., Lin, D., Guo, S., Dong, H., Zhang, J., Deng, L., Liu, R., Tang, H., and Dong, A., *Contribution of hydrophobic/hydrophilic modification on cationic chains of poly(ε-caprolactone)-graft-poly(dimethylamino ethylmethacrylate) amphiphilic co-polymer in gene delivery.* Acta Biomaterialia, 2014. **10**(2): p. 670-679.
261. Shi, S., Shi, K., Tan, L., Qu, Y., Shen, G., Chu, B., Zhang, S., Su, X., Li, X., Wei, Y., and Qian, Z., *The use of cationic MPEG-PCL-g-PEI micelles for co-delivery of Msurvivin T34A gene and doxorubicin.* Biomaterials, 2014. **35**(15): p. 4536-4547.
262. Sun, T.-M., Du, J.-Z., Yao, Y.-D., Mao, C.-Q., Dou, S., Huang, S.-Y., Zhang, P.-Z., Leong, K.W., Song, E.-W., and Wang, J., *Simultaneous Delivery of siRNA and Paclitaxel via a "Two-in-One" Micelleplex Promotes Synergistic Tumor Suppression.* ACS Nano, 2011. **5**(2): p. 1483-1494.
263. Anderson, J.M. and Shive, M.S., *Biodegradation and biocompatibility of PLA and PLGA microspheres.* Advanced Drug Delivery Reviews, 2012. **64**: p. 72-82.
264. Lasprilla, A.J.R., Martinez, G.A.R., Lunelli, B.H., Jardini, A.L., and Filho, R.M., *Poly-lactic acid synthesis for application in biomedical devices — A review.* Biotechnology Advances, 2012. **30**(1): p. 321-328.
265. Nair, L.S. and Laurencin, C.T., *Biodegradable polymers as biomaterials.* Progress in Polymer Science, 2007. **32**(8–9): p. 762-798.
266. Cheng, J., Teply, B.A., Sherifi, I., Sung, J., Luther, G., Gu, F.X., Levy-Nissenbaum, E., Radovic-Moreno, A.F., Langer, R., and Farokhzad, O.C., *Formulation of functionalized PLGA-PEG nanoparticles for in vivo targeted drug delivery.* Biomaterials, 2007. **28**(5): p. 869-876.
267. Marques, J.G., Gaspar, V.M., Markl, D., Costa, E.C., Gallardo, E., and Correia, I.J., *Co-delivery of Sildenafil (Viagra®) and Crizotinib for synergistic and improved anti-tumoral therapy.* Pharmaceutical research, 2014. **31**(9): p. 2516-2528.
268. Venkatraman, S.S., Jie, P., Min, F., Freddy, B.Y.C., and Leong-Huat, G., *Micelle-like nanoparticles of PLA-PEG-PLA triblock copolymer as chemotherapeutic carrier.* International Journal of Pharmaceutics, 2005. **298**(1): p. 219-232.
269. He, G., Ma, L.L., Pan, J., and Venkatraman, S., *ABA and BAB type triblock copolymers of PEG and PLA: a comparative study of drug release properties and "stealth" particle characteristics.* International Journal of Pharmaceutics, 2007. **334**(1): p. 48-55.
270. Song, Z., Feng, R., Sun, M., Guo, C., Gao, Y., Li, L., and Zhai, G., *Curcumin-loaded PLGA-PEG-PLGA triblock copolymeric micelles: Preparation, pharmacokinetics and distribution in vivo.* Journal of Colloid and Interface Science, 2011. **354**(1): p. 116-123.
271. Yu, Y., Chen, C.-K., Law, W.-C., Mok, J., Zou, J., Prasad, P.N., and Cheng, C., *Well-defined degradable brush polymer–drug conjugates for sustained delivery of paclitaxel.* Molecular Pharmaceutics, 2012. **10**(3): p. 867-874.
272. Munier, S., Messai, I., Delair, T., Verrier, B., and Ataman-Önal, Y., *Cationic PLA nanoparticles for DNA delivery: Comparison of three surface polycations for DNA binding, protection and transfection properties.* Colloids and Surfaces B: Biointerfaces, 2005. **43**(3–4): p. 163-173.
273. Bivas-Benita, M., Romeijn, S., Junginger, H.E., and Borchard, G., *PLGA-PEI nanoparticles for gene delivery to pulmonary epithelium.* European Journal of Pharmaceutics and Biopharmaceutics, 2004. **58**(1): p. 1-6.
274. Jeong, J.H. and Park, T.G., *Poly(L-lysine)-g-poly(D,L-lactic-co-glycolic acid) micelles for low cytotoxic biodegradable gene delivery carriers.* Journal of Controlled Release, 2002. **82**(1): p. 159-166.
275. Li, Y., Zhu, Y., Xia, K., Sheng, R., Jia, L., Hou, X., Xu, Y., and Cao, A., *Dendritic Poly(L-lysine)-b-Poly(L-lactide)-b-Dendritic Poly(L-lysine) Amphiphilic Gene Delivery Vectors: Roles of PLL Dendritic Generation and Enhanced Transgene Efficacies via Termini Modification.* Biomacromolecules, 2009. **10**(8): p. 2284-2293.

276. Mishra, D., Kang, H.C., and Bae, Y.H., *Reconstitutable charged polymeric (PLGA)2-b-PEI micelles for gene therapeutics delivery.* Biomaterials, 2011. **32**(15): p. 3845-3854.
277. Zhao, Z.-X., Gao, S.-Y., Wang, J.-C., Chen, C.-J., Zhao, E.-Y., Hou, W.-J., Feng, Q., Gao, L.-Y., Liu, X.-Y., Zhang, L.-R., and Zhang, Q., *Self-assembly nanomicelles based on cationic mPEG-PLA-b-Polyarginine(R15) triblock copolymer for siRNA delivery.* Biomaterials, 2012. **33**(28): p. 6793-6807.
278. Fu, C., Sun, X., Liu, D., Chen, Z., Lu, Z., and Zhang, N., *Biodegradable tri-block copolymer poly (lactic acid)-poly (ethylene glycol)-poly (L-lysine)(PLA-PEG-PLL) as a non-viral vector to enhance gene transfection.* International Journal of Molecular Sciences, 2011. **12**(2): p. 1371-1388.
279. Liu, P., Yu, H., Sun, Y., Zhu, M., and Duan, Y., *A mPEG-PLGA-b-PLL copolymer carrier for adriamycin and siRNA delivery.* Biomaterials, 2012. **33**(17): p. 4403-4412.
280. Su, W.-P., Cheng, F.-Y., Shieh, D.-B., Yeh, C.-S., and Su, W.-C., *PLGA nanoparticles codeliver paclitaxel and Stat3 siRNA to overcome cellular resistance in lung cancer cells.* International Journal of Nanomedicine, 2012. **7**: p. 4269.
281. Patil, Y.B., Swaminathan, S.K., Sadhukha, T., Ma, L., and Panyam, J., *The use of nanoparticle-mediated targeted gene silencing and drug delivery to overcome tumor drug resistance.* Biomaterials, 2010. **31**(2): p. 358-365.

Section II

Minicircle biosynthesis and evaluation of peptide ligands

CHAPTER 5

Improved Minicircle DNA Biosynthesis for Gene Therapy Applications

Human Gene Therapy Methods, 2014
DOI: 10.1089/hgtb.2013.020

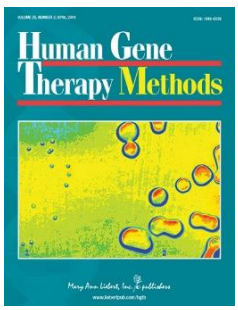

Volume 25, issue 2

Motivation

The biosynthesis of mcDNA with the φC31/I-SceI technology presents several improvements in comparison with other mcDNA production processes. The following research was performed as an attempt to further characterize and optimize minicircles production in recombinant organisms since several parameters of this technology remain poorly explored. Such study was anticipated to impact the final quality of mcDNA biopharmaceutical batches.

HUMAN GENE THERAPY METHODS 25:93–105 (April 2014)

DOI: 10.1089/hgtb.2013.020

Improved Minicircle DNA Biosynthesis for Gene Therapy Applications

Vítor M. Gaspar,[1] Cláudio J. Maia,[1] João A. Queiroz,[1] Chantal Pichon,[2] Ilídio J. Correia,[1] and Fani Sousa[1]

Abstract

Minicircular DNA (mcDNA) biopharmaceuticals have recently risen as a valuable alternative for the development of a next generation of bioactive therapeutics because they are more efficient and safer than standard plasmid DNA (pDNA). To date, the relatively insufficient knowledge regarding mcDNA biosynthesis is currently hindering its manufacture in suitable amounts for clinical trial evaluations. Addressing this limitation is therefore mandatory to bring forth the full therapeutic potential of this cutting-edge technology. Herein, we describe for the first time new processing parameters that improve the overall yield of mcDNA obtained from bacterial fermentations. We provide details for further in-line monitoring and optimization in view of the current good manufacturing guidelines. Our results show that by rising growth temperature to 42°C, an increase in the overall minicircle producer plasmid yield is attained, while biomass amounts are reduced. Moreover, by monitoring in real time the dynamic recombination of parental plasmids to mcDNA, we found that this event is more efficient at specific time points, regardless of the growth temperature and inductor concentration used. These are important findings since mcDNA can be recovered with higher yields at these determined key stages. Indeed, the manipulation of these parameters resulted in a 2.21-fold increase in mcDNA production compared with the established growth temperatures for this technology. Overall, our findings highlight that to achieve maximum productivity while attaining pharmaceutical-grade mcDNA preparations, process design and biosynthesis optimization must take into account key parameters such as temperature, inductor concentration, and recovery time.

Introduction

In the last couple of decades, DNA biopharmaceuticals have attracted an increasing interest because of their exceptional potential for application in several disease scenarios that currently remain very challenging and difficult to overcome (Kay, 2011; Santos *et al.*, 2012). Spanning from the use in novel DNA vaccines to the design of therapeutic approaches focused on cancer or tissue engineering, these remarkable biomolecules may represent a novel generation of bioactive medications in the near future (Kimelman Bleich *et al.*, 2012). Until now, plasmid DNA (pDNA) was considered the primary expression vector to develop biopharmaceuticals for human use, with various investigations presently underway worldwide (Carnes *et al.*, 2011; Ismail *et al.*, 2012). However, the translation of pDNA-based approaches into actual pharmaceutics is still severely held up by numerous concerns associated with pDNA structure–activity correlations (Gill *et al.*, 2009). In fact, pDNA vectors generally comprise bacterial sequences and CpG motifs, which trigger adverse immune responses if delivered to mammalian hosts, raising serious biocompatibility issues (Ismail *et al.*, 2012; Mayrhofer and Iro, 2012). The presence of antibiotic selection markers in DNA vectors is also an additional drawback, since risky resistance gene transfer into human bacterial flora may naturally occur (Salyers *et al.*, 2004). Apart from this, silencing of transgene expression in eukaryotic cells occurs shortly after pDNA administration, which is a major obstacle that further emphasizes plasmid-associated limitations in therapeutic applications (Chen *et al.*, 2004, 2008). In order to overcome these restrictions, recent reports are unraveling the therapeutic potential of an innovative technology that relies on tailored minicircular DNA (mcDNA) expression cassettes (Chabot *et al.*, 2013; Kwon *et al.*, 2012). Minicircles are engineered nucleic acids that completely lack bacterial backbone sequences and their inherent cytotoxic effects (Kobelt *et al.*, 2013).

[1]Centro de Investigação em Ciências da Saúde, Universidade da Beira Interior, Covilhã 6200-506, Portugal.
[2]Centre de Biophysique Moléculaire CNRS UPR4301, INSERM, and University of Orléans, F-45071 Orléans Cedex 2, France.

Actually, smaller mcDNA is endowed with a unique miniaturized design that accounts for their improved diffusion and increased biological activity (Chen *et al.*, 2003). Notably, not only is minicircle-mediated expression prolonged *in vivo*, but also higher therapeutic protein levels are produced compared with its pDNA counterparts (Chabot *et al.*, 2013).

To date, the available high-throughput technologies of mcDNA manufacture for nonviral gene therapy are established on site-specific recombination systems (e.g., ParA resolvase and Cre recombinase) that convert template pDNA into minimal DNA circles during fermentation usually performed at 37°C (Jechlinger *et al.*, 2004; Wong *et al.*, 2012). These techniques have been recently optimized with the outcome of an upgraded mcDNA production bioprocess via the expression of ΦC31 serine recombinase in a genetically modified *Escherichia coli* strain (Kay *et al.*, 2010). In this improved system, parental plasmids (PP) that encode the information of standard pDNA are initially replicated and then dynamically converted into minicircles and miniplasmids (mP) by the action of ΦC31 recombinase (Osborn *et al.*, 2011). Thus, this interesting event driven by L-arabinose addition, at a temperature of 32°C, generates two distinct expression vectors that encode either the therapeutic genes of interest (mcDNA) or bacterial-derived sequences (namely, those present in mP) (Kay *et al.*, 2010). After this induction, an endonuclease (I-SceI) that targets specific degradation sites in mP and PP backbones is also activated to mediate their elimination (Fig. 1). Despite that this is a complex methodology, its robustness renders it feasible, rapid, and with yields similar to those of generic pDNA biosynthesis (Chen *et al.*, 2005; Kay *et al.*, 2010). However, to accelerate mcDNA translation into novel biopharmaceuticals, the design of cost-effective manufacture processes that assure scalability and clinical-grade quality is still a prerequirement that must be attained. In fact, unlike pDNA, very few reports address actual bioprocess design parameters that may be manipulated to increase mcDNA production, while assuring product consistency (Chen *et al.*, 2005).

Therefore, we characterized the first commercially available mcDNA producing system by analyzing bacterial growth conditions that could influence the overall minicircle yield, and monitored in real time the mcDNA generation from its parental template, to shed light on events that have not been explored so far.

Materials and Methods

Materials

The minicircle-producing *E. coli* strain ZYCY10P3S2T and the 7.06 kbp pMC.CMV-MCS-EF1-GFP-SV40 PolyA PP containing the pUC19 replication origin and recombinase recognition sites were obtained from System Biosciences. Bacterial culture reagents that include yeast extract and tryptone were purchased from Biokar Diagnostics. Glycerol was obtained from Himedia. L-arabinose, Luria Broth (LB)-agar, and LB powder were purchased from Sigma Aldrich, and DNA ladder was provided by Vivantis Technologies. Safe Green DNA was obtained from NZYTech. Ready-to-use Maxima SYBR green quantitative polymerase chain reaction (qPCR) master mix was purchased from Fermentas (Thermo Scientific Bio). All other reagents were of analytical grade and used as received.

Fermentation conditions

In order to evaluate the effect of different growth conditions on the amplification of PP, the genetically modified *E. coli* ZYCY10P3S2T strain was primarily transformed with the kanamycin-resistant pMC expression cassette according to the manufacturer's instructions. After transformation, several colonies present in LB-agar plates (50 μg/ml, kanamycin) were isolated for posterior studies. All bacterial cultures were performed in 1-liter Erlenmeyer's containing 250 ml of Terrific Broth medium (Tryptone [20 g/liter]; yeast extract [24 g/liter], glycerol [4 ml/liter]; 0.017 *M* KH_2PO_4, 0.072 *M* K_2HPO_4, pH 7.0) in a refrigerated orbital shaker (Agitorb 200 IC; Aralab) at constant stirring (250 rpm) and variable temperature conditions (37°C and 42°C). Batch fermentations were inoculated from an over-night prefermentation (OD_{600nm} = 2.6) to achieve a starting OD_{600nm} of 0.2. In order to track PP amplification during the course of fermentation, bacterial samples were collected at different time periods, immediately pelleted (20 min, 6,000 g, 4°C), and stored at −20°C for subsequent

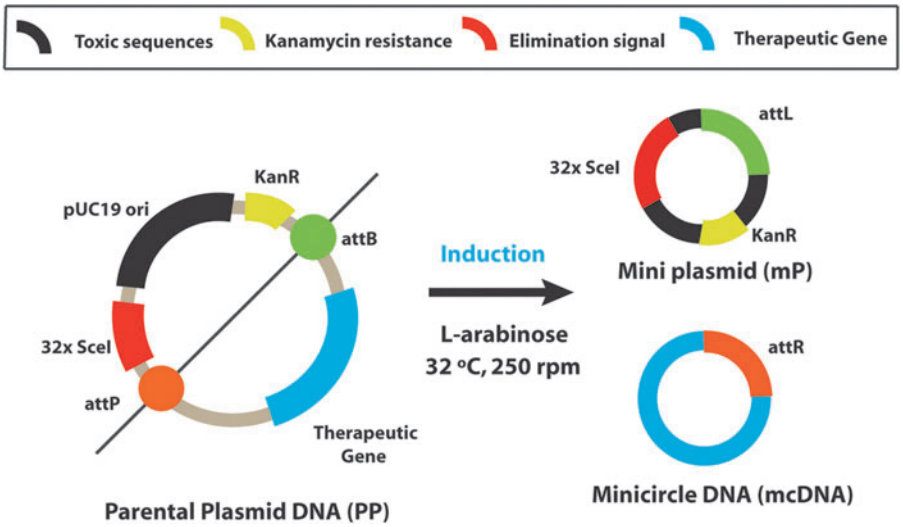

FIG. 1. Schematics of mcDNA-producing technology from PP. Upon induction with L-arabinose, the minicircle-producing plasmid is converted into mcDNA, and miniplasmids, by the action of ΦC31 recombinase that recognizes attB and attP recombination sequences. Simultaneously, the endonuclease I-SceI is activated to destroy PP and miniplasmids by recognition of the 32 *Sce*I binding sites present in the vectors. mcDNA, minicircular DNA; PP, parental plasmids. Color images available online at www.liebertpub.com/hgtb

analysis. Simultaneously, samples for biomass analysis (OD_{600nm}) were also withdrawn and analyzed immediately by UV-Vis spectroscopy (Shimadzu UV-1700 spectrophotometer). For each condition tested, at least three independent fermentations were performed. In addition to the 7.06 kbp PP, a smaller construct of 4.88 kbp was also designed. Briefly, the original PP template was reduced in size by digestion with *Sac*I (New England Biolabs) restriction enzyme by following the manufacturer's instructions. The linearized smaller PP was then blunt ligated with T4DNA ligase overnight at 4°C. After confirming the formation of the smaller PP backbone, competent *E. coli* ZYCY10P3S2T were transformed with this construct by using a method previously described by Roychoudhury *et al.* (2009). The single colonies that contained the smaller PP plasmid were then selected for posterior studies.

Induction conditions

The induction of mcDNA production was promoted as previously reported in the literature with some adjustments (Kay *et al.*, 2010). Initially, bacterial cultivations were grown at different temperatures until the end of the determined exponential phase. Minicircle production was then induced by the addition of a sterile L-arabinose solution (20% w/v) to the desired final concentrations (0.01% and 0.1%). Upon induction, the pH of all fermentations was monitored and adjusted to pH 7.0 by the addition of 1 *M* sterile NaOH, whenever necessary. The recombination process was then allowed to proceed for an additional 5 hr period with constant stirring at 250 rpm, at a temperature of 32°C. Additionally, the bacterial cultures were induced as previously described by Kay *et al.* (2010), in order to evaluate if the presence of residual species was decreased. Briefly, a sterile minicircle induction mix (250 ml of LB medium, 10 ml of 1 *M* NaOH), containing L-arabinose to the desired final concentrations (0.1% and 0.01%), was added to the bacterial cultures at the end of the exponential phase. The biosynthesis of mcDNA from the PP template was then performed as described above.

Dry cell weight determination

The dry cell weight of the genetically modified mcDNA producer strain was determined as previously described (Silva *et al.*, 2009), with slight modifications. Briefly, aliquots (1 ml) of cell cultivations were recovered by centrifugation (6,000 × *g*, 20 min, 4°C) in preweighed tubes. Afterward, cell sediments were then washed twice with NaCl (0.9% w/v) and placed in a drying oven at 85°C for 48 hr. All experiments were performed in triplicates. Dry cell weight was then determined from a standard curve ($y = 2.176x + 0.0338$; $R^2 = 0.9981$). For this specific strain one unit OD_{600nm} corresponded to a dry cell weight of 0.437 g/liter.

Bacterial lysis and DNA isolation

The recovery of both intact smaller PP and DNA minicircles from bacterial cultures was performed with the NucleoSpin Plasmid Miniprep Recovery Kit (Macherey-Nagel) according to the manufacturer's instructions, with some modifications. In summary, bacterial pellets recovered from fermentation were resuspended in prechilled buffer, and afterward incubated with lysis buffer by gently agitating for 5 min at room temperature. The neutralized lysate was clarified, and applied in spin columns, where it was then purified through extensive washing (4°C) using the double of the recommended volume. DNA elution was finally promoted by the addition of elution buffer (45 μl) after an incubation period of 2 min at 4°C. The yield of recovered template plasmids was determined by UV-Vis spectrophotometry at A_{260nm}. The purity of PP and mcDNA samples was monitored before all analysis (A_{260nm}/A_{280nm} and A_{260nm}/A_{230nm}) in a Nanophotometer (Implen).

Quantitative PCR

The conversion process of smaller PP into minicircles and mP was monitored by real-time PCR in a Multi-color iCycler iQ5 system (Bio-Rad Laboratories) to determine the presence of the expression vectors during induction. For this purpose a set of specific primers for each species was designed: (i) Parental plasmid primers for pUC19 origin (ColE1) (forward [fw]: 5′-TCCTGTTACCAGTGGCTGCT; reverse [rv]: 5′-AGTTCGGTGTAGGTCGTTCG) were used to amplify a fragment of 151 bp. (ii) Miniplasmid primers for attL recombination site (fw: 5′-GGGCGTGCCCTTGAGTTC; rv: 5′-CGTTGGCTACCCGTGATATT) were used to amplify a 248 bp fragment. (iii) DNA minicircle primers for attR recombination site (fw: 5′-TGGGGTAACCTTTGGGCT; rv: 5′-AAGTCCCGTTGATTTTGGTG) were developed to amplify a 248 bp fragment. The qPCR efficiency of primers sets for each specific vector was determined by serial dilutions of DNA samples in a given range (1:10; 1:100; 1:1,000; and 1:10,000). Efficiencies between 90% and 110% were obtained, which are considered acceptable for real-time PCR (Pfaffl, 2001). PCRs were carried out in 20 μl reactions containing 10 μl SYBR green mastermix, 300 n*M* of each primer, and 1 μl of extracted DNA. The physical conditions included an initial denaturation step of 10 min at 95°C, followed by 35 cycles of denaturation (10 sec at 95°C), annealing (30 sec at 60°C), and extension (10 sec at 72°C). The amplified PCR fragments were checked by melting-curves. The reactions were heated from 55°C to 95°C with 10 sec hold at each temperature (0.05°C/sec). Melting reactions were carried out by step-wise heating (0.05°C/sec) from 55°C to 95°C, with 10 sec holds at every temperature. DNA samples were run at least in triplicate for each assay. Data analysis, baseline adjustments, and fluorescence threshold setting above background values were executed in iQ5 software v 2.0. Relative fold differences were calculated using the formula $2^{-\Delta\Delta Ct}$ as previously reported in the literature (Pfaffl, 2001). The minicircle/parental and parental/minicircle ratios were also calculated from qPCR data analysis. The conversion of the previous results to heat-map coding was performed according to the rules of significance arithmetic (Mathematica v. 8.0, Wolfram|Alpha).

Agarose gel electrophoresis

Agarose gel electrophoresis was performed in a horizontal system (Cleaver Scientific) using a 1% agarose gel stained with ethidium bromide (0.5 μg/ml). Electrophoresis was run at 90 V for 35 min in TAE buffer. The gels were then imaged using an Uvitec Cambridge Fire-reader UV transilluminator equipped with a CCD camera (Uvitec Cambridge).

Statistical analysis

Different groups were compared by one-way analysis of variance, with the *post-hoc* Newman–Keuls test. A value of $p < 0.05$ was considered statistically significant. All the calculations were performed on Graphpad Prism 5 trial software (Graphpad Software).

Results

Bacterial growth and PP amplification

Bacterial growth rate of the novel *E. coli* ZYCY10P3S2T strain bearing the minicircle-producer template plasmid was initially characterized to determine its evolution profile during cultivation. For this purpose, two different temperatures (37°C and 42°C) were studied in order to primarily establish optimal growth conditions that could maximize PP production in this initial stage. As the results in Fig. 2A demonstrate, bacterial amplification at 37°C results in higher cell levels than those obtained at a higher temperature. Remarkably, regardless of the fermentation conditions, both strategies reached maximum cell number at 12 hr after inoculation (Fig. 2A). During the course of fermentation, the structural instability of the PP template plasmids was also addressed. Concerning the latter, electrophoretic analysis reveals that PP degradation was promoted neither at 37°C nor at 42°C. In fact, it can be readily observed that template vectors maintained their characteristic open circular and supercoiled isoforms at all sampling times (Fig. 2B–D). Moreover, the results obtained after restriction digestion reveal that no genomic DNA contamination is present (Fig. 2B). These noteworthy results suggest that the various genome modifications of the producer strain did not impair PP biosynthesis under these conditions.

The effect of temperature settings on biomass accumulation during fermentation was also evaluated since this is an important process-associated parameter that can influence the final yield of PP DNA, and consequently the mcDNA biopharmaceutical manufactured. Regarding this feature, our findings demonstrate that higher biomass production is obtained when bacterial growth is performed at 37°C. Inversely, biomass production at 42°C was decreased significantly, a 0.74-fold reduction (Fig. 3A). However, this noticeable decline is translated into a 1.29-fold increase in PP-specific yield in comparison with the yields obtained at 37°C (Fig. 3B).

Further characterization of bacterial-specific growth rates under variable temperature conditions demonstrates that an increase in temperature to 42°C is correlated with lower specific growth rates of the minicircle-producing strain (Table 1). Actually, for the same size of PP templates, a $0.013\,hr^{-1}$ decrease in bacterial growth rate occurs when cultivations are performed at higher temperature (42°C).

Evaluation of mcDNA dynamic biosynthesis

The evaluation of mcDNA manufacture and elimination of contaminating species inherent to the recombination process is also one of the most significant manufacture parameters associated with this novel technology. Essentially, the removal or reduction of contaminants at this stage may have a positive impact on subsequent purification stages and unlock the full clinical potential of this engineered bioprocess. Therefore, we unraveled the time-dependent dynamics of the mcDNA manufacture process by using a highly sensitive technique. When we consider the course of recombination, our findings illustrate that this is a remarkably complex and versatile event in which conversion of PP to mP and mcDNA starts to take place immediately upon L-arabinose addition and temperature decrease to 32°C, regardless of the initial cultivation settings (37°C or 42°C) (Fig. 4C and F). The results presented in heat-map coding demonstrate that the fraction of miniplasmids formed during conversion is rather low throughout the entire process (Fig. 4A and D), whereas PP templates have shown to be present during the course of recombination, meaning that despite their programmed transformation to DNA minicircles and mPs, this event is not completely promoted in all parental vectors. In fact, particularly for cultivations initially set at 37°C, a slight increase in PP species is attained at 4 hr, in comparison with other

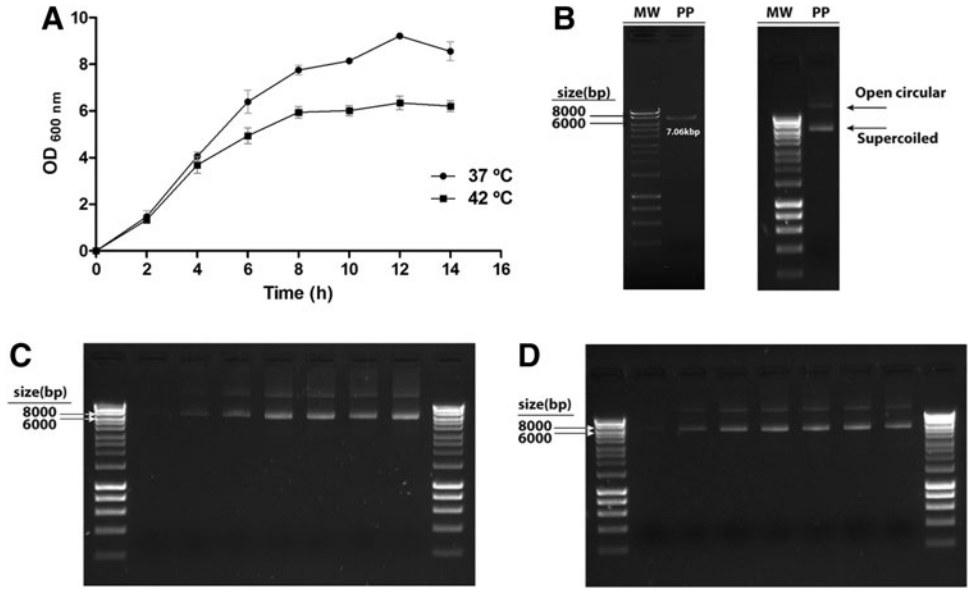

FIG. 2. Bacterial growth profiles. **(A)** Growth curve of *Escherichia coli* ZYCY10P3S2T minicircle-producing strain at two temperatures (37°C and 42°C). Values presented are mean ± s.d., $n = 3$. **(B)** Restriction digestion of parental DNA and representation of the different plasmid topoisoforms. **(C** and **D)** Time-course evaluation of total parental DNA biosynthesis, at 37°C and 42°C, respectively. MW, molecular weight marker; s.d., standard deviation.

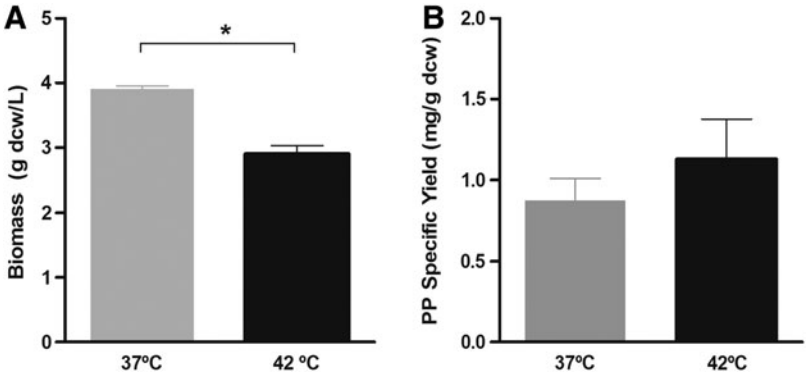

FIG. 3. Biomass and PP yield obtained in batch fermentation. **(A)** Biomass accumulation at different temperature conditions. **(B)** Overall PP-specific yield at the final phase of exponential growth at 37°C and 42°C. Values represent mean ± s.d., $n = 3$, $^*p < 0.05$.

periods (2 and 3 hr), a finding that is not observed at 42°C, where the relative amounts of PP vectors actually decrease across time after L-arabinose induction (0.01% w/v) (Fig. 4D and F). Regarding mcDNA biosynthesis, it is also important to emphasize that in the first hour after induction, only residual minicircle amounts are detected (Fig. 4). In addition, by analyzing the results presented in Fig. 4A–C, it is also noticeable that as the recombination time is extended (2–5 hr), higher amounts of mcDNA are achieved. Interestingly, this characteristic is observed for both conditions tested (Fig. 4D–F), suggesting that the expression of ΦC31 serine recombinase requires a certain amount of time to attain its complete functionality and prompt minicircle formation. Moreover, it should be underlined that mcDNA production spikes are attained at both temperatures (Fig. 4B and E). These highly important insights are further emphasized by time-dependent differences observed for 37°C and 42°C, with the latter reaching its maximum mcDNA conversion after 5 hr, while the former peaks at 4 hr postinduction (Fig. 4B and E).

In order to further explore mcDNA-related production process parameters that may influence overall yield, we also investigated the time-dependent effect of higher L-arabinose amounts at the induction stage. We hypothesized that a rate-limiting parameter in the induction stage could be the quantity of the inductor since the ΦC31 recombinase activity is in tight control of the araDAB system inducible by L-arabinose (Kay, 2011). Interestingly, our findings reveal that an increased inductor concentration significantly transforms conversion dynamics in both strategies (Fig. 5A and B). In fact, as depicted in Fig. 5, mcDNA biosynthesis profile during the induction period is markedly different since maximum mcDNA biosynthesis is obtained at 5 hr after induction for 37°C and mcDNA concentration increases proportionally with time (Fig. 5B), whereas mcDNA production had its maximum 4 hr after induction, at 42°C, and then it decreased at 5 hr (Fig. 5E). Furthermore, the overall PP-mcDNA relative conversion occurs to an higher extent with 0.1% L-arabinose in comparison with the induction conditions described in the literature (0.01% L-arabinose) (Kay *et al.*, 2010) (Figs. 4 and 5). These results are corroborated by agarose gel electrophoresis, where an increased mcDNA production and its time-specific peaks can be readily observed (Fig. 5C, lane 5, and 5F, lane 4).

Table 1. Effect of Temperature Conditions on Specific Growth Rate

Temperature (°C)	*Parental plasmid (kbp)*	*Specific growth rate (hr^{-1})*
37	7.06	0.162
42	7.06	0.149

The results presented in Fig. 6 demonstrate the quantification of specific mcDNA yield obtained under the various conditions manipulated during the recombination stage. As shown, the overall yield of minicircular biopharmaceuticals manufactured with 0.01% L-arabinose is very similar between both temperatures tested, and only a minor increase in mcDNA synthesis was observed for the cultivation performed at higher temperature. Notwithstanding, further analysis reveals that the induction performed with 0.1% L-arabinose promoted higher mcDNA recovery yields (Fig. 6B). In fact, concerning fermentations performed at 37°C, the manipulation of the inductor concentration results in a 0.88-fold increase in mcDNA-specific quantity ($p < 0.05$). Additionally, the same tendency was verified for 42°C; however, under these particular experimental settings, a noteworthy 2.21-fold increase was achieved, emphasizing the relevance of this parameter (Fig. 6B).

In order to further complement the improvements obtained at 42°C in PP and mcDNA yield, another growth strategy based on the induction at 6 hr of growth was tested. This L-arabinose induction was also performed in an attempt to evaluate a possible reduction in the presence of PP residual species in the final mcDNA titers. This is important because not only the yield but also the purity of each mcDNA biopharmaceuticals preparations is required for therapeutic applications. The results shown in Fig. 7 reveal that similar to the other strategies, trace amounts of PP templates are present during the different recombination stages (Fig. 7B and C). In Fig. 7 it is demonstrated that in this approach the maximum mcDNA conversion occurs at 5 hr after L-arabinose induction. In addition, promoting bacterial growth only up to 6 hr yields lower PP-specific yield, in comparison to that obtained at 42°C (Fig. 3B). Moreover, the mcDNA yield at 42°C with induction at 6 hr of growth is 4.37-fold lower than that obtained at 42°C with induction in the end of the exponential phase (Fig. 6), indicating that this strategy is less valuable than those formerly investigated.

A global analysis of the mcDNA-PP correlation ratios in the different production methods tested is presented in

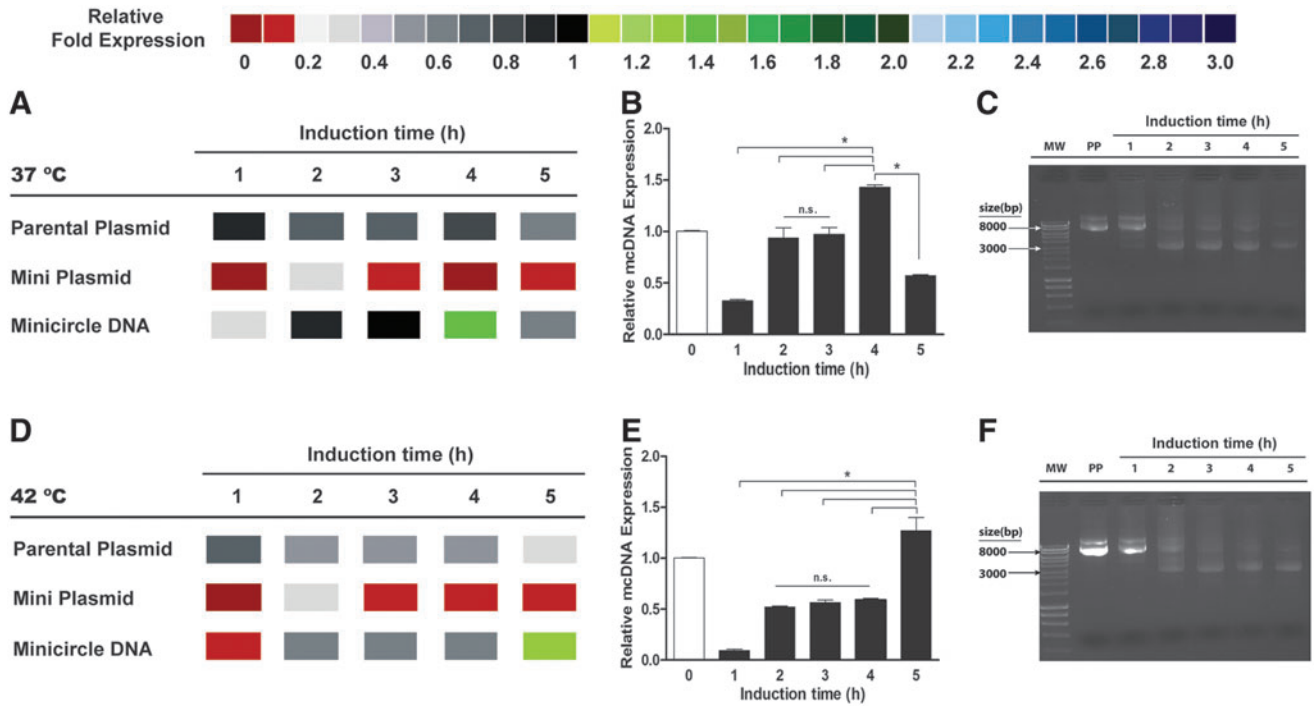

FIG. 4. Minicircle production dynamics during the course of the recombination process induced with 0.01% L-arabinose. **(A** and **D)** Color-coded heat map generated from qPCR data analysis, representing the different species of growth at 37°C and 42°C, respectively. **(B** and **E)** Expression to PP amount at induction ($t=0$), during the course of induction in bacterial cultivations that were initiated at 37°C and 42°C, respectively. Values represent mean ± s.d., $n=3$, $^*p<0.05$. **(C** and **F)** Time-course agarose gel electrophoresis of extracted samples at specific stages. PP, template parental plasmid; qPCR, quantitative polymerase chain reaction. Numbers represent different sample recovery points. Color images available online at www.liebertpub.com/hgtb

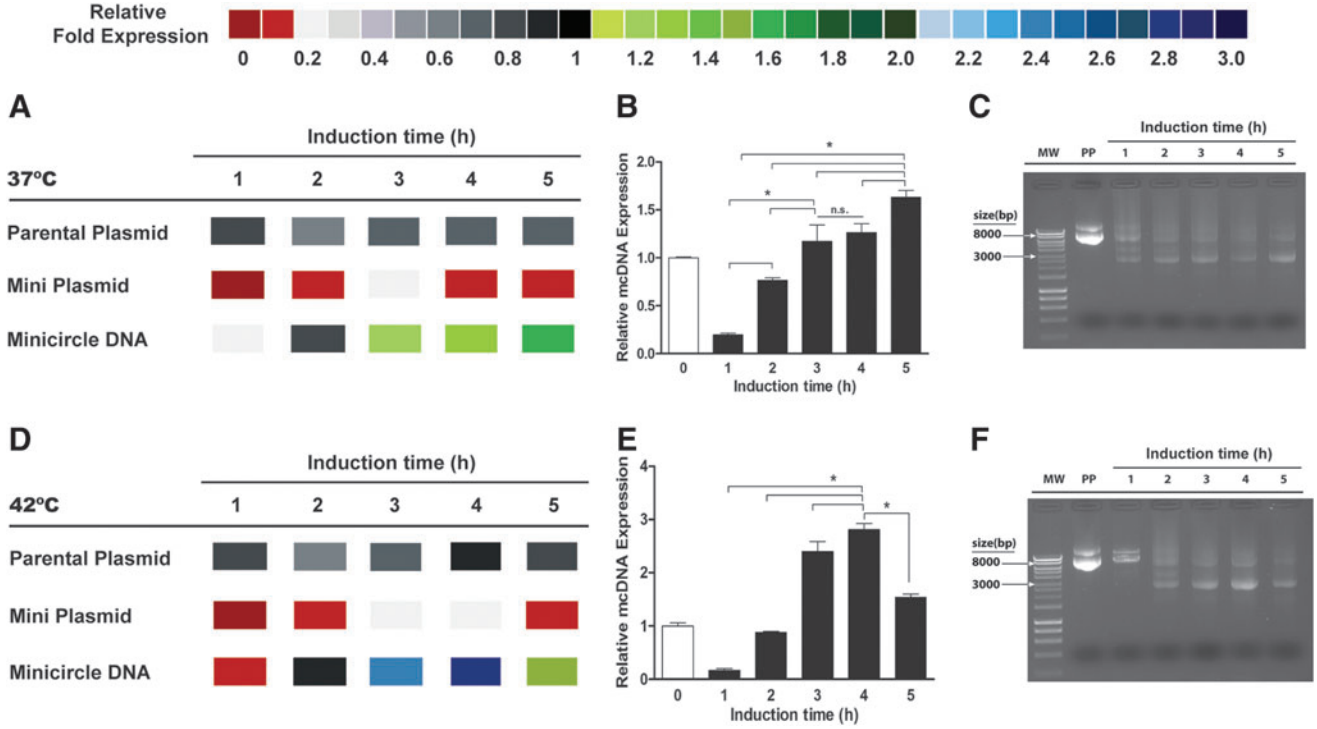

FIG. 5. Minicircle production dynamics during the recombination process induced with 0.1% L-arabinose. **(A** and **D)** Color-coded heat maps generated from qPCR data analysis, representing the different species grown at 37°C and 42°C, respectively. **(B** and **E)** Relative mcDNA expression to PP amount at induction ($t=0$), during induction in bacterial cultivations at 37°C and 42°C, respectively. Values represent mean ± s.d., $n=3$, $^*p<0.05$. **(C** and **F)** Time-course agarose gel electrophoresis of extracted samples at specific stages. Numbers represent different sample recovery points. Color images available online at www.liebertpub.com/hgtb

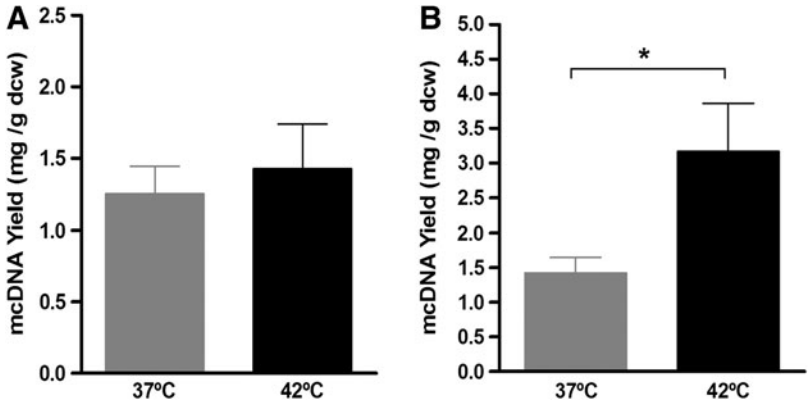

FIG. 6. mcDNA-specific yields determined by qPCR. **(A** and **B)** mcDNA yields obtained at the peaks of mcDNA biosynthesis during induction with 0.01% L-arabinose (37°C, 4 hr; 42°C, 5 hr) and 0.1% L-arabinose (37°C, 5 hr; 42°C, 4 hr), respectively. Values represent mean ± s.d., $n = 3$, $^*p < 0.05$.

Table 2. As the results demonstrate, the mcDNA/parental ratio is higher at 42°C with induction at the end of the exponential phase (0.1% L-arabinose) when compared with the other two strategies, showing the presence of less PP species in these samples. Interestingly, the mcDNA/PP ratio obtained in this condition is markedly higher (Table 2), with a 3.14-fold increase in the mcDNA/PP ratio. It is also important to emphasize that in comparison with the 0.01% L-arabinose induction, less PP species are present in all the mcDNA preparations obtained with the 0.1% induction strategy (Table 2).

After establishing the optimal growth conditions and induction stages for the 7.06 kbp PP plasmid, the proposed methodologies were also applied in the bacterial amplification of a smaller construct with 4.88 kbp (smaller PP) that has been engineered from the original PP backbone. As schematized in Fig. 8, the smaller PP backbone yields a smaller mcDNA expression cassette (880 bp). The construction of this new plasmid was confirmed by agarose gel electrophoresis as shown in Fig. 8B. The bacterial amplification of the smaller PP vector was also evaluated at 37°C and 42°C as described above. As the results in Fig. 8C indicate, the smaller PP-

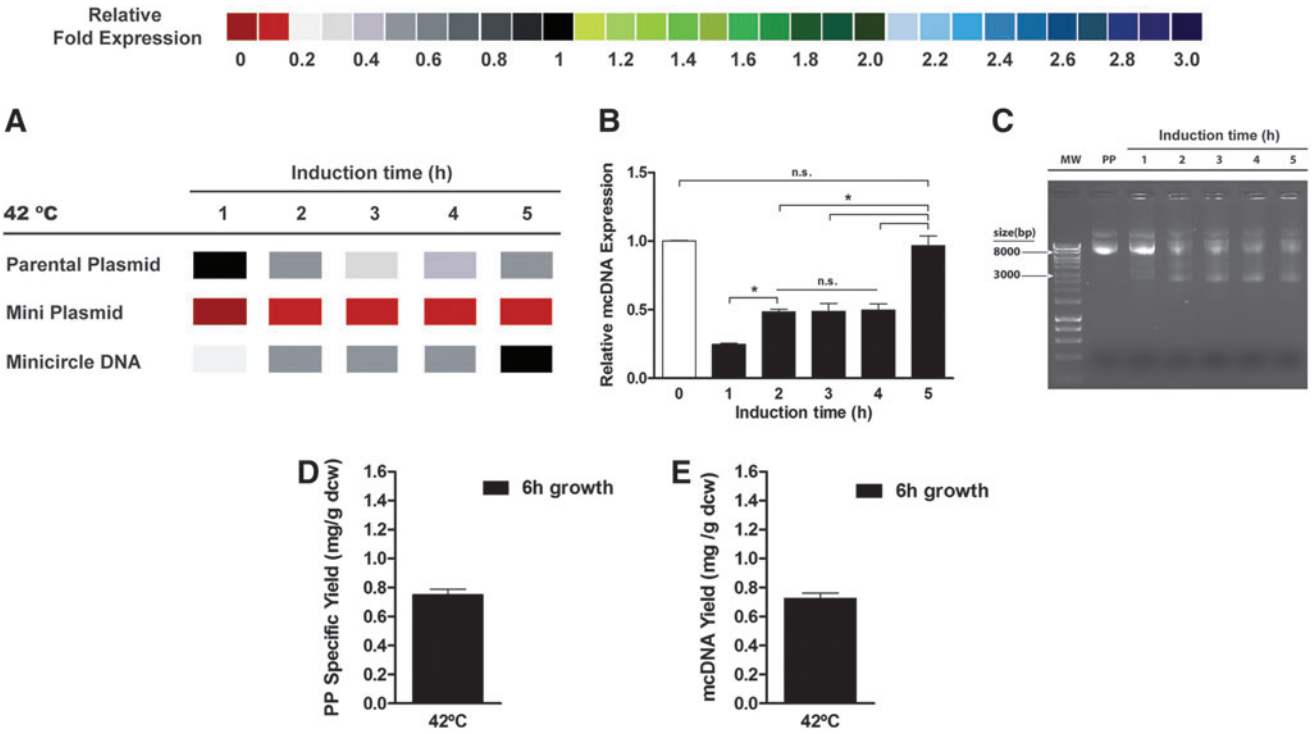

FIG. 7. mcDNA production dynamics during the recombination process induced with 0.1% L-arabinose. **(A)** Color-coded heat maps generated from qPCR data analysis, representing the different species grown at 42°C, for 6 hr. **(B)** Relative mcDNA expression to PP amount at induction ($t = 0$). **(C)** Time-course agarose gel electrophoresis of extracted samples at specific stages of the induction process. Numbers represent different sample recovery points. **(D)** PP-specific yield obtained after 6 hr of growth at 42°C. **(E)** mcDNA yields obtained at the peaks of mcDNA biosynthesis during induction with 0.1% L-arabinose. Values represent mean ± s.d., $n = 3$, $^*p < 0.05$. Color images available online at www.liebertpub.com/hgtb

Table 2. Relationship Between Minicircular DNA and Parental Plasmid Presence in the Various Growth Conditions

Parental plasmid size (bp)	*L-arabinose concentration (%)*	*Growth temperature (°C)*	*Induction time*	*Parental/minicircle ratio*	*Minicircle/parental ratio*
7,063	0.01	37	End exponential phase	0.645 ± 0.041	1.821 ± 0.027
		42	End exponential phase	0.708 ± 0.041	1.374 ± 0.141
	0.1	37	End exponential phase	0.468 ± 0.016	2.137 ± 0.073
		42	End exponential phase	0.149 ± 0.005	6.706 ± 0.230
		42	Log phase (6 hr)	0.487 ± 0.022	2.096 ± 0.107

specific yield at 42°C is 1.78-fold higher than that obtained at 37°C, indicating a major improvement.

After establishing that the smaller PP production is also improved at 42°C, the optimal induction conditions and smaller mcDNA generation were investigated. The time-dependent dynamics of the production of the smaller mcDNA cassette reveals that the maximum yield for 37°C and 42°C is obtained between 3 and 5 hr. The correlation of this data with the presence of smaller PP species presented in the heat maps reveals that during this time frame, the recovery of the mcDNA preparations at 4 or 5 hr is more valuable since the fractions of smaller PP vectors are decreased on these periods, a fact that is observed at both 37°C and 42°C (Fig. 9A and D). Interestingly, the analysis of the smaller mcDNA relative expression illustrates that smaller PP to smaller mcDNA conversion is more effective at 42°C (Fig. 9B and E).

Regarding the smaller mcDNA-specific yield, the results indicate that there is a notable difference in the overall yield between the two growth temperatures. In fact, the smaller mcDNA yield at 42°C is 2.26-fold higher than that at 37°C bacterial cultivations. These findings are in agreement with those obtained for the bigger mcDNA expression cassette, suggesting that this is indeed the best production strategy.

In relation to the presence of the different PP species in the smaller mcDNA preparations, the results presented in Table 3 demonstrate that similar to the other parental vector with larger size, the bacterial cultivations performed at 42°C promote a decrease in the presence of template plasmids as revealed by the higher minicircle/parental ratio of these titers. This is accomplished alongside with an increase in smaller mcDNA generation as shown in Fig. 10, indicating that this particular construct should also be amplified in *E. coli* and grown at 42°C.

To evaluate if the presence of template plasmid species could be further reduced after growth at 42°C, the mcDNA induction was evaluated in the conditions that were

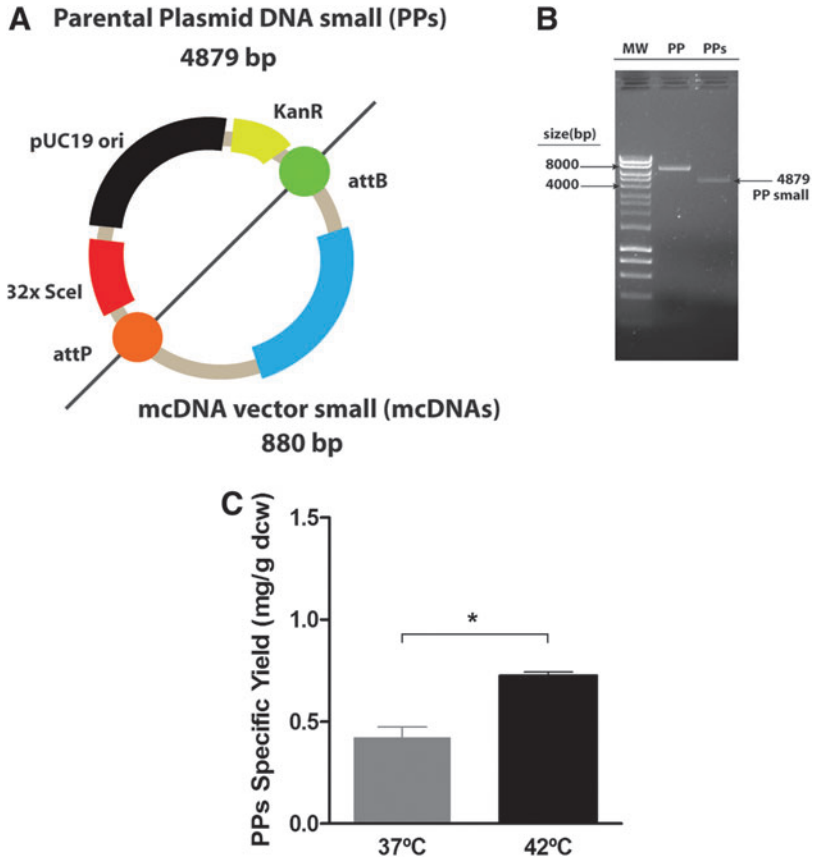

FIG. 8. Smaller PP design and growth yield. **(A)** Schematics of smaller PP with smaller backbone and smaller mcDNA size. **(B)** Representative agarose gel electrophoresis of the presence of the newly engineered construct. **(C)** Overall smaller PP yields obtained at the final phase of exponential growth at 37°C and 42°C. Values represent mean ± s.d., $n = 3$, $^*p < 0.05$. Color images available online at www.liebertpub.com/hgtb

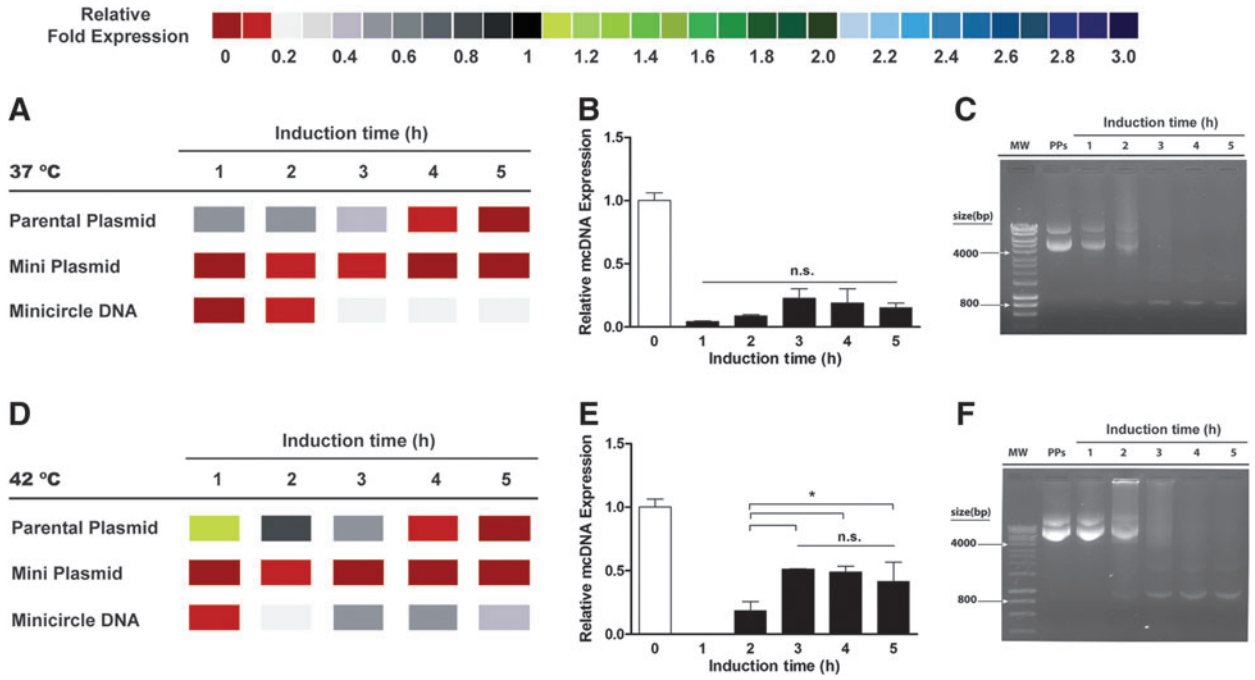

FIG. 9. Smaller mcDNA production dynamics during the recombination process induced with 0.1% L-arabinose. **(A** and **D)** Color-coded heat maps generated from qPCR data analysis, representing the different species grown at 37°C and 42°C, respectively. **(B** and **E)** Relative smaller mcDNA expression to smaller PP amount at induction ($t=0$), during induction in bacterial cultivations at 37°C and 42°C, respectively. Values represent mean ± s.d., $n=3$, $^*p<0.05$. **(C** and **F)** Time-course agarose gel electrophoresis of extracted samples at specific stages. Numbers represent different sample recovery points. Color images available online at www.liebertpub.com/hgtb

originally described by Kay *et al.* (2010) (Fig. 11A). This particular induction strategy is based on the addition of a minicircle induction mix that comprises L-arabinose to promote the recombination process. The results obtained with this strategy reveal that by performing bacterial growth at 42°C and inducing with the inductor mix, the overall yield of mcDNA is improved in both the smaller and the larger expression vectors (7.06 and 4.88 kbp). The efficiency of the recombination process is also improved for both plasmids in comparison with the induction performed without the mix (Fig. 11C, F, I, and L). Particularly, more than fivefold relative mcDNA expression is reached at 2–3 hr for the larger plasmids (Fig. 11L), a marked increase in comparison with the strategy mentioned in Fig. 5E. This improvement in the recombination efficiency was attained with all L-arabinose concentrations (Fig. 11I and L). Regarding the smaller vectors, a slightly higher recombination efficiency is also observed compared with the induction without the mix (Figs. 9E and 11C). This is more pronounced with 0.01% L-arabinose concentration for both plasmids. Regarding the presence of PP contaminants, the results demonstrate an overall reduction of template species in all conditions in which the induction mix was used to initiate the recombination process (Fig. 11). Interestingly, the preparations of the smaller mcDNA vectors show insignificant PP template contamination (Fig. 11B and E), a result that is similar to that obtained without the inductor mix (Fig. 9A and D). In respect to the larger vectors, the residual PP species are highly reduced with the addition of the induction mix containing 0.01% L-arabinose (Fig. 11H and J). For this particular vector, the optimal recovery of mcDNA preparations was obtained 3 hr after recombination. At this time point, mcDNA and residual amounts of PP achieved the best compromise to recover the biopharmaceuticals of interest with the highest yield and a significant reduction in trace amounts of contaminants (Fig. 11H).

Discussion

Nowadays the rapidly developing field of nucleic acid-based bioactives has led to a demanding expansion in the manufacture of pharmaceutical-grade genetic material at scales suitable for its envisioned applications (Kwon *et al.*, 2013). However, despite the major breakthroughs in the

Table 3. Relationship Between Smaller Minicircular DNA and Smaller Parental Plasmid Presence in the Various Growth Conditions

Parental plasmid size (bp)	*Growth temperature (°C)*	*Induction*	*Parental/minicircle ratio*	*Minicircle/parental ratio*
4,879	37	End exponential phase	1.349 ± 0.442	0.859 ± 0.280
	42	End exponential phase	0.709 ± 0.003	1.782 ± 0.008

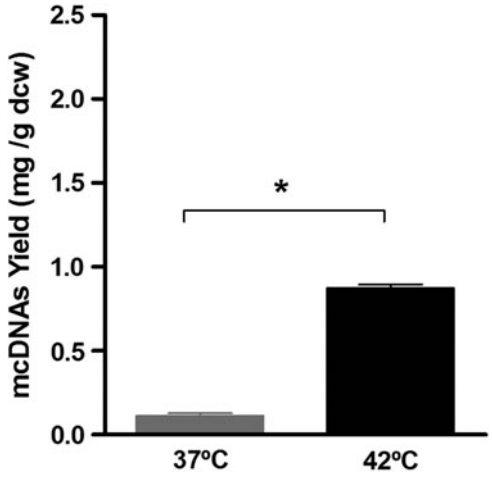

FIG. 10. Smaller mcDNA yields obtained at the peaks of smaller mcDNA biosynthesis during induction with 0.1% L-arabinose (37°C and 42°C, 3 hr). Values represent mean ± s.d., $n = 3$, $*p < 0.05$.

production processes of recombinant pDNA gene expression vectors (Carnes *et al.*, 2006; Silva *et al.*, 2011), their associated biocompatibility and efficiency issues hardly render them the most appropriate for future application.

Herein, we present a recently developed approach that covers the previous restrictions, by not only improving all aspects deemed essential for therapeutic approval, but also doing so via a straightforward and rapid manufacturing process (Kay *et al.*, 2010). Nevertheless, up to now this biosynthesis methodology has never been investigated, and its associated mcDNA yields are only equivalent to those of standard pDNA, falling short in comparison with optimized production strategies (Silva *et al.*, 2009). Hence, in order to further unlock the potential of this approach, we manipulated process-dependent parameters that could improve minicircle DNA synthesis and prompt its widespread use.

In a first stage, the growth curves of minicircle-producing bacteria were characterized in an attempt to describe the behavior of this genetically modified *E. coli* strain and establish optimal growth temperatures. For this purpose, cells were cultivated at both 37°C and 42°C. The latter temperature condition was chosen because it has been previously described that plasmid amplification can be improved in vectors that withhold the pUC origin of replication by performing growth at higher temperatures (42°C) (Wong *et al.*, 1982; Carnes *et al.*, 2006). This particular characteristic is also imprinted in the commercial PP template that originates DNA minicircles, and thus stands as a valuable approach to improve biosynthesis. In fact, our findings reveal that under conventional growth conditions described in the literature for mcDNA amplification (37°C) (Chen *et al.*, 2005), higher biomass concentrations and low template plasmid yields are obtained (Fig. 3), whereas a temperature increase to 42°C improved PP amplification to some extent and lowered final biomass amounts. These interdependent yield–biomass parameters are often associated with the metabolic burden imposed when high-copy plasmids are amplified, as in the case of PP (Ow *et al.*, 2006). Interestingly, this metabolic load is also correlated with the specific growth rate, because it has been reported by Ow *et al.* (2006) that under stressful conditions bacterial cell-wall formation genes are downregulated. Our results are in stark agreement with these previous observations, since the specific growth rate obtained at 42°C is lower than that of 37°C (Table 1). Furthermore, our data show that this key parameter may also be a useful tool to manipulate process design (Bohle and Ross, 2011).

In order to further validate the general applicability of the improved production parameters in the manufacture of DNA minicircles, the amplification of a smaller PP template was also investigated. The obtained results indicate that regardless of the used template vector, the yield of PP is improved when bacterial cultivations are performed at 42°C (Fig. 8). These are noteworthy findings because they provide strong foundations for the scaling up of the mcDNA recombination technology into pilot or industrial-scale production. In addition, the results presented in Fig. 2B and C emphasize the noteworthy stability of the amplified PP template during cultivation, before any induction events. From this stand point, it becomes clear that despite all strain genetic modifications and the complexity of this technology, before induction, its features are comparable with those encountered in general pDNA bacterial fermentations.

Most importantly, in addition to the amplification of PP, other critical parameters inherent to mcDNA manufacture could provide further insights that influence the development of novel biosynthesis processes. Taking this into account, we also evaluated the dynamic events that govern PP-to-mcDNA conversion, a process that, to the best of our knowledge, has never been assessed so far. Therefore, through the development of a unique online monitoring approach based on qPCR, we were able to unravel new stages where mcDNA synthesis is improved (Figs. 4 and 5). Actually, our findings reveal that the recombination process is essentially dependent on (i) temperature (32°C), (ii) conversion time, and (iii) inductor concentration. The manipulation of the inductor quantity assumes further importance since it promoted a 2.21-fold increase in mcDNA synthesis in comparison with standard conditions (Fig. 6A and B). Remarkably, the application of this strategy was translated into mcDNA titers (8.84 ± 2.37 mg/liter, 42°C, 0.1% L-arabinose for 4 hr, 7.06 kbp PP) that are higher than those reported in the literature performed at 37°C and 0.01% L-arabinose induction for 5 hr (4.83 ± 0.60 mg/liter, for a 8.8 kbp plasmid) (Kay *et al.*, 2010), a very relevant detail for the future development of cost-effective biopharmaceuticals (Gonçalves *et al.*, 2011; Silva *et al.*, 2012). However, it is yet mandatory to also correlate this outcome with the kinetics of conversion, since our assessments revealed that the recombination process is characterized by the production peaks at key points (Figs. 4, 5, 7, and 9). Indeed, a global analysis of all the species present during the recombination process for both vectors tested exposes the existence of mcDNA and residual amounts of PP and miniplasmids. The last fact is likely correlated with the action of I-SceI endonuclease that targets these undesirable contaminants for degradation, however, not entirely as demonstrated in Figs. 4, 5, and 7. Also, it is important to underline that during conversion, the template PP species are still slightly present, an interesting finding suggestive of both PP conversion and PP production during this stage (Fig. 4 and Fig. 5C and F). In order to evaluate whether the induction time had influence on the overall yield-purity of the mcDNA preparations, a new methodology based on bacterial

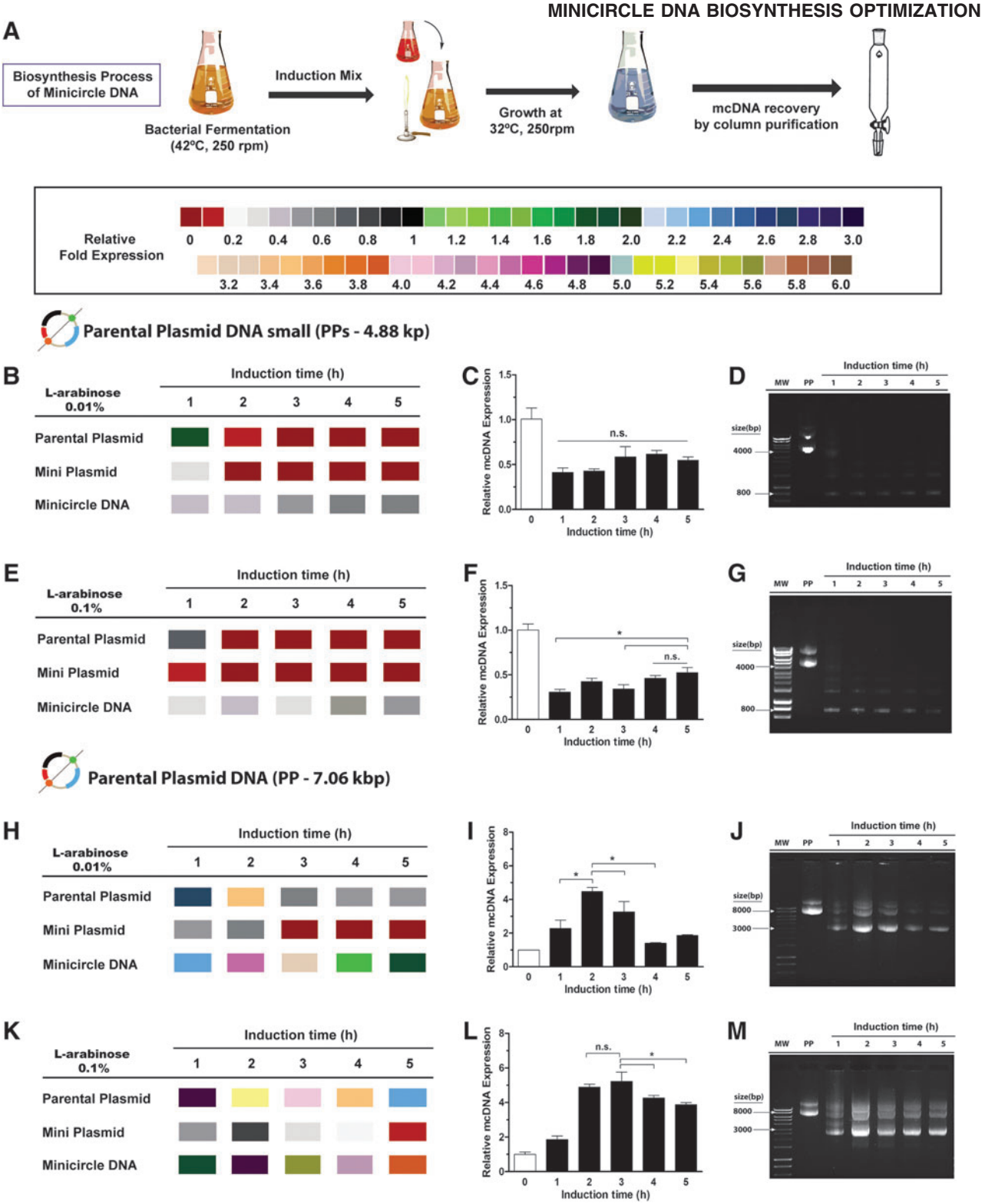

FIG. 11. Production dynamics of mcDNA and smaller mcDNA at 42°C with the addition of the minicircle induction mix including various L-arabinose concentrations (0.1% and 0.01%). **(A)** Schematics of the growth–recombination process with the addition of the minicircle induction mix. **(B** and **E)** Color-coded heat maps generated from qPCR data analysis of small PP vectors induced with the mix containing 0.01% and 0.1% L-arabinose, respectively. **(C** and **F)** Relative smaller mcDNA expression to smaller PP amount at induction ($t=0$); **(D** and **G)** Time-course agarose gel electrophoresis at specific stages of the induction process with the addition of the minicircle induction mix. **(H** and **K)** Color-coded heat maps generated from qPCR data analysis of PP vectors induced with the mix containing 0.01% and 0.1% L-arabinose, respectively. **(I** and **L)** Relative mcDNA expression to PP amount at induction ($t=0$). **(J** and **M)** Time-course agarose gel electrophoresis at specific stages of the induction process with the addition of the minicircle induction mix. Numbers represent different sample recovery points. All data represent mean ± s.d., $n=3$, $^*p<0.05$. Color images available online at www.liebertpub.com/hgtb

cultivations at 42°C and induction at 6 hr of growth was explored. The results obtained for this strategy reveal, however, that not only is mcDNA yield markedly decreased, but also the presence of PP templates is increased (Table 2), indicating that inducing recombination at the end of the exponential phase is a more valuable approach to achieve maximum yield and purity.

In addition to these strategies and always with the aim to further reduce PP contamination and improve mcDNA yield, bacterial fermentations grown at 42°C were also induced by using the procedure originally described by Kay *et al.* (2010) that comprises the addition of a mix to promote the recombination process. With this strategy, the optimal preparations were obtained with 0.01% L-arabinose (Fig. 11). This result is in agreement with those previously reported (Kay *et al.*, 2010) and that demonstrates the robustness of this approach. This is a very important process parameter since the manufacturing cost of mcDNA biopharmaceuticals at larger scales is significantly reduced. Interestingly, the conjugation of the growth at 42°C and the use of the minicircle induction mix remarkably improved not only the overall recombination yield but also the purity of the mcDNA preparations (Fig. 11) in comparison with the aforementioned strategy of L-arabinose addition alone. Regarding the presence of residual PP species, the results demonstrate that after induction, recovering smaller mcDNA (4.88 kbp) preparations between 3 and 5 hr is the best strategy to obtain a high yield of smaller mcDNA and negligible PP contamination (Fig. 11B and E).

In the larger size minicircle preparations, our findings illustrate that the recombination process is more effective, yielding a higher amount of mcDNA and lower residual plasmids than the induction strategy of L-arabinose addition alone. This improvement is obtained at the lowest L-arabinose concentration tested (0.01%) (Fig. 11H), a finding that is in agreement with that of the original report (Kay *et al.*, 2010). These results assume great relevance for the optimization of the whole bioprocess and for its feasibility to be scaled up.

It is also important to point out that regardless of the induction parameters, a slight difference in the trace amounts of residuals species is observed during recombination for the different-size plasmids (7.06 and 4.88 kbp), with the smaller constructs generally yielding less PP contamination. We hypothesize that this interesting fact could be associated with plasmid-induced metabolic stress imposed by the biosynthesis of plasmid vectors in *E. coli* bacteria as recently reviewed in the literature (Silva *et al.*, 2012). This burden is characterized by the reprogramming of the metabolic pathways to sustain plasmid biosynthesis and it is more prevalent for bacterial hosts that amplify larger size plasmids (Kay *et al.*, 2003). This metabolic stress could influence the expression of the recombination mediators, in such a way that the expression of the I-SceI homing endonuclease could be reduced. As a consequence, less PP templates are eliminated in the bacterial cultivations with the larger constructs. This hypothesis is supported by the results of the specific plasmid yield of both constructs at 42°C. The specific yield for the smaller mcDNA constructs (4.88 kbp) (Fig. 8C) is lower than that obtained for the mcDNA vectors (7.06 kbp) (Fig. 3B), indicating that a higher amount of biomass is produced during fermentation of the smaller PP. An increased biomass is correlated with less bacterial stress (Silva *et al.*, 2012), suggesting that the trace amounts of PP templates obtained might be associated with the existence of certain metabolic burden imposed during the production–recombination process.

In general, and regardless of the construct size, the results show a clear existence of precise periods where recombination takes place to a significantly higher extent, indicating that the recovery of the bioactive molecules of interest at precise fermentation phases may have an impact on process development, downstream purification, and consequently on its envisioned applications.

Overall, in this work we have explored the bioprocess of a novel DNA minicircle production technology to characterize and manipulate design parameters that can be improved to achieve maximum productivity while reducing manufacturing costs of DNA-based biopharmaceuticals. We were able to establish precise growth and induction conditions on which the general recovery yield of minicircles was significantly increased, regardless of the used PP template. Therefore, we found that promoting bacterial growth at 42°C and inducing recombination with the procedure originally described by Kay *et al.* (2010) is the best strategy to improve both the process yield and the overall purity of the mcDNA preparations in comparison with the growth approaches without the induction mix. Moreover, concerning L-arabinose concentration, the addition of the induction mix with 0.01% L-arabinose is the best parameter for this bioprocess (Fig. 11), a result that is in agreement with those previously reported in the literature (Kay *et al.*, 2010). The precise time at which PP-to-mcDNA conversion achieves its peak is dependent on the original template PP since the 7.06 kbp plasmid presented a maximum mcDNA yield–lower PP correlation at 3 hr after induction (Fig. 11H and I). On the other hand, the maximum production of the PPs (4.88 kbp) was achieved between 3 and 5 hr (Fig. 11B and C). Altogether, these findings emphasize the importance of addressing the recombination process of each parental template in order to improve both overall process yield and mcDNA preparations purity degree. These optimal conditions assume further importance when we take into consideration that mcDNA biological activity and safety surpasses that of the widely employed pDNA expression vectors. Moreover, from the best of our knowledge this was the first time that the dynamics of the recombination process were evaluated and characterized. Their establishment is likely to provide novel foundations for further bioprocess developments and engineering of pilot and industrial production platforms in a near future.

In conclusion, gathering the findings herein described and combining them with the native potential of mcDNA biomolecules may open a whole new range of possibilities for their anticipated translation into clinical application.

Acknowledgments

This work was supported by the Portuguese Foundation for Science and Technology (FCT; PTDC/EME-TME/103375/2008, PTDC/EBB-BIO/114320/2009, and PEst-C/SAU/UI0709/2011 COMPETE). V.M.G. acknowledges a PhD fellowship from FCT (SFRH/BD/80402/2011).

Author Disclosure Statement

No competing financial interests are disclosed by the authors.

References

Bohle, K., and Ross, A. (2011). Plasmid DNA production for pharmaceutical use: role of specific growth rate and impact on process design. Biotechnol. Bioeng. 108, 2099–2106.

Carnes, A., Hodgson, C., and Williams, J. (2006). Inducible *Escherichia coli* fermentation for increased plasmid DNA production. Biotechnol. Appl. Biochem. 45, 155–166.

Carnes, A.E., Luke, J.M., Vincent, J.M., *et al.* (2011). Plasmid DNA fermentation strain and process-specific effects on vector yield, quality, and transgene expression. Biotechnol. Bioeng. 108, 354–363.

Chabot, S., Orio, J., Schmeer, M., *et al.* (2013). Minicircle DNA electrotransfer for efficient tissue-targeted gene delivery. Gene Ther. 20, 62–68.

Chen, Z., He, C., Ehrhardt, A., and Kay, M. (2003). Minicircle DNA vectors devoid of bacterial DNA result in persistent and high-level transgene expression *in vivo*. Mol. Ther. 8, 495–500.

Chen, Z., He, C., Meuse, L., and Kay, M. (2004). Silencing of episomal transgene expression by plasmid bacterial DNA elements *in vivo*. Gene Ther. 11, 856–864.

Chen, Z., He, C., and Kay, M. (2005). Improved production and purification of minicircle DNA vector free of plasmid bacterial sequences and capable of persistent transgene expression *in vivo*. Hum. Gene Ther. 16, 126–131.

Chen, Z.Y., Riu, E., He, C.Y., *et al.* (2008). Silencing of episomal transgene expression in liver by plasmid bacterial backbone DNA is independent of CpG methylation. Mol. Ther. 16, 548–556.

Gill, D.R., Pringle, I.A., and Hyde, S.C. (2009). Progress and prospects: the design and production of plasmid vectors. Gene Ther. 16, 165–171.

Gonçalves, G.A., Bower, D.M., Prazeres, D.M.F., *et al.* (2011). Rational engineering of *Escherichia coli* strains for plasmid biopharmaceutical manufacturing. Biotechnol. J. 7, 251–261.

Ismail, R., Allaudin, Z.N., and Lila, M.A. (2012). Scaling-up recombinant plasmid DNA for clinical trial: current concern, solution and status. Vaccine 30, 5914–5920.

Jechlinger, W., Azimpour Tabrizi, C., Lubitz, W., and Mayrhofer, P. (2004). Minicircle DNA immobilized in bacterial ghosts: *in vivo* production of safe non-viral DNA delivery vehicles. J. Mol. Microbiol. Biotechnol. 8, 222–231.

Kay, M.A. (2011). State-of-the-art gene-based therapies: the road ahead. Nat. Rev. Genet. 12, 316–328.

Kay, A., O'Kennedy, R., Ward, J., and Keshavarz-Moore, E. (2003). Impact of plasmid size on cellular oxygen demand in *Escherichia coli*. Biotechnol. Appl. Biochem. 38, 1–7.

Kay, M.A., He, C.Y., and Chen, Z.Y. (2010). A robust system for production of minicircle DNA vectors. Nat. Biotechnol. 28, 1287–1289.

Kimelman Bleich, N., Kallai, I., Lieberman, J.R., *et al.* (2012). Gene therapy approaches to regenerating bone. Adv. Drug Deliv. Rev. 64, 1320–1330.

Kobelt, D., Schleef, M., Schmeer, M., *et al.* (2013). Performance of high quality minicircle DNA for in vitro and in vivo gene transfer. Mol. Biotechnol. 53, 80–89.

Kwon, M.J., An, S., Choi, S., *et al.* (2012). Effective healing of diabetic skin wounds by using nonviral gene therapy based on minicircle vascular endothelial growth factor DNA and a cationic dendrimer. J. Gene Med. 14, 272–278.

Kwon, K.C., Verma, D., Singh, N.D., *et al.* (2013). Oral delivery of human biopharmaceuticals, autoantigens and vaccine antigens bioencapsulated in plant cells. Adv. Drug Deliv. Rev. 65, 782–799.

Mayrhofer, P., and Iro, M. (2012). Minicircle-DNA. In *Gene Vaccines.* Thalhamer, J [Hrsg.] (Springer, Wien), *pp*. 297–310.

Osborn, M.J., Mcelmurry, R.T., Lees, C.J., *et al.* (2011). Minicircle DNA-based gene therapy coupled with immune modulation permits long-term expression of alpha-L-iduronidase in mice with mucopolysaccharidosis type I. Mol. Ther. 19, 450–460.

Ow, D.S.W., Nissom, P.M., Philp, R., *et al.* (2006). Global transcriptional analysis of metabolic burden due to plasmid maintenance in *Escherichia coli* DH5α during batch fermentation. Enzyme Microb. Technol. 39, 391–398.

Pfaffl, M.W. (2001). A new mathematical model for relative quantification in real-time RT-PCR. Nucleic Acids Res. 29, e45.

Roychoudhury, A., Basu, S., and Sengupta, D.N. (2009). Analysis of comparative efficiencies of different transformation methods of *E. coli* using two common plasmid vectors. Indian J. Biochem. Biophys. 46, 395–400.

Salyers, A.A., Gupta, A., and Wang, Y. (2004). Human intestinal bacteria as reservoirs for antibiotic resistance genes. Trends Microbiol. 12, 412–416.

Santos, J.L., Nouri, A., Fernandes, T., *et al.* (2012). Gene delivery using biodegradable polyelectrolyte microcapsules prepared through the layer-by-layer technique. Biotechnol. Prog. 28, 1088–1094.

Silva, F., Passarinha, L., Sousa, F., *et al.* (2009). Influence of growth conditions on plasmid DNA production. J. Microbiol. Biotechnol. 19, 1408–1414.

Silva, F., Lourenço, O., Maia, C., *et al.* (2011). Impact of plasmid induction strategy on overall plasmid DNA yield and *E. coli* physiology using flow cytometry and real-time PCR. Process Biochem. 46, 174–181.

Silva, F., Queiroz, J.A., and Domingues, F.C. (2012). Evaluating metabolic stress and plasmid stability in plasmid DNA production by *Escherichia coli*. Biotechnol. Adv. 30, 691–708.

Wong, E.M., Muesing, M.A., and Polisky, B. (1982). Temperature-sensitive copy number mutants of CoIE1 are located in an untranslated region of the plasmid genome. Proc. Natl. Acad. Sci. USA 79, 3570–3574.

Wong, S.P., Argyros, O., and Harbottle, R.P. (2012). Vector systems for prenatal gene therapy: principles of non-viral vector design and production. Methods Mol. Biol. 891, 133–167.

Address correspondence to:
Dr. Fani Sousa
Centro de Investigação em Ciências da Saúde
Universidade da Beira Interior
Av. Infante D. Henrique
6200-506 Covilhã
Portugal

E-mail: fani.sousa@fcsaude.ubi.pt

Received for publication January 17, 2013;
accepted after revision November 19, 2013.

Published online: November 26, 2013.

CHAPTER 6

Sensitive Detection of Peptide - Minicircle DNA Interactions by Surface Plasmon Resonance

Analytical Chemistry, 2013
DOI: 10.1021/ac303288x

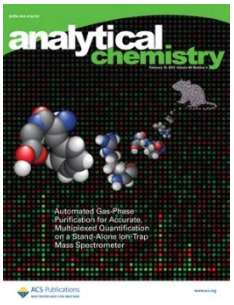

Volume 85, issue 4

Motivation

The use of mcDNA technology involves the optimization of production parameters in recombinant organisms as demonstrated in the previous study. However, from an integrative perspective that involves manufacturing and application, it also is important to develop new technologies that could purify or isolate mcDNA vectors and ultimately assure their pharmaceutical-grade quality. Taking this into consideration the following study was performed to investigate new ligands that could be used in the future for mcDNA purification or isolation under precise conditions.

analytical chemistry

Article

pubs.acs.org/ac

Sensitive Detection of Peptide–Minicircle DNA Interactions by Surface Plasmon Resonance

Vítor M. Gaspar,[†] Carla Cruz,[†] João A. Queiroz,[†] Chantal Pichon,[‡] Ilídio J. Correia,[†] and Fani Sousa*[,†]

[†]CICS-UBI - Centro de Investigação em Ciências da Saúde, Universidade da Beira Interior, Covilhã, Portugal

[‡]Centre de Biophysique Moléculaire CNRS UPR4301, INSERM and University of Orléans, F-45071 Orléans cedex 2, France

Supporting Information

ABSTRACT: Minicircle DNA (mcDNA) is recently becoming an exciting source of genetic material for therapeutic purposes due to its exceptional biocompatibility and efficiency over typical DNA. However, its widespread use is yet restrained because of the absence of an efficient technology that allows its purification. Here, the precise conditions of mcDNA interaction with novel arginine-arginine dipeptide ligands were explored to promote binding and recovery of these biopharmaceuticals. Such interactions were investigated by taking advantage of a highly sensitive method based on surface plasmon resonance (SPR) to screen, in real-time, for ligand-coupled biomolecules, while preserving mcDNA integrity. Through this analytic approach, we detected dynamic binding responses that are dependent on buffer type, mcDNA electrokinetic potential, and temperature conditions. Remarkably, the results obtained revealed that the ligands possess high affinity to mcDNA molecules under low salt buffers, and low affinity in the presence of salt, suggesting that electrostatic interactions mainly govern ligand–analyte coupling. These findings provide important insights for an active manipulation of parameters that promote mcDNA recovery and purification. Above all, this study showed the crucial importance of SPR for future screening of other ligands that, like the one described herein, can be used to design mcDNA recovery platforms which will have significant impact in biopharmaceutical-based therapeutics.

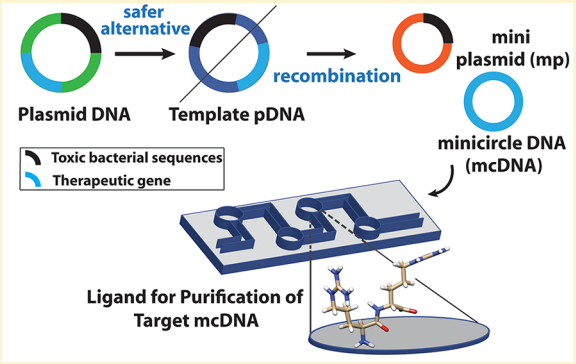

There has been an ever-growing interest in DNA-based therapies on behalf of both scientific and medical communities since the first clinical trial was approved by the US Food and Drug Administration (FDA) in the early 1990s.[1] In fact, the potential to treat impairing pathologies, such as cancer, AIDS, or central nervous system (CNC) disorders, through the insertion of exogenous genetic material in defective cells, arises as a particularly promising approach from a therapeutic point of view.[2] One of the major objectives of nonviral gene therapy is the development of vectors that are suitable for gene transfer into human cells. To date, plasmid DNA (pDNA) remains the most used biopharmaceutical for such applications.[3] However, serious safety concerns have recently arisen.[4] These are correlated with the intrinsic immunostimulatory capacity of bacterial sequences present in pDNA structure and which ultimately cause severe side effects.[5] Furthermore, because of these factors, pDNA activity in vivo is markedly reduced after a short period of time, rendering pDNA-based treatments rather ineffective.[6] Altogether, these yet unmet prerequisites have significantly limited its widespread application.[5] Currently, the advent of a novel technology based on minicircle DNA (mcDNA) biomolecules has presented the opportunity to develop safer and more proficient therapeutic approaches.[7] Unlike plasmids, mcDNA is completely devoid of bacterial sequences.[8] Their small size allows them to have a greater diffusivity, which accounts for their improved therapeutic efficacy when administered to cell lines using chemical methods[8] or nanoparticles.[9] Moreover, mcDNA notably possesses an improved in vivo performance, with a persistent expression of therapeutic genes being attained for prolonged periods without being silenced.[6]

The promising applicability of mcDNA was recently enhanced with the development of a minicircle production technology that relies on exploiting bacterial machinery to generate DNA with improved yield and the potential for scaleup.[10] This cutting-edge method relies on bacteriophage phiC31 serine recombinase that mediates site-specific recombination events in template pDNA.[11] This so-termed parental plasmid (PP) is a template that bears a bacterial expression cassette, as well as sequences for enzyme recognition (*attB* and *attP*).[12] Additionally, it also contains the therapeutic gene of interest and its associated promoter sequences that allow its expression in eukaryotic cells.[7,9a] The biosynthesis of mcDNA from the parental backbone is inducible and occurs at a specific site, in which phiC31 catalyzes the division of PP into two species: (i) miniplasmids (mP) that contain the undesirable

Received: November 12, 2012
Accepted: January 22, 2013
Published: January 22, 2013

bacterial sequences and (ii) the mcDNA biomolecules.[11] Following recombination, PP and mP are degraded by endonucleases that identify a cutting sequence in their structure.[13] However, this last stage of the process is not completely effective and PP is not totally removed.[11] To overcome this drawback and supply highly pure mcDNA biopharmaceuticals, a purification stage is thus preemptively required.

Numerous purification methods such as hydrophobic interaction, ionic-exchange chromatography, membrane ultrafiltration, or magnetic separation are currently available for pDNA,[14] though none of these have concerned mcDNA purification.[15] Actually, our group has previously engineered and optimized pDNA-affinity purification methods that yield pharmaceutical-grade DNA (without endotoxins or bacterial proteins) in its biologically active supercoiled isoform.[16] These platforms take advantage of biomimetic interactions between amino acids and DNA strands at a molecular level to achieve a selective purification.[17] Interestingly, similar biorecognition interactions were also described by Liu and co-workers when analyzing phiC31−DNA complexes, these being events particularly evident for an array of key phiC31 affinity sequences that include arginine amino acids.[18] The search for innovative ligands is however demanding and must rely on high-throughput analytical technologies that are extremely sensitive.[19] As recently reported by Cruz and co-workers, SPR arises as a particularly effective technique for the analysis of ligands suitable for DNA purification.[20] From this standpoint, herein we devised a straightforward and versatile strategy based on SPR to screen for the potential of arginine dipeptides as novel affinity ligands for mcDNA recognition and also to establish parameters that may positively influence ligand−mcDNA biomolecular interactions, in such a way that recovery of the target molecules is attained.

EXPERIMENTAL SECTION

Materials. The 7.06 kbp pMC.CMV-MCS-EF1-GFP-SV40PolyA, kanamycin-resistant, parental plasmid and the *Escherichia coli* (*E.coli*) ZYCY10P3S2T minicircle producer strain were purchased from System Biosciences (Mountain View, CA). Arginine-arginine dipeptides were obtained from GenScript (Piscataway, NJ). A 1 kbp DNA ladder was provided by Vivantis Technologies (Oceanside, CA). Borate buffer, bacterial culture reagents, disodium hydrogen phosphate, *N*-(2-hydroxyethyl)piperazine-*N*′-(2-ethanesulfonic acid) (HEPES free acid), sodium hydrogen phosphate, and tris-(hydroxymethyl)aminomethane (Tris base) were purchased from Sigma Aldrich (Sintra, Portugal). Carboxymethyl dextran-modified gold surface sensor chip CM5, surfactant P20, HBS-N buffer (100 mM HEPES, 1.5 M NaCl, 0.05% P20, pH 7.4), *N*-ethyl-*N*′-(3-dimethylaminopropyl)carbodiimide hydrochloride (EDC), and *N*-hydroxysuccinimide (NHS) were obtained from GE Healthcare Ltd. (Barcelona, Spain).

Bacterial Growth and mcDNA Biosynthesis. To set up the production of mcDNA, competent *E. coli* ZYCY10P3S2T cells were initially transformed with the PP template according to the manufacturer's instructions. Bacteria were then seeded in LB-agar plates containing kanamycin (50 μg/mL), and transformed colonies were selected for further studies. To promote bacterial amplification, a prefermentation (v = 25 mL) containing Terrific Broth medium (TB) (nitrogen source, tryptone (20 g/L); carbon source, glycerol (4 mL/L); protein and nitrogen source, yeast extract (24 g/L); buffering salts, 0.017 M KH_2PO_4, 0.072 M K_2HPO_4, pH 7.0) was inoculated with transformed cells, and growth was carried out in fed-batch mode at 37 °C, 250 rpm (Agitorb 200 IC, Aralab) until an $OD_{600\ nm} \cong 2.6$ was reached. The cells were then used to inoculate a scaled up fermentation (v = 250 mL) with a starting $OD_{600\ nm} \cong 0.2$ that was subsequently incubated overnight at 37 °C, 250 rpm. In the following day at late log phase, minicircle DNA production was induced by using a modification of a previously described method.[11] Briefly, a sterile 20% L-arabinose solution was added to the overnight culture to a final concentration of 0.01%, to induce the BAD.phiC31 promoter to express the serine recombinase that mediates mcDNA and mP production. Afterward, the culture was grown for an additional 5 h period at 30 °C, 250 rpm, and then recovered by centrifugation (4 °C, 6000 rpm, 20 min).

Primary Isolation of mcDNA. The recovery of mcDNA from bacterial cultures and isolation from other bacterial contaminants was performed through alkaline lysis with the commercial Qiagen Plasmid Maxi kit (Qiagen Inc., Valencia, Spain) following the manufacturer's instructions with slight modifications. Briefly, induced ZYCY10P3S2T cells were lysed with two times the volume of kit solutions that is described in the original protocol. After lysis and prior to primary purification, the resulting cell debris were then removed by a two-step centrifugation protocol (19 000g, 30 min, 4 °C). Bacterial RNA and genomic DNA were subsequently separated from the extracted samples by anion exchange chromatography using a silica resin. Lastly, the recovery of the target DNA bound to the column was accomplished using an elution buffer containing 1.35 times higher salt concentration than that originally recommended. The eluted species were precipitated with 1 volume of 2-propanol and afterward resuspended in a suitable buffer for SPR experiments. With these minor modifications, the overall mcDNA recovery yield was significantly improved in comparison to the standard protocol. The purity of the isolated samples was further confirmed with UV−vis spectrophotometry by determining the 260/280 nm absorbance ratio (Shimadzu 1700, Shimadzu Inc., Japan). All samples had purity values that ranged between 1.8 and 2.0.

The integrity of mcDNA samples isolated from *E. coli* cells was also examined by electrophoresis using 1% low-melting agarose gel supplemented with ethidium bromide. Electrophoresis was performed at a running voltage of 100 V for 35 min, at room temperature, in Tris-acetate−EDTA (TAE) buffer, pH 8.0 ± 0.2. Agarose gels were visualized using a UV transilluminator (UVItec, Cambridge, UK, λ = 362 nm).

Peptide Immobilization. All SPR analyses were performed by using a Biacore T200 Biosensor (Biacore, GE Healthcare, Sweden) equipped with a CM5 research grade sensor chip. Prior to immobilization, the signal response of the CM5 chip was normalized (BIA normalizing solution, 70%), and a pH scouting experiment was performed to determine the optimal immobilization pH according to the immobilization level desired by comparing the responses (in RU) obtained at each pH of the sensorgram with the desired response in RU. Following this standard procedure, 1 M arginine-arginine dipeptides (Arg-Arg, 97% purity) (Scheme 1) in 0.1 M borate, pH 8.5, were immobilized onto the hydrophilic carboxymethyl-dextran (CM) polymeric chains through amine coupling chemistry, using HBS-N as a running buffer. To promote chemical attachment, the carboxylic acid (COOH) moieties of dextran in flow cell 1 and 2 (Fc-1 and Fc-2) were initially activated by injecting a 1:1 mixture of EDC (0.4 M) and NHS

dx.doi.org/10.1021/ac303288x | *Anal. Chem.* 2013, 85, 2304−2311

Scheme 1. Arginine-Arginine Dipeptides Used To Exploit Possible Biomolecular Interactions with mcDNA

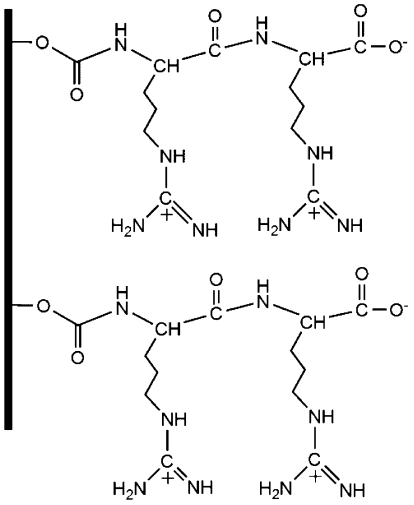

(0.1M) at a flow rate of 5 μL/min, (T = 25 °C). To promote ligand immobilization, the Arg-Arg dipeptide was then injected in Fc-2 for 7 min, at 25 °C (93×10^{-3} mol/L immobilized, 0.465pmol/mm^2 ligand sites). Fc-1 was used as reference for all experiments. To quench the unreacted COOH groups in Fc-2 and Fc-1, 1 M ethanolamine-HCl solution, pH 8.5, was injected onto the sensor chip surface (7 min, 5 μL/min), followed by a baseline stabilization period with HBS-N.

SPR Specific Binding Assays. To address ligand−analyte biomolecular interactions, SPR experiments were performed with several buffers that are suitable for use with DNA biomolecules: (i) 10 mM Tris-HCl, pH 8.0; (ii) 100 mM HEPES, pH 7.4; (iii) 10 mM phosphate, pH 8.0; (iv) 300 mM NaCl in 10 mM Tris-HCl, pH 8.0; (v) HBS-N, pH 7.4 (100 mM HEPES, 1.5 M NaCl). Variable temperature conditions (10 °C and 25 °C) were also investigated to address their possible influence on the establishment of binding interactions. Minicircle samples used for injection were prepared by serial dilutions to the desired concentration range with adequate buffers for each experiment. At least duplicate injections of each mcDNA solution and a buffer blank were flowed over the Arg-Arg surface, as well as over the reference surface at a flow rate of 1 μL/min with constant data acquisition (10 Hz). No regeneration solution was required because all mcDNA solutions are removed from the surface. In addition, PP control samples (concentration range: 2.63 μM to 0.001 μM) were also flowed over the different peptide surfaces studied, as described above (Supporting Information Figure S2).

Following mcDNA injection, the association and dissociation phases were monitored for 420 and 100 s, respectively. After the last stage, an additional stabilization period of 100 s was carried out. To correct the bulk refractive index, the signal obtained for the reference surface was subtracted from sensorgrams for the Arg-Arg immobilized surface. In addition, subtraction of the blank injection responses (running buffer without mcDNA) were performed. The equilibrium dissociation constants (K_D) were determined by fitting averaged response data (RU) in the steady-state region (300 to 400 s) to an affinity model, $[R_{eq}] = R_{max} - (1/(1 + K_D/[A]))$, where R_{eq} represents the amount of analyte complexed with the ligand on the surface, [A] is the analyte concentration, and R_{max} is the maximum binding capacity of the surface. R_{max} was also determined by the previous mathematical model. All numerical integrations were performed in BIAevaluation software v.4.1 and Biacore T200 evaluation software v 1.0 (Biacore, GE Healthcare, Sweden).

Zeta Potential. For the determination of DNA zeta potential in different buffers, a Zetasizer Nano Zs instrument was used (Malvern Instruments, Worcestershire, UK). Sample measurements were performed in a disposable folded capillary cell, and data was acquired after 50 runs in monomodal mode. Buffer solutions without DNA were used as references for all measurements. Simultaneously to zeta potential acquisition, the conductivity of the samples was also analyzed. The experiments were performed in triplicate both at 10 °C and 25 °C. Electrokinetic mobility was then converted to zeta potential assuming the Smoluchowsky approximation[21]

RESULTS AND DISCUSSION

Minicircle DNA Biosynthesis and Isolation. DNA minicircles have the potential to become the next generation of biopharmaceuticals due to their invaluable characteristics as therapeutic biomolecules. Furthermore, the recent improvements in mcDNA production process open the possibility to obtain genetic material in quantities that are suitable for gene expression studies and clinical trials.[10] From this standpoint, DNA biosynthesis was therefore promoted in a standard bacterial culture, in which selective enzymes were activated with L-arabinose, to convert PP template DNA into minicircles in high yield. As demonstrated by Figure 1, the recovered mcDNA

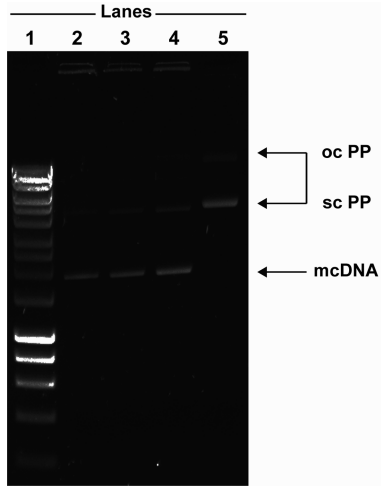

Figure 1. Agarose gel electrophoresis of recovered DNA from a bacterial culture of ZYCY10P3S2T. Lane 1: DNA molecular weight marker; lanes 2 to 4: recovered mcDNA after biosynthesis and induction in three independent fermentations; lane 5: template PP DNA before induction with L-arabinose (sc, supercoiled; oc, open circular).

is structurally stable and no linear isoforms of the biopharmaceutical were detected (Figure 1, lanes 2 to 4). Actually, our findings reveal that after upstream processing with the optimized isolation conditions, mcDNA fully upholds its naturally occurring supercoiled (sc) isoform (Figure 1, lane 2). Contrary to the linear (ln) or open circular (oc) DNA forms, this topological conformation is particularly relevant when therapeutic applications are envisioned. In fact, it has been previously demonstrated that expression of the therapeutic genes is more effective when mediated by sc DNA both in vitro

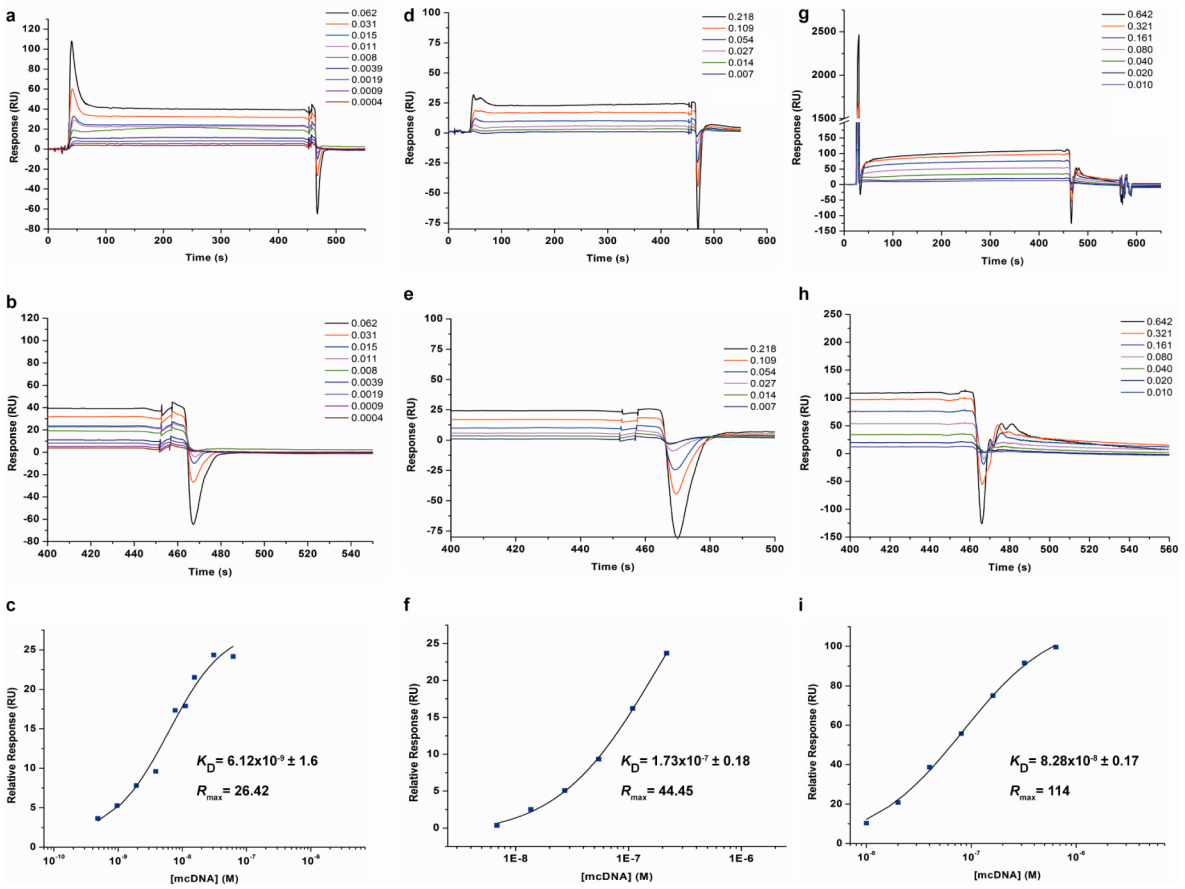

Figure 2. SPR analysis of mcDNA biopharmaceutical interaction with Arg-Arg dipeptide ligands in different buffers, at 25 °C. Sensorgrams and binding analysis: (a, b, and c) 10 mM Tris-HCl buffer, pH 8.0; (d, e, and f) 100 mM HEPES buffer, pH 7.4; (g, h, and i) 10 mM phosphate buffer, pH 8.0.

and in vivo.[22] Moreover, Chandock and co-workers also reported that superhelical DNA structures favor localized unwinding events of its strands, thus contributing to a more effective expression and an improved overall therapeutic effect.[23] These results assume further importance in light of the current good manufacturing practices (cGMP) that demand the use of pharmaceutical-grade DNA mostly in the sc isoform.[24] However, it is also important to emphasize that residual PP species still remain in mcDNA preparations (Figure 1). The presence of these residual contaminants is highly correlated with the bioprocess itself because the enzymes responsible for the degradation of the original template are unable to completely eliminate parental DNA.[25] Interestingly, this pattern of activity largely influences the final yield of mcDNA because both degradative/recombination-mediating enzymes are activated simultaneously.[11] If PP DNA is completely degraded prior to its recombination, the mcDNA recovery yield is significantly compromised. Because of this indispensable unbalance between degradation/recombination, the PP templates, which also contain bacterial sequences, are still recovered. Henceforth, the purification of mcDNA formulations arises as a critical requirement for the development of safe therapeutic applications.

Analysis of Specific Biomolecular Interactions by SPR. The new Arg-Arg dipeptides were immobilized on two CM5 SPR sensor chips to evaluate mcDNA binding. SPR not only allows the quantification of ligand−analyte binding events with extreme accuracy but also offers the perfect system design to test for experimental conditions similar to those provided by standard chromatography instruments (buffer, pH, and temperature manipulation) where usually the purification of DNA biomolecules is accomplished.[26] To set up the SPR binding assays, dipeptide immobilization was performed via amine coupling chemistry at an optimal pH of 8.52. These conditions ensure that the guanidine functional groups of the arginine amino acid are positively charged and the α-NH_2 group of the dipeptides is attached to the reactive ester groups of the CM5 chip. The latter parameter is of utmost importance because our group has previously demonstrated that the guanidine functional group of arginine establishes different affinity interactions with DNA, depending on its conformation.[27] These previous results regarding amino acid−DNA interactions have also contributed to the further exploration of this novel Arg-Arg dipeptide, because similar affinity interactions might be established. Hence, to evaluate the existence of such biomolecular recognition of the guanidine functional groups of arginine by mcDNA, different experimental conditions were investigated. As shown in the sensorgrams of Figure 2, in the range of concentrations tested, dipeptide−mcDNA bioaffinity interactions were present for Tris-HCl, phosphate, and HEPES buffers, at 25 °C (Figure 4). When HBS-N buffer (100 mM HEPES, 1.5 M NaCl) was used, no interaction was established. Furthermore, our results also reveal that when a moderate salt concentration (300 mM NaCl buffer) was used, negligible binding responses were obtained (<2 RU), implying that binding and elution of mcDNA may be manipulated with this

dx.doi.org/10.1021/ac303288x | Anal. Chem. 2013, 85, 2304−2311

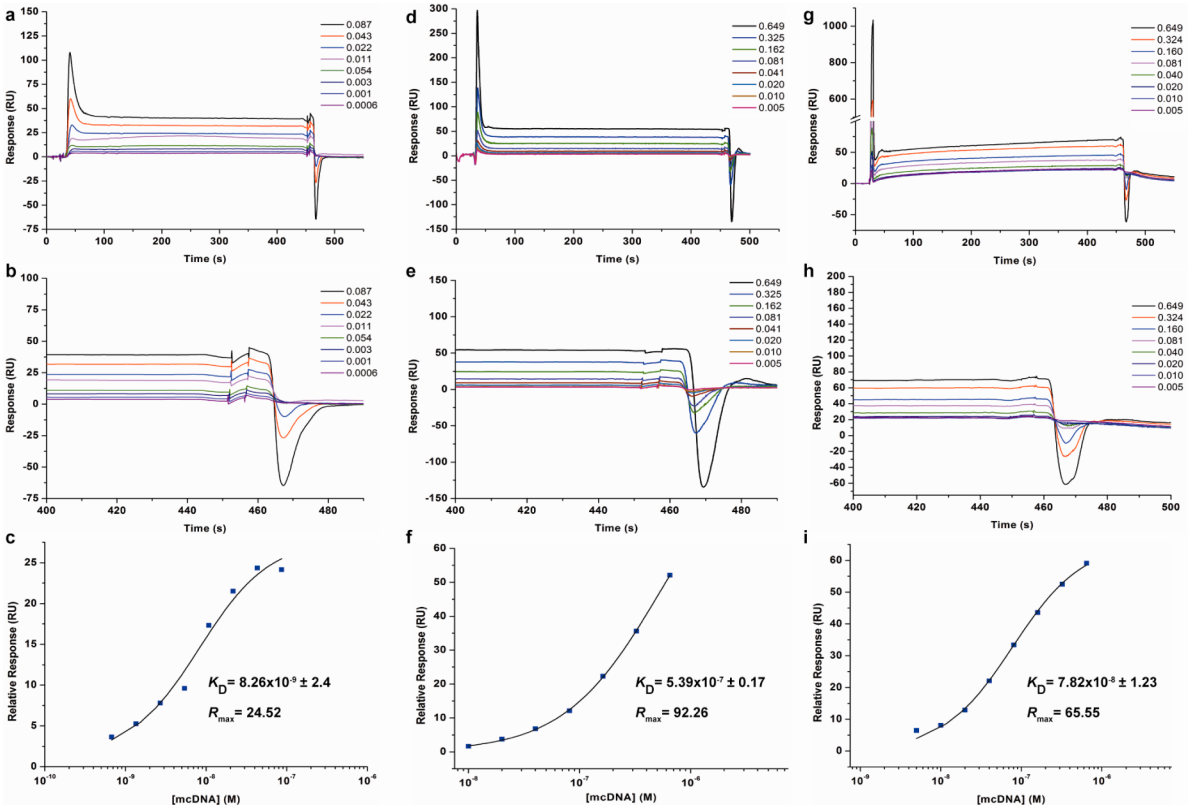

Figure 3. SPR analysis of mcDNA biopharmaceutical interaction with Arg-Arg in different buffers, at 10 °C. Sensorgrams and binding analysis: (a, b, and c) 10 mM Tris-HCl buffer, pH 8.0; (d, e, and f) 100 mM HEPES buffer, pH 7.4; (g, h, and i) 10 mM phosphate buffer, pH 8.0.

parameter. Additionally, alternative dipeptides (arginine-histidine and histidine-arginine) were also screened as novel ligands for mcDNA; however, the binding capacity for these biopharmaceuticals was insignificant under all tested conditions (Supporting Information Figure S1). Also, no binding response was obtained in the array of buffers tested when the original PP plasmid was injected (Supporting Information Figure S2). Interestingly, the SPR sensorgrams obtained with the Arg-Arg dipeptide present markedly square shaped response profiles that illustrate swift dissociation and association rates (k_{off}/k_{on}) (Figure 2a,c,e). These results suggest that mcDNA biomolecules are rapidly recognized by the Arg-Arg dipeptides, and that the ongoing interactions are also reversible. This is a relevant characteristic of these ligands because they must favor the occurrence of affinity interactions and allow an easy release of the target molecules, to promote their selective recovery.[28] A closer analysis of sensorgram shape also reveals a remarkable dissociation phase (450 s) with total mcDNA detachment characterized by a steep profile (Figures 2 and 3, parts b, e, and h). Actually, this demonstrates the avidity of the ligands for mcDNA molecules, i.e., when a binding site is available, it readily interacts with the target molecule.

With the aim to further characterize the influence of different buffers in ligand−analyte interactions in a quantitative mode, mathematical analysis was also performed by using binding responses at the plateau region where the rates of association/dissociation are equally coordinated (Figure 2). Steady-state data was best fitted to a single-site biomolecular interaction binding model for all buffers tested. The overall affinity of the mcDNA to the Arg-Arg surface was higher ($K_D > 10^{-6}$ M). The equilibrium dissociation constants (K_D) demonstrate that Tris-HCl promotes higher ligand−analyte affinity interactions (K_D = 6.12×10^{-9} M) in comparison with phosphate (K_D = 8.28×10^{-8} M) or HEPES (K_D = 1.73×10^{-7} M). Our results are in stark agreement with those reported in the literature, where Tris-HCl buffer was used to promote the establishment of affinity interactions between DNA and selective ligands, such as hydroxyapatite[14b] or arginine.[27]

Notwithstanding, the effect of temperature in mcDNA−ligand binding interaction was also studied. In fact, this is a critical parameter in DNA purification because lower temperatures stabilize the compact superhelical topoisoform and prevent its conversion into open circular form.[22a] Definitely, the maintenance of this unique topology not only is advantageous for its biological application, but it also increases the binding interactions with amino acid ligands due to torsion deformations that expose the phosphate groups present in nucleic acids.[29]

The resonance response results achieved at lower temperature (10 °C) are shown in Figure 3. As the representative sensorgrams demonstrate, the profile of the binding responses is similar to that obtained at 25 °C, illustrating that ligand−analyte interactions also take place under these conditions (Figure 3a,c,e). Furthermore, the binding dissociation constants reveal that Tris-HCl buffer (K_D = 8.26×10^{-9} M) promotes affinity interactions to a higher extent followed by phosphate (K_D = 7.82×10^{-8} M) and HEPES (K_D = 5.39×10^{-7} M). Affinity decreased 3-fold when temperature was decreased for HEPES and decreased slightly (1.3 fold) for Tris-HCl, although for phosphate buffer, the affinity increase is negligible. Regardless of the buffer type, a decrease in temperature influences analyte−ligand affinity interactions, with an increase in K_D being attained for all buffers at 10 °C (Figures 2 and 3). A decrease in affinity interactions at relatively lower temper-

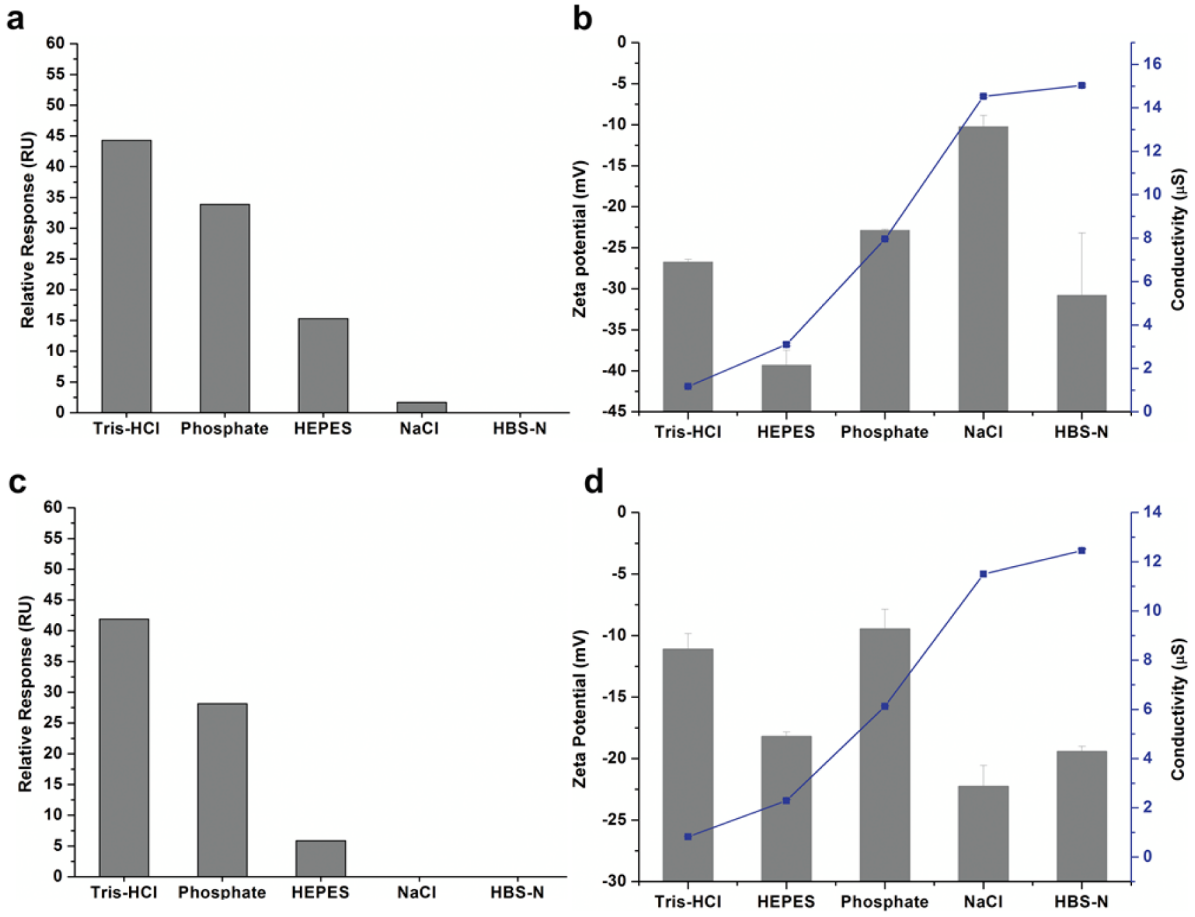

Figure 4. Electrokinetic potential and SPR binding analysis. (a and c) Relative resonance response (RU) with different running buffers at 380 s after injection of mcDNA at a concentration of 0.040 μM, at 25 °C and 10 °C, respectively; (b and d) left-*y* axis: mcDNA zeta potential in different buffers; right *y*-axis: buffer conductivity, at 25 °C and 10 °C, respectively.

atures is consistent with the previously reported results by Sousa et al., in which pDNA retention in an arginine−agarose chromatography support was reduced at low temperatures (≤10 °C).[27] In addition, the performance of the novel dipeptides was also evaluated at 37 °C; however, the binding affinities were lower than those obtained both at 25 °C and 10 °C (Supporting Information Figure S3). Nevertheless, the purification of DNA biopharmaceuticals performed at lower temperatures presents advantages regarding nucleic acid stability. In addition, industrial purification of gene-based therapeutics is severely restricted at higher temperatures, such as 37 °C, because of economic costs.[5] All these important insights provided by SPR data emphasize not only the fact that affinity interactions are established with the candidate ligand but also that it possesses a distinctive behavior under a wide range of conditions.

Electrokinetic Mobility and Conductivity Analysis. Analytical characterization of the physicochemical behavior of mcDNA under different conditions may bring forth additional knowledge on how these novel biomolecules interact with possible ligands under precise conditions. Therefore, the electrokinetic mobility of mcDNA and conductivity were also determined. The mcDNA zeta potential was negative for all conditions tested, indicating that mcDNA preserves its overall negative surface charge (Figure 4b,d). A negative zeta potential value is very relevant for the establishment of electrostatic-based interactions with the positively charged dipeptide. In addition, because of the unique structure of the ligand, the binding interaction between DNA and amino acid is reinforced by H-bonds.[22a]

As mentioned previously for SPR data, the distinct buffer environments affected the interaction strength, with an increase in binding up to 40% for Tris-HCl in comparison with NaCl and HBS-N (Figures 4a,c) at temperature 25 °C and 10 °C, respectively). The affinity interactions obtained with the array of buffers under the different conditions are summarized in Table 1. This is correlated not only with the negative zeta potential but also with the specific conductance of this buffer and its neutral charge at pH 8.0 (Figure 4b,d). Temperature conditions also influenced the electrokinetic mobility with the

Table 1. Representative mcDNA−Dipeptide Binding Interactions under Different Buffer Conditions[a]

	Buffers				
	Tris-HCl	HEPES	Phosphate	NaCl	HBS-N
25 °C	+++	+	++	-	--
10 °C	+++	+	++	--	--

[a]+++, Strongest binding interactions; --, no binding interactions.

dx.doi.org/10.1021/ac303288x | *Anal. Chem.* 2013, 85, 2304−2311

potential increasing from −26.7 mV to −11.1 mV at 10 °C for Tris-HCl. Despite this effect, the responses obtained by SPR were similar at both temperatures, suggesting that Tris-HCl is a valuable choice for promoting mcDNA−ligand binding interactions in future applications (Figure 4a,c). HEPES and phosphate buffer coupling responses were also verified, with higher binding events being more evident for HEPES. The occurrence of favorable affinity interactions with these two particular buffers is essentially correlated with their chemical nature. HEPES is a zwitterion at pH 7.4 and thus interacts with the mcDNA biopharmaceuticals in opposite modes. Actually, HEPES may possibly disturb the electrostatic potentials around the dissolved biomolecules by displacing the dynamic guy-chapman electric double layer[21] and consequently changing the overall surface charge by shielding DNA with positive charge in a phenomenon described as solvent penetration.[22a] Moreover, HEPES may also repel mcDNA nucleotides, leading to more compact structures with exposed phosphate groups and higher negative spatial charge.[30] The balance of these events dictates the behavior of nucleic acids, and as our results demonstrate, the DNA zeta potential in HEPES is more negative than in phosphate (Figure 4b,d). Remarkably, mcDNA−ligand interactions are higher for the latter, suggesting that HEPES may also interfere in mcDNA−dipeptide coupling. Nevertheless, the higher binding response for phosphate (Figure 4a,b) also provides insights regarding the actual capacity to establish affinity interactions with this buffer. Polyelectrolyte solutions, such as phosphate buffer, contain counterions that solvate DNA molecules, influencing not only the net surface charge but also, as described by Bauman and co-workers, the actual elasticity of the biomolecules,[31] which in turn impacts mcDNA−ligand interactions. The zeta potential of mcDNA in phosphate at 25 °C is more negative than at 10 °C, suggesting that the increased binding response observed for higher temperatures can be correlated with the occurrence of stronger electrostatic interactions.

Apart from the above-mentioned buffers, sodium-containing buffers (300 mM NaCl and HEPES) demonstrated opposite effects. Indeed, for these buffers, no binding responses were recorded at 10 °C and negligible response (<2.5 RU) was detected at 25 °C (Figure 4a,c). Regarding the contribution of other parameters, HBS-N (100 mM HEPES, 1.5 M NaCl) presents a shift in conductivity from 12.5 μS to 15.0 μS with increasing temperature, while mcDNA zeta potential values remain rather unchanged. Moreover, it becomes important to emphasize that for HEPES buffer alone (no mcDNA), electrophoretic mobility was not significantly different at the tested temperatures (25 °C: −9.92 mV; 10 °C: −6.54 mV, results not shown). Taking this into consideration, the absence of binding interactions is likely correlated with the high salt concentration of the HBS-N buffer. Actually, similar salt concentration-dependent effects have also been reported in the literature for pDNA−arginine interactions.[32]

Concerning 300 mM NaCl in 10 mM Tris-HCl, our findings emphasize that mcDNA electrokinetic potential withstands a relevant shift toward less negative values at 25 °C. However, it should be emphasized that this change does not take into account the buffer contribution. In this specific circumstance, NaCl zeta potential is highly different at 10 °C (−3.54 mV) from that of 25 °C (−16 mV, data not shown). Thus, only in this particular case, subtracting the contribution of the buffer alone masks the real zeta potential of mcDNA. Therefore, the binding signal observed at 25 °C illustrates the existence of electrostatic interactions between biopharmaceuticals and the surrounding counter-species that are strong enough to provide binding. This phenomena caused by the electrolytes arises from dynamic ionic hydration effects because sodium ions tend to interact with both the major and minor groove of DNA molecules[33] originating a densely packed molecule that possesses an electric-double layer composed of counterions (Na^+ and Cl^-). This remarkably dynamic ionic atmosphere associated with free ions in solution consequently influences the immediate interactions with the dipeptide ligand.[21] The description of these parameters and binding conditions provides invaluable information for further manipulation of mcDNA recovery, under precise conditions (Table 1). Overall, Tris-HCl at both temperatures was the best buffer to establish mcDNA−dipeptide binding interactions; in contrast, HBS-N is a suitable buffer to promote mcDNA elution.

■ CONCLUSIONS

In this study, we have explored the capacity of novel dipeptide ligands to interact with mcDNA by using SPR analysis under different conditions that are generally employed for the recovery and purification of pharmaceutical-grade genetic material in the industry. From the range of ligands investigated, arginine dipeptides are the most suitable for the establishment of biomolecular interactions with DNA minicircles. Therefore, various experimental parameters for ligand−mcDNA binding and recovery were thoroughly characterized, and an optimal set of buffers and temperature conditions was defined. Moreover, the additional analysis of mcDNA electrokinetic potential provided important insights into the physicochemical characteristics of these novel biopharmaceuticals. To the best of our knowledge, this is the first time that the electrokinetic potential of mcDNA was investigated. This characterization assumes further importance, taking into consideration that this parameter influences biomolecular interactions that mcDNA may establish for instance with candidate ligands, cell membranes, or biomaterials. Furthermore, this was also the first time that SPR was used for the evaluation of innovative ligands for minicircle purification.

Overall, gathering these important insights together opens up the possibility to devise dynamic recovery strategies for these promising biopharmaceuticals that mostly rely on the manipulation of the key conditions that were investigated. The development of such platforms will have a tremendous impact in the development of safer and more effective therapeutic approaches for a broad range of pathologies.

■ ASSOCIATED CONTENT

Supporting Information

Additional information as noted in the text. This material is available free of charge via the Internet at http://pubs.acs.org.

■ AUTHOR INFORMATION

Corresponding Author

*Tel: +351 275 329 002. Fax: +351 275 329 099. E-mail: fani.sousa@fcsaude.ubi.pt.

Notes

The authors declare no competing financial interest.

■ ACKNOWLEDGMENTS

The authors thank Prof. Ricardo Louro for all his help with the acquisition of zeta potential data. This work was supported by

the Portuguese Foundation for Science and Technology (FCT) (PTDC/EME-TME/103375/2008, PTDC/EBB-BIO/114320/2009, and PEst-C/SAU/UI0709/2011 COMPETE). Vítor M. Gaspar acknowledges a Ph.D. fellowship from FCT (SFRH/BD/80402/2011). Carla Cruz also acknowledges a postdoctoral grant from FCT (SFRH/BPD/46934/2008).

REFERENCES

(1) Moran, N. *Nat. Biotechnol.* **2012**, *30*, 807−809.
(2) Giacca, M. *Introduction to Gene Therapy*; Springer: New York, 2010.
(3) Subramanian, G. *Biopharmaceutical Production Technology*; Wiley-VCH: New York, 2012.
(4) Mayrhofer, P.; Iro, M. In *Gene Vaccines*; Thalhamer, J.; Weiss, R.; Scheiblehofer, S., Eds.; Springer-Verlag: Duesseldorf, 2012; pp 297−310.
(5) Ismail, R.; Allaudin, Z. N.; Lila, M. A. M.; Rahman, N. M. A. N. A. *Vaccine* **2012**, *30*, 5914−5920.
(6) Chen, Z. Y.; Riu, E.; He, C. Y.; Xu, H.; Kay, M. A. *Mol. Ther.* **2008**, *16*, 548−556.
(7) Osborn, M. J.; McElmurry, R. T.; Lees, C. J.; DeFeo, A. P.; Chen, Z.-Y.; Kay, M. A.; Naldini, L.; Freeman, G.; Tolar, J.; Blazar, B. R. *Mol. Ther.* **2011**, *19*, 450−460.
(8) Chabot, S.; Orio, J.; Schmeer, M.; Schleef, M.; Golzio, M.; Teissie, J. *Gene Ther.* **2012**, 1−7, DOI: 10.1038/gt.2011.215.
(9) (a) Kobelt, D.; Schleef, M.; Schmeer, M.; Aumann, J.; Schlag, P. M.; Walther, W. *Mol. Biotechnol.* **2012**, 1−10. (b) Zhang, C.; Gao, S.; Jiang, W.; Lin, S.; Du, F.; Li, Z.; Huang, W. *Biomaterials* **2010**, *31*, 6075−6086.
(10) Kwon, M. J.; An, S.; Choi, S.; Nam, K.; Jung, H. S.; Yoon, C. S.; Ko, J. H.; Jun, H. J.; Kim, T. K.; Jung, S. J.; Park, J. H.; Lee, Y.; Park, J. S. *J. Gene Med.* **2012**, *14*, 272−8, DOI: 10.1002/jgm.2618.
(11) Kay, M. A.; He, C. Y.; Chen, Z. Y. *Nat. Biotechnol.* **2010**, *28*, 1287−1289.
(12) Chen, Z.; He, C.; Kay, M. *Human Gene Ther.* **2005**, *16*, 126−131.
(13) Huang, M.; Chen, Z. Y.; Hu, S.; Jia, F.; Li, Z.; Hoyt, G.; Robbins, R. C.; Kay, M. A.; Wu, J. C. *Circulation* **2009**, *120*, S230.
(14) (a) Perçin, I.; Karakoç, V.; Akgöl, S.; Aksöz, E.; Denizli, A. *Mater. Sci. Eng., C* **2012**, *32*, 1133−1140. (b) Hilbrig, F.; Freitag, R. *Biotechnol. J.* **2012**, *7*, 90−102.
(15) Mayrhofer, P.; Blaesen, M.; Schleef, M.; Jechlinger, W. *J. Gene Med.* **2008**, *10*, 1253−1269.
(16) (a) Sousa, F.; Prazeres, D.; Queiroz, J. *J. Gene Med.* **2009**, *11*, 79−88. (b) Sousa, A.; Tomaz, C.; Sousa, F.; Queiroz, J. *J. Chromatogr., A* **2011**, *1218*, 8333−43.
(17) Sousa, F.; Cruz, C.; Queiroz, J. A. *J. Mol. Recognit.* **2010**, *23*, 505−518.
(18) Liu, S.; Ma, J.; Wang, W.; Zhang, M.; Xin, Q.; Peng, S.; Li, R.; Zhu, H. *PloS One* **2010**, *5*, e8863.
(19) Pattnaik, P. *Appl. Biochem. Biotechnol.* **2005**, *126*, 79−92.
(20) Cruz, C.; Cabrita, E. J.; Queiroz, J. A. *Anal. Bioanal. Chem.* **2011**, *401*, 983−993.
(21) Schellman, J. A.; Stigter, D. *Biopolymers* **1977**, *16*, 1415−1434.
(22) (a) Gaspar, V. M.; Correia, I. J.; Sousa, Â.; Silva, F.; Paquete, C. M.; Queiroz, J. A.; Sousa, F. *J. Controlled Release* **2011**, *156*, 212−222. (b) Quaak, S. G. L.; den Berg, J. H. v.; Oosterhuis, K.; Beijnen, J. H.; Haanen, J. B. A. G.; Nuijen, B. *J. Controlled Release* **2009**, *139*, 153−159.
(23) Chandok, G.; Kapoor, K.; Brick, R.; Sidorova, J.; Krasilnikova, M. *Nucleic Acids Res.* **2011**, *39*, 2103−2115.
(24) (a) Urthaler, J.; Schuchnigg, H.; Garidel, P.; Huber, H. In *Gene Vaccines*; Thalhamer, J.; Weiss, R.; Scheiblehofer, S., Eds.; Springer-Verlag: Duesseldorf, 2012; pp 311−330 (b) Cai, Y.; Rodriguez, S.; Rameswaran, R.; Draghia-Akli, R.; Juba, R. J., Jr.; Hebel, H. *Vaccine* **2010**, *28*, 2046−2052.
(25) System Biosciences, 2010, version 1-112310.
(26) Sousa, A.; Bicho, D.; Tomaz, C.; Sousa, F.; Queiroz, J. *J. Chromatogr., A* **2011**, *1218*, 1701−1706.
(27) Sousa, F.; Matos, T.; Prazeres, D.; Queiroz, J. *Anal. Biochem.* **2008**, *372*, 432−434.
(28) Hage, D. S. *Encyclopedia of Analytical Chemistry*; Wiley: New York, 2012
(29) Kanaar, R.; Cozzarelli, N. *Curr. Opin. Struct. Biol.* **1992**, *2*, 369−379.
(30) Turro, N.; Barton, J.; Tomalia, D. *Acc. Chem. Res.* **1991**, *24*, 332−340.
(31) Baumann, C. G.; Smith, S. B.; Bloomfield, V. A.; Bustamante, C. *Proc. Natl. Acad. Sci. U.S.A.* **1997**, *94*, 6185−6190.
(32) Sousa, F.; Prazeres, D.; Queiroz, J. *Biomed. Chromatogr.* **2009**, *23*, 160−165.
(33) Ben-Yaakov, D.; Andelman, D.; Podgornik, R.; Harries, D. *Curr. Opin. Colloid Interface Sci.* **2011**, *16*, 542−550.

dx.doi.org/10.1021/ac303288x | *Anal. Chem.* 2013, 85, 2304−2311

Supplementary Information

Sensitive Detection of Peptide - Minicircle DNA Interactions by Surface Plasmon Resonance

Analytical Chemistry, 2013
DOI: 10.1021/ac303288x

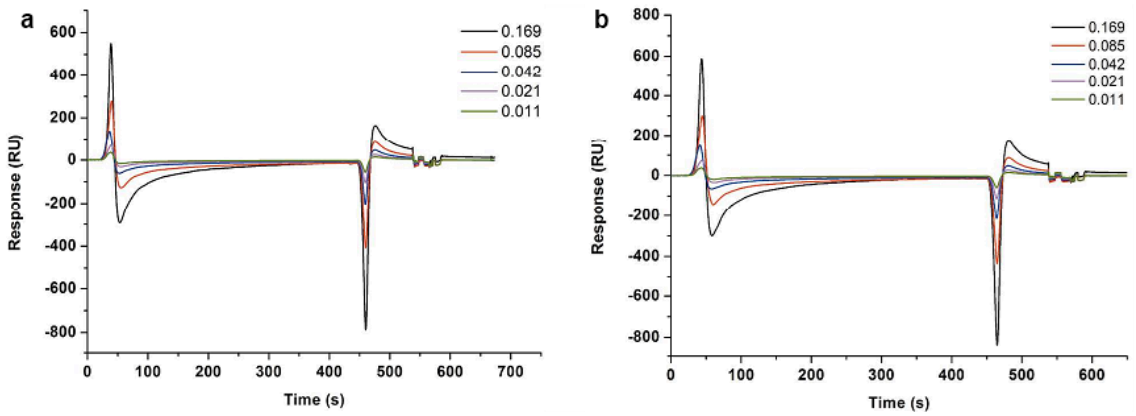

Figure S1. Representative SPR analysis of mcDNA biopharmaceuticals interaction with additional dipeptide ligands in 10 mM Tris.HCl buffer, at 25 °C. Sensorgrams of mcDNA binding to: a) Histidine-Arginine dipeptides; b) Arginine-Histidine dipeptides.

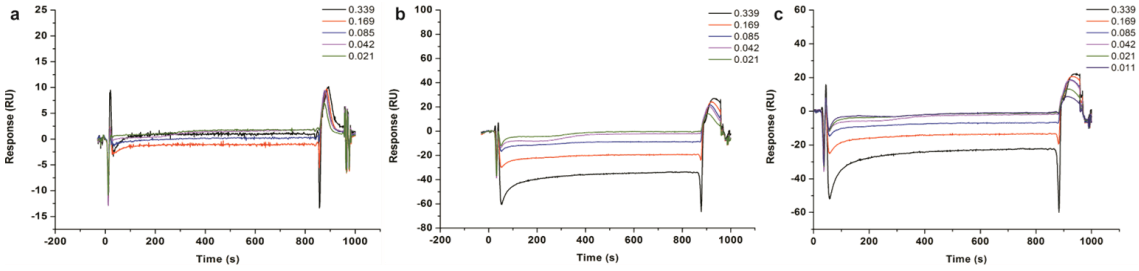

Figure S2. Representative SPR analysis of PP interaction with various ligands in 10 mM Tris.HCl buffer, at 25 °C. Sensorgrams of: a) Arginine-Arginine; b) Histidine-Arginine; c) Arginine-Histidine dipeptides.

Section III

Formulation of multifunctional delivery systems

CHAPTER 7

Biofunctionalized Nanoparticles with pH-responsive and Cell Penetrating Blocks for Gene Delivery

Nanotechnology, 2013

DOI: 10.1088/0957-4484/24/27/275101

Volume 24, number 27

Motivation

The advances in the manufacture and recovery of DNA preparations described in the previously presented studies may prove to be beneficial for enhancing minicircles applicability in therapeutic applications. However, the delivery of such biopharmaceuticals to the human host still remains a major challenge for currently available delivery technologies. From this standpoint the following study was performed to design a biofunctional chitosan-based nanocarrier with improved properties for delivery of DNA biopharmaceuticals to cancer cells.

Nanotechnology **24** (2013) 275101 (16pp) doi:10.1088/0957-4484/24/27/275101

Biofunctionalized nanoparticles with pH-responsive and cell penetrating blocks for gene delivery

V M Gaspar[1], J G Marques[1], F Sousa[1], R O Louro[2], J A Queiroz[1] and I J Correia[1,3]

[1] CICS-UBI—Centro de Investigação em Ciências da Saúde, Universidade da Beira Interior, Covilhã, Portugal
[2] ITQB-UNL—Instituto de Tecnologia Química e Biológica, Universidade Nova de Lisboa, Av. da República, Oeiras 2780-157, Portugal

E-mail: icorreia@ubi.pt

Received 5 November 2012, in final form 17 March 2013
Published 13 June 2013
Online at stacks.iop.org/Nano/24/275101

Abstract
Bridging the gap between nanoparticulate delivery systems and translational gene therapy is a long sought after requirement in nanomedicine-based applications. However, recent developments regarding nanoparticle functionalization have brought forward the ability to synthesize materials with biofunctional moieties that mimic the evolved features of viral particles. Herein we report the versatile conjugation of both cell penetrating arginine and pH-responsive histidine moieties into the chitosan polymeric backbone, to improve the physicochemical characteristics of the native material. Amino acid coupling was confirmed by 2D TOCSY NMR and Fourier transform infrared spectroscopy. The synthesized chitosan–histidine–arginine (CH–H–R) polymer complexed plasmid DNA biopharmaceuticals, and spontaneously assembled into stable 105 nm nanoparticles with spherical morphology and positive surface charge. The functionalized delivery systems were efficiently internalized into the intracellular compartment, and exhibited remarkably higher transfection efficiency than unmodified chitosan without causing any cytotoxic effect. Additional findings regarding intracellular trafficking events reveal their preferential escape from degradative lysosomal pathways and nuclear localization. Overall, this assembly of nanocarriers with bioinspired moieties provides the foundations for the design of efficient and customizable materials for cancer gene therapy.

S Online supplementary data available from stacks.iop.org/Nano/24/275101/mmedia

(Some figures may appear in colour only in the online journal)

1. Introduction

The delivery of genetic material into cells is a remarkably promising approach for the treatment of a wide range of incurable pathologies with growing worldwide occurrence, such as immune deficiencies, cancer or diabetes [19]. However, despite the fact that nucleic acid-based therapies are endowed with major safety improvements, the successful outcome of effective translational therapies remains a rather challenging issue [19]. To a certain extent, this is due to the high predisposition for degradation of plasmid DNA (pDNA) biopharmaceuticals in the extracellular environment, and their inability to cross major cellular barriers [15]. Such limitations may however be overcome with the inclusion of pDNA in specialized synthetic nanosized delivery systems.

Considering the numerous nanodevices developed in recent years, those comprised of cationic polymeric biomaterials are definitely receiving an ever-growing attention, mostly

[3] Address for correspondence: Centro de Investigação em Ciências da Saúde, Faculdade de Ciências da Saúde, Universidade da Beira Interior, Avenida Infante D Henrique, 6200-506 Covilhã, Portugal.

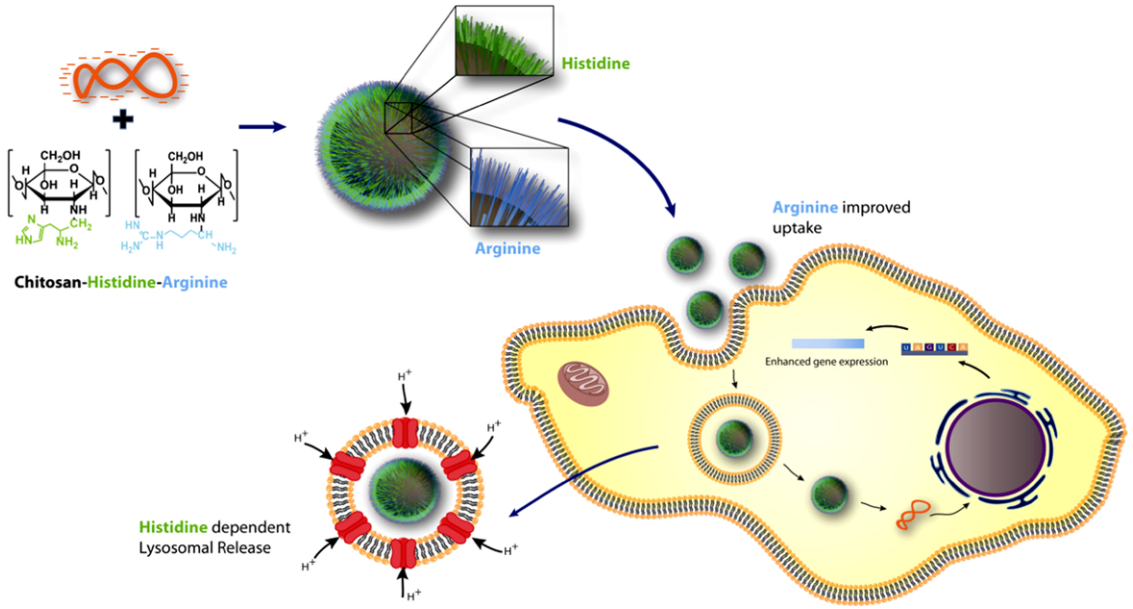

Figure 1. Illustration of the dual bioconjugation of histidine and arginine amino acid residues onto the chitosan polymeric backbone. Nanoparticle synthesis and improved biological activity of the self-assembled nanoparticles and their intracellular trafficking is also depicted.

due to their underlying nucleic acid condensing capacity, via mild electrostatic interactions [54]. Amongst these, chitosan emerges as a nanocarrier of exceptional interest since it possesses a set of valuable characteristics, such as low immunogenicity, biocompatibility and most importantly, highly positive surface charge density [32]. In fact, this intrinsic attribute assumes additional importance upon DNA complexation, since the immediately assembled polyplex nanoparticles promptly safeguard the genetic information by sterically blocking the deleterious activity of endogenous nucleases [7]. However, once the nanoparticulate carriers are loaded with the biopharmaceutical of interest, they face several extracellular and intracellular barriers that severely hinder transport and translocation to the nucleus, where gene expression will ultimately occur [39]. Indeed, these barriers assume further importance since they are the major cause for the relative inability of non-viral delivery systems to achieve sustainable and therapeutically relevant transgene expression levels [39, 4]. Therefore, it becomes clear that polyplex-based delivery systems must also possess the ability to promote cellular internalization, as well as the capacity to mediate critical downstream intracellular trafficking events, which include the escape from lysosomal pathways [58], microtubule-associated transport across the cytoplasm [41], and shuttling onto the nucleus [24]. Understanding and addressing these issues and limitations is a critical requirement for devising rational biocompatible nanomaterials that improve the therapeutic potential of nanomedicine-based approaches.

From this standpoint, the recently reported conjugation of functional and bioinspired ligands, such as cell penetrating peptides and amino acid moieties, in the surface of polyplex nanocarriers emerges as a particularly advantageous and efficient strategy to improve cellular uptake [7, 20]. Indeed, short peptide residues, such as the human immunodeficiency virus (HIV)-1 TAT sequence (48–60), are able to cross the cellular membrane by mediating interactions with cell-surface negative proteoglycans such as heparan sulfate or sialic acid, and subsequently achieve internalization of anti-tumoral drugs [53] and pDNA biopharmaceuticals [18, 20]. It is important to point out that this cell penetrating capacity mainly relies on the existence of arginine-rich sequences [33]. Interestingly, it has been demonstrated that the conjugation of arginine amino acid residues, surface grafted to nanocarriers, is enough to promote their cellular uptake [3, 18, 21]. The cellular uptake mechanism of these carriers is also a parameter that assumes a critical role since, as mentioned above, these events ultimately influence gene expression efficiency and consequently the overall therapeutic effect [61].

However, apart from internalization, nanocarrier efficiency may be affected due to particle entrapment and degradation in the lysosomal compartments, to which they are initially guided [25, 3]. Regarding this fact, several reports have proved that lysosomal escape is sharply increased as a function of the inherent buffering capacity of the delivery system [36, 7]. For this purpose the inclusion of another amino acid moiety, namely histidine, has proved itself as a remarkably beneficial alternative. In fact, imprinting histidine on the surface of nanomaterials maintains their biocompatibility, and also enhances their buffering capacity in the pH range of lysosomes (pH 6–5) [35]. The latter is a critical parameter since it influences the transfection efficiency of these gene delivery systems [7, 50]. Recently, our group has developed a chitosan-based delivery system that had the capacity to load pDNA upon crosslinking with an anionic counterion [14]. However, by using water soluble chitosan and grafting novel biofunctional moieties this system can be further improved to achieve higher transfection efficiency.

Taking this into account, as schematized in figure 1, herein we devised a novel sequential approach to conjugate

both pH-responsive histidine moieties and cell penetrating arginine residues, onto the chitosan polymeric backbone as a strategy to efficiently overcome key cellular barriers and maximize its inherent potential as a non-viral gene delivery system of reference when therapeutic applications are envisioned.

2. Materials and methods

2.1. Materials

Ultrapure chitosan hydrochloride (CH) (Protasan UP CL 113, MW ≈ 110 kDa, deacetylation degree of 83%) was obtained from Novamatrix (Sandvika, Norway). L-histidine, L-arginine, fluorescein isothiocyanate isomer I (FITC), rhodamine B isothiocyanate (RITC), 2-nitrophenyl β-D-galactopyranoside (ONPG), *N*-hydroxysuccinimide (NHS), *N*-(3-dimethylaminopropyl)-*N*′-ethylcarbodiimide hydrochloride (EDC), *N*,*N*,*N*′,*N*′-tetramethylethylenediamine (TEMED) and cell culture Dulbecco's modified Eagle's medium—high glucose (DMEM) were purchased from Sigma-Aldrich (St Louis, MO, USA). 3-(4,5-dimethylthiazol-2-yl)-5-(3-carboxymethoxyphenyl)-2-(4-sulfophenyl)-2H-tetrazolium (MTS) was obtained from Promega (Madison, WI, USA). HeLa (Human negroid cervix epithelioid carcinoma—CCL-2) cells were purchased from ATCC (Middlesex, UK). The 6.05 kbp pVAX1-LacZ plasmid encoding for β-galactosidase, Hoescht 33342®, Backman Cell Light 2.0®, LysoTracker® Red DND-99, and transfection reagents including Opti-MEM® and Lipofectamine 2000® were obtained from Invitrogen (Carlsbad, CA, USA). All other reagents were used as received.

2.2. Methods

2.2.1. Synthesis of chitosan-histidine-arginine. Amino acid coupling of both L-histidine and L-arginine residues onto pharmaceutical grade chitosan (dry matter content: 96.1%; endotoxin levels: <53 EU g^{-1}; protein content: 0.09%) was performed in a two-step reaction by amidation of the primary amine groups present in chitosan glucosamine (GlcN) monomers using EDC/NHS as coupling agents, as described by Liu *et al*, 2010, with slight modifications [26]. Briefly, chitosan was dissolved in 10 mM TEMED/HCL buffer (pH 6.0) to a final concentration of 1% (w/v) at room temperature (approximately 24 °C). Subsequently, NHS was dissolved in TEMED/HCL buffer, (0.55 mol mol^{-1} EDC) and added to the chitosan solution under intense magnetic stirring. EDC was also dissolved in 10 mM TEMED/HCL buffer (1.5 mol mol^{-1} L-Histidine) and added to the reaction. L-Histidine dissolved in 10 ml of buffer (0.7 mol mol^{-1} GlcN) was then incorporated into the mixture and the coupling reaction proceeded for 24 h. To remove traces of unreacted components the CH–H conjugate was dialyzed for five days against deionized water with daily changes of the dialysant. The purified CH–H polymer was recovered by freeze-drying (Scanvac CoolSafe™, ScanLaf A/S, Lynge, Denmark) for 24 h. The chitosan-H modified polymer backbone was then functionalized with L-arginine (0.7 mol mol^{-1} GlcN), as aforementioned. After the two-step coupling reaction the multifunctional polymer, CH–H–R, was stored in an inert atmosphere.

2.2.2. Characterization of amino acid grafted chitosan. The grafting of amino acid residues onto the chitosan backbone was analyzed by 1D and 2D proton nuclear magnetic resonance (^{1}H NMR) spectroscopy in a Brüker Avance III 400 MHz spectrometer (Brüker Scientific Inc., NY, USA). Prior to acquisition, the different polymer-amino acid conjugates were dissolved in 1 ml of 9:1 (v/v) H_2O/D_2O (pH 5.88). The ^{1}H 1D homonuclear spectra were collected using pre-saturation for water suppression, at 298 K, with a spectral width of 10.00 kHz. Spectra were processed with an exponential window function with 3 Hz of line broadening Regarding the 2D TOCSY homonuclear experiments, the spectra were collected in phase sensitive mode with different spin-lock times (40–100 ms), with gradient-based excitation sculpting (W5) for water elimination, and a spectral width of 10.00 kHz both in t_1 and t_2. 1024 data points were acquired in F2 and 256 increments were used in F1. The data was processed with 8192 by 4096 data points in both dimensions using a QSINE window function. All data were processed with the software TOPSPIN 3.0. Additionally, the amino acid coupling was also accessed by Fourier transform infrared spectroscopy (FTIR). The infrared spectra were recorded in a Nicolet iS10 spectrometer (Thermo Scientific Inc., MA, USA) by acquisition of 256 interferograms with a 4 cm^{-1} spectral resolution. The determination of the substitution degree of the polymer backbone was performed by FTIR spectroscopy, as previously reported in the literature [36].

2.2.3. Potentiometric titration. To address the proton buffering capacity of the functionalized CH–H and CH–H–R, the polymers were dissolved to a final concentration of 0.1 M, as reported by Chang and co-workers [6]. In addition, the buffering capacity of the different ratios of CH–H was also addressed. The titration was performed with the addition of 5 μl aliquots of 0.1 M NaOH and continuously monitored in a Metrohm 827 pH-meter (Metrohm, Titrino, Switzerland).

2.2.4. Formulation of nanoparticles. For the synthesis of functionalized nanoparticles, CH–H–R was dissolved in 5 mM sodium acetate buffer (pH 4.5) to a concentration of 10 mg ml^{-1} and was used as a stock solution. The pVAX1-LacZ plasmid was amplified in a bacterial culture of *Escherichia coli* (*E. coli*) DH5α cells and the pMC.CMV-MCS-EF1-GFP was amplified in *E-coli* ZYCY10P3S2T strain. Both plasmids were recovered by alkaline lysis and purified with the Qiagen Plasmid Maxi Kit as formerly reported [15]. The pDNA stock solution was prepared in 5 mM sodium acetate buffer (pH 4.5) with a concentration of 800 μg ml^{-1}. Amino acid-coupled nanoparticles were formulated at different molar ratios of amine/phosphate groups. As a nomenclature amine/phosphate ratios (N:P ratios) represent the amine groups present in chitosan and phosphate groups present in the pDNA biomolecules. The

calculation of the different charge ratios was carried with a MATLAB programmed routine (Prentice-Hall, Inc, NJ, USA), where an average mass per charge of 330 Da for pDNA was used for the computation of the ratios tested. The nanoparticles were prepared by adding pDNA (10 μg ml^{-1}) to the polymer solution (diluted at an appropriate concentration) at a 1:4 (v/v) ratio. The solution was then vigorously mixed for 1 min using a vortex. Afterwards, the complexes were allowed to stabilize for 30 min and recovered by centrifugation at 18 000 g for 30 min at 4 °C.

2.2.5. Electrophoretic mobility shift assay (EMSA) and enzymatic protection. The electrophoretic mobility profile of pDNA was accessed by agarose electrophoresis using a 1% agarose gel stained with ethidium bromide (0.5 μg ml^{-1}). Electrophoresis was run at 100 V for 45 min in Tris-Acetate-EDTA (TAE) buffer. The extent of enzymatic degradation mediated by serum nucleases was analyzed by incubation of the nanoparticles in a cell culture medium containing 10% fetal bovine serum (FBS), at 37 °C, for 4 h.

To address degradation mediated by DNases, nanoparticles were incubated with DNAse I (2 U μl^{-1}, in 5 mM $MgCl_2$, pH 7.4) for 30 min at 37 °C. After the incubation period, the reaction was stopped with 10 mM EDTA, and analyzed by gel electrophoresis. In addition, pDNA degradation was also quantitatively determined by UV–vis analysis. The experiments were carried out by constantly recording absorbance values ($\lambda = 260$ nm), at 37 °C, for 30 min in a Shimadzu-1700 spectrophotometer (Shimadzu Inc, Japan). Throughout the assay, the temperature oscillation was monitored with a laser thermometer (registered variation of ±0.2 °C).

2.2.6. Nanoparticle physicochemical characterization. For size characterization, nanoparticle samples were stabilized after synthesis for 30 min and immediately analyzed. The hydrodynamic radius was determined by dynamic light scattering (DLS) on a Zetasizer Nano Zs instrument (Malvern Instruments, Worcestershire, UK), at 25 °C, with detection of backscattered light at a 173° angle, in order to minimize dust contamination. The collected particle diffusion coefficients were converted to average size with the Stokes–Einstein model, by using Cumulant analysis and the non-negative least squares algorithm (NNLS). For zeta (ζ) potential experiments, nanoparticle samples were prepared as described above. The experiments were performed on a zeta dip cell, with the acquisition of 100 measurements for each sample. Zeta potential was then automatically calculated with the Smoluchowski equation for aqueous suspensions in the Zetasizer software (v 6.2).

Nanoparticle morphology was analyzed by scanning electron microscopy (SEM). Briefly, one drop of 0.1% (w/v) phosphotungstic acid (PTA) stained nanoparticles was dispersed in a cover glass and subsequently dried overnight at 37 °C. Prior to image acquisition, the samples were mounted on aluminum stubs and sputter coated with gold. Nanoparticle samples were then examined on a Hitachi S-2700 (Tokyo, Japan) electron microscope at an accelerating voltage of 20 kV with different magnifications and acquisition modes.

2.2.7. Cell culture. HeLa cells were seeded in 25 cm^2 T-flasks, grown in DMEM medium, supplemented with 10% (v/v) fetal bovine serum (FBS), and 1% antibiotics/antimicotics at 37 °C, in an incubator with a humidified atmosphere containing 5% CO_2.

2.2.8. Cytotoxicity assays. The cellular cytotoxicity of the synthesized biofunctional CH–H–R polymer, as well as the pDNA loaded nanoparticles, was addressed by the MTS assay. In brief, 24 h prior to the experiments HeLa cells were seeded at a density of 1×10^4 cells/well into 96-well flat bottom culture plates with 150 μl of DMEM-10% FBS. The following day, cell culture medium was removed and replaced by fresh medium. The cells were then immediately incubated with different concentrations of the synthesized polymer (diluted in DMEM-10% FBS). Additionally, HeLa cells were also incubated with pDNA loaded CH–H–R nanoparticles (pDNA concentration—2.5 μg cm^{-2}) for 4 h in antibiotic free medium, afterwards the medium was exchanged to DMEM-10% FBS with antibiotics. Both experiments were performed at 24 and 48 h, as previously described by our group [15]. Afterwards, the medium was exchanged and a mixture of MTS/phenazine metasulfate (PMS) was added to each well. Incubation with MTS reagent proceeded for 4 h according to the manufacturer instructions. Following incubation, the absorbance measurements of the soluble brown formazan produced were performed in a microplate reader (Sanofi, Diagnostics Pauster) at 492 nm. A total of five replicates were performed. Cells incubated with absolute ethanol were used as positive control for cytotoxicity.

2.2.9. Flow cytometry analysis of nanoparticle cellular uptake. Characterization of the nanoparticle uptake was performed by flow cytometry. For uptake experiments, culture plates ($\varnothing = 35$ mm) were seeded with 8×10^5 cells and grown for 24 h in DMEM-10% FBS. CH–H–R nanoparticles were prepared with freshly labeled FITC-pDNA (1 μg cm^{-2}) (see supplementary information for details available at stacks.iop.org/Nano/24/275101/mmedia) and resuspended in culture medium without antibiotics immediately before their addition to the plate. The particles were allowed to interact with cells for 4 h and removed soon afterwards by rinsing twice with ice cold PBS. The cells were then harvested with 0.18% trypsin—5 mM EDTA, pelleted and resuspended in 300 μl of PBS for flow cytometry. Sample analysis was performed on a BD FACSCalibur flow cytometer equipped with 488 and 633 nm lasers. Data collection was accomplished in the CellQuest^{TM} Pro software, where the fluorescent signals of 1×10^4 events present in the region of interest (ROI) were recorded with the FL-1 (530/30) band pass filter. Flow cytometry data was analyzed in FlowJo software (Treestar, Inc., CA, USA) and is presented as mean fluorescence intensity (MFI).

2.2.10. In vitro transfection. Transfection experiments were performed at a pDNA concentration of 1 μg cm^{-2} unless otherwise stated. For these experiments HeLa cells

were cultured in 96-well black/clear bottom plates (Greiner Bio-One, Frickenhausen,Germany) at a density of 1×10^4 cells/well in DMEM containing 10% FBS and incubated for 24 h. At the time of transfection, CH–H–R/pDNA nanoparticles were added to each well and incubated for 4 h. After that period, the cells were washed with PBS and the medium exchanged to DMEM-F12—10% FBS with antibiotics. The expression of the GFP reporter gene was analyzed 24 h after transfection by confocal microscopy, and by using a plate reader spectrofluorimeter (Spectramax Gemini XS, Molecular Devices, California, USA) using the 9-point well scanning method and high PMT sensitivity. The acquired data was processed by using the SOFTmax PRO Software. LP 2000 was used as a reference delivery system in all transfection assays. Transfection with this cationic liposome-based formulation was carried out according to the manufacturer's instructions.

2.2.11. Confocal microscopy and intracellular trafficking. The visualization of cellular uptake, intracellular trafficking of nanoparticles, and GFP expression was addressed by confocal laser scanning microscopy (CLSM). Prior to experiments μ-Slide 8 well Ibidi chamber coverslips (Ibidi GmbH, Germany) were coated with 0.01 mg ml^{-1} collagen in PBS for 30 min. Following the coating procedure, confluent cell monolayers were trypsinized and seeded in each well at a density of 2×10^4 cells/well, 40 h before visualization. For imaging experiments, pDNA was labeled with two distinct fluorochromes, namely FITC and RITC (see supplementary information for details available at stacks.iop.org/Nano/24/275101/mmedia), in order to avoid crosstalk between green channels. Imaging of nanoparticle uptake was initially performed by transfecting cells with a Backman Cell Light 2.0® Actin-GFP probe, 16 h prior to acquisition, according to the manufacturer protocol. The cells were afterwards incubated with nanoparticles bearing RITC-labeled pDNA and these were removed after 4 h by rinsing twice with PBS. Cells were then fixed with 4% paraformaldehyde in PBS and the cell nucleus stained with Hoechst 33342®. In addition, the intracellular distribution of pDNA was also analyzed 24 h after incubation with FITC-pDNA loaded nanoparticles. Thirty minutes prior to imaging, the late lysosomal compartments were stained with LysoTracker® Red DND-99 dye (50 nM). After incubation, cells were rinsed ten times with PBS, fixed, and stained with Hoechst nuclear probe, as outlined above. For GFP expression visualization 2×10^4 cells were seeded in μ-Slide 8 well Ibidi chamber coverslips and transfected, as reported in section 2.2.10. All GFP data was acquired with constant laser power and PMT gain in order to avoid fluorescence artifacts. Imaging was performed with a Zeiss LSM 710 laser scanning confocal microscope (Carl Zeiss SMT Inc., USA) equipped with a Plan-Apochromat 63x/NA 1.4 DIC II, oil objective. All images were acquired with proper sampling in order to comply with the Nyquist–Shannon criteria to minimize image aliasing. For all experiments the images were collected in Z-stack mode, with the optimal slice interval determined by the Abbe/Rayleigh diffraction limit, in the LSM 710 software, where subsequent 3D reconstruction and maximum intensity projections were processed. 3D reconstructions were also performed using Imaris software (trial version 5.5, Bitplane, Switzerland). For quantitative multicolor colocalization analysis all the acquired images were initially segmented by deconvolution in order improve the signal-to-noise ratio (SNR) (ImageJ software [42]). Colocalization was then executed also in ImageJ, with the Costes *et al* 2004, automatic threshold approach for Mander's colocalization coefficients [11].

2.2.12. Statistics. Comparison between multiple groups was determined using one-way analysis of variance (ANOVA), with the Student–Newman–Keuls test. A value of $p < 0.05$ was deemed statistically significant. All the calculations were performed on OriginPro 8.1 trial software (OriginLab corporation, MA, USA).

3. Results and discussion

3.1. Characteristics of amino acid functionalized chitosan

The synthesis of amino acid functionalized chitosan comprised the bioconjugation of histidine moieties on the polymer backbone, and subsequent coupling with arginine residues (figure 2(A)). The chemical coupling of both amino acid monomers to chitosan was confirmed by proton nuclear magnetic resonance (^{1}H NMR) (figure 2), and Fourier transform infrared spectroscopy (see supplementary information figure S1 available at stacks.iop.org/Nano/24/275101/mmedia).

The ^{1}H NMR spectra of the CH–H conjugate reveal the presence of additional peaks with the characteristic chemical shifts of the C-2 and C-4 protons of the histidine imidazole ring ($\delta = 7.5$ ppm and $\delta = 8.48$ ppm, respectively), indicating its successful coordination to the polymeric backbone (figure 2(C); 1, 2). Regarding arginine conjugation our results demonstrate that these moieties are indeed linked to the polymeric chain, as illustrated by the resonance peak assigned to NH protons of the amine coupling ($\delta = 8.13$ ppm) (figure 2(D), number 3), suggesting that regardless of the different structure of the chosen amino acids, both can be bound to the polymeric chain.

With respect to the dual grafting methodology, the existence of distinctive imidazole and guanidine associated resonance peaks reveals the successful double functionalization of chitosan (CH–H–R) (figure 2(E); 1, 2, 3). Aside from this, a complementary analysis of 2D homonuclear total correlation spectra (2D TOCSY) provided analysis of the structural stability of the immobilized molecules, since each individual amino acid has a unique pattern of resonances. The results showed the existence of cross-peaks at $\delta = 7.14/3.18$ ppm and $\delta = 7.14/1.78$ ppm, which were assigned to the correlation of εNH with δH and βH protons of arginine (figure 2(F); number 5 and 6). Furthermore, the fingerprint signals of the imidazole functional group were also identified by the cross-peak at $\delta = 7.5/8.48$ ppm

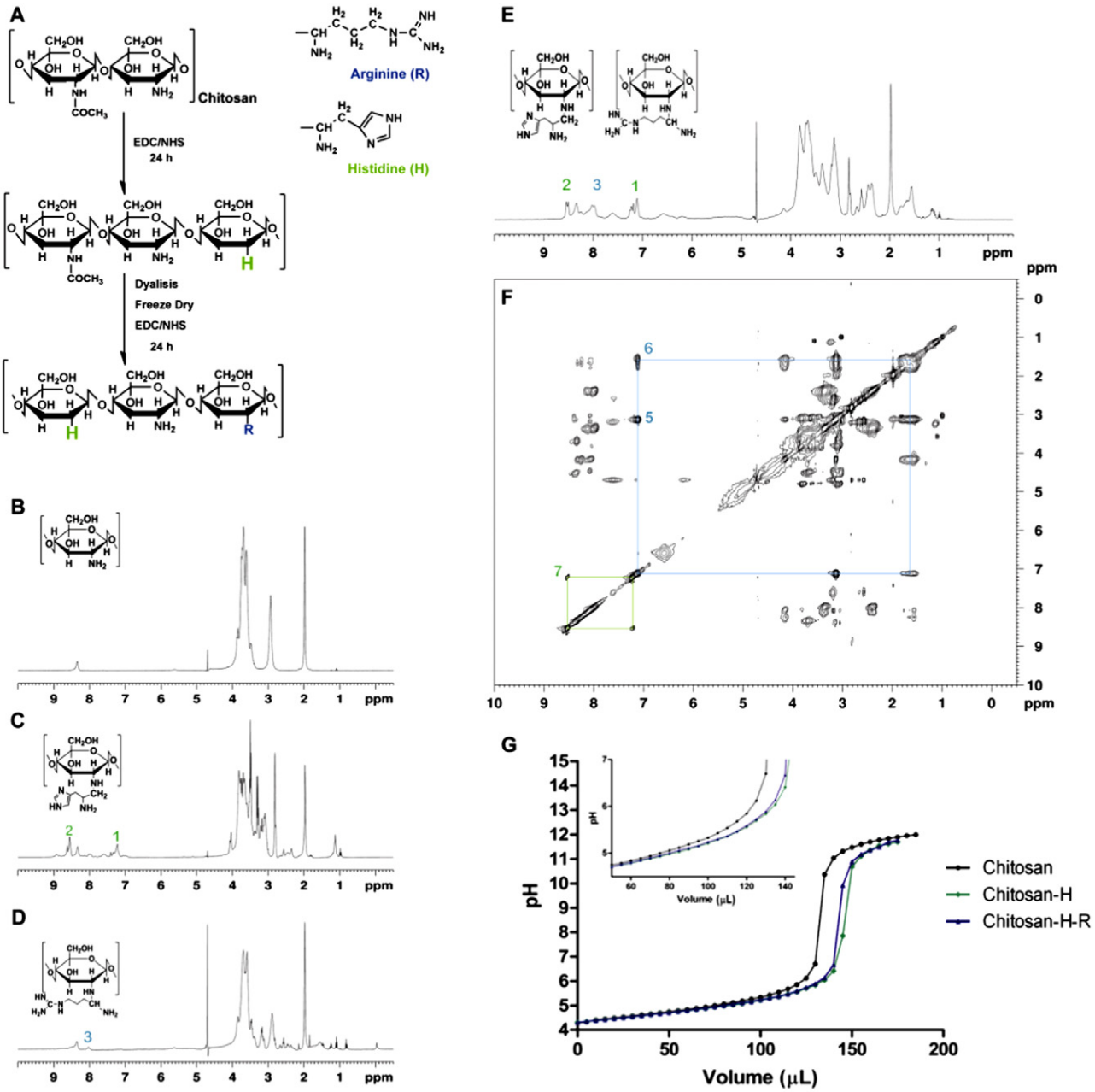

Figure 2. Amino acid bioconjugation and characterization. (A) Schematics of the two-step sequential chemical conjugation of histidine and arginine into the chitosan backbone. (B)–(E) ^{1}H 1D NMR spectra of chitosan hydrochloride, CH–H, CH–R, and CH–H–R, respectively. (F) 2D TOCSY NMR spectra of CH–H–R. The green and blue bounding boxes indicate the cross-peaks within the spin systems of histidine and arginine, respectively. (G) Buffering capacity plot of CH–H (green), CH–H–R (blue) and unmodified chitosan (black). The numbers presented in the NMR spectra are assigned to characteristic resonance peaks of the amino acids.

(figure 2(F); number 7). All the 2D TOCSY assignments were performed according to the amino acid spin systems reported in the literature [44, 60]. Assuming the latter, it becomes relevant to address if the buffering capacity of the novel CH–H–R polymer was increased. As the pH titration results in figure 2(G) depict, functionalization increases the buffering capacity in the pH range of lysosomal compartments, a valuable characteristic that influences the release of nanoparticulated systems from deleterious intracellular pathways [36].

3.2. Synthesis and physicochemical properties of functional nanoparticles

Polyplex nanoparticles were synthesized by promoting a highly attractive electrostatic interaction between the positively charged CH–H–R backbone and the negatively charged pDNA molecules. The CH–H–R ability to complex pDNA was screened as a function of the molar ratio of amines in unmodified chitosan to pDNA phosphate residues (N:P ratio). Our results demonstrated that at an N:P ratio of 5, pDNA was completely entrapped in

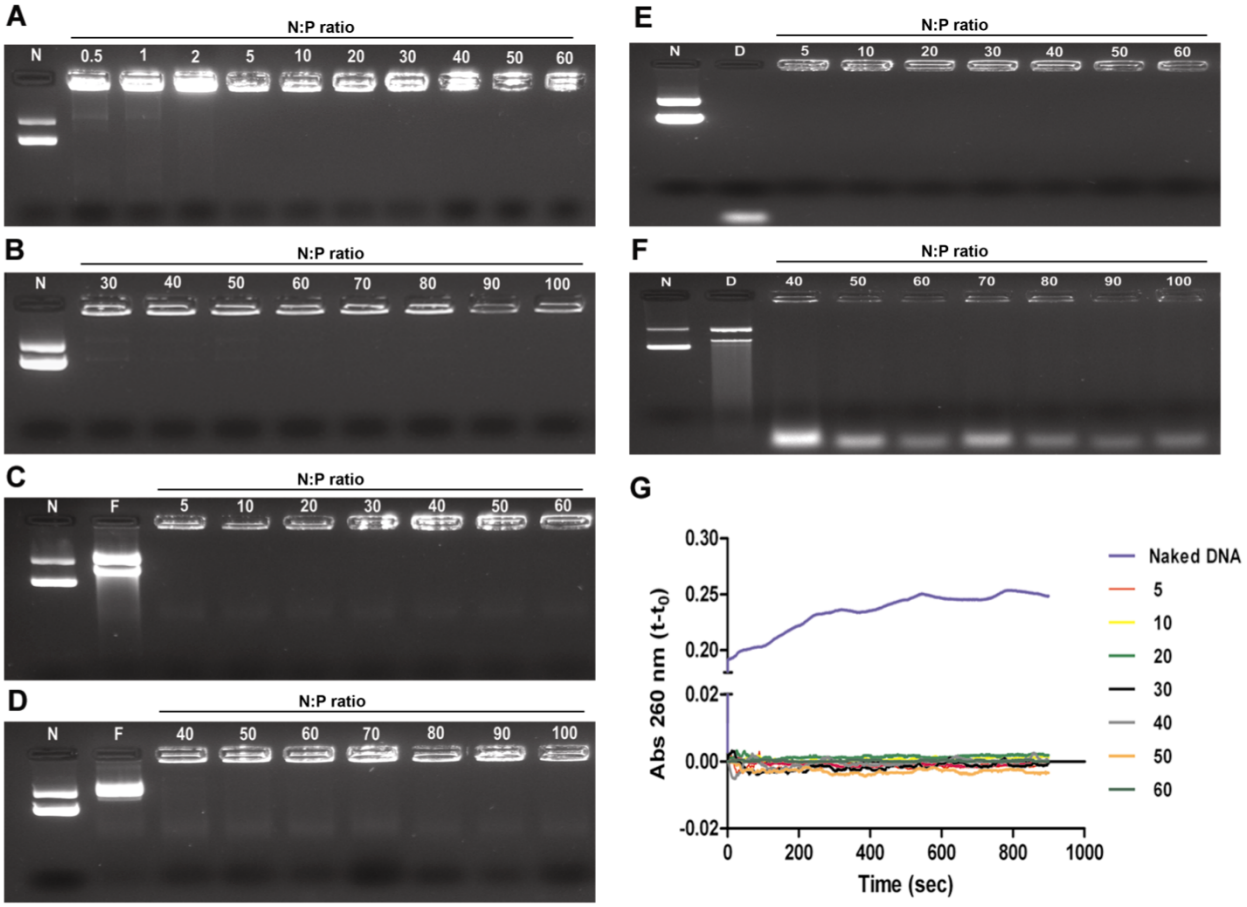

Figure 3. Electrophoretic mobility shift assay and serum stability. Agarose gel electrophoresis of: (A) and (B) pDNA complexation by CH–H–R and unmodified chitosan, respectively. Lane N—Naked pDNA. (C) and (D) Nanoparticles in DMEM—10% FBS for 4 h. Numbered lanes represent the different N:P ratios tested. Lane F—Naked DNA incubated in serum-containing medium. (E) and (F) Functionalized and unfunctionalized chitosan nanoparticles incubated with DNase I. Lane D—Naked DNA incubated with DNAse I. (G) Variation of pDNA absorbance at 260 nm during incubation with DNase I, for 30 min (pH 7.4, 37 °C).

the polymer, a fact supported by a major retardation in the electrophoretic migration of pDNA (figure 3(A)). Whereas, at the same ratio the unmodified polymer was unable to fully condense the DNA molecule (supplementary information figure S2 available at stacks.iop.org/Nano/24/275101/mmedia), and only at a N:P ratio of 60 did a significantly dominant electrostatic interaction that affected pDNA gel electrophoretic mobility occur with no pDNA bands appearing (figure 3(B)).

These findings illustrate that functionalization also provides significant improvement regarding the encapsulation of pDNA. Actually, these enhanced interactions are expected to be a consequence of privileged amino acid–nucleic acid pairing [29], in addition to the polymer-pDNA pre-existing complexation. The capacity of the CH–H–R nanoparticles to protect the condensed pDNA biopharmaceuticals from competing negatively charged proteins, such as gamma-globulin or transferrin [38], and from nuclease mediated degradation was confirmed by nanoparticle incubation in serum. Our results showed that all the biofunctional nanoparticles maintained their retardation profile, implying their capacity to upkeep encapsulation of the genetic material, whilst protecting it from nucleases present in serum-supplemented culture medium [49] (figure 3(C)). The latter is an essential attribute, since nanoparticles must resist the capacity of serum nucleases to rapidly degrade naked DNA (pDNA $t_{1/2}$—0.15–21 min [40]). In addition, also chitosan nanoparticles were able to maintain condensation at all ratios (figure 3(D)). Moreover, to ensure that nanoparticles can indeed safeguard the encapsulated genetic material they were also incubated with a specific nuclease that possesses high affinity for DNA (DNase I). The electrophoretic profile obtained confirms that the genetic material is well shielded in the biofunctionalized CH–H–R nanoparticles (figure 3(E)). In contrast, for chitosan-DNA a clear degradation band was observed (figure 3(F)). These results corroborate the ability of CH–H–R to preserve pDNA structure, suggesting that the inclusion of the amino acid blocks is also advantageous for pDNA protection [46]. An additional quantitative assay based on the hyperchromicity of pDNA [34] was performed to further address DNA protection [36]. As demonstrated in figure 3(G), the absorbance values of naked DNA undergo an immediate increase after incubation, indicating that nucleic acid cleavage has occurred. In contrast, all formulations of CH–H–R maintain DNA structure. Following this preliminary screening, the amino acid bearing nanodevices were also

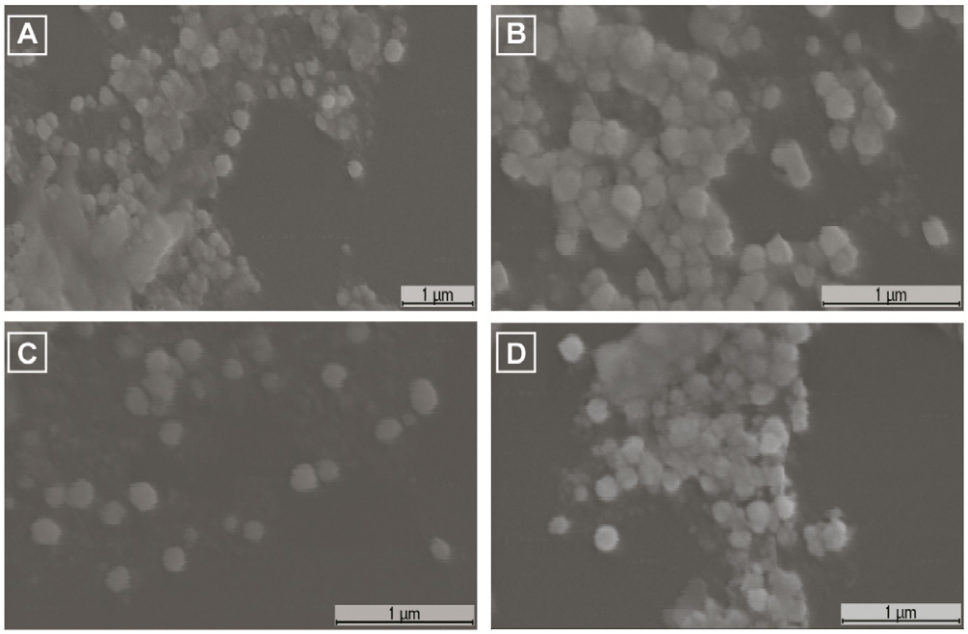

Figure 4. Scanning electron microscopy images of nanoparticles. (A) Unmodified chitosan nanoparticles (N:P 60). (B)–(D), CH–H–R nanoparticles synthesized at different molar ratios of N:P 40; 50 and 60, respectively. (E) Forty-five degree angle image of amino acid bearing chitosan nanoparticles (N:P 60).

Table 1. Physicochemical characterization of the nanoparticles formulated with unmodified chitosan or its amino acid functionalized derivate.

	N:P ratio	Average size (nm)	PDI	Zeta potential (mV)
CH	60	178.5	0.336	$+35.9 \pm 6.31$
	70	275.4	0.287	$+26.7 \pm 6.57$
	80	212.1	0.243	$+39.0 \pm 4.86$
CH–H–R	40	110.5	0.555	$+24.1 \pm 9.5$
	50	105.7	0.244	$+33.7 \pm 4.85$
	60	119.2	0.300	$+37.4 \pm 8.22$

characterized in terms of their ability to form stable colloidal nanoparticles with appropriate physicochemical characteristics for delivery applications. Our results showed that, nanoparticles synthesized either with chitosan (N:P 60) or CH–H–R form stable particles at specific ratios (N:P 40 to 60), and also possess spherical-like morphologies (figures 4(A)–(D)). At these formulation conditions, total complexation of the pDNA biomolecules occurs (∼100% pDNA entrapment as measured by UV–vis spectroscopy, data not shown). In addition, zeta potential also plays an important role in particle-membrane affinity interactions [38], and in the internalization of the delivery system [37].

At the nano-bio interface, internalization is mainly driven by electrostatic forces involving negatively charged proteoglycans and positively charged nanoparticles [37, 38]. Our results showed that all formulations have positive zeta (ζ) potential values within the range of colloidal stability ($\zeta > 24$ mV) (table 1). Moreover, a tendency for an increase in surface charge dependent on the N:P ratio was observed for the nanoparticles formulated with CH–H–R, whereas those synthesized only with chitosan presented variable results, a finding mainly attributed to the existence of free polymeric chains in solution (table 1).

These findings illustrate that the interaction between CH–H–R and the pDNA backbone is electrostatically and thermodynamically favored to a higher extent in comparison to the native material. This fact is also supported by the presence of unreacted chitosan after complexation, as depicted in figure 4(A). The occurrence of these privileged electrostatic interactions with the CH–H–R polymer arises due to the presence of amino acid moieties. In fact, as previously reported by our group, arginine [48] and histidine [47] can form extremely specific contacts with pDNA, to an extent that different plasmid topological conformations can be recognized. In the foundation of these pairing preferences are histidine-nucleobase T-shaped strong electrostatic interactions [10], and also arginine-induced hydrogen bonds, especially those formed with guanine bases [29, 8]. Interestingly, arginine plays a particularly significant role in the magnitude of pDNA loading because it also promotes the establishment of van der Waals forces with the DNA minor groove [18]. The increase in the cationic net charge of the CH–H–R polymer backbone must also be accounted, due to its ejection of monovalent counter-ions that surround DNA strands [13]. Overall, the remarkable interconnection between every single one of these dynamic

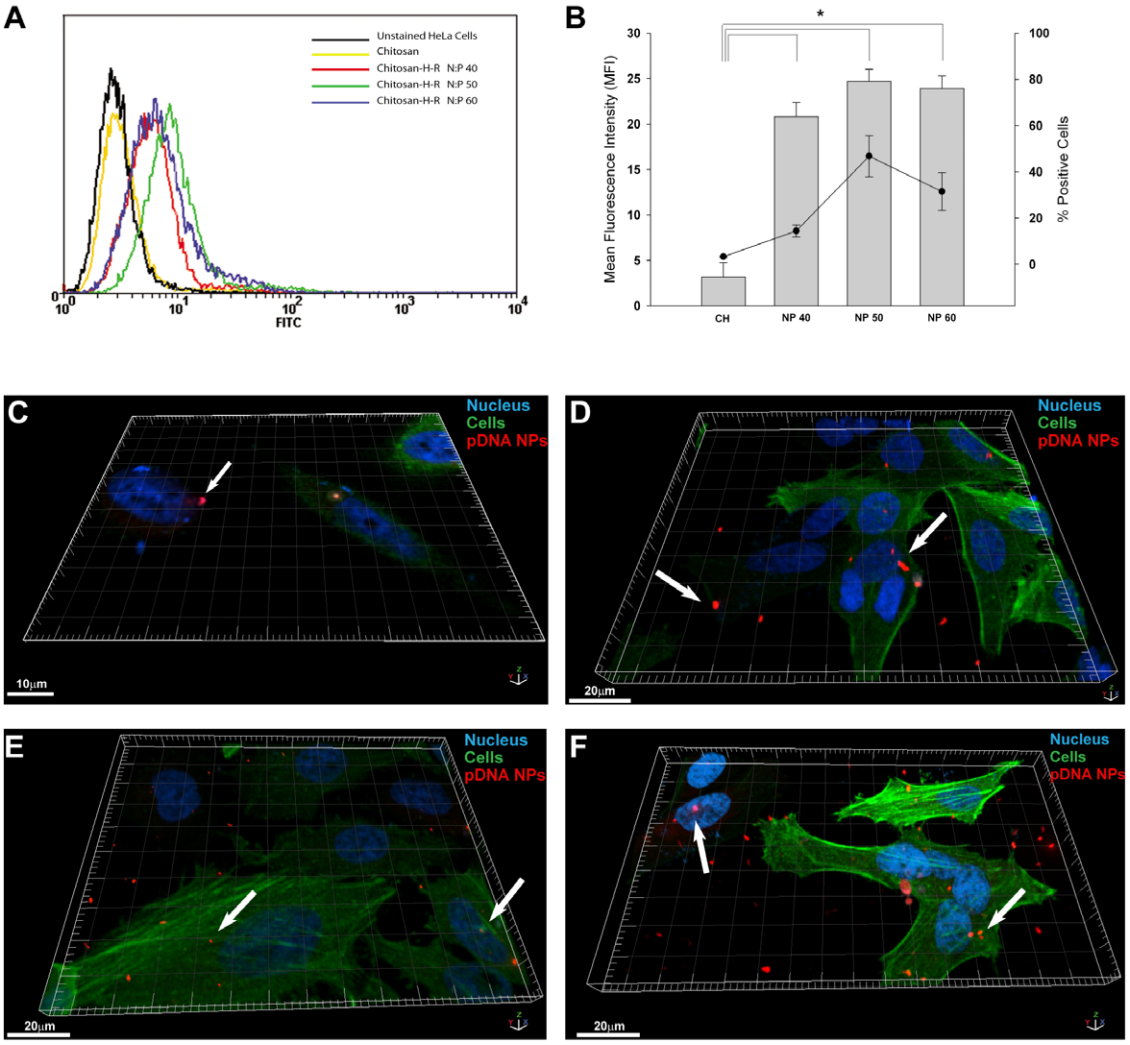

Figure 5. Nanoparticle cellular uptake. (A) Representative flow cytometry histograms of uptake. Black—negative control (unstained cells); yellow—unmodified chitosan nanoparticles (N:P 60); red—biofunctional CH–H–R nanoparticles (N:P 40); green—biofunctional CH–H–R nanoparticles (N:P 50); blue—biofunctional CH–H–R nanoparticles (N:P 60). (B) Quantification of the mean fluorescence intensity with the different nanoparticle formulations. CH—unmodified chitosan. Each bar represents the mean ± s.d. ($n = 3$), $*(p < 0.001)$. CLSM analysis of nanoparticle cellular uptake and localization. (C)–(F) 3D reconstruction of maximum intensity projections of cells transfected with chitosan nanoparticles (N:P 60) or biofunctional chitosan nanoparticles (N:P 40; 50; 60) respectively. Green channel—actin-GFP staining of the intracellular compartment; blue channel—nuclear staining with Hoescht 33342®; red channel—RITC labeled pDNA nanoparticles (indicated with white arrows).

interactions leads to higher cohesive forces and ultimately to the rearrangement into a densely packed nanoparticulated structure with a given size distribution [13].

Regarding nanoparticle size, our results demonstrated that chitosan nanoparticles increase in size above N:P 60, with the nanoparticles having sizes greater than 200 nm [13] (table 1). Remarkably, the size analysis of synthesized CH–H–R amino acid-nanoparticles supports the existence of the additional pDNA binding affinities and cross-interactions described above, since these nanocarriers possess smaller sizes in comparison with unmodified chitosan (table 1). Accordingly, Ho *et al* [18] recently reported a decrease in nanoparticle size when chitosan-DNA complexation was mediated alongside by arginine residues, a fact that was ascribed to a rearrangement of the DNA groove geometry in the denser complexes. Interestingly, the obtained results reveal that the novel CH–H–R nanoparticles have suitable sizes for the establishment of particle–cell interactions and, consequently, cell uptake [17, 52].

3.3. Nanoparticle-induced gene expression and intracellular trafficking

Taking the former into account, the actual capacity of the assembled functional nanomaterials to transpose extracellular barriers and achieve internalization was also investigated. Figure 5(A) shows that the nanoparticles bearing multifunctional moieties on their surface were internalized to a higher degree in comparison to the unmodified chitosan complexes. In fact, as demonstrated in figure 5(B), there is a significant difference in uptake between chitosan and CH–H–R formulations, suggesting that amino acid-based biofunctionalization is also beneficial at the cell entry stage.

Predominantly, the CH–H–R particles with larger N:P ratios (50 and 60) were to a certain extent more internalized than those formulated at a lower N:P ratio (figures 5(A) and (B)). This noteworthy event might be descriptive of some variability in particles that are formulated with the same polymeric material. Indeed, these findings must be addressed, taking into consideration the dynamic molecular interactions and forces such as Coulombic electrostatic and steric attractive van der Waals forces that are established in the cell-particle interface [38]. Therefore the larger effective positive surface charge obtained for particles with higher ratios accounts for their improved internalization capacity [38] (figure 5(A) and table 1). Regarding the single substituted formulations, these possess lower uptake in comparison with CH–H–R nanocarriers (CH–R—MFI 19.2; and CH–H—MFI 14.9, supplementary information, figure S6 available at stacks.iop.org/Nano/24/275101/mmedia).

The cell uptake capacity of CH–H–R is also emphasized by confocal microscopy (figures 5(C)–(F)), since the amount of fluorescently labeled pDNA that reaches the intracellular compartment is higher when the biofunctional CH–H–R particles are employed as delivery systems in detriment of their unmodified counterparts. An individual analysis of the different amino acid bearing carriers reveals that the particles formulated at N:P 40 are less prone to cellular uptake (figure 5(D)), whereas N:P 50 and 60 are extensively localized within their target cells (figures 5(E) and (F)). However, it should be emphasized that the results obtained for nanoparticle uptake may be affected by asynchronous malignant cell division, which may lead to different rates of particle internalization [22]. In fact, as recently described by Kim *et al* [22], cells with different cycle phases internalize nanoparticles with similar rates up to 24 h, but after this period nanocarrier uptake is influenced by the different cell cycle phases. Nevertheless, asynchronous cell division *in vitro* closely mimics the *in vivo* tumor microenvironment characterized by cell proliferation, and hence also provides important information for *in vivo* nanocarrier performance.

Once located within the intracellular compartment, CH–H–R nanoparticles are trafficked in the various cellular uptake routes, a fact that is clearly noticeable in figures 5(E) and (F), where their presence in the cytoplasm can be readily visualized (white arrows). These cell trafficking events play a critical role in the biological fate of novel CH–H–R carriers. Actually, it has been previously described that nanosized carriers containing arginine-rich sequences may translocate directly to the cell cytoplasm via energy-independent pathways, facilitating uptake [28]. Recently, chitosan-H and chitosan-R have been described to also enter into cells via energy-dependent routes such as endocytosis, either caveolin or clathrin-mediated [16, 43]. Therefore, lysosomal release may also assume a significant role in nanoparticle trafficking and biological processing [4, 23]. A buffering capacity study revealed that at higher ratios the buffering capacity is indeed improved (supplementary information figure S3 available at stacks.iop.org/Nano/24/275101/mmedia), corroborating the findings of intracellular trafficking analysis (figures 6(A), (C) and (E)) [31]. The latter results are further supported by other reports which demonstrated an increase in the buffering capacity of non-viral delivery systems upon conjugation with histidine moieties [7].

Lysosomal escape analysis by CLSM demonstrated CH–H–R N:P 40 nanoparticles were extensively localized in lysosomes (figure 6), whereas those with higher ratios were scarcely accumulated within these compartments (figures 6(C) and (E)). A direct visual comparison between the results obtained for the nanoparticulated systems N:P 50 and 60, suggests that the latter are less prone to lysosomal localization, therefore indicating a higher endosomolytic activity. In addition, colocalization histograms and their statistical analysis showed that the biofunctional nanoparticles formulated at N:P 60 had a greater ability to escape from these vesicles since they presented the lowest values of the Mander's overlap coefficient (figure 6(H), tM values). With respect to the single formulations, both CH–R N:P 40 (tM—0.172) and CH–H N:P 30 (tM—0.0749) nanoparticles had Mander's coefficients in the range of those found for N:P 50 and N:P 60, with nanoparticles being localized both in the cytoplasm and few in the lysosomal compartments, as shown in CLSM analysis (supplementary figure S8 available at stacks.iop.org/Nano/24/275101/mmedia). 3D reconstruction provided further insights regarding the differences observed for different ratios, with the CH–H–R N:P 60 revealing less colocalization (figures 6(C), (F) and (G)). During this release from lysosomal vesicles the pDNA remains enclosed in the polymer mesh due to the action of attractive electrostatic interactions promoted by the cationic nature of chitosan, arginine, and also histidine, which becomes positively charged in lysosomal compartments [9]. The nuclear localization of pDNA was also confirmed by 3D analysis, as shown in figures 7(A) and (B), emphasizing the capacity of this novel approach for therapeutic applications.

The cytotoxic profile of the CH–H–R polymer was determined to address its feasibility as a biomaterial for nanodevice formulation. As the results demonstrate, at 24 h the viability of the cells incubated with different concentrations of the functionalized polymer is similar to that obtained with unmodified chitosan (figure 8(A)). It should be highlighted that the usual concentration range of incubated polymer described in the literature has its maximum value at 100 μg ml^{-1} [45], herein we extended this value to 200 μg ml^{-1} and noticed that no impairment in cell proliferation was promoted, suggesting that the novel CH–H–R carriers are suitable for therapeutic applications (>96% viability) (figure 8(A)). In fact, the CH–H–R delivery system also possesses biocompatibility features comparable to those of other proficient nanocarriers formulated with biocompatible biomaterials, such as those comprised of silk-elastin conjugates, described by Xia *et al* [57].

In addition, the characterization of biocompatibility on an extended time scale was also performed, and results presented in figure 8(B) show, at 48 h, the cells remained viable and no significant difference between chitosan and its functional derivatives was found. This provides important additional characterization of the nanomaterial biocompatibility, since the metabolites of delivery systems are frequently overlooked

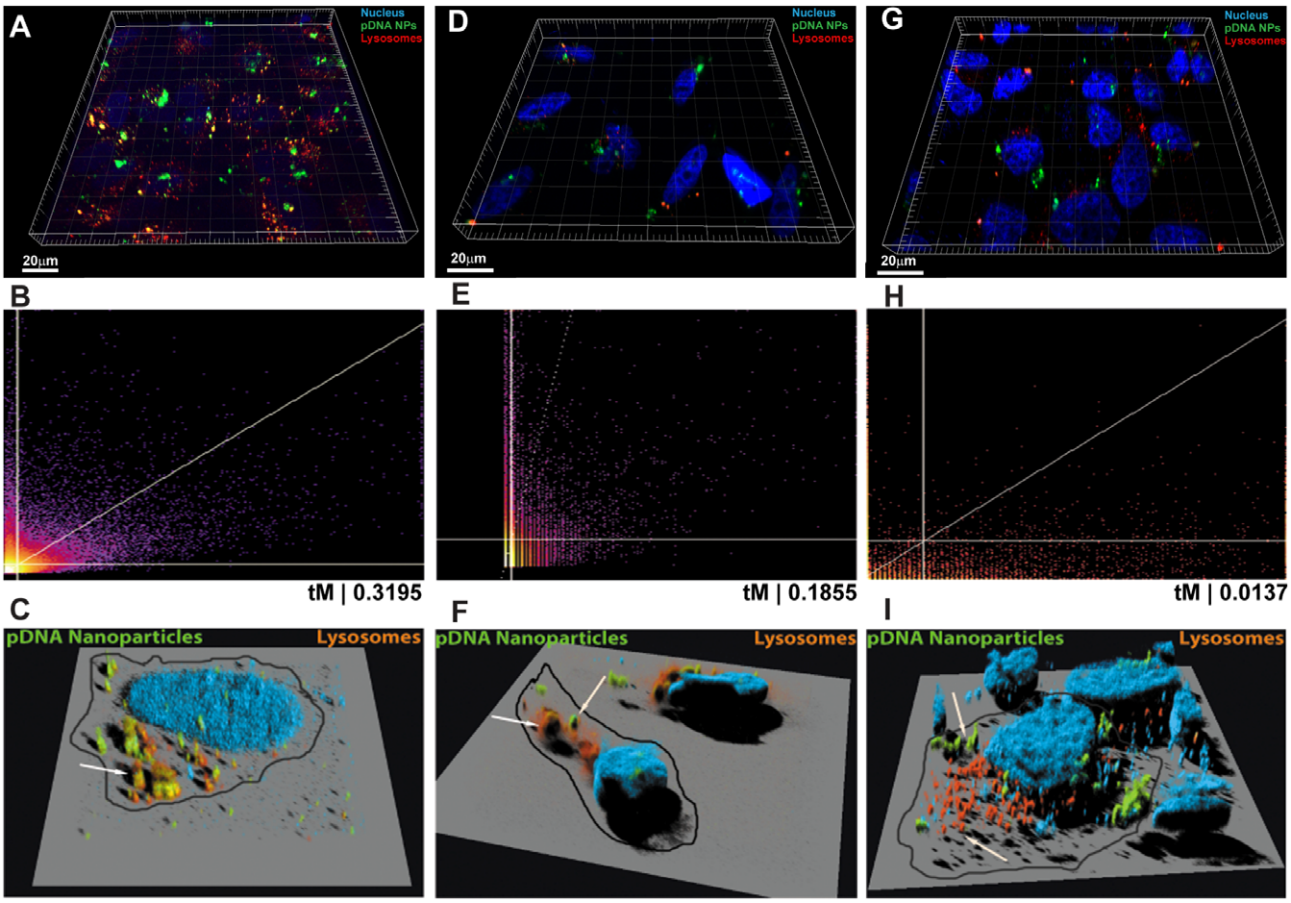

Figure 6. Intracellular trafficking and colocalization of biofunctionalized nanoparticles. (A), (D) and (G), Colocalization profiles of the different CH–H–R nanoparticles (N:P 40, 50 and 60, respectively) visualized by confocal laser scanning microscopy. Green channel—FITC-labeled pDNA; red channel—staining of the lysosomal compartments with LysoTracker® Red DND-99 dye; blue channel—nuclear staining with Hoescht 33342®. (B), (E), (H) Representative colocalization histograms of the biofunctional nanoparticles formulated at N:P 40; 50 and 60 respectively. The numerical analysis was performed with the Mander's colocalization coefficients (tM) automatically determined by a thresholding algorithm. (C), (F), (I) 3D SFP volume rendering of HeLa cells transfected with CH–H–R nanoparticles.

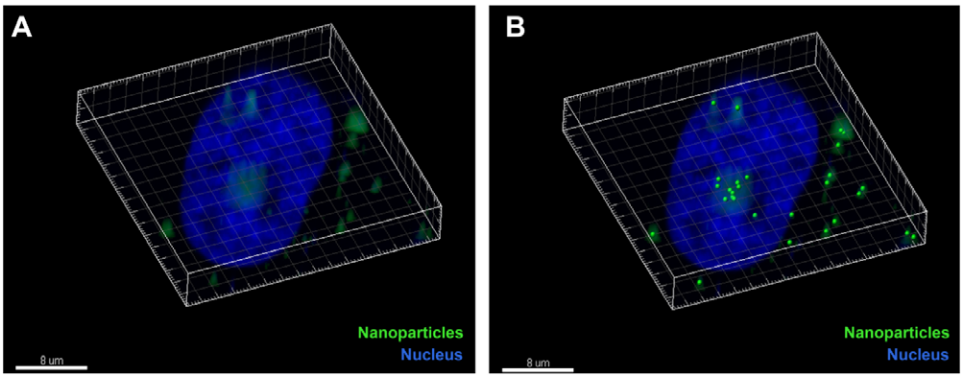

Figure 7. CLSM analysis of nuclear localization. (A) HeLa cell nucleus and cytoplasm transfected with CH–H–R N:P 60 nanoparticles. (B) Spot detection of labeled pDNA. Green channel—FITC-labeled pDNA; blue channel—nuclear staining with Hoechst 33342®.

after nanoparticle cell internalization. The biocompatibility of the functional particles with encapsulated pDNA biopharmaceuticals was also determined, and demonstrated in figure 8. CH–H–R nanoparticles can achieve higher biocompatibility than commercial formulations, even at high pDNA concentrations (2.5 μg cm^{-2}). At this pDNA concentration, the biofunctional nanoparticles accomplish high cell viability levels at 24 h, (figure 8(A)). Furthermore, during the time frame of the assay, an increase in cellular proliferation can be observed at 48 h (≈90%) for the CH–H–R

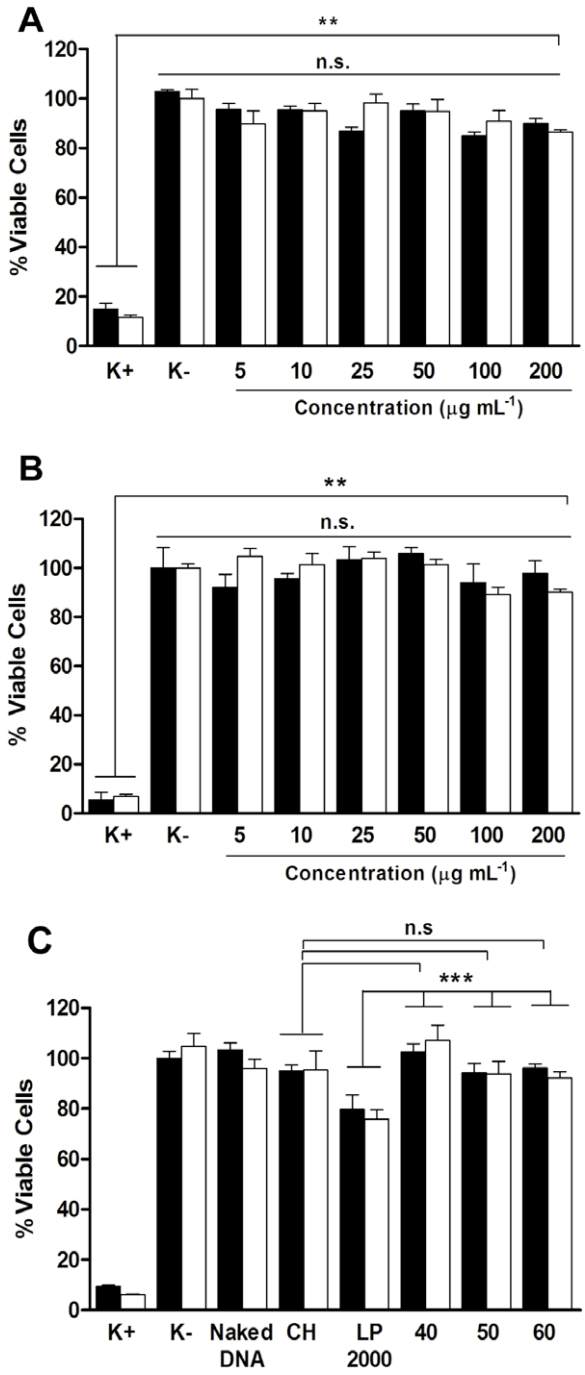

Figure 8. Cytotoxicity of nanoparticles. (A) and (B) Cytotoxicity index of the native polymer (black bars), and the arginine-histidine functionalized polymer (white bars) at 24 and 48 h, respectively, at different concentrations (μg ml^{-1}). (C) Cytotoxicity profile after incubation with CH, Lipofectamine 2000 (LP 2000) and the biofunctional nanoparticles at various ratios, at 24 h (black bars) and 48 h (white bars), respectively. $K-$ stands for the negative control for cytotoxicity (live cells); $K+$ denotes the positive control for cytotoxicity (absolute ethanol incubated cells, i.e., dead cells). Each bar represents the mean $\pm$ s.d. ($n = 5$).

particles (figure 8(B)), implying that the transfected cells are metabolically active after delivery. These results highlight the advantage of the amino acid functionalization in maintaining the biocompatibility of the novel nanodevices.

Evaluating the biocompatibility of anti-cancer nanocarriers is crucial for *in vivo* administration, as recently recommended by the cytotoxicity-related regulatory guidelines (ASTM E2526) [2], since nanoparticle accumulation and off-target cytotoxicity can affect healthy organs (e.g., liver, kidneys and lungs) and contribute to poor disease prognosis.

As our previous results demonstrated that pDNA is carried into the nucleus, the transfection efficiency of the novel delivery system was also characterized. The resulting gene expression levels attained when the CH–H–R nanodevices were employed was slightly lower than those obtained for Lipofectamine (LP) 2000 (figure 9(A)). This slight difference is also observed in GFP fluorescence images. However, it should be underlined that LP 2000 transfection is highly cytotoxic and took place under serum-free conditions, whilst CH–H–R transfection is performed with serum-supplemented medium (10% FBS). Nevertheless, our findings assume further importance, since accessing the efficiency of these delivery systems in *in vivo* mimicking conditions provides important insights on their effectiveness for administration in humans. Moreover, DNA release from the above-mentioned delivery systems is yet another parameter that needs to be taken into consideration in the analysis of figure 9(A). Mainly LP 2000 releases its pDNA cargo with burst-release kinetics [59].

Conversely, chitosan nanoparticles possess a sustained DNA release profile along a given time frame [5]. This controlled release is crucial, since the continuous discharge of genetic material can compensate for silencing of the plasmid vectors and sustain therapeutic levels for longer periods without cytotoxic side-effects associated with cationic lipids. Additionally, the expression levels attained by CH–H–R N:P 60 nanoparticles are approximately 4.4-fold higher when compared with those of native chitosan (figure 8(D)). When compared with their single substituted formulations, CH–H–R carriers formulated at N:P 60 attain 2.2-fold higher expression than CH–H, and 2-fold higher expression than CH–R. These markedly differences are further visualized in CLSM images, with a clear difference in fluorescence intensity and number of transfected cells being observed for the different formulations (figures 9(B)–(G)). In fact, it can be observed that the CH–H–R N:P 60 formulation presents higher GFP fluorescence when compared to the native and single modified chitosan. Moreover, the administration of this particular formulation also yields a higher GFP fluorescence intensity than the N:P 40 and 50 formulations (figure 9(G)).

This remarkable improvement is not only a consequence of the improved intrinsic physicochemical properties but also a contribution of the functional histidine and arginine components. In fact, further analysis of the results regarding nanoparticle-induced expression show that the carriers formulated at N:P 60 yield superior gene expression than the particles with lower ratios (figure 8(D)). In comparison to the transfection efficiency attained with other CH–H systems reported in the literature [36], the novel biofunctionalized nanodevices possess a remarkable improvement in cellular uptake ($\approx$40% transfected cells) and gene expression when compared to that of CH–H alone,

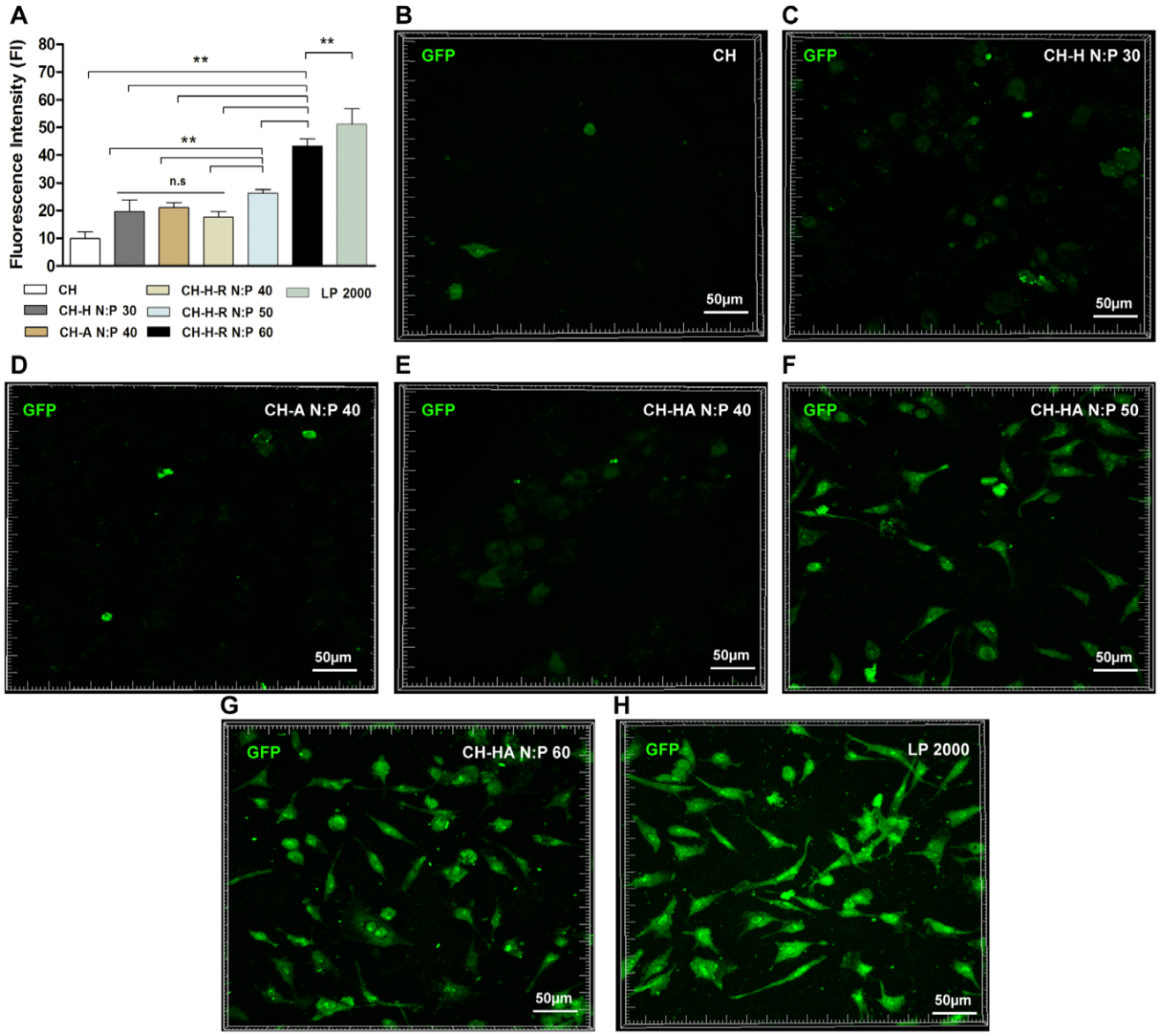

Figure 9. Transfection efficiency of the dual functionalized nanocarriers, their single modified and native counterparts. (A) Quantitative spectrofluorimetric analysis of GFP expression. Each bar represents the mean ± s.d. ($n = 3$). $**p < 0.01$; $***p < 0.0001$; n.s.—non significant. (B)–(H) CLSM analysis of nanoparticle-mediated GFP expression in cancer cells. Nanoparticle transfection was performed with serum-containing medium, whilst, LP 2000 control transfection was performed in serum-free medium.

reported previously by Moreira *et al* (<15% transfected cells) [36]. Likewise, a similar comparison with previously reported CH–R grafting methodology by Ho *et al* [18], reveals that the inclusion of histidine further enhances nanoparticle lysosomal escape. This is important, since the latter significantly lowers the probability that the particles become trapped in these vesicles [30] or get recycled back to the extracellular medium [27] which would markedly influence the overall therapeutic effect. A comparison with other recently engineered systems designed for gene delivery, such as that described by Aldawsari and co-workers [1], where arginine was conjugated with a dendrimer network, emphasizes the necessity to further include additional moieties to overcome the various physiological barriers (e.g. cell membrane, lysosomal release, nuclear membrane) encountered during transfection in an adaptive mode. In fact these adaptive and stimuli responsive nanoparticle systems are currently becoming an ever promising approach for the successful delivery of genes and drugs, as recently reviewed by Wang *et al* [55]. This novel concept is integrated in our delivery system with the addition of histidine, since its unique characteristics make it responsive to the surrounding environment cues. In fact, the pH-responsive behavior of histidine ($pKa = 6.5$) is a valuable property for gene delivery in acidic tumor tissues [55, 12]. In these sites histidine undergoes a charge reversal and becomes positively charged [56]. This feature associated with the presence of arginine further improves cell uptake at the tumor site, thus emphasizing the interest in having more than one functional block in the polymer backbone. Recently, Wu *et al* developed

a complex micellar delivery system that includes histidine residues to take advantage of these events and increase drug delivery into the intracellular compartment [56]. In the particular case of CH–H–R nanoparticles designed for cancer gene delivery, this adaptive response assumes even further relevance in addition to the charge shift at the tumor site and lysosomal release. Actually, the inclusion of histidine in the functionalized polymer also influences cargo release on the cytoplasm and nucleus, since at physiological pH, histidine residues are not positively charged, and thus contribute to a looser nanocarrier structure, which may promote diffusion of the genetic material. This reveals the importance of not having merely a passive block such as arginine, but also of adding residues with a dynamic behavior that may assist different stages of transfection. This is a major breakthrough in comparison with other systems comprised of single amino acid modifications [36], or others that rely on complex chemical modifications to ultimately achieve the similar objectives [51]. The latter is fundamental, since amino acids are biocompatible and cost-effective bioactive blocks, in contrast with others that are too expensive for pharmaceutical applications.

4. Conclusions

Overall, we devised a versatile strategy of dual bioconjugation of amino acid blocks onto the polymeric chain of chitosan through a general, facile and reproducible grafting methodology. Our findings demonstrated that the inclusion of amino acids improved DNA encapsulation and the transfection efficiency of the assembled nanosystems, rendering them relevant alternatives to currently available nanodevices. Moreover, the findings herein described the relevance of amino acid functionalization at the nano-bio interface where nanoparticles interact with cellular barriers. It is also important to emphasize that chitosan-amino acid materials are cost-effective materials for the engineering of the efficient nanomedicines projected for therapeutic applications. To bring forth the full therapeutic potential of these nanocarriers in *in vivo* applications, the developed multifunctional nanoparticles will be further tailored with biocompatible polymers that improve circulation time, and also with targeting blocks to increase their specificity to target cells. In conclusion, the effectiveness and versatility of CH–H–R nanoparticles will unlock the possibility to advance the delivery of biopharmaceuticals in a cost-effective and efficient mode.

Acknowledgments

The authors would like to thank to Eng. Ana Paula for her help with the acquisition of SEM images and Ângela Sousa for her help regarding plasmid pVax1-LacZ samples. This work was supported by the Portuguese Foundation for Science and Technology (FCT), (PTDC/EME-TME/103375/2008, PTDC/EBB-BIO/114320/2009, and PEst-C/SAU/UI0709/2011 COMPETE). Vítor M Gaspar also acknowledges a PhD fellowship from FCT (SFRH/BD/80402/2011). All the authors have declared that they have no conflict of interest.

References

[1] Aldawsari H, Edrada-Ebel R, Blatchford D R, Tate R J, Tetley L and Dufès C 2011 Enhanced gene expression in tumors after intravenous administration of arginine-, lysine- and leucine-bearing polypropylenimine polyplex *Biomaterials* **32** 5889–99

[2] ASTM 2008 *Standard Test Method for Evaluation of Cytotoxicity of Nanoparticulate Materials in Porcine Kidney Cells and Human Hepatocarcinoma Cells* ASTM standard E2526, 6

[3] Beloor J, Choi C S, Nam H Y, Park M, Kim S H, Jackson A, Lee K Y, Kim S W, Kumar P and Lee S K 2011 Arginine-engrafted biodegradable polymer for the systemic delivery of therapeutic siRNA *Biomaterials* **33** 1640–50

[4] Bonner D K, Leung C, Chen-Liang J, Chingozha L, Langer R and Hammond P T 2011 Intracellular trafficking of polyamidoamine–poly (ethylene glycol) block copolymers in DNA delivery *Bioconjug. Chem.* **22** 1519–25

[5] Bozkir A and Saka O M 2004 Chitosan nanoparticles for plasmid DNA delivery: effect of chitosan molecular structure on formulation and release characteristics *Drug Deliv.* **11** 107–12

[6] Chang K L, Higuchi Y, Kawakami S, Yamashita F and Hashida M 2010 Efficient gene transfection by histidine-modified chitosan through enhancement of endosomal escape *Bioconjug. Chem.* **21** 1087–95

[7] Chang K L, Higuchi Y, Kawakami S, Yamashita F and Hashida M 2011 Development of lysine-histidine dendron modified chitosan for improving transfection efficiency in HEK293 Cells *J. Controll. Release* **156** 195–202

[8] Cheng A, Chen W, Fuhrmann C and Frankel A 2003 Recognition of nucleic acid bases and base-pairs by hydrogen bonding to amino acid side-chains *J. Mol. Biol.* **327** 781–96

[9] Cho W S, Duffin R, Thielbeer F, Bradley M, Megson I L, MacNee W, Poland C A, Tran C L and Donaldson K 2012 Zeta potential and solubility to toxicions as mechanisms of lung inflammation caused by metal/metal oxide nanoparticles *Toxicol. Sci.* **126** 469–77

[10] Churchill C D M and Wetmore S D 2009 Noncovalent interactions involving histidine: the effect of charge on π–π stacking and T-shaped interactions with the DNA nucleobases *J. Phys. Chem.* B **113** 16046–58

[11] Costes S V, Daelemans D, Cho E H, Dobbin Z, Pavlakis G and Lockett S 2004 Automatic and quantitative measurement of protein-protein colocalization in live cells *Biophys. J.* **86** 3993–4003

[12] Danhier F, Feron O and Préat V 2010 To exploit the tumor micro environment: passive and active tumor targeting of nanocarriers for anti-cancer drug delivery *J. Controll. Release* **148** 135–46

[13] Dias R and Lindman B 2008 *DNA Interactions with Polymers and Surfactants* (New York: Wiley)

[14] Gaspar V, Sousa F, Queiroz J and Correia I 2011 Formulation of chitosan–TPP–pDNA nanocapsules for gene therapy applications *Nanotechnology* **22** 015101

[15] Gaspar V M, Correia I J, Sousa Â, Silva F, Paquete C M, Queiroz J A and Sousa F 2011 Nanoparticle mediated delivery of pure P53 supercoiled plasmid DNA for gene therapy *J. Controll. Release* **156** 212–22

[16] Gu Z, Rolfe B E, Thomas A C, Campbell J H, Lu G and Xu Z P 2011 Cellular trafficking of low molecular weight heparin incorporated in layered double hydroxide

nanoparticles in rat vascular smooth muscle cells *Biomaterials* **32** 7234–40
[17] Gullotti E and Yeo Y 2009 Extracellularly activated nanocarriers: a new paradigm of tumor targeted drug delivery *Mol. Pharmaceut.* **6** 1041–51
[18] Ho Y C, Liao Z X, Panda N, Tang D W, Yu S H, Mi F L and Sung H W 2011 Self-organized nanoparticles prepared by guanidine-and disulfide-modified chitosan as a gene delivery carrier *J. Mater. Chem.* **21** 16918–27
[19] Kay M A 2011 State-of-the-art gene-based therapies: the road ahead *Nature Rev. Genet.* **12** 316–28
[20] Khafagy E S and Morishita M 2012 Oral biodrug delivery using cell-penetrating peptide *Adv. Drug Deliv. Rev.* **64** 531–9
[21] Khalil I A, Hayashi Y, Mizuno R and Harashima H 2011 Octaarginine- and pH sensitive fusogenic peptide-modified nanoparticles for liver gene delivery *J. Controll. Release* **156** 374–80
[22] Kim J A, Åberg C, Salvati A and Dawson K A 2011 Role of cell cycleon the cellular uptake and dilution of nanoparticles in a cell population *Nature Nanotechnol.* **7** 62–8
[23] Laga R, Carlisle R, Tangney M, Ulbrich K and Seymour L W 2012 Polymer coatings for delivery of nucleic acid therapeutics *J. Controll. Release* **161** 537–53
[24] Lam A and Dean D 2010 Progress and prospects: nuclear import of nonviral vectors *Gene Therapy* **17** 439–47
[25] Lechardeur D, Verkman A S and Lukacs G L 2005 Intracellular routing of plasmid DNA during non-viral gene transfer *Adv. Drug Deliv. Rev.* **57** 755–67
[26] Liu L, Bai Y, Song C, Zhu D, Song L, Zhang H, Dong X and Leng X 2010 The impact of arginine-modified chitosan–DNA nanoparticles on the function of macrophages *J. Nanoparticle Res.* **12** 1637–44
[27] Love S A and Haynes C L 2010 Assessment of functional changes in nanoparticle-exposed neuroendocrine cells with amperometry: exploring the generalizability of nanoparticle-vesicle matrix interactions *Anal. Bioanal. Chem.* **398** 677–88
[28] Lu C W, Hung Y, Hsiao J K, Yao M, Chung T H, Lin Y S, Wu S H, Hsu S C, Liu H M and Mou C Y 2007 Bifunctional magnetic silica nanoparticles for highly efficient human stem cell labeling *Nano Lett.* **7** 149–54
[29] Luscombe N, Laskowski R and Thornton J 2001 Amino acid–base interactions: a three-dimensional analysis of protein-DNA interactions at anatomic level *Nucl. Acids Res.* **29** 2860
[30] Ma X, Wu Y, Jin S, Tian Y, Zhang X, Zhao Y, Yu L and Liang X J 2011 Gold nanoparticles induce auto phagosome accumulation through size-dependent nanoparticle uptake and lysosome impairment *ACS Nano* **5** 8629–39
[31] Malmo J, Sørgård H, Vårum K M and Strand S P 2012 siRNA delivery with chitosan nanoparticles: molecular properties favoring efficient gene silencing *J. Controll. Release* **158** 261–8
[32] Mao S, Sun W and Kissel T 2009 Chitosan-based formulations for delivery of DNA and siRNA *Adv. Drug Deliv. Rev.* **61** 12–27
[33] Margus H, Padari K and Pooga M 2012 Cell-penetrating peptides as versatile vehicles for oligonucleotide delivery *Mol. Therapy* **20** 525–33
[34] Minetti C A S A, Remeta D P and Breslauer K J 2008 A continuous hyperchromicity assay to characterize the kinetics and thermodynamics of DNA lesion recognition and base excision *Proc. Natl Acad. Sci.* **105** 70–5
[35] Modi S, Swetha M, Goswami D, Gupta G D, Mayor S and Krishnan Y 2009 ADNA nanomachine that maps spatial and temporal pH changes inside living cells *Nature Nanotechnol.* **4** 325–30
[36] Moreira C, Oliveira H, Pires L, Simões S, Barbosa M and Pęgo A 2009 Improving chitosan-mediated gene transfer by the introduction of intracellular buffering moieties into the chitosan backbone *Acta Biomater.* **5** 2995–3006
[37] Morille M, Passirani C, Vonarbourg A, Clavreul A and Benoit J 2008 Progress in developing cationic vectors for non-viral systemic gene therapy against cancer *Biomaterials* **29** 3477–96
[38] Nel A E, Madler L, Velegol D, Xia T, Hoek E M V, Somasundaran P, Klaessig F, Castranova V and Thompson M 2009 Understanding biophysicochemical interactions at the nano-bio interface *Nature Mater.* **8** 543–57
[39] Pack D W, Hoffman A S, Pun S and Stayton P S 2005 Design and development of polymers for gene delivery *Nature Rev. Drug Discov.* **4** 581–93
[40] Parra-Guillén Z, González-Aseguinolaza G, Berraondo P and Trocóniz I 2010 Gene therapy: a pharmacokinetic/ pharmacodynamic modelling overview *Pharmaceut. Res.* **27** 1487–97
[41] Pichon C, Billiet L and Midoux P 2010 Chemical vectors for gene delivery: uptake and intracellular trafficking *Curr. Opin. Biotechnol.* **21** 640–5
[42] Rasband W S 2008 ImageJ http://rsbweb.nih.gov/ij/
[43] Ren J, Shen S, Wang D, Xi Z, Guo L, Pang Z, Qian Y, Sun X and Jiang X 2012 The targeted delivery of anticancer drugs to brain glioma by PEGylated oxidized multi-walled carbon nanotubes modified with angiopep-2 *Biomaterials* **33** 3324–33
[44] Sachs D H, Schechter A N and Cohen J S 1971 Nuclear magnetic resonance titration curves of histidine ring protons *J. Biol. Chem.* **246** 6576
[45] Santos J L, Pandita D, Rodrigues J, Pêgo A P, Granja P L and Balian Gand Tomás H 2010 Receptor-mediated gene delivery using PAMAM dendrimers conjugated with peptides recognized by mesenchymal stem cells *Mol. Pharmaceut.* **7** 763–74
[46] Sousa F, Cruz C and Queiroz J A 2010 Amino acids–nucleotides biomolecular recognition: from biological occurrence to affinity chromatography *J. Mol. Recognit.* **23** 505–18
[47] Sousa F, Freitas S, Azzoni A R, Prazeres D M F and Queiroz J 2006 Selective purification of supercoiled plasmid DNA from clarified cell lysates with a single histidine–agarose chromatography step *Biotechnol. Appl. Biochem.* **45** 131–40
[48] Sousa F, Prazeres D and Queiroz J 2009 Improvement of transfection efficiency by using supercoiled plasmid DNA purified with arginine affinity chromatography *J. Gene Med.* **11** 79–88
[49] Stern R 1970 A nuclease from animal serum which hydrolyzes double-stranded RNA *Biochem. Biophys. Res. Commun.* **41** 608–14
[50] Thomas J J and Sharma C P 2012 Unraveling the intracellular efficacy of dextran–histidine polycation as an efficient non-viral gene delivery system *Mol. Pharmaceut.* **9** 121–34
[51] Van Butsele K, Cajot S, Van Vlierberghe S, Dubruel P, Passirani C, Benoit J P, Jérôme R and Jérôme C 2009 pH-Responsive flower-type micelles formed by a biotinylated poly (2-vinylpyridine)-block-poly (ethylene oxide)-block-poly (ε-caprolactone) triblock copolymer *Adv. Funct. Mater.* **19** 1416–25
[52] Venkataraman S, Hedrick J L, Ong Z Y, Chuan Y, Ee P L R, Hammond P T and Yang Y Y 2011 The effects of polymeric nanostructure shape on drug delivery *Adv. Drug Deliv. Rev.* **63** 1228–46

[53] Wang J *et al* 2012 Star-shape copolymer of lysine-linked di-tocopherol polyethylene glycol 2000 succinate for doxorubicin delivery with reversal of multidrug resistance *Biomaterials* **33** 6877–88
[54] Wang Y, Byrne J D, Napier M E and DeSimone J M 2012 Engineering nanomedicines using stimuli-responsive biomaterials *Adv. Drug Deliv. Rev.* **64** 1021–30
[55] Wang Y, Byrne J D, Napier M E and Desimone J M 2012 Engineering nanomedicines using stimuli-responsive biomaterials *Adv. Drug Deliv. Rev.* **64** 1021–30
[56] Wu H, Zhu L and Torchilin V P 2012 pH-sensitive poly(histidine)-PEG/DSPE-PEG co-polymer micelles for cytosolic drug delivery *Biomaterials* **34** 1213–22
[57] Xia X X, Xu Q, Hu X, Qin G and Kaplan D L 2011 Tunable self-assembly of genetically engineered silk–elastin-like protein polymers *Biomacromolecules* **12** 3844–50
[58] Xiang S, Tong H, Shi Q, Fernandes J C, Jin T, Dai K and Zhang X 2011 Uptake mechanisms of non-viral gene delivery *J. Controll. Release* **158** 371–8
[59] Xu Y and Szoka F C 1996 Mechanism of DNA release from cationic liposome/DNA complexes used in cell transfection *Biochemistry* **35** 5616–23
[60] Yamazaki T, Pascal S M, Singer A U, Forman-Kay J D and Kay L E 1995 NMR pulse schemes for the sequence-specific assignment of arginine guanidino 15N and 1H chemical shifts in proteins *J. Am. Chem. Soc.* **117** 3556–64
[61] Yue Z G, Wei W, Lv P P, Yue H, Wang L Y, Su Z G and Ma G H 2011 Surface charge affects cellular uptake and intracellular trafficking of chitosan-based nanoparticles *Biomacromolecules* **12** 2440–6

Supplementary Information

Biofunctionalized Nanoparticles with pH-responsive and Cell Penetrating Blocks for Gene Delivery

Nanotechnology, 2013
DOI: 10.1088/0957-4484/24/27/275101

7.1. Methods

7.1.1. Plasmid DNA Fluorescent Labelling

Plasmid DNA (pDNA) labelling was performed with, fluorescein isothiocyanate isomer I (FITC) and rhodamine B isothiocyanate (RITC). The FITC fluorescently labeled pDNA was synthesized by a method previously described by our group [56]. Briefly, to activate the fluorescent probe, FITC (10 mg) was initially mixed with 2-(4-aminophenyl)-ethylamine in a DMF solution overnight at room temperature (approximately 23 °C) under stirring to prepare FITC-aniline. Afterwards the aniline conjugated FITC was reacted with $NaNO_2$ in 0.5 M HCl at 0 ºC under magnetic stirring, for 5 min. The reaction was stopped by the addition of 100 µL of a 1M NaOH solution. The resulting FITC-diazonium salt was then mixed with the pVax1-*LacZ* plasmid under mild horizontal magnetic stirring for 25 min, at 4 °C (0.2 M carbonate buffer solution, pH 9.0). The FITC labeled pDNA was then recovered by precipitation with 4 volumes of ice cold isopropanol and pelleted by centrifugation (16 000 g, 30 min, 4 °C). The recovered pDNA was additionally washed two times with ice cold ethanol to remove traces of the fluorescent probe. Labeling of pDNA with RITC was carried out as previously described by Santos and collaborators [84], with slight modifications. Briefly, 0.8 mg of pDNA was diluted in 3 mL of a sodium carbonate ice cold solution (0.1 M, pH = 9.0) and was then mixed with 3 µL of an RITC stock solution prepared at a concentration of 100 mM in dimethyl sulfoxide. The reaction was carried out at room temperature under horizontal stirring for 5 h. The resulting RITC labeled pDNA was subsequently recovered and washed as abovementioned.

7.2. Results and Discussion

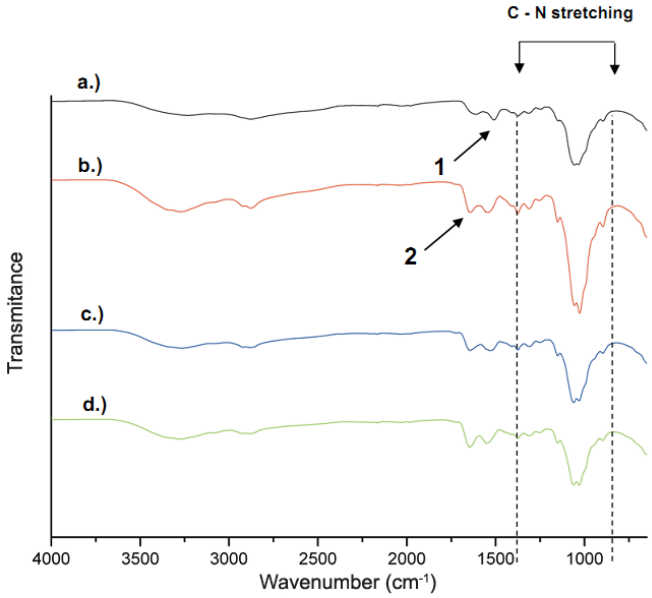

Figure S1. Representative FTIR spectra of the bioconjugation reaction. a.) Unmodified chitosan hydrochloride. The absorption peak 1 was assigned to the N-H bending (≈ 1560 cm^{-1}) (amide II) of the glucosamine monomer of chitosan. b.) Histidine-grafted chitosan

(CH-H; substitution degree (SD) – 29.02 %). After conjugation the spectral analysis demonstrates an increase in the amide I peak (peak 2, ≈ 1654 cm^{-1}), suggesting the synthesis of extra amide bonds which are formed during the coupling reaction. c.) Arginine-grafted chitosan (CH-R; SD – 26.30 %). An analysis of the obtained spectra reveals an increase in the N-H bending peak correspondent to amide I as aforementioned, further confirming the conjugation of arginine in the polymer backbone. d.) Chitosan-histidine-arginine conjugate (CH-H-R SD – 48.58 %; Histidine SD – 27.51 %; Arginine SD – 21.07 %). The results obtained showed a markedly increase in the amide I bending peak denoting that after the sequential two-step conjugation the amino acids are grafted in the polymer backbone.

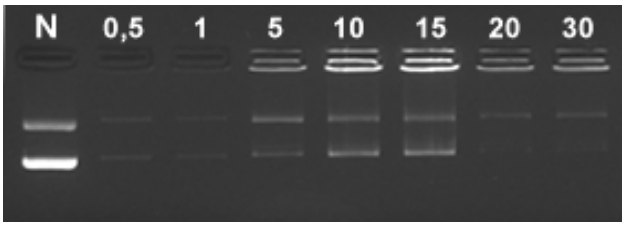

Figure S2. Agarose gel electrophoresis of pDNA complexation with chitosan hydrochloride at different N:P molar ratios indicated in comparison with the naked pDNA sample (N).

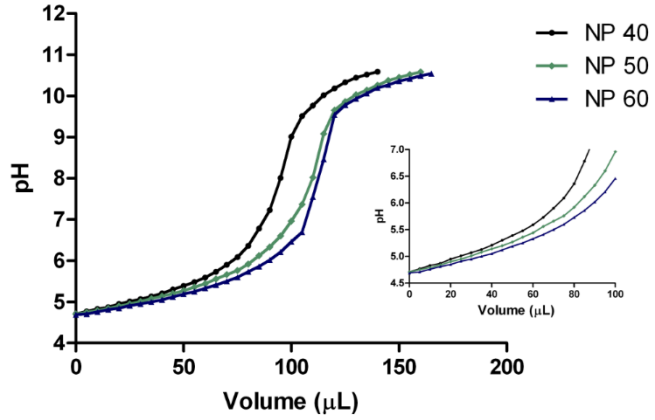

Figure S3. Buffer capacity plot of the different ratios of CH-H-R polymer formulations. CH-H-R N:P 40 (black), CH-H-R N:P 50 (green), CH-H-R N:P 60 (blue).

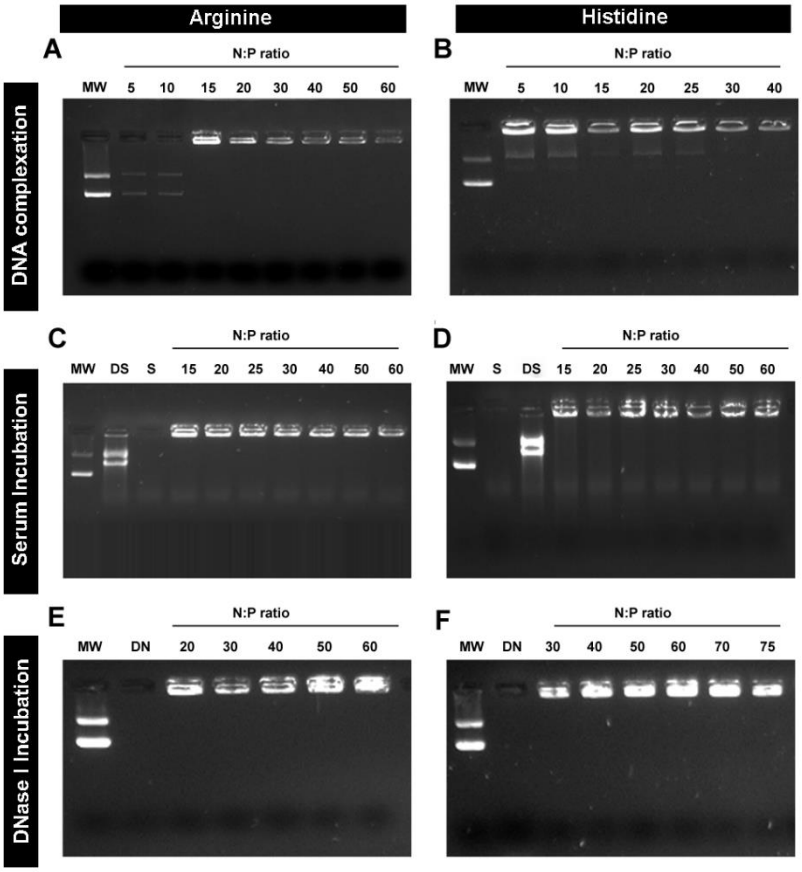

Figure S4 – Agarose gel electrophoresis of amino acid substituted CH. A and B) DNA complexation assays of CH-R and CH-H, respectively; C and D) FBS resistance assays of CH-R and CH-H nanoparticles, respectively; E and F) DNAseI incubation of CH-R and CH-H nanoparticles, respectively. MW – native DNA sample (open circular and supercoiled); DS – naked DNA incubated in FBS serum; S – FBS serum; DN – naked DNA incubated with DNAseI.

Table 1. Physicochemical characterization of the best N:P formulation ratios of amino acid substituted chitosan nanoparticles.

	N:P Ratio	Average Size (nm)	PDI	Zeta Potential (mV)
CH-H	30	125.4	0.415	+ 25.4 ± 6.14
CH-R	40	139.6	0.240	+ 22.7 ± 12.2

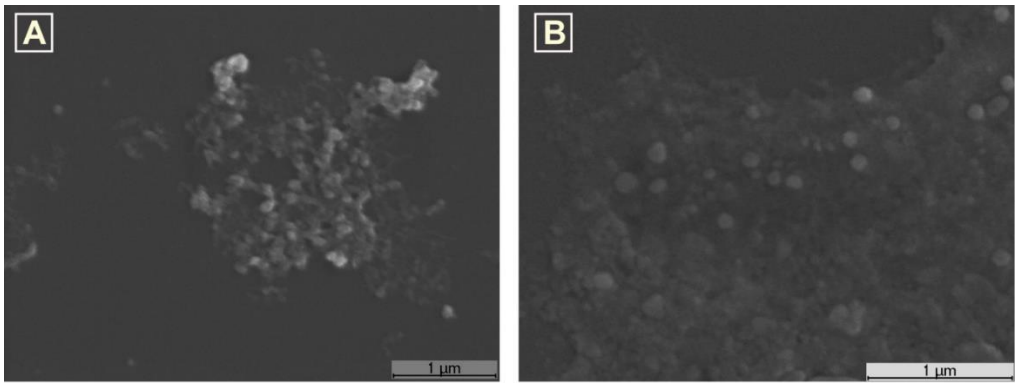

Figure S5 - SEM micrographs of biofunctional nanoparticles. A) CH-H nanoparticles at N:P 30; B) CH-R nanoparticles at N:P 40.

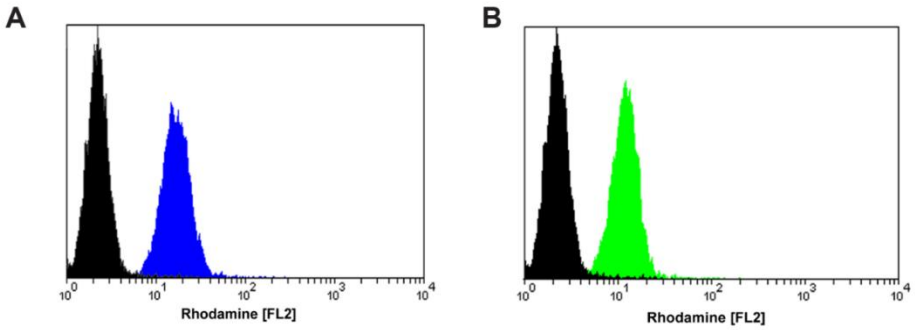

C

Sample	MFI	% Cells
CH-H	14.9	21.44
CH-R	19.2	30.82

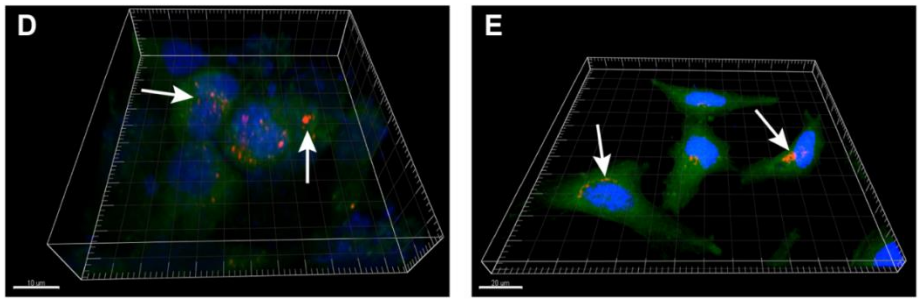

Figure S6 - Nanoparticle cellular uptake. A) Representative flow cytometry histograms of cell uptake. Black – Negative control (unstained cells); Blue – Biofunctional CH-R nanoparticles (N:P 40). B) Representative flow cytometry histograms of cell uptake. Black – Negative control (unstained cells); Green – Biofunctional CH-H nanoparticles (N:P 30). C) Quantification of the mean fluorescence intensity (MFI) and percentage of transfected cells with the different nanoparticle formulations (CH-H and CH-R, respectively). D) CLSM analysis of nanoparticle cellular uptake and localization of CH-R. E) CLSM analysis of nanoparticle cellular uptake and localization of CH-H. Green channel – Actin-GFP staining of the intracellular compartment; Blue channel – Nuclear staining with Hoechst 33342®; Red channel– RITC labeled pDNA (indicated with white arrows).

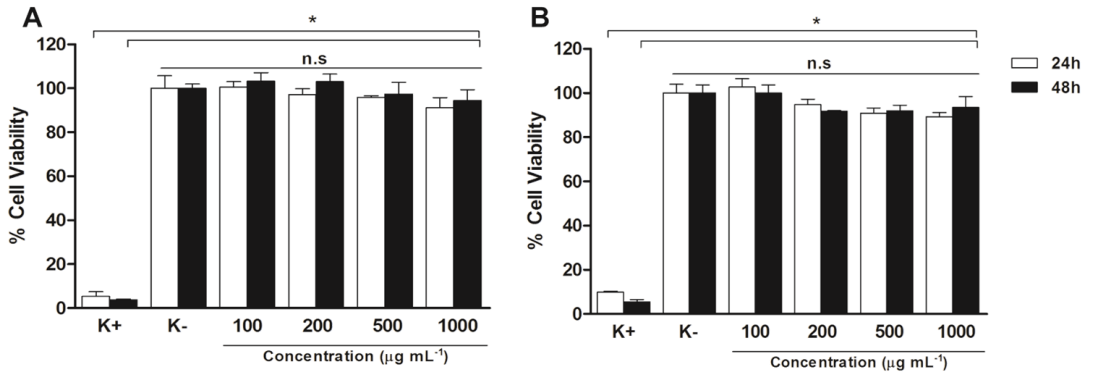

Figure S7 - Cytotoxicity of nanoparticles. A) Cytotoxicity index of the CH-R polymer; B) Cytotoxicity index of the CH-H polymer. White bars – 24 h and Black bars- 48 h, at different concentrations (μg mL^{-1}).

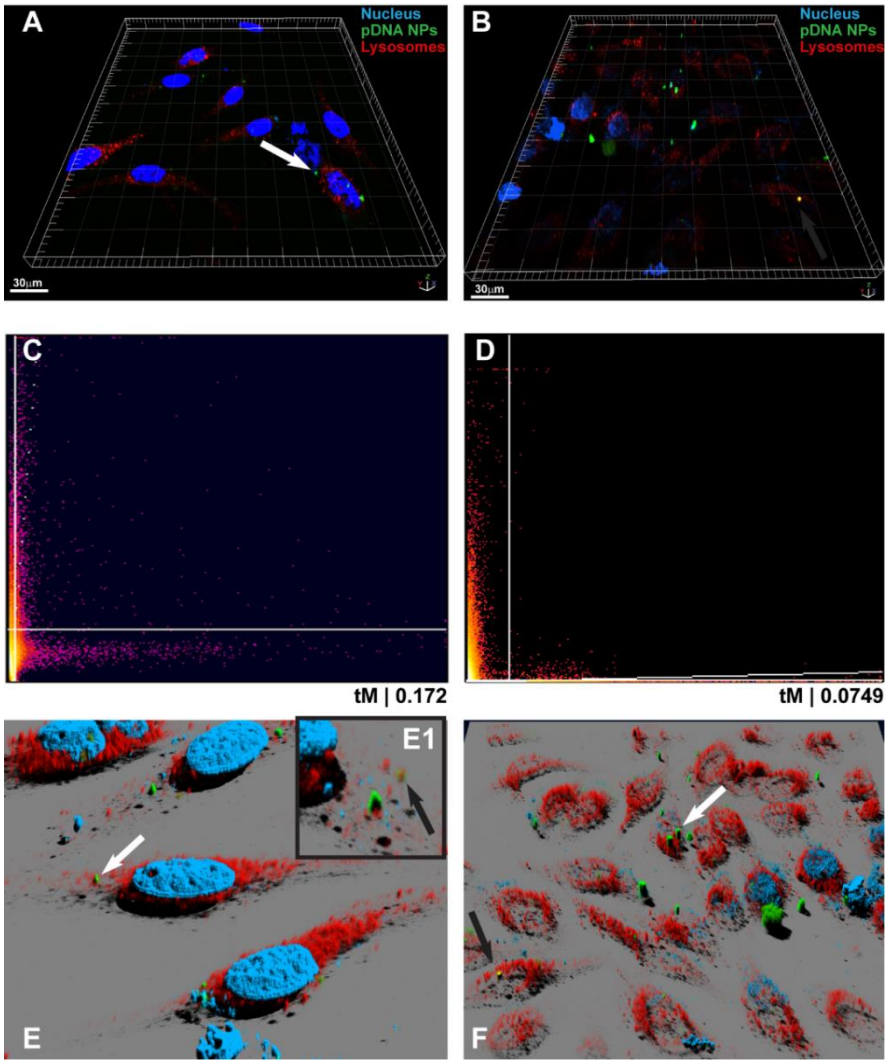

Figure S8 - Intracellular trafficking and colocalization of biofunctionalized nanoparticles. A and B) CLSM images of intracellular trafficking of CH-R and CH-H nanoparticles, respectively; C and D) Representative colocalization profiles of the different nanoparticles (CH-R, and CH-H, respectively) The numerical analysis was performed with the Manders colocalization coefficients (tM) automatically determined by a threshold algorithm. E) 3D reconstruction volume rendering of cells transfected with CH-R nanoparticles; E1) Magnified 3D reconstruction, black arrow indicates nanoparticles inside the lysosome; F) 3D reconstruction volume rendering of cells transfected with CH-R nanoparticles. Green channel – FITC labeled pDNA; Red channel – Staining of the lysosomal compartments with LysoTracker® Red DND-99 dye; Blue channel - Nuclear staining with Hoechst 33342®. White arrows indicate pDNA/nanoparticles (NPs). Black arrows indicate colocalized lysosomes-pDNA NPs.

7.3. References

1. Gaspar, V., Sousa, F., Queiroz, J., and Correia, I., *Formulation of chitosan-TPP-pDNA nanocapsules for gene therapy applications.* Nanotechnology, 2011. **22**: p. 015101.
2. Santos, J.L., Pandita, D., Rodrigues, J., Pêgo, A.P., Granja, P.L., Balian, G., and Tomás, H., *Receptor-mediated gene delivery using pamam dendrimers conjugated with peptides recognized by mesenchymal stem cells.* Molecular Pharmaceutics, 2010. **7**(3): p. 763-774.

CHAPTER 8

Folate-Targeted Multifunctional Amino Acid-Chitosan Nanoparticles for Improved Cancer Therapy

Pharmaceutical Research, 2015
DOI: 10.1007/s11095-014-1486-0

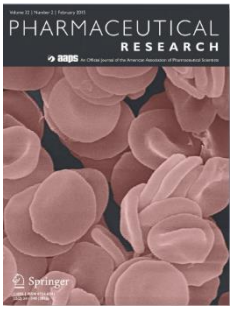

Volume 32, issue 2

Motivation

Gathering the important insights obtained with the *in vitro* testing of chitosan-histidine-arginine nanocarriers these systems were further modified with cancer cell targeting ligands in the following study. This approach was devised to improve the cell selectivity as this parameter may be beneficial towards reducing off-target effects following administration. Overall, such approach was anticipated to positively impact not only the cell selectivity buy also the cellular uptake and gene transfer efficiency of chitosan-DNA nanovehicles.

Pharm Res
DOI 10.1007/s11095-014-1486-0

RESEARCH PAPER

Folate-Targeted Multifunctional Amino Acid-Chitosan Nanoparticles for Improved Cancer Therapy

Vítor M. Gaspar • Elisabete C. Costa • João A. Queiroz • Chantal Pichon • Fani Sousa • Ilídio J. Correia

Received: 21 May 2014 / Accepted: 15 August 2014

ABSTRACT

Purpose Tumor targeting nanomaterials have potential for improving the efficiency of anti-tumoral therapeutics. However, the evaluation of their biological performance remains highly challenging. In this study we describe the synthesis of multifunctional nanoparticles decorated with folic acid-PEG and dual amino acid-modified chitosan (CM-PFA) complexed with DNA and their evaluation in organotypic 2D co-cultures of cancer-normal cells and also on 3D multicellular tumor spheroids models.

Methods The physicochemical characterization of CM-PFA multifunctional carriers was performed by FTIR, ^{1}H NMR and DLS. 2D co-culture models were established by using a 1:2 cancer-to-normal cell ratio. 3D organotypic tumor spheroids were assembled using micromolding technology for high throughput screening. Nanoparticle efficiency was evaluated by flow cytometry and confocal microscopy.

Results The CM-PFA nanocarriers (126–176 nm) showed hemocompatibility and were internalized by target cells, achieving a 3.7 fold increase in gene expression. *In vivo*-mimicking 2D co-cultures confirmed a real affinity towards cancer cells and a negligible uptake in normal cells. The targeted nanoparticles penetrated into 3D spheroids to a higher extent than non-targeted nanocarriers. Also, CM-PFA-mediated delivery of p53 tumor suppressor promoted a decrease in tumor-spheroids volume.

Conclusion These findings corroborate the improved efficiency of this delivery system and demonstrate its potential for application in cancer therapy.

Electronic supplementary material The online version of this article (doi:10.1007/s11095-014-1486-0) contains supplementary material, which is available to authorized users.

V. M. Gaspar • E. C. Costa • J. A. Queiroz • F. Sousa • I. J. Correia (✉)
CICS-UBI – Health Sciences Research Centre, Universidade da Beira Interior, Avenida Infante D. Henrique, 6200-506 Covilhã, Portugal
e-mail: icorreia@ubi.pt

C. Pichon
Centre de Biophysique Moléculaire, CNRS UPR4301, Inserm and University of Orléans, 45071 cedex 02 Orléans, France

KEY WORDS cancer therapy · gene delivery · targeted nanoparticles · 2D co-cultures · 3D tumor spheroids

INTRODUCTION

Targeted delivery through specialized nanocarriers currently attracts remarkable attention since bioactive molecules can be selectively transported into malignant tissues with improved efficiency and limited systemic toxicity (1). In line with this focus, nanosized systems are currently being developed for the delivery of a broad range of anti-tumoral therapeutics that span from plasmid DNA (pDNA (2)), small interfering RNA (siRNA (3)), polyphenolic compounds (Resveratrol, tea catechins (4)), up to general pharmaceuticals (Doxorubicin, Paclitaxel and Cisplatin (5)).

Nevertheless, despite these advances, the majority of the nanocarriers engineered so far present limited *in vivo* targeting capacity, generally taking advantage of a probabilistic accumulation in cancer cells through the so-termed enhanced permeability and retention effect (EPR) (6). The EPR effect is a consequence of an uncontrolled angiogenesis which originates disorganized and leaky vascular networks that have characteristic fenestrations with sufficiently large sizes for passive nanocarrier extravasation into diseased tissues (100 - 300 nm) (7,8). However, this range is highly variable, depends on tumor type, location, and vascular density, both at the periphery and tumor core (9). To further hinder accumulation, solid tumors have a high interstitial fluid pressure, an additional barrier that affects nanoparticle convective diffusion and tissue penetration (10). Consequently, these properties significantly impair the pharmacokinetic/pharmacodynamic profile and therapeutic effectiveness of non-targeted delivery systems (9,11). In order to overcome these issues various classes of targeting ligands such as antibodies (Herceptin®(12)), aptamer bioconjugates (13), homing

Published online: 04 September 2014

peptides (14), and other macromolecules including lectins (12), transferrin (Tf) (15), and folic acid (FA) (12), are available for cell targeting. In this context, selecting ligands that bind surface receptors prone to internalization is a valuable strategy to deliver drugs and DNA biopharmaceuticals that are only active in the cytoplasm or nucleus (2). For this objective, FA is a particularly advantageous biomolecule since it can bind to the folate receptor (FR) with high affinity under physiological conditions ($Kd \approx 1 \times 10^{-10}$ M), and is then readily internalized via receptor-mediated endocytosis (16,17). The fact that folate receptors have minimal expression in most tissues and are highly expressed in breast, cervical, ovary and prostate cancers (18,19), further contributes for their potential to be used as a target for cancer therapy (17,20). In a recent report, Aranda *et al.*, 2013, demonstrated that the use of folate-conjugated cyclodextrin derivatives significantly enhanced gene transfer into FR-positive cancer cells, with target-specific polyplexes achieving a 1.7 fold increased expression in comparison with plain nanocarriers (21). On the other hand, folate functionalization by itself has shown certain limitations in promoting penetration into deep tumor regions, a fact that presents a major issue in current nanomedicines under production. Such could be overcome, by combining FR targeting with cell penetrating moieties like the TAT penetrating protein (22). In the same way, our group has recently reported the formulation of amino acid modified nanoparticles that remarkably improve cell penetration through the use of arginine moieties and also stimulate endosomal release of pDNA carriers by the pH responsive behaviour of histidine, in an effort to improve the therapeutic outcome (23).

However, up until recently, testing the biological activity after nanocarrier modification with targeting ligands or penetration enhancers remained extremely challenging during pre-clinical stages (24). A fact mainly attributed to the lack of *in vitro* tools capable of providing data that can be correlated with the complex *in vivo* conditions (25). This necessity assumes additional importance in light of the current restrictions of animal use and also of the rigorous toxicity-efficiency tests demanded by regulatory organisms (FDA, EMEA) before nanomedicines clinical approval (26). In this stand point, the advent of 2D co-cultures and 3D solid tumor models presents a relevant breakthrough (27,28). Co-culture models have various advantages over standard single cell culture, in such a way that the targeting capacity of nanocarriers can be simultaneously tested in a heterogeneous culture of malignant and normal cells (25). These assays thus provide valuable insights in to true cell-selectivity. In addition, 3D multicellular tumor spheroids (MCTS) is another useful platform for testing the development of nanocarriers since these microtissues can closely mimic *in vitro* the complex tumor architecture, mass transfer limitations, cell-cell contacts, pH gradients and necrotic regions with high accuracy (26). Besides, by using novel nano/micro manufacturing technologies for MCTS production, a large number of uniform spheroids can be produced simultaneously, contributing for robust assays and data acquisition (29).

Therefore, herein we report the formulation of a multifunctional nanocarrier comprised by folate-PEG and amino acid moieties (CM-PFA) to improve cell targeting and penetration. The biological performance of this novel nanocarrier was evaluated in 2D co-cultures and 3D solid tumor models produced by micropatterned scaffolds. Altogether our results show that this delivery system has improved cell uptake, tumor penetration and also gene expression in 3D spheroids.

MATERIALS AND METHODS

Materials

Folic acid, branched Polyethylenimine (PEI) (Mw≈25 kDa), L-cysteine, L-histidine, L-arginine, Triethylamine (TEA), cysteamine. HCl, Fluorescein isothiocyanate isomer I (FITC), Rhodamine B isothiocianate (RITC), N- Hydroxysuccinimide (NHS), 4-(2-Hydroxyethyl)piperazine-1-ethanesulfonic acid (HEPES), Resazurin, cell culture Dulbecco's Modified Eagle's Medium – high glucose (DMEM-HG) and DMEM-F12 were purchased from Sigma–Aldrich (Sintra, Portugal). Fetal bovine serum (FBS) was acquired from Biochrom (Biochrom AG, Berlin). N-(3-Dimethylaminopropyl)-N'-ethylcarbodiimide hydrochloride (EDAC) was obtained from MerckMillipore (Nothingham, UK). Homobifunctional Poly(ethylene glycol) maleimide (MAL-PEG-MAL, MW≈3500 Da) was acquired from Nanocs Inc (New York, USA). Pharmaceutical-grade chitosan UP CL 113 (MW≈110 kDa; Deacetylation degree: 83%; Heavy metals <16 ppm, Proteins: 0.09%; Endotoxins <51 EU/gram) was purchased from Novamatrix (Sandvika, Norway). HeLa (Human negroid cervix epitheloid carcinoma - CCL-2) cells were acquired from ATCC (Middlesex, UK). Human dermal fibroblasts (hFIB) were obtained from Promocell (Heidelberg, Germany). The fluorescent probes Hoechst 33342® and Backman Cell Light 2.0® Actin-GFP, were obtained from Invitrogen (Carlsbad, CA, USA). Anti-F-actin CruzFluor® 647 conjugate antibody was a kind gift from Santa Cruz Biotechnology (Santa Cruz, CA, USA). All the buffers and reagents used were of technical or analytical grade.

Methods

A complete description of all the methods technical details is provided in supplementary information.

Synthesis of Folate- PEG-Amino Acid Modified Chitosan

The synthesis of amino acid-modified chitosan (CM) was performed through selective amidation of the polymer primary amines by using EDC/NHS coupling chemistry as previously reported by our group (23). The inclusion of PEG into CM polymer was promoted via thiol-maleimide Michael-type addition reaction. For the synthesis of folate-grafted polymers (CM-PFA) an excess of FA-SH was reacted with CM-P via Michael type thiol-maleimide coupling, as previously described by Zhang and co-workers, 2010 (30). To remove unreacted folic acid the product was initially dialyzed (MWCO 3500 Da) against 5 L of 0.1 M sodium bicarbonate solution during 4 days, in the dark. The use of sodium carbonate leads to the formation of sodium folate, i.e., the soluble salt of folic acid allowing its removal. Afterwards, the product was dialyzed against 5 L of water for additional 4 days in the dark. The recovered product was then freeze dried for 48 h, and stored at 4°C until further use, in the dark, to protect folic acid from degradation (yield, 81.9%). Characterization of CM-PFA multifunctional polymers was performed through ^{1}H NMR spectroscopy and Fourier transform infrared spectroscopy (FTIR) (Fig. S1, S2, S3 and S4).

Formulation of Targeted Multifunctional Nanocarriers

For the formulation of CM-PFA/pDNA polyplexes a stock solution of modified polymers was prepared in 5 mM sodium acetate (NaAct) buffer (pH 4.5). The CM-PFA/pDNA polyplexes were assembled at different molar ratios of polymer amines to pDNA phosphate groups (N/P ratio). The moles of free amine groups in chitosan were obtained from the polymer deacetylation degree (83%). The primary amines of chitosan and the amines of arginine (guanidine group) and histidine (imidazole group protonated at pH 4.5) were used for calculation of the N/P complexation ratio. The moles of phosphate groups were extrapolated from pDNA size (7060 bp), considering that double strand DNA base pairs have 660 g/mol/bp. Amine-phosphate ratio was calculated according to equation 1:

$$ {}^{N}/_{P}\text{ratio} = \frac{\text{moles of amines in the polymer}}{\text{moles of phosphate groups in pDNA}} \quad (1) $$

The nanoparticles were prepared by adding pDNA to the polymer solution at a 1:4 (*v*/*v*) ratio, under vigorous stirring for 2 min. The formed particles were then recovered by centrifugation at 18 000 g for 30 min. For PEI/pDNA, the polyplexes were produced in HEPES buffered glucose (N:P ratio =5; HBG - 20 mM HEPES, 5% glucose, pH=7.1) as recommended in the literature (31).

Nanocarriers Physicochemical Characterization

The hydrodynamic radius and zeta potential of the nanocarriers was determined through dynamic light scattering (DLS) by using a Zetasizer Nano ZS particle analyzer (Malvern Instruments, Worcestershire, UK) Nanocarriers morphology was evaluated by Scanning Electron Microscopy (SEM) as previously described (23). All images were acquired in high vacuum mode and with an accelerating voltage of 20 kV. Image post-processing was performed in Rontec EDWIN software v. 4.1.

Cytotoxicity Assays

The cytotoxicity of CM-PFA polymers and CM-PFA/pDNA nanocarriers was evaluated by the Resazurin assay. In brief, HeLa or hFIB cells were cultured at 37°C, in an incubator with a controlled atmosphere (5% CO_2, 95% O_2, humid atmosphere) until attaining 80 – 85% confluence. The cells were then sub-cultured at an initial density of 8×10^3 cells per well in 96-well culture plates containing DMEM-HG (HeLa) or DMEM-F12 (hFIB) and 10% FBS. After attachment, cells were incubated with different concentrations of CM-PFA polymers (5–200 μg/mL). All experiments were performed at 24, 48 and 72 h. At these predetermined time points Resazurin (1%*w*/*v*) was incubated in each well for a 4 h period, in the dark (37°C, 5% CO_2, 95% O_2). The resultant resorufin pink dye present in culture medium was then transferred to fluorescence plates for immediate analysis (96-well black clear bottom; Greiner Bio-one, Frickenhausen, Germany). Fluorescence measurements were performed in a Spectramax Gemini XS spectrofluorometer (λ_{ex}=560 and λ_{em}=590 nm) (Molecular Devices LLC, USA). Optical micrographs were acquired by using an Olympus CX41 optical microscope attached to an Olympus SP-500 UZ digital camera.

Cell Uptake in Monocultures

Nanocarriers cellular uptake in single HeLa cultures was evaluated by flow cytometry and confocal laser scanning microscopy (CLSM) based on methodologies previously established by our group (23,25). Flow cytometry analysis was performed in a BD FACSCalibur flow cytometer (Becton Dickinson Inc., USA) equipped with green (488 nm) and red (633 nm) lasers. For each experiment a total of 1×10^4 events were collected in the region of interest (ROI) corresponding to HeLa cells. Data acquisition was carried out in the CellQuest™ Pro software. Data processing and statistical analysis was performed in the trial version of FlowJo software v. 10.0.6 (Tree Star, Ashland, Oregon, USA).

For CLSM analysis HeLa cells were innitially cultured at a density of 2×10^4 cells per cm^2, in fibronectin coated μ-slide 8-

well imaging plates (Ibidi GmbH, Germany). After 4 h of nanoparticle incubation the cells were fixed with 4% (*w/v*) paraformaldehyde (PFA) for 10 min at room temperature (RT), permeabilized for 30 min (1% Triton X-100, phosphate buffer saline (PBS)), and stained with the Anti-F-actin CruzFluor® 647 conjugate antibody for 1 h, RT. After rinsing for 6 times with PBS the cells were incubated with Hoechst 33342® for 15 min, RT. Fluorescence images were acquired in a Zeiss LSM 710 confocal microscope (Carl Zeiss SMT Inc., USA). Image processing was carried out in Fiji (32), and Imaris software (Bitplane, Switzerland).

GFP Expression

For transgene expression GFP was used as a model reporter gene. The experiments were performed in 96-well black-clear bottom plates seeded with 1×10^4 HeLa cells per well. Transfection was carried out at a pDNA concentration of 1 μg/cm^2 and by incubating nanoparticles in medium containing FBS and administering to cancer cells during 4 h. After this period the particles were removed. GFP expression was analyzed after 48 h by using a plate reader spectrofluorometer (Molecular Devices, California, USA). In addition, the visualization of GFP expression was carried out by CLSM also after 48 h of transfection.

Targeted Delivery in 2D Co-culture Models

Co-cultures of malignant and normal cells were designed by simultaneously seeding HeLa and hFIB cells in 6-well plates in a 1:2 ratio, using a total number of 2×10^4 cells/well. Co-cultures were maintained in DMEM-HG medium for 24 h prior to all experiments. Targeting specificity was determined in 2D co-cultures by CLSM and flow cytometry. To distinguish normal and cancer cells, HeLa cells were previously transfected with a baculovirus containing an Actin-GFP fusion construct by following the manufacturer's instructions (Backman Cell Light 2.0® Actin-GFP). Co-cultures grown in DMEM-HG / 10% FBS were then incubated with targeted and non-targeted nanocarriers for 4 h. Flow cytometry analysis of co-culture populations was performed in Actin-GFP expressing HeLa cells and unstained fibroblasts. The data of non-treated controls is provided in Supplementary information (Figure S9).

3D Tumor Spheroids Penetration and Gene Expression

Organotypic 3D tumor spheroids of HeLa cells were assembled by using a 3D precision micromold hydrogel scaffold with an array of 81-wells, as previously reported by Napolitano and co-workers (33). In brief, hydrogel micromolds were produced with 2% (*w/v*) liquid agarose by casting a negative scaffold from the original template. After drying, the molds were equilibrated overnight with culture medium. HeLa cells were then seeded to a suitable density and were left to deposit in the various recesses for 4–6 h. MCTS were then grown in the dark (37°C, 5% CO_2, 95% O_2, humid environment), until they reached a mean diameter ranging between 700 and 800 μm. For uptake experiments MCTS were incubated with RITC-pDNA labeled nanoparticles. The spheroids were then rinsed with PBS, fixed (4% PFA, 1 h, RT) and imaged by CLSM. 3D GFP transgene expression was promoted by incubating MCTS with nanoparticles and was then visualized by CLSM after 48 h. All CLSM images were acquired in z-stack mode with an average step of 6.17 μm. 3D reconstruction was performed either in Zeiss Zen software (2010) or Imaris software. The antitumoral effect of the tumor suppressor gene p53 in 3D microtissues was then analyzed. In brief, for p53 gene expression MCTS were transfected with CM-PFA nanocarriers loaded with the pcDNA3-FLAG-p53 expression cassette and spheroids volume was monitored by optical microscopy during 5 days. Measurement of spheroids volume variations were analyzed by image segmentation using automatic image threshold and applying a 2D mask (Fiji software).

Statistical Analysis

One-way analysis of variance (ANOVA), with the post-hoc Newman-Keuls test was used for comparing data of control (negative/positive) and multiple experimental groups. A confidence interval of 95% ($p<0.05$) was considered statistically significant. Data analysis was performed in GraphPad Prism v.6.0 (trial version; GraphPad software Inc, CA, USA).

RESULTS AND DISCUSSION

Synthesis and Formulation of CM-PFA Nanocarriers

The synthesis of folate-targeted multi-amino acid nanocarriers was performed by modifying the native polymeric backbone of low molecular weight chitosan primary amines with various amino acids and also FA-PEG as schematized in Fig. 1a. The successful inclusion of all biofunctional moieties was confirmed by FTIR and ^{1}H NMR spectroscopy (Fig. S1 and S4). The results obtained from ^{1}H NMR spectroscopy reveal that the PEG degree of substitution of chitosan was 46.02 ± 1.38% ($n=3$) (Supplementary information). Also, as demonstrated by Fig. S1 and S2, all the PEG blocks have FA targeting molecules since the characteristic maleimide peak of PEG disappears after thiol-maleimide conjugation between CM-P and FA. These results are corroborated by FTIR data which indicates the presence of the FA characteristic bands as shown in Fig. S4.

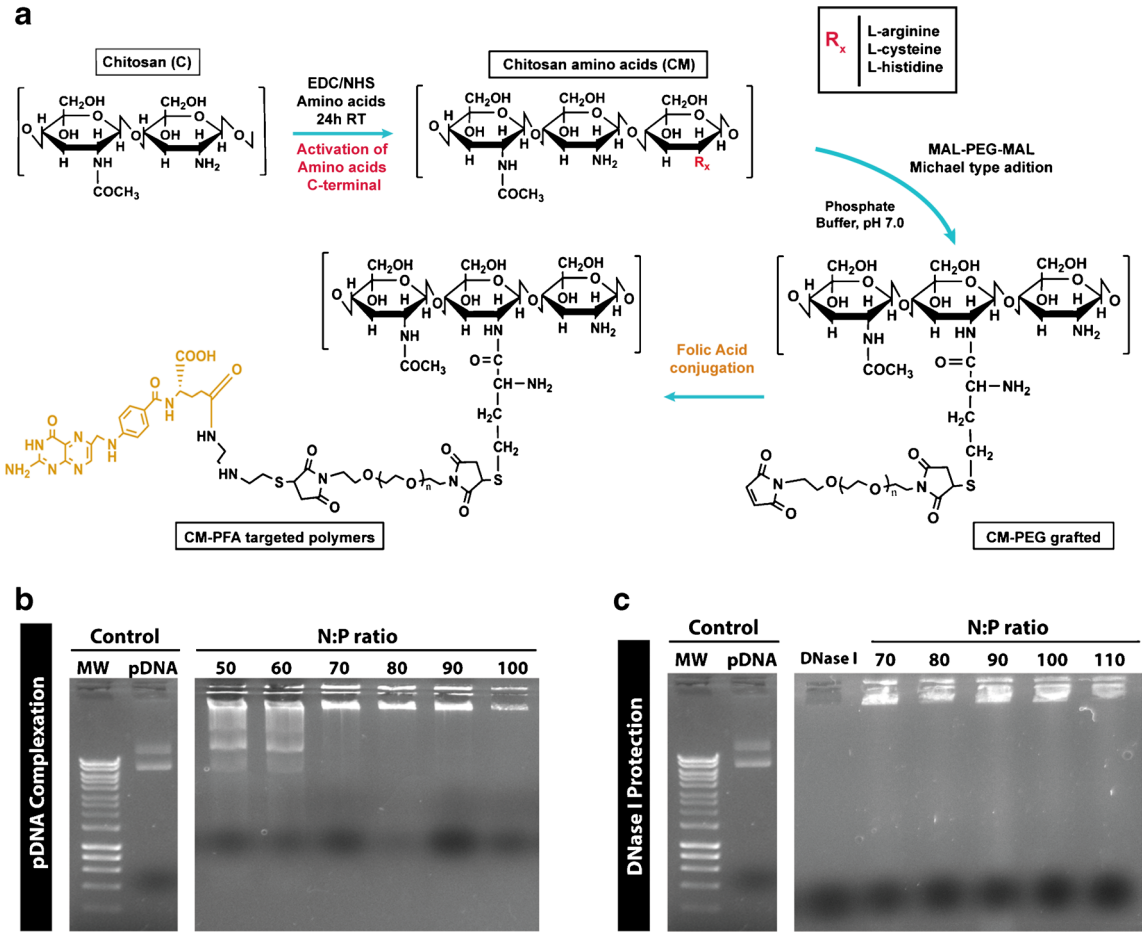

Fig. 1 CM-PFA polymers synthesis and complexation with pDNA. (**a**) Schematics of the chemical functionalization of the native chitosan backbone with amino acids, PEG and FA moieties. (**b**) Agarose gel electrophoresis of CM-PFA/pDNA complexation assay at various amine to phosphate ratios. (**c**) Agarose gel electrophoresis of endonuclease protection assay (DNaseI, 2 U^{-1} , in 5 mM $MgCl_2$, pH 7.4; during 30 min, at 37°C). MW-represents the DNA molecular weight marker. pDNA-represents control naked DNA.

Following CM-PFA synthesis the DNA complexation capacity of the polymer was investigated by agarose gel electrophoresis. The formulation of CM-PFA/pDNA nanocarriers was based on the establishment of attractive electrostatic interactions between polymer amines to pDNA phosphate groups with subsequent self-assembly into nanosized complexes stabilized by grafted PEG chains and decorated with FA. The self-assembled CM-PFA nanoparticles achieve total DNA complexation at a N:P 70 ratio (Fig. 1b). On the other hand, complexes formulated without the FA functionality but with the PEG hydrophilic shell (CM-P) achieve complexation at N:P 40 (Fig. S5). The recovery of the nanocarriers by centrifugation is important to remove free polymer that has not completed with pDNA. The results demonstrate that the CM-PFA complexes formed are highly stable and capable of protecting pDNA from nuclease-mediated destruction as demonstrated in Fig. 1c. This is an important parameter since free DNA is rapidly degraded by serum endonucleases after systemic administration and also in lysosomal compartments (34,35). Therefore protecting DNA biopharmaceuticals is of critical importance since the final therapeutic effect is completely dependent on their structural stability and biological activity (2).

Physicochemical Characterization and Cytotoxicity

The physicochemical characterization of the most stable CM-PFA nanoparticles regarding size, surface charge and morphology is shown in Fig. 2. Overall targeted carriers presented average diameters ranging from 126 nm to 176 nm, with the N:P 90 formulation yielding the smallest particles. The size of non-targeted systems obtained with CM-P polymers was slightly higher than that of the FA-decorated carriers (193 nm to 290 nm) (Fig. S6). The zeta potential of non-targeted carriers was highly positive (+18 to +27 mV), whereas, FA-targeted carriers exhibited slightly negative surface charge, a critical factor for *in vivo* applications (36). From these formulations the CM-PFA N:P 100 particles shown the most negative surface charge (Fig. 2c). The formulations of N:P 70 and N:P 90 demonstrated zeta potentials in the range of

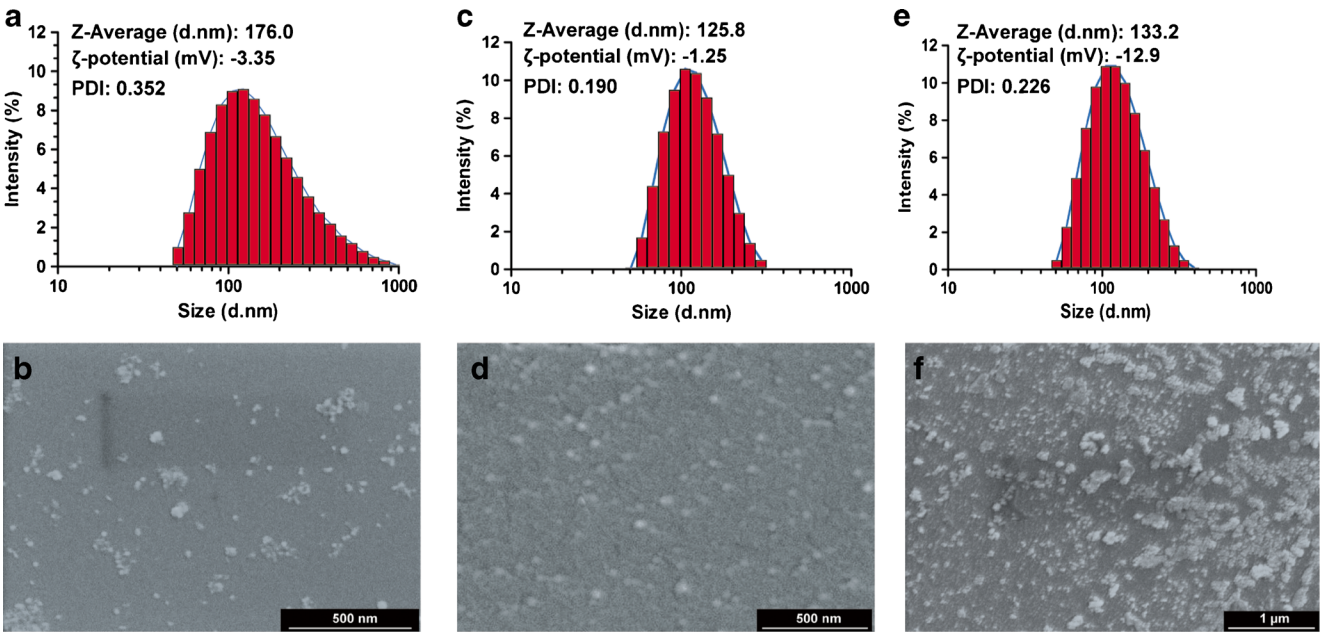

Fig. 2 DLS and morphological characterization of CM-PFA/pDNA nanocarriers. (**a**, **c** and **e**) Size distribution histograms, average size and zeta potential of nanocarriers formulated at N:P 70, 90 and 100, respectively. (**b**, **d** and **f**) SEM micrographs of the morphological characteristics of nanoparticles formulated at the before mentioned ratios.

neutrality (ζ ± 10 mV). From the tested formulations the N:P 70 carriers present the broadest particle size distribution, whereas the N:P 90 nanocarriers exhibited a polydispersity index (PDI) value of 0.19 (Fig. 2c) indicating that the particle size has a narrow distribution (i.e., PDI < 0.2 (37)). These results suggest that this formulation (N:P 90) is particularly suitable for therapeutic applications. The N:P 100 carriers present a PDI slightly higher than 0.2, a value representative of some polydispersity (Fig. 2e). Regarding the morphological characteristics all carriers have displayed spherical-like shapes as revealed by SEM analysis (Fig. 2b, d and f).

To evaluate the potential for intravenous administration the *in vitro* hemocompatibility was studied by quantifying erythrocytes lysis (Fig. 3). The quantitative and qualitative results, indicate a negligible effect on RBCs after incubation with concentrations up to 500 µg/mL (<1% of hemoglobin released). These results are in accordance with the guidelines issued by international agencies (ISO/TR 7406) regarding the critically safe hemolytic ratio, since less than 5% of hemoglobin is released (38). Moreover, as shown in Fig. 3b, SEM analysis reveals that RBCs maintained their characteristic round-shape with a confined central pallor (39), further indicating that CM-PFA based carriers could be administered via intravenous route without deleterious effects for these cells.

In vitro cytotoxicity assays were also performed in both HeLa and hFIB cell lines and have shown that more than 90% viability was obtained at various concentrations and up to 72 h of incubation (Fig. S7). These findings demonstrate the potential of FA-targeted systems for pDNA delivery without eliciting severe toxicity.

Targeted Carriers Cell Uptake and Gene Expression in Single Cultures of Cancer Cells

The effect of FA functionalization of the surface of nanocarriers was expected to increase cellular uptake in folate receptor positive (FR+) cancer cells. Therefore, HeLa cells which over-express the receptors of folic acid according to several reports in the literature (19,40), were selected as target cells for pDNA specific delivery. After cancer cells were treated with equivalent concentrations of either CM-PFA or CM-P nanocarriers for 4 h, the FA functionalized carriers exhibited an evident and significantly higher cellular uptake than non-targeted systems ($p < 0.05$) (Fig. S9 a and b). Among the different formulations of targeted nanoparticles no substantial differences in cellular uptake were observed ($p < 0.05$) (Fig. 4a).

This improved uptake originated a considerably higher GFP transgene expression in cancer cells as shown in Fig. 5a. Actually, in comparison with plain CM-P carriers the targeted particles achieve a noteworthy 3.7 fold increased gene expression (Fig. 5a).

The three different formulations of CM-PFA carriers did not displayed significant differences in gene expression, however since the N:P 90 formulation presents the most suitable conjugation of physicochemical characteristics and biological activity as recently summarized by Ernsting *et al.*, 2013 (36), these carriers were selected for posterior experiments. A visual

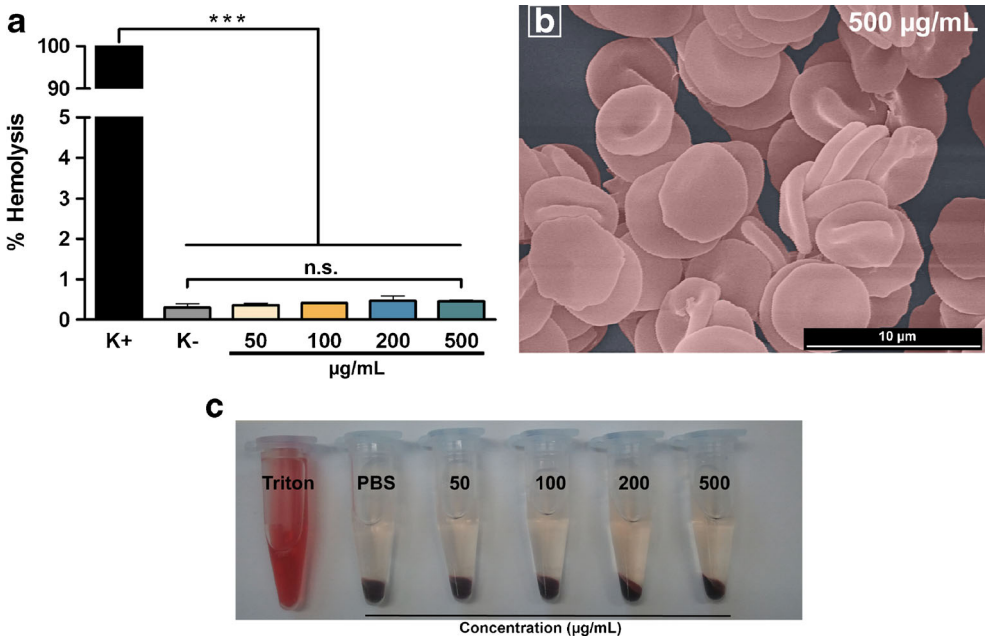

Fig. 3 Hemocompatibility assays of CM-PFA functional polymers. (**a**) UV–vis quantification of RBCs released hemoglobin after incubation with a range of polymer concentrations for 1 h, 37°C. (**b**) Representative pseudo-colored SEM micrograph of RBCs morphology after incubation. (**c**) Optical photograph of the supernatants recovered after the assay for posterior quantification of hemoglobin release. Triton-X 100 was used as positive control for RBCs lysis (K+). PBS was used as negative control. Data is represented as mean ± s.d., $n = 3$; ***$p < 0.001$.

comparison of GFP expression also noticeably reveals the fluorescence intensity differences obtained between PEI 25kDa, non-targeted carriers and FA-decorated systems (Fig. 5b to f). These findings demonstrate the improved delivery and targeting capacity of multifunctional CM-PFA systems in comparison with plain carriers. The relatively low transfection efficiency obtained with PEI is likely due to the transfection conditions used such as the inclusion of serum in the culture medium. This is important since serum presence mimics the *in vivo* conditions. Overall, the fact that gene expression and cellular uptake are simultaneously enhanced supports the hypothesis that including FA-targeting capacity in amino acid-modified nanocarriers further increases their therapeutic efficacy.

To actually confirm that the enhanced cellular uptake and gene expression was directly associated with receptor mediated endocytosis via FR+ cells, a competitive binding assay for the target receptor was performed. For this purpose HeLa cells were incubated with various concentrations of free folic acid and short afterwards with targeted nanocarriers. The obtained results reveal an average 89% decrease in GFP gene expression upon addition of 5 mM of folic acid, and only residual expression is obtained at higher concentration (10 mM) (Fig. S8). Such major reduction supports the concept that CM-PFA carriers are mostly internalized via FR biorecognition.

Targeted Delivery in HeLa:hFIB 2D Co-cultures

2D co-culture models are excellent testing platforms for evaluating the realistic targeting specificity in conditions that closely resemble the actual tumor microenvironment in terms of cell heterogeneity (25). In fact, in comparison with standard *in vitro* cultures, these models offer a more complete approach that takes into account not only the establishment of close cell-cell contacts, but also the cooperative cancer-normal cells response to drugs or genes with anti-tumoral activity (25,41). This combined reaction is commonly associated with the development of an innate resistant phenotype and may affect the therapeutic effectiveness and biological performance of targeted delivery (41). Actually, as recently demonstrated in the seminal work of Straussman *et al.*, 2012, the stromal components of the tumor microenvironment, particularly fibroblasts, assure cancer cells resistance to various anti-tumoral drugs by growth factors secretion (41). This is an important parameter that cannot be evaluated in standard unicellular cultures. Taking this into account, the selectivity of FA-targeted delivery was also evaluated in 2D co-cultures of HeLa and hFIB cells. For these assays, a 1:2 ratio of HeLa:hFIB cells was used as previously recommended in the literature (42). The co-cultured cells remained viable during the course of all experiments and exhibited the characteristic morphologies of both HeLa and hFIB cells as shown in Fig. S7. Fluorescence images revealed that incubation of non-targeted nanocarriers in co-cultures promotes indiscriminate internalization, with CM-P nanoparticles being localized in both HeLa and hFIb cells (Fig. 6a, c, e and g).

On the contrary, upon CM-PFA administration to 2D co-cultures an evident selectivity towards target cancer cells was observed since extensive uptake occurs in HeLa cells and very few fibroblasts have internalized

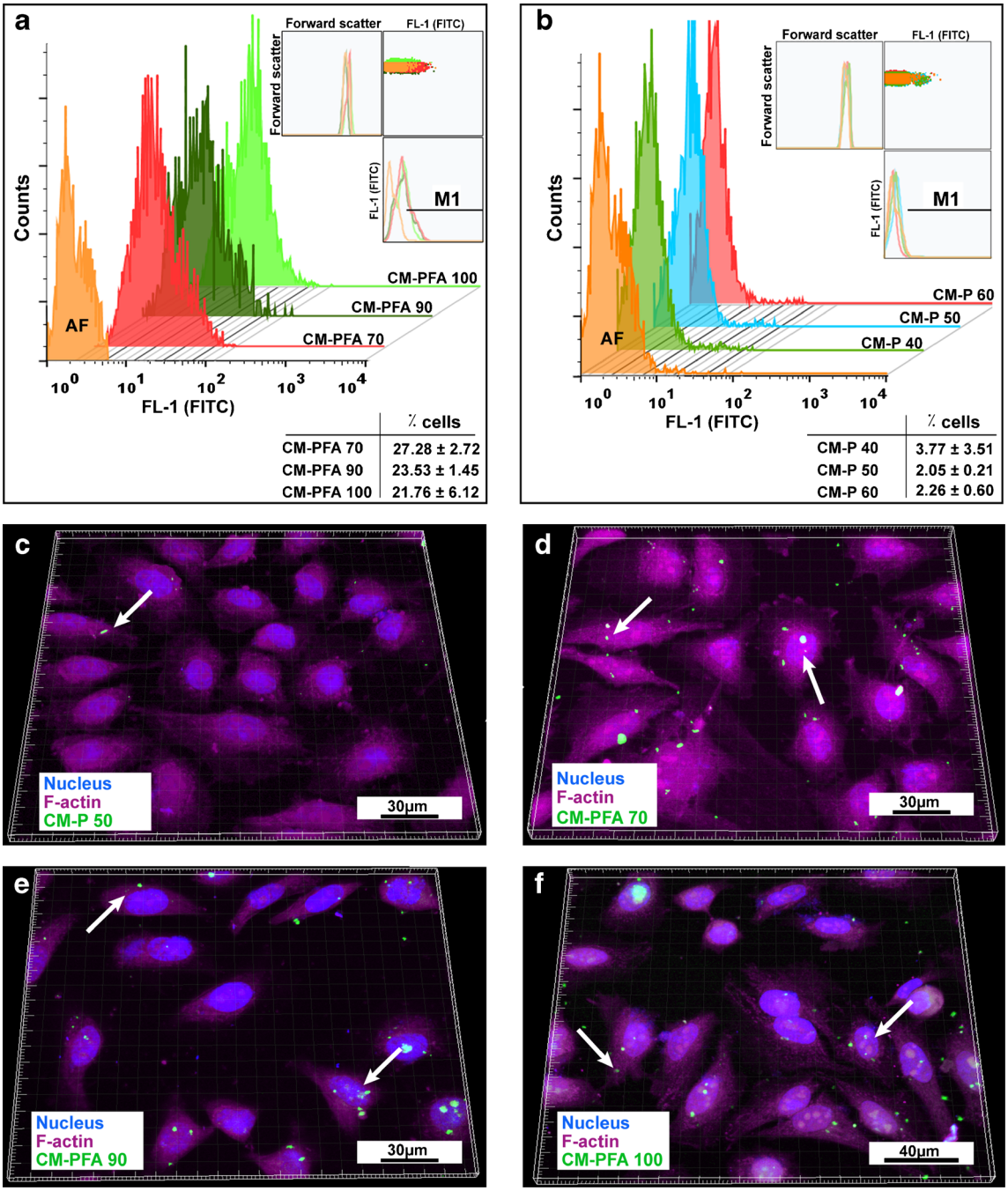

Fig. 4 Flow cytometry and CLSM analysis of nanocarriers uptake in monocultures of HeLa cells. (**a** and **b**) Cellular uptake analysis of targeted CM-PFA and non-targeted CM-P/ FITC-pDNA loaded nanocarriers, respectively. Data represents mean ± s.d., $n = 3$. AF- represents non-treated cells. M1-represents the marker used for analysis of FL-1 positive cells. (**c**) Representative non-targeted nanocarriers cellular uptake.(**d, e** and **f**) Nanoparticle cellular uptake of CM-PFA systems formulated at various ratios. *Blue channel*: Hoechst 33342® labeled nucleus; *Purple channel:* Actin-F-actin Alexa 647 conjugate antibody; *Green Channel*: Pseudocolored CM-PFA/RITC labeled pDNA nanocarriers. *White arrows* indicate nanoparticles.

nanoparticles (Fig. 6b, d, f and h). These results indicate that CM-PFA/pDNA nanocarriers present a genuine affinity for FR+ cells even in the presence of stromal fibroblasts. To further complement these results with a more broad evaluation of targeted nanoparticles uptake in co-cultured cell populations we also studied cell targeting selectivity by flow cytometry in order to obtain a quantitative analysis of CM-PFA particle uptake in cancer cells and normal cells. To distinguish normal cell populations from HeLa cells the latter were stained with an Actin-GFP fusion protein. This approach allowed the separation of both cell types and an individual analysis of

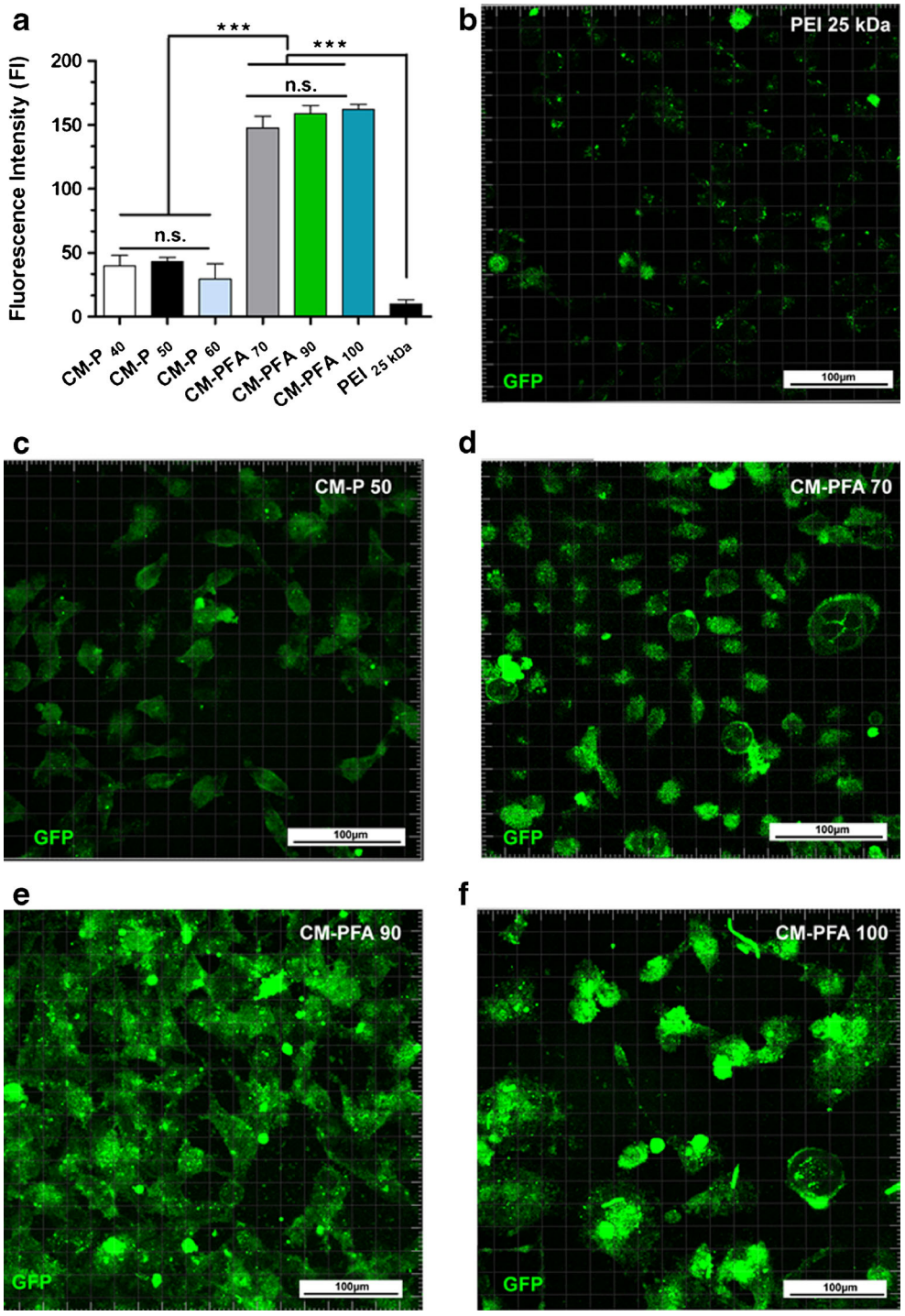

Fig. 5 GFP gene expression in mono-cultured cancer cells. (**a**) Quantification of nanocarriers-mediated GFP expression. PEI 25 kDa N:P 5 carriers were used as controls. (**b** to **f**) Representative fluorescence images of GFP expression. Data is presented as mean ± s.d., $n = 5$, ***$p < 0.001$. n.s.- non significant.

particle internalization. Our findings demonstrated that approximately 30% of HeLa cells have internalized FA-decorated particles, whilst cellular uptake in hFIB cells was negligible (0.84%) (Fig. 7f).

Therefore, when CM-PFA (N:P 90) nanoparticles were administered to a co-culture of FR+ HeLa cells and hFIB (Folate receptor negative) (40), the pDNA cargo is mostly delivered in target cells. Overall, flow cytometry results were consistent with those obtained by fluorescence microscopy. It is essential to underline that these findings were attained in co-cultures that have a higher number of fibroblasts in respect to cancer cells (2:1 ratio). Achieving this degree of selectivity, even in the presence of a higher amount of normal cells, is important to limit off-target events and reduce non-specific cytotoxicity.

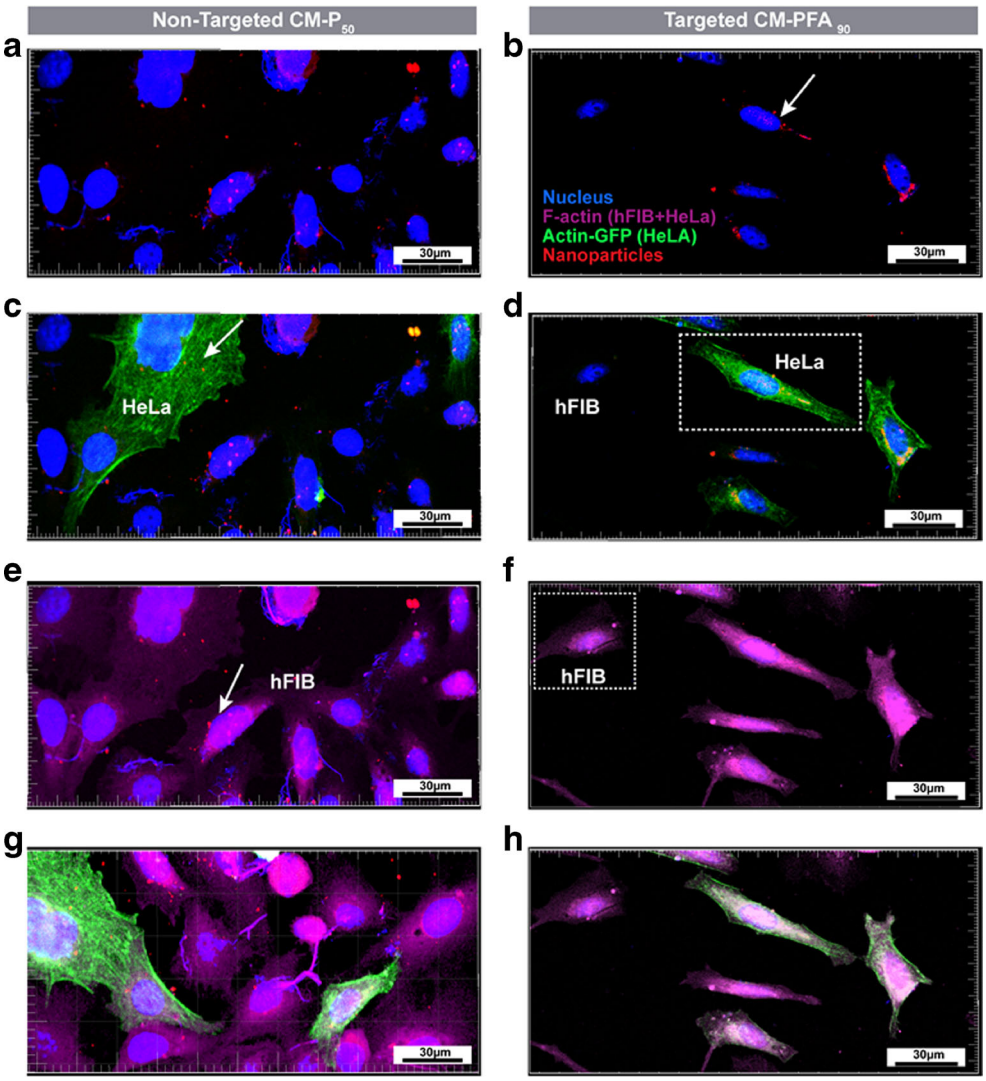

Fig. 6 CLSM analysis of nanocarriers uptake in 2D co-cultures of HeLa and hFIB cells (1:2 ratio). (**a**, **c**, **e** and **g**) Fluorescence images of non-targeted nanoparticles uptake. (**b**, **d f** and **h**) Fluorescence images of FA-targeted CM-PFA/pDNA nanoparticles. *Blue channel*: Hoechst 33342® labeled nucleus; *Purple channel*: Anti-F-actin Alexa 647 conjugate antibody; *Green Channel*: Actin-GFP expressing HeLa cells. *Red channel*: RITC labeled pDNA. *White arrows* indicate nanoparticles.

Nanocarriers Penetration and Anti-tumoral Activity in 3D Microtissues

Self-assembly of HeLa 3D spheroids was carried out in hydrogel micro-molded scaffolds as schematized in Fig. 8a. 3D spheroid models are a unique platform for testing novel nanocarriers since they provide *in vitro* a correlation with *in vivo* solid tumors and are excellent models to study drug or nanoparticle penetration (26). Actually, these 3D models mimic *in vitro* tumors that are poorly vascularized. Penetration into this type of tumors is an issue since generally a poor diffusive transport and limited spatial distribution into deep tumor regions is obtained after drug or nanoparticle administration (43). The assembled 3D spheroid models had sizes in the range of 700–800 µm, an important parameter since it has been described by that spheroids larger than 500 µm possess all the features of solid tumors (e.g. solid structure, necrotic regions, pH and waste gradients) (44). The spheroids also displayed a highly reproducible and defined spherical shape as demonstrated in the optical micrographs of (Fig. 9a to c).

Assuring this high degree of reproducibility is currently only possible due to the use of micromolding-based technologies (33). This manufacturing method presents several improvements in comparison with standard spheroid production techniques and is presently the best high-throughput approach to produce a large number of reproducible microtissues (26). Therefore, the tumor penetration mediated by CM-PFA targeted nanocarriers was evaluated in 3D MCTS in an attempt to investigate nanocarriers therapeutic potential. The CM-PFA targeted nanoparticles achieved considerable penetration in comparison to non-targeted and control PEI25kDa particles (Fig. 8e, f and g). Moreover, a significantly higher number of cells were positive for CM-PFA incubated spheroids as evidenced by the dense and red signal (nanoparticles) observed in Fig. 8d.

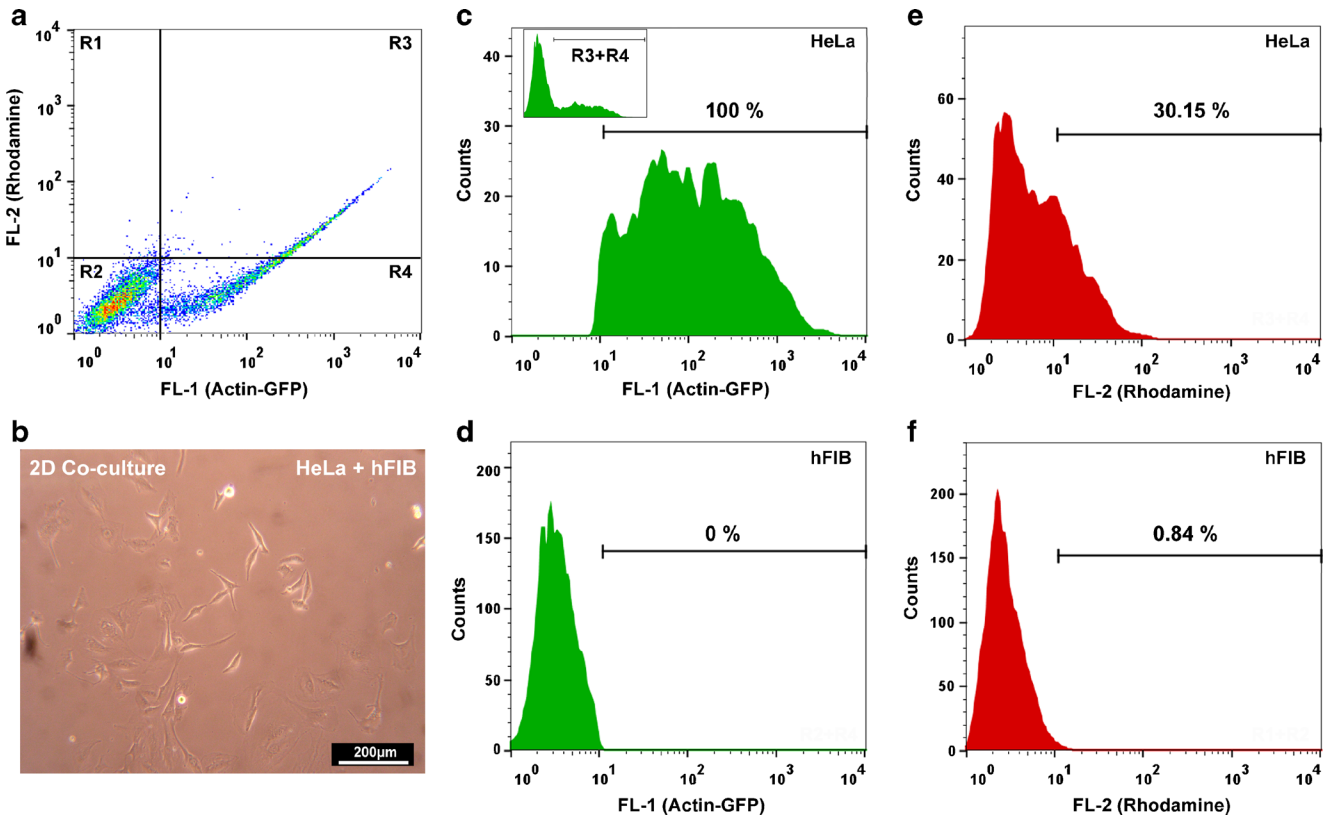

Fig. 7 Flow cytometry analysis of targeting selectivity in 2D co-culture populations. (**a**) Pseudocolor dot-plots of co-cultured HeLa-GFP and hFIB cells. (**b**) Representative optical contrast photograph of 2D co-cultures of HeLa and hFIB cells. (**c** and **d**) Histograms of Actin-GFP fluorescence (FL-1) in HeLa and hFIB cells, respectively. 100% represents the GFP-actin gate used for separating HeLa from hFIB (**e** and **f**) Histograms of CM-PFA/RITC-pDNA nanoparticles (FL-2) in HeLa and hFIB cells, respectively.

We hypothesize that these differences in 3D uptake can be correlated with the effects of FA targeting, but also of zeta potential influence on tumor penetration as recently reviewed by Ernsting *et al.*, 2013 (36). It has been reported that particles with highly positive zeta potential exhibit very limited penetration and distribute non-homogenously inside tumors, whereas particles with zeta potential in the range of (±10 mV) travel further into deep tumor regions and in an homogenous mode (36). Taking into account that control particles (PEI 25kDa) and non-targeted CM-PFA have highly positive surface charge (+25.7 and +18.5 mV, Fig. S4) they are more likely to interact with negatively charged cell glycosaminoglycans (e.g. hyaluronic and sialic acid) and thus showed limited penetration in 3D MCTS. Moreover, as demonstrated in Fig. 2, CM-PFA nanocarriers formulated at N:P 90 present a suitable surface charge for tumor penetration (−1.25 mV). In comparison with nanoparticles functionalized with F3 peptides such as those reported by Hu *et al.*, 2013, the CM-PFA systems achieve approximately 1.86 fold higher tumor penetration, indicating their effectiveness (45). These interesting results obtained in 3D MCTS evidence the necessity of further exploring the effects of targeting and particle surface charge on the extent of tumor penetration in other types of delivery systems. This data can be important in the future to shed light on the most important parameters for improving 3D tissue penetration.

Regarding 3D gene expression, the synthesized CM-PFA systems originated evident GFP expression in MCTS. Actually, has shown by the results of Fig. 9h and the 3D reconstruction (Fig. 9d and g), CM-PFA carriers promoted considerable GFP expression. A quantitative analysis revealed that FA-targeted nanocarriers attained a 8.9 fold higher gene expression in comparison to that of PEI 25kDa nanocarriers and a 7.8 fold higher expression than that of non-targeted CM-P nanoparticles (Fig. 9h, $p<0.001$, $n=10$). To further confirm this therapeutic potential targeted carriers were loaded with a gene expression cassette that encodes the p53 gene with the objective to trigger an anti-tumoral response mediated by this renowned tumor suppressor.

The obtained results after particle administration showed that the administration of CM-PFA/pcDNA3-FLAG-p53 loaded nanocarriers promoted spheroids disruption after 5 days (Fig. 10d to f) in comparison with control spheroids that proliferated during the time of the assay (Fig. 10a to c). A high throughput analysis ($n=25$) based on the automatic segmentation of a large number of treated and non-treated

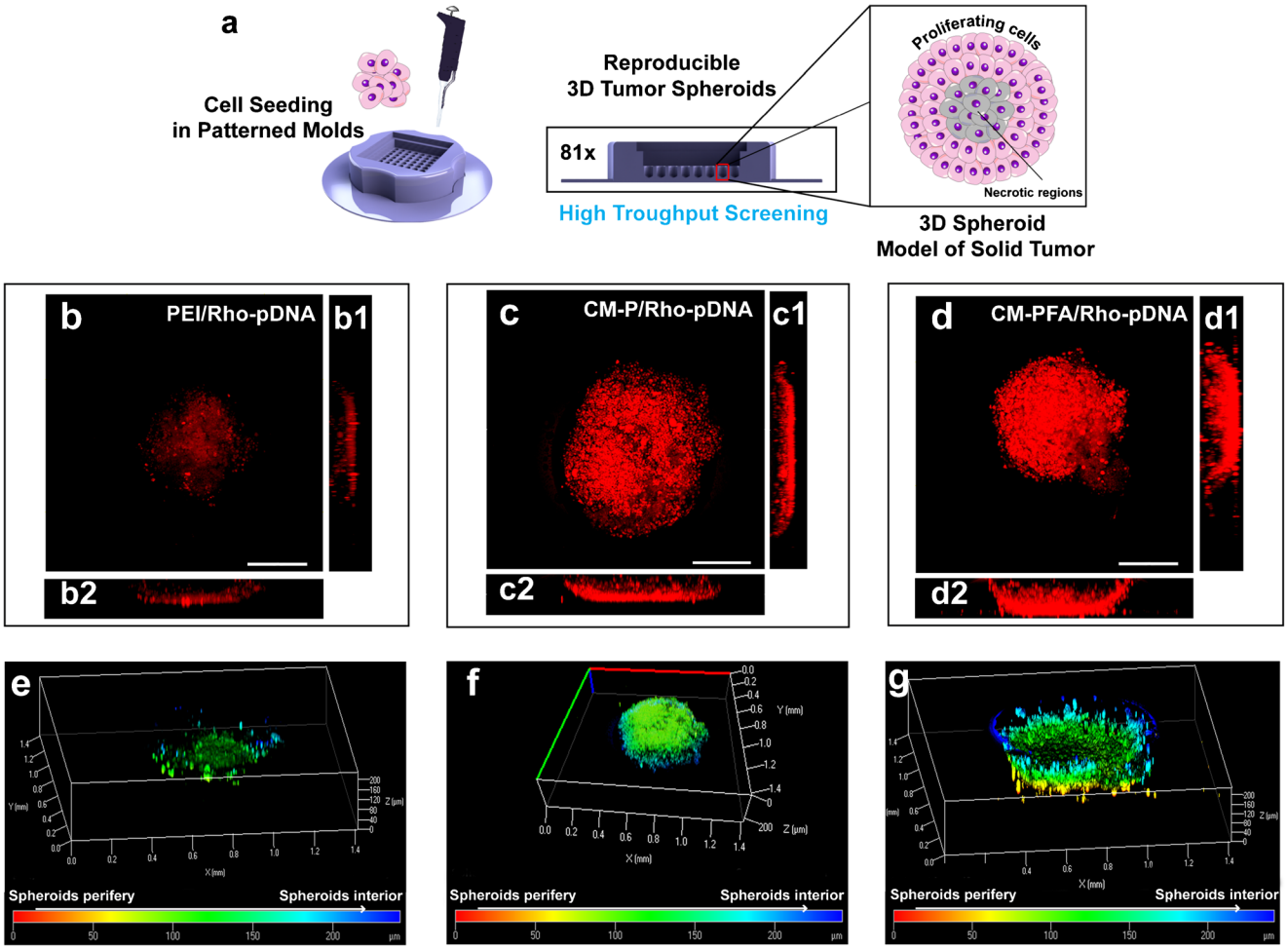

Fig. 8 Analysis of nanoparticle penetration in 3D microtissues. (**a**) Schematics of 3D spheroids manufacture using scaffolds. (**b**, **c** and **d**) Orthogonal projections of PEI 25kDa, CM-P N:P 50, CM-PFA N:P 90 RITC-pDNA loaded nanocarriers penetration in 3D spheroids, respectively. *Red channel*: RITC-pDNA. (**e**, **f** and **g**) Color coded depth analysis of targeted and non-targeted carriers penetration in 3D tumor spheroids. Color bar represents depth in micrometers (μm). PEI 25kDa were used as controls.

spheroids showed that 3D MCTS undergo an average 39% volume reduction after a single p53 administration (Fig. 10g). These findings demonstrate the capacity of CM-PFA systems in terms of both penetration and gene delivery into solid tumor models that closely mimic *in vivo* tumors. These findings emphasize that the novel features of chitosan given by the amino acids modification and folate targeting increase its effectiveness. In fact, in comparison with other chitosan-based drug delivery systems such as those reported by Kim and co-workers (46) this novel chitosan derivative (CM-PFA) presents low cytotoxicity since at 200 µg/mL more than 95% of the cells remain viable (Fig. S7). This is an important characteristic since a higher dose can be delivered without severe side effects. Moreover, the inclusion of amino acids and folic acid in the nanocarriers promotes an enhanced uptake in target cells (Fig. 7) and also an improved lysosomal escape as our group previously demonstrated (23). This improved capacity is associated with the inclusion of both histidine and arginine which promote an escape via the proton sponge effect (23). An effective escape from these vesicles is associated with an improved gene expression. As such, this amino acid modified system presents higher transgene expression in comparison with other folate targeted chitosan nanocarriers such as those described by Shen and co-workers (47). More importantly these systems have evidenced their effectiveness also in 3D tumor models

Fig. 9 GFP expression in 3D tumor microtissues. (**a**, **b** and **c**) Optical ▶ contrast microscopy analysis of 3D tumor spheroids morphology after incubation with control (PEI 25kDa), non-targeted and FA-targeted nanocarriers, respectively. Confocal images of GFP expression in 3D spheroids incubated with targeted (N:P 90) (**d**1 to **d**6), non-targeted (N:P 50) (**d**7 to **d** 12) and control (PEI 25kDa) nanocarriers (**d**13 to **d**18). *Green channel*: GFP expression. *Grey-white channel*: differential interference contrast (DIC) images. The white squares around the 3D spheroids are the recesses of the micro-molded scaffold in which the microtissues are grown. Scale bar represents 700 μm. GFP expression in 3D spheroids mediated by control (PEI 25kDa) (**e**, **e**1 and **e**2), non-targeted (**f**, **f**1 and **f**2) and targeted carriers (**g**, **g**1 and **g**2). (**h**) Analysis of GFP fluorescence intensity in 3D. Data is presented as mean ± s.d., $n = 10$, $^{***}p < 0.001$.

since a significant reduction in the volume of tumor spheroids was obtained (Fig. 10). These results led us to conclude that the CM-PFA system presents suitable characteristics for therapeutic applications.

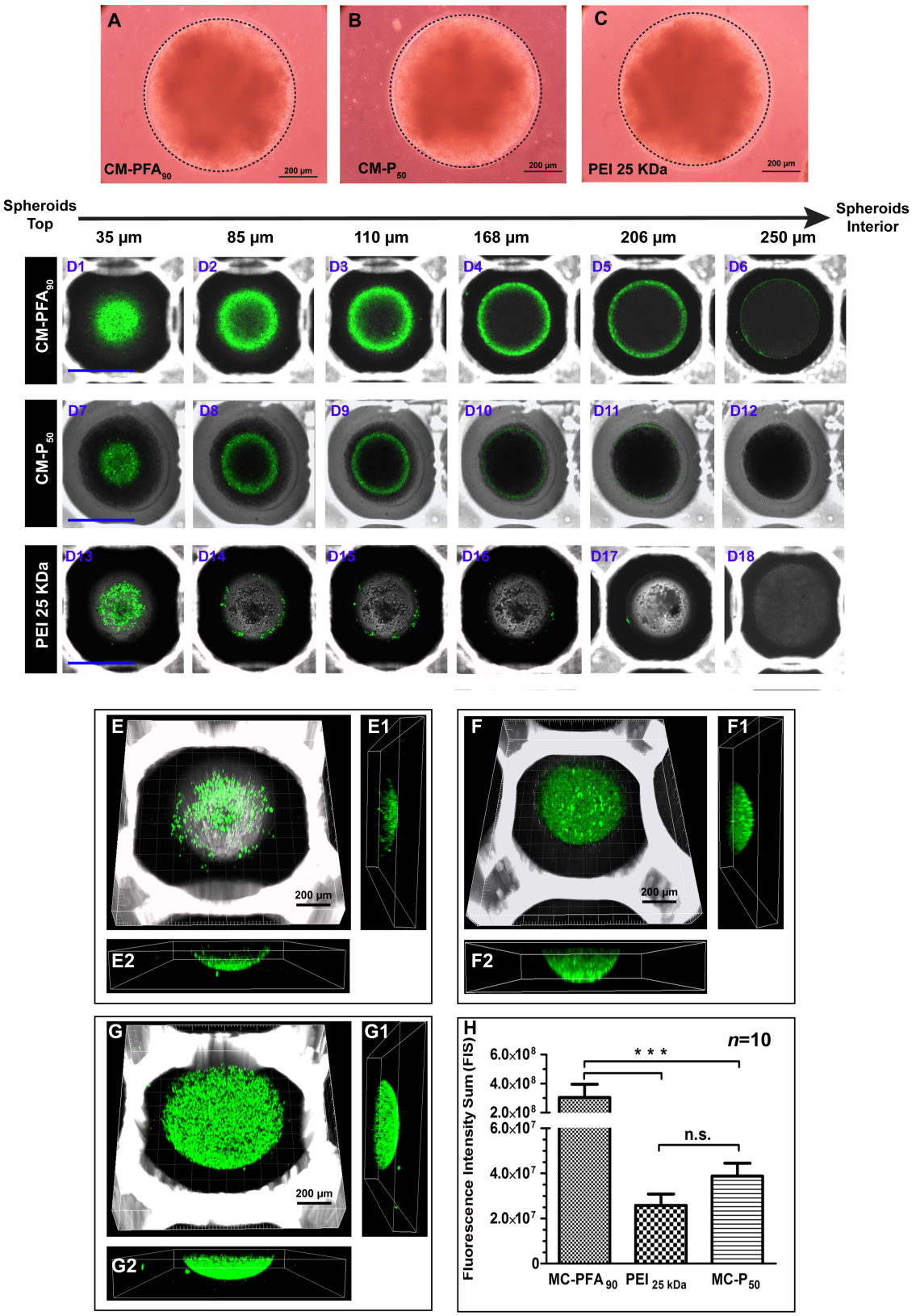

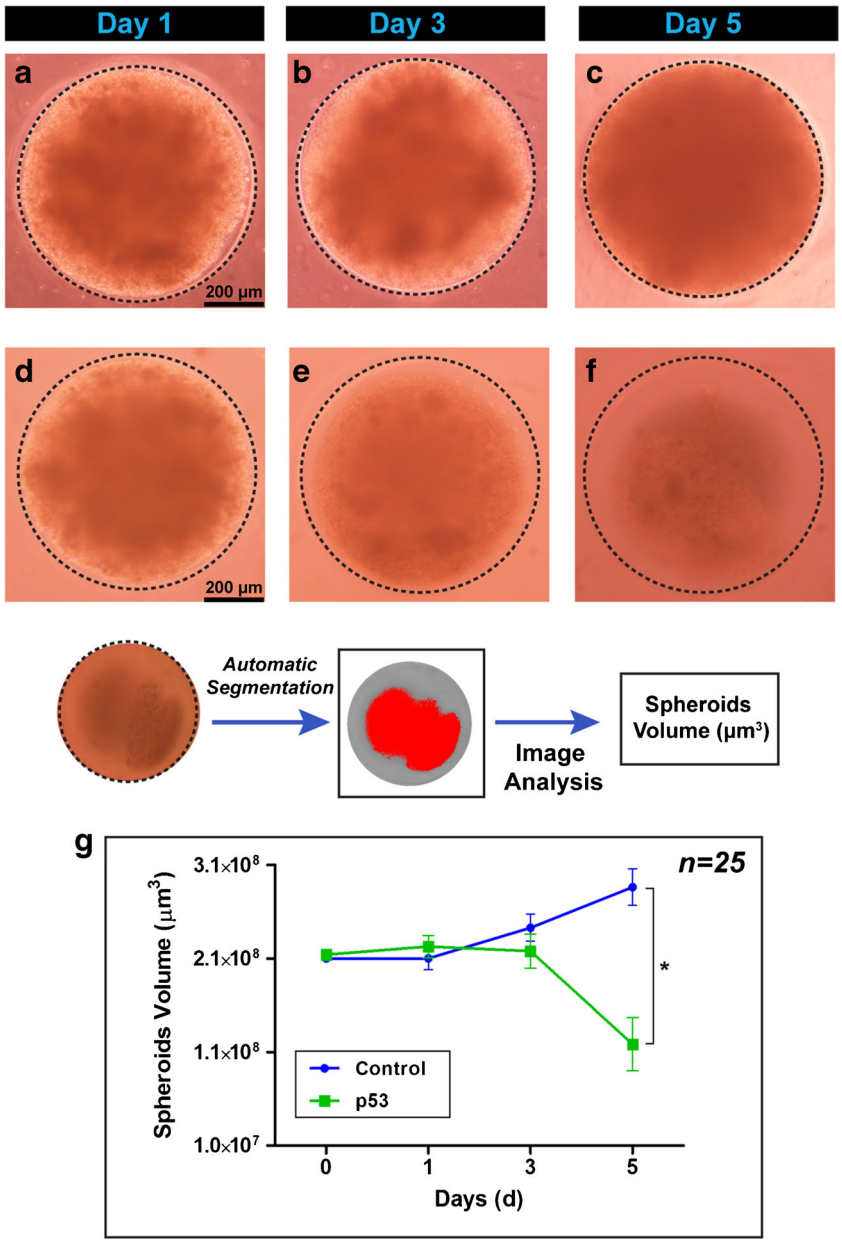

Fig. 10 Evaluation of p53 anti-tumoral activity following CM-PFA delivery of the pcDNA3-FLAG-p53 plasmid to 3D tumor spheroids. Optical contrast microscopy images of non-treated spheroids (**a**, **b** and **c**) and p53 treated spheroids (**d**, **e** and **f**). (**g**) High throughput analysis of spheroids volume reduction after pcDNA3-FLAG-p53 administration during 5 days. Quantification was performed via automatic imaging segmentation. Data is presented as mean ± s.d., $n = 25$, $^{*}p < 0.05$.

CONCLUSIONS

In this study we synthesized a folate receptor-targeted and PEG grafted amino acid functionalized chitosan-based system for delivery of pDNA biopharmaceuticals into target cancer cells. This novel system assembled in to small nanosized nanoparticles with high hemocompatibility and low cytotoxicity demonstrating proper characteristics for *in vivo* application. The grafted PEG chains further contribute for the stability in physiological conditions and the amino acid moieties have previously shown to enhance exogenous gene expression.

This system exhibited improved cellular uptake and increased GFP expression in monocultures of cancer cells in comparison with non-targeted carriers. Folic acid decoration promoted the establishment of a genuine affinity towards FR+ cancer cells even when closely co-cultured with higher numbers of normal cells. To the best of our knowledge this was the first time that FA-targeted nanocarriers affinity towards target receptors was evaluated in dynamic 2D co-culture models that contained both cancer and stromal fibroblasts. The obtained results provide a rationale for future evaluation of other nanocarriers targeted for different cell receptors.

Moreover, the manufacture of 3D spheroid models with micro-molded templates unlocked the possibility to use testing platforms that provided highly reproducible microtissue models and allowed a high throughput analysis of different experimental conditions. From this standpoint the data gathered in 3D MCTS evidences that these carriers possess

considerable efficiency and also demonstrates that a homogeneous gene expression occurs in 3D. This fact led to an antitumoral effect upon CM-PFA-mediated delivery of the p53 tumor suppressor to 3D MCTS. A part from this, the results obtained with 3D spheroids also indicate that in the future studies concerning the effect of targeting moieties and particle physicochemical properties on tissue penetration should be further characterized. The *in vivo* efficacy and maximum tolerated dose of these nanocarriers will be evaluated in a near future.

Overall, the results led us to conclude that CM-PFA/pDNA nanocarriers present significant potential for future application in cancer therapy.

ACKNOWLEDGMENTS

The authors would like to acknowledge Eng. Ana Paula for her help with the acquisition of SEM images. This work was supported by the Portuguese Foundation for Science and Technology (FCT), (PTDC/EBB-BIO/114320/2009 and PEst-C/SAU/UI0709/2011). Vítor M. Gaspar is grateful for the PhD fellowship from FCT (SFRH/BD/80402/2011). All the authors do not disclose any conflict of interest.

REFERENCES

1. Zhang X-Q, Xu X, Bertrand N, Pridgen E, Swami A, Farokhzad OC. Interactions of nanomaterials and biological systems: implications to personalized nanomedicine. Adv Drug Deliv Rev. 2012;64:1363–84.
2. Gaspar VM, Correia IJ, Sousa Â, Silva F, Paquete CM, Queiroz JA, *et al*. Nanoparticle mediated delivery of pure P53 supercoiled plasmid DNA for gene therapy. J Control Release. 2011;156:212–22.
3. Ragelle H, Vandermeulen G, Préat V. Chitosan-based siRNA delivery systems. J Control Release. 2013;172:207–18.
4. Carocho M, Ferreira ICFR. The role of phenolic compounds in the fight against cancer–a review. Anti-Cancer Agents Med Chem (Formerly Current Medicinal Chemistry-Anti-Cancer Agents). 2013;13(1236–58).
5. Cho H, Lai TC, Kwon GS. Poly (ethylene glycol)-block-poly (ε-caprolactone) micelles for combination drug delivery: evaluation of paclitaxel, Cyclopamine and Gossypol in Intraperitoneal Xenograft Models of Ovarian Cancer. J Control Release. 2013;166:1–9.
6. Maeda H. Tumor-selective delivery of macromolecular drugs via the EPR effect: background and future prospects. Bioconjug Chem. 2010;21:797–802.
7. Bergersand G, Benjamin LE. Tumorigenesis and the angiogenic switch. Nat Rev Cancer. 2003;3:401–10.
8. Decuzzi P, Pasqualini R, Arap W, Ferrari M. Intravascular delivery of particulate systems: does geometry really matter? Pharm Res. 2009;26:235–43.
9. van de Ven AL, Kim P, Haley OH, Fakhoury JR, Adriani G, Schmulen J, *et al*. Rapid tumoritropic accumulation of systemically injected plateloid particles and their biodistribution. J Control Release. 2012;158:148–55.
10. Florence AT. "Targeting" nanoparticles: the constraints of physical laws and physical barriers. J Control Release. 2012;164:115–24.
11. Hollis CP, Weiss HL, Leggas M, Evers BM, Gemeinhart RA, Li T. Biodistribution and bioimaging studies of hybrid paclitaxel nanocrystals: lessons learned of the EPR effect and image-guided drug delivery. J Control Release. 2013;172:12–21.
12. Danhier F, Feron O, Préat V. To exploit the tumor microenvironment: passive and active tumor targeting of nanocarriers for anticancer drug delivery. J Control Release. 2010;148:135–46.
13. Farokhzad OC, Cheng J, Teply BA, Sherifi I, Jon S, Kantoff PW, *et al*. Targeted nanoparticle-aptamer bioconjugates for cancer chemotherapy in vivo. Proc Natl Acad Sci. 2006;103:6315–20.
14. Chen R, Braun GB, Luo X, Sugahara KN, Teesalu T, Ruoslahti E. Application of a proapoptotic peptide to intratumorally spreading cancer therapy. Cancer Res. 2013;73:1352–61.
15. Choe U-J, Rodriguez AR, Lee BS, Knowles SM, Wu AM, Deming TJ, *et al*. Endocytosis and intracellular trafficking properties of transferrin-conjugated block copolypeptide vesicles. Biomacromolecules. 2013;14:1458–64.
16. Panand J, Feng S-S. Targeting and imaging cancer cells by folate-decorated, quantum dots (QDs)-loaded nanoparticles of biodegradable polymers. Biomaterials. 2009;30:1176–83.
17. Chen C, Ke J, Zhou XE, Yi W, Brunzelle JS, Li J, *et al*. Structural basis for molecular recognition of folic acid by folate receptors. Nature. 2013;500:486–9.
18. Mi Y, Liu Y, Feng S-S. Formulation of docetaxel by folic acid-conjugated d-α-tocopheryl polyethylene glycol succinate 2000 (Vitamin E TPGS2k) micelles for targeted and synergistic chemotherapy. Biomaterials. 2011;32:4058–66.
19. Garcia-Bennett A, Nees M, Fadeel B. In search of the holy grail: folate-targeted nanoparticles for cancer therapy. Biochem Pharmacol. 2011;81:976–84.
20. Wu M, Gunning W, Ratnam M. Expression of folate receptor type α in relation to cell type, malignancy, and differentiation in ovary, uterus, and cervix. Cancer Epidemiol Biomark Prev. 1999;8:775–82.
21. C. Aranda, K. Urbiola, A. Méndez Ardoy, J.M. García Fernández, C. Ortiz Mellet, and C.T. de Ilarduya. Targeted gene delivery by new folate–polycationic amphiphilic cyclodextrin–DNA nanocomplexes in vitro and in vivo. European Journal of Pharmaceutics and Biopharmaceutics. 2013;85:390–7.
22. Kogure K, Akita H, Yamada Y, Harashima H. Multifunctional envelope-type nano device (MEND) as a non-viral gene delivery system. Adv Drug Deliv Rev. 2008;60:559–71.
23. Gaspar V, Marques J, Sousa F, Louro R, Queiroz J, Correia I. Biofunctionalized nanoparticles with pH-responsive and cell penetrating blocks for gene delivery. Nanotechnology. 2013;24:275101.
24. HogenEschand H, Nikitin AY. Challenges in pre-clinical testing of anti-cancer drugs in cell culture and in animal models. J Control Release. 2012;164:183–6.
25. Costa EC, Gaspar VM, Marques JG, Coutinho P, Correia IJ. Evaluation of nanoparticle uptake in co-culture cancer models. PLoS One. 2013;8:e70072.
26. Mehta G, Hsiao AY, Ingram M, Luker GD, Takayama S. Opportunities and challenges for use of tumor spheroids as models to test drug delivery and efficacy. J Control Release. 2012;164:192–204.
27. H.-l. Ma, Q. Jiang, S. Han, Y. Wu, J. Cui Tomshine, D. Wang, Y. Gan, G. Zou, and X.-J. Liang. Multicellular tumor spheroids as an in vivo-like tumor model for three-dimensional imaging of chemotherapeutic and nano material cellular penetration. Molecular imaging. 2012;11:487–98.
28. Vargo-Gogolaand T, Rosen JM. Modelling breast cancer: one size does not fit all. Nat Rev Cancer. 2007;7:659–72.
29. Yoshii Y, Waki A, Yoshida K, Kakezuka A, Kobayashi M, Namiki H, *et al*. The use of nanoimprinted scaffolds as 3D culture models to facilitate spontaneous tumor cell migration and well-regulated spheroid formation. Biomaterials. 2011;32:6052–8.

30. Zhang C, Gao S, Jiang W, Lin S, Du F, Li Z, *et al*. Targeted minicircle DNA delivery using folate–poly(ethylene glycol)–polyethylenimine as non-viral carrier. Biomaterials. 2010;31:6075–86.
31. van Gaal EV, van Eijk R, Oosting RS, Kok RJ, Hennink WE, Crommelin DJ, *et al*. How to screen non-viral gene delivery systems in vitro? J Control Release. 2011;154:218–32.
32. Schindelin J, Arganda-Carreras I, Frise E, Kaynig V, Longair M, Pietzsch T, *et al*. Fiji: an open-source platform for biological-image analysis. Nat Methods. 2012;9:676–82.
33. Napolitano AP, Dean DM, Man AJ, Youssef J, Ho DN, Rago AP, *et al*. Scaffold-free three-dimensional cell culture utilizing micromolded nonadhesive hydrogels. Biotechniques. 2007;43:494–500.
34. Fujiwara Y, Kikuchi H, Aizawa S, Furuta A, Hatanaka Y, Konya C, *et al*. Direct uptake and degradation of DNA by lysosomes. Autophagy. 2013;9:1167–71.
35. Chang KL, Higuchi Y, Kawakami S, Yamashita F, Hashida M. Development of lysine-histidine dendron modified chitosan for improving transfection efficiency in HEK293 cells. J Control Release. 2011;156:195–202.
36. Ernsting MJ, Murakami M, Roy A, Li S-D. Factors controlling the pharmacokinetics, biodistribution and intratumoral penetration of nanoparticles. J Control Release. 2013;172:782–94.
37. Johnson RN, Kopecková P, Kopecek J. Synthesis and evaluation of multivalent branched HPMA copolymer − fab' conjugates targeted to the B-cell antigen CD20. Bioconjug Chem. 2008;20:129–37.
38. Maya S, Kumar LG, Sarmento B, Sanoj Rejinold N, Menon D, Nair SV, *et al*. Cetuximab conjugated O-carboxymethyl chitosan nanoparticles for targeting EGFR overexpressing cancer cells. Carbohydr Polym. 2013;93:661–9.
39. Ford J. Red blood cell morphology. Int J Lab Hematol. 2013;35:351–7.
40. Ditto AJ, Shah KN, Robishaw NK, Panzner MJ, Youngs WJ, Yun YH. The Interactions between l-tyrosine based nanoparticles decorated with folic acid and cervical cancer cells under physiological flow. Mol Pharm. 2012;9:3089–98.
41. Straussman R, Morikawa T, Shee K, Barzily-Rokni M, Qian ZR, Du J, *et al*. Tumour micro-environment elicits innate resistance to RAF inhibitors through HGF secretion. Nature. 2012;487:500–4.
42. Delinassiosand J, Kottaridis S. Interactions between human fibroblasts and HeLa cells in vitro. Biol Cell. 1984;50:9–16.
43. Gao Y, Li M, Chen B, Shen Z, Guo P, Wientjes MG, *et al*. Predictive models of diffusive nanoparticle transport in 3-dimensional tumor cell spheroids. AAPS J. 2013;15:816–31.
44. LaBarbera DV, Reid BG, Yoo BH. The multicellular tumor spheroid model for high-throughput cancer drug discovery. Expert Opin Drug Discov. 2012;7:819–30.
45. Hu Q, Gu G, Liu Z, Jiang M, Kang T, Miao D, *et al*. F3 peptide-functionalized PEG-PLA nanoparticles co-administrated with tLyp-1 peptide for anti-glioma drug delivery. Biomaterials. 2012;34:1135–45.
46. Kim Y-K, Minai-Tehrani A, Lee J-H, Cho C-S, Cho M-H, Jiang H-L. Therapeutic efficiency of folated poly (ethylene glycol)-chitosan-graft-polyethylenimine-Pdcd4 complexes in H-ras12V mice with liver cancer. Int J Nanomedicine. 2013;8:1489–98.
47. Shen J-M, Guan X-M, Liu X-Y, Lan J-F, Cheng T, Zhang H-X. Luminescent/magnetic hybrid nanoparticles with folate-conjugated peptide composites for tumor-targeted drug delivery. Bioconjug Chem. 2012;23:1010–21.

Supplementary Information

Folate-Targeted Multifunctional Amino Acid-Chitosan Nanoparticles for Improved Cancer Therapy

Pharmaceutical Research, 2015
DOI: 10.1007/s11095-014-1486-0

8.1. Methods

8.1.1. Synthesis of Folate- PEG-Amino acid modified chitosan

The synthesis of L-histidine, L-arginine and L-cysteine-modified chitosan was performed through selective amidation of the polymer primary amines by using EDC/NHS coupling chemistry as previously reported by our group [1]. From this point onwards the resulting chitosan multi-amino acid modified polymer will be termed multifunctional chitosan (CM). The percentage of arginine and histidine moieties grafted into the polymer chain was 20.2 ± 6.7 and 23.6 ± 2.5 (n=3), respectively, determined by FTIR analysis as previously reported by our group [1]. The inclusion of PEG into CM polymer was promoted via thiol-maleimide Michael-type addition reaction. Briefly, the lyophilized CM polymer was dissolved in 10 mM phosphate buffer (1 % w/v) and reacted with an excess of MAL-PEG-MAL under stirring for 48 h at room temperature (RT), in N_2 atmosphere, to yield the CM-P polymer. The modified CM-P was then purified by dialysis (MWCO 12 000-14 000 Da) against water for 6 days, and freeze dried for 48 h (yield, 86.3 %). The average of PEG moieties to CM was 46.02 ± 1.38 % (n=3) determined by proton nuclear magnetic resonance (^{1}H NMR) analysis as recently described in the literature [2]. Following the synthesis of CM-P, folic acid (FA) was modified with pendant thiol groups as previously reported by Zhang and co-workers, 2010 [3]. Initially, FA (3.39 mmol), was dissolved in anhydrous DMSO containing TEA. The mixture was continuously stirred in the dark, overnight, under N2 inert atmosphere. After complete dissolution the carboxylic acid end group of FA was activated with NHS (3.45 mmol) and EDC (3.45 mmol) for 48 h, under N_2. The mixture was then precipitated three times with ethyl acetate, recovered by filtration and washed five times with ethanol (EtOH) (yield, 60.8 %). The crude FA-NHS (0.93 mmol) was dissolved in anhydrous DMSO/TEA (5:1 v/v) and then an excess of cysteamine.HCl was reacted with the NHS ester, for 48 h, in N_2 atmosphere, in the dark. The FA-SH product was recovered as before mentioned (yield, 62.4%). For the synthesis of folate-grafted polymers (CM-PFA) an excess of FA-SH was reacted with CM-P via Michael type thiol-maleimide coupling, as previously described. The crude product was then purified by dialysis for a total of 8 days. To remove unreacted folic acid the crude product was initially dialyzed (MWCO 3500 Da) against 5 L of 0.1 M sodium bicarbonate solution during 4 days, in the dark. The use of sodium carbonate leads to the formation of sodium folate (soluble salt of folic acid) allowing its removal. Afterwards, the product was dialyzed against 5 L of water for additional 4 days in the dark. The recovered product was then freeze dried for 48 h, and stored at 4 ºC until further, in the dark, to protect folic acid from degradation (yield, 81.9 %). Characterization of CM-PFA multifunctional polymers was performed through 1H NMR spectroscopy and Fourier transform infrared spectroscopy (FTIR). The characterization of the modified polymers was performed through ^{1}H NMR spectroscopy by using a Brüker Avance III spectrometer operating at 400 MHz (Brüker Scientific Inc., N.Y., USA). Chemical shifts are represented in parts per million (ppm) and referenced to $CDCl_3$ (δ ~ 7.26 ppm), water (δ ~ 4.70 ppm) or DMSO (δ ~ 2.50 ppm) solvent peak. The spectra were recorded with a spectral width (SW) of 8 ppm, 64k data points, at 298 K.

The quantification of PEG substitution in chitosan was performed as recently described by Novoa-Carballal and co-workers, 2013, [2]. Briefly, the CM-P polymer (10 mg) was dissolved in a solution containing D_2O/0.2 % DCl/$NaNO_2$ and heated at 70 ºC for 5 min. This procedure led to a visible decrease in viscosity as reported by Novoa-Carballal. The sample was then transferred to an NMR tube (5 mm) and extensively vortexed. Spectra acquisition was performed at 298 K (Figure S3). The acquired data was processed in the TOPSPIN 3.1 and MestReNova v. 6.0 software.

The chemical modification of the polymers was additionally evaluated by Fourier transform infrared spectroscopy (FTIR) (Figure S2). The spectra were recorded in a Nicolet iS10 FTIR spectrometer (Thermo Scientific Inc., MA, USA) equipped with a Smart iTR diamond module. For each sample, 512 spectra were collected, at a 4 cm^{-1} spectral resolution and with a spectral width ranging from 4000 cm-1 to 650 cm^{-1} as previously reported [1]. Peak picking and background subtraction was performed in the OMNIC Spectra Software (Thermo Scientific).

8.1.2. Formulation of targeted multifunctional nanocarriers

For the synthesis of CM-PFA/pDNA polyplexes a stock solution of modified polymers was prepared in 5 mM sodium acetate (NaAct) buffer (pH 4.5). The 7.06 kbp pMC.CMV-MCS-EF1-GFP-SV40PolyA plasmid was amplified in a bacterial culture of *E. coli* ZYCY10P3S2T cells and recovered with the Qiagen Plasmid Maxi Kit as recently reported by our group [4]. The pcDNA3-FLAG-p53 plasmid was amplified in an *E. coli* bacterial culture as formerly reported [5]. The purity of pDNA samples was evaluated by UV-vis spectrophotometry ($\lambda_{260}/\lambda_{280}$). Prior to nanoparticle production a pDNA stock solution was prepared in 5 mM NaAct buffer with a concentration of 2 mg. mL^{-1}. The delivery systems were assembled at different molar ratios of polymer amines to pDNA phosphate groups (N/P ratio). The nanoparticles were prepared by adding pDNA to the polymer solution at a 1:4 (v/v) ratio, under vigorous stirring for 2 min. The formed particles were then recovered by centrifugation at 18 000 g for 30 min. The ratios of pDNA complexation with the CM-PFA polymers were determined by evaluating the modification of the electrophoretic mobility of pDNA biomolecules in an agarose gel as previously described [1]. For PEI/pDNA, the polyplexes were produced in HEPES buffered glucose (N/P= 5; HBG; 20 mM HEPES, 5 % glucose, pH= 7.1) as recommended in the literature [6].

8.1.3. Nanocarriers physicochemical characterization

The hydrodynamic radius and zeta potential of the nanocarriers was determined through dynamic light scattering (DLS) by using a Zetasizer Nano ZS particle analyzer (Malvern Instruments, Worcestershire, UK) equipped with a 633 nm He-Ne laser (4 mW). The analysis of CM-PFA samples was performed at 298 K, in a disposable folded capillary cell. For size measurements, the events obtained from a scattering angle of 173º were recorded and converted into size by the Stokes-Einstein model. For zeta potential determination electrophoretic data was converted to zeta potential using Henry's and Smoluchowsky approximation. All data was treated with the Malvern Zetasizer Software.

Nanocarriers morphology was evaluated by Scanning Electron Microscopy (SEM) as previously described [1]. Briefly, fresh CM-PFA/pDNA complexes formulated at various ratios were prepared and dispersed in aluminum stubs. After water removal, the samples were coated with a thin layer of gold and imaged in a Hitachi S-2700 (Tokyo, Japan) electron microscope. All images were acquired in high vacuum mode and with an accelerating voltage of 20 kV. Image post-processing was performed in Rontec EDWIN software v. 4.1.

8.1.4. Cytotoxicity assays

The cytotoxicity of CM-PFA polymers and CM-PFA/pDNA nanocarriers was evaluated by the Resazurin assay. In brief, HeLa or hFIB cells were cultured at 37 °C, in an incubator with a controlled atmosphere (5 % CO_2, 95 % O_2, humidity) until attaining 80 – 85 % confluence. The cells were then sub-cultured at an initial density of 8 x 10^3 cells per well in 96-well culture plates containing DMEM-HG (HeLa) or DMEM-F12 (hFIB) and 10 % FBS. After attachment, cells were incubated with different concentrations of CM-PFA polymers (5 - 200 $\mu g.mL^{-1}$). In addition, HeLa cells were also incubated with CM-PFA/pDNA nanoparticles for 4 h. After this period the medium was exchanged to fresh medium supplemented with antibiotics. All experiments were performed at 24, 48 and 72 h. At these predetermined time points Resazurin (1 % w/v) was incubated in each well for a 4 h period, in the dark (37 ºC, 5 % CO_2, 95 % O_2). The resultant resorufin red dye present in culture medium was then transferred to fluorescence plates for immediate analysis (96-well black clear bottom; Greiner Bio-one, Frickenhausen, Germany). Fluorescence measurements were performed in a Spectramax Gemini XS spectrofluorometer (λ_{ex}= 560 and λ_{em}= 590 nm) (Molecular Devices LLC, USA). Optical micrographs were acquired by using an Olympus CX41 optical microscope attached to an Olympus SP-500 UZ digital camera. Non-incubated cells were used as negative controls (K-) and absolute EtOH treated cells were used as positive controls (K+).

8.1.5. Cell uptake in monocultures

Nanocarriers cell uptake in single HeLa cultures was evaluated by flow cytometry and confocal laser scanning microscopy (CLSM) based on methodologies previously established by our group [1, 7]. For these studies pDNA was labelled with RITC was carried out as previously described by our group [1]. Briefly, pDNA (800 µg) was diluted in a sodium carbonate ice cold solution (V= 3 mL, 0.1 M sodium carbonate, pH = 9.0) and was then mixed with 3 µL of RITC (100 mM). The reaction was carried out at room temperature under horizontal stirring for 5 h. The resulting RITC labeled pDNA was subsequently recovered by isopropanol precipitation and washed until no fluorescence was detected in the supernatant.

For flow cytometry analysis, the cells were seeded in 6-well culture plates (3 x 10^5 cells per well) containing DMEM-HG medium supplemented with 10 % FBS. On the following day CM-PFA nanoparticles were prepared with RITC labeled pDNA, and administered to cells for 4 h. After this stage, free particles were thoroughly removed by various washing steps with PBS. The cells were then recovered by trypsinization (0.18 % trypsin/ 5 mM EDTA), pelleted and resuspended

in 500 µL of PBS. Analysis was performed in a BD FACSCalibur flow cytometer (Becton Dickinson Inc., USA) equipped with green (488 nm) and red (633nm) lasers. For each experiment a total of 1 x 10^4 events were collected in the ROI corresponding to HeLa cells. All samples were run in low flow rate to assure limited cell numbers per second (< 400). The events associated with nanoparticle-positive cells were recorded in the FL-2 channel (585/42 nm (Rhodamine)). Data acquisition was carried out in the CellQuest™ Pro software. Data processing and statistical analysis was performed in the trial version of FlowJo software v. 10.0.6 (Tree Star, Ashland, Oregon, USA).For CLSM analysis HeLa cells were initially cultured at a density of 2 x 10^4 cells per cm^2, in fibronectin coated µ-slide 8-well imaging plates (Ibidi GmbH, Germany). After 4 h of nanoparticle incubation the cells were fixed with 4 % (w/v) paraformaldehyde (PFA) for 10 min at room temperature (RT), permeabilized for 30 min (1 % Triton X-100, PBS), and stained with the Anti-F-actin CruzFluor® 647 conjugate antibody for 1 h, RT. After rinsing for 6 times with PBS the cells were incubated with Hoechst 33342® fluorophore for 15 min, RT. The cells were visualized after washing with PBS several times during 10 min. Fluorescence images were acquired in a Zeiss LSM 710 confocal microscope having a Plan-Apochromat 63x/DIC II oil immersion objective and a 34 channel QUASAR photomultiplier detector (Carl Zeiss SMT Inc., USA). Image processing was carried out in Fiji [8] and Imaris software (Bitplane, Switzerland).

8.1.6. GFP expression in HeLa cultures

For transgene expression GFP was used as a model reporter gene. The experiments were performed in 96-well black-clear bottom plates seeded with 1 x 10^4 HeLa cells per well. Transfection was carried out at a pDNA concentration of 1 µg/cm^2 and by incubating nanoparticles in cancer cells during 4 h. After this period the particles were removed. GFP expression was analyzed after 48 h by using a plate reader spectrofluorometer (Molecular Devices, California, USA). Data from each well was acquired with the 9-point scanning mode to improve robustness (SoftMax PRO software v.4.0). In addition, the visualization of GFP expression was carried out by CLSM also after 48 h of transfection.

8.1.7. Targeted delivery in 2D co-culture models

For the establishment of co-culture models, HeLa cells and hFIB were grown separately in 25 cm^2 T-flasks containing complete DMEM-HG or DMEM-F12 medium, respectively (10 % FBS, 1 % antibiotic-antimitotic). After achieving confluence, both cell types were recovered by trypsinization and viable cells were manually counted in a hemocytometer by using the trypan blue dye exclusion assay (0.4 % trypan blue in PBS). Co-cultures of malignant and normal cells were then designed by simultaneously seeding HeLa and hFIB cells in 6-well plates in a 1:2 ratio, using a total number of 2 x 10^4 cells/well. Co-cultures were maintained in DMEM-HG medium during 24 h prior to all experiments. Targeting specificity was determined in 2D co-cultures by CLSM and flow cytometry. Microscopy experiments were carried out by co-seeding HeLa and hFIB cells in fibronectin coated µ-slide imaging plates as above mentioned. To distinguish normal and cancer cells, HeLa was previous transfected with a baculovirus

containing an Actin-GFP fusion construct by following the manufacturer's instructions (Backman Cell Light 2.0® Actin-GFP). Co-cultures grown in DMEM-HG / 10 % FBS were then incubated with targeted and non-targeted nanocarriers for 4 h. All cells were then fixed, permeabilized and stained with the Anti-F-actin CruzFluor® 647 conjugate antibody. Flow cytometry analysis of co-culture populations was performed in Actin-GFP expressing HeLa cells and unstained fibroblasts. A total of 1 x 10^4 events were collected in the ROI corresponding to both HeLa and hFIB cells. The events associated with nanoparticle-positive cells were recorded in the FL-2 channel (585/42 nm (Rhodamine)), HeLa cells events were collected in the FL-1 channel (520/30 nm (Actin-GFP)). Data acquisition and processing was performed in the CellQuest™ Pro software and FlowJo software v.10.0.6, respectively.

8.1.8. 3D Tumor spheroids penetration and gene expression

Organotypic 3D tumor spheroids of HeLa cells were assembled by using a 3D precision micromold hydrogel scaffold with an array of 81-wells, as previously reported by Napolitano and co-workers [9]. In brief, hydrogel micromolds were produced with 2 % (w/v) liquid agarose by casting a negative scaffold from the original template. After drying, the molds were equilibrated overnight with culture medium. HeLa cells were then seeded to a suitable density and were left to deposit in the various recesses for 4 - 6 h. MCTS were then grown in the dark (37 °C, 5 % CO_2, 95 % O_2, humid environment), until they reached a mean diameter ranging between 700-800 µm. For uptake experiments MCTS were incubated with RITC-pDNA labeled nanoparticles. The spheroids were then rinsed with PBS, fixed (4 % PFA, 1 h, RT) and imaged by CLSM. 3D GFP transgene expression was promoted by incubating MCTS with nanoparticles and was then visualized by CLSM after 48 h. All CLSM images were acquired in z-stack mode with an average step of 6.17 µm. 3D reconstruction was performed either in Zeiss Zen software (2010) or Imaris software. Depth coding analysis was carried out by using transparent 3D reconstruction conjugated with the color coded depth algorithm. All GFP images were acquired with the same gain/laser intensity parameters for proper comparison between different experimental conditions. Fluorescence intensity sum in the MCTS volume and GFP intensity across the spheroid were computed by using Fiji image-analysis software [8]. The antitumoral effect of the tumor suppressor gene p53 in 3D microtissues was then analyzed. In brief, for p53 gene expression MCTS were transfected with CM-PFA nanocarriers loaded with the pcDNA3-FLAG-p53 expression cassette and spheroids volume was monitored by optical microscopy during 5 days. Measurement of spheroids volume variations were analyzed by image segmentation using automatic image threshold and applying a 2D mask (Fiji software). The isolated spheroid area was converted to volume (µm^3) assuming a spherical shape. Spheroid volume was calculated by using an image with a defined scale for calibration.

8.2. Results

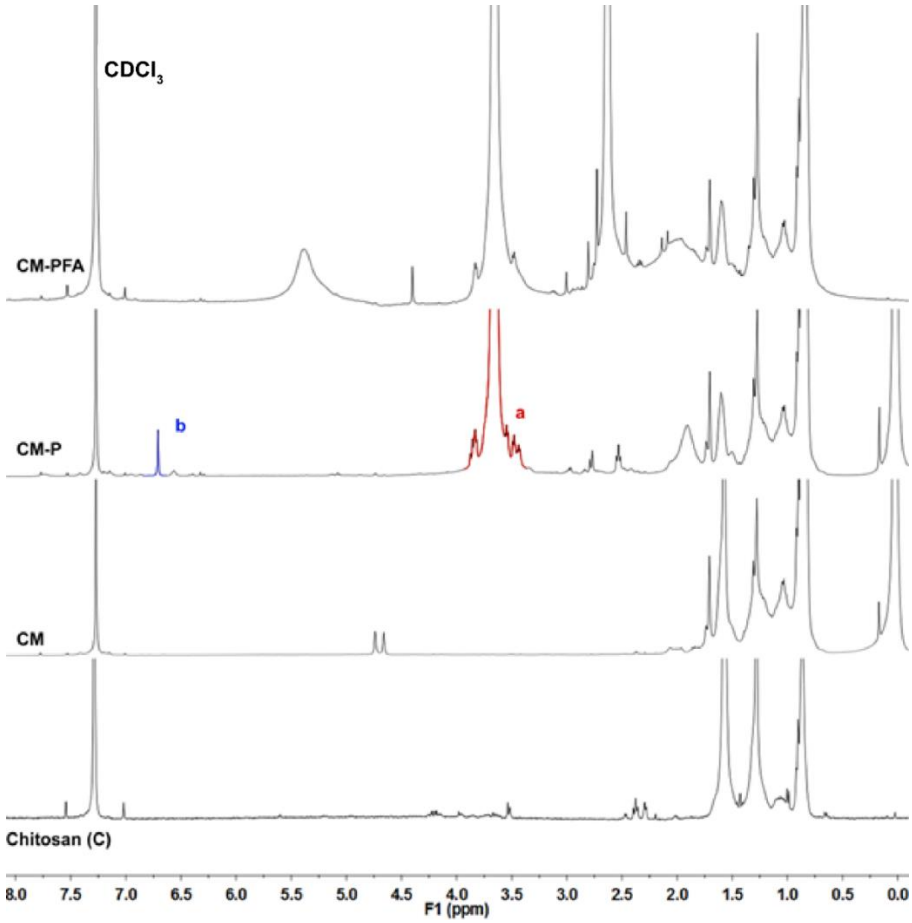

Figure S1. ^{1}H NMR analysis of the step-wise synthesis of the multifunctional CM-PFA polymer. After coupling of CM with maleimide-PEG-maleimide a characteristic peak (δ ≈ 3.9-4.0 ppm; (a), red peak) of PEG methylene protons appears. Moreover, a characteristic peak (δ ≈ 6.70 ppm; (b), blue peak) is also present and is assigned to the maleimide end capping functionality of PEG demonstrating that the conjugation of CM with MAL-PEG-MAL through maleimide coupling chemistry was successful. The peak corresponding to the maleimide functionality disappears, which suggests that FA is successfully grafted into PEG and also indicates that FA-SH- reacted with all available MAL-PEG residues.

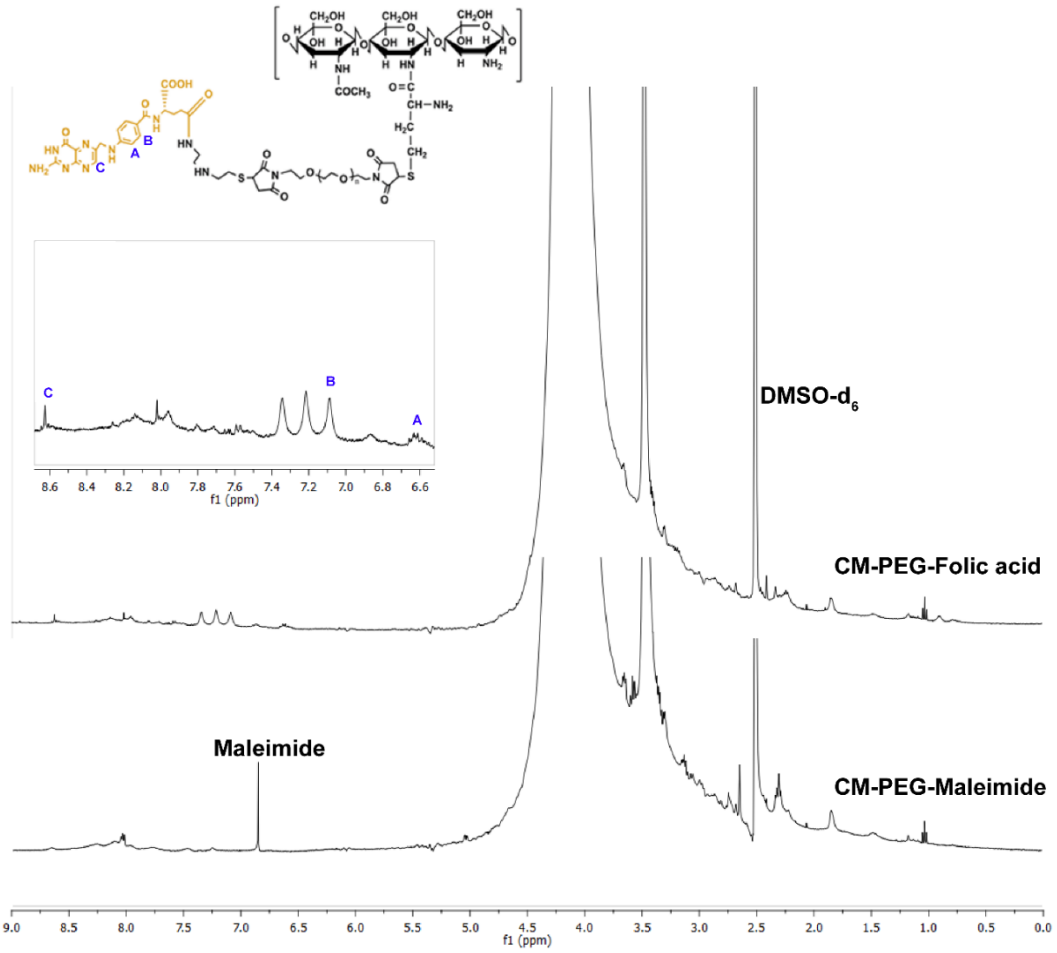

Figure S2. ^{1}H NMR analysis of the step-wise synthesis of the multifunctional CM-PFA polymer. After coupling of Folic acid the characteristic peak of PEG-maleimide protons disappears (δ ≈ 6.70 ppm). The resulting CM-PFA polymer shows the characteristic folic acid proton peaks at (δ ≈ 6.6 ppm (A); δ ≈ 7.1 ppm (B) and δ ≈ 8.6 ppm) which confirms the successful inclusion of folic acid. Peak assignment was performed according to the literature [10].

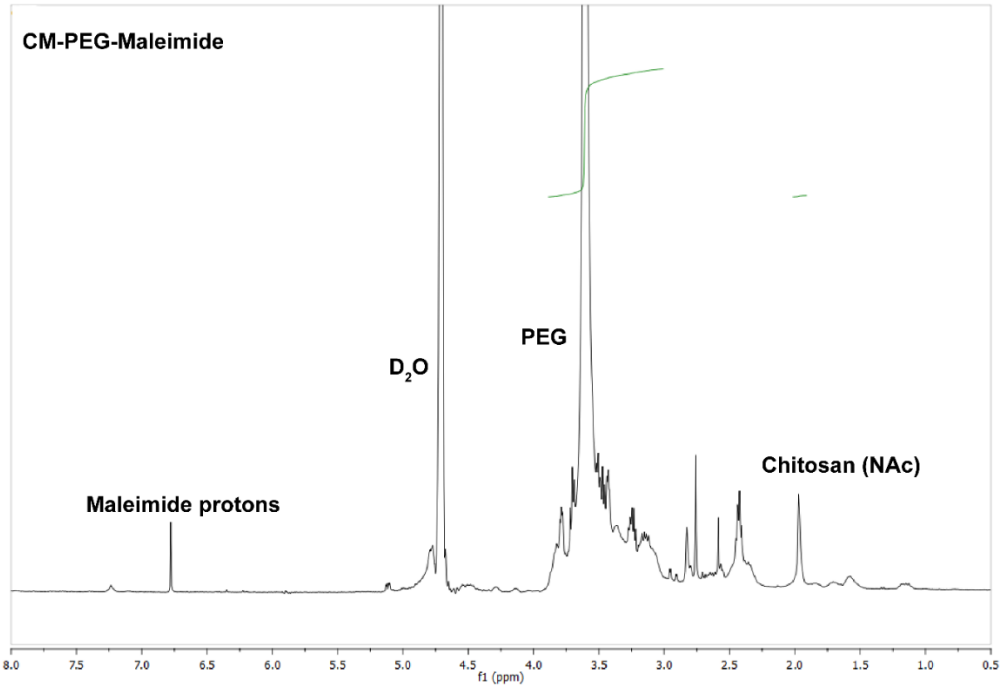

Figure S3. ^{1}H NMR analysis of the step-wise synthesis of the multifunctional CM-PFA acquired in D_2O/0.2% DCL/$NaNO_2$. The green integrals demonstrate the signals used for determination of PEG substitution degree according to Novoa-Carballal and co-workers [2]. NAc represents the N-acetyl groups of chitosan.

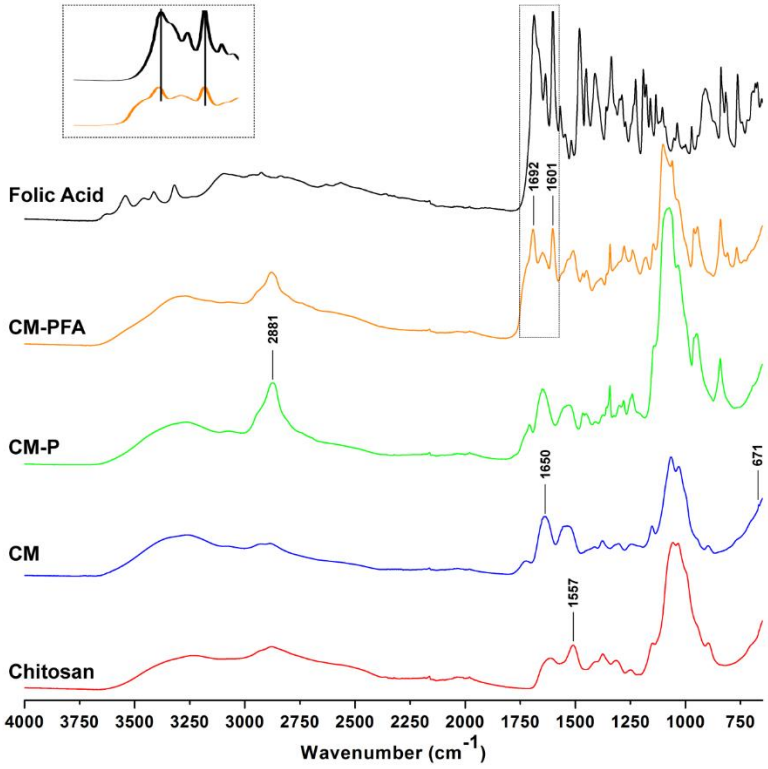

Figure S4. Fourier transform infra-red (FITR) spectra of CM-PFA synthesis. Chitosan UP CL 113. The absorption peak of the N-H bending is observed at ≈ 1560 cm^{-1} (amide II) of the glucosamine monomer of chitosan. CM – L-histidine, L-cysteine, L-arginine modified chitosan. Following amino acid conjugation the FTIR spectra exhibits an increase in the amide I peak (≈ 1650 cm^{-1}), indicating the formation of amide bonds during EDC/NHS coupling, demonstrating the successful inclusion of amino acids into the chitosan backbone. The small peak displayed at ≈ 671 cm^{-1} is assigned to –SH groups of L-cysteine. CM-P – Maleimide-PEG grafted CM polymer. The band present at 2881 cm^{-1} is assigned to aliphatic hydrocarbons of the hydrophilic PEG chains. CM-PFA – Folic acid decorated CM-P polymer. The characteristic IR peaks

of folic acid appear at ≈ 1692 cm^{-1} and ≈1601 cm^{-1}, suggesting a successful inclusion and the formation of FA-targeted polymers. Folic acid – free folic acid IR spectra.

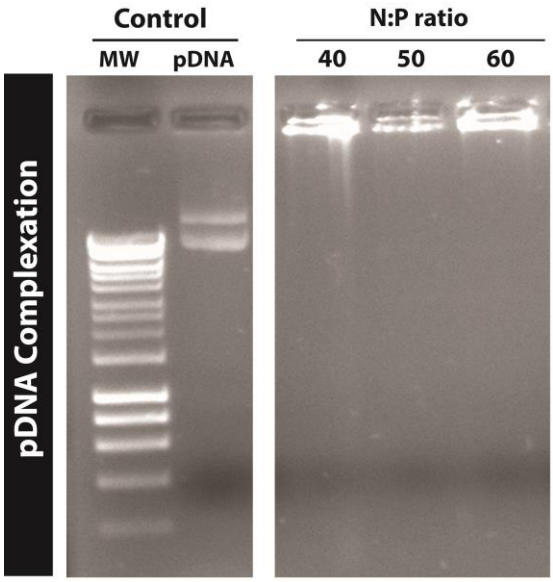

Figure S5. Agarose gel electrophoresis of CM-P mediated pDNA complexation at various N:P ratios. MW - represents molecular weight marker. pDNA lane represents native DNA sample (supercoiled + open circular).

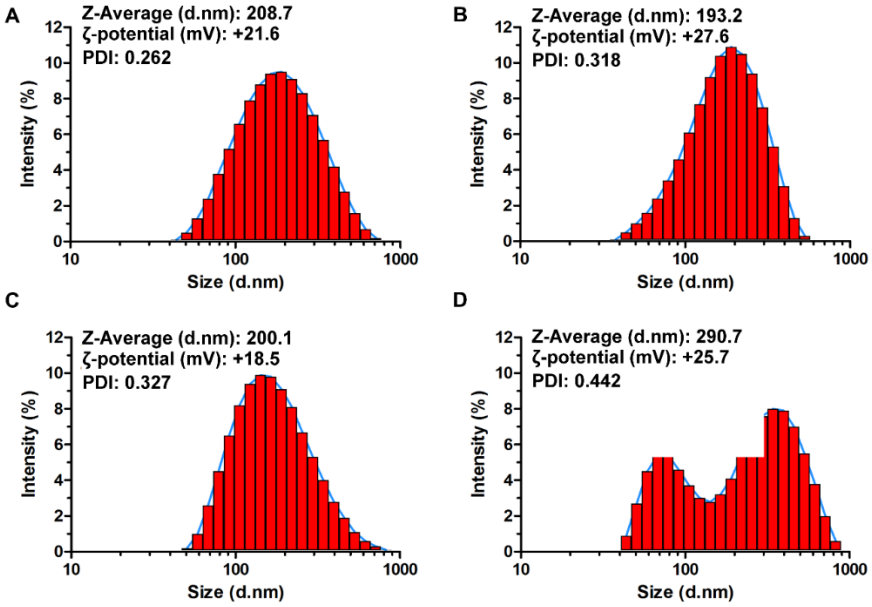

Figure S6. DLS characterization of non-targeted nanoparticles by DLS. (A, B and C) CM-P/pDNA particles formulated at N:P ratio of 40; 50 and 60, respectively. (D) PEI25 kDa/pDNA nanoparticles formulated at N:P 5 ratio.

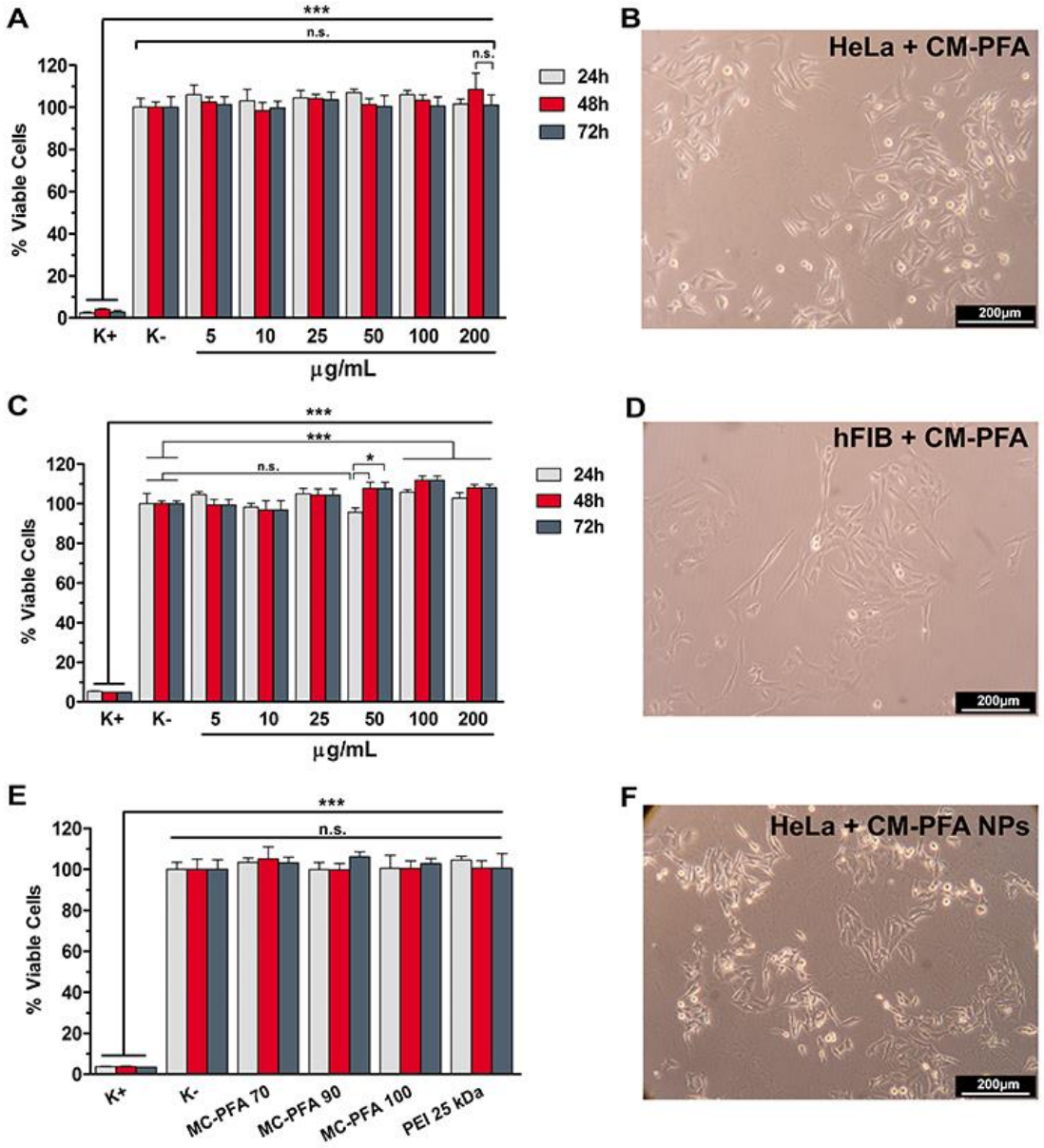

Figure S7. Cytotoxicity evaluation of CM-PFA nanocarriers in malignant and normal cells. (A and C) Cell viability of HeLa and hFIB cells, following incubation with a range of CM-PFA concentrations. (B and D) Optical contrast microscopy analysis of *in vitro* cultured HeLa and hFIB cells in the presence of CM-PFA polymers after 3 days. Representative optical micrographs of HeLa cells depict the maintenance of their epithelial-like shape after this period. In the same way, normal human fibroblasts exhibited high viability, and even some proliferation after 48 and 72 h of incubation with the highest CM-PFA concentrations (50 to 200 $\mu g.mL^{-1}$). (E and F) Evaluation of HeLa cell viability and morphology after incubation with CM-PFA/pDNA nanocarriers. K+ represents the positive control and K- non treated cells. Fibroblasts maintain their typical spindle-like morphology, an indicative that the cells remained healthy. With regard to the incubation with CM-PFA/pDNA nanoparticles formulated at different ratios, no significant differences were obtained in comparison with non-treated cells or PEI25kDa/pDNA (N:P of 5) control particles.

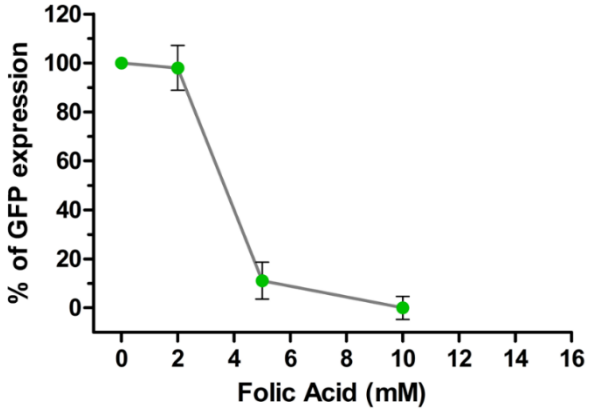

Figure S8. Effect of the addition of various folic acid concentrations to culture medium on GFP expression mediated by CM-PFA targeted nanocarriers. Data represents mean ± s.d., *n*=3.

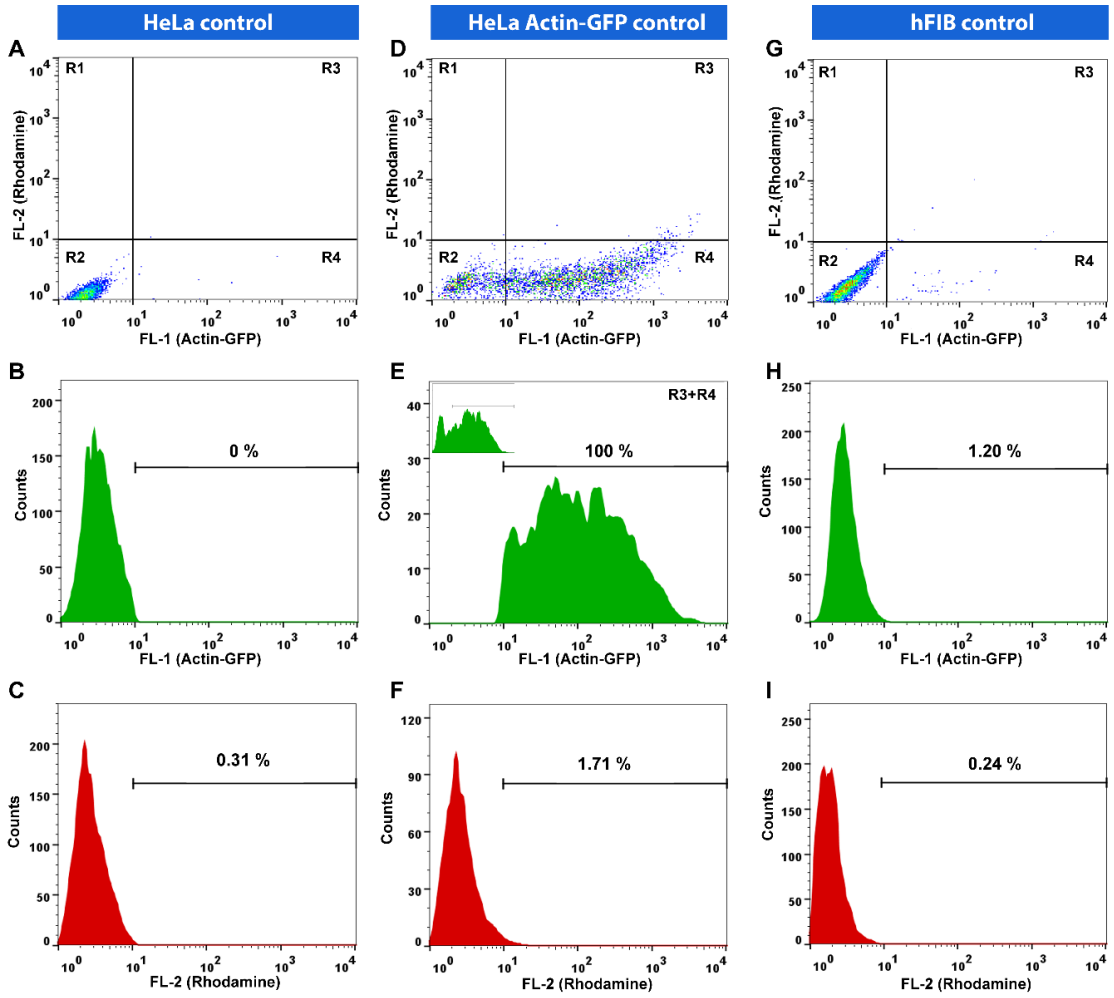

Figure S9. Flow cytometry analysis of non-treated cells. (A, D and G) Pseudocolor dot-plots of HeLa, HeLa-GFP and hFIB cells, respectively. (B, E and H) Control histograms of Actin-GFP fluorescence (FL-1). (C, F and I) Control histograms of Rhodamine fluorescence (FL-2).

8.3. References

1. Gaspar, V.M., Marques, J.G., Sousa, F., Louro, R., Queiroz, J.A., and Correia, I.J., *Biofunctionalized nanoparticles with pH-responsive and cell penetrating blocks for gene delivery*. Nanotechnology, 2013. **24**(27): p. 275101.
2. Novoa-Carballal, R., Riguera, R., and Fernandez-Megia, E., *Disclosing an NMR-Invisible Fraction in Chitosan and PEGylated Copolymers and Its Role on the Determination of Degrees of Substitution*. Molecular pharmaceutics, 2013. **10**(8): p. 3225-3231.
3. Zhang, C., Gao, S., Jiang, W., Lin, S., Du, F., Li, Z., and Huang, W., *Targeted minicircle DNA delivery using folate-poly(ethylene glycol)-polyethylenimine as nonviral carrier*. Biomaterials, 2010. **31**(23): p. 6075-6086.
4. Gaspar, V.M., Cruz, C., Queiroz, J.A., Pichon, C., Correia, I.J., and Sousa, F., *Sensitive Detection of Peptide-Minicircle DNA Interactions by Surface Plasmon Resonance*. Analytical Chemistry, 2013. **85**(4): p. 2304-2311.
5. Gaspar, V.M., Correia, I.J., Sousa, Â., Silva, F., Paquete, C.M., Queiroz, J.A., and Sousa, F., *Nanoparticle Mediated Delivery of Pure P53 Supercoiled Plasmid DNA for Gene Therapy*. Journal of Controlled Release, 2011. **156**(2): p. 212–222.
6. van Gaal, E.V., van Eijk, R., Oosting, R.S., Kok, R.J., Hennink, W.E., Crommelin, D.J., and Mastrobattista, E., *How to screen nonviral gene delivery systems in vitro?*. Journal of Controlled Release, 2011. **154**(3): p. 218-232.
7. Costa, E.C., Gaspar, V.M., Marques, J.G., Coutinho, P., and Correia, I.J., *Evaluation of Nanoparticle Uptake in Co-culture Cancer Models*. PLoS ONE, 2013. **8**(7): p. e70072.
8. Schindelin, J., Arganda-Carreras, I., Frise, E., Kaynig, V., Longair, M., Pietzsch, T., Preibisch, S., Rueden, C., Saalfeld, S., and Schmid, B., *Fiji: an open-source platform for biological-image analysis*. Nature Methods, 2012. **9**(7): p. 676-682.
9. Napolitano, A.P., Dean, D.M., Man, A.J., Youssef, J., Ho, D.N., Rago, A.P., Lech, M.P., and Morgan, J.R., *Scaffold-free three-dimensional cell culture utilizing micromolded nonadhesive hydrogels*. Biotechniques, 2007. **43**(4): p. 494.
10. Nair, L., Jagadeeshan, S., Nair, A., and Kumar, G.V., *Folic Acid Conjugated δ-Valerolactone-Poly (ethylene glycol) Based Triblock Copolymer as a Promising Carrier for Targeted Doxorubicin Delivery*. PLoS ONE, 2013. **8**(8): p. e70697.

CHAPTER 9

Poly(2-ethyl-2-oxazoline)-PLA-g-PEI Amphiphilic Triblock Micelles for Co-delivery of Minicircle DNA and Chemotherapeutics

Journal of Controlled Release, 2014
DOI: 10.1016/j.jconrel.2014.06.040

Volume 189

Motivation

The co-delivery of drug-mcDNA combinations holds a tremendous potential for therapeutic applications, particularly because various disease hallmarks could be targeted simultaneously. The formerly developed chitosan nanocarriers presented efficient gene transfer, however, their intrinsic physicochemical properties are incompatible with drug-gene co-delivery in a singular carrier. Therefore, the following study was designed with the aim to explore the potential of combinatorial therapy and to evaluate the feasibility of synthesizing an amphiphilic nanocarrier that could be used as a platform for simultaneous delivery of mcDNA and small molecule drugs.

Journal of Controlled Release 189 (2014) 90–104

Contents lists available at ScienceDirect

Journal of Controlled Release

journal homepage: www.elsevier.com/locate/jconrel

Poly(2-ethyl-2-oxazoline)–PLA-g–PEI amphiphilic triblock micelles for co-delivery of minicircle DNA and chemotherapeutics

Vítor M. Gaspar [a], Cristine Gonçalves [b], Duarte de Melo-Diogo [a], Elisabete C. Costa [a], João A. Queiroz [a], Chantal Pichon [b], Fani Sousa [a], Ilídio J. Correia [a,*]

[a] CICS-UBI, Health Sciences Research Center, University of Beira Interior, 6200-506 Covilhã, Portugal
[b] Centre de Biophysique Moléculaire, CNRS UPR4301, Inserm et Université d'Orléans, 45071 Orléans cedex 02, France

ARTICLE INFO

Article history:
Received 25 April 2014
Accepted 21 June 2014
Available online 28 June 2014

Keywords:
Co-delivery
Minicircle DNA
Anti-tumoral drugs
Micellar carriers
Cancer therapy

ABSTRACT

The design of nanocarriers for the delivery of drugs and nucleic-acids remains a very challenging goal due to their physicochemical differences. In addition, the reported accelerated clearance and immune response of pegylated nanomedicines highlight the necessity to develop carriers using new materials. Herein, we describe the synthesis of amphiphilic triblock poly(2-ethyl-2-oxazoline)–PLA-g–PEI (PEOz–PLA-g–PEI) micelles for the delivery of minicircle DNA (mcDNA) vectors. In this copolymer the generally used PEG moieties are replaced by the biocompatible PEOz polymer backbone that assembles the hydrophilic shell. The obtained results show that amphiphilic micelles have low critical micellar concentration, are hemocompatible and exhibit stability upon incubation in serum. The uptake in MCF-7 cells was efficient and the nanocarriers achieved 2.7 fold higher expression than control particles. Moreover, mcDNA-loaded micelleplexes penetrated into 3D multicellular spheroids and promoted widespread gene expression. Additionally, to prove the concept of co-delivery, mcDNA and doxorubicin (Dox) were simultaneously encapsulated in PEOz–PLA-g–PEI carriers, with high efficiency. Dox–mcDNA micelleplexes exhibited extensive cellular uptake and demonstrated anti-tumoral activity. These findings led us to conclude that this system has a potential not only for the delivery of novel mcDNA vectors, but also for the co-delivery of drug–mcDNA combinations without PEG functionalization.

1. Introduction

Nucleic acid-based non-viral therapeutics have been receiving an ever growing focus in the last decade due to their unique potential for attacking critical cancer hallmarks [1]. In this context, various efforts have been put forward to develop more efficient transgene expression cassettes that can express tumor suppressor genes or anti-tumoral mediators for longer periods and at levels that generate the desirable therapeutic outcome [2].

Minicircle DNA (mcDNA) is a class of non-viral gene expression vectors that presents excellent characteristics for the development of an efficient and long-lasting cancer therapy [3–5]. Originally described in a patent by Cameron and Schleef [6], in 1995, DNA minicircles present the following key characteristics: i.) a double stranded DNA molecule, ii.) in open circular or supercoiled isoform, iii.) devoid of bacterial origin of replication, iv.) without antibiotic resistance genes and v.) containing a specific recombinant region resulting from site specific recombination [6]. This recombinant region results from the excision of the original plasmid template (parental plasmid), which in bacteria, originates a mini-plasmid (containing all bacterial elements and antibiotic resistance genes) and the DNA minicircle containing mainly the eukaryotic promoter and the therapeutic transgene of interest [7,8]. Latter in 1997, Darquet et al., developed luciferase expressing mcDNA and purified it from their parental and miniplasmid contaminants. Following purification by cesium chloride gradient, the biological activity of DNA minicircles was tested in various cell lines and the results demonstrated that mcDNA achieved up to 10-fold higher activity than the original parental plasmid [7]. These unique characteristics endowed mcDNA with a clear potential for therapeutic applications.

Kay and co-workers, in 2010, revolutionized the DNA minicircle producing technology with a seminal work describing a procedure based on site-specific recombination mediated by bacteriophage C31 in which the miniplasmid and parental plasmid precursor were eliminated in bacteria by I-SceI homing endonuclease, yielding a more pure supercoiled mcDNA preparation without laborious purification stages [8]. Recently, our group has reported an improvement in this mcDNA production process in a way that higher yields of minicircles are obtained, while preserving purity [9]. These advances contribute for the applicability and safety of mcDNA, since there is a minimized risk of contaminant-associated immunological response, after its delivery to the host [8]. Adding to this improved safety profile, mcDNA

* Corresponding author at: Av. Infante D. Henrique, 6200-506 Covilhã, Portugal. Tel.: +351 275 329 002; fax: +351 275 329 099.
E-mail address: icorreia@ubi.pt (I.J. Correia).

http://dx.doi.org/10.1016/j.jconrel.2014.06.040
0168-3659/

administration has recently shown to maintain transgene therapeutic levels *in vivo* for up to one year [10]. Also, it has been described that these minimalistic cassettes have superior resistance to the shear forces applied during sonication or nebulization, being thus suitable for administration via microbubbles or nebulizers [11].

Combining this promising technology with different chemotherapeutics can be beneficial for cancer treatment since it is recognized that standard chemotherapy administration becomes inefficient throughout time and leads to the establishment of drug resistance [12]. Due to these drawbacks, drug-gene combinations are becoming ever-more interesting since they open the opportunity to enhance the therapeutic effect [13]. Fan et al., described the co-delivery of plasmid DNA coding for tumor necrosis factor alpha related apoptosis-inducing ligand (TRAIL) and a chemotherapeutic drug, this co-delivery improved the anti-tumoral effect and prolonged mice survival time in comparison with single drug administration [14]. The advantages of combining drug and nucleic acids for cancer therapy is also evidenced by Hu et al., which have delivered surviving small interfering RNA (siRNA) and paclitaxel through supramolecular micelles [14]. This combination resulted in a synergistic apoptotic effect and suppressed cancer growth *in vivo* [14]. Nevertheless, mcDNA can further improve these approaches since it can be used to express therapeutic genes for longer periods.

However, the simultaneous delivery of drug-nucleic acid combinations is very challenging due to the physicochemical differences of these molecules, requiring therefore a rationale nanocarrier design with various properties including positive surface charge and hydrophobicity [13,15]. Alike plasmids, DNA minicircles can be degraded by serum nucleases and also have poor cell penetration due to their negative charge [16]. So, the development of nanosized systems for mcDNA delivery is still a necessity, and very few reports have addressed it so far [16,17].

Different types of nanocarriers have been produced for the delivery of nucleic acids individually or in combination with small drugs, these include but are not limited to: i.) solid lipid nanoparticles [18], ii.) silica nanoparticles [19], and iii.) polymeric micelles [20,21]. Such systems generally have a poly(ethylene glycol) (PEG)-based shell in their surface for reducing unspecific adsorption of serum proteins (including albumin), opsonins and complement system mediators [22]. The steric barrier formed by PEG decreases the formation of a protein corona in the surface of the nanocarriers, reducing their uptake by the reticuloendothelial system (RES) and increasing circulation time [23]. These characteristics have made PEG one of the most used polymers for medical applications, being introduced in Food and Drug Administration (FDA) approved nanomedicines for cancer therapy (Doxil®, Genexol-PM®) and used in nanocarriers currently evaluated in clinical trials, including the Dox–Pluronic micelle *SP1049C* for metastatic cancer therapy and the *NK911*, PEG–Dox–poly(aspartic acid) carriers [24]. However, concerns regarding PEG immunogenicity and efficiency have been recently observed. As demonstrated by Ishida and co-workers, the repeated administration of amphiphilic pegylated carriers (e.g. liposomes, micelles) originates an immunological response mediated by anti-PEG IgM produced during the first administration [25]. This phenomenon has been described as accelerated blood clearance (ABC), and produces a dramatic modification in the pharmacokinetic profile of PEG nanocarriers reducing their localization in the target tumor tissues and increasing accumulation in the liver and spleen [26]. Recently, ABC was directly associated with the size of the PEG chain, density, and type of hydrophobic domain, emphasizing the necessity of addressing this issue that has also shown to have clinical incidence [26,27]. Among the materials that can be an alternative to PEG, bioinspired oxazolines, have been described to offer particularly valuable characteristics as stealth polymers [28].

Poly(2-oxazolines) (POx) are obtained from 2-substituted oxazolines, by ring-opening polymerization, a highly controlled process that yields very well defined polymers with suitable polydispersity (PDI) for therapeutic applications (PDI < 1.2) [29]. During synthesis, POx end-group functionalization (eg. amines, hydroxyl) can be easily controlled, a property that contributes for the versatility of these polymers. POx are generally non-ionic, hydrophilic and non-toxic materials that can also provide a steric barrier and reduce the protein corona similarly to PEG [30]. In addition, POx have been successfully conjugated to proteins and small drugs to improve their blood circulation time [31]. A recent report by Ulbricht et al., 2014, demonstrated that these polymers are biodegradable via reactive oxygen species *in vivo* in a time and concentration dependent mode [32]. More importantly, as demonstrated by Qiu and co-workers, POx-based micelles exhibited an improved anti-tumoral efficacy attributed to the "stealth" properties of the nanocarriers, indicating the suitability of this material for nanoparticle functionalization [33].

These results evidence that oxazolines can be a potentially advantageous alternative to PEG-based nanocarriers.

Therefore, this study reports the successful synthesis of a novel micellar nanocarrier based on poly(2-ethyl-2-oxazoline) (PEOz)–PLA-g–PEI for the individual delivery of mcDNA and also for the co-delivery of minicircles and chemotherapeutics in a strategy to overcome the need of pegylation and the lack of nanocarriers for mcDNA delivery. Overall the self-assembled micelleplexes exhibited suitable characteristics for both *in vitro* and *in vivo* administration of minicircle DNA with high efficacy and negligible cytotoxicity. Moreover, the amphiphilic design of the triblock copolymers provided the necessary characteristics to co-encapsulate mcDNA and Dox despite their physicochemical differences. Altogether our findings demonstrate the potential of these nanocarriers to be used for delivery of novel mcDNA and its combinations with small anti-tumoral drugs.

2. Materials and methods

2.1. Materials

The 7.06 kbp pMC.CMV-MCS-EF1-GFP-SV40PolyA template plasmid and the ZYCY10P3S2T minicircle producing strain were purchased from System Biosciences (Moutain view, CA, USA). Poly(2-ethyl-2-oxazoline) (Mw ≈ 5000 Da) and linear polyethylenimine (PEI) (Mw ≈ 2500 Da) were purchased from Polysciences (Polysciences Inc., Eppelheim, Germany). Doxorubicin hydrochloride, rhodamine B isothiocyanate (RITC), resazurin, Dulbecco's Modified Eagle's Medium — F12 (DMEM-F12), branched PEI (Mw ≈ 25 kDa) were purchased from Sigma-Aldrich (Sintra, Portugal). Stannous octoate ($Sn(Oct)_2$) was acquired from Cymit Química (Barcelona, Spain). L-lactide, tetrahydrofuran (THF), 1,1′-carbonyldiimidazole (CDI) and triethylamine (TEA) were obtained from Tokyo Chemical Industry Europe (TCI Europe, Antwerp, Belgium). The cell cytotoxicity kit containing 3-(4,5-dimethylthiazol-2-yl)-5-(3-carboxymethoxyphenyl)-2-(4-sulfophenyl)-2H-tetrazolium (MTS) and phenazine methosulfate (PMS) were obtained from Promega (Madison, WI, USA). MCF-7 mammary gland/breast cancer cells (Michigan Cancer Foundation-7) (ATCC® HTB-22™) cells and 4T1 mammary carcinoma cells (ATCC® CRL2539™) were acquired from ATCC (Middlesex, UK). Human skin fibroblasts (hFIBs) were purchased from Promocell (Heidelberg, Germany). Hoechst 33342® and wheat germ agglutinin (WGA)-Alexa 594 conjugate fluorescent probes, were purchased from Invitrogen (Carlsbad, CA, USA). All other reagents used were of analytical grade and used as received.

2.2. Methods

2.2.1. Synthesis of PEOz–PLA-g–PEI triblock copolymers

The synthesis of the triblock copolymer was performed by using a two-stage sequential procedure. Initially, PEOz–PLA was synthesized through ring opening polymerization of L-Lactide (LA) by using $Sn(Oct)_2$ as catalyst and the terminal hydroxyl group (–OH) of PEOz as initiator, as recently described by our group [34]. In brief, L-lactide

(LA) and PEOz initiator (50% w/w of LA) were added to a reaction flask under N_2 inert atmosphere and dissolved in dry toluene. Subsequently, ($Sn(Oct)_2$) (0.5% w/v) was added to the flask and the polymerization proceeded for 8 h, at 120 °C. At the end of the reaction the solvent was evaporated by rotary evaporation (Rotavap® R-215, Büchi, Switzerland) and the PEOz–PLA crude polymer was recovered by methanol (MetOH) precipitation. The resulting product was then purified by dialysis in acetone and water for 5 days, and freeze dried (yield: 95.3%). The PEOz–PLA block copolymer was then conjugated with PEI amines via CDI mediated coupling. For the activation of PLA–OH groups PEOz–PLA (296 mmol) and CDI (0.32 mol/mol PEOz–PLA) were dissolved in anhydrous THF under an inert atmosphere during 4 h. Subsequently, PEI (1.1 mol/mol PEOz–PLA) was added to the flask and the reaction proceeded at 60 °C, in an inert atmosphere (N_2) and under reflux for 48 h. The triblock copolymer was purified by dialysis (MWCO 3500 Da) for 6 days using water as dyalisant. The final product was then freeze dried and a fine white powder was obtained. Characterization of PEOz–PLA-g–PEI was performed by ^1H NMR spectroscopy, Fourier transform infrared (FTIR), matrix assisted time of flight mass spectroscopy (MALDI–TOF) and differential scanning calorimetry (DSC) (Supplementary information Figs. S1 to S4).

2.2.2. Determination of the critical micellar concentration

The critical micellar concentration (CMC) of the amphiphilic polymers was determined by the standard pyrene encapsulation method, as described in the literature [35]. The use of pyrene provides a rapid and precise method to determine the CMC of amphiphilic polymers in a solution since this fluorescent probe changes its absorption spectra according to the polarity of its environment. Due to this property, pyrene characteristic fluorescence emission (ratio of intensities of pyrene first and third vibronic peaks; $\lambda_{ex} = 333$ nm and $\lambda_{ex} = 335$ nm, often described as the 1:3 method) can be used to estimate the polarity level of its surroundings [36]. This is only possible since hydrophobic pyrene molecules are often aggregated in a solution. Upon contact with amphiphilies these aggregates are destabilized and the polymers interact with the probe. With cationic amphiphilies this phenomena is characterized by a slight reduction in emission intensity just before CMC and then enhancement of intensity after the critical point [36]. The value of CMC is calculated from the intersection of the two straight lines obtained in 1:3 method plot. For CMC determination serial dilutions (0.001 to 2000 μg/mL) were prepared from a PEOz–PLA-g–PEI stock solution (4 mg/mL). Pyrene (0.6 μM) was then added to the polymer solutions and the resulting mixture was sonicated for 30 min. The CMC was extrapolated from the pyrene fluorescence peaks ($\lambda_{ex} = 333$ nm and $\lambda_{ex} = 335$ nm; $\lambda_{em} = 390$ nm) obtained after sample analysis in a Spectramax Gemini XS spectrofluorometer (Molecular Devices LLC, USA).

2.2.3. Preparation of PEOZ–PLA-g–PEI micellar carriers

The micellar carriers were prepared by using two different methods in order to load mcDNA individually or in combination with Dox. For all experiments mcDNA was produced by using template parental plasmids that were amplified in a bacterial culture of *Escherichia coli* (*E. coli*) ZYCY10P3S2T cells. Minicircle biosynthesis was then induced by L-arabinose addition as recently optimized by our group [9]. The production of nucleic acid-loaded micelles was performed by using different molar ratios of PEI amines to mcDNA phosphate groups (N/P ratio). Initially, the PEOz–PLA-g–PEI triblock copolymers were dissolved in HEPES buffered glucose (20 mM HEPES, 5% glucose, pH 7.1) at desired concentrations, and sonicated during 30 min. The micelleplexes were then prepared by adding mcDNA to micelles and vortexed for 1 min. The resulting particles were then recovered by centrifugation at 18,000 *g* for 30 min. The optimal PEOz–PLA-g–PEI/mcDNA (micelleplexes) N/P ratios were determined by agarose gel electrophoresis as previously described by our group [37].

2.2.4. Micellar carrier physicochemical characterization

Dynamic light scattering (DLS) analysis was used to determine the hydrodynamic diameter and zeta potential of the different mcDNA-loaded micelleplexes. The measurements were performed in a Zetasizer Nano ZS particle analyzer (Malvern Instruments, Worcestershire, UK) equipped with a He–Ne laser, at 25 °C. For DLS analysis particle samples were produced as mentioned before and resuspended in ultrapure water. Size characterization was performed in a fully automatic mode and with a scattering angle of 173°. Particle zeta potential measurements were performed in disposable capillary cells and computed by using Henry's [F(Ka) 1.5], and Smoluchowsky models. All the data was examined in Zetasizer software v 7.03.

Micelleplex morphology was analyzed by atomic force microscopy (AFM) as previously described with slight modifications [38]. In brief, micelleplexes were drop-casted into freshly cleaved muscovite mica slides and dried at room temperature (RT). Imaging was performed in a AFM Veeco Dimension 3100 microscope (Veeco, Santa Barbara, CA, USA) operated at a frequency of 300 Hz. All images were acquired in tapping mode by using a Tap300A1-G tip (Budget Sensors, Combo, US). Image data was post-processed in the WSxM 5.0 software [39].

2.2.5. Micelle stability assays

Minicircle DNA loaded PEOz–PLA-g–PEI nanocarriers' kinetic stability was studied in phosphate buffered saline (PBS) containing 10% v/v fetal bovine serum (FBS) and sodium dodecyl sulfate (SDS) destabilizing agent as reported in the literature [40]. Briefly, micelleplexes (1.32 mg/mL) were incubated with PBS/10% FBS and aqueous SDS (2.5 mg/mL) at 37 °C for predetermined time intervals. Differences in micelle size during incubation were then monitored by DLS using a Zetasizer Nano ZS equipment (Malvern Instruments, Worcestershire, UK) as mentioned before.

2.2.6. In vitro hemolysis

Nanocarriers' hemolytic effect in red blood cells (RBCs) was investigated by using freshly collected blood from euthanized Wistar rats as reported in the literature [34]. All the procedures used to manipulate animal models were in agreement with the European regulatory guidelines set for care and use of laboratory animals (Directive 2010/63/UE). The experiments were performed by specialized personal and in facilities certified by the Portuguese Veterinary Department for animal research. Briefly, blood samples were collected via cardiac puncture and immediately transferred to EDTA containing tubes to avoid coagulation. RBCs were then isolated from 1 mL samples by centrifugation (4500 rpm for 10 min) and washed four times with PBS. Purified RBC suspensions were then incubated with different micelleplex formulations during 4 h at 37 °C in a shaking water bath (75 rpm). After the incubation period all samples were centrifuged (6000 rpm, 10 min) and the supernatant recovered for analysis. Hemoglobin released from RBCs was quantified through spectrophotometry ($\lambda = 540$ nm) by using a Shimadzu UV-1700 spectrophotometer (Shimadzu Inc., Japan). PBS and Triton X-100 were used as negative and positive controls, respectively.

2.2.7. Micelles biocompatibility

The biocompatibility of PEOz–PLA-g–PEI nanocarriers was studied by the resazurin assay as previously reported by our group [37]. In brief, MCF-7 cells were cultured in DMEM-F12 medium supplemented with 10% FBS in a humidified and controlled atmosphere (5% CO_2) at 37 °C. For the assays confluent cell monolayers were then subcultured in 96 well plates at a density of 8×10^3 cells per well. In the following day, cancer cells were incubated with different concentrations of blank micelles (10–1000 μg/mL). In addition, normal hFIB cells were also incubated with blank nanocarriers. Biocompatibility was evaluated at 24, 48 and 72 h. At these predetermined intervals resazurin (1% w/v) was incubated in each well during 4 h, in the dark (37 °C, 5% CO_2). The resultant resorufin products were transferred to fluorescence plates for

analysis by spectrofluorimetry (96-well black clear bottom; Greiner Bio-one, Frickenhausen, Germany). All the measurements were performed in a Spectramax Gemini XS spectrofluorometer ($\lambda_{ex} = 560$ and $\lambda_{em} = 590$ nm) (Molecular Devices LLC, USA). Untreated cells were used as negative controls (K−) and absolute EtOH treated cells were used as positive controls (K+).

2.2.8. Nanocarriers' cellular uptake and intracellular trafficking

Micelleplex uptake in cancer cells was initially investigated by flow cytometry. For this purpose MCF-7 cells were seeded in sterile 6-well culture plates (3×10^5 cells/well). In the following day, micelleplexes prepared with RITC-labeled mcDNA were incubated during 4 h in serum supplemented DMEM-F12. Free particles were thoroughly removed by rinsing with PBS. Afterwards, the cells were recovered by trypsinization, pelleted and resuspended in 500 μL of PBS-5% FBS. Flow cytometry analysis was performed in a BD FACSCalibur flow cytometer (Becton Dickinson Inc., USA) in which a total of 1×10^4 events were collected in the region of interest (ROI) corresponding to MCF-7 cells. Micelleplex-positive events were recorded in the FL-2 channel by the red/orange emission filter (585/42 nm). Raw data processing and statistical analysis were performed in FlowJo software v. 10.0.6 (Tree Star, Trial version, Ashland, Oregon, USA).

Additionally CLSM was used to visualize micelleplex uptake and lysosomal release in MCF-7 cells as previously reported by our group [37]. In brief, MCF-7 cells were cultured at a density of 2×10^4 cells/cm^2, cell culture treated μ-slide 8-well imaging plates (Ibidi GmbH, Germany). After cell adhesion, micelleplexes loaded with FITC-mcDNA were incubated for 4 h. The cells were then fixed (4% paraformaldehyde, 10 min) and stained with the WGA-Alexa 594® conjugate. Cells were then rinsed several times with PBS and labeled with Hoechst 33342® nuclear probe (2 μM). Confocal images were acquired in a Zeiss LSM 710 confocal microscope equipped with a Plan-Apochromat 63x/DIC II objective (Carl Zeiss SMT Inc., USA). Raw image data was post processed in Fiji [41] and Imaris software (Bitplane, Switzerland).

2.2.9. In vitro gene expression in 2D cultures

Minicircle DNA mediated GFP expression in MCF-7 breast cancer cells was evaluated through spectrofluorimetry by using a plate reader spectrofluorometer (Molecular Devices, California, USA). For these assays cancer cells were seeded at a density of 1×10^4 cells/well in 96-well black-clear bottom plates. All transfection experiments were performed in DMEM-F12/10% FBS culture medium to mimic physiological conditions. The cells were transfected with a mcDNA concentration of 1 μg/cm^2 and GFP fluorescence intensity was then quantified 48 h after transfection. Additionally, the visualization of GFP expression was carried out by CLSM.

2.2.10. 3D tumor spheroids penetration and gene expression

Breast cancer 3D multicellular tumor spheroids (MCTSs) were produced by using precision micromolds with a design containing arrays of 81-wells as reported by Napolitano et al., 2007 [42]. Briefly, agarose hydrogel micromolds were formed under aseptic conditions by casting melted agarose (2% w/v) into the original template to obtain a negative mold. After drying at room temperature and sterilization with UV light, MCF-7 cells were seeded in the patterned molds at a suitable density to attain a diameter between 500 and 600 μm. MCTSs were cultured in DMEM-F12/10% FBS medium that was renewed by partially (50% of fresh medium) when considered necessary in order to preserve soluble factors secreted by cells in 3D culture. The evaluation of RITC-mcDNA micelleplex uptake in 3D MCTS was performed by CLSM using the procedures described for 2D cultures.

mcDNA mediated GFP expression in 3D was promoted by administering micelleplexes (0.4 μg mcDNA/spheroid) and then visualizing expression by CLSM after 48 h. For spheroids visualization a series of z-stacks were acquired along the volume of the MCTS and then reconstructed to 3D in the Zeiss Zen SP2 software (2010) or Imaris v.7.2.3 software. All images and stacks were acquired with similar laser and detector gain parameters for comparison and quantification purposes. Posterior GFP fluorescence intensity analysis in the MCTS volume was quantified in Fiji image-analysis software [41].

2.2.11. In vivo mcDNA expression

Female Balb/c mice (3 weeks old, ~20 g) obtained from Harlem (France) were manipulated and kept according to the guidelines issued by the French Ministry of Agriculture for experiments with laboratory animals (C. Pichon accreditation, Law 87848). Animal experimentation was performed in facilities equipped and accredited for animal research (agreement B 45-234-12, Délégation des Services vétérinaires du Loiret). The animals were maintained in a 12 light/12 dark, light cycle and fed with standard chow food (Laboratory Rodent Diet 5001; PMI Feeds, Richmond, VA). All animals were housed at 22 °C, and had free access to water and food during the course of experiments.

Orthotopic 4T1 breast tumor models that commonly metastasize to the lungs were produced by injecting 6×10^6 4T1 tumor cells into the mammary fat pad of randomly selected mice. For posterior studies, mice were randomly distributed in groups ($n = 2$). Control mice and tumor bearing mice were placed in different cages during the experiments. For mcDNA *in vivo* expression, tumor bearing mice (tumor volume 150–200 mm^3) were injected intratumorally with micelleplexes (10 μg of mcDNA). Two days after nanocarriers' administration the mice were euthanized by methoxyfluorane (Methofane®) inhalation. For GFP expression visualization the tumors were then resected and immediately imaged in a Nikon Multizoom AZ100 *in vivo* imaging microscope equipped with a Neo scCMOS camera (Nikon Instruments Inc., Melville, NY).

2.2.12. Drug-nucleic acids co-delivery in PEOz–PLA-g–PEI

The capacity of the PEOz–PLA-g–PEI polymers to simultaneously deliver mcDNA and Dox was also evaluated. For this purpose, the film-casting method was combined with sonication/electrostatic complexation to investigate the feasibility of producing mcDNA–Dox in micelles. Briefly, PEOz–PLA-g–PEI (5 mg) and Dox base (500 μg/mL, 1.5 eq. TEA) were initially mixed in 1 mL chloroform/MetOH (1:1 v/v). The solvent was evaporated by rotary evaporation and the polymer-drug film was hydrated with double deionized water and sonicated for 30 min. To remove trace amounts of surface bound Dox and TEA the micelles were transferred to dialysis bags (MWCO 3500) and dialyzed in water for 2 h, in the dark. Dox-loaded micelles were then dissolved to the desired concentrations, complexed with mcDNA and recovered, as mentioned above. The resulting nanocarriers were characterized by DLS and FTIR spectroscopy. Dual loaded micelle cell uptake was also investigated by flow cytometry and CLSM as described before.

2.2.13. Drug encapsulation and in vitro release

Dox encapsulation efficiency in micellar carriers was evaluated through ultra performance liquid chromatography (UPLC) by using a Agilent 1200 UPLC system equipped with a ZORBAX Eclipse C18 Rapid Resolution HT column (Agilent Technologies, CA, USA). Drug encapsulation efficiency and loading capacity was determined as previously reported by our group [34]. All chromatographic runs were performed with Acetonitrile/Na_2HPO_4 (0.015 M, pH 7.4) with 0.01% (v/v) TEA (32:68) as mobile phase. Supernatant samples from micelles production were analyzed for Dox content (230 nm) at a flow rate of 1 mL/min and a temperature of 24 °C. Protriptyline (294 nm) was used as internal standard in all runs.

Drug release from micelles was studied by resuspending the carriers in release medium (PBS, pH 7.4) in order to assure sink conditions. Release was performed at 37 °C in a shacking water bath (45 rpm). Supernatant samples were collected at predetermined intervals and then analyzed by UPLC.

2.2.14. Micelleplex anti-tumoral activity

The anti-tumoral activity of mcDNA–Dox micelleplexes in breast cancer cells was evaluated by the MTS assay as previously reported with slight modifications [34]. Initially, 8×10^3 cells were seeded in 96 well plates containing DMEM-F12/10% FBS culture medium. One day after seeding, the cells were incubated with different micelle concentrations for 4 h. After incubation the medium was replaced to remove unbound micelles. Cell viability was then determined at 48 h after administration by adding MTS/PMS to each well and incubating it for 4 h in the dark (37 °C, 5% CO_2). Non-treated and dead cells (EtOH treated cells) were used as negative and positive controls, respectively.

2.2.15. Statistical analysis

One-way analysis of variance (ANOVA), complemented by the post-hoc Newman–Keuls test were used for statistical analysis. A confidence interval (CI) of 95% (p value < 0.05) was considered statistically significant. Raw data analysis was carried out in GraphPad Prism v.6.0 (trial version; GraphPad software Inc., CA, USA).

3. Results and discussion

3.1. Synthesis and characterization of micellar carriers

The synthesis of ABC-type triblock copolymers comprised by poly(2-ethyl-2-oxazoline)–poly(L-lactide)–polyethylenimine (PEOz–PLA-g–PEI, from here forward designated by PPP) was performed by a two-step reaction as schematized in Fig. 1A.

Initially, PEOz–PLA was synthesized through ROP of L-lactide by using the hydroxyl end group of PEOz as template. The resulting PLA hydrophobic chain had a Mn of 3349 Da as determined by ^{1}H NMR (Fig. S2). The inclusion of linear PEI in the diblock co-polymer was then promoted by carbonyldiimidazole-mediated coupling of PLA hydroxyl group to the amines of PEI. The successful synthesis of the triblock copolymer was confirmed by FTIR and ^{1}H NMR spectroscopy (Figs. S1 and S2). MALDI–TOF–TOF data further revealed that the triblock copolymer had a uniform molecular weight distribution (Supplementary Fig. S4). In addition, DSC thermograms showed an increased melting temperature (T_m) in the diblock and triblock

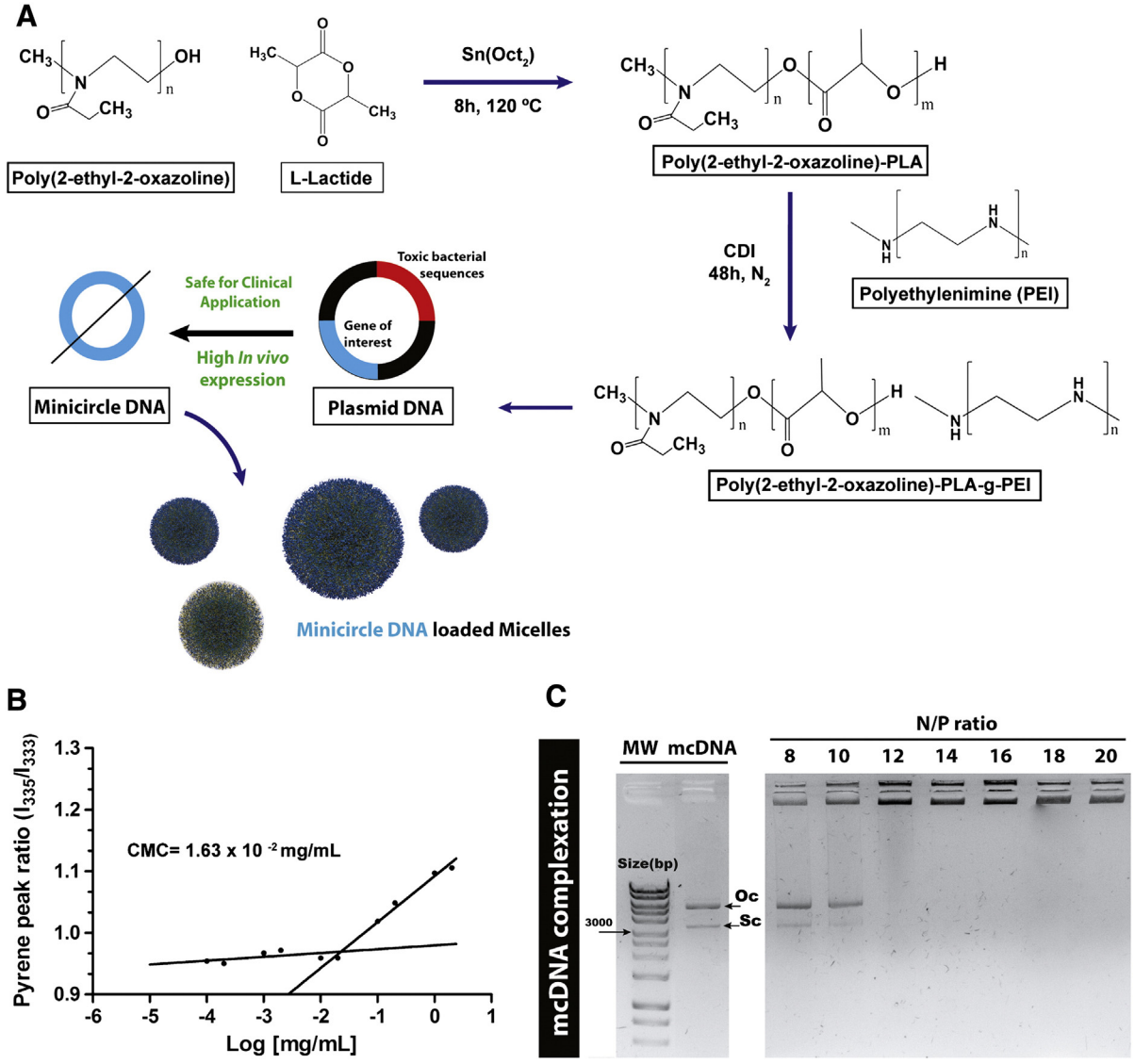

Fig. 1. PEOz–PLA-g–PEI (PPP) triblock copolymer synthesis and characterization. A.) Schematics of the synthesis process. B.) CMC determination. C.) Representative gel electrophoresis of minicircle DNA (mcDNA) complexation by the triblock copolymers at various N/P ratios, for all ratios above N/P 12 (including N/P30 or above) the DNA is complexed with the polymer in the tested conditions. MW — DNA ladder molecular weight marker, mcDNA (3064 bp) — non-complexed DNA, Oc — open circular and Sc — supercoiled isoform, respectively. N/P ratio — amine to phosphate ratio of PEI/mcDNA.

copolymers when compared to the PEOz homopolymer, also indicating an effective conjugation (Fig. S3).

The capacity of the amphiphilic copolymers to form micellar structures was evaluated by determining their critical micellar concentration (CMC). The results demonstrate that generally these conjugates self-assemble into micelles at relatively low concentrations (Fig. 1B), showing their high stability and potential to be used as nanocarriers. The obtained CMC of the PPP copolymers was lower than other delivery systems such as those described by Li et al. (D-alpha tocopheryl polyethylene glycol succinate–PLA (TPGS–PLA); CMC = 2.06×10^{-2} mg/mL) [43]. Following this characterization the actual capacity of the PPP carriers to condense mcDNA was investigated. In this context, our group has recently characterized the zeta potential of DNA minicircles in various buffers and different temperatures in an attempt to shed light on the forces involved during mcDNA interaction with positively charged macromolecules [44]. Since these parameters ultimately influence nanocarrier production, the formulation of mcDNA micelleplexes was promoted in conditions that would favor polyelectrolyte condensation (HBG buffer, pH 7.1). As the agarose gel electrophoresis characterization demonstrates the PPP copolymers fully condensed mcDNA at N/P 12 (Fig. 1C). This successful loading is important since as described by Endres and co-workers, PEI blocks could be entrapped to some extent in the micelles hydrophobic core due to phase mixing [45]. Even if this phenomenon partially occurs the results reveal that the spatial structure of the micelles allows an effective interaction of PEI amines with mcDNA, and consequently its full complexation (Fig. 1 C).

3.2. Physicochemical characterization of PPP nanocarriers

The physicochemical characterization of the most suitable nanocarrier formulations regarding hydrodynamic size and surface charge is shown in Fig. 2. The micelleplexes produced at different N/P ratios generally exhibited a particle size ranging from 140 nm to 280 nm (Fig. 2). The N/P 30 formulation yielded the smallest micelleplexes and with a relatively low polydispersity index (PDI = 0.270). The zeta potential varied with different formulations and was generally negative (−41 mV to −8 mV) apart from that of the N/P 30 micelleplexes (+0.63 mV). Regarding the morphological characteristics, AFM images display that the nanocarriers have well defined spherical shapes and size comparable to that obtained by DLS analysis (Fig. 2E and F).

3.3. Nanocarriers' stability and biocompatibility

The kinetic stability of mcDNA micelleplexes was assessed by monitoring changes in the hydrodynamic size at various time intervals through DLS. Initially, to determine stability in disrupting conditions the carriers were incubated with an aqueous solution of SDS in a concentration (2.5 mg/mL) that is reported to promote the disassembly of amphiphilic block copolymer systems. As the results in Fig. 3 demonstrate, mcDNA-PPP micelles size increased along time from 140 nm to ~350 nm (Fig. 3A), suggesting that the nanocarriers' structure is slightly destabilized after 24 h, but remains totally intact. On the contrary, other types of micellar carriers have shown to immediately disassemble in contact with SDS, under similar conditions [40]. To further characterize micelleplex performance in physiological conditions we also investigated the particle size stability in PBS/10% FBS to reproduce the osmolarity, salt concentrations and serum found *in* vivo [46]. The results of Fig. 3A indicate that the nanocarriers kept their size and narrow distribution along time with no significant differences being observed when compared with particles incubated in formulation buffer (HBG, pH 7.1), emphasizing their potential for therapeutic applications. Importantly, these findings indicate that PEOz is a suitable substitute for PEG, and that it could provide similar surface shielding as already described in the literature [28,47].

The potential of mcDNA-PPP carriers to be administered via intravenous injection was analyzed *in vitro* by determining erythrocytes lysis upon direct contact. As the results in Fig. 3B demonstrate, the various formulations of micelleplexes have a negligible effect on RBCs membrane (~1% of hemolyzed erythrocytes), with no significant differences being obtained in comparison with PBS incubated cells. The absence of hemolysis is important since the amount of released hemoglobin is below the 5% threshold set forth in the guidelines issued by international agencies (ISO/TR 7406) in what concerns the critically safe hemolytic ratio of medical devices [48].

To complement mcDNA-PPP nanocarriers' characterization, *in vitro* biocompatibility assays were performed in hFIB and MCF-7 cells. Breast cancer cells remain alive during 72 h after their incubation with various

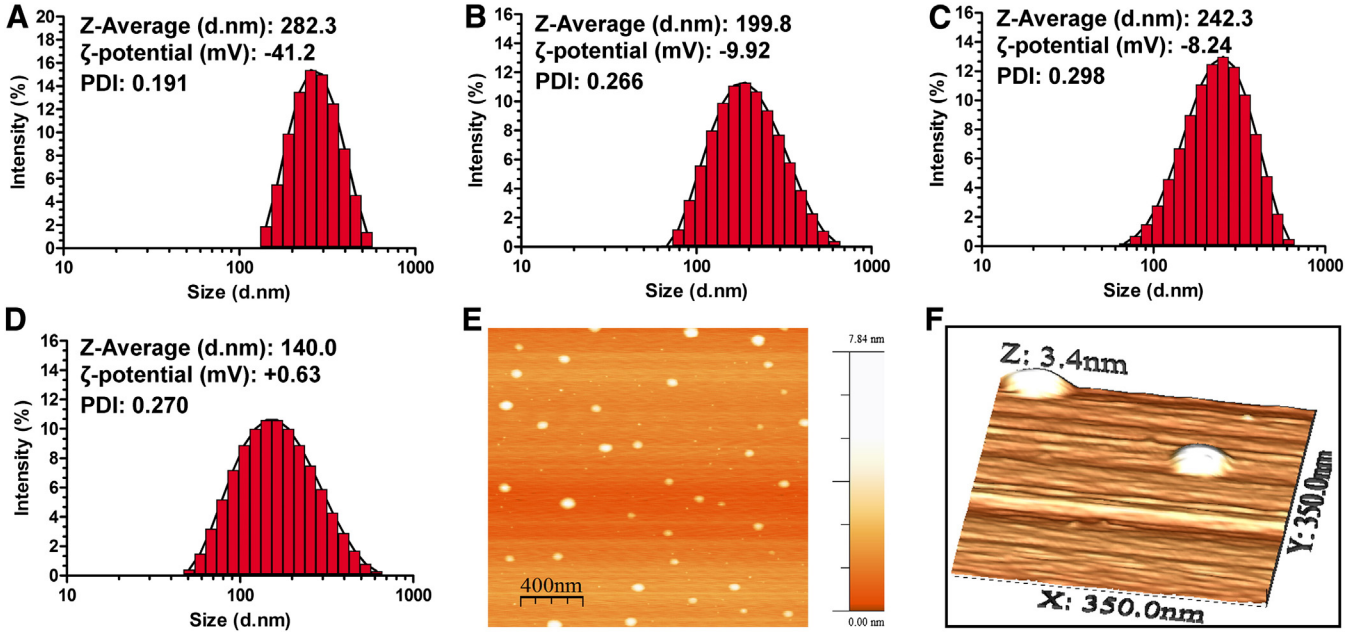

Fig. 2. Characterization of nanocarriers. DLS analysis of mcDNA micelleplexes formulated at various N/P ratios: A.) 12, B.) 14, C.) 16, D.) 30, E.) representative 2D AFM image of micelleplexes (N/P 30), and F.) 3D reconstruction of mcDNA micelleplexes.

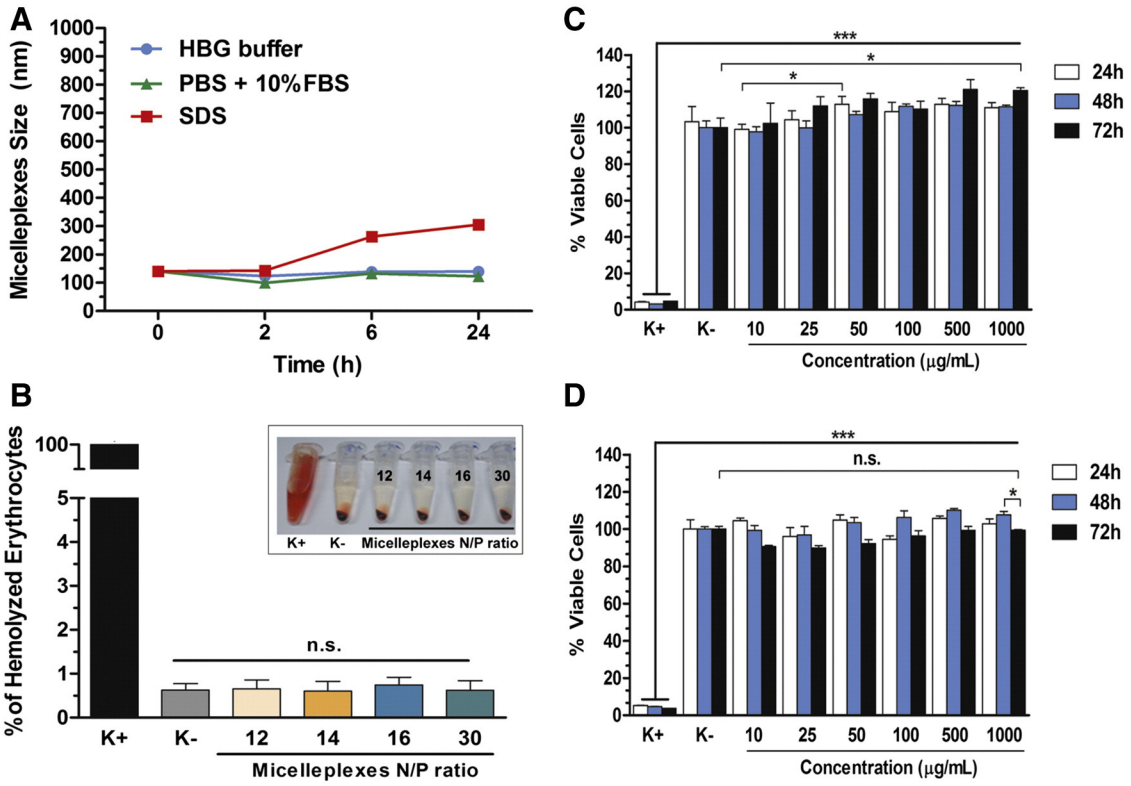

Fig. 3. Micelleplex stability and biocompatibility. A.) Time course micelle stability assay of micelles formulated at N/P 30. Micelleplexes incubated in HBG buffer were used as negative controls. B.) RBC hemolysis assay; optical images of pelleted RBCs after incubation. K+ represents the positive control (Triton X-100 permeabilized RBCs). K − represents the negative control (PBS incubated RBCs). Data represents mean ± s.d. n.s — not significant, n = 3. C and D.) Evaluation of cell viability after incubating the different concentrations of PPP blank micelles in MCF-7 and hFIB cells, respectively. K− and K+ were used as negative and positive controls, respectively. Data represents mean ± s.d. *$p < 0.05$; ***$p < 0.001$; n.s. — not significant; $n = 5$.

polymer concentrations (Fig. 3C). Moreover, PPP micelles have shown negligible toxicity when incubated with normal human skin fibroblasts (Fig. 3D), as cell viability remained above 90% during the course of incubation and with concentrations up to 1000 μg/mL.

3.4. Micelleplex uptake and gene expression in 2D cultures

Cell uptake efficiency of mcDNA-loaded PPP micelleplexes in cancer cells showed that all the tested formulations achieve internalization to a similar extent. Actually, the mean fluorescence intensity (MFI) was not considerably different among the formulations tested (Fig. 4B). However, as shown in Fig. 4A and B, the N/P 30 formulation exhibits a significantly higher percentage of nanocarrier positive cells, suggesting that these particular micelles could be more effective.

Variations in micellar carrier cell uptake efficiency were further confirmed by confocal microscopy. As displayed in Fig. 4C and D (white arrows) the nanocarriers that were produced at N/P 30 exhibit uptake in a higher number of cells in comparison with their N/P 12 counterparts. Such differences in internalization efficiency are likely associated with micelle zeta potential differences (Fig. 2). In fact, the N/P 30 micelles present a slightly positive charge in comparison with the other formulations, a factor that can increase the interaction with the negatively charged glycosaminoglycans (e.g. sialic acid, heparan sulfate) in the cell membrane and thus lead to a higher percentage of nanocarrier positive cells. These results thus highlight the discovery of an optimal N/P ratio for mcDNA delivery (N/P 30).

Additionally, micelles lysosomal localization was explored with the aim to elucidate their possible sequestration in these degradative compartments. Interestingly, as demonstrated by confocal images and colocalization analysis (Tm = 0.093, Fig. 4F), mcDNA-loaded particles were not confined in lysosomes, an important factor since they become readily available to deliver DNA to the cytoplasm or nucleus. In fact, FITC-labeled mcDNA vectors are visible in the nucleus of some MCF-7 cells (Fig. 4D, white arrows). This availability and high uptake efficiency of the N/P 30 micelles yielded a 2.9 fold higher gene expression in comparison with control nanocarriers (Fig. 5A). To assure that this green fluorescence visualized in confocal micrographs was from intracellular located GFP, the cells were additionally stained with a membrane probe (WGA-Alexa 594®) to delimit the cell membranes (Fig. 5C and E). The expression of the transgene suggests that mcDNA reaches the nuclear compartment after delivery by PPP micelleplexes as shown in Fig. 5B. Gene expression data demonstrates that the N/P 30 mcDNA-micelleplexes achieve the highest transgene expression of all tested formulations as revealed by GFP quantification and CLSM analysis (Fig. 5A and B), thus confirming their superior efficiency. Owing to these characteristics the N/P 30 mcDNA-micelleplexes were selected for subsequent studies.

3.5. Nanocarriers' uptake and expression in 3D tumor spheroids

Despite 2D cell cultures provide a rapid platform for evaluating the biological performance of novel nanocarriers throughout pre-clinical development stages, they remain highly limited in closely reproducing the *in vivo* tumor microenvironment [49]. In truth, it is highly challenging to address in 2D the real 3D architecture of the tumor mass, the close cell–cell contacts, pH/nutrient gradients and mass transfer limitations found in *in vivo* tumors [50]. The recently developed micromolding technologies for 3D cell culture have come to bridge this important gap in a way that tumor microtissues which mimic the *in vivo* microenvironment can be produced *in vitro* under highly reproducible conditions (Fig. 6A). The 3D spheroids produced by using the patterned micromolds had well defined spherical shape and size ranging from 500 to 600 μm (Fig. 6B), a key parameter that allows these models to

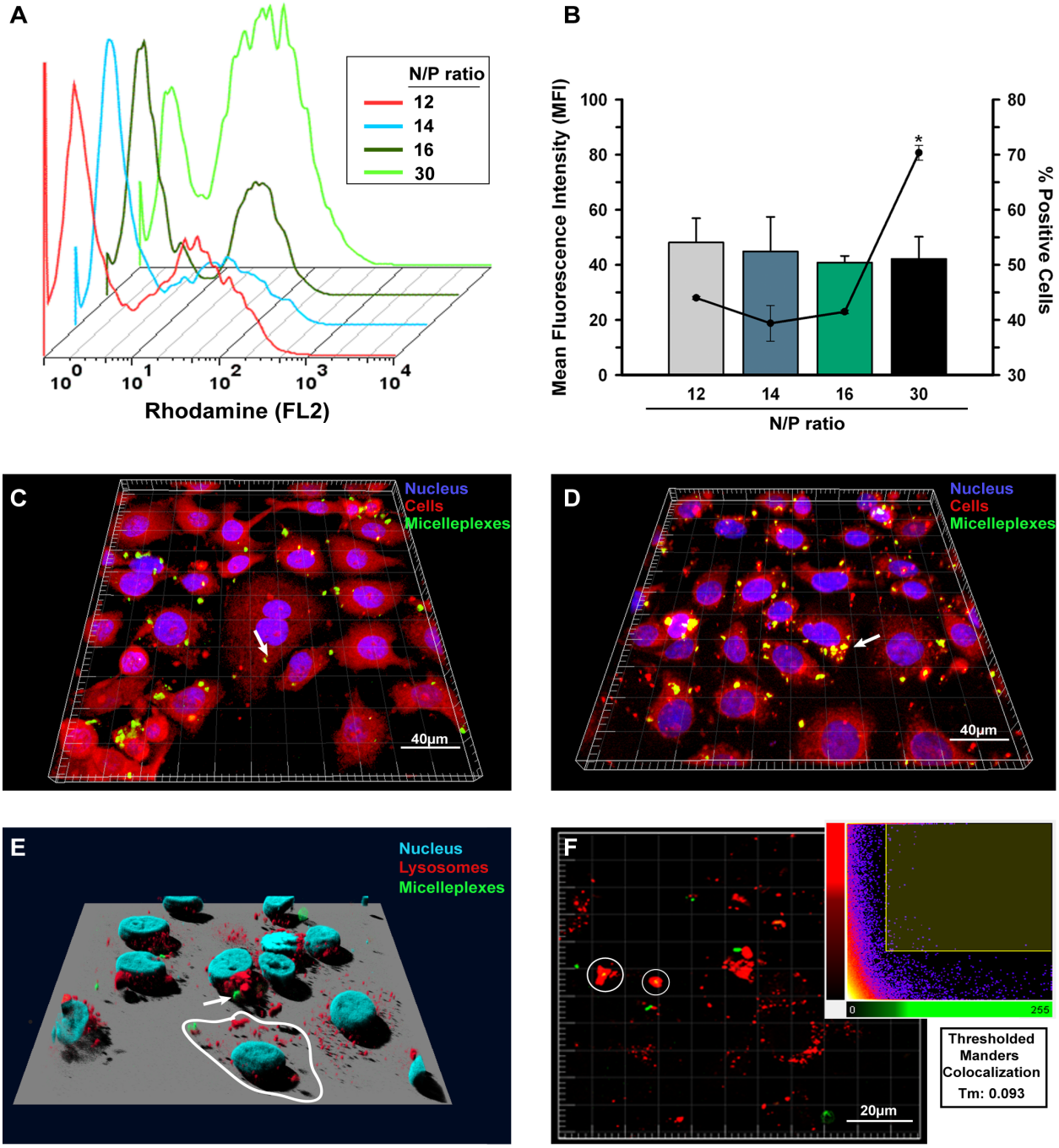

Fig. 4. Micelleplex uptake in MCF-7 cells. A.) Representative histograms of RITC-mcDNA micelleplex uptake. B.) Flow cytometry analysis of RITC-mcDNA PPP nanocarriers' uptake. Data represents mean ± s.d., $n = 3$. C and D.) Representative CLSM images of N/P 12 and N/P 30 micelleplex internalization in breast cancer cells, respectively. Blue channel: nucleus. Red channel: cell membrane WGA-Alexa 594®. Green channel: FITC-labeled mcDNA E.) 3D reconstruction of micelleplex intracellular trafficking. F.) Threshold Manders (Tm) colocalization analysis of mcDNA-micelleplexes (N/P 30) in lysosomes. Blue channel: nucleus; green channel: FITC-labeled mcDNA; red channel: lysosomes (Lysotracker Red DND-99®). White arrows indicate FITC-mcDNA. (For interpretation of the references to color in this figure legend, the reader is referred to the web version of this article.)

form necrotic regions which resemble those found in the majority of solid tumors [50].

In an attempt to unravel the potential of PPP micelleplexes for the administration to solid tumors, mcDNA-mediated GFP expression was evaluated in the assembled 3D microtissues. For this purpose 3D spheroids were incubated with different micelle formulations to evaluate penetration and distribution of gene expression in the tumor volume. GFP positive cells were detected in the spheroid interior, demonstrating that the delivery systems penetrate into 3D MCTS (Fig. 6C and D). This gene expression is also exhibited in z-stack images of spheroids models, in which fluorescence is visible (Fig. 6E1 to E24). As demonstrated in Fig. 6E gene expression is homogeneous in the spheroid and is observed deep in the spheroid (Fig. 6E17 to E24). Achieving gene expression in deeper spheroid regions is very important since it influences the number of cells exposed to the therapeutic molecules. A quantitative analysis of GFP intensity indicated that mcDNA-PPP N/P 30 micelles were the most efficient (Fig. 6D). The highest gene expression mediated by N/P 30 micelles is in accordance to the data obtained in 2D *in vitro* cultures. Such, indicates that this particular formulation is more effective in comparison with the other micellar carriers tested and that it should be the

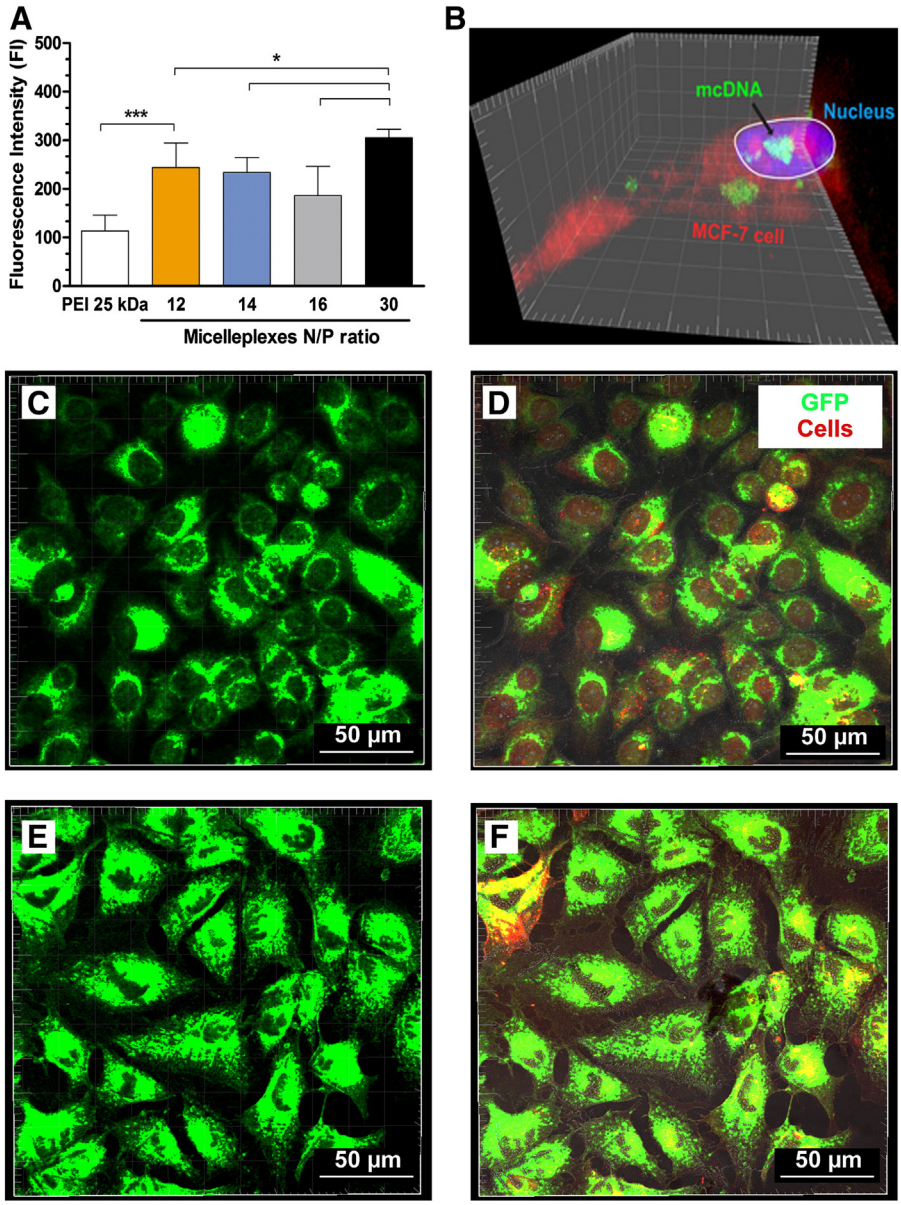

Fig. 5. mcDNA micelleplexes 2D *in vitro* gene expression. A.) Quantitative analysis of GFP fluorescence in MCF-7 cells. Data is presented as mean ± s.d., $n = 5$, $^{*}p < 0.05$, and $^{***}p < 0.001$. n.s. — not significant. B.) 3D confocal micrograph of FITC-mcDNA in the nuclear compartment of MCF-7 cells. C and E.) Representative maximum intensity projection (MIP) of GFP expression after 48 h in MCF-7 cells, mediated by the micelleplexes formulated at N/P ratios of 12 and 30, respectively. D and F.) Merged images of N/P 12 and 30 micelleplexes mediated GFP expression, respectively. PEI 25 kDa/mcDNA were used as control particles. Green channel: GFP. Red channel: cell membrane (WGA-Alexa 594®).

most suitable for tumor administration. The correlation of 3D spheroids data with *in vivo* administration showed that the N/P 30 micelleplexes were also able to promote GFP expression when administered in 4T1 breast cancer tumor models as demonstrated in Fig. 7. For *in vivo* assays orthotopic 4T1 breast cancer tumor models were successfully induced in Balb/c mice by injection into the mammary foot pad (Fig. 7A, B and C). All tumors were then treated with PPP micelleplexes and gene expression was evaluated by *ex vivo* fluorescence imaging. The obtained results show an intense GFP expression in comparison with non-treated tumor (Fig. 7D and G). These findings suggest that the administered PPP micelles remained in the tumor tissue after intratumoral administration. *Ex vivo* imaging also showed that transgene expression was relatively distributed in the tumor mass and not limited to a small area (Fig. 7H). An absence of gene expression in other organs (spleen and kidney) was observed and negligible expression was visualized in the liver and lung (Fig. S5).

3.6. Co-delivery of mcDNA and chemotherapeutics

Since the nanocarriers were capable of delivering mcDNA to cancer cells, the co-delivery of minicircles and chemotherapeutics was investigated in an attempt to take further advantage of the PPP amphiphilic triblock copolymer design (Fig. 8, schematics A). The simultaneous delivery of these macromolecules in a single delivery system is exceptionally challenging since they present very different physicochemical characteristics such as recently reviewed by Li and co-workers [13]. Dual loaded micelles were formulated by initially encapsulating Dox in the micelles hydrophobic core through the solvent displacement method followed by sonication. With this technique the drug and triblock copolymer are dissolved in an organic solvent which is subsequently evaporated. The film that is formed is then resuspended in water and micelles self-assembly is promoted by sonication. In this way, Dox is encapsulated in the hydrophobic core formed by PLA.

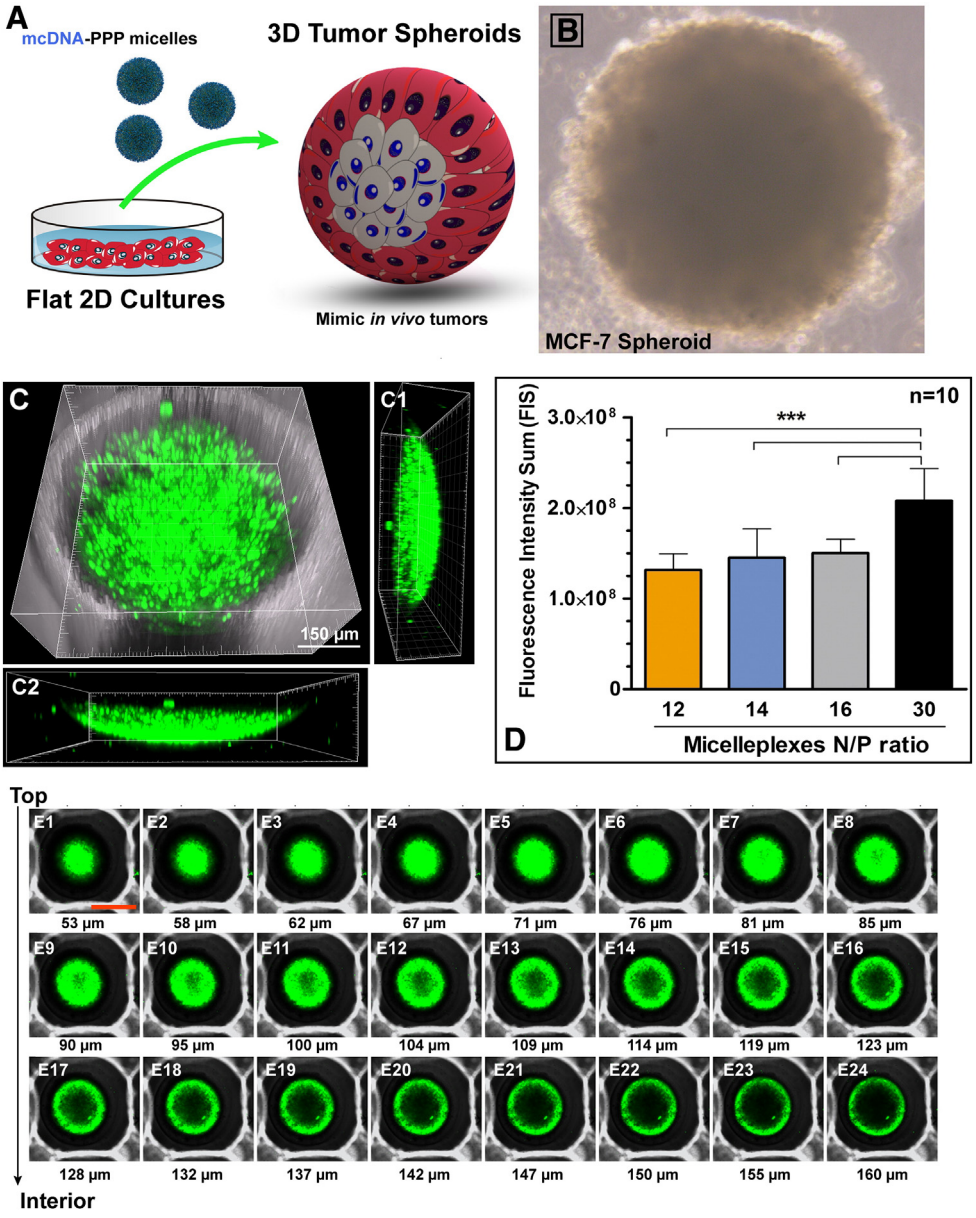

Fig. 6. Evaluation of mcDNA-micelleplex GFP expression in 3D tumor spheroids mediated by N/P 30 micelles. A.) Schematics of the assays in 3D *in vitro* models of solid tumors, 3D spheroids. B.) Optical micrograph of MCF-7 spheroid. C.) 3D reconstruction and orthogonal projection of GFP expressing tumor spheroids. D.) GFP fluorescence intensity sum in the 3D spheroids volume. Data is presented as mean ± s.d., $n = 10$, and ***$p < 0.001$. E1 to E24.) Representative CLSM images of GFP expression along the 3D volume. Green channel: GFP. Scale bar represents 500 μm. N/P 30 micelles.

Following Dox micelles assembly, mcDNA loading is promoted by the electrostatic complexation between the negatively charged phosphate groups in mcDNA and the positively charged amines of PEI. The establishment of this electrostatic interaction is promoted by rapid vortexing that culminates with micelleplex formation. The nanocarriers will thus be dual loaded with Dox–mcDNA after this two-step methodology. To evaluate mcDNA loading its complexation with PEI was studied by agarose gel electrophoresis. The PPP N/P 30 micellar formulation was selected for investigating co-delivery due to its smaller size and neutral surface charge. This particular choice was further supported by N/P 30 micelles improved uptake and gene expression in 2D and 3D models (Figs. 4–6). Moreover, this formulation was chosen since as demonstrated by molecular mechanics the potential mean force of PEI–DNA interaction is higher even when DNA is overneutralized by PEI amines [51], which assures its total aggregation. In fact, the obtained results confirm that the inclusion of an anti-tumoral drug in the micellar core does not affect nanocarriers' ability to condense mcDNA (Fig. 8B). These results emphasize a very interesting aspect of the synthesized delivery system since it demonstrates its versatility towards the encapsulation of various bioactive molecules by different molecular forces. On one side Dox is encapsulated in the micelle core by the establishment of hydrophobic forces with the PLA block, and from the other mcDNA is condensed with the amines of PEI. The interaction of PEI and negatively charged nucleic acids such as mcDNA is very interesting since it occurs under mild conditions that assure the maintenance of DNA structure [52]. This interaction is mainly governed by electrostatic interactions and also hydrogen bonding that together contribute for the potential mean force of PEI–DNA interactions as revealed by molecular dynamics simulation [51].

DLS analysis showed that the mcDNA–Dox micelleplexes produced have an average size of ~190 nm and a PDI of 0.319 (Fig. 8C), indicating a potential for tumor accumulation through the EPR effect [53]. In

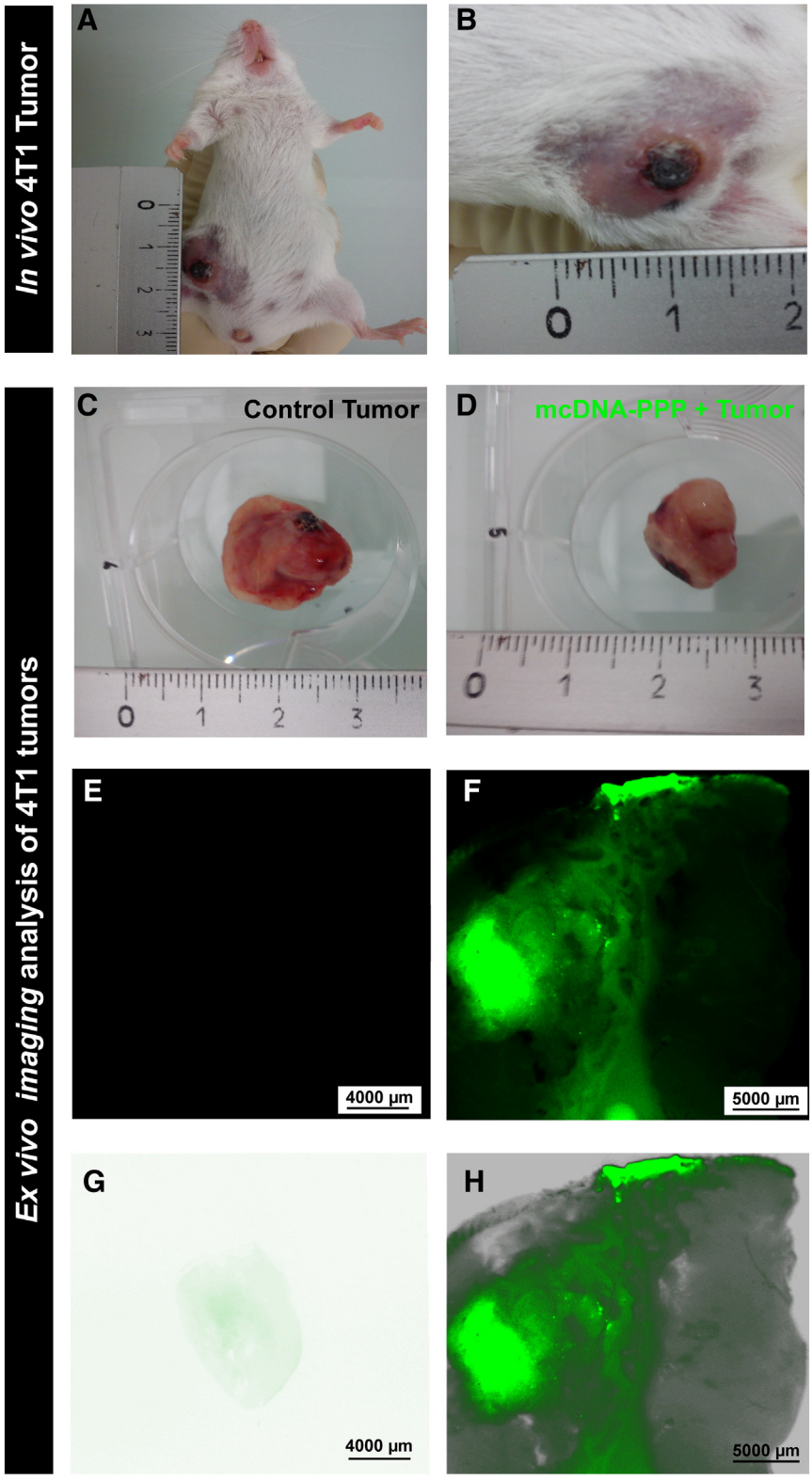

Fig. 7. *In vivo* evaluation of mcDNA expression mediated by PPP micelles (N/P 30). A and B.) Representative image of 4T1 tumor bearing mice models. C and D.) Surgical removed control (non-injected) and treated tumor (mcDNA-PPP micelles (N/P 30)), respectively. E and F.) *Ex vivo* GFP channel fluorescence micrographs of control and treated tumor sections after 48 h, respectively. G and H.) *Ex vivo* merged channel images (GFP and differential interference contrast (DIC)), of control and treated tumor sections. Green channel: GFP; gray channel: DIC.

contrast, PPP micelles produced only with Dox demonstrated a significantly higher average size (Fig. S6), a finding that may be correlated with the fact that PEI chains are not condensed as occurs in the case of mcDNA-loaded nanocarriers.

The presence of Dox in the PLA hydrophobic core was studied by FTIR analysis, which has revealed an increase in the C–H stretching band (2932 cm^{-1}) in drug loaded micelle (Fig. 8D). This increase in band intensity is assigned to the presence of Dox [54].

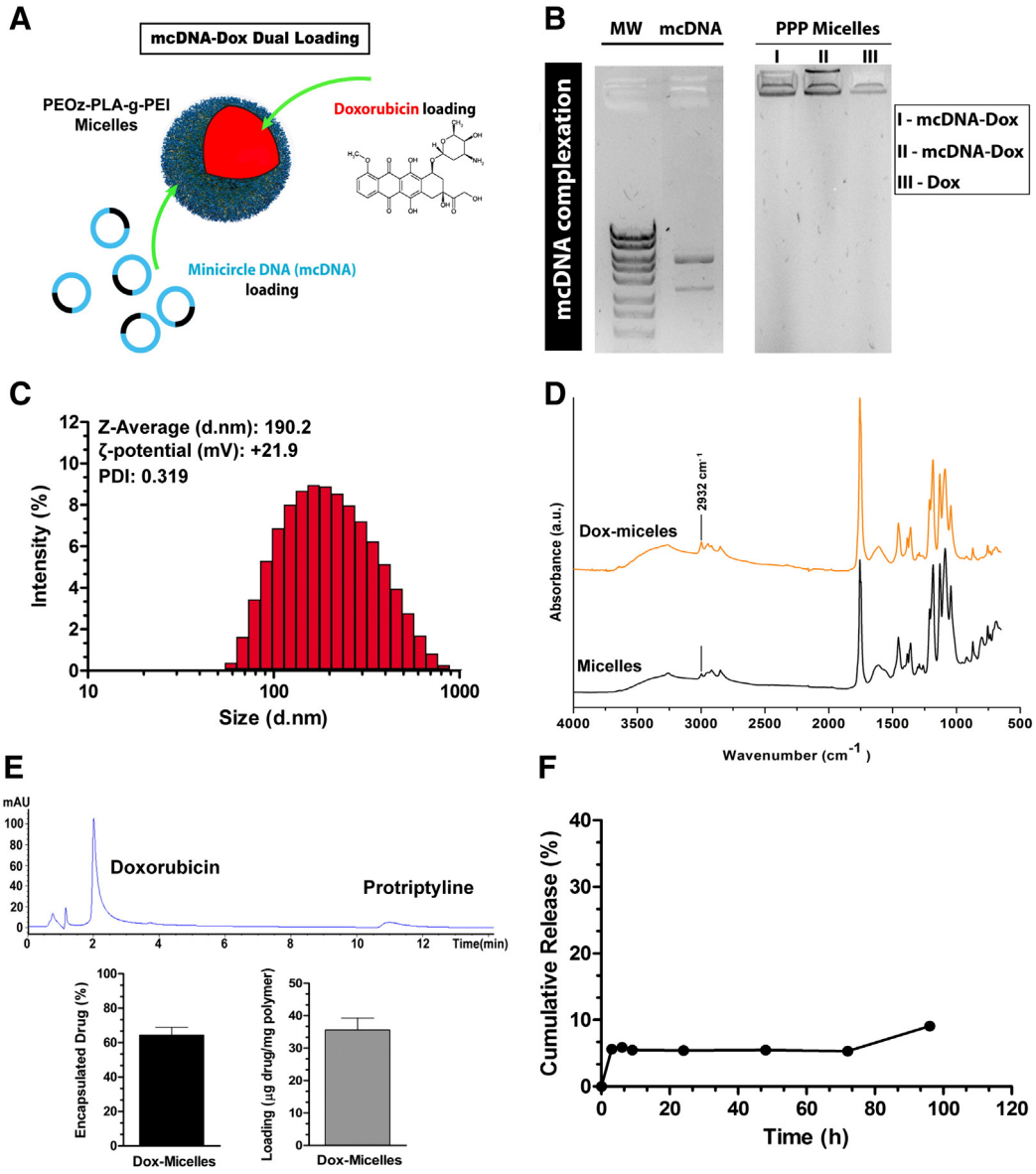

Fig. 8. Physicochemical characterization of mcDNA–Dox dual loaded PPP micelleplexes. A.) Schematics of the dual loading concept. B.) Agarose gel electrophoresis of mcDNA complexation in Dox–PPP micelles (N/P 30). I and II — mcDNA–Dox micelles. III — Dox-micelles. MW — represents molecular weight ladder; mcDNA — represents naked DNA. C.) DLS analysis of mcDNA–Dox PPP nanocarriers' size and zeta potential. D.) FTIR spectroscopy of blank and Dox-loaded micelles. E.) UPLC chromatographic analysis of Dox encapsulation and loading efficiency. Data represents mean ± s.d., $^{*}p < 0.05$, and n = 3. F.) UPLC analysis of Dox cumulative release from PPP nanocarriers.

The UPLC-based analysis of drug encapsulation efficiency in PPP carriers evidences that the PLA hydrophobic core is capable of entrapping Dox with high efficacy (>64%). Moreover, the PPP triblock copolymers have a higher drug loading capacity (~36%) in comparison to other delivery systems for example like those comprised by pegylated liposomes [55]. Drug release profile of PPP micelles was significantly prolonged in time and no apparent initial burst release was observed (Fig. 8F). We hypothesize that the increase in Dox release observed at 75 h might be correlated with degradation/erosion of the copolymer micelles.

3.7. Dual loaded nanocarriers uptake and anti-tumoral effect

Considering that the synthesized PPP copolymers are capable of simultaneously loading mcDNA and Dox, the biological activity of these micelleplexes was investigated to evaluate their potential to be used for therapeutic applications. Intracellular uptake was assessed through flow cytometry by analyzing Dox fluorescence. After cell treatment with Dox-micelles or mcDNA–Dox micelleplexes for 4 h, the dual loaded carriers demonstrated a slightly lower amount of particles inside cells in comparison with single Dox-micelles (Fig. 9B). This difference is consistent with the surface charge differences of Dox-micelles (+42.3 mV, Fig. S6) and mcDNA–Dox micelleplexes (+21.9 mV, Fig. 8C). But bearing in mind that single Dox micelles have a higher average size (~344 nm) and highly positive surface charge these particles would be less effective when administered *in vivo* in comparison with dual loaded micelles. Nevertheless, both carriers (single and dual loaded) exhibited similar uptake efficiencies with more than 95% positive cells being transfected, revealing that they are very effective. In comparison with free Dox administration, PPP micelles generally promoted an increased intracellular concentration of the anti-tumoral drug, an important finding if a higher therapeutic effect is aimed to be obtained (Fig. 9B). Confocal micrographs confirm the extensive uptake of dual loaded micelles with some of the carriers being localized in the cell nucleus (gold arrows in Fig. S7). Assuring this nuclear localization is crucial since Dox targets cell replication mechanisms and intercalates with DNA triggering damage responses [56]. The anti-tumoral activity of dual-loaded carriers was

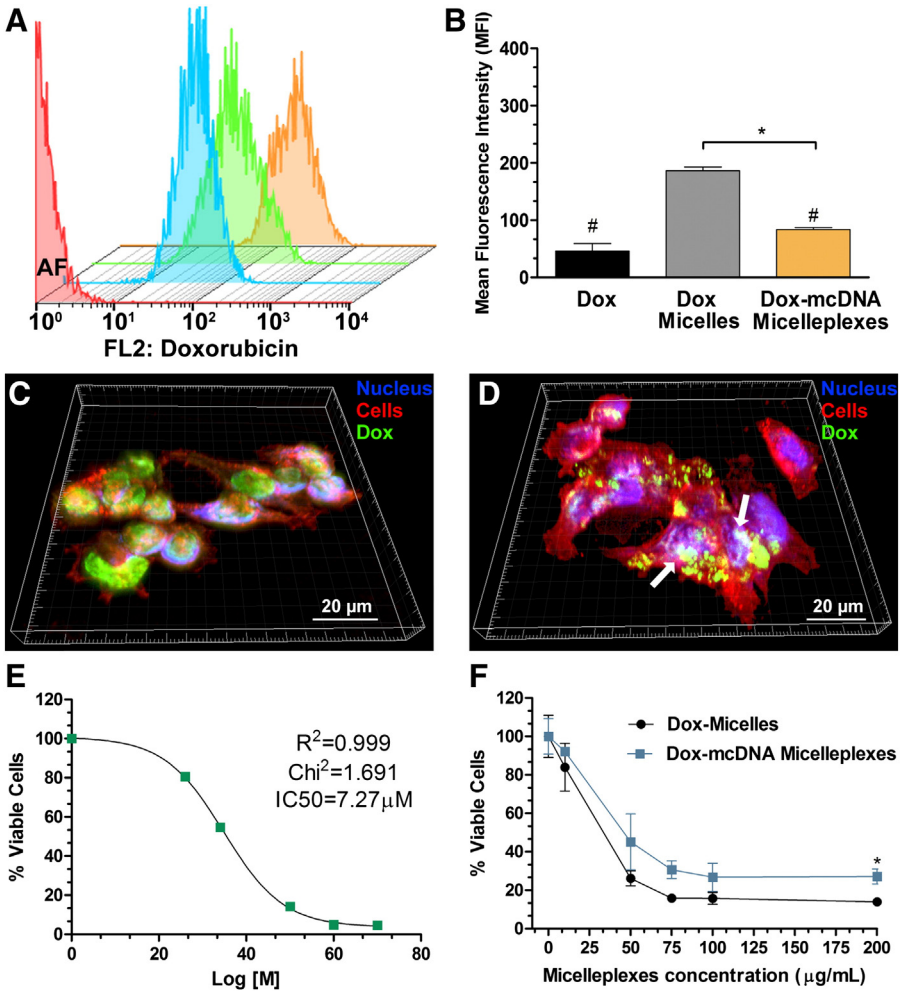

Fig. 9. mcDNA–Dox dual loaded micelleplex evaluation in MCF-7 cancer cells. A.) Representative flow cytometry histograms of nanocarriers' uptake (N/P 30). Blue: free Dox (5 μg/mL); green: mcDNA–Dox micelleplexes; orange: Dox-micelles. B.) Cell uptake analysis of single and dual loaded PPP nanocarriers. C and D.) Confocal micrographs of Dox-loaded and mcDNA–Dox loaded micelleplexes, respectively. E.) Dox IC50 determination in MCF-7 cells. F.) Anti-tumoral activity of PPP micelleplexes. Data represents mean ± s.d., $^{*}p < 0.05$, $^{\#}p < 0.05$, and n = 5.

confirmed in MCF-7 cells. The IC50 of free Dox is slightly higher than that generally described in the literature (1.12 μM, [57]), indicating that cells were possibly more resistant. Despite this, an anti-tumoral activity was observed for both single and dual loaded nanocarriers at relatively low concentrations (100–200 μg/mL, Fig. 9F). These results, also show that dual micelles exhibit slightly higher viability than single loaded micelles. However, as mentioned, dual-loaded micelles have more suitable physicochemical characteristics for *in vivo* administration. From a therapeutic perspective, the co-delivery of drug–mcDNA presents much more advantages in comparison with single drug treatments. As an example, it is generally recognized that cancer cells often become resistant to chemotherapeutics due to efflux transporters, hence, if mcDNA vectors are co-delivered with drugs they can encode tumor suppressor genes that can further potentiate the therapeutic outcome. In addition, recent reports have emphasize the co-delivery of drug-siRNA either to reverse P-gp mediated drug resistance or to target important proliferation pathways as reviewed by Li and co-workers [13]. The novelty of combining mcDNA with drugs is that this vector can achieve prolonged gene expression *in vivo*, for up to one year, without being silenced as recently described by Viecelli et al., 2014 [10]. This property can be explored to express small haipin RNA (shRNA) during prolonged periods of time overcoming the issues of multiple administration and loss of RNA activity, since the cell is continuously producing the therapeutic biomolecules. These evidences emphasize the potential of delivering mcDNA–drug combinations which has been a rather unexplored area so far.

4. Conclusions

In summary, we have developed a novel amphiphilic triblock copolymer that self-assembles into nanosized carriers. This system has proven to complex recently created minicircle DNA vectors that have superior safety and gene expression efficiency. The PPP micelleplexes were highly stable in physiologic conditions and biocompatible proving that PEOz is a suitable substitute for the generally used PEG moieties which have shown adverse *in vivo* effects. Both mcDNA and dual loaded micelles were very efficient in achieving cell internalization which was consistent with the effective gene expression and anti-tumoral activity that was obtained. *In vivo* assays are currently ongoing in order to evaluate the co-delivery of mcDNA–Dox in tumor bearing mice.

Above all, the PPP carriers have demonstrated that this triblock copolymer is versatile for a range of applications that include mcDNA delivery and its combinations with chemotherapeutics. To the best of our knowledge this is the first time that co-delivery of mcDNA and anti-tumoral drugs is described. Our findings open a new range of possibilities regarding the design of effective systems that are not based on PEG, paving the way towards a change in the paradigm of using pegylation to avoid RES uptake.

In the future this system can also be used for other therapeutic applications rather than those focused just on cancer therapy. Its chemical structure is highly adaptable, in such a way that it allows further modification with cell targeting moieties or imaging macromolecules for nanodiagnostics/theranostic applications.

Acknowledgments

The authors would like to acknowledge Dr. Frédérick Foucher for all the help in sample preparation and acquisition of AFM images, and Dr. Anthony Delalande and Dr. Patrick Barille for all the help. The authors would also like to acknowledge Dr. Alexandra Foucault for the help in *ex vivo* image acquisition. This work was supported by the Portuguese Foundation for Science and Technology (FCT), (PTDC/EBB-BIO/114320/2009 and PEst-C/SAU/UI0709/2011). Vítor M. Gaspar acknowledges an individual PhD fellowship from FCT (SFRH/BD/80402/2011). All the authors do not disclose any conflict of interest.

Appendix A. Supplementary data

Supplementary data to this article can be found online at http://dx.doi.org/10.1016/j.jconrel.2014.06.040.

References

[1] V.M. Gaspar, I.J. Correia, Â. Sousa, F. Silva, C.M. Paquete, J.A. Queiroz, F. Sousa, Nanoparticle mediated delivery of pure P53 supercoiled plasmid DNA for gene therapy, J. Control. Release 156 (2011) 212–222.
[2] M. Brenner, M.-C. Hung, Cancer Gene Therapy by Viral and Non-viral Vectors, John Wiley & Sons, 2014.
[3] M.A. Kay, State-of-the-art gene-based therapies: the road ahead, Nat. Rev. Genet. 12 (2011) 316–328.
[4] L.E.G. Maniar, J.M. Maniar, Z.-Y. Chen, J. Lu, A.Z. Fire, M.A. Kay, Minicircle DNA vectors achieve sustained expression reflected by active chromatin and transcriptional level, Mol. Ther. 21 (2013) 131–138.
[5] J. Mairhofer, R. Grabherr, Rational vector design for efficient non-viral gene delivery: challenges facing the use of plasmid DNA, Mol. Biotechnol. 39 (2008) 97–104.
[6] M. Grund, M. Schleef, Minicircle Patents: A Short IP Overview of Optimizing Nonviral DNA Vectors, Minicircle and Miniplasmid DNA Vectors: The Future of Nonviral and Viral Gene Transfer, 2013. 1–6.
[7] A. Darquet, B. Cameron, P. Wils, D. Scherman, J. Crouzet, A new DNA vehicle for nonviral gene delivery: supercoiled minicircle, Gene Ther. 4 (1997) 1341.
[8] M.A. Kay, C.Y. He, Z.Y. Chen, A robust system for production of minicircle DNA vectors, Nat. Biotechnol. 28 (2010) 1287–1289.
[9] V.M. Gaspar, C.J. Maia, J.A. Queiroz, C. Pichon, I.J. Correia, F. Sousa, Improved minicircle DNA biosynthesis for gene therapy applications, Hum. Gene Ther. Methods 25 (2014) 93–105.
[10] H.M. Viecelli, R.P. Harbottle, S.P. Wong, A. Schlegel, M.K. Chuah, T. VandenDriessche, C.O. Harding, B. Thöny, Treatment of phenylketonuria using minicircle-based naked-DNA gene transfer to murine liver, Hepatology (2014) (in press).
[11] D. Catanese, J. Fogg, D. Schrock, B. Gilbert, L. Zechiedrich, Supercoiled minivector DNA resists shear forces associated with gene therapy delivery, Gene Ther. 19 (2011) 94–100.
[12] M. Wang, K. Alberti, S. Sun, C.L. Arellano, Q. Xu, Combinatorially designed lipid-like nanoparticles for intracellular delivery of cytotoxic protein for cancer therapy, Angew. Chem. 126 (2014) 2937–2942.
[13] J. Li, Y. Wang, Y. Zhu, D. Oupický, Recent advances in delivery of drug–nucleic acid combinations for cancer treatment, J. Control. Release 172 (2013) 589–600.
[14] H. Fan, Q.-D. Hu, F.-J. Xu, W.-Q. Liang, G.-P. Tang, W.-T. Yang, In vivo treatment of tumors using host-guest conjugated nanoparticles functionalized with doxorubicin and therapeutic gene pTRAIL, Biomaterials 33 (2012) 1428–1436.
[15] L.K. Bogart, G. Pourroy, C.J. Murphy, V. Puntes, T. Pellegrino, D. Rosenblum, D. Peer, R. Lévy, Nanoparticles for imaging, sensing, and therapeutic intervention, ACS Nano 8 (2014) 3107–3122.
[16] M. Keeney, S.-G. Ong, A. Padilla, Z. Yao, S. Goodman, J.C. Wu, F. Yang, Development of poly(β-amino ester)-based biodegradable nanoparticles for nonviral delivery of minicircle DNA, ACS Nano 7 (2013) 7241–7250.
[17] M.J. Osborn, R.T. McElmurry, C.J. Lees, A.P. DeFeo, Z.-Y. Chen, M.A. Kay, L. Naldini, G. Freeman, J. Tolar, B.R. Blazar, Minicircle DNA-based gene therapy coupled with immune modulation permits long-term expression of [alpha]-L-Iduronidase in mice with mucopolysaccharidosis type I, Mol. Ther. 19 (2011) 450–460.
[18] O. Taratula, A. Kuzmov, M. Shah, O.B. Garbuzenko, T. Minko, Nanostructured lipid carriers as multifunctional nanomedicine platform for pulmonary co-delivery of anticancer drugs and siRNA, J. Control. Release 171 (2013) 349–357.
[19] W.X. Mai, T. Xia, H. Meng, Development of pharmaceutically adapted mesoporous silica nanoparticles for siRNA delivery, Advanced Delivery and Therapeutic Applications of RNAi, 2013. 187–205.
[20] L. Zhu, F. Perche, T. Wang, V.P. Torchilin, Matrix metalloproteinase 2-sensitive multifunctional polymeric micelles for tumor-specific co-delivery of siRNA and hydrophobic drugs, Biomaterials 35 (2014) 4213–4222.
[21] C. Liu, F. Liu, L. Feng, M. Li, J. Zhang, N. Zhang, The targeted co-delivery of DNA and doxorubicin to tumor cells via multifunctional PEI-PEG based nanoparticles, Biomaterials 34 (2013) 2547–2564.
[22] M. Lundqvist, Nanoparticles: tracking protein corona over time, Nat. Nanotechnol. 8 (2013) 701–702.
[23] R.I. El-Gogary, N. Rubio Carrero, J.T.-W. Wang, W.T. Al-Jamal, M. Bourgognon, H. Kafa, M. Naeem, R. Klippstein, V. Abbate, F. Leroux, Polyethylene glycol conjugated polymeric nanocapsules for targeted delivery of quercetin to folate-expressing cancer cells in vitro and in vivo, ACS Nano 8 (2014) 1384–1401.
[24] N. Kamaly, Z. Xiao, P.M. Valencia, A.F. Radovic-Moreno, O.C. Farokhzad, Targeted polymeric therapeutic nanoparticles: design, development and clinical translation, Chem. Soc. Rev. 41 (2012) 2971–3010.
[25] T. Ishida, X. Wang, T. Shimizu, K. Nawata, H. Kiwada, PEGylated liposomes elicit an anti-PEG IgM response in a T cell-independent manner, J. Control. Release 122 (2007) 349–355.
[26] A.S. Abu Lila, H. Kiwada, T. Ishida, The accelerated blood clearance (ABC) phenomenon: clinical challenge and approaches to manage, J. Control. Release 172 (2013) 38–47.
[27] R. Saadati, S. Dadashzadeh, Z. Abbasian, H. Soleimanjahi, Accelerated blood clearance of pegylated plga nanoparticles following repeated injections: effects of polymer dose, peg coating, and encapsulated anticancer drug, Pharm. Res. 30 (2013) 985–995.
[28] A. Mero, G. Pasut, L.D. Via, M.W. Fijten, U.S. Schubert, R. Hoogenboom, F.M. Veronese, Synthesis and characterization of poly(2-ethyl 2-oxazoline)-conjugates with proteins and drugs: suitable alternatives to PEG-conjugates? J. Control. Release 125 (2008) 87–95.
[29] R. Hoogenboom, H. Schlaad, Bioinspired poly(2-oxazoline) s, Polymers 3 (2011) 467–488.
[30] R. Luxenhofer, G. Sahay, A. Schulz, D. Alakhova, T.K. Bronich, R. Jordan, A.V. Kabanov, Structure-property relationship in cytotoxicity and cell uptake of poly(2-oxazoline) amphiphiles, J. Control. Release 153 (2011) 73–82.
[31] T.X. Viegas, M.D. Bentley, J.M. Harris, Z. Fang, K. Yoon, B. Dizman, R. Weimer, A. Mero, G. Pasut, F.M. Veronese, Polyoxazoline: chemistry, properties, and applications in drug delivery, Bioconjug. Chem. 22 (2011) 976–986.
[32] J. Ulbricht, R. Jordan, R. Luxenhofer, On the biodegradability of polyethylene glycol, polypeptoids and poly(2-oxazoline) s, Biomaterials 35 (2014) 4848–4861.
[33] L.-Y. Qiu, L. Yan, L. Zhang, Y.-M. Jin, Q.-H. Zhao, Folate-modified poly(2-ethyl-2-oxazoline) as hydrophilic corona in polymeric micelles for enhanced intracellular doxorubicin delivery, Int. J. Pharm. 456 (2013) 315–324.
[34] J.G. Marques, V.M. Gaspar, D. Markl, E.C. Costa, E. Gallardo, I.J. Correia, Co-delivery of Sildenafil (Viagra®) and Crizotinib for synergistic and improved anti-tumoral therapy, Pharm. Res. (2014) 1–13.
[35] J. Aguiar, P. Carpena, J. Molina-Bolıvar, C. Carnero Ruiz, On the determination of the critical micelle concentration by the pyrene 1:3 ratio method, J. Colloid Interface Sci. 258 (2003) 116–122.
[36] G. Basu Ray, I. Chakraborty, S.P. Moulik, Pyrene absorption can be a convenient method for probing critical micellar concentration (cmc) and indexing micellar polarity, J. Colloid Interface Sci. 294 (2006) 248–254.
[37] V. Gaspar, J. Marques, F. Sousa, R. Louro, J. Queiroz, I. Correia, Biofunctionalized nanoparticles with pH-responsive and cell penetrating blocks for gene delivery, Nanotechnology 24 (2013) 275101.
[38] V.r. Bennevault-Celton, A. Urbach, O. Martin, C. Pichon, P. Guégan, P. Midoux, Supramolecular assemblies of histidinylated α-cyclodextrin in the presence of DNA scaffold during CDplexes formation, Bioconjug. Chem. 22 (2011) 2404–2414.
[39] I. Horcas, R. Fernández, J.M. Gómez-Rodríguez, J. Colchero, J. Gómez-Herrero, A.M. Baro, WSXM: a software for scanning probe microscopy and a tool for nanotechnology, Rev. Sci. Instrum. 78 (2007).
[40] Y. Li, K. Xiao, J. Luo, W. Xiao, J.S. Lee, A.M. Gonik, J. Kato, T.A. Dong, K.S. Lam, Well-defined, reversible disulfide cross-linked micelles for on-demand paclitaxel delivery, Biomaterials 32 (2011) 6633–6645.
[41] J. Schindelin, I. Arganda-Carreras, E. Frise, V. Kaynig, M. Longair, T. Pietzsch, S. Preibisch, C. Rueden, S. Saalfeld, B. Schmid, Fiji: an open-source platform for biological-image analysis, Nat. Methods 9 (2012) 676–682.
[42] A.P. Napolitano, D.M. Dean, A.J. Man, J. Youssef, D.N. Ho, A.P. Rago, M.P. Lech, J.R. Morgan, Scaffold-free three-dimensional cell culture utilizing micromolded nonadhesive hydrogels, Biotechniques 43 (2007) 494.
[43] P. Li, P. Lai, C. Lin, Reversal of multidrug resistance using poly(L-lactide)-Vitamin E TPGS micelles in breast cancer cell, Biomedical and Pharmaceutical Engineering, 2009. ICBPE'09. International Conference on, IEEE, 2009, pp. 1–5.
[44] V.M. Gaspar, C. Cruz, J.A. Queiroz, C. Pichon, I.J. Correia, F. Sousa, Sensitive detection of peptide–minicircle DNA interactions by surface plasmon resonance, Anal. Chem. 85 (2013) 2304–2311.
[45] T.K. Endres, M. Beck-Broichsitter, O. Samsonova, T. Renette, T.H. Kissel, Self-assembled biodegradable amphiphilic PEG–PCL–lPEI triblock copolymers at the borderline between micelles and nanoparticles designed for drug and gene delivery, Biomaterials 32 (2011) 7721–7731.
[46] S. Kulthe, N. Inamdar, Y. Choudhari, S. Shirolikar, L. Borde, V. Mourya, Mixed micelle formation with hydrophobic and hydrophilic Pluronic block copolymers: implications for controlled and targeted drug delivery, Colloids Surf. B: Biointerfaces 88 (2011) 691–696.
[47] N. Adams, U.S. Schubert, Poly(2-oxazolines) in biological and biomedical application contexts, Adv. Drug Deliv. Rev. 59 (2007) 1504–1520.

[48] S. Maya, L.G. Kumar, B. Sarmento, N. Sanoj Rejinold, D. Menon, S.V. Nair, R. Jayakumar, Cetuximab conjugated O-carboxymethyl chitosan nanoparticles for targeting EGFR overexpressing cancer cells, Carbohydr. Polym. 93 (2013) 661–669.
[49] G. Mehta, A.Y. Hsiao, M. Ingram, G.D. Luker, S. Takayama, Opportunities and challenges for use of tumor spheroids as models to test drug delivery and efficacy, J. Control. Release 164 (2012) 192–204.
[50] B. Weigelt, M.J. Bissell, The need for complex 3D culture models to unravel novel pathways and identify accurate biomarkers in breast cancer, Adv. Drug Deliv. Rev. 69–70 (2014) 42–51.
[51] S. Bagai, C. Sun, T. Tang, Potential of mean force of polyethylenimine-mediated DNA attraction, J. Phys. Chem. B 117 (2012) 49–56.
[52] R. Dias, B. Lindman, DNA Interactions With Polymers and Surfactants, Wiley Online Library, 2008.
[53] C. Cui, Y.-N. Xue, M. Wu, Y. Zhang, P. Yu, L. Liu, R.-X. Zhuo, S.-W. Huang, Cellular uptake, intracellular trafficking, and antitumor efficacy of doxorubicin-loaded reduction-sensitive micelles, Biomaterials 34 (2013) 3858–3869.
[54] R. Jayakumar, A. Nair, N.S. Rejinold, S. Maya, S. Nair, Doxorubicin-loaded pH-responsive chitin nanogels for drug delivery to cancer cells, Carbohydr. Polym. 87 (2012) 2352–2356.
[55] W. Gao, B. Xiang, T.-T. Meng, F. Liu, X.-R. Qi, Chemotherapeutic drug delivery to cancer cells using a combination of folate targeting and tumor microenvironment-sensitive polypeptides, Biomaterials 34 (2013) 4137–4149.
[56] C.F. Thorn, C. Oshiro, S. Marsh, T. Hernandez-Boussard, H. McLeod, T.E. Klein, R.B. Altman, Doxorubicin pathways: pharmacodynamics and adverse effects, Pharmacogenet. Genomics 21 (2011) 440.
[57] D.Y. Lu, M. Huang, C.H. Xu, W.Y. Yang, C.X. Hu, L.P. Lin, L.J. Tong, M.H. Li, W. Lu, X.W. Zhang, Anti-proliferative effects, cell cycle G2/M phase arrest and blocking of chromosome segregation by probimane and MST-16 in human tumor cell lines, BMC Pharmacol. 5 (2005) 11.

Supplementary Information

Poly(2-ethyl-2-oxazoline)-PLA-g-PEI Amphiphilic Triblock Micelles for Co-delivery of Minicircle DNA and Chemotherapeutics

Journal of Controlled Release, 2014
DOI: 10.1016/j.jconrel.2014.06.040

9.1. Results

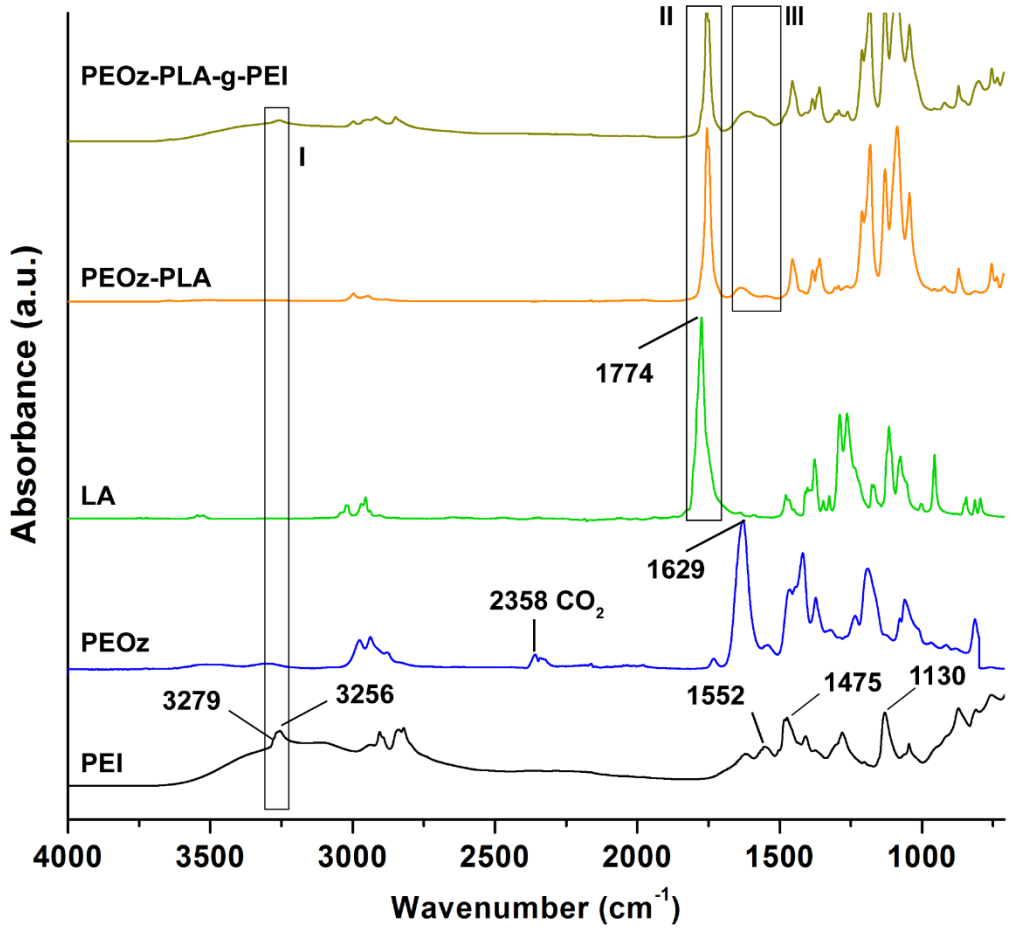

Figure S1. FTIR spectroscopy of PEOz-PLA-g-PEI copolymers step-wise synthesis. The peak observed at 1130 cm^{-1} is assigned to the –C-N stretch [1]. The absorption peak of the CH_2 bend is observed at 1475 cm^{-1}. At 1552 cm^{-1} the -NH_2 bend vibration can also be observed. The PEI characteristic –NH_2 symmetric stretch and –NH_2 asymmetric stretch are visible at 3256 cm^{-1} and 3279 cm^{-1}, respectively (Box I). The PEOz characteristic strong ester (C-O) stretching band is observed at 1629 cm^{-1} [2]. The LA spectra reveals the characteristic C=O stretching adsorption band, which is visible also in the PEOz-PLA copolymer (Box II). In the PEOz-PLA-g-PEI triblock copolymer spectra the characteristic bands of its polymeric elements are visible, particularly Box I and III confirm that PEI was successfully grafted to the PEOz-PLA diblock copolymer due to the presence of amine bands.

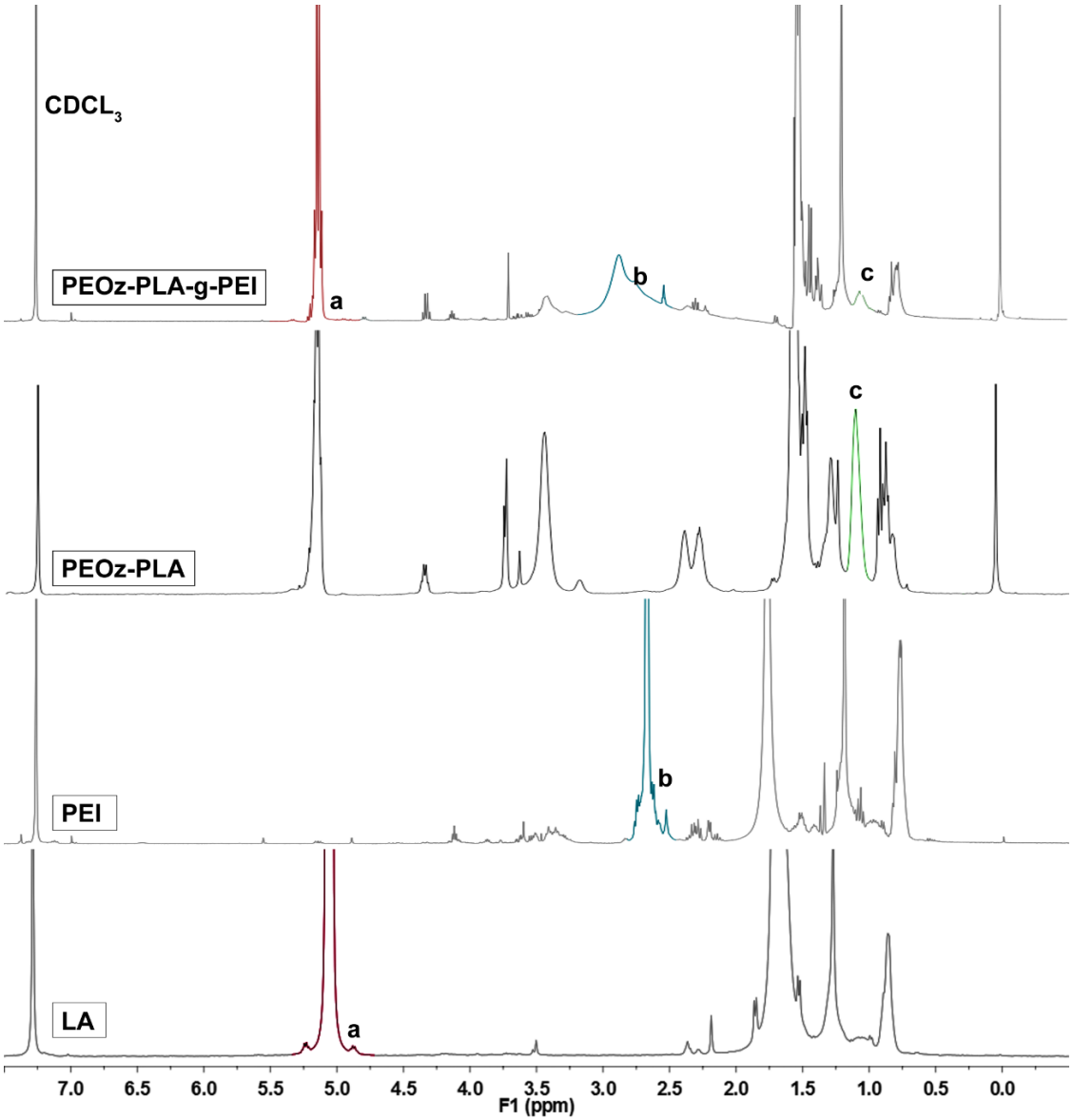

Figure S2. ^{1}H NMR analysis of the step-wise synthesis of PEOz-PLA-g-PEI triblock copolymers. Following ROP of LA the resulting PEOz-PLA diblock exhibits the characteristic methyne (R_1-CH=R_2) protons δ ~ 5.1 ppm **(a - red)**, of the PLA monomer [3]. The methyl proton peaks (CH_3) of PEOz are also observed in the diblock copolymer δ ~ 1.1 ppm **(c - green)** [4]. PEI conjugation was confirmed by the existence of the characteristic methylene (-CH_2) proton resonance peaks **(b - blue)** (δ ~ 2.6 - 2.8 ppm) [5].

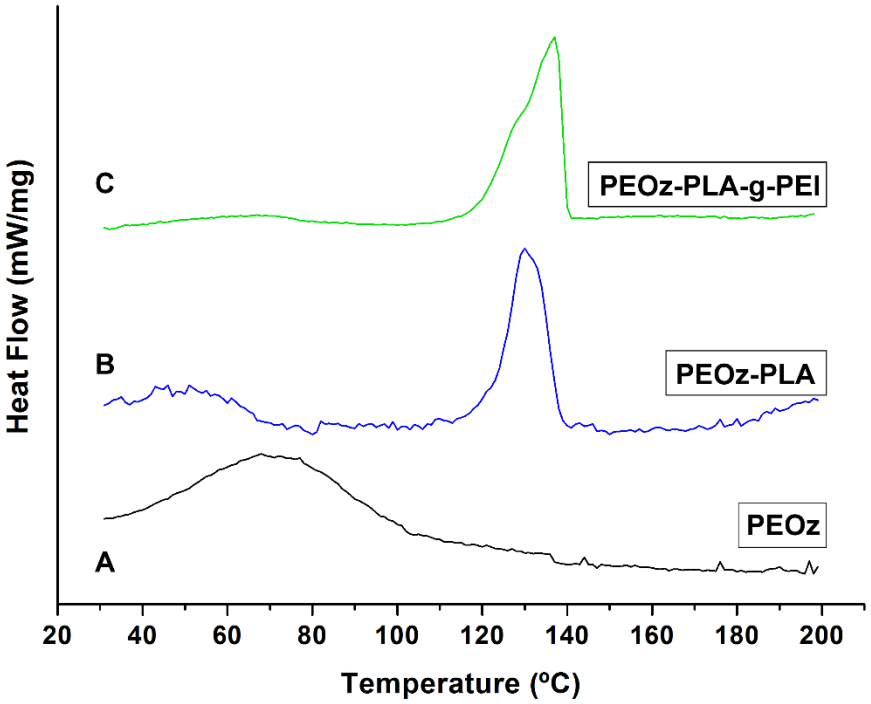

Figure S3. DSC thermograms of the synthesized diblock and triblock copolymers. **A.)** PEOz single polymer (T_m= 70 ºC). **B.)** PEOz-PLA diblock copolymer (T_m= 131 ºC). C.) PEOz-PLA-g-PEI triblock copolymer (T_m= 137 ºC).

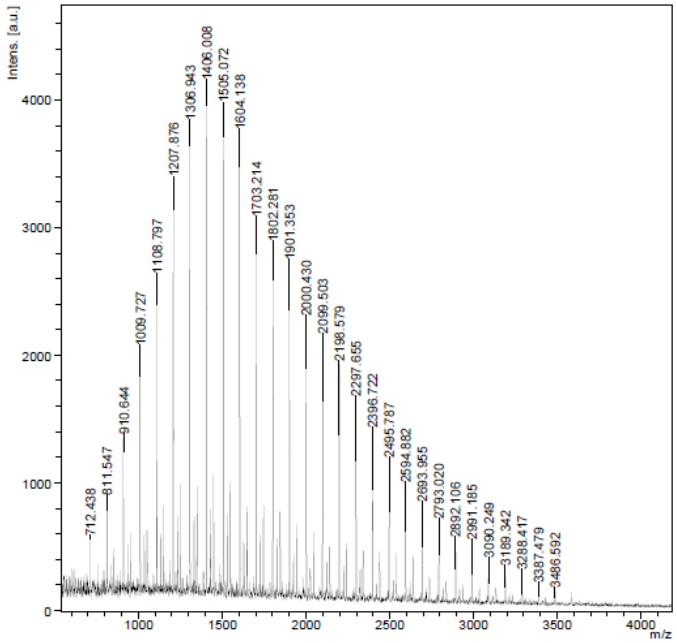

Figure S4. MALDI TOF spectra of PEOz-PLA-g-PEI copolymers. The spectra was acquired in a matrix comprised by 1 mM Dichloromethane/Methanol 50/50, diluted (1:100) in Methanol, 1:1 DHB 20 mg/mL in Acetonitrile/H_2O/TFA

50/49.9/0.1 mixture. The spectra reveals the presence of the mass distribution signals of PEOz repeating unit m/z = 99 Da (higher intensity peaks marked), PEI m/z = 43 Da and PLA m/z=72 (lowest intensity peaks). The triblock copolymer presents a homogenous molecular weight distribution.

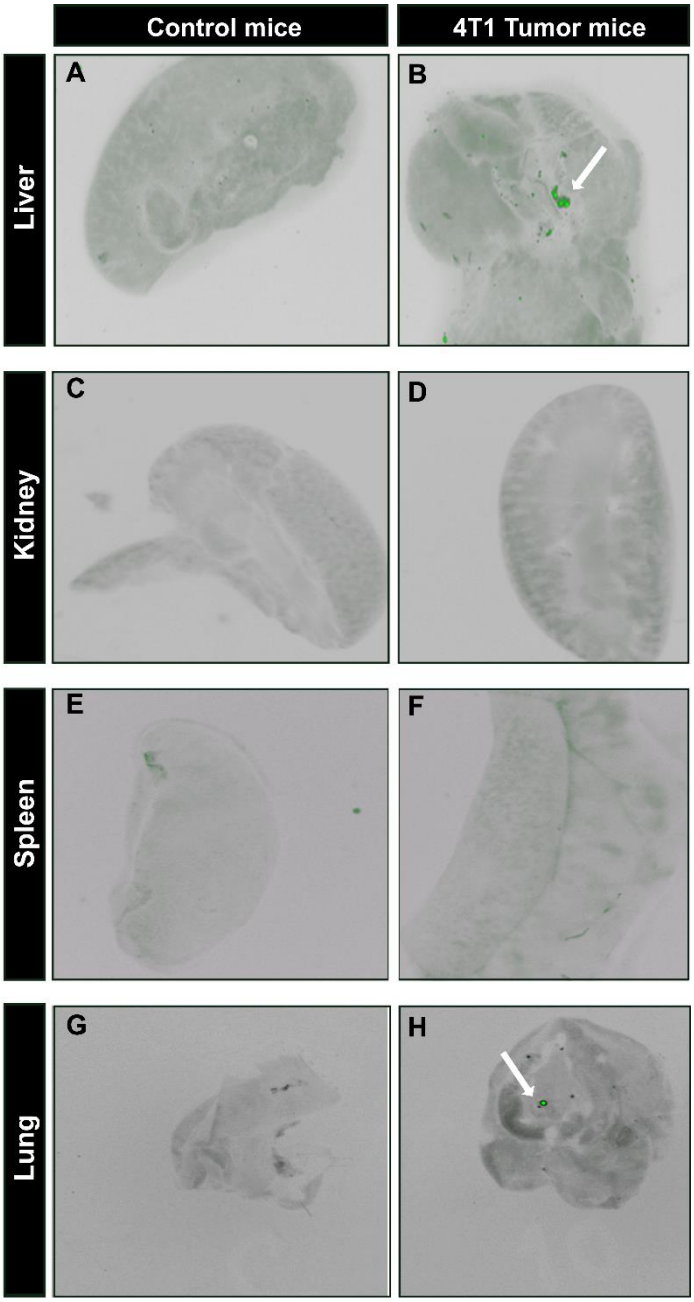

Figure S5. Ex vivo evaluation of mcDNA expression mediated by PPP micelles in different organs of control and 4T1 tumor bearing mice administered with micelles **A and B.)** Liver ex vivo analysis. **C and D.)** Kidney ex vivo analysis. **E and F.)** Ex vivo spleen analysis. **G and H.)** Ex vivo lung analysis. Grey channel: DIC Green Channel: GFP. White arrow indicates GFP.

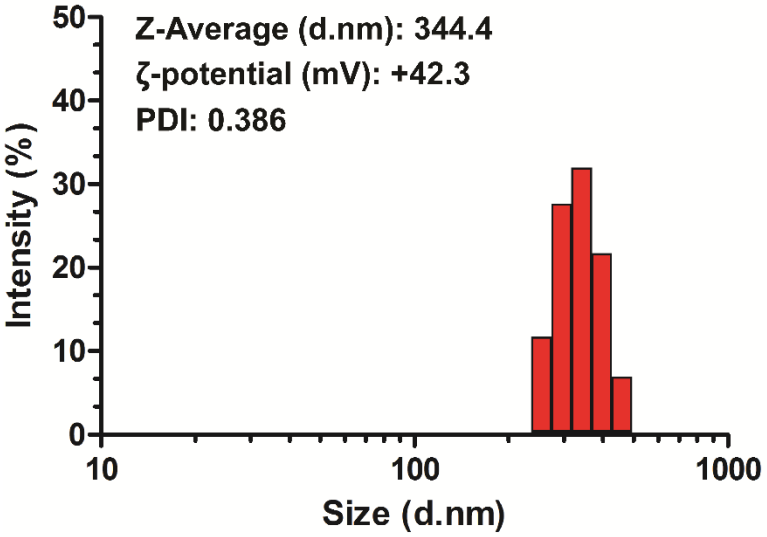

Figure S6. DLS analysis of average size and zeta potential of single Dox-loaded PPP micellar carriers.

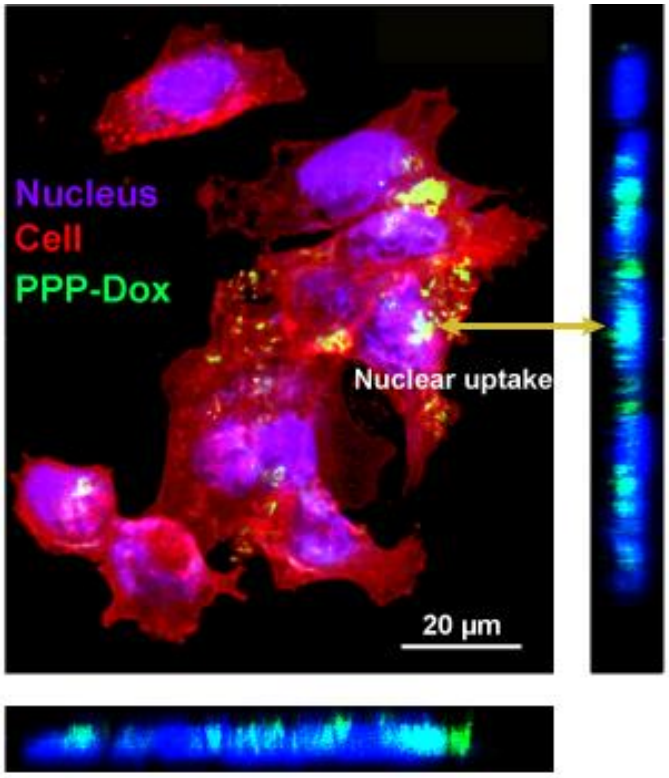

Figure S7. Confocal micrograph in orthogonal projection showing the nuclear localization of mcDNA-Dox loaded PPP micelles (Golden arrows). The xz and yz lateral projections demonstrate the nucleus and internalized nanocarriers. Blue channel: Nucleus stained with Hoechst 33342®; Red channel: Cell membrane stained with WGA-Alexa 594® conjugate. Green Channel: Doxorubicin.

9.2. References

1. Peng, C., Thio, Y., and Gerhardt, R., *Conductive paper fabricated by layer-by-layer assembly of polyelectrolytes and ITO nanoparticles*. Nanotechnology, 2008. **19**(50): p. 505603.
2. Jerca, V.V., Nicolescu, A., Vasilescu, D., Albu, A., and Vuluga, D.M., *Synthesis and structure of 2-ethyl-2-oxazoline macromonomers with styryl end-groups*. UPB Scientific Bulletin Series B, 2009. **71**: p. 29-36.
3. Li, F., Li, S., El Ghzaoui, A., Nouailhas, H., and Zhuo, R., *Synthesis and gelation properties of PEG-PLA-PEG triblock copolymers obtained by coupling monohydroxylated PEG-PLA with adipoyl chloride*. Langmuir, 2007. **23**(5): p. 2778-2783.
4. Cheon Lee, S., Kim, C., Chan Kwon, I., Chung, H., and Young Jeong, S., *Polymeric micelles of poly (2-ethyl-2-oxazoline)-block-poly (ε-caprolactone) copolymer as a carrier for paclitaxel*. Journal of Controlled Release, 2003. **89**(3): p. 437-446.
5. Xu, Z., Wan, X., Zhang, W., Wang, Z., Peng, R., Tao, F., Cai, L., Li, Y., Jiang, Q., and Gao, R., *Synthesis of biodegradable polycationic methoxy poly (ethylene glycol)-polyethylenimine-chitosan and its potential as gene carrier*. Carbohydrate Polymers, 2009. **78**(1): p. 46-53.

CHAPTER 10

Gas-generating TPGS-PLGA Microspheres loaded with Nanoparticles (NIMPS) for co-delivery of minicircle DNA and antitumoral drugs

Colloids and Surfaces B: Biointerfaces, 2015
DOI: 10.1016/j.colsurfb.2015.07.004

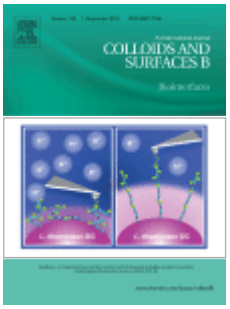

Volume 134

Motivation

The co-delivery of drug-gene combinations may provide important improvements in cancer therapy. Nevertheless, it is also important to control the response of nanocarriers in the biological environment to increase efficacy and reduce off-target effects. Such dynamic response could be manifested by a modification of the carriers structural properties or the controlled release of the different payloads under specific biological conditions, at the diseased site. The following study was developed to fabricate smart nanocarriers that respond to biological cues and trigger their cargo release.

Colloids and Surfaces B: Biointerfaces 134 (2015) 287–294

Contents lists available at ScienceDirect

Colloids and Surfaces B: Biointerfaces

journal homepage: www.elsevier.com/locate/colsurfb

Gas-generating TPGS-PLGA microspheres loaded with nanoparticles (NIMPS) for co-delivery of minicircle DNA and anti-tumoral drugs

Vítor M. Gaspar[a], André F. Moreira[a], Elisabete C. Costa[a], João A. Queiroz[a], Fani Sousa[a], Chantal Pichon[b], Ilídio J. Correia[a,*]

[a] CICS-UBI—Health Sciences Research Center, University of Beira Interior, 6200-506 Covilhã, Portugal
[b] Centre de Biophysique Moléculaire, CNRS UPR4301, Inserm and University of Orléans, 45071 Orléans cedex 02, France

ARTICLE INFO

Article history:
Received 22 January 2015
Accepted 1 July 2015
Available online 9 July 2015

Keywords:
Microspheres
Nanoparticles
Drugs
Minicircle DNA
Co-delivery

ABSTRACT

Drug-DNA combination therapies are receiving an ever growing focus due to their potential for improving cancer treatment. However, such approaches are still limited by the lack of multipurpose delivery systems that encapsulate drugs and condense DNA simultaneously. In this study, we describe the successful formulation of gas-generating pH-responsive D-α-tocopherol PEG succinate-poly(D,L-lactic-co-glycolic acid) (TPGS-PLGA) hollow microspheres loaded with both Doxorubicin (Dox) and minicircle DNA (mcDNA) nanoparticles as a strategy to co-deliver these therapeutics. For this study mcDNA vectors were chosen due to their increased therapeutic efficiency in comparison to standard plasmid DNA. The results demonstrate that TPGS-PLGA microcarriers can encapsulate Dox and chitosan nanoparticles completely condense mcDNA. The loading of mcDNA-nanoparticles into microspheres was confirmed by 3D confocal microscopy and co-localization analysis. The resulting TPGS-PLGA-Dox-mcDNA nanoparticle-in-microsphere hybrid carriers exhibit a well-defined spherical shape and neutral surface charge. Microcarriers incubation in acidic pH produced a gas-mediated Dox release, corroborating the microcarriers stimuli-responsive character. Also, the dual-loaded TPGS-PLGA particles achieved 5.2-fold higher cellular internalization in comparison with non-pegylated microspheres. This increased intracellular concentration resulted in a higher cytotoxic effect. Successful transgene expression was obtained after nanoparticle-mcDNA co-delivery in the microspheres. Overall these findings support the concept of using nanoparticle-microsphere multipart systems to achieve efficient co-delivery of various drug-mcDNA combinations.

1. Introduction

In the last decades the relative ineffectiveness of clinically administered anti-cancer therapeutics has highlighted the necessity to develop novel treatments that can improve cancer prognosis and patient survival rates [1]. To deal with this unfavorable scenario efforts are being focused on the combinatorial administration of multiple bioactive molecules such as: (i.) anti-tumoral drugs, (ii.) proteins, (iii.) natural compounds, (iv.) antibodies and (v.) nucleic acids (*e.g.* DNA, RNA), as a strategy to achieve an improved therapeutic effect in comparison to stand-alone treatments [2]. From all combinatorial therapies, those based on drug-DNA co-administration have shown to be particularly promising for targeting multiple cancer hallmarks [3–5].

Chemotherapy-nucleic acid combinations generally take advantage of drugs intrinsic anti-tumoral activity together with DNA capacity to surpass additional genetic abnormalities of cancer cells. Such coordinated action is expected to result in a synergistic effect, and ultimately, in tumor regression [5,6]. Despite its remarkable potential, this treatment modality remains limited by drugs systemic cytotoxicity and by the establishment of cell drug resistance due to exocytosis via drug efflux pumps [7]. Adding to these facts, standard non-viral DNA expression vectors are unstable in blood circulation and relatively ineffective in promoting prolonged gene expression *in vivo* [8,9]. These factors affect the feasibility of co-administering free drugs and naked DNA through the various administration routes (*e.g.* intravenous, oral) and contribute for the reduced application of combinatorial therapies in the clinic.

A valuable strategy to overcome these drawbacks is the formulation of micro and nanoparticles that can transpose biological

* Corresponding author at: Av. Infante D. Henrique, 6200-506 Covilhã, Portugal. Fax: +351 275 329 099.
E-mail address: icorreia@ubi.pt (I.J. Correia).

http://dx.doi.org/10.1016/j.colsurfb.2015.07.004
0927-7765/

barriers and deliver small molecule-gene combinations into unhealthy cells. To load multiple therapeutics simultaneously the delivery systems must display hydrophilic or hydrophobic character for drug encapsulation and positively charged groups for DNA condensation [10]. Designing micro or nanocarriers with such versatile properties remains highly challenging, and to date very few materials exhibited suitable physicochemical properties to achieve this goal. In this context, Zhang et al., used peptide-functionalized DSPE/PEG liposomes to perform the co-delivery of Paclitaxel and microRNA antagomir-10b (miRNA-10b) in order to delay tumor growth and lung metastasis dissemination [11]. Recently, triblock copolymer micellar delivery systems for co-delivery of Doxorubicin (Dox) and minicircle DNA (mcDNA) have been developed in our group to attain an improved therapeutic effect [10]. mcDNA was selected, as exogenous gene expression vector, because it is devoid of bacterial backbone, which is responsible for inducing transgene silencing and eliciting severe immunological responses from the host [12]. Besides, mcDNA provides higher levels of transgene expression both *in vitro* and *in vivo* in comparison with standard DNA [13]. While these drug-gene co-delivery studies reveal a positive outcome from dual administration *via* nanodevices, the release of therapeutics was not actively controlled. Manipulating drug or gene release in a spatially and temporally controlled mode at the target site is crucial for further improving carriers biological performance and maximize the efficacy of combinatorial therapy [2,14].

Stimuli-responsive carriers are a viable option to fulfill this purpose since cargo release can be promoted by different extracellular and intracellular signals [15,16]. Redox potential variation, enzymes, light, temperature and pH are some of the stimulus that can be exploited for creating dynamic delivery systems that sense and react to their surrounding environment [17,18]. Response to pH changes is a particularly valuable strategy for cancer therapy since acid-triggered release can be promoted at the tumor microenvironment and in cancer cells lysosomal compartments [19]. Gas-generating pH-sensitive carriers are an advanced class of efficient stimuli-sensitive delivery systems that generate carbon dioxide gas (gCO_2), as a response to surrounding acidic environments. Such gas production is generally mediated by bicarbonate salts (sodium bicarbonate ($NaHCO_3$), or ammonium bicarbonate (NH_4HCO_3)), that are encapsulated inside the delivery systems. The pH responsiveness is conferred by the reaction between hydrogencarbonate anion (HCO_3^-) with acid medium, which in turn produces gCO_2 bubbles that trigger the formation of pores in particles shell and cargo release [19]. The therapeutic applicability of gCO_2-based pH-responsive systems was recently demonstrated by Liu et al. with the delivery of NH_4HCO_3 and Dox-loaded Cholesterol-mPEG$_{2000}$-DSPE liposomes [20]. The delivery of pH-sensitive liposomes to multi-drug resistant (MDR) breast cancer cells resulted in an increased intracellular drug concentration and improved cytotoxic activity [20]. To the best of our knowledge such gas-triggered delivery systems are yet to be explored for drug-mcDNA combinatorial therapy.

Therefore, this study reports the successful formulation of nanoparticle-in-microsphere hybrid delivery systems (NIMPS) based on pH-responsive TPGS-PLGA microspheres and amino acid modified chitosan nanoparticles as a strategy for promoting the dual delivery of mcDNA and Dox to cancer cells. In this multipart system amino acid-modified chitosan nanoparticles provide complexation of mcDNA gene expression vectors. Modification of chitosan with amino acids, namely L-histidine and L-arginine, further grants the polymer backbone a pH-responsive capacity as our group previously reported [21]. This functionalization enhances nanocarriers biological performance, as well as gene expression efficiency [21], making it a good candidate for mcDNA delivery to cancer cells. The rationale of further employing TPGS as a coating for gas-generating PLGA-$NaHCO_3$ microcarriers is established on previous evidence that this polymer enhances both cellular uptake and particles stability in physiological medium in comparison to standard poly(vinyl alcohol) (PVA) [22]. Overall, our findings demonstrate that the use of FDA approved, TPGS and PLGA biodegradable polymers as materials for microparticles production assures the biocompatibility of the NIMPS system and its potential for translation to therapy. Moreover, NIMPS demonstrated a gas-mediated pH-sensitive drug release in acidic medium and an improved cellular uptake in cancer cells. Transgene expression mediated by mcDNA vectors was confirmed after nanoparticles delivery, corroborating the co-administration concept. As a final point, Dox delivery in NIMPS resulted in a cytotoxic effect comparable to that of free drug, a result that demonstrates the potential of using this multipart system for co-delivery of different mcDNA-chemotherapeutics combinations.

2. Materials and methods

For a detailed description of the materials and methods the reader is referred to the electronic Supplementary information.

2.1. Methods

2.1.1. Preparation of Doxorubicin-loaded gas-generating hollow microspheres

PLGA and TPGS-PLGA hollow microspheres were formulated by using the water-in-oil-in-water double-emulsion (W/O/W) solvent diffusion-evaporation method reported by Liu et al. with slight modifications [19]. Blank microparticles were prepared by the W/O/W method without Dox incorporation in the first aqueous phase. Dox-loaded microspheres with poly(vinyl alcohol) (PVA) or TPGS coating are termed micro-PVA-Dox and micro-TPGS-Dox, respectively.

2.1.2. Preparation of mcDNA Amino acid-Chitosan nanoparticles

Prior to preparation of chitosan-mcDNA nanoparticles the cationic biopolymer was chemically modified with L-arginine and L-histidine via *N*-(3-Dimethylaminopropyl)-*N*′-ethylcarbodiimide hydrochloride/*N*-Hydroxysuccinimide (EDC/NHS) coupling chemistry to yield multifunctional Chitosan–Arginine–Histidine (CH–HR) as our group previously reported [21]. All nanoparticles were formulated at the amine-to-phosphate ratio of 60 (N/P 60) since this formulation has previously presented optimal stability, biological performance and transfection efficiency [21]. mcDNA complexation by CH–HR was confirmed by agarose gel electrophoresis [23]. Nanocarriers loading into Micro-TPGS-Dox microspheres was accomplished by adding CH–HR-mcDNA nanoparticles in the primary aqueous phase of the W/O/W assembly process. The resulting Micro-TPGS-Dox-(CH–HR-mcDNA) nanoparticle-in-microsphere systems are designated by NIMPS from herein onwards.

2.1.3. Delivery systems physicochemical characterization

Microspheres and nanoparticles size was analysed by dynamic light scattering (DLS) in a Zetasizer NanoZS (Malvern Instruments, Worcestershire, UK). Three independent measurements were performed in disposable folded capillary cells (DTS1070), at 25 °C, and with a 173° scattering angle. Microspheres morphology was evaluated by scanning electron microscopy (SEM) by using a Hitachi S-3400N scanning electron microscope (Hitachi, Japan). The existence of the gas-generating agent ($NaHCO_3$) in PLGA microspheres core was determined by X-ray diffraction spectroscopy (XRD).

2.1.4. Drug encapsulation and in vitro release

Drug encapsulation efficiency in all PLGA microsphere formulations was determined through UV–vis spectrophotometry at

λ = 485 nm by using a Shimadzu–1700 spectrophotometer (Shimadzu Inc., Japan). Drug encapsulation efficiency was calculated as reported in the literature [24]. Drug release from microspheres was evaluated by the dialysis method, in duplicate independent experiments. Drug release was carried out at 37 °C in a water bath, with magnetic stirring (500 rpm), in the dark. Supernatant samples were collected at various time-points and the drug content was analyzed by UV–vis spectrophotometry.

2.1.5. Cellular uptake

The cellular uptake of drug-loaded microparticles (micro-PVA-Dox, micro-TPGS-Dox) and Dox-mcDNA dual loaded NIMPS was evaluated by flow cytometry. This analysis was carried out in a BD FACSCalibur flow cytometer (Becton Dickinson Inc., USA). Data acquisition was performed with the CellQuest software where 1×10^4 events were collected in the region of interest assigned to HeLa cells. Additionally, particles cellular uptake was visualized by confocal laser scanning microscopy (CLSM). Confocal images were acquired in a Zeiss LSM 710 confocal microscope (Carl Zeiss SMT Inc., USA). 3D reconstruction, colocalization analysis and image processing was performed in Zeiss Zen 2010, ImageJ and Imaris software (Bitplane, Switzerland).

2.1.6. In vitro gene expression in 2D cultures

mcDNA-GFP expression in cancer cells was evaluated by spectrofluorimetry [23]. For this assay, HeLa cells were cultured in 96 well black-clear bottom plates at a density of 1×10^4 cells per well. Gene expression was quantified after 48 h by using a plate reader spectrofluorometer (Spectramax Gemini XS, Molecular Devices LLC, USA), at λ_{ex} = 488 nm and λ_{em} = 519 nm. In addition, GFP expression was also visualized and quantified by CLSM by using a Zeiss LSM 710 confocal microscope (Carl Zeiss SMT Inc., USA), equipped with a Plan-Apochromat 63x/1.4 oil objective. For all experiments, 3D *z*-stacks of randomly distributed cell fields (n = 3) were acquired. GFP fluorescence intensity in cells volume was quantified by using the Imaris software (Bitplane, Switzerland).

2.1.7. Cytotoxic activity

The cytotoxic activity of Dox-loaded microspheres and mcDNA-Dox dual loaded NIMPS was evaluated by the MTS assay as previously described [10]. Dead cells (70% EtOH), and non-treated cells were used as positive and negative controls, respectively.

2.1.8. Statistical analysis

One-way analysis of variance (ANOVA) with the post-hoc Newman–Keuls test were used for statistical analysis of three or more groups. Student's *t*-test was used for comparison between two groups. A p value below 0.05 was considered statistically significant.

3. Results and discussion

3.1. Formulation of gas-generating PLGA microspheres

Gas-generating pH responsive hollow PLGA microspheres were produced by the double emulsion water-on-oil-water (W/O/W) solvent diffusion-evaporation method as schematized in supplementary Fig. S1A. Initially the first water phase comprised by the gas-generating agent $NaHCO_3$ and by the PVA surfactant, were mixed with the oil phase containing PLGA dissolved in dichloromethane. Primary emulsification was promoted by the action of ultrasound waves which generated well-defined PLGA droplets by disrupting the oil–water interface (Supplementary Fig. 1A).

The resulting microcarriers were subsequently mixed with the second water phase comprised either by PVA or TPGS (Supplementary Fig. S1A). TPGS was used as an alternative to PVA for microspheres production because the PLGA–$NaHCO_3$-PVA–PVA systems generally described in the literature have shown relatively low cellular uptake and also reduced stability in biological fluids [25]. Thus, as a strategy to improve microcarriers biological performance, TPGS was used as the surfactant in a second emulsification that involves high speed homogenization (Supplementary Fig. S1A). Following the establishment of the W/O/W double emulsion the organic solvent was diffused by mixing and evaporated under reduced pressure which led to the formation of spherical PLGA microspheres coated with TPGS or PVA (Supplementary Fig. S1B and D). The produced micro-TPGS carriers had lower polydispersity than micro-PVA formulations, suggesting that the coating process yields more homogeneous particles when this surfactant is used in the end of the process. Micro-TPGS microspheres also exhibit a slightly larger size when compared to their PVA counterparts, a finding that can be attributed to the PEG shell that is formed in particles surface. Particle surface charge characterization shows that the inclusion of TPGS causes a slight decrease in zeta potential (Supplementary Fig. S1C and E). These findings are in accordance with those obtained by Mu et al. which studied the impact of different surfactants in Paclitaxel-loaded PLGA nanoparticles. The inclusion of TPGS resulted in larger sized nanocarriers with more negative surface charge in comparison with those formulated PVA [26].

Following the successful formulation of TPGS coated PLGA microspheres the presence of the gas-generating agent in the carriers was analyzed by X-ray diffraction. As demonstrated in Fig. 2A the characteristic peaks of $NaHCO_3$ crystalline structure are present in microsphere formulations, indicating the effective encapsulation of the bicarbonate salt in particles during the assembly process. The broad XRD peak centered at $2\Theta \sim 19.5^\circ$ is assigned to amorphous PLGA microspheres (Fig. 1A). Interestingly, no significant differences in $NaHCO_3$ characteristic diffraction peaks is observed between micro-PVA and micro-TPGS formulations suggesting that the addition of TPGS in the end of the process does not affect $NaHCO_3$ encapsulation.

The potential of PLGA gas-generating microspheres to encapsulate anti-tumoral drugs was evaluated by including Doxorubicin (Dox) in the first aqueous phase of the assembly process. As the results in Fig. 1B demonstrate the encapsulation efficiency for both formulations is higher than 95% and no significant difference between micro-TGPS-Dox and micro-PVA-Dox particles is obtained. Drug encapsulation in particles core also had negligible influence in particles morphology. In fact, as observed in SEM micrographs all formulations maintained their characteristic spherical shape (Fig. 1C and D). Interestingly, the physicochemical characterization of drug loaded microspheres reveals that encapsulation of Dox in micro-TPGS carriers leads to the production of smaller particles (*z*-average size = 1877 nm) when compared to blank TPGS-based formulations (*z*-average size = 2362 nm) (Supplementary Fig. S2 A and B). Microspheres surface charge is also changed upon drug encapsulation in micro-PVA-Dox and micro-TPGS-Dox formulations, with the latter presenting a neutral zeta potential (ζ = −9.17 mV). This neutrality is highly important for the therapeutic efficiency of micro or nanoparticle formulations since it has been previously demonstrated that particles zeta potential in the range of neutrality (+10 mV to −10 mV) achieve optimal for tumor penetration [27].

3.2. Microcarriers biological characterization

To further characterize the biological properties of micro-sized delivery systems, *in vitro* biocompatibility assays were performed in HeLa cells. The obtained results show that HeLa cells remain

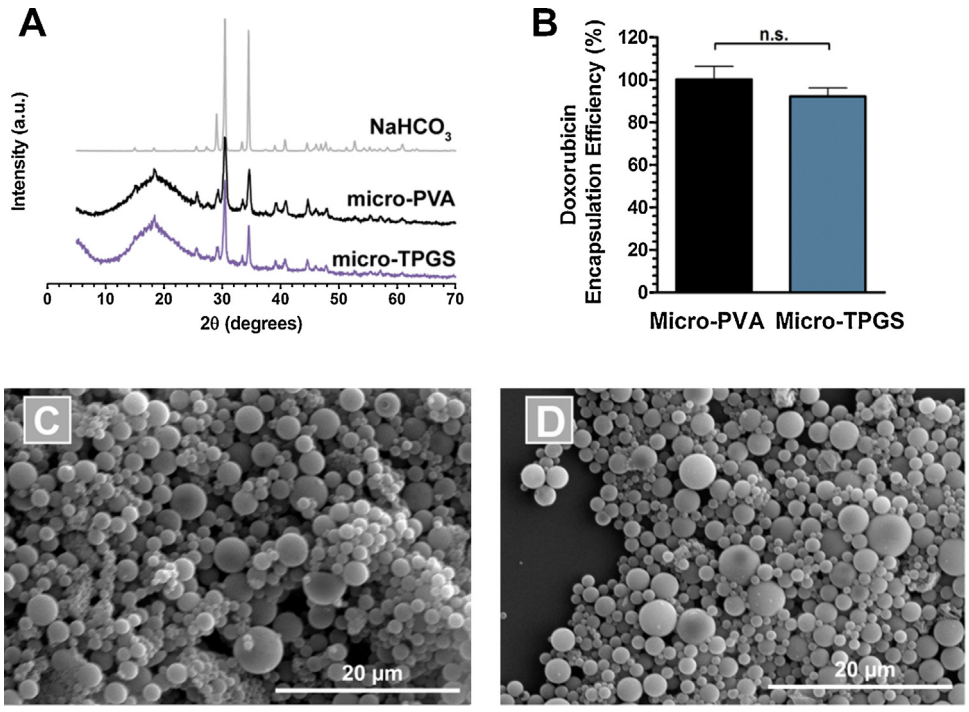

Fig. 1. Microcarriers physicochemical characterization. (A.) XRD analysis of microsphere formulations. (B.) Dox encapsulation in different microsphere formulations. Data is presented as mean ± s.d., $n = 3$. (C and D.) SEM micrographs of micro-PVA-Dox and micro-TPGS-Dox formulations, respectively.

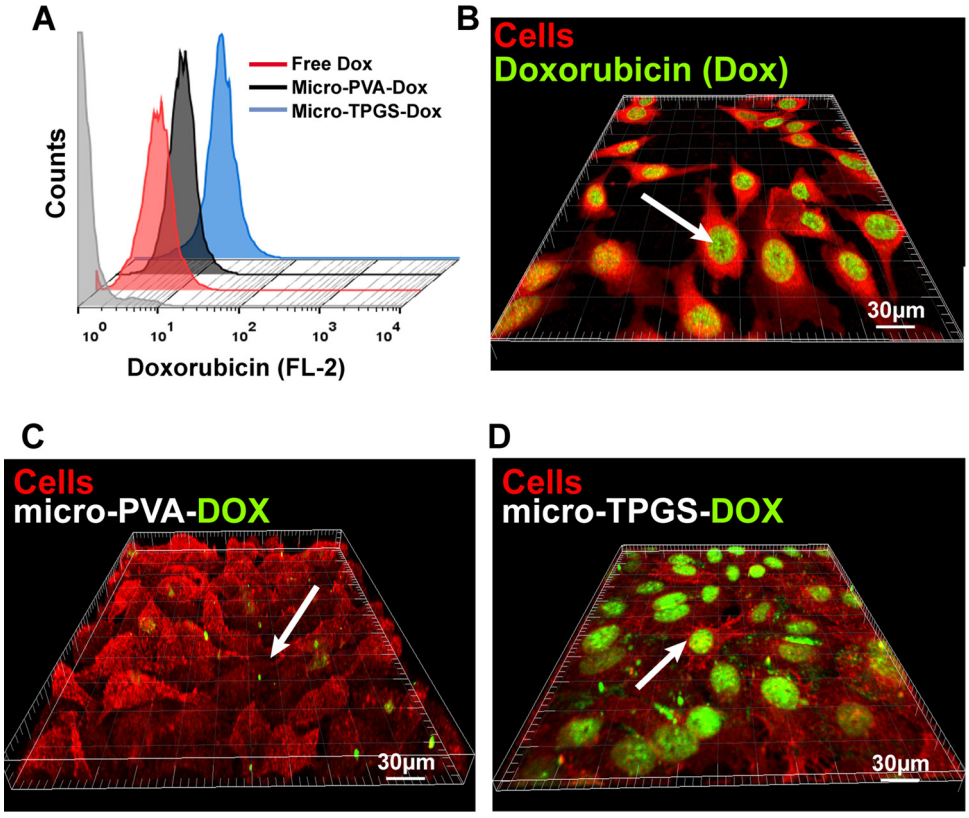

Fig. 2. Analysis of drug loaded microspheres uptake in HeLa cancer cells. (A.) Representative histograms of microcarriers and free drug cellular uptake (Grey histogram: cells autofluorescence). CLSM visualization of free Dox (B.), micro-PVA-Dox microspheres (C.), and micro-TPGS-Dox microspheres (D.) cellular uptake and intracellular localization. Red channel: WGA-Alexa Fluor® 594 conjugate; Green channel: Doxorubicin. (For interpretation of the references to color in this figure legend, the reader is referred to the web version of this article.)

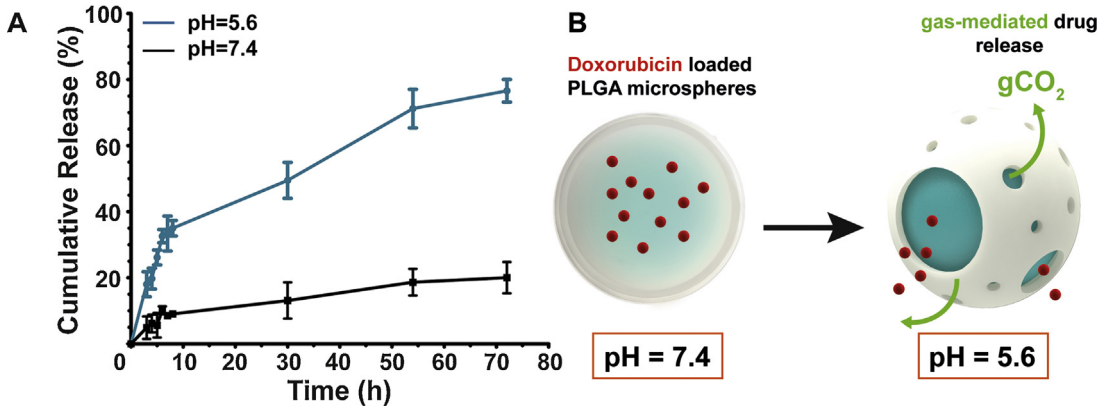

Fig. 3. Analysis of drug release from pH-responsive TPGS-coated PLGA microspheres. (A.) Cumulative Dox release at physiological and acidic pH. (B.) Schematics that depicts the underlying principle of gas-generation in acidic environment with subsequent particles shell disruption and drug release.

metabolically active up until 72 h when incubated with micro-PVA or micro-TPGS particles (Supplementary Fig. S3A and C).

The cellular uptake capacity of both formulations in physiological conditions was also evaluated by using flow cytometry. The obtained results depicted in Fig. 2A indicate that micro-PVA-Dox carriers exhibit a cellular uptake comparable to that of free drug. In addition, micro-TPGS-Dox achieve approximately a 5.2-fold higher cellular uptake in comparison to their micro-PVA-Dox counterparts (Supplementary Fig. S4A and B), indicating that the inclusion of TPGS enhances the biological efficiency of gas-generating PLGA microspheres. These results are in agreement with those recently reported by Kulkarni and Feng, 2013, in which the inclusion of TPGS in polystyrene particles surface has shown to significantly increase cellular uptake in comparison with unmodified particles [28].

The cellular uptake and intracellular localization of Dox loaded microcarriers was additionally confirmed by confocal microscopy. As depicted in Fig. 2B the administration of free drug leads to its intracellular accumulation particularly in the nuclear compartment (white arrows). In contrast, micro-PVA-Dox exhibit a widespread distribution in the intracellular compartment and few cells display Dox in the nuclear compartment (Fig. 2C, white arrows and Supplementary Fig. S4, D1 and D2). The micro-TPGS-Dox carriers also have a random intracellular distribution (white arrows), however, a clear accumulation of the anti-tumoral drug in the nuclear compartment is visible (Fig. 2D, white arrows; Supplementary Fig. S4, E1 and E2). We hypothesize that such difference is correlated with the enhanced cellular uptake efficiency of micro-TPGS-Dox carriers. From a therapeutic point of view achieving this increased intracellular concentration and nuclear localization is critical for improving the overall therapeutic efficacy as Dox intracellular targets are mainly localized in the nuclear compartment [29]. The cellular uptake of microcarriers with this hydrodynamic size has also been reported in the literature [25]. In fact, the interesting work of Ke et al. explored the cellular uptake routes of PLGA-PVA microspheres, revealing that this event is an energy dependent process and that macropynocytosis plays a significant role in microcarriers internalization [25].

3.2. Stimuli-responsive drug release

Since TPGS-based microcarriers present an improved cellular uptake efficiency, their responsiveness to acidic milieu was investigated.

The stimuli-dependent release is promoted via a pH-triggered disruption of particles core–shell structure (schematics of Fig. 3B). Such responsiveness of micro-TPGS-Dox microcarriers is governed by the generation of gCO_2 bubbles that are produced *via* reaction of sodium bicarbonate with acid ($NaHCO_3 + HCl \rightarrow NaCl + H_2CO_3$; $H_2CO_3 \rightarrow CO_{2(g)} + H_2O$) [30]. Eventually, the resulting gCO_2 bubbles diffuse through particles shell and originate pores which stimulate a rapid release of the anti-tumoral drug (Fig. 3B). Drug release assays were performed both in physiological and acidic conditions in an attempt to mimic a stimuli-controlled drug release in the acidic tumor microenvironment or acidic cell compartments. As the results demonstrate the immersion of TPGS-coated PLGA microspheres in acidic medium results in a rapid and extensive Dox release (Fig. 3A). In fact, the particles that were exposed to pH 5.6 exhibit a 3.88-fold higher drug release at 8 h, when compared to their equivalents immersed in physiological conditions (pH 7.4) (Fig. 3A). This tendency is also maintained after 70 h of incubation. It is important to emphasize that at physiological pH the microcarriers have negligible burst release since only 13% of loaded drug is released at 30 h (Fig. 3A). Retention of the anti-tumoral drug in the particles core is crucial to reduce off-target cytotoxic effects upon their administration *in vivo* [14].

Additionally, SEM imaging was used to complement the characterization of microsphere structural stability in environments with different pH. The results in Supplementary Fig. S5 show that micro-TPGS carriers preserve their structural and morphological integrity upon incubation in physiological conditions, while microspheres exposed to acidic medium display various holes in their shell due to the effervescent reaction promoted by $NaHCO_3$ and acid (White square, Supplementary Fig. S5 B2 and B3). Particles disintegration is also confirmed by the significant amount of free polymer present in SEM micrographs (Supplementary Fig. S5 B1 to B3, white arrows). Such findings confirm the stimuli-responsive profile of micro-TPGS particles, contributing for the envisioned control over drug release at the target tumor site.

3.3. Formulation of drug-gene loaded pH-responsive PLGA Microspheres (NIMPS)

Since TPGS-coated microcarriers demonstrate a pH-responsive profile and also an improved cellular uptake, the co-delivery of drugs and genes was investigated by combining micro-TPGS-Dox with mcDNA-loaded amino acid chitosan amino acid nanoparticles (CH-HR) as a strategy to promote the dual delivery of these therapeutics (schematics of Fig. 4).

Prior to NIMPS formulation the production of CH–HR-mcDNA nanoparticles was investigated. mcDNA chitosan nanoparticles were assembled via electrostatic attraction between the negatively charged phosphate groups of mcDNA and the cationic groups in the polymer backbone under mild conditions. The amino acid modification of chitosan with L-arginine and L-histidine (CH–HR), also contributes for the condensation of genetic material, namely plasmid DNA (pDNA), as our group previously demonstrated [21].

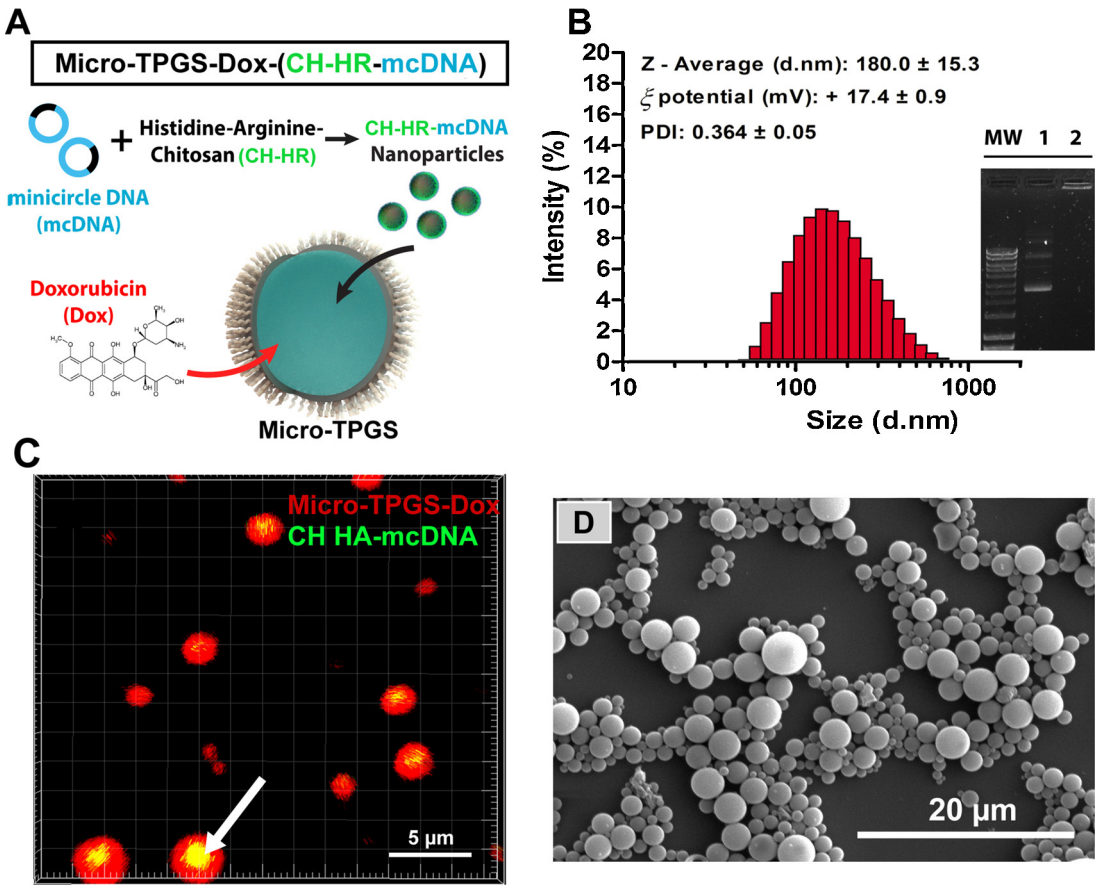

Fig. 4. Production of nanoparticle-in-microsphere (NIMPS) hybrid delivery systems. (A.) Schematics of the hybrid delivery systems comprised by micro-TPGS-Dox and CH-HR-mcDNA loaded nanoparticles (not drawn in scale). (B.) DLS and agarose electrophoresis analysis of DNA minicircles condensation and CH-HR-mcDNA nanoparticles assembly. MW—molecular weight marker. Lane 1—free mcDNA. Lane 2—CH-HR-mcDNA (C.) Confocal microscopy micrographs of NIMPS dispersed in an imaging chamber. Red channel: Doxorubicin encapsulated in microspheres. Green channel: FITC-labelled mcDNA. Yellow channel: merged red and green channels. White arrows indicate FITC-mcDNA. (D.) SEM micrograph of NIMPS. (For interpretation of the references to color in this figure legend, the reader is referred to the web version of this article.)

In this study, this improved chitosan derivative has also shown to completely condense novel mcDNA vectors as evidenced by agarose gel electrophoresis (Fig. 4B). These findings assume further importance since few reports have explored mcDNA vectors condensation by cationic biomaterials so far [10,31,32]. The resulting mcDNA nanoparticles have an average size below 200 nm and a positive zeta potential (Fig. 4B).

The production of NIMPS was carried out by including CH–HR-mcDNA nanoparticles in the first aqueous phase. The resulting hybrid delivery systems exhibit an average size of 2502 nm and are homogeneous (PDI: 0.208, Supplementary Fig. S6A). The dual loaded carriers also display a less negative zeta potential (ζ: -1.89 ± 0.2 mV) when compared to single loaded micro-TPGS-Dox formulations (ζ: -9.17 ± 0.6 mV) (Supplementary Fig. S6A). This increase in zeta potential corroborates the successful encapsulation of positively charged nanoparticles in microcarriers core. The resulting NIMPS also maintain their spherical morphology (Fig. 4D), indicating that the addition of nanoparticles does not significantly affect microspheres assembly.

To confirm the presence of mcDNA nanoparticles inside the PLGA microcarriers, the dual system was also analyzed by confocal microscopy. As displayed in Fig. 4C the fluorescence signal corresponding to mcDNA-FITC nanoparticles is coincident with micro-TPGS-Dox carriers. This fact is supported by co-localization analysis (Supplementary Fig. S7). A 3D reconstruction of microspheres volume further confirmed the presence of mcDNA-loaded nanoparticles in microspheres interior (Supplementary Fig. S6B).

3.4. NIMPS cellular uptake and gene expression

The cellular uptake analysis of NIMPS demonstrates that the hybrid carriers exhibit higher internalization in cancer cells ($87.1 \pm 4.1\%$ cells) in comparison to micro-TPGS-Dox counterparts ($72.9 \pm 6.1\%$ cells) (Supplementary Fig. S8A). Confocal microscopy images additionally confirmed that NIMPS are localized in the intracellular compartment and that Dox is present in cancer cells nucleus (Supplementary Fig. S8B, white arrows).

To complement NIMPS characterization the gene expression mediated by mcDNA-GFP when co-delivered with Dox was assessed. The results demonstrate that GFP expression achieved by CH–HR-mcDNA nanoparticles is slightly higher than that obtained with NIMPS. However, this difference is not significant (Supplementary Fig. S8E and F), and may be attributed to the fact that mcDNA-nanoparticles must be released from microcarriers before being localized in the cytoplasm as emphasized by Jain and Amiji that developed nanoparticle-in-microsphere systems for oral delivery [33]. Besides, these results demonstrate that mcDNA-nanoparticles delivered in NIPMS achieve successful GFP expression.

3.5. Delivery systems cytotoxic activity

The cytotoxic activity of both single and dual-loaded delivery systems produced throughout this study was investigated to provide evidence about NIMPS therapeutic potential.

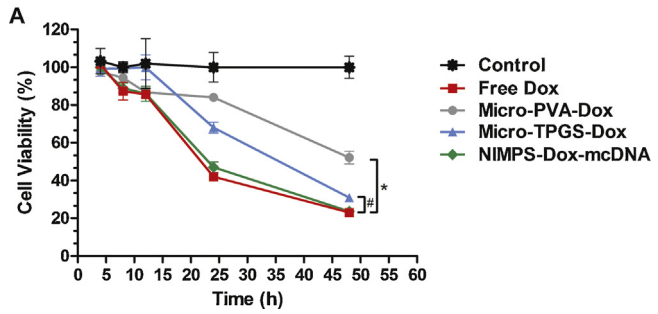

Fig. 5. Cytotoxic activity of single-loaded microcarriers and dual-loaded delivery systems (micro-TPGS-Dox/CH-HR-mcDNA) in HeLa cancer cells. Control: non-treated HeLa cells. Particles were administered at a dose of 200 μg mL^{-1}. Data is represented as mean ± s.d., $n = 5$, $^{*}p < 0.05$, $^{\#}p < 0.01$.

As the depicted in Fig. 5 micro-TPGS-Dox carriers display 1.7-fold higher cytotoxicity in comparison to their PLGA-PVA equivalents. Similarly, NIMPS exhibit a significantly higher cytotoxic activity when compared with single loaded micro-TPGS-Dox particles (Fig. 5; $^{\#}p < 0.01$). Taken together, the results indicate that the inclusion of TPGS enhances the overall biological performance and cytotoxic activity of gas-generating PLGA microcarriers. Also, the encapsulation of mcDNA in the form of CH–HR polyplexes originated transgene expression of mcDNA non-viral vectors, which are reported to be more effective than standard DNA both *in vitro* and *in vivo* [9]. From a therapeutic point of view this is a crucial factor since cancer treatment may be improved by using mcDNA vectors that encode anti-tumoral genes (*e.g.* P53 or TRAIL [34,35]), and combining their action with the cytotoxic activity of chemotherapeutics, to achieve a synergistic anti-tumoral effect.

PLGA–$NaHCO_3$–PVA based microspheres for Dox delivery to cancer cells have been previously described in the literature [25]. Herein, we have taken advantage of this simple and cost-effective technology to formulate pH-responsive microspheres with further improved cellular uptake, and also demonstrated the possibility to efficiently co-delivery nanoparticle-mcDNA in these systems. Due to its stability NIMPS provide the possibility to be locally delivered to cervix cancer location and respond to the acidic pH of this tumor [36,37]. This is a major advantage when compared as example to other nanoparticulated PLGA-based systems (PLGA-PEI) for co-delivery and which are unable to respond to biological stimuli [38]. The micron-size of the NIMPS system may prove beneficial in the future for inclusion in tandem or ovoid devices that are generally used in the clinics to locally apply treatment for this particular type of cancer [39]. In addition, the recently described potential of using gas generation for theranostic applications based in ultrasound imaging further expands the applicability of these carriers [40].

4. Conclusions

In summary, in this study we have developed a pH-responsive nanoparticle-in-microsphere hybrid delivery system comprised by gas-generating PLGA-TPGS-Dox microcarriers and by amino acid chitosan nanoparticles loaded with mcDNA vectors. This multipart delivery platform has proven to respond to acidic pH and release its cargo in a spatiotemporally controlled mode. Micro-TPGS-Dox microspheres have also displayed an improved cellular uptake in comparison to standard PLGA-PVA microcarriers. Adding to this, the concept of using nanoparticles inside microspheres for combinatorial therapy was supported by the evidence that the resulting NIMPS formulations have the highest cellular uptake, accomplish transgene expression, and above all exhibit an improved cytotoxic activity. It is also important to emphasize that to the best of our knowledge this was the first time that mcDNA-loaded nanoparticles were included in PLGA microspheres as a strategy to co-deliver anti-tumoral drugs and genetic material. NIMPS are in fact a valuable addition to the relatively few number of delivery systems that are currently capable of delivering DNA minicircles and chemotherapeutics simultaneously. In fact, considering the drawbacks associated with stand-alone cancer treatments such as those based on single drug administration these findings encourage the applicability of this hybrid system for exploring new drug-gene combinations and to bridge the gap between pre-clinical research and realistic clinical application.

In the future the versatility of PLGA microspheres to encapsulate both hydrophilic/hydrophobic drugs and the possibility of including cancer cell targeting biomolecules in TPGS structure will surely prove to be beneficial for the development of a delivery platform that is based on FDA approved materials. Additionally, 3D tumor spheroids can be used in the future for testing the therapeutic efficiency of NIMPS in high-throughput models that more closely mimic *in vivo* tumors.

Acknowledgments

The authors would like to acknowledge Sónia Miguel for the help in the acquisition of SEM images. This work was supported by the Portuguese Foundation for Science and Technology (FCT), (PEst-C/SAU/UI0709/2011 and PEst-OE/SAU/UI0709/2014)). Vítor M. Gaspar acknowledges an individual PhD fellowship from FCT (SFRH/BD/80402/2011). The third author acknowledges a fellowship (CENTRO-07-ST24-FEDER-002014) from "Programa Operacional Regional do Centro 2007-2013 QREN" ("Mais Centro" program).

Appendix A. Supplementary data

Supplementary data associated with this article can be found, in the online version, at http://dx.doi.org/10.1016/j.colsurfb.2015.07.004

References

[1] S. Mitragotri, P.A. Burke, R. Langer, Overcoming the challenges in administering biopharmaceuticals: formulation and delivery strategies, Nat. Rev. Drug Discov. 13 (2014) 655–672.
[2] A. Jhaveri, P. Deshpande, V. Torchilin, Stimuli-sensitive nanopreparations for combination cancer therapy, J. Controlled Release 190 (2014) 352–370.
[3] J. Li, Y. Guo, Y. Kuang, S. An, H. Ma, C. Jiang, Choline transporter-targeting and co-delivery system for glioma therapy, Biomaterials 34 (2013) 9142–9148.
[4] Y. Wang, S. Gao, W.-H. Ye, H.S. Yoon, Y.-Y. Yang, Co-delivery of drugs and DNA from cationic core–shell nanoparticles self-assembled from a biodegradable copolymer, Nat. Mater. 5 (2006) 791–796.
[5] S.W. Morton, M.J. Lee, Z.J. Deng, E.C. Dreaden, E. Siouve, K.E. Shopsowitz, N.J. Shah, M.B. Yaffe, P.T. Hammond, A Nanoparticle-Based Combination Chemotherapy Delivery System for Enhanced Tumor Killing by Dynamic Rewiring of Signaling Pathways, Sci. Signal. 7 (2014) ra44.
[6] B. Yu, C. Tang, C. Yin, Enhanced antitumor efficacy of folate modified amphiphilic nanoparticles through co-delivery of chemotherapeutic drugs and genes, Biomaterials 35 (2014) 6369–6378.
[7] D. de Melo-Diogo, V.M. Gaspar, E.C. Costa, A.F. Moreira, D. Markl, E. Gallardo, I.J. Correia, Combinatorial delivery of Crizotinib–Palbociclib–Sildenafil using TPGS–PLA micelles for improved cancer treatment, Eur. J. Pharm. Biopharm. 88 (2014) 718–729.
[8] S.B. Uppada, T. Erickson, L. Wojdyla, D.N. Moravec, Z. Song, J. Cheng, N. Puri, Novel delivery system for T-oligo using a nanocomplex formed with an alpha helical peptide for melanoma therapy, Int. J. Nanomed. 9 (2014) 43-53.
[9] W.M. Dietz, N.E. Skinner, S.E. Hamilton, M.D. Jund, S.M. Heitfeld, A.J. Litterman, P. Hwu, Z.-Y. Chen, A.M. Salazar, J.R. Ohlfest, Minicircle DNA is superior to plasmid DNA in eliciting antigen-specific CD8 + T-cell responses, Mol. Ther. 21 (2013) 1526–1535.
[10] V.M. Gaspar, C. Gonçalves, D. de Melo-Diogo, E.C. Costa, J.A. Queiroz, C. Pichon, F. Sousa, I.J. Correia, Poly(2-ethyl-2-oxazoline)–PLA-g–PEI amphiphilic triblock micelles for co-delivery of minicircle DNA and chemotherapeutics, J. Controlled Release 189 (2014) 90–104.
[11] Q. Zhang, R. Ran, L. Zhang, Y. Liu, L. Mei, Z. Zhang, H. Gao, Q. He, Simultaneous delivery of therapeutic antagomirs with paclitaxel for the management of

metastatic tumors by a pH-responsive anti-microbial peptide-mediated liposomal delivery system, J. Controlled Release 197 (2015) 208–218.
[12] V. Gaspar, D. d. Melo-Diogo, E. Costa, A. Moreira, J. Queiroz, C. Pichon, I. Correia, F. Sousa, Minicircle DNA vectors for gene therapy: advances and applications, Expert Opin. Biol. Ther. 15 (2015) 353–379.
[13] D. Kobelt, M. Schleef, M. Schmeer, J. Aumann, P.M. Schlag, W. Walther, Performance of high quality minicircle DNA for in vitro and in vivo gene transfer, Mol. Biotechnol. 53 (2012) 80–89.
[14] J.V. Natarajan, C. Nugraha, X.W. Ng, S. Venkatraman, Sustained-release from nanocarriers: a review, J. Controlled Release 193 (2014) 122–138.
[15] Y. Wang, M.S. Shim, N.S. Levinson, H.W. Sung, Y. Xia, Stimuli-responsive materials for controlled release of theranostic agents, Adv. Funct. Mater. 24 (2014) 4206–4220.
[16] N.R. Ko, J. Cheong, A. Noronha, C.J. Wilds, J.K. Oh, Reductively-sheddable cationic nanocarriers for dual chemotherapy and gene therapy with enhanced release, Colloids Surf. B: Biointerfaces 126 (2015) 178–187.
[17] G. Saravanakumar, W.J. Kim, Stimuli-responsive polymeric nanocarriers as promising drug and gene delivery systems, in: Intracellular Delivery II, Springer, 2014, 2015, pp. 55–91.
[18] M. Cai, M. Leng, A. Lu, L. He, X. Xie, L. Huang, Y. Ma, J. Cao, Y. Chen, X. Luo, Synthesis of amphiphilic copolymers containing zwitterionic sulfobetaine as pH and redox responsive drug carriers, Colloids Surf. B: Biointerfaces 126 (2015) 1–9.
[19] J. Liu, Y. Huang, A. Kumar, A. Tan, S. Jin, A. Mozhi, X.-J. Liang, Ph-sensitive nano-systems for drug delivery in cancer therapy, Biotechnol. Adv. 23 (2014) 693–710.
[20] J. Liu, H. Ma, T. Wei, X.-J. Liang, CO 2 gas induced drug release from pH-sensitive liposome to circumvent doxorubicin resistant cells, Chem. Commun. 48 (2012) 4869–4871.
[21] V. Gaspar, J. Marques, F. Sousa, R. Louro, J. Queiroz, I. Correia, Biofunctionalized nanoparticles with pH-responsive and cell penetrating blocks for gene delivery, Nanotechnol. 24 (2013) 275101.
[22] Z. Zhang, S.-S. Feng, The drug encapsulation efficiency, *in vitro* drug release, cellular uptake and cytotoxicity of paclitaxel-loaded poly(lactide)–tocopheryl polyethylene glycol succinate nanoparticles, Biomaterials 27 (2006) 4025–4033.
[23] V.M. Gaspar, E.C. Costa, J.A. Queiroz, C. Pichon, F. Sousa, I.J. Correia, Folate-targeted multifunctional amino acid-chitosan nanoparticles for improved cancer therapy, Pharm. Res. 32 (2015) 562–577.
[24] J.G. Marques, V.M. Gaspar, D. Markl, E.C. Costa, E. Gallardo, I.J. Correia, Co-delivery of sildenafil (viagra(r)) and crizotinib for synergistic and improved anti-tumoral therapy, Pharm. Res. 31 (2014) 2516–2528.
[25] C.-J. Ke, W.-L. Chiang, Z.-X. Liao, H.-L. Chen, P.-S. Lai, J.-S. Sun, H.-W. Sung, Real-time visualization of pH-responsive PLGA hollow particles containing a gas-generating agent targeted for acidic organelles for overcoming multi-drug resistance, Biomaterials 34 (2013) 1–10.
[26] L. Mu, P.-H. Seow, S.-N. Ang, S.-S. Feng, Study on surfactant coating of polymeric nanoparticles for controlled delivery of anticancer drug, Colloid Polym. Sci. 283 (2004) 58–65.
[27] M.J. Ernsting, M. Murakami, A. Roy, S.-D. Li, Factors controlling the pharmacokinetics, biodistribution and intratumoral penetration of nanoparticles, J. Controlled Release 172 (2013) 782–794.
[28] S.A. Kulkarni, S.-S. Feng, Effects of particle size and surface modification on cellular uptake and biodistribution of polymeric nanoparticles for drug delivery, Pharm. Res. 30 (2013) 2512–2522.
[29] A.F. Moreira, V.M. Gaspar, E.C. Costa, D. de Melo-Diogo, P. Machado, C.M. Paquete, I.J. Correia, Preparation of end-capped pH-sensitive mesoporous silica nanocarriers for on-demand drug delivery, Eur. J. Pharm. Biopharm. 88 (2014) 1012–1025.
[30] J.S. Fordtran, S.G. Morawski, C.A. Santa Ana, F. Rector Jr, Gas production after reaction of sodium bicarbonate and hydrochloric acid, Gastroenterology 87 (1984) 1014–1021.
[31] M. Keeney, S.-G. Ong, A. Padilla, Z. Yao, S. Goodman, J.C. Wu, F. Yang, Development of poly(β-amino ester)-based biodegradable nanoparticles for nonviral delivery of minicircle DNA, ACS Nano 7 (2013) 7241–7250.
[32] C. Zhang, S. Gao, W. Jiang, S. Lin, F. Du, Z. Li, W. Huang, Targeted minicircle DNA delivery using folate–poly(ethylene glycol)–polyethylenimine as non-viral carrier, Biomaterials 31 (2010) 6075–6086.
[33] S. Jain, M. Amiji, Nanoparticles-in-microsphere oral delivery systems (NiMOS) for nucleic acid therapy in the gastrointestinal tract, in: Mucosal Delivery of Biopharmaceuticals, Springer, 2014, pp. 283–312.
[34] E. Pazarentzos, N.D. Mazarakis, Anticancer gene transfer for cancer gene therapy, in: Anticancer Genes, Springer, 2014, pp. 255–280.
[35] T.H. Kim, H.H. Jiang, C.W. Park, Y.S. Youn, S. Lee, X. Chen, K.C. Lee, PEGylated TNF-related apoptosis-inducing ligand (TRAIL)-loaded sustained release PLGA microspheres for enhanced stability and antitumor activity, J. Controlled Release 150 (2011) 63–69.
[36] B.A. Webb, M. Chimenti, M.P. Jacobson, D.L. Barber, Dysregulated pH: a perfect storm for cancer progression, Nat. Rev. Cancer 11 (2011) 671–677.
[37] G. Schwickert, S. Walenta, K. Sundfør, E.K. Rofstad, W. Mueller-Klieser, Correlation of high lactate levels in human cervical cancer with incidence of metastasis, Cancer Res. 55 (1995) 4757–4759.
[38] W.-P. Su, F.-Y. Cheng, D.-B. Shieh, C.-S. Yeh, W.-C. Su, PLGA nanoparticles codeliver paclitaxel and Stat3 siRNA to overcome cellular resistance in lung cancer cells, Int. J. Nanomed. 7 (2012) 4269.
[39] L. Fokdal, K. Tanderup, S.B. Hokland, L. Røhl, E.M. Pedersen, S.K. Nielsen, M. Paludan, J.C. Lindegaard, Clinical feasibility of combined intracavitary/interstitial brachytherapy in locally advanced cervical cancer employing MRI with a tandem/ring applicator *in situ* and virtual preplanning of the interstitial component, Radiother. Oncol. 107 (2013) 63–68.
[40] K.H. Min, H.S. Min, H.J. Lee, D.J. Park, J.Y. Yhee, K. Kim, I.C. Kwon, S.Y. Jeong, O.F. Silvestre, X. Chen, Y.-S. Hwang, E.-C. Kim, S.C. Lee, pH-controlled gas-generating mineralized nanoparticles: a theranostic agent for ultrasound imaging and therapy of cancers, ACS Nano 9 (2015) 134–145.

Supplementary Information

Gas-generating TPGS-PLGA Microspheres loaded with Nanoparticles (NIMPS) for Co-delivery of Minicircle DNA and Antitumoral Drugs

Colloids and Surfaces B: Biointerfaces, 2015
DOI: 10.1016/j.colsurfb.2015.07.004

10.1. Materials and Methods

10.1.1. Materials

PLGA (lactide:glycolic acid ratio 75:25, MW: 66 000- 107 000 Da), poly(vinyl alcohol) (PVA, MW ≅ 31000 Da), Triethylamine (TEA), Resazurin, N-Hydroxysuccinimide (NHS), D-α-tocopheryl polyethylene glycol 1000 succinate (TPGS), Fluorescein isothiocyanate isomer I (FITC), Dulbecco's modified Eagle's medium-high glucose (DMEM-HG) were purchased from Sigma-Aldrich (St Louis, MO, USA). Ultrapure, low molecular weight, chitosan hydrochloride (Protasan UP CL 113) was obtained from Novamatrix (Sandvika, Norway). The pMC.CMV-MCS-EF1-GFP-SV40PolyA (7.06 kbp) parental plasmid and the ZYCY10P3S2T minicircle producing strain were acquired from System Biosciences (Mountain view, CA, USA). N-(3-Dimethylaminopropyl)-N'-ethylcarbodiimide hydrochloride (EDC) was obtained from MerckMillipore. (Nothingham, UK). HeLa (Human negroid cervix epithelioid carcinoma) (ATCC® CCL-2™) was acquired from ATCC (Middlesex, UK) and Human skin fibroblasts (hFIB) were acquired from Promocell (Heidelberg, Germany). Phenazine methosulfate (PMS) and 3-(4,5-dimethylthiazol-2-yl)-5-(3-carboxymethoxyphenyl)-2-(4-sulfophenyl)-2H-tetrazolium) (MTS) were obtained from Promega. (Madison, WI, USA). Doxorubicin hydrochloride was purchased from Tocris (Bristol, UK). Hoechst 33342® and wheat germ agglutinin (WGA)-Alexa 594® conjugate fluorescent probes were purchased from Invitrogen (Carlsbad, CA, USA). All other reagents and salts were of analytical grade and were used without further purification.

10.1.2. Methods

10.1.2.1. Preparation of Doxorubicin-loaded gas-generating hollow microspheres

PLGA and TPGS-PLGA hollow microspheres were formulated by using the water-in-oil-in-water double-emulsion solvent diffusion-evaporation method reported by Ke and co-workers with slight modifications [1]. The first aqueous phase was comprised by a mixture of PVA, $NaHCO_3$ and hydrophobic Doxorubicin (Dox) and the second aqueous phase was formed either by PVA or TPGS as a strategy to manufacture microspheres with different coating materials (schematized in Figure 1A). Doxorubicin hydrochloride salt was converted into the hydrophobic base by adding TEA (1.5 eq.) and stirred for 30 min prior to particles formulation. For the assembly of gas-generating pH-responsive microspheres, the hydrogen carbonate source $NaHCO_3$ (2.5 mg) and the antitumoral drug Dox (200 µg) were initially added to 1 mL aqueous PVA solution (10 $mg.mL^{-1}$) and stirred for 15 min (600 rpm) at room temperature (RT). Then, 2 mL of PLGA solution (5 $mg.mL^{-1}$ in dichloromethane (DCM), organic phase) were dropped into the aqueous phase and the primary emulsification was carried out by using an ultrasonication bath for 30 min (Branson® 5510E-DTH, output 135 W, Branson Ultrasonics, Connecticut, USA), to promote PLGA microparticles assembly. Subsequently, 6 mL of PVA (20 $mg.mL^{-1}$) or TPGS (0.3 $mg.mL^{-1}$) were added to the primary W/O emulsion. The resulting mixture was homogenized at 1100 rpm, for 30 min, in an ice bath, by using a homogenizer (Ystral® X10/25 (Ystral GmbH, Ballrechten-

Dottingen, Germany). The final W/O/W double-emulsion was then transferred into 16 mL of double distilled and deionised water (ddH_2O, 0.22 μm filtered, ρ=17.9 $M\Omega.cm^{-1}$) and stirred overnight under reduced pressure to promote organic solvent diffusion-evaporation and particle shell solidification. The, PLGA-$NaHCO_3$-Dox microspheres were then recovered by centrifugation (1000 rpm, 30 min, RT). All the formulations were washed 3 times with ddH_2O and used immediately. Blank microparticles were prepared by the above mentioned W/O/W method without Dox incorporation in the first aqueous phase. Dox-loaded microspheres with PVA or TPGS coating are termed micro-PVA-Dox and micro-TPGS-Dox, respectively.

10.1.2.2. Preparation of mcDNA Amino acid-Chitosan nanoparticles

Prior to preparation of chitosan-mcDNA nanoparticles the cationic biopolymer was chemically modified with L-arginine and L-histidine via EDC/NHS coupling chemistry to yield multifunctional Chitosan-Arginine-Histidine (CH-HR) as our group previously reported [2]. To generate mcDNA for all experiments, parental plasmids were initially amplified in a laboratory scale bacterial fermentation of the genetically modified ZYCY10P3S2T *E.coli* strain (42 ºC, 250 rpm). At the end of exponential growth mcDNA production was induced by addition of L-arabinose as previously optimized by our group [3]. mcDNA (3.06 kbp) was subsequently purified with a commercial DNA purification kit (NZYMaxiprep, NZYTech, Lda., Portugal). CH-HR-mcDNA nanocarriers were formulated via electrostatic interaction between the polymer-amino acid amines and DNA phosphate groups under mild conditions [2]. In brief, mcDNA at the desired concentration was added drop-wise to the CH-HR polymer solution (5 mM acetate buffer, pH=4.5) at a 1:4 (v/v) ratio and vortexed for 1 min. Nanocarriers were then stabilized by incubation at RT for 30 min, and recovered by centrifugation (30 min, 14 000 rpm). All nanoparticles were formulated at the amine-to-phosphate ratio of 60 (N/P 60) since this formulation has previously presented optimal stability, biological performance and transfection efficiency [21]. mcDNA complexation by CH-HR was confirmed by agarose gel electrophoresis [24]. Nanocarriers loading into Micro-TPGS-Dox microspheres (45 μg mcDNA/ microspheres formulation) was accomplished by adding CH-HR-mcDNA nanoparticles in the primary aqueous phase of the W/O/W assembly process. The resulting Micro-TPGS-Dox-(CH-HR-mcDNA) nanoparticle-in-microsphere systems are designated by NIMPS from herein onwards.

10.1.2.3. Delivery systems physicochemical characterization

Microspheres and nanoparticles size was analysed by Dynamic Light Scattering (DLS) in a Zetasizer NanoZS (Malvern Instruments, Worcestershire, UK), equipped with a 633 nm He–Ne laser. Particles zeta potential was determined by measuring electrophoretic mobility. All measurements were carried out in triplicate (n=3) in disposable folded capillary cells (DTS1070), at 25 ºC, and with a 173° scattering angle. The data was analysed in Malvern Zetasizer software by using the cumulants analysis and the Smoluchowski equation (v.7.11). Microspheres morphology was evaluated by scanning electron microscopy (SEM). Prior to imaging, particle solutions were dropped into a round cover glass and left to dry overnight.

Afterwards, the samples were mounted on aluminium stubs and sputter coated with gold by using a Quorum Q150R ES sputter coater (Quorum Technologies, UK). All the images were acquired in a Hitachi S-3400N scanning electron microscope (Hitachi, Japan), at an accelerating voltage of 20 kV and various magnifications.

The existence of the gas-generating agent ($NaHCO_3$) in PLGA microspheres was determined by X-ray diffraction spectroscopy (XRD). In brief, microspheres were collected by centrifugation and freeze dried for 24 h. Powder samples were then recovered and deposited in silica slides using a double-sided adhesive. Data was acquired by using a Rigaku Geiger Flex D-max III/c diffractometer (Rigaku Americas Corporation, USA) with a 2Θ scanning range from 5° to 70°.

10.1.2.4. Drug encapsulation and *in vitro* release

Drug encapsulation efficiency in all PLGA microsphere formulations was determined through UV-vis spectrophotometry at λ=485 nm by using a Shimadzu–1700 spectrophotometer (Shimadzu Inc., Japan). Drug encapsulation efficiency was calculated as reported in the literature [5]. Drug release from microspheres was evaluated by the dialysis method, in duplicate independent experiments. Briefly, drug-loaded microspheres were resuspended in phosphate buffer saline (PBS, pH = 7.4 and pH = 5.0) and transferred into a dialysis bag (MWCO 1000 Da). Drug release was carried out at 37 ºC in a water bath, with magnetic stirring (500 rpm), in the dark. Supernatant samples were collected at various time-points and the drug content was analyzed by UV-vis spectrophotometry.

10.1.2.5. Biocompatibility assays

The biocompatibility of blank Micro-PVA and Micro-TPGS carriers was evaluated by the resazurin assay, as previously described [6]. Briefly, HeLa cells were cultured in DMEM-HG medium supplemented with 10 % FBS and placed in a sterile incubator with humidified and controlled atmosphere (37 °C, 5 % CO_2). For all biocompatibility assays, HeLa cells were sub-cultured in 96-well flat bottom culture plates at a density of 8 x 10^3 cells per well. After 24 h in culture, cancer cells were incubated with different concentrations of Micro-PVA or Micro-TPGS formulations (10-1000 $\mu g.mL^{-1}$). Microparticles biocompatibility was evaluated at 24, 48 and 72 h. At pre-determined intervals, the medium of each well was replaced and cells were incubated with fresh medium containing resazurin 10 % ($v.v^{-1}$), for the period of 4 h, in the dark (37 ºC, 5 % CO_2). The resulting resorufin product present in the culture medium was transferred to 96-well black clear bottom plates (Greiner Bio-one, Frickenhausen, Germany). Resorufin fluorescence intensity was quantified in a plate reader spectrofluorometer (Spectramax Gemini XS, Molecular Devices LLC, USA), at λ_{ex}=560 nm and λ_{em}=590 nm. HeLa Cells incubated with ethanol (EtOH, 70 % $v.v^{-1}$) were used as positive controls (K+). Untreated cells were used as negative controls (K-).

10.1.2.6. Cellular uptake

The cellular uptake of drug-loaded microparticles (micro-PVA-Dox, micro-TPGS-Dox) and Dox-mcDNA dual loaded NIMPS was evaluated by flow cytometry. For this analysis, HeLa cells were seeded in 12 well culture plates at a density of 1 x 10^4 cells per well. In the following day, cancer cells were incubated with different particle formulations (200 $\mu g.mL^{-1}$), for 4 h, at 37 ºC, in DMEM-HG-10 % FBS medium in order to mimic physiological conditions. Subsequently, the cells were extensively rinsed with PBS, detached with 0.18 % trypsin and resuspended in 500 µL of PBS-5 % FBS. Flow cytometry analysis was carried out in a BD FACSCalibur flow cytometer (Becton Dickinson Inc., USA). Data acquisition was performed with the CellQuest software where 1 x 10^4 events were collected in the region of interest assigned to HeLa cells. Flow cytometry dot plots and histograms were analysed in the trial version of FlowJo software v. 10.0.6 (Tree Star, Trial version, Ashland, Oregon, USA).

In addition, particles cellular uptake was visualized by confocal laser scanning microscopy (CLSM). In brief, HeLa cells were cultured in fibronectin coated µ-Slide 8-well slides (Ibidi GmbH, Munich, Germany), at a density of 2 x 10^4 cells/well. In the following day, cells were incubated with different formulations (200 $\mu g.mL^{-1}$) during 4 h. Afterwards, each well was rinsed with PBS, fixed in paraformaldehyde (4 % PFA, 15 min, RT), and incubated with WGA-Alexa Fluor® 594 conjugate to label cell surface glycoproteins. HeLa cells nucleus was labeled with the Hoechst 33342® nuclear probe (2 µM, 10 min, RT). Confocal images were acquired in a Zeiss LSM 710 confocal microscope (Carl Zeiss SMT Inc., USA). 3D reconstruction, colocalization analysis and image processing was performed in Zeiss Zen 2010, ImageJ and Imaris software (Bitplane, Switzerland). CLSM analysis was also used to visualize the inclusion of CH-HR-mcDNA nanoparticles in micro-TPGS-Dox microspheres. For this purpose mcDNA was labelled with FITC as previously reported [6].

10.1.2.7. *In vitro* gene expression in 2D cultures

mcDNA-GFP expression in cancer cells was evaluated by spectrofluorimetry [4]. For this assay, HeLa cells were cultured in 96 well black-clear bottom plates at a density of 1 x 10^4 cells per well. In the following day, transfection was performed with mcDNA-CH-HR nanoparticles or mcDNA-loaded NIMPS for 4 h, in DMEM-HG-10 % FBS with a concentration of 1 µg mcDNA per cm^2. After incubation the particles were removed by replacing the culture medium. Gene expression was quantified after 48 h by using a plate reader spectrofluorometer (Spectramax Gemini XS, Molecular Devices LLC, USA), at λ_{ex}=488 nm and λ_{em}=519 nm. In addition, GFP expression was also visualized and quantified by CLSM. Briefly HeLa cells were seeded (1 x 10^4 cells/well) in cell culture treated µ-Slide 8-well imaging slides. After 48 h of transfection, the cells were fixed with 4 % PFA and imaged in a Zeiss LSM 710 confocal microscope (Carl Zeiss SMT Inc., USA), equipped with a Plan-Apochromat 63x/1.4 oil objective. For all experiments, 3D z-stacks of randomly distributed cell fields (n=3) were acquired. GFP fluorescence intensity in cells volume was quantified by using the Imaris software (Bitplane, Switzerland).

10.1.2.8. Cytotoxic activity

The cytotoxic activity of Dox-loaded microspheres and mcDNA-Dox dual loaded NIMPS was evaluated by the MTS assay. For this purpose, cancer cells were seeded (10 x 10^3 cells/well), in 96 well culture plates containing DMEM-HG-10 % FBS.In the following day, the culture medium was exchanged and the cells were incubated with the different microcarriers (200 $\mu g.mL^{-1}$) during 4, 8, 12, 24 and 48 h. Cell viability was evaluated at each time point by adding 20 µL of MTS/PMS to each well and incubating during 4 h, in the dark (37 °C, 5% CO_2). Absorbance measurements of the soluble brown formazan were carried out in a microplate reader (Anthos 2020, Biochrom UK), at λ=492 nm. Dead cells (70 % EtOH), and non-treated cells were used as positive and negative controls, respectively.

10.1.2.9. Statistical analysis

One-way analysis of variance (ANOVA) with the post-hoc Newman–Keuls test were used for statistical analysis of three or more groups. Student's t-test was used for comparison between two groups. A p value below 0.05 was considered statistically significant. Data analysis was carried out in GraphPad Prism v.6.0 (GraphPad software Inc., CA, USA; trial version).

10.2. Results and Discussion

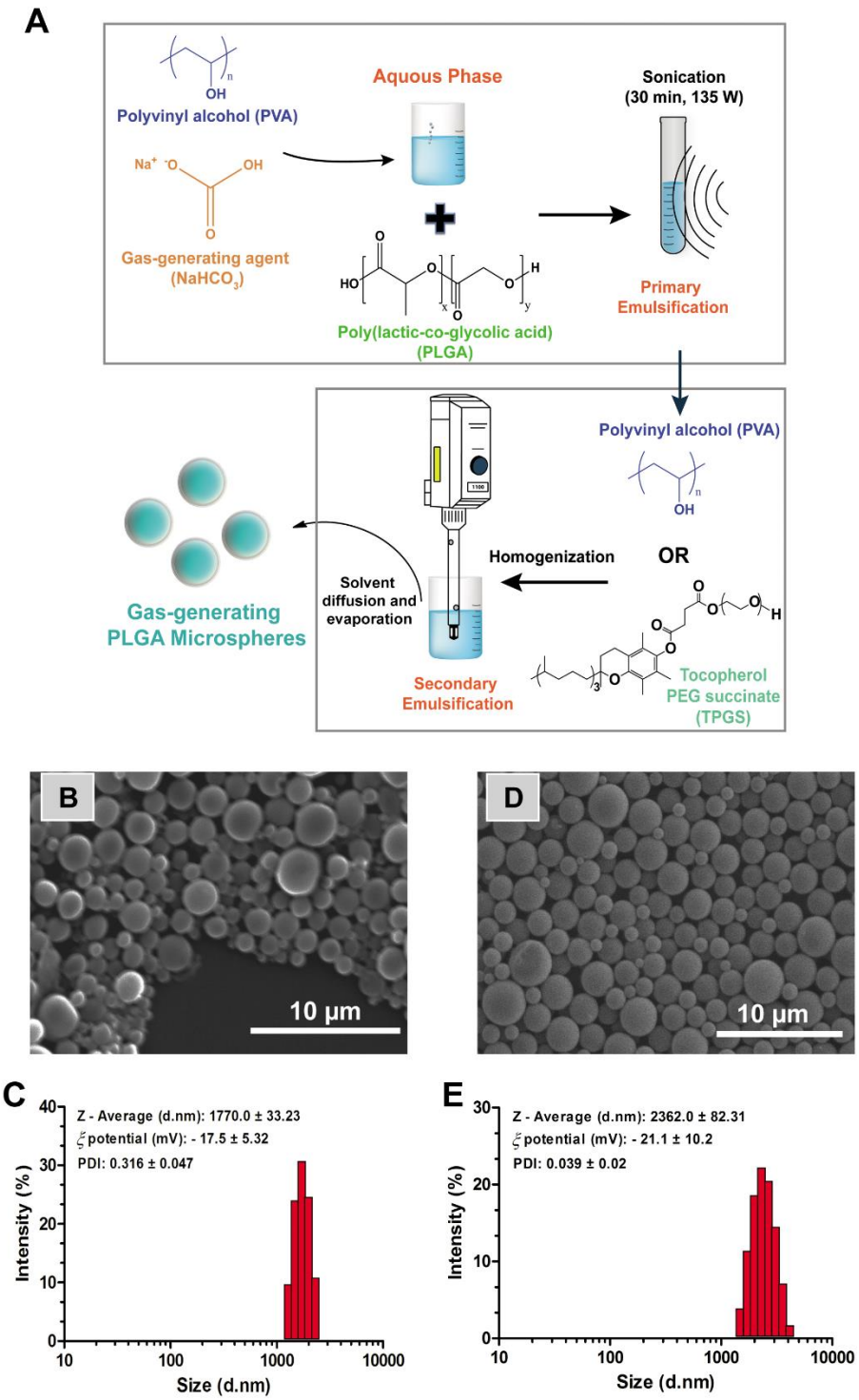

Figure S1. Production of gas-generating pH-responsive PLGA microspheres. (A.) Schematics of microspheres production process. (B and D.) SEM micrographs of micro-PVA and micro-TPGS formulations, respectively. (C and E.) DLS analysis of micro-PVA and micro-TPGS particles, respectively. Data is presented as mean ± s.d., *n*=3.

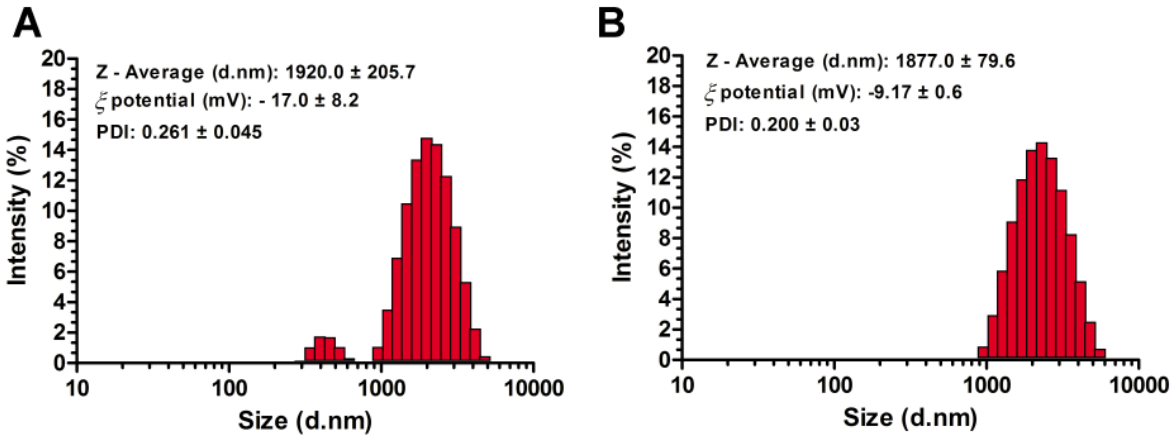

Figure S2. DLS analysis of Doxorubicin loaded micro-PVA (A.) and micro-TPGS carriers (B.), respectively. Data is presented as mean ± s.d., *n*=3.

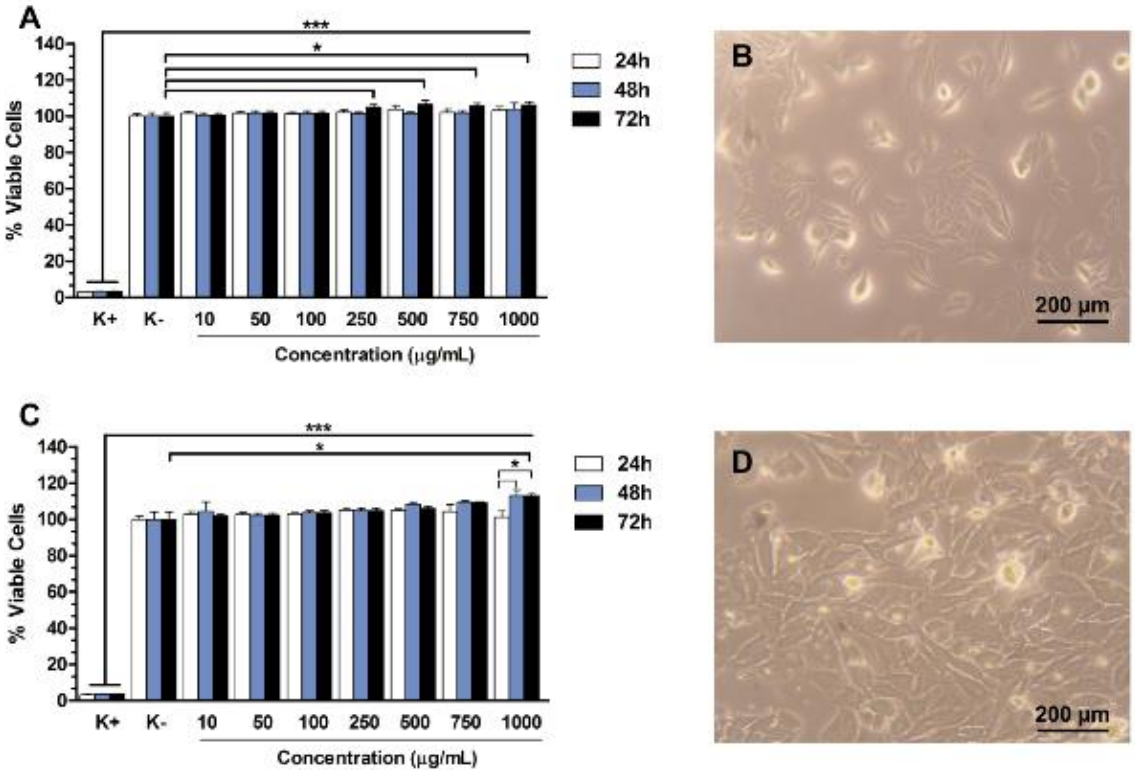

Figure S3. Biocompatibility of microsphere formulations. (A and C.) Evaluation of cell viability after incubation of different concentrations of blank micro-PVA and micro-TPGS carriers at various time-points. Data is presented as mean ± s.d., *p<0.05, ***p<0.01, *n*=5. (B and D.) Representative optical micrographs of HeLa cells incubated with microspheres. Results show a high percentage of living HeLa cells (>98 %), thus corroborating the biocompatibility of these delivery systems. Cancer cells morphology and cell-cell contacts are also maintained after incubation with the highest concentration of microspheres after 72 h, indicating that these carriers do not significantly affect normal cell functions such as cell adhesion.

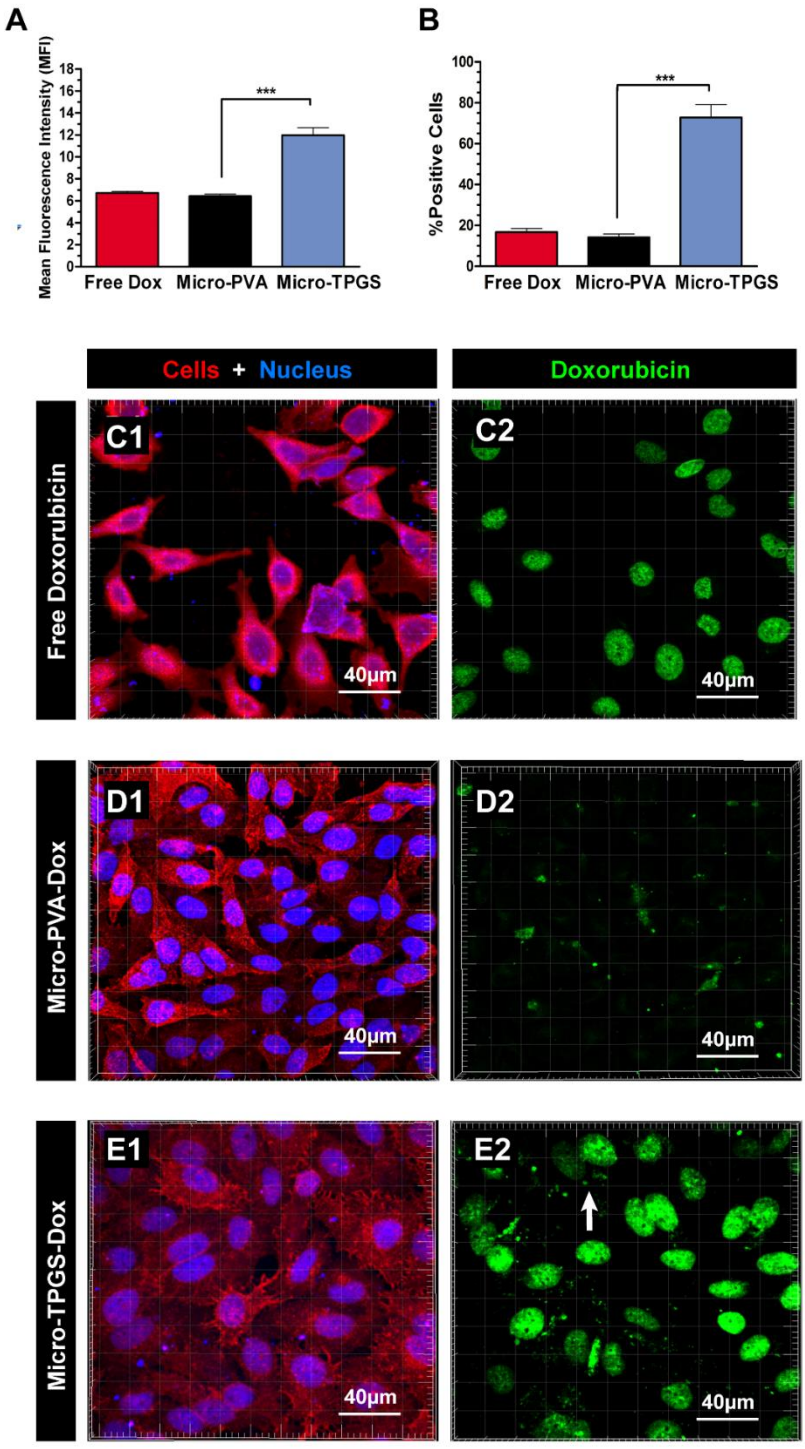

Figure S4. Analysis of drug loaded microspheres uptake in HeLa cancer cells. (A.) Analysis of Dox mean fluorescence intensity in HeLa cells after microcarriers incubation for 4 h. (B.) Percentage of Dox positive cells. Data represents mean ± s.d., *n*=3. (C1 and C2.) CLSM visualization of free Dox cellular uptake and intracellular localization. (D1 and E2.) CLSM visualization of micro-PVA-Dox microspheres cellular uptake and intracellular localization. (E1 and E2.) CLSM visualization of micro-TPGS-Dox microspheres uptake and intracellular localization. Red channel: WGA-Alexa Fluor® 594 conjugate; Blue channel: Hoechst 33342®; Green channel: Doxorubicin; Merged channel: z-stack 3D reconstruction and merged RGB channels.

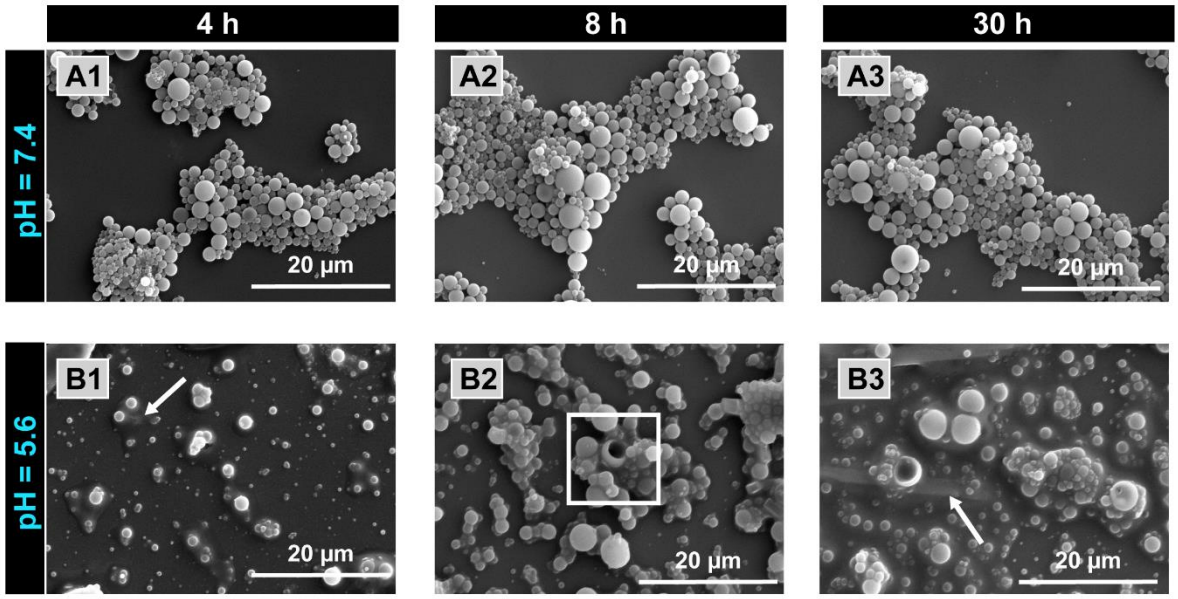

Figure S5. SEM analysis of pH-responsive microspheres. (A1, A2 and A3.) TPGS-coated PLGA microspheres structure at various time-points during drug release assays (pH = 7.4). (B1, B2 and B3.) TPGS-coated PLGA microspheres structure at various time points during the release assays (pH = 5.6). White square represents disrupted microspheres. White arrow represents free polymer.

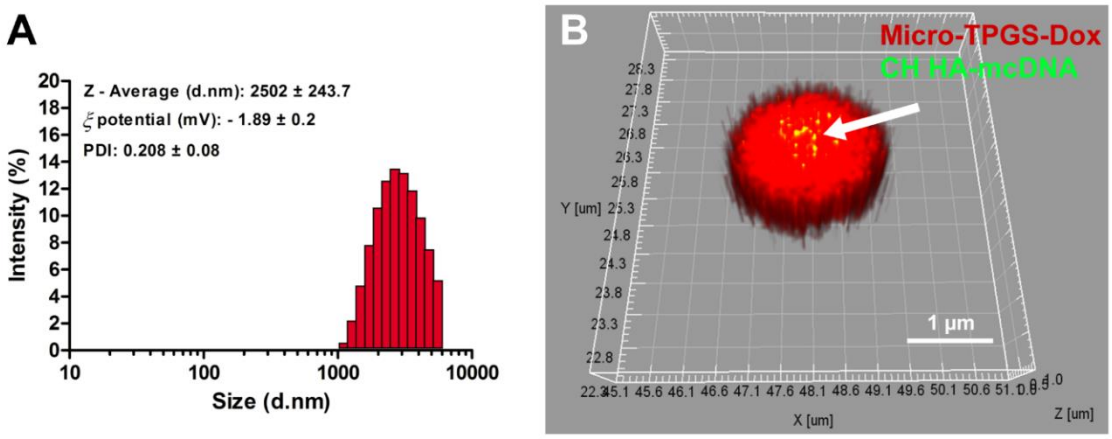

Figure S6. (A.) DLS analysis of nanoparticle in microsphere hybrid systems NIMPS after encapsulation of CH-HR-mcDNA in micro-TPGS-Dox carriers. Data is represented as mean ± s.d., *n*=3. (B.) Representative NIMPS 3D reconstruction. Red channel: Doxorubicin encapsulated in microspheres. Green channel: FITC-labelled mcDNA. Yellow channel: merged red and green channels. White arrows indicate FITC-mcDNA.

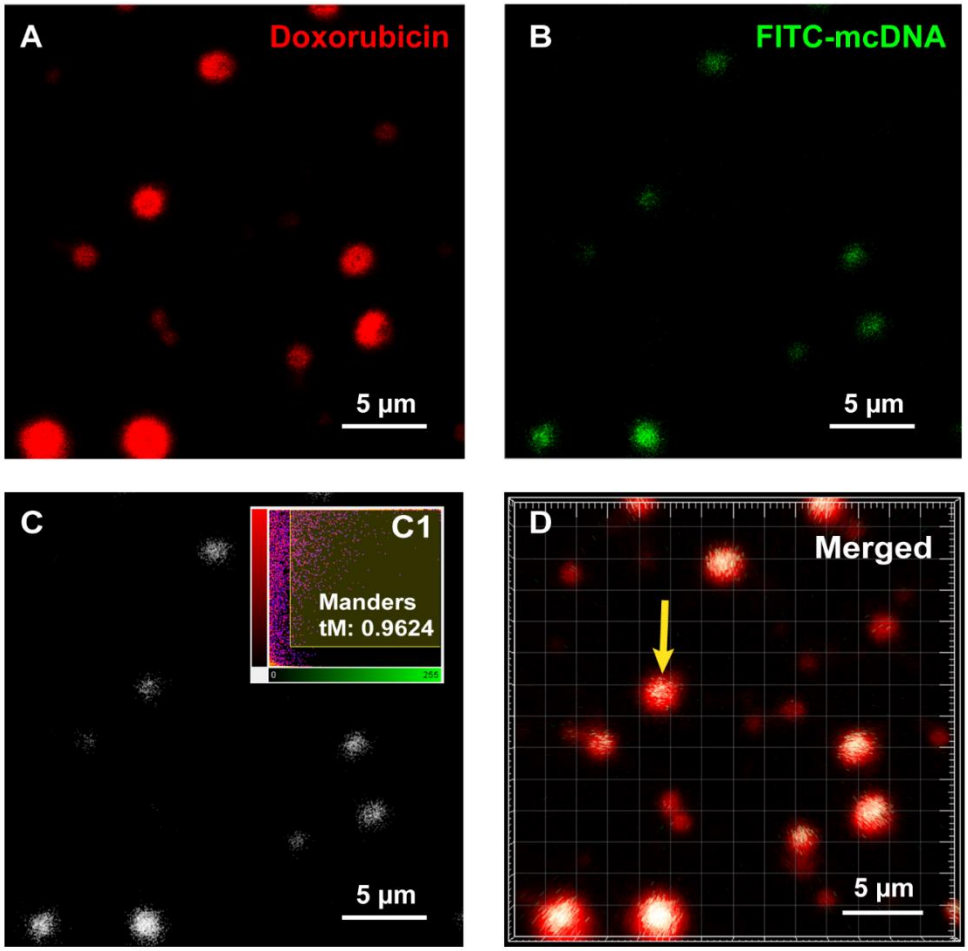

Figure S7. Confocal microscopy analysis of CH-HR nanoparticles inclusion in micro-TPGS-Dox microcarriers. (A.) Doxorubicin loaded PLGA-$NaHCO_3$-TPGS microspheres. (B.) FITC-mcDNA loaded in CH-HR nanoparticles that were subsequently encapsulated in PLGA microspheres. (C and C1.) Colocalization channel of Doxorubicin fluorescence and FITC-mcDNA fluorescence. Colocalization analysis was performed by using threshold manders colocalization algorithm (tM: 0.9264). (D.) Merged channels represent the colocalization of FITC-mcDNA and Dox, indicating that the nanocarriers are inside the microspheres (Gold arrow).

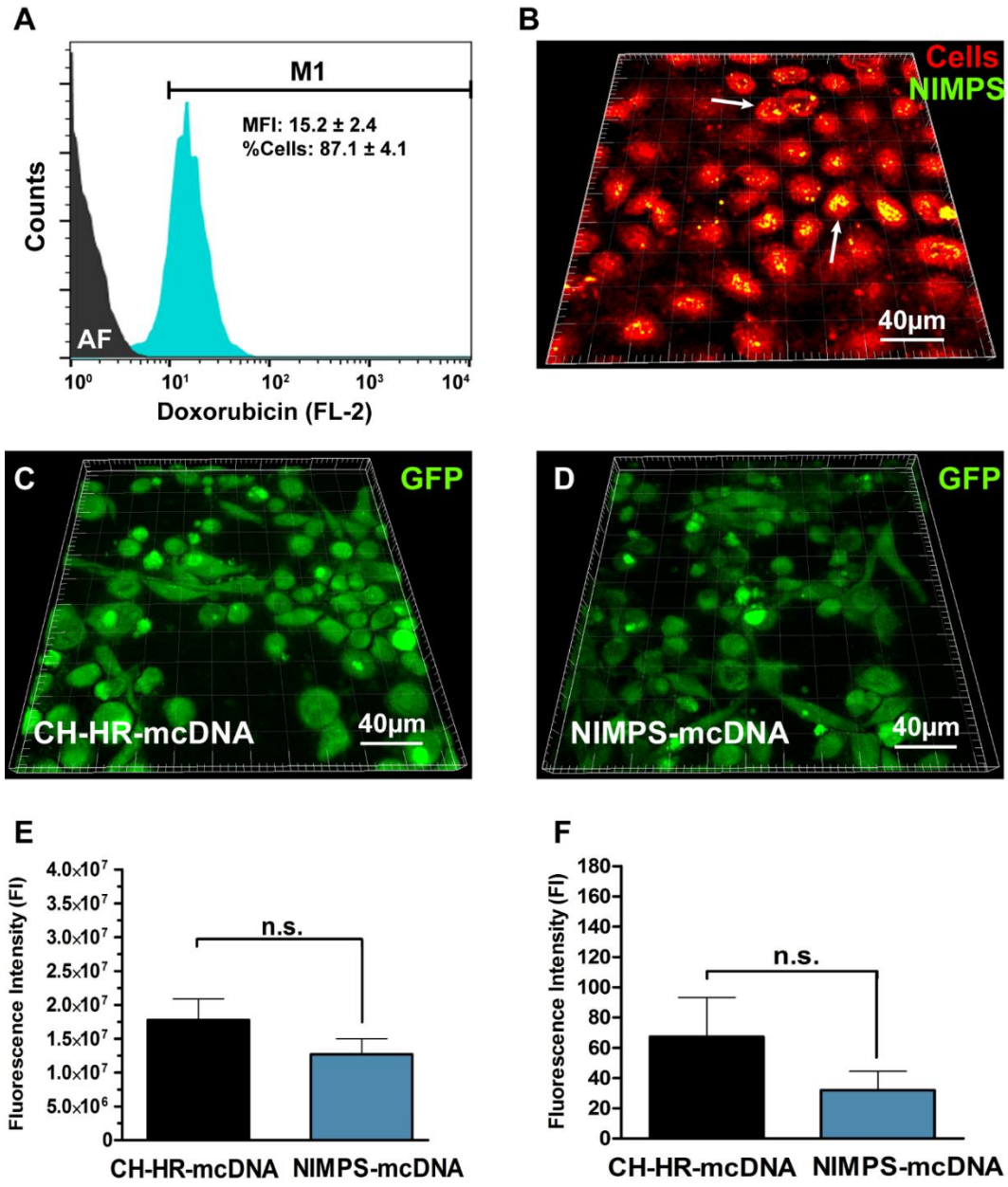

Figure S8. Evaluation of NIMPS biological performance. (A.) Cellular uptake of NIMPS systems after 4 h incubation in HeLa cancer cells. (B.) Confocal microscopy analysis of NIMPS cellular uptake. (C and D.) Confocal microscopy analysis of GFP expression mediated by mcDNA vectors delivered by CH-HR nanocarriers and hybrid NIMPS systems, respectively. (E and F) Quantification of GFP fluorescence intensity by confocal microscopy and spectrofluorimetry, respectively. Data represents mean ± s.d., *n*= 3, n.s. – not significant.

10.3. References

1. Ke, C.-J., Chiang, W.-L., Liao, Z.-X., Chen, H.-L., Lai, P.-S., Sun, J.-S., and Sung, H.-W., *Real-time visualization of pH-responsive PLGA hollow particles containing a gas-generating agent targeted for acidic organelles for overcoming multi-drug resistance.* Biomaterials, 2013. **34**(1): p. 1-10.
2. Gaspar, V., Marques, J., Sousa, F., Louro, R., Queiroz, J., and Correia, I., *Biofunctionalized nanoparticles with pH-responsive and cell penetrating blocks for gene delivery.* Nanotechnology, 2013. **24**(27): p. 275101.
3. Gaspar, V.M., Maia, C.J., Queiroz, J.A., Pichon, C., Correia, I.J., and Sousa, F., *Improved Minicircle DNA Biosynthesis for Gene Therapy Applications.* Human gene therapy methods, 2014. **25**(2): p. 93-105.
4. Gaspar, V.M., Costa, E.C., Queiroz, J.A., Pichon, C., Sousa, F., and Correia, I.J., *Folate-Targeted Multifunctional Amino Acid-Chitosan Nanoparticles for Improved Cancer Therapy.* Pharmaceutical research, 2015. **32**(2): p. 562-577.
5. Marques, J.G., Gaspar, V.M., Markl, D., Costa, E.C., Gallardo, E., and Correia, I.J., *Co-delivery of Sildenafil (Viagra®) and Crizotinib for Synergistic and Improved Anti-tumoral Therapy.* Pharmaceutical research, 2014. **31**(9): p. 2516-2528.
6. Gaspar, V.M., Gonçalves, C., de Melo-Diogo, D., Costa, E.C., Queiroz, J.A., Pichon, C., Sousa, F., and Correia, I.J., *Poly (2-ethyl-2-oxazoline)–PLA-g–PEI amphiphilic triblock micelles for co-delivery of minicircle DNA and chemotherapeutics.* Journal of Controlled Release, 2014. **189**: p. 90-104.

CHAPTER 11

Bioreducible Poly(2-ethyl-2-oxazoline)-PLA-PEI-SS triblock Copolymer Micelles for Co-delivery of DNA minicircles and Doxorubicin

Journal of Controlled Release, 2015

DOI: 10.1016/j.jconrel.2015.07.011

Volume 213

Motivation

As before demonstrated in chapter 9 the physicochemical characteristics and the *in vivo* performance of triblock micellar carriers also makes this platform highly desirable for application in co-delivery of drug-gene combinations. In an attempt to further explore its potential and create a smarter platform that could respond to biological stimuli the triblock copolymers were chemically modified to react to redox conditions. Such modification was anticipated to provide additional improvements in gene transfer efficacy.

Journal of Controlled Release 213 (2015) 175–191

Contents lists available at ScienceDirect

Journal of Controlled Release

journal homepage: www.elsevier.com/locate/jconrel

Bioreducible poly(2-ethyl-2-oxazoline)–PLA–PEI-SS triblock copolymer micelles for co-delivery of DNA minicircles and Doxorubicin

Vítor M. Gaspar [a], Patrick Baril [b], Elisabete C. Costa [a], Duarte de Melo-Diogo [a], Frédéric Foucher [b], João A. Queiroz [a], Fani Sousa [a], Chantal Pichon [b], Ilídio J. Correia [a,*]

[a] CICS-UBI — Health Sciences Research Center, University of Beira Interior, 6200-506 Covilhã, Portugal
[b] Centre de Biophysique Moléculaire, CNRS UPR4301, Inserm and University of Orléans, 45071 Orléans cedex 02, France

ARTICLE INFO

Article history:
Received 20 April 2015
Received in revised form 8 July 2015
Accepted 9 July 2015
Available online 13 July 2015

Keywords:
Bioreducible micelles
Cancer therapy, Chemotherapeutics
Co-delivery
Minicircle DNA

ABSTRACT

The co-delivery of minicircle DNA (mcDNA) and small anti-cancer drugs via stimuli-sensitive nanocarriers is a promising approach for combinatorial cancer therapy. However, the simultaneous loading of drugs and DNA in nanosized delivery systems is remarkably challenging. In this study we describe the synthesis of triblock copolymer micelles based on poly(2-ethyl-2-oxazoline)–poly(L-lactide) grafted with bioreducible polyethylenimine (PEOz–PLA-g–PEI-SS) for co-delivery of supercoiled (sc) mcDNA vectors and Doxorubicin (Dox). These amphiphilic carriers take advantage of non-fouling oxazolines to confer biological stability, of PLA to provide a hydrophobic core for drug encapsulation and of bioreducible PEI-SS to provide mcDNA complexation and an on-demand stimuli-responsive release. The obtained results show that mcDNA-loaded micelleplexes penetrate into *in vitro* tumor spheroid models with specific kinetics and exhibit a higher gene expression when compared to non-bioreducible nanocarriers. Moreover, *in vivo* bioluminescence imaging showed that gene expression is detected up to 8 days following mcDNA-micelles intratumoral administration. Furthermore, drug–gene co-delivery in PEOz–PLA-g–PEI-SS carriers was verified by successful encapsulation of both Dox and mcDNA with high efficacy. Moreover, dual-loaded micelleplexes presented significant uptake and a cytotoxic effect in 2D cultures of cancer cells. The co-delivery of mcDNA-Dox to B16F10-Luciferase tumor bearing mice resulted in a reduction in tumor volume and cancer cells viability. Overall, such findings indicate that bioreducible triblock micelles are efficient for focal delivery *in vivo* and have potential for future application in combinatorial DNA-drug therapy.

1. Introduction

Combinatorial therapy encloses a remarkable potential to overcome the issues of conventional oncology treatments since an enhanced therapeutic outcome can be obtained by co-administration of multiple bioactive molecules [1]. A multi-modal regimen is advantageous for cancer therapy because various hallmarks of this complex disease can be targeted simultaneously [2]. In turn, this cooperative action is anticipated to result in an additive or synergistic effect that promotes significant tumor regression [3]. From a therapeutic perspective such increase in efficacy is highly beneficial since recent reports continue to emphasize that the stand-alone administration of cytotoxic drugs is insufficient and often leads to acquisition of cancer drug resistance [4,5]. In line with this evidence, Chen and co-workers demonstrated that this suboptimal efficiency is also obtained following *in vivo* administration of plasmid DNA (pDNA) biopharmaceuticals as it results in a relatively short-lived expression of therapeutic transgenes [4].

Aiming to bridge this gap, in the last years substantial efforts have been focused on exploring the co-administration of DNA–drug combinations [1,6]. In practice, this treatment modality can take advantage of two main strategies: (i) the use of exogenous DNA vectors encoding interfering RNA (e.g., shRNA) for sensitizing cancer cells to chemotherapeutics action [2,7], and (ii) the use of DNA biopharmaceuticals to encode tumor suppressor genes which act in synergy with drugs cytotoxic activity [8]. The latter has recently started to be explored in a phase I clinical trial that involves administration of free (non-encapsulated) anti-cancer drugs Topotecan and Cyclophosphamide, in combination with p53-encoding DNA vectors delivered by transferrin-targeted liposomes (clinicaltrials.gov, NCT02354547). However, alike other examples, this approach involves the delivery of chemotherapeutics through systemic administration a factor that may consequently lead to dose-related toxicity.

To overcome these deleterious side effects, different types of delivery systems are being actively developed for co-administration of drug–gene combinations within a single nanocarrier [9]. Simultaneous encapsulation is highly advantageous since it increases not only drugs therapeutic index, but also protects exogenous DNA vectors from

* Corresponding author at: Av. Infante D. Henrique, 6200-506 Covilhã, Portugal.
E-mail address: icorreia@ubi.pt (I.J. Correia).

http://dx.doi.org/10.1016/j.jconrel.2015.07.011
0168-3659/

immediate degradation in biological fluids [10,11]. In addition, the facilitated delivery of chemotherapeutics and nucleic acids to the same cell highly favorable to achieve drug–gene synergy.

However, the formulation of nanodevices for DNA–drug co-loading remains extremely challenging due to the different physicochemical properties of these molecules [10]. Moreover, to achieve maximal therapeutic efficiency from this dual delivery strategy it is also essential to assure an optimal compromise between drug release and efficient transgene expression since the onset of drug-induced toxicity may interfere with DNA expression. To this end, block copolymer micellar carriers, with their inherent structural versatility offer an ideal platform for co-administration of multiple therapeutic. In this context, our group has previously developed poly(2-ethyl-2-oxazoline)–poly(L-lactide)-g–polyethylenimine (PEOz–PLA-g–PEI) triblock copolymers for co-delivery of Doxorubicin and minicircle DNA (mcDNA) [10]. These amphiphilic nanocarriers take advantage of poly(2-ethyl-2-oxazoline) polymers to confer a stealth character, being an alternative to poly(ethylene glycol) (PEG) [10]. Such property assumes great importance in light of the reported accelerated blood clearance of pegylated nanocarriers [12,13]. Besides this, 2-oxazoline-based polymers have demonstrated to be non-toxic and biodegradable *in vitro* and *in vivo*, which are important properties that support their use for the assembly of novel delivery systems [14]. In addition, in the PEOz–PLA-g–PEI triblock carrier the poly(L-lactide) core is used as a reservoir for hydrophobic anti-cancer drugs and polyethylenimine for mcDNA complexation and facilitate intracellular trafficking. The use of mcDNA vectors provides further advantages in comparison to standard pDNA biopharmaceuticals. In contrast to pDNA, minicircles are devoid of the bacterial backbone and immunostimulatory CpG motifs. These unique characteristics associated to their smaller size, significantly increases their safety and *in vivo* efficacy [15]. This enhanced biological performance has been recently evidenced by Kobelt and co-workers which reported that *in vivo* administration of mcDNA induces higher levels of transgene expression in comparison to plasmid-based vectors [16].

Despite these improvements in both nanocarriers and DNA vectors, it has been demonstrated that imprinting stimuli-responsive properties in nanoformulations designed for co-delivery may provide an added biological efficacy since a more controlled biodegradation and site-specific, on-demand release can be promoted [17]. To date, various types of stimuli such as pH, redox conditions, enzymes, magnetic fields, ultrasound or light have been explored for promoting modifications in nanocarrier structure in biological environment. Exploiting redox conditions is particularly interesting for cancer therapy as it was reported that cancer cells have increased intracellular glutathione (GSH) levels [18]. This provides a further reductive environment which can be used to exploit thiol–disulfide exchange reactions. In essence, this approach takes advantage of different redox conditions naturally found in the extracellular space and intracellular compartments to prompt a site-specific release upon nanocarrier cellular internalization. Such event is highly dynamic and can occur both in the cytoplasm and nucleus as these are reported to be highly reductive compartments [18]. Due to this fact various types of gene delivery systems for cancer therapy have been designed to take advantage of thiol–disulfide exchange. However, to date, few reports have explored the formulation of bioreducible micellar carriers that can promote a stimuli-responsive co-delivery of drug-minicircle combinations to cancer cells.

From this standpoint, with the aim to control biodegradation and improve transgene expression efficiency, the cationic block of PEOz–PLA-g–PEI micelles was modified with redox responsive disulfide (S–S) moieties to imprint a sensitive character in these co-delivery systems. Overall, the bioreducible carriers exhibited a stimuli-responsive character and possess the attributes for simultaneous Doxorubicin (Dox) encapsulation and supercoiled mcDNA condensation. The administration of mcDNA-loaded micelleplexes to different 3D tumor models showed that bioreducible carriers achieve higher transgene expression efficiency when compared to their non-responsive counterparts. The single loaded and dual loaded micelleplexes also mediated significant gene expression following *in vivo* administration to tumor bearing mice. Moreover, local administration of Dox–mcDNA dual loaded micelleplexes *in vivo* promoted a decrease in tumor volume. Altogether, these results support the concept of adding bioreducible moieties to improve gene transfer and also demonstrate that PEOz–PLA-g–PEI-SS nanocarriers can be used for drug–DNA combinatorial cancer therapy.

2. Materials and methods

For a complete description of additional materials and methods used throughout the article the reader is referred to the Supplementary materials.

2.1. Materials

Branched polyethylenimine (PEI) (Mw ≈ 1300 Da), poly (2-ethyl-2-oxazoline) (Mw ≈ 5000 Da), Pyrene, anhydrous toluene, Resazurin, Fluorescein isothiocyanate isomer I (FITC), and Rhodamine B isothiocyanate (RITC) were obtained from Sigma-Aldrich (Sintra, Portugal). 1,1′-carbonyldiimidazole (CDI), L-lactide, anhydrous tetrahydrofuran (THF) and triethylamine (TEA) were acquired from Tokyo Chemical Industry Europe (TCI Europe, Antwerp, Belgium). N′N′-Cystamine bisacrylamide was purchased from Polysciences, Inc. (Warrington, PA). Stannous octoate ($Sn(Oct)_2$) was purchased from Cymit Química (Barcelona, Spain). Doxorubicin hydrochloride was obtained from Biogen Cientifica S.L. (Madrid, Spain). The ZYCY10P3S2T minicircle producing *Escherichia coli* (*E. coli*) strain and the parental plasmid pMC.CMV-MCS-EF1-GFP-SV40PolyA (7.06 kbp) were purchased from System Biosciences (Mountain view, CA, US). The p3NF-luc-3NF (5.5 kbp) encoding firefly luciferase and bearing the 3NF motif to favor nuclear import by $NF_K\beta$ was constructed in a previous study [19]. B16F10 (Mus musculus skin melanoma cell line; ATCC® CRL-6475™) and HeLa CCL-2 (Human negroid cervix epithelioid carcinoma; ATCC® CCL-2™) were purchased to ATCC (Middlesex, UK). Hoechst 33342®, wheat germ agglutinin (WGA)-Alexa 594® conjugate and LysoTracker™ Red DND-99 were obtained from Invitrogen (Carlsbad, CA, US). All other reagents were of analytical grade and used without further purification.

2.2. Methods

2.2.1. Synthesis of bioreducible PEI

Bioreducible PEI (PEI-SS) was synthesized by Michael type addition chemistry between PEI (Michael donor) and N′N′-Cystamine bisacrylamide (CBA) (Michael acceptor) as previously described by Sun and co-workers [20], with slight modifications. In brief, PEI (1.72 g) was dispersed in 20 mL of aqueous methanol (MetOH) (10% v/v). The reaction flask was mounted in a water jacketed Graham condenser and stirred at 45 °C, under a nitrogen (N_2) atmosphere, in the dark. In another flask, CBA was dissolved in 12 mL of a MetOH solution (100% v/v) in the dark (CBA:PEI molar ratio 1:6). This solution was added drop-wise to PEI and the reaction was left to proceed for 4 h in the dark, at 45 °C, under N_2. Subsequently, 10% w/v PEI, in 2 mL MetOH, was added to the under stirring, in order to consume unreacted acrylamide groups for an additional period of 2 h. The reaction was stopped by addition of 40 mL, room temperature, double deionized water (0.22 μm filtered; 18.1 MΩ·cm). The resulting mixture was then acidified to pH 4.0 with 1 M HCl and dialyzed (MWCO 3500 Da) against water during 3 days. Then, the dialysis purified PEI-SS solution was acidified again to pH 4.0 with 1 M HCl and freeze dried for 48 h.

2.2.2. Synthesis of triblock copolymers

The synthesis of triblock copolymers bearing bioreducible PEI-SS was performed through a two-stage procedure [10]. Initially, PEOz–PLA was synthetized through cationic ring opening polymerization (CROP) of L-lactide by using PEOz hydroxyl group as the initiator and

$Sn(Oct)_2$ as the catalyst [10]. For this synthesis, L-lactide (LA) and PEOz (1:0.5 w/w ratio) were added to a Schlenk reaction flask under N_2 atmosphere. The powder reagents were then dissolved with anhydrous toluene at 100 °C under stirring. Upon complete dissolution the CROP catalyst (0.5% w/v) was added and the reaction was carried out under reflux at 120 °C for 8 h in an inert atmosphere. The crude product was subsequently recovered by using rotary evaporation (Rotavap® R-215, Büchi, Switzerland), followed by precipitation in MetOH. The resulting PEOz–PLA copolymer was then dialyzed (MWCO 3500 Da) and collected as a white powder after freeze drying [10]. The assembly of the triblock copolymer was then promoted by conjugation of PEOz–PLA to PEI-SS through carbonyldiimidazole-mediated chemistry [10]. In brief, PEOz–PLA hydroxyl group was activated in anhydrous THF with excess CDI, under N_2 atmosphere for 4 h. Afterwards, previously dissolved PEI-SS was added drop-wise to the Schlenk flask under vigorous stirring (1:1 w/w ratio PEOz–PLA:PEI-SS), and the reaction proceeded at 60 °C, under N_2 for 48 h. The resulting copolymer was subsequently purified by dialysis (MWCO 3500 Da) for 5 days against water and freeze dried. From herein onwards the bioreducible PEOz–PLA-g–PEI-SS copolymers will be termed PPP-SS.

The amine weight fraction per PPP-SS copolymer mass was determined by the copper (Cu^{2+}) assay by using a standard curve with PEI-SS ($y = 3.099x + 0.427$; $R^2 = 0.993$) as reported in the literature [21] (60.77 ± 0.86%). Further characterization of polymers was performed by ^1H NMR spectroscopy and high resolution electrospray ionization mass spectrometry (HR ESI-MS) (Supplementary information).

2.2.3. Determination of critical micellar concentration

Triblock copolymers critical micellar concentration (CMC) in double deionized water was determined by using the ratio of the first and third vibronic peaks of pyrene fluorochrome (1:3 ratio) [10]. Prior to all experiments a fresh stock solution containing PPP-SS copolymers (4 $mg \cdot mL^{-1}$) was prepared. For CMC determination, different dilutions were prepared from a stock solution (2000 $\mu g \cdot mL^{-1}$ to 0.001 $\mu g \cdot mL^{-1}$), and incubated with pyrene (0.6 μM). The polymers–pyrene mixture was then sonicated for 30 min, at RT, and analyzed in a Spectramax Gemini XS spectrofluorometer (Molecular Devices LLC, US). CMC was calculated from pyrene fluorescence peaks (λ_{ex} = 333 nm, λ_{ex} = 335 nm; λ_{em} = 390 nm) by using the peak 1:peak 3 ratio.

2.2.4. Formulation of supercoiled mcDNA-loaded bioreducible micelleplexes

For all experiments mcDNA vectors were obtained from a bacterial culture of *E. coli* ZYCY10P3S2T by following an optimized fermentation protocol that involves the addition of 0.01% w/v L-arabinose to induce parental-to-minicircle recombination [22]. Supercoiled mcDNA vectors were then recovered from the native minicircle preparations (containing open circular and supercoiled), through affinity chromatography by using a monolith disk with di-peptide arginine ligands (Supplementary information). DNA-loaded bioreducible PPP-SS micelleplexes were then formulated as previously described by our group [10]. In brief, triblock copolymers were initially prepared from a stock solution, diluted to desired concentrations and submitted to sonication for 30 min. Subsequently, supercoiled (sc) mcDNA-loaded micelleplexes were then assembled through electrostatic interaction by using different amines to phosphate ratios (N/P ratio). For micelleplexes formation, mcDNA was added dropwise to PPP-SS polymer solutions (20 mM HEPES, 5% glucose, pH 7.1 (HBG)), and the mixture was vortexed for 1 min at maximum speed. After 30 min of stabilization at RT, the micelleplexes were recovered by centrifugation (18,000 *g*, 30 min). mcDNA complexation by PPP-SS copolymers at different N/P ratios was evaluated by agarose gel electrophoresis [10].

2.2.5. Micelles physicochemical characterization

Micellar carrier hydrodynamic size and zeta potential were characterized by Dynamic Light Scattering (DLS) with a Zetasizer Nano ZS (Malvern Instruments, Worcestershire, UK). All measurements were performed in a zeta disposable folded capillary cell (DTS1070), at 25 °C, and at a scattering angle of 173°, with filtered solutions (0.22 μm). Zetasizer software v.7.11 was used for data analysis. Micelleplexes morphological characterization was evaluated by Atomic Force Microscopy (AFM) [10]. For AFM analysis freshly prepared micelleplexes were dropped into muscovite mica and left to dry at RT overnight. Images were acquired in tapping mode in a 300 Hz AFM Veeco Dimension 3100 microscope (Veeco, Santa Barbara, CA, US), equipped with a Tap300A1-G cantilever tips (ω = 300 kHz, kc = 40 N/m, Budget Sensors, Combo, US). AFM image analysis and post-processing were performed in the WSxM 5.0 free software [23].

2.2.6. Micelles biocompatibility

The biocompatibility of PPP-SS micellar carriers was determined through the resazurin assay. Micelles biocompatibility was assessed in HeLa and B16F10 cancer cells. Both cell lines were cultured with DMEM-high glucose (DMEM-HG) supplemented with 10% FBS in a sterilized incubator with a humidified and controlled atmosphere (37 °C, 5%, CO_2). For biocompatibility assays, the cells were sub-cultured in 96 well plates at a density of 8×10^3 cells/well (HeLa), and 4×10^3 cells/well (B16F10). In the following day, the culture medium was exchanged and the cells were incubated with medium containing micelleplexes formulated at different N/P ratios. After incubation for 24 and 48 h, the medium of each well was exchanged and incubated with fresh medium containing 10% (v/v) resazurin (1 $mg \cdot mL^{-1}$) during 4 h (in the dark, 37 °C, 5%, CO_2). The produced pink resorufin was then transferred to a 96-well black clear bottom fluorescence plates (Greiner Bio-one, Frickenhausen, Germany) and quantified in a spectrofluorometer (Spectramax Gemini XS, Molecular Devices LLC, US), using a excitation/emission wavelength of λ_{ex} = 560 nm and λ_{em} = 590 nm. Non-treated cells were used as negative controls (K−) and ethanol (EtOH) treated cells were used as positive controls (K+).

For biocompatibility assays in 3D multicellular tumor spheroids (MCTS), HeLa cells (8×10^5 cells) or B16F10 cells (1.8×10^6 cells) were seeded in agarose micromolds containing 81-recesses (3D Petri Dish®, Microtissues Inc., Providence RI, US) for spheroids assembly. Following 6 days of culture, 6 spheroids of each mold (6 spheroids, $n = 5$ wells) were incubated with micelleplexes formulated at different N/P ratios (0.4 μg mcDNA/spheroid). After 24 and 48 h of incubation the medium of each well was exchanged and incubated with fresh medium containing 10% (v/v) resazurin during 4 h. The resulting resorufin product was quantified as before mentioned. Non-treated 3D spheroids were used as negative controls (K−) and ethanol (EtOH) treated spheroids were used as positive controls (K+).

2.2.7. Nanocarrier cellular uptake and intracellular trafficking in 2D cultures

McDNA-loaded micelleplexes cellular uptake in HeLa cells was evaluated by flow cytometry. For this analysis HeLa cells were seeded in 12-well plates at a density of 2×10^5 cells/well. In the following day micelleplexes loaded with RITC-labeled mcDNA were incubated during 4 h in serum containing medium (DMEM-HG/10% FBS). Cells were extensively rinsed with PBS, harvested with trypsin and resuspended in 500 μL of PBS-5% FBS. Fluorescence labeling of mcDNA was performed as previously reported by our group [24]. Flow cytometry analysis was then carried out in a BD FACSCalibur flow cytometer in the FL-2 channel (BP 585/42 nm) (Becton Dickinson Inc., US). Data acquisition was performed in CellQuest software where a total of 1×10^4 events were recorded in the region of interest assigned to HeLa cells. In addition, the cellular uptake of free Doxorubicin (Dox) and dual loaded micelleplexes containing Dox–mcDNA was performed in B16F10 cells as before described. The events assigned to Doxorubicin fluorescence were recorded in FL-2 channel. The trial version of FlowJo software v.10.0.6 (Ashland, Oregon, USA) was used for data analysis.

Confocal laser scanning microscopy (CLSM) was also used to visualize micelleplexes internalization in cancer cells and to access their

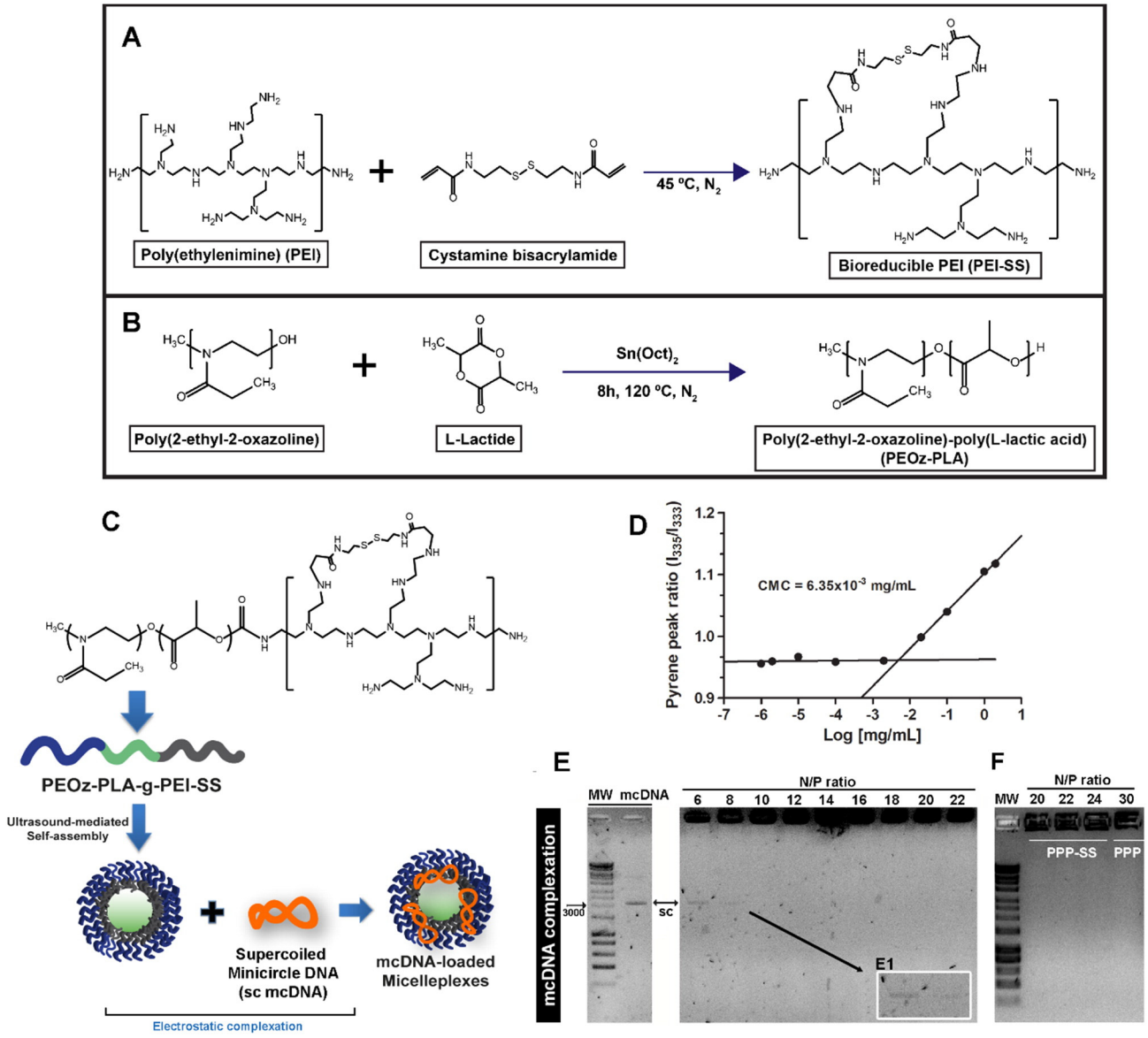

Fig. 1. Bioreducible PEOz–PLA-g–PEI-SS triblock copolymer synthesis and formulation. (A and B) Schematics of the different chemical synthesis stages. (C) Schematics of PPP-SS/mcDNA micelles self-assembly. (D) Determination of micelles CMC by pyrene method. (E) Agarose gel electrophoresis of supercoiled minicircle DNA (sc mcDNA) electrostatic complexation by PPP-SS triblock copolymers at different amine to phosphate ratios (N/P). (E1) Zoomed box of non-complexed sc mcDNA vectors. (F) Agarose gel electrophoresis of bioreducible mcDNA micelleplexes (PPP-SS) formulated at N/P ratios ranging from 20 to 24 and of non-bioreducible micelleplexes (PPP N/P 30). MW — HyperLadder™ 1 kb Plus, DNA marker (Bioline Ltd., London, UK). mcDNA lane — Non-complexed mcDNA; sc — supercoiled isoform.

capacity to escape lysosomal compartments. Briefly, cancer cells were cultivated in μ-Slide 8-well flat bottom imaging plates (Ibidi GmbH, Germany), at a density of 2×10^4 cells/cm^2. In the following day, micelleplexes prepared with FITC-labeled mcDNA were incubated during 4 h, in DMEM-HG/10% FBS medium. Afterwards, cells were fixed with paraformaldehyde 4% for 15 min and rinsed with PBS. Cells were then stained with WGA-Alexa Fluor® 594 conjugate and Hoechst 33342® nuclear probe. For intracellular trafficking studies, cells were incubated with FITC-mcDNA/PPP-SS micelleplexes as described before. Following different periods of incubation (6 and 24 h of uptake), lysosomal compartments were stained with LysoTracker™ Red DND-99 (75 nM) for 30 min prior to cell fixation with PFA. Imaging experiments were performed in a Zeiss LSM 710 confocal microscope (Carl Zeiss SMT Inc., US) and processed in Zeiss Zen (SP2, 2010) and Imaris software (Bitplane, Switzerland). Manders coefficient colocalization analysis was performed in Imaris software (Bitplane, Switzerland).

2.2.8. 3D tumor spheroids penetration and transgene expression

3D tumor spheroids of HeLa and B16F12 cells with a diameter ranging from 800 to 900 μm were produced by using precision agarose micromolds containing 81-recesses (3D Petri Dish®, Microtissues Inc., Providence RI, US). All MCTS were cultured in DMEM-HG/10% FBS (37 °C, 5% CO_2) with partial medium exchange when necessary in order to preserve secreted factors by 3D cultured cells. Micelleplexes uptake in 3D MCTS was evaluated with CLSM by incubating RITC-labeled mcDNA/PPP-SS nanocarriers at different time points (8, 12 and 24 h) in DMEM-HG/10% FBS culture medium.

In addition, the capacity of mcDNA-loaded micelleplexes to promote transgene expression in 3D MCTS was also evaluated. For this purpose spheroids were incubated with mcDNA-GFP/PPP-SS micelleplexes (0.4 μg mcDNA/spheroid) during 24 h in DMEM-HG/10% FBS medium. 3D transgene expression was characterized at 48 h by evaluating GFP fluorescence through CLSM. Non-bioreducible PEOz–PLA-g–PEI (PPP) micelleplexes were used as non-bioreducible controls [10]. Lipofectamine

2000® (LP 2000) was used as positive control for gene expression (2.5 μL LP 2000 per 1 μg of mcDNA as reported in the literature [25]). For visualization of 3D MCTS sequential z-stack images (≈5 μm), were acquired along the spheroids volume in a Zeiss LSM 710 (HeLa cells) and 510 META (B16F10 cells) confocal microscope equipped with a 10×/0.30 Plan Neofluar objective. Image analysis and 3D reconstruction were performed in Zeiss Zen (SP2, 2010) and Imaris software (Bitplane, Switzerland). Images were acquired with equal laser and detector gain parameters for comparison and quantification purposes.

2.2.9. Drug–DNA co-delivery in bioreducible micellar carriers

Doxorubicin loaded micelles were formulated by using the solvent displacement-film casting-hydration method [10]. In brief, of PPP-SS copolymers (5 mg) and Dox (500 μg, 1.5 eq. TEA) were dissolved in 1 mL chloroform/MetOH (1:1 v/v) in a round bottom flask. The solvent was then evaporated by rotary evaporation (Rotavap® R-215, Büchi, Switzerland), and the film hydrated with double deionized water. The resuspended polymer–drug film was then sonicated for 30 min and dialyzed against water for 2 h in order to remove traces of TEA and non-loaded Dox. Drug encapsulation efficiency was determined by spectrofluorimetry (Spectramax Gemini XS, Molecular Devices LLC, US), using an excitation/emission wavelength of $\lambda_{ex} = 488$ nm and $\lambda_{em} = 590$ nm. To produce dual loaded carriers Dox-loaded micelles were incubated with mcDNA as before mentioned.

2.2.10. Micelleplexes cytotoxic activity in 2D cultures

The cytotoxic activity of PPP-SS–Dox–mcDNA micellar carriers in B16F10 cells was evaluated by the MTS assay (Promega, Madison, WI, US). In brief, 4×10^3 cells were seeded in 96 well plates containing DMEM-F12/10% FBS culture medium and cultured for 24 h. In the following day cells were incubated with different micelle formulations during for 4 h. Cell viability was then determined at 48 h by adding MTS/PMS solution to each well and incubating for 4 h in the dark (37 °C, 5% CO_2). Non-treated and non-viable cells (EtOH treated cells) were used as negative and positive controls, respectively.

2.2.11. Kinetics of Dox-induced cytotoxicity and influence in GFP gene expression

The onset of Dox-induced cytotoxicity was evaluated by the resazurin assay as before mentioned. In brief, B16F10 cells were seeded in 96 well plates with a density of 5×10^3 cells per well. In the following day the cells were incubated with bioreducible PPP-SS–Dox–mcDNA micelleplexes or non-bioreducible PPP–Dox–mcDNA control particles (100 μg·mL), during 4 h. Following the incubation period the culture medium (DMEM-HG/ 10% FBS) was replaced by fresh medium. At different time points the cells were incubated with 10% (v/v) resazurin ($1\ mg \cdot mL^{-1}$) for 4 h. Cell viability was determined by quantification of resorufin product as before mentioned.

The influence of Dox-cytotoxicity in GFP transgene expression was evaluated by CLSM. For this purpose B16F10 cells (20×10^3 cells per well) were seeded in μ-slide 8-well imaging chambers (Ibidi GmbH, Germany). In the following day, cells were incubated with bioreducible and non-bioreducible micelleplexes for 4 h. Afterwards, the medium was replaced by fresh medium as above and cells were fixed with 4% PFA at given time points (4, 6 and 12 h). The cell nucleus was then labeled with Hoechst 33342® as above described. Imaging was performed in a Zeiss LSM 710 equipped with a 63×/DIC oil objective. To avoid image artifacts from overspill of GFP and Doxorubicin fluorescence, spectral imaging and tuning of the acousto-optic tunable filter (AOTF) were used. At least 10 random fields of cells were acquired to perform GFP fluorescence intensity quantification.

2.2.12. In vivo transgene expression

For *in vivo* experiments, immunocompetent, C57BL/6JRj female mice (6 weeks old, ~20 g) (Janvier Labs, Saint-Berthevin, France) were manipulated and housed according to the guidelines issued by the French Ministry of Agriculture for experiments with laboratory animals (C. Pichon accreditation, Law 87848). Animal experimentation was performed in specialized facilities accredited for animal research (Agreement B 45-234-12, Délégation des Services vétérinaires du Loiret). All the mice were housed with a 12 light/12 dark light cycle, at 22 °C, in ventilated filter-top cages and with access to food and water *ad libitum*.

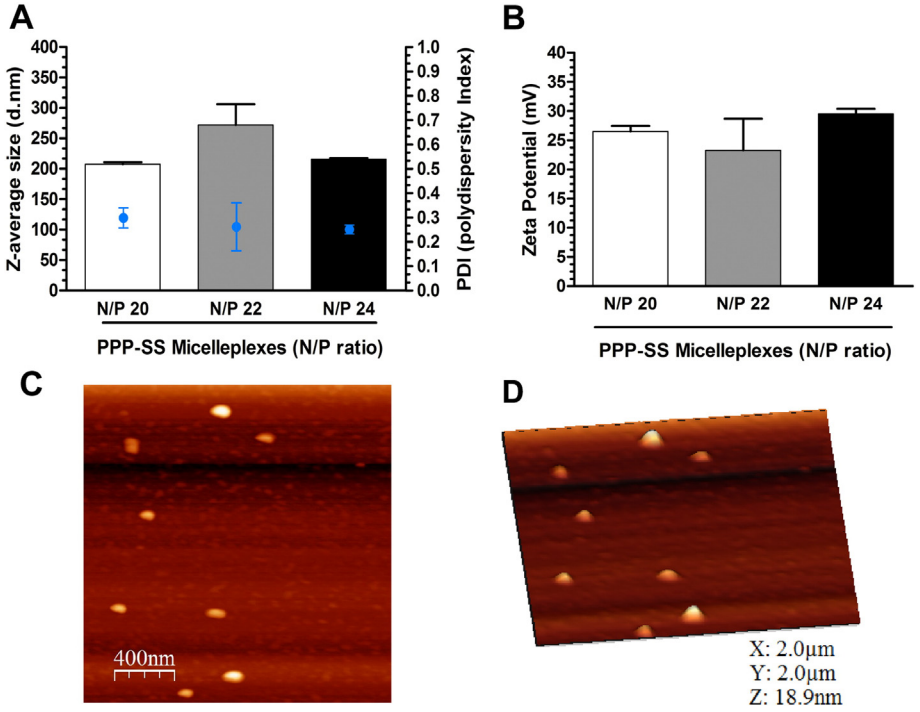

Fig. 2. Characterization of mcDNA loaded bioreducible micelleplexes. (A) DLS analysis of micelles size. Columns represent size; Blue dots represent PDI. (B) Zeta potential measurements of different micelleplexes formulations. Data represents mean ± s.d., $n = 3$. (C and D) Characterization of micelleplexes morphology by AFM imaging.

For evaluation of *in vivo* gene expression, murine B16F10 cells (1×10^6 cells per mice) were implanted subcutaneously in C57BL/6JRj mice. Following implantation, the tumors were allowed to grow for 10 days. Afterwards, different doses of PPP-SS micelleplexes loaded with luciferase expressing p3NF-Luc-3NF prepared in 50 μl of 20 mM HEPES, 5% glucose, pH 7.1, (HBG) were administered via intratumoral (i.t.) injection directly into the primary tumor of B16F10 mouse melanoma models. Luciferase transgene expression was then visualized by bioluminescence imaging 48 h latter using the IVIS® Lumina II pre-clinical *in vivo* imaging system (Xenogen Caliper Life Sciences, Hopkinton, MA, US), equipped with a CCD camera as previously reported [28]. Bioluminescence signals emitted from the tumor were acquired from a region-of-interest (ROI) draw manually and finally quantify using the Living Image® software Instrument and imaging scanner calibration was assured by weekly testing with standardized bioluminescence sources.

2.2.13. In vivo therapeutic efficacy

The therapeutic activity of micelle formulations was evaluated in luciferase-expressing B16F10 melanoma tumor models. For this purpose, freshly cultured B16F10-Luc cells (1×10^6 cells per mice) were subcutaneously implanted in 6 week old C57BL/6JRj female mice. After 14 days post-implantation (experimental day 0) tumor bearing mice were randomly assigned into three different groups ($n = 5$) and intratumorally injected with 50 μL of the different formulations. The mice from control group I were administered with transport media (HBG), whereas the mice from group II were treated with free (non-

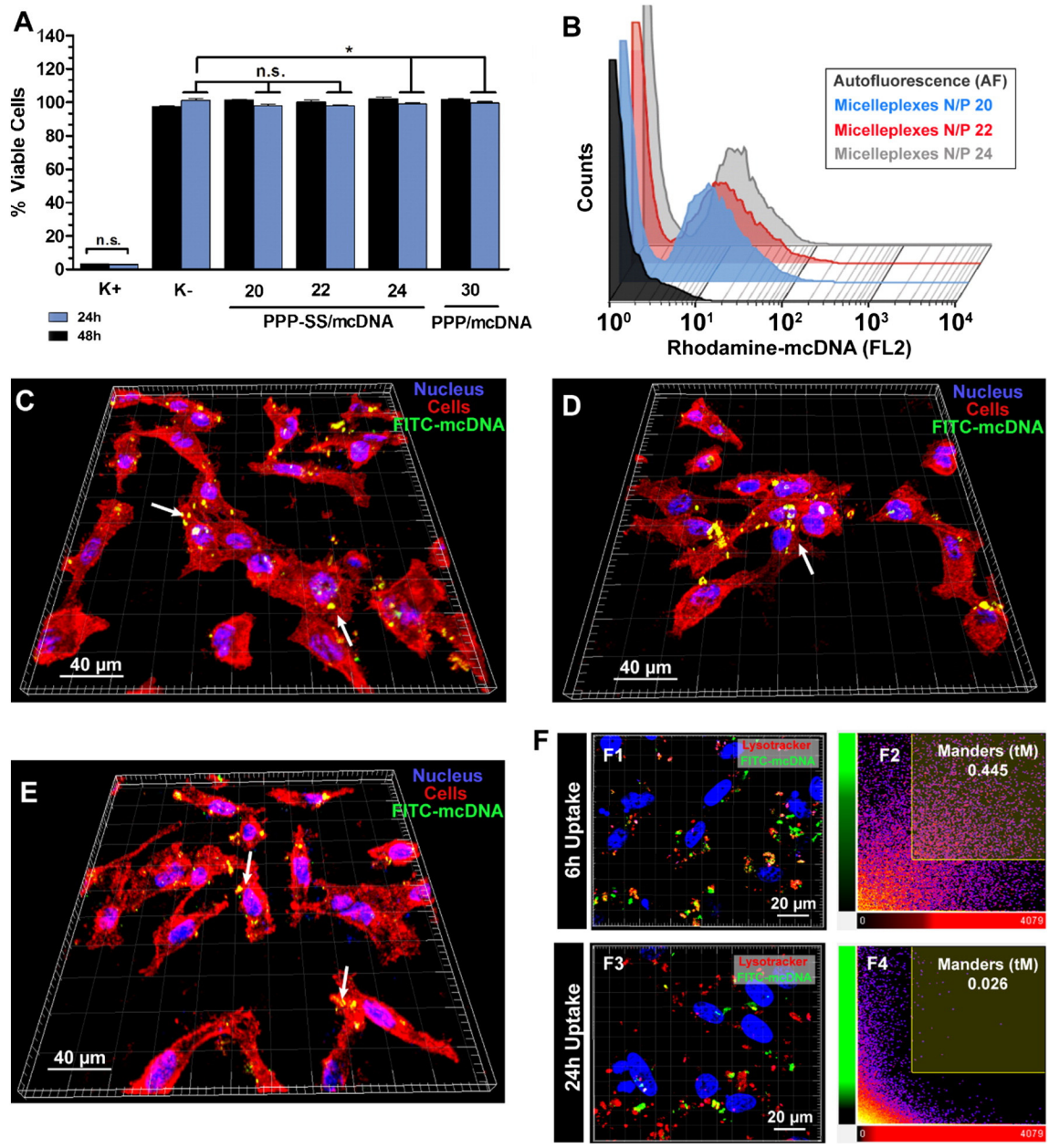

Fig. 3. Characterization of micelleplexes biological properties in HeLa cells. (A) Analysis of cell viability, at 24 and 48 h, following incubation with different micelleplexes formulated at various N/P ratios. Data represents mean ± s.d., $n = 5$. K+ represents EtOH treated cells (positive control for cytotoxicity). K − represents non-treated cells (negative control for cytoxicity). (B) Representative flow cytometry histograms of PPP-SS micelleplexes cellular uptake. (C, D and E) CLSM analysis of FITC-mcDNA/PPP-SS micelleplexes at various N/P ratios of 20, 22 and 24, respectively. Blue channel: Hoechst 33342® nucelar probe; red channel: WGA-Alexa 594®; green Channel: FITC-labeled mcDNA. White arrows indicate FITC-mcDNA. (F1 and F3) CLSM imaging of FITC-mcDNA/micelleplexes intracellular trafficking in lysosomal compartments at different time points (6 and 24h). Red channel: Lysotracker™ red DND-99; green channel: FITC-mcDNA. (F2 and F4) Manders colocalization plots of FITC-mcDNA/micelleplexes (N/P ratio 20). (For interpretation of the references to color in this figure legend, the reader is referred to the web version of this article.)

encapsulated) Dox (5 mg·kg^{-1}), diluted from stock solution into HBG, while the mice from group III were treated with Dox–mcDNA micelleplexes at equivalent drug dosage (5 mg·kg^{-1}, in HBG). Therapeutic efficacy was analyzed by measuring the tumor volume and B16F16-Luc tumors luminescence at 3-day intervals. Tumor size was analyzed by measuring the minor diameter (d) and major diameter (D) using a digital caliper. Tumor volume was determined by using the following formula $V = ½(D \cdot d^2)$ as reported in the literature [26]. Relative tumor volume was then extrapolated from caliper measurements.

In addition, the viability of tumor B16F10-Luc cancer cells was visualized and quantified by bioluminescence imaging during the various time points of the experimental period by using an IVIS® Lumina II pre-clinical *in vivo* imaging system (Xenogen Caliper Life Sciences, Hopkinton, MA, US) as mentioned before.

2.2.14. Histological analysis

Mice from different groups were sacrificed at the end of the study (humane end-point), and tumors were excised for histological analysis. The tissues were then immersed in 10% neutral-buffered formalin, embed in paraffin, sectioned in a microtome (5 μm sections, Leica CM1900, Leica Microsystems, Heidelberg, Germany) and stained with Hematoxylin–Eosin (H&E). In addition, melanin deposits were labeled by Fontana-Masson staining as previously reported in the literature [27]. Tissue sections were visualized in a Zeiss Axio Imager Z1 microscope and post-processed in Axiovision software (Carl Zeiss SMT Inc., US).

2.2.15. Statistical analysis

Statistical analysis was performed by using one-way analysis of variance (ANOVA), followed by the post-hoc Newman–Keuls test. A confidence interval (CI) of 95% ($p < 0.05$) was considered statistically significant. Data analysis was performed in GraphPad Prism v.5.0 (trial version; GraphPad software Inc., CA, USA).

3. Results and discussion

3.1. Synthesis and characterization of bioreducible micellar carriers

The synthesis of bioreducible triblock copolymers comprised by PEOz–PLA-g–PEI-SS was performed by initially modifying PEI with cystamine bisacrylamide (CBA) (Fig. 1A). The crosslinking of PEI *via* CBA occurs by the reaction of acrylamide groups with primary and secondary amines of PEI thus crosslinking the polymer with disulfide bonds. A part from this the establishment of CBA-PEI intermolecular forces is also plausible due to the establishment of H-bonds between CBA

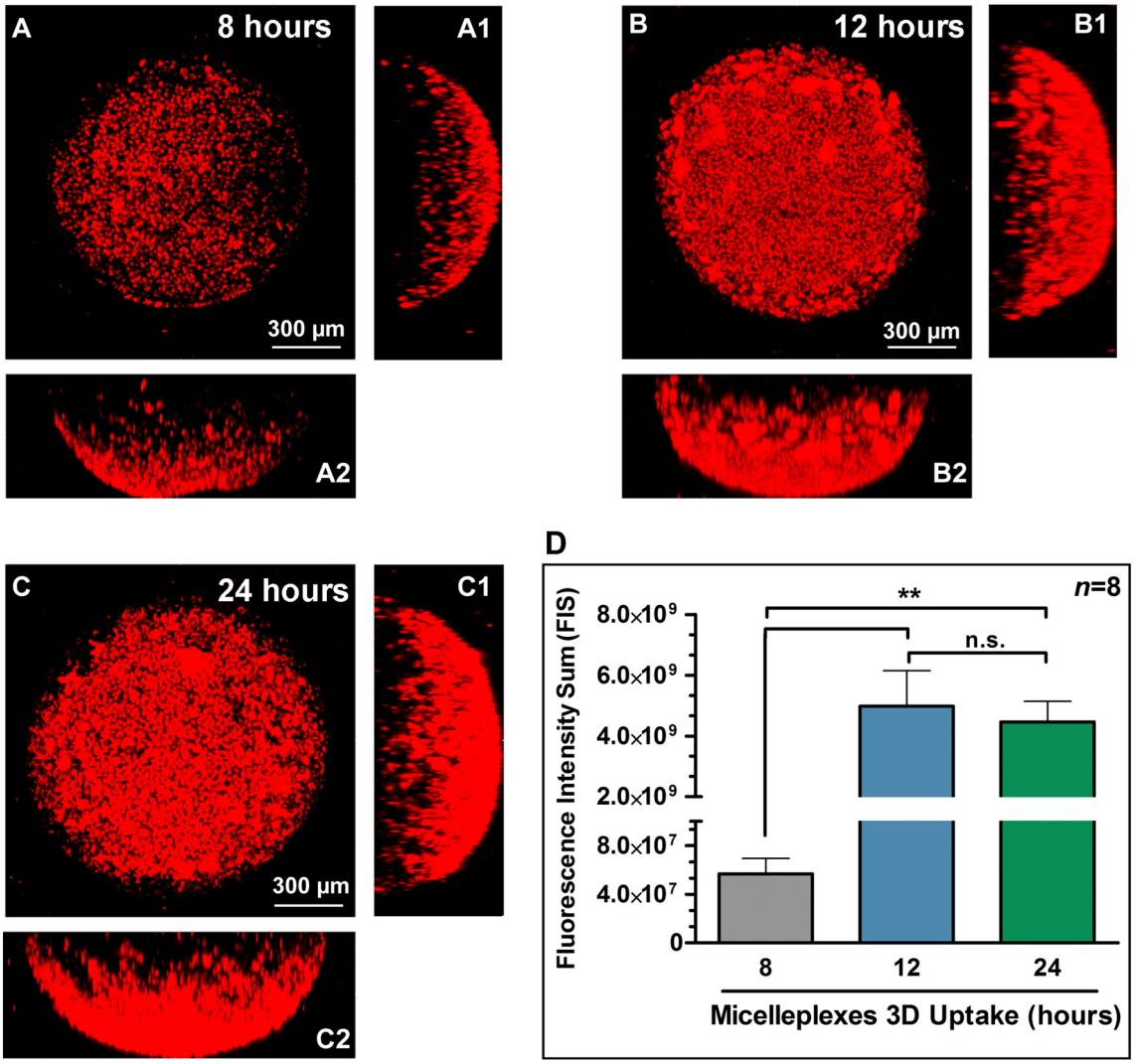

Fig. 4. Kinetic of micelleplexes uptake in HeLa 3D MCTS. (A, B and C) Representative CLSM 3D and orthogonal reconstruction of MCTS incubated with RITC-mcDNA micelleplexes (N/P 20) at 8, 12, and 24h, after administration. (D) Quantification of RITC fluorescence intensity in the 3D volume of MCTS. Data represents mean ± s.d., $n = 8$. Red channel: RITC-mcDNA/micelleplexes.

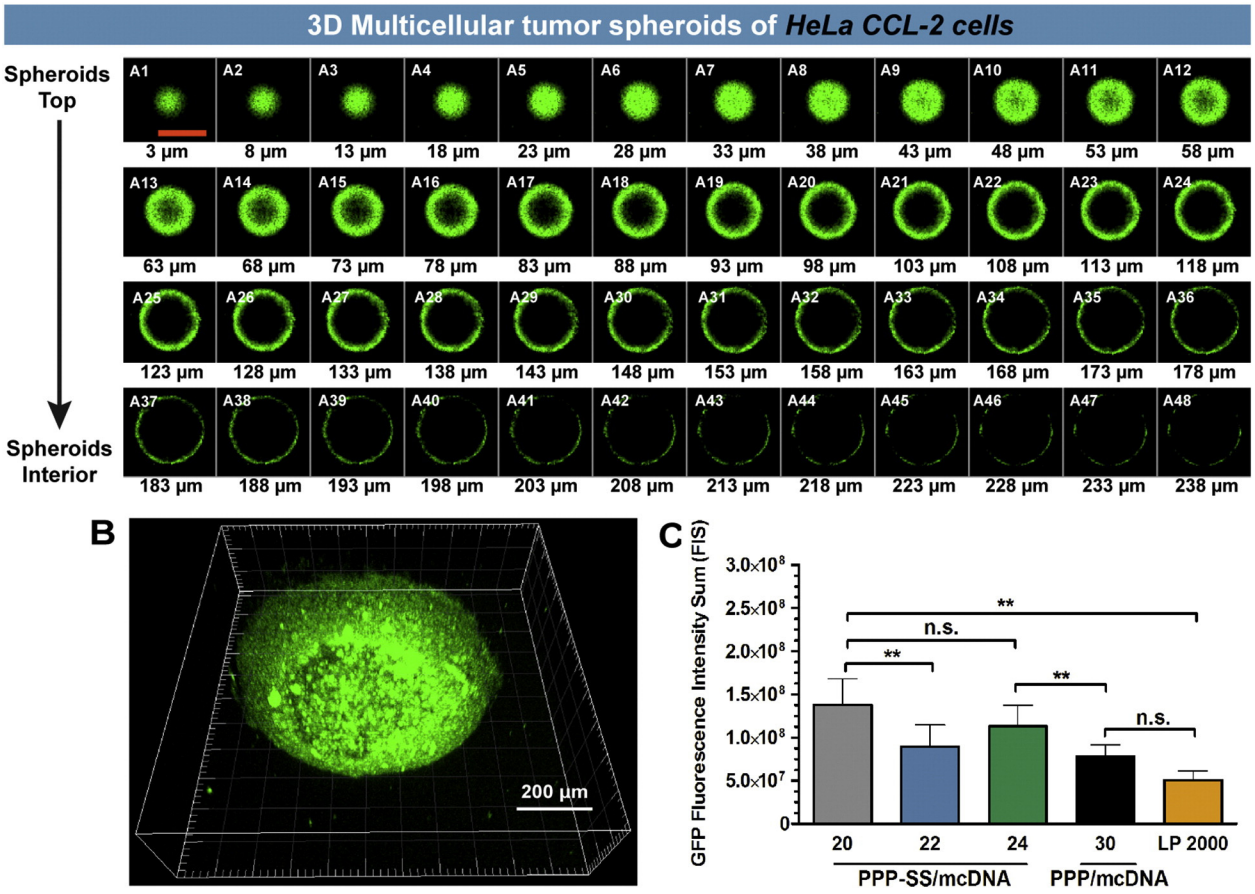
3D Multicellular tumor spheroids of HeLa CCL-2 cells
Spheroids Top
Spheroids Interior
A1 3 µm
A2 8 µm
A3 13 µm
A4 18 µm
A5 23 µm
A6 28 µm
A7 33 µm
A8 38 µm
A9 43 µm
A10 48 µm
A11 53 µm
A12 58 µm
A13 63 µm
A14 68 µm
A15 73 µm
A16 78 µm
A17 83 µm
A18 88 µm
A19 93 µm
A20 98 µm
A21 103 µm
A22 108 µm
A23 113 µm
A24 118 µm
A25 123 µm
A26 128 µm
A27 133 µm
A28 138 µm
A29 143 µm
A30 148 µm
A31 153 µm
A32 158 µm
A33 163 µm
A34 168 µm
A35 173 µm
A36 178 µm
A37 183 µm
A38 188 µm
A39 193 µm
A40 198 µm
A41 203 µm
A42 208 µm
A43 213 µm
A44 218 µm
A45 223 µm
A46 228 µm
A47 233 µm
A48 238 µm
B
200 µm
C
GFP Fluorescence Intensity Sum (FIS)
3.0x10^8
2.5x10^8
2.0x10^8
1.5x10^8
1.0x10^8
5.0x10^7
0
**
n.s.
**
**
n.s.
20
22
24
30
LP 2000
PPP-SS/mcDNA
PPP/mcDNA

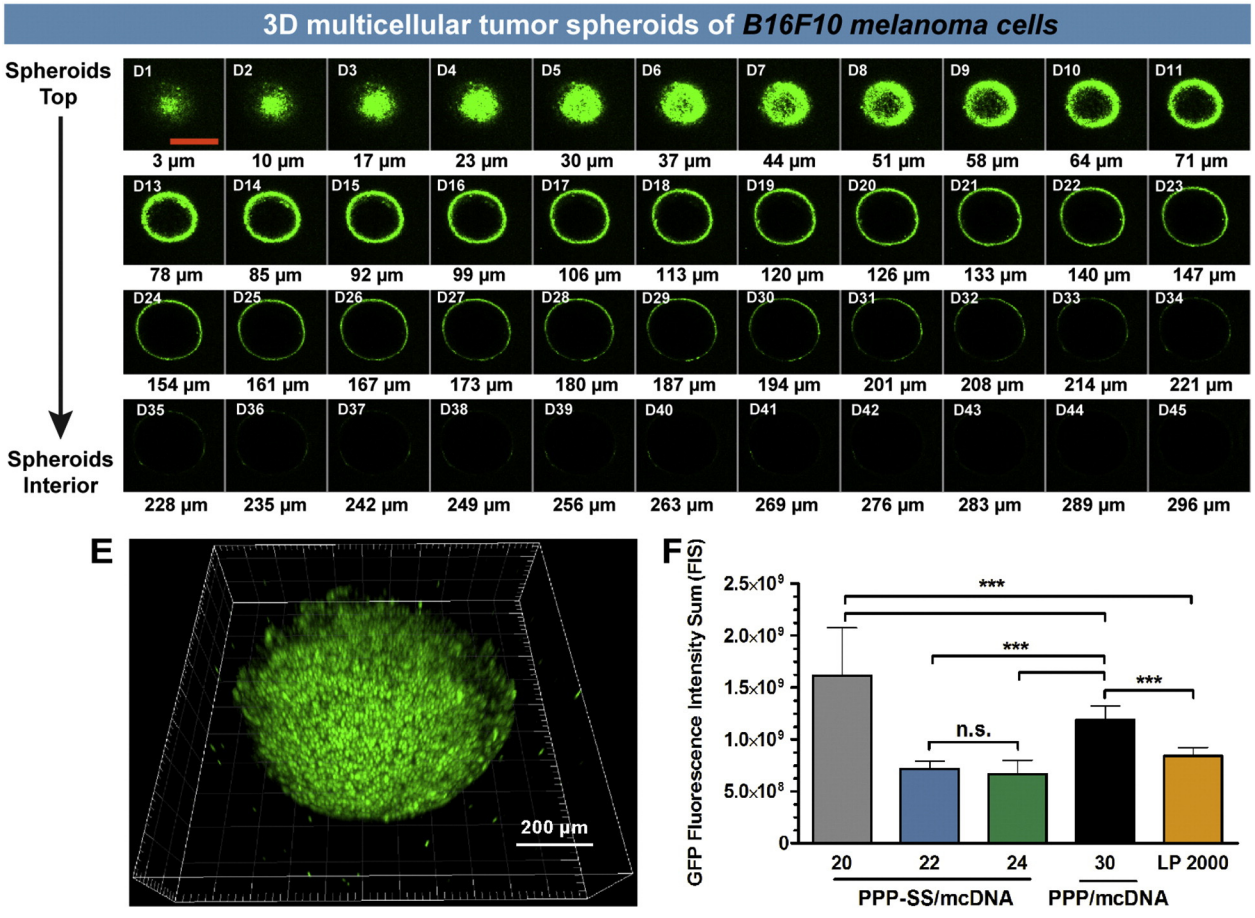
3D multicellular tumor spheroids of B16F10 melanoma cells
Spheroids Top
Spheroids Interior
D1 3 µm
D2 10 µm
D3 17 µm
D4 23 µm
D5 30 µm
D6 37 µm
D7 44 µm
D8 51 µm
D9 58 µm
D10 64 µm
D11 71 µm
D13 78 µm
D14 85 µm
D15 92 µm
D16 99 µm
D17 106 µm
D18 113 µm
D19 120 µm
D20 126 µm
D21 133 µm
D22 140 µm
D23 147 µm
D24 154 µm
D25 161 µm
D26 167 µm
D27 173 µm
D28 180 µm
D29 187 µm
D30 194 µm
D31 201 µm
D32 208 µm
D33 214 µm
D34 221 µm
D35 228 µm
D36 235 µm
D37 242 µm
D38 249 µm
D39 256 µm
D40 263 µm
D41 269 µm
D42 276 µm
D43 283 µm
D44 289 µm
D45 296 µm
E
200 µm
F
GFP Fluorescence Intensity Sum (FIS)
2.5x10^9
2.0x10^9
1.5x10^9
1.0x10^9
5.0x10^8
0
***
***
***
n.s.
20
22
24
30
LP 2000
PPP-SS/mcDNA
PPP/mcDNA

secondary amines and PEI. Fig. 1 A provides a representation of CBA-PEI reaction and the final cationic polymer structure is expected to be a mesh-like structure which is disassembled in reducible conditions as previously demonstrated by different reports [20,28].

Successful production of PEI containing disulfide linkages was confirmed by ^{1}H NMR analysis (Supplementary Fig. S1). High-resolution mass spectrometry of bioreducible PEI (PEI-SS) further confirmed the modification of the cationic polymer as evidenced by the existence of different fragments of charged species in comparison to native PEI (Supplementary Fig. S2).

In an additional reaction PLA was synthesized by CROP of L-lactide ring to yield a hydrophobic polymer chain which subsequently yielded an amphiphilic diblock copolymer (PEOz–PLA). The chemical conjugation of PEI-SS to PEOZ–PLA was then mediated by carbonyldiimidazole activation of PEOz–PLA hydroxyl group and subsequent conjugation to PEI-SS amines (Fig. 1C). The conjugation was confirmed through ^{1}H NMR spectra which shows the existence of PEOz and PEI-SS characteristic peaks (Supplementary Fig. S1). After confirming successful synthesis, the self-assembly properties of this novel copolymer combination in aqueous media was investigated. As demonstrated by the results obtained from pyrene fluorescence measurements the bioreducible PPP-SS polymers have an amphiphilic character and readily self-assemble into micellar carriers in water, at very low concentrations (CMC = 6.35×10^{-3} mg·mL^{-1}, Fig. 1 D). Interestingly, the bioreducible triblock copolymer exhibits a significantly lower CMC when compared to their non-bioreducible PEOz–PLA–PEI equivalents previously synthesized (1.63×10^{-2} mg·mL^{-1} [10]). It is hypothesized that this lower CMC is associated with the introduction of additional hydrocarbon chains from CBA into PEI polymer backbone. It will be interesting to further address this parameter at higher CBA:PEI ratios and its influence on triblock micelles assembly. Such findings indicate that PPP-SS micelles are more stable and support their potential application for drug–gene co-delivery.

Prior to formulation of nucleic acid-loaded micelleplexes, the supercoiled (sc) mcDNA isoform was isolated by affinity chromatography (Supplementary Fig. S3). The recovery of sc mcDNA isoform is highly beneficial from a therapeutic perspective since this specific topology has been attributed to a higher transgene expression efficiency, as our group previously reported [29]. Natively mcDNA is produced in sc isoform, however, during downstream processing and manipulation DNA may relax into less condensed open circular (oc) or linear species [30]. Moreover, it is important to emphasize that FDA regulatory guidelines demand that DNA biopharmaceuticals must have at least 80% supercoiled content for vaccine applications [30], although a higher content in this isoform is beneficial for gene expression efficiency as our group previously demonstrated [31]. Therefore, to obtain optimal transgene expression and to comply with these demands a monolith disk chromatographic column was used for isolation of this topoisoform. The results obtained by electrophoresis of recovered fractions demonstrate that under precise experimental conditions sc mcDNA can be effectively isolated from a preparation containing both oc and sc isoforms (Supplementary Fig. S3).

Following this isolation, the complexation of sc mcDNA by bioreducible PPP-SS previously formed by ultrasound-mediated self-assembly (Supplementary Fig. S5) was then evaluated. This preliminary self-assembly allows the formation of a micellar-like structure before mcDNA complexation. Investigating condensation particularly of the sc mcDNA isoform is highly important since due to torsional deformations the zeta potential of sc and oc isoforms is different as we have

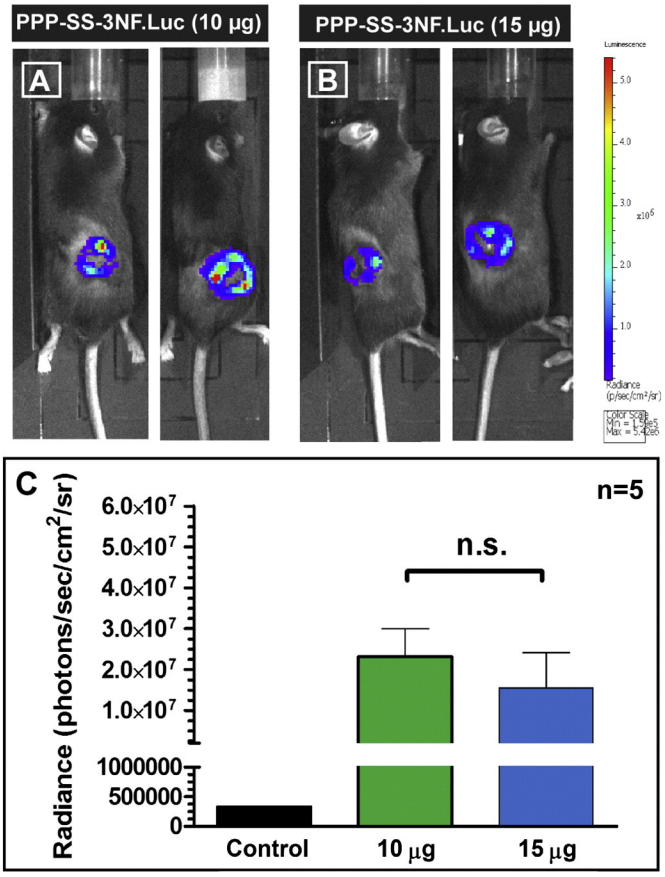

Fig. 6. Gene expression analysis following administration of p3NF-Luc-3NF/PPP-SS micelleplexes (N/P 20). (A and B) *In vivo* bioluminescence imaging of tumor bearing mice. (C) Quantification of *in vivo* gene expression after 48 h of i.t. injection with different doses. Data represents mean ± s.d., $n = 5$. Control mice were injected with HBG media (Black bar).

previously shown [29]. Results of agarose gel electrophoresis demonstrate that complexation was observed at lower ratios (N/P 8 to 10). However, note that a faint band of non-condensed sc mcDNA was still present (Fig. 1E and 1 E1 and Supplementary Fig. S4). Furthermore, no bands were visualized at N/P 14 indicating that there was a complete mcDNA complexation at this ratio.

Taking this into account the different ratios were subsequently characterized for their size and zeta potential. Fig. 2A shows the most suitable formulations for biological application, having exhibited sizes ranging from 207 to 272 nm. The N/P 20 formulation showed the smallest size and an adequate polydispersity (PDI < 0.28). These mcDNA-loaded micelleplexes formulations presented a smaller size than their blank-self assembled counterparts (Supplementary Fig. S5). Morphological characterization through AFM imaging revealed that sc mcDNA loaded micelleplexes have a quasi-spherical or slightly ellipsoidal morphology (Fig. 2 C and D). Finally, the zeta potential of all formulations was positive and in the range of colloidal stability (23.3 mV to 29.5 mV, Fig. 2B). In comparison to blank self-assembled micelles (33.0 mV, Supplementary Fig. S5), the PPP-SS–mcDNA carriers presented a reduction in zeta potential due to the electrostatic complexation with negatively charged nucleic acids. The zeta potential of bioreducible

Fig. 5. Evaluation of GFP transgene expression in 3D MCTS of HeLa and B16F10 cells at 48 h. (A and D) Representative CLSM Z-stacks acquired along the 3D MCTS volume (PPP-SS/mcDNA micelleplexes N/P 20). Red scale bar represents 500 μm. (B and E) Representative 3D reconstruction (maximum intensity projection) of HeLa and B16F10 tumor spheroids transfected with micelleplexes, respectively. Green channel: GFP. (C and F) Analysis of GFP fluorescence following administration of bioreducible micelleplexes and non-bioreducible triblock copolymer micelles (non-bioreducible PPP/mcDNA (N/P 30) — black bars; bioreducible PPP-SS/mcDNA micelleplexes formulated at various N/P ratios; LP-2000 — Lipofectamine 2000/mcDNA control polyplexes). The PPP–mcDNA complexes were used at N/P 30 ratio since this was the optimal formulation previously optimized by our group [10]. (For interpretation of the references to color in this figure legend, the reader is referred to the web version of this article.)

micelleplexes is also higher than that of non-bioreducible carriers previously synthesized [10], we hypothesize that this difference could be correlated with the addition of CBA and to the branched nature of the PEI:CBA polymer which may change the electrostatic condensation of mcDNA and amines exposure.

3.2. Stimuli-responsive properties and micelleplexes biological performance

The biocompatibility of bioreducible micelleplexes formulated at various ratios was analyzed *in vitro* in 2D culture of HeLa cancer cells at different time points. All micelleplexes tested present more than 90% cell viability at 48 h (Fig. 3 A), indicating the suitability of these carriers for delivery of bioactive molecules without significant cytotoxicity. In addition, these results were also corroborated by the biocompatibility results obtained in B16F10 melanoma cell line (Supplementary Fig. S6).

Evaluation of mcDNA-loaded micelleplexes cellular uptake showed that at 4 h all formulations (N/P 20 to 24) achieved similar uptake efficacy in 2D *in vitro* cell cultures (Fig. 3B). These results were further confirmed by confocal microscopy analysis of cellular uptake. As evidenced in Fig. 3 C to E, micellar carriers were internalized with similar patterns, without any significant difference between formulations being visualized.

The stimuli-responsive feature of PPP-SS micelleplexes was also evaluated both by agarose gel electrophoresis, by Picogreen-mediated quantification or by FRET. As revealed by agarose gel electrophoresis, when mcDNA-loaded nanocarriers were incubated in disulfide-reducing conditions for 4 h, a portion of mcDNA was released as shown by the free band observed in the gel in addition to the condensed form that remained in the well (Supplementary Fig. S7 A). Moreover, the quantification of mcDNA release from PPP-SS micelleplexes indicated that a 7.2 fold higher increase in DNA release was obtained in

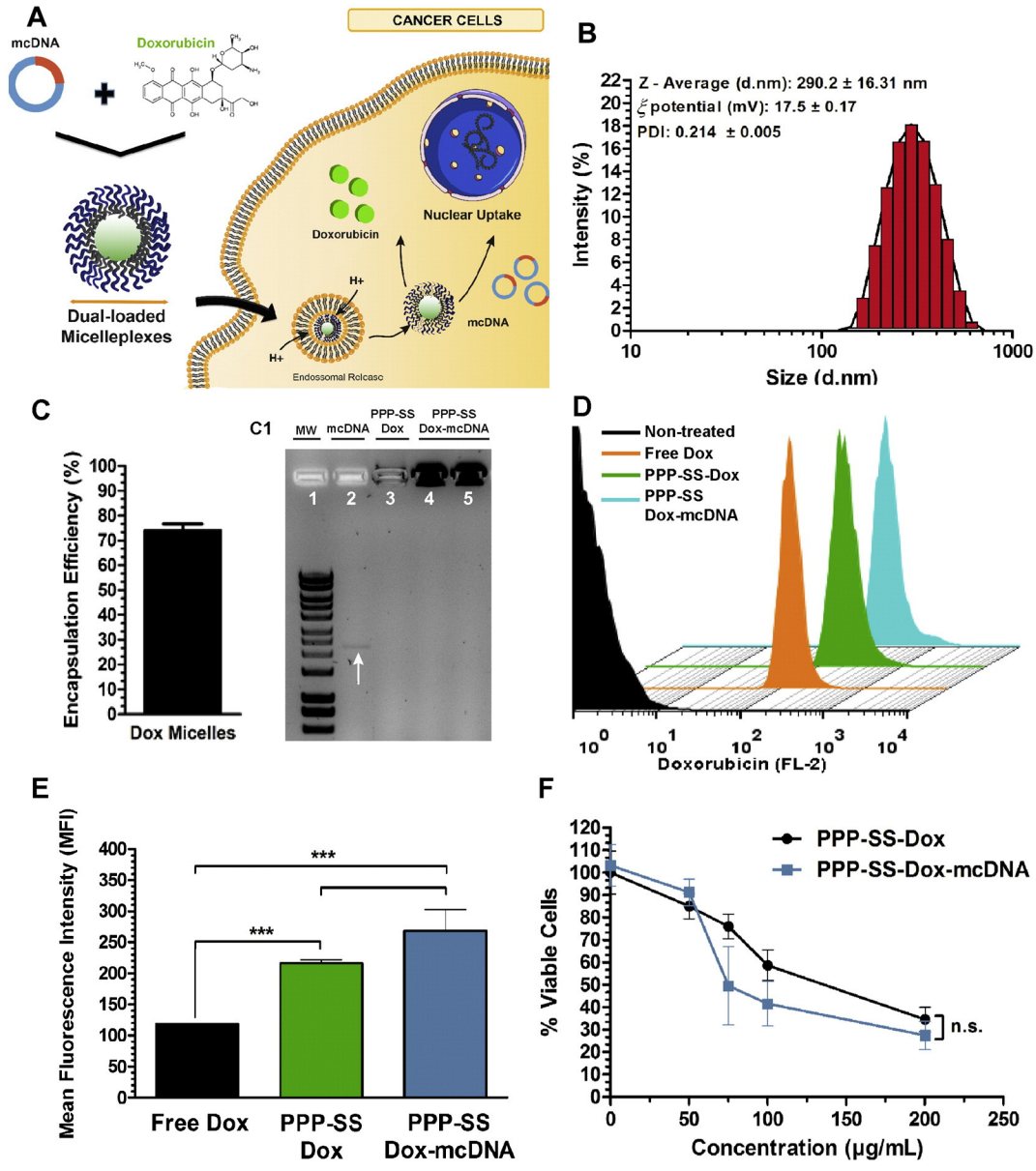

Fig. 7. Co-delivery of drug–mcDNA in bioreducible PPP-SS micelleplexes. (A) Schematics of co-delivery concept. (B) DLS characterization of Dox–mcDNA loaded micelleplexes (N/P 20). (C) Analysis of encapsulation efficiency and Agarose gel electrophoresis of mcDNA complexation in PPP-SS–Dox micelleplexes. Data represents mean ± s.d., $n = 3$. MW — DNA ladder; mcDNA — naked sc mcDNA (white arrow). (D) Representative flow cytometry histograms of dual loaded carriers cellular uptake in B16F10 melanoma cells. Black histogram — non-treated cells, orange histogram — Dox treated cells, green histogram — PPP-SS–Dox treated cells, blue histogram — PPP-SS–Dox–mcDNA treated cells. (E) Flow cytometry analysis of drug and drug–mcDNA micelleplexes. Data represents mean ± s.d., $n = 3$. (E) Cytotoxic activity of micelleplexes formulations in B16F10 cells after 48 h following incubation with different formulations. Data represents mean ± s.d., $n = 5$. ***$p < 0.01$. (For interpretation of the references to color in this figure legend, the reader is referred to the web version of this article.)

comparison to non-bioreducible micelleplexes incubated in redox conditions (Supplementary Fig. S7 C). Regarding DNA release with dextran sulfate as a competing polyanion, no significant differences in the released nucleic acid fraction was obtained between PPP-SS–mcDNA and PPP–mcDNA micelleplexes (Supplementary Fig. S7 D).

These interesting results corroborate the bioreducible character of PPP-SS triblock copolymers and suggest that not all mcDNA was promptly released. This was expected as the reaction between CBA and PEI was performed at 1:6 molar ratio. To further investigate if micelleplexes maintained this stimuli-responsiveness in cancer cells CLSM-FRET analysis was performed by using mcDNA-Cy3/PPP-SS-Cy5 (Supplementary information). FRET signals were obtained at 4 h, indicating that a portion of mcDNA remained tightly complexed to internalized micellar carriers (purple signal, FRET on). In addition, there is also evidence of a portion of released/loosely condensed mcDNA, as indicated by the green signal, revealing an absence of FRET (off) (Supplementary Fig. S7 F), which corroborates the results obtained in Picogreen assay. From a therapeutic perspective, it is beneficial to achieve this on-demand redox responsive release at the cytosol since this event is anticipated to change the onset, site-of-release, duration and efficacy of gene expression as it will be further discussed. In addition, FRET analysis of non-bioreducible micelleplexes reveals that the majority of mcDNA was complexed to the micelleplexes and only residual mcDNA-Cy3 was uncondensed/released (Supplementary Fig. S7 G).

Next, the kinetic of intracellular trafficking of mcDNA-loaded bioreducible micelleplexes was investigated. Image analysis shown in Fig. 3 F1 to F4 suggests that there was a time-dependent lysosomal localization, as confirmed by the co-staining with Lysotracker™. A significant fraction of micelles was confined within lysosomal compartments as evidenced by Manders colocalization analysis at 6 h (Fig. 3 F1). After 24 h, there was a decrease of micelleplexes found in lysosomes (tM (6 h): 0.445; tM (24 h): 0.026; Fig. 3 F3 and F4). Moreover, isolated green spots were found in the cytoplasm. Combined together, these observations could suggest that micellar carriers efficiently escaped from these degradative compartments. This escape is an important parameter for posterior transgene expression since the entrapment of mcDNA-micelleplexes in these compartments leads to their posterior degradation. The mechanisms of polyplexes lysosomal escape to the cytoplasm are still under active debate and studies are underway to precisely determine this phenomenon. We hypothesize that the decrease in lysosomal colocalization of the micelleplexes from 6 to 24 h (Fig. 3 F) may be associated to the so termed "proton sponge effect" induced by the buffering capacity of this cationic polymer or possibly also to the escape through holes in the lysosomal membranes caused by PEI as demonstrated by Bieber and co-workers using electron microscopy [32]. Regarding the proton sponge effect, this phenomenon is based on the buffering capacity of PEI which induces V-ATPase activity to pump protons and also leads to the accumulation of chloride ions (Cl^-) and water in the lysosomes [33]. Consequently, and due to water influx, lysosomal compartments swell and burst, releasing their contents [34]. The lysosomal release of PEI containing gene delivery systems has also been reported by Ganas and co-workers. In this report, a PEI-based delivery system was developed for delivery of siRNA to cancer cells and polyplexes lysosomal release was proposed to be correlated with the proton sponge effect [34]. However, in the future it would be interesting to evaluate if the triblock copolymer micelleplexes could also contribute to lysosomal release mediated by different mechanisms due their structural arrangement and polymer combinations.

Taking into consideration the bioreducible character of the triblock copolymer nanocarriers, it is also important to discuss lysosomal release in this context. Although, the redox-state of lysosomal compartments has not yet been fully elucidated, available evidence indicates the existence of endo-lysosomal redox enzymes (gamma-interferon-inducible lysosomal thiol reductase — GILT [18]) that can promote thiol–disulfide exchange if certain cofactors such as cysteine are present [35]. Hence, if a bioreducible nanocarrier is trapped inside the lysosomes, the therapeutic mcDNA could be released into this compartment. Such would be highly deleterious since the acidic pH, characteristic of these compartments, has been reported to promote DNA depurination *via* acid-catalyzed hydrolysis of the purine–glycosyl bond, which in turn would significantly affect DNA expression efficacy and the therapeutic outcome [36]. As such, the release from lysosomal compartments is likely to be beneficial for the maximization of therapeutic genes expression efficiency [37,38].

The results of 2D cellular uptake confirmed that mcDNA loaded bioreducible micelleplexes were internalized by cells. However, it is important to emphasize that an increasing body of knowledge evidences that 2D *in vitro* cultures offer a simplistic representation of *in vivo* solid tumors and a poor *in vitro*/*in vivo* correlation is generally obtained [39]. Therefore, the next experiments were carried out in 3D *in vitro* models.

3.3. Micelleplexes uptake and gene expression in 3D tumor spheroids

By contrast to 2D culture, 3D *in vitro* models of solid tumors mimic the *in vivo* scenario in terms of cellular spatial distribution, cell–cell contacts, nutrient, pH gradients, as well as proliferation/necrosis patterns. They are emerging as valuable pre-clinical platforms for testing novel carriers designed for cancer therapy [39]. Hence, micelleplexes internalization was also evaluated in 3D multicellular tumor spheroids (MCTS) (Fig. 4 A to C). For these experiments, spheroids were assembled in a micromold with 81-recesses, this allowed achieving a high reproducibility regarding spheroid shape and size. This feature unlocked the possibility to explore high throughput imaging of a significant number of spheroids in each experimental condition. The results obtained with this methodology reveal that micelleplexes uptake in 3D MCTS increases from 8 to 12 h of incubation (Fig. 4 D).

Interestingly, no significant differences in uptake at 12 or 24 h were obtained, indicating that a plateau was achieved after 12 h of incubation (Fig. 4 D). Regarding the biocompatibility of bioreducible micelleplexes in 3D cultures, the microtissues were actively proliferating and no cytotoxicity was observed both in HeLa and in B16F10 3D multicellular tumor spheroids (Supplementary Fig. S8).

Following the confirmation that the bioreducible micelleplexes were efficiently delivered into 3D MCTS and that cell viability was unaffected, the expression of mcDNA-GFP transgene was also evaluated in these models (Fig. 5).

As demonstrated by confocal images of 3D MCTS sections, mcDNA-loaded micelleplexes successfully mediated GFP transgene expression both in HeLa cervix carcinoma cells and in B16F10 melanoma cells (Fig. 5 A and D). The 3D reconstruction and serial Z-stacks show that GFP expression was clearly detected in spheroids surface, remaining superficial. This is in line with the results of uptake experiments performed in 3D spheroids, which show this distribution.

Overall, this data indicates that a significant portion of cancer cells was transfected. Furthermore, gene expression analysis in HeLa cells demonstrates that bioreducible micelleplexes (N/P 20) exhibited an improved GFP expression efficiency in comparison to non-bioreducible PEOz–PLA-g–PEI nanocarriers which our group previously produced [10] (Fig. 5 C, black bars). This improved efficacy was also validated in B16F10 MCTS (Fig. 5 F). These findings could be correlated not only with the physicochemical properties of these nanocarriers but also with their bioreducible feature, since more mcDNA was released from PPP-SS micelleplexes upon incubation in reducible conditions (Supplementary Fig. S7 C).

Moreover, in comparison to Lipofectamine 2000 used as positive control, the bioreducible PPP-SS micelleplexes achieved a 2.7 fold higher expression in 3D HeLa spheroids and a 1.9 fold higher in 3D B1610 cells. Such results corroborate the improved biological performance of PPP-SS micelles and indicate that the redox responsive character in the intracellular reducing environment of cancer cells positively influences transgene expression efficiency. Altogether, these findings

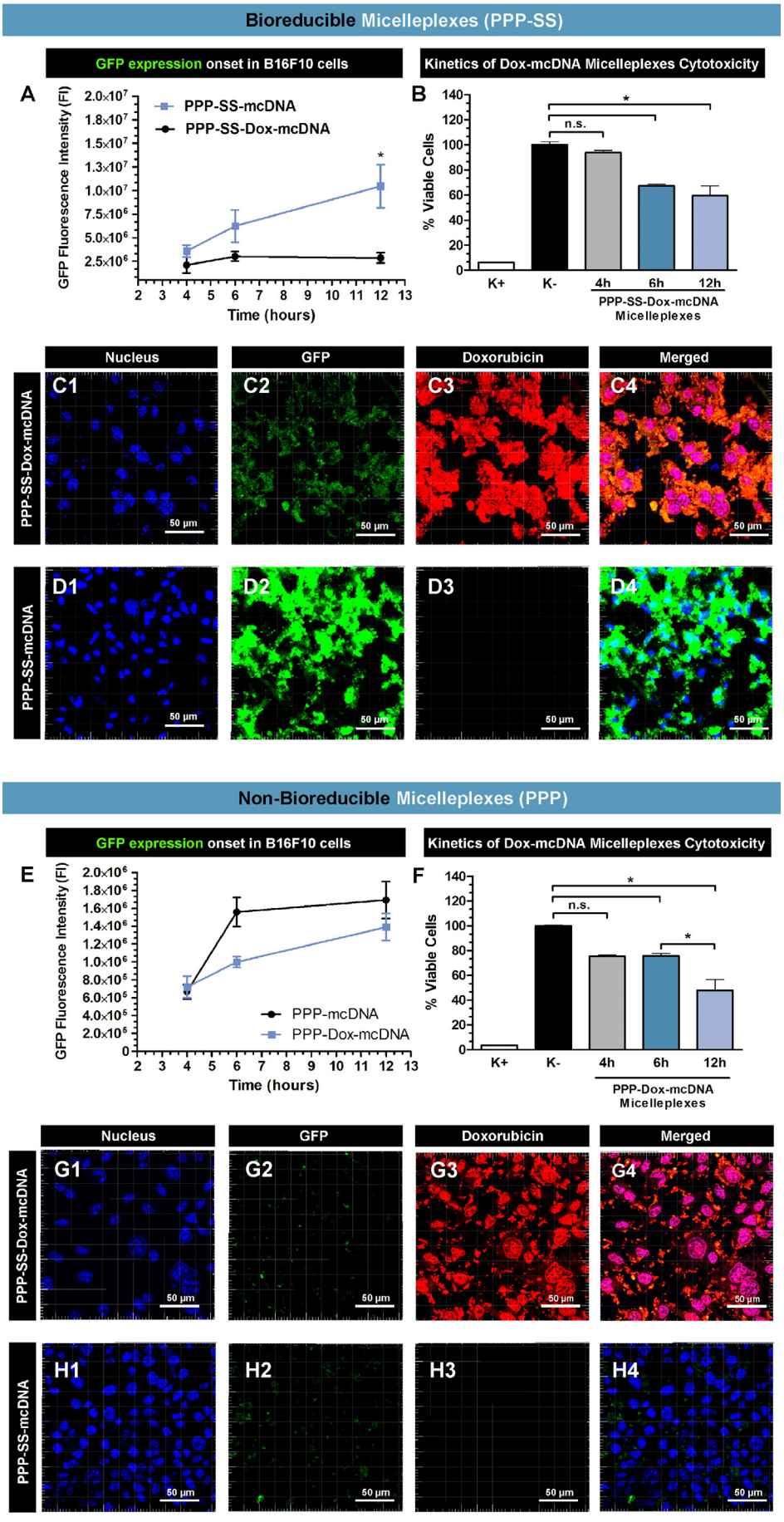
Bioreducible Micelleplexes (PPP-SS)
GFP expression onset in B16F10 cells
Kinetics of Dox-mcDNA Micelleplexes Cytotoxicity
A
GFP Fluorescence Intensity (FI)
PPP-SS-mcDNA
PPP-SS-Dox-mcDNA
Time (hours)
B
% Viable Cells
n.s.
K+
K-
4h
6h
12h
PPP-SS-Dox-mcDNA Micelleplexes
Nucleus
GFP
Doxorubicin
Merged
PPP-SS-Dox-mcDNA
PPP-SS-mcDNA
C1
C2
C3
C4
D1
D2
D3
D4
50 μm
Non-Bioreducible Micelleplexes (PPP)
GFP expression onset in B16F10 cells
Kinetics of Dox-mcDNA Micelleplexes Cytotoxicity
E
F
PPP-mcDNA
PPP-Dox-mcDNA
PPP-Dox-mcDNA Micelleplexes
G1
G2
G3
G4
H1
H2
H3
H4

are in agreement with various reports which have demonstrated that the administration of reduction-responsive gene delivery systems leads to an improved gene expression [40]. Recently, Piao and co-workers, reported that the formulation of a bioreducible, self-crosslinking polymeric carrier also leads to a significant improvement of *in vivo* gene expression when compared to non-bioreducible polyplexes [41].

3.4. In vivo transgene expression

To further evaluate the therapeutic potential of bioreducible triblock copolymer micelles their capacity to mediate gene expression in *in vivo* tumor models was investigated. For this purpose mcDNA-loaded carriers were administered to mice bearing B16F10 subcutaneous melanoma tumors via intratumoral (i.t.) injection.

Bioluminescence imaging revealed that a substantial luciferase expression was obtained after 48 h (Fig. 6). Interestingly, no significant differences were found in mice injected with different DNA doses (10 μg and 15 μg, Fig. 6 B), suggesting that administration with 10 μg is sufficient to achieve the desired transgene expression. Moreover luminescence signals were still observed after 8 days indicating that a prolonged gene expression could be obtained even upon a single micelleplexes injection of bioreducible PPP-SS micelleplexes (Supplementary Fig. S10). This feature is interesting and highly beneficial from a therapeutic perspective as the therapeutic transgenes can exert their effect in a prolonged time window without the need to repeat the administration of the delivery system.

Regarding the parameters that are required for *in vivo* transgene expression mediated by bioreducible micellar carriers, it is important to emphasize the possible influence of the thiol pool in the tumor interstitium for the overall gene expression efficiency. In effect, although the redox state of this particular constituent of tumor microenvironment is not fully characterized, it has been recently described that the thiol pool in the interstitial fluid surrounding tumor cells may be altered due to the fact that many tumors overexpress redox enzymes to the extracellular space as a protective measure against oxidative stress [18]. Moreover, evidence of an increased extracellular thiol pool in actively dividing cancer cells has also been reported [18]. Such parameter must be taken into account for mcDNA-mediated delivery by bioreducible nanocarriers *in vivo* since it may have an influence in the premature release of these biopharmaceuticals into the tumor interstitium. As a consequence, the nucleic acids could be exposed to the action of endonucleases and be degraded before they exert their therapeutic effect.

3.5. Micelleplexes in vitro co-delivery and cytotoxic activity

Next experiments were dedicated to evaluate the ability of these systems to promote the simultaneous delivery of chemotherapeutics and mcDNA.

Co-delivery of DNA and anti-cancer drugs in a single delivery system is of interest for cancer therapy as various disease hallmarks can be simultaneously targeted (Fig. 7 A, schematics). However, Drug–DNA co-delivery is extremely challenging due to the physicochemical differences between these two bioactive molecules. In fact, DNA complexation benefits from the existence of positive chemical groups, whereas, the drugs encapsulation generally requires existence of hydrophobic depots for the encapsulation of anti-cancer pharmaceutics with poor water solubility.

PPP-SS micelles were initially assembled by using the film casting method to promote Doxorubicin (Dox) encapsulation. This approach yielded small sized micelles (average size 116 nm, Supplementary Fig. S11) with highly positive zeta potential. These carriers presented high Dox encapsulation efficiency (74 ± 2.64%, Fig. 7C) indicating that the PLA hydrophobic core provides a suitable reservoir for this model anti-cancer drug. Subsequently, Dox-loaded micelles were then used for mcDNA complexation and as shown by agarose gel electrophoresis nucleic acid condensation was successful (Fig. 7 C1). The resulting Dox–mcDNA micelleplexes had a slightly larger size and lower zeta potential (Fig. 7 B). This decrease in zeta potential is in agreement with that obtained with previously produced Dox–mcDNA PPP non-bioreducible micelles [10].

Cellular uptake of dual loaded micelleplexes in 2D cultures was evaluated. B16F10 cancer cells were incubated with Dox–mcDNA bioreducible micelleplexes for 4 h (Fig. 7 D and 7 E). The high value of cell-associated fluorescence intensity corresponding to Dox fluorescence, indicated that these particles were efficiently taken up by cells compared to free (non-encapsulated) Dox and their non-bioreducible PPP micelleplexes. The characterization of Dox-release from mcDNA–Dox loaded micelleplexes revealed that the anticancer drug was released with a sustained profile and no significant burst release was observed (Supplementary Fig. S9 A). In comparison to the non-bioreducible micelleplexes, the bioreducible carriers present a similar release profile [10]. In addition, a time-course analysis of Dox release in B16F10 cells also demonstrates the increase in Dox fluorescence along time, as well as its preferential localization in the nuclear compartment, an advantageous finding since this is the main local of action of the anthracycline (Supplementary Fig. S9. B to F).

The cytotoxic activity of micelleplexes was also evaluated and as shown in Fig. 7 E, both single and dual loaded bioreducible formulations possessed a cytotoxic activity, with no significant differences between these formulations being observed.

To complement this characterization of the dual delivery system, the onset of Dox cytotoxicity and its possible influence in GFP transgene expression efficiency were assessed. As shown in Fig. 8 A and B, when Dox-induced toxicity altered the cell viability (6 and 12 h) the expression of GFP transgene promoted by PPP-SS–Dox–mcDNA was lower than that obtained with PPP-SS–mcDNA alone. Still, in comparison to non-bioreducible micelleplexes the PPP-SS–Dox–mcDNA present a 2.1 fold higher GFP expression on the onset of significant Dox-induced cytotoxicity at 12 h, indicating also its improved efficacy in this context (Fig. 8 A and E).

Moreover these findings demonstrate that the sustained drug release profile of these micelleplexes is clearly beneficial in comparison to that of other systems that have a burst drug release of anti-cancer therapeutics at early stages [42]. In this context, the bioreducible character of the delivery system is also important since a prompt redox responsive release of mcDNA once the carriers are in the cytoplasm may more rapidly promote gene expression before significant cytotoxicity is established. Such balance between kinetics of cytotoxicity-gene expression can be translated in a more effective therapeutic effect when a transgene encoded in mcDNA triggers cells apoptosis or sensitizes cancer cells to the action of anti-cancer drugs. It will be interesting also to take into consideration the efficacy of

Fig. 8. Evaluation of the onset of Dox induced cytotoxicity and GFP gene expression following co-delivery of Dox-mcDNA dual-loaded micelleplexes to B16F10 cells at various time points. (A and E) Kinetic of GFP gene expression after delivery of bioreducible and non-bioreducible micelleplexes, respectively. Data represents mean ± s.e.m., $^{*}p < 0.05$. (B and F) Cell viability analysis at the onset of Dox-induced cytotoxicity. Data represents mean ± s.e.m., $n = 3$, $^{*}p < 0.05$. n.s. — non-significant. (C and D) Representative confocal micrographs of bioreducible PPP-SS–Dox–mcDNA and PPP-SS–mcDNA transfected B16F10 cells after 12h of nanocarrier administration, respectively. (E and F) Representative confocal micrographs of non-bioreducible PPP–Dox–mcDNA and PPP–mcDNA transfected B16F10 cells after 12h of administration, respectively. Blue channel: Hoechst 33342® labeled cell nucleus. Green Channel: GFP. Red channel: Doxorubicin. Merged: merged channels. (For interpretation of the references to color in this figure legend, the reader is referred to the web version of this article.)

mcDNA that needs to be delivered to the nucleus of already dying cells, further studies on this parameter could help maximizing the overall therapeutic effect.

From a therapeutic perspective the Dox–mcDNA bioreducible micelleplexes have a higher potential to achieve an improved anti-cancer effect due to the delivery of two bioactive molecules with regards

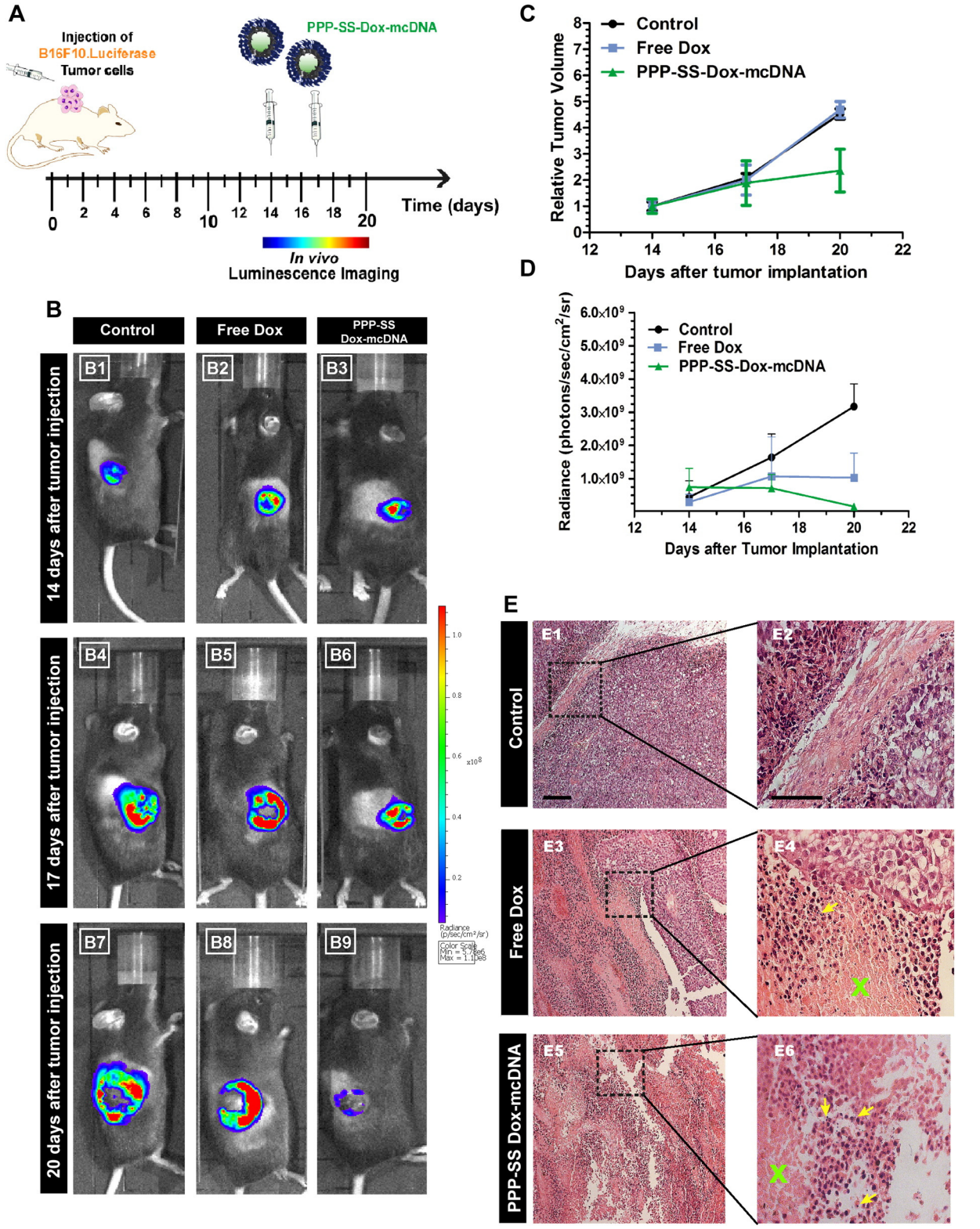

Fig. 9. Evaluation of micelles therapeutic activity in B16F10-Luc tumor bearing mice. (A) Schematics of the administration regime (two intratumoral injections at 14 and 17 days after tumor implantation). (B) Bioluminescence-based follow up of tumor burden during the experimental period. (C) Relative tumor volume measurements at different time points. (D) Quantitative analysis of luciferase radiance throughout the whole experimental procedure. Control — HBG injected tumor; Free Dox group — Dox injected tumors (5 mg·kg^{-1}, in HBG); PPP-SS Dox–mcDNA micelleplexes (N/P 20) group — 5 mg·kg^{-1} equivalents Dox dose in HBG. Data represents mean ± s.e.m., $n = 5$. (E) Hematoxylin and Eosin (H&E) stained tumor sections collected at day 20 post-implantation. Yellow arrows indicate pyknotic nuclei. Green X demarcates necrotic tumor regions. Black scale indicates 50 μm. (For interpretation of the references to color in this figure legend, the reader is referred to the web version of this article.)

to a single one, these dual loaded formulations were selected for posterior *in vivo* studies.

3.6. Dual loaded micelleplexes in vivo therapeutic activity

The *in vivo* therapeutic activity of dual loaded micelleplexes was evaluated in fully established melanoma tumor models of B16F10 cells that stably express luciferase gene (B16F10-Luc). Drug–mcDNA loaded nanocarriers were locally (i.t.) administered at different time points in a two-stage regime (Fig. 9 A).

Following tumor implantation and micelleplexes administration, the therapeutic efficacy and tumor burden were evaluated by monitoring tumor volume overtime, as well as the bioluminescence signals emitted from cancer cells. As shown in Fig. 9 C there is a similar tumor growth between control and free Dox groups, indicating that the administration of the drug alone does not immediately result in tumor volume reduction.

In sharp contrast, the relative tumor volume of mice injected with dual-loaded micelles was significantly lower in comparison to that of control or free (non-encapsulated) Dox treated tumors (Fig. 9 C), suggesting that bioreducible micelles mediate an effective anti-tumoral response. We hypothesize that this increased therapeutic activity is due to micelle-mediated delivery which is anticipated to increase of Dox bioavailability in the intracellular compartment of cancer cells.

Bioluminescence analysis revealed a reduction of the signals in free Dox treated mice despite the tumor volume remains similar to control non-treated group. By contrast, mice treated with Dox–mDNA bioreducible micelleplexes presented both a reduced tumor volume and lower luciferase expression. The explanation that could be raised from these observations is that in the case of mice treated with free Dox, it is possible that tumors became hypoxic reducing the luciferase activity to occur, which is not the case in control mice (Fig. 9 B and D). Such reduction in luciferase bioluminescence in hypoxic tumors has also been previously described by Khalil and co-workers [43]. In this report, it was concluded that luciferase bioluminescence is strongly reduced either by acute or chronic hypoxia *in vivo* in a xenograft tumor model comprised by U87-Luc human malignant glioma cells, and thus emphasizes the importance of addressing this parameter, especially in solid tumors [43]. For mice treated with Dox–mDNA bioreducible micelleplexes, the decrease of tumor volume is correlated with the luminescence signals suggesting that this latter could be due to the cytotoxicity effect reducing tumor growth.

Such findings are supported by the H&E histological analysis of tumor sections which reveals the existence of a significant amount of shrunken cells with condensed cytoplasm and pyknotic nuclei (Fig. 9 E6), particularly in Dox–mcDNA-micelleplexes treated group. The therapeutic effect was also confirmed by analysis of Fontana-Masson stained tumor sections which reveal a significant reduction in melanin production in tumor tissues of dual loaded micelleplexes group of mice when compared to tumor tissues from control and free Dox groups (Fig. 10 A to F).

To further complement these results and proof the concept of dual delivery, the *in vivo* reporter transgene expression was also evaluated when dual loaded micelles were administered to B16F10 melanoma tumors. A successful gene expression was attained following simultaneous administration of Dox and mcDNA in micelles (Supplementary Fig. S12). This important finding shows that the micellar carriers are capable of simultaneously promoting an anti-tumoral effect via delivery of chemotherapeutics, but also to mediate gene expression from mcDNA. This successful *in vivo* performance supports the earlier described design of the bioreducible triblock copolymers and emphasizes the potential of using these systems for focal co-administration to melanoma. Herein, the gene expression vectors express reporter transgenes (GFP and Luciferase). The inclusion of therapeutic transgenes of interest such as p53 or the addition of shRNA in these cassettes will be performed to assess new combinations of chemotherapeutic and tumor suppressor nucleic acids in the future.

The synthesized bioreducible micelleplexes were superior to the triblock copolymer micelles that our group previously synthesized in terms of transgene expression in vitro cultures both in 2D cultures, as well as in 3D multicellular tumor spheroids. They also achieved a therapeutic effect *in vivo* indicating that disulfide linkages provided a gain-of-function in terms of biological performance. In comparison with other bioreducible systems in the literature, the PPP-SS bioreducible micelles present improvements regarding the use of PEOz as non-fouling material in alternative to the generally used PEG. This is highly desirable

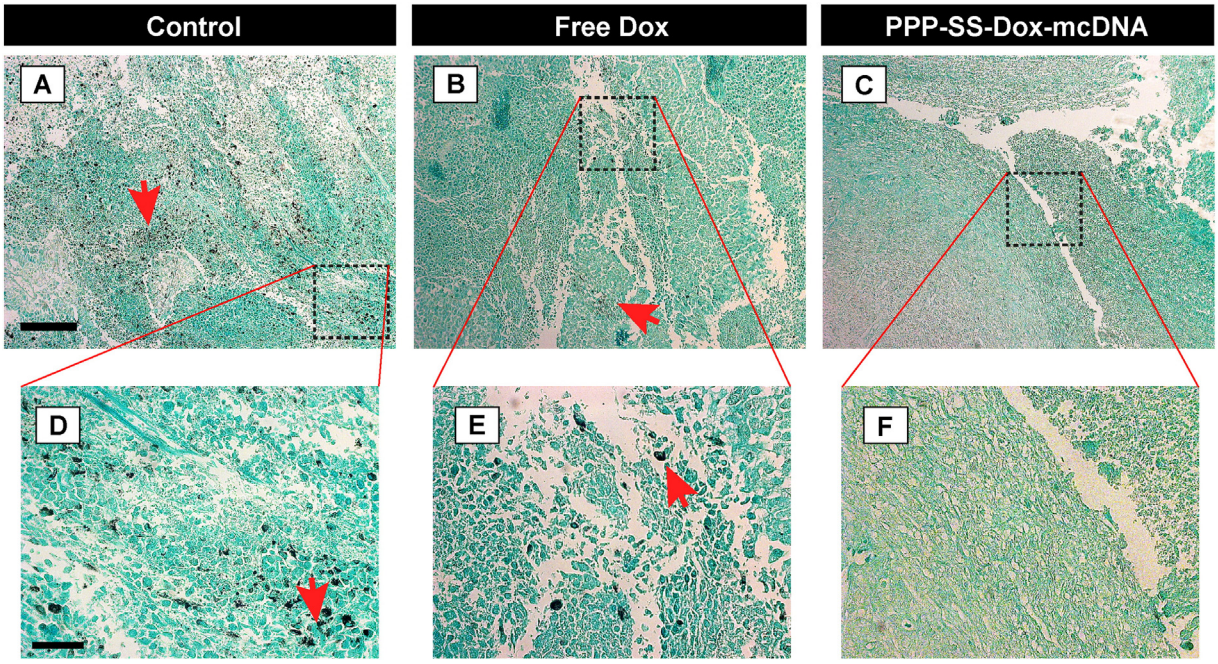

Fig. 10. Histological analysis of Fontana-Masson stained tumor sections at 20 days post-implantation. (A and D) Control group. (B and E) Free (non-encapsulated) Dox. (C and F) Dual loaded micelleplexes treated tumors. Black bar represents 50 μm. Red arrows represent melanin deposits. (For interpretation of the references to color in this figure legend, the reader is referred to the web version of this article.)

especially in light of recent reports that emphasize the issues associated with multiple administrations of pegylated nanocarriers and their accelerated blood clearance [44].

4. Conclusions

In this study we developed bioreducible amphiphilic triblock copolymers that can be used for on-demand site-specific mcDNA delivery to cancer cells. The micelleplexes exhibited superior gene expression when compared to non-bioreducible nanocarriers. Moreover, this system demonstrated to efficiently mediate co-delivery of drugs–mcDNA both *in vitro* and *in vivo*. Such efficiency was demonstrated by the anti-tumoral effect obtained following focal delivery of Dox–mcDNA micelleplexes to melanoma tumors. Further *in vivo* evidence of drug–gene co-delivery corroborated the capacity to promote gene expression even following delivery of anti-cancer therapeutics.

PPP-SS bioreducible carriers were useful for both single gene delivery and drug–gene co-delivery. Next studies will be devoted to a complete characterization of these nanocarriers following their intravenous administration to evaluate maximum tolerated dose, their biodistribution, the tumor extravasation capacity and therapeutic efficacy. The shielding of cationic charge and addition of targeting ligands will also be addressed. Moreover, further modification of the hydrophobic block with bioreducible or pH responsive moieties that comprises micelles could be beneficial for a spatiotemporally controlled drug release in the tumor microenvironment or intracellular compartment of cancer cells.

Acknowledgments

The authors would like to acknowledge Dr. Guillaume Gabant for the help in sample preparation and HR ESI-MS analysis. The authors would also like to acknowledge Dr. Cristine Gonçalves for all her help during experiments and to BIA Separations for having kindly provided the monolithic disk. This work was supported by the Portuguese Foundation for Science and Technology (FCT), (PTDC/EBB-BIO/114320/2009 and PEst-C/SAU/UI0709/2011). Vítor M. Gaspar acknowledges an individual PhD fellowship from FCT (SFRH/BD/80402/2011). Duarte de Melo-Diogo acknowledges an individual PhD fellowship from FCT (SFRH/BD/103506/2014). Elisabete C. Costa also acknowledged a fellowship from "Programa Operacional Regional do Centro 2007–2013 QREN" (CENTRO-07-ST24-FEDER-002014), and currently acknowledges an individual fellowship from FCT (SFRH/BD/103507/2014). The authors do not have any conflict of interest in the work presented herein.

Appendix A. Supplementary data

Supplementary data to this article can be found online at http://dx.doi.org/10.1016/j.jconrel.2015.07.011.

References

[1] S.M. Mignani, M. Bryszewska, B. Klajnert-Maculewicz, M. Zablocka, J.-P. Majoral, Advances in combination therapies based on nanoparticles for efficacious cancer treatment: an analytic report, Biomacromolecules 16 (2015) 1–27.
[2] J. Li, Y. Wang, Y. Zhu, D. Oupický, Recent advances in delivery of drug–nucleic acid combinations for cancer treatment, J. Control. Release 172 (2013) 589–600.
[3] N.S. Gandhi, R.K. Tekade, M.B. Chougule, Nanocarrier mediated delivery of siRNA/miRNA in combination with chemotherapeutic agents for cancer therapy: current progress and advances, J. Control. Release 194 (2014) 238–256.
[4] Z.Y. Chen, E. Riu, C.Y. He, H. Xu, M.A. Kay, Silencing of episomal transgene expression in liver by plasmid bacterial backbone DNA is independent of CpG methylation, Mol. Ther. 16 (2008) 548–556.
[5] W.M. Dietz, N.E. Skinner, S.E. Hamilton, M.D. Jund, S.M. Heitfeld, A.J. Litterman, P. Hwu, Z.-Y. Chen, A.M. Salazar, J.R. Ohlfest, Minicircle DNA is superior to plasmid DNA in eliciting antigen-specific CD8+ T-cell responses, Mol. Ther. 21 (2013) 1526–1535.
[6] H. Yu, Z. Xu, X. Chen, L. Xu, Q. Yin, Z. Zhang, Y. Li, Reversal of lung cancer multidrug resistance by pH-responsive micelleplexes mediating co-delivery of siRNA and paclitaxel, Macromol. Biosci. 14 (2014) 100–109.
[7] X. Dai, C. Tan, Combination of microRNA therapeutics with small-molecule anticancer drugs: mechanism of action and co-delivery nanocarriers, Adv. Drug Deliv. Rev. 81 (2015) 184–197.
[8] Z. Yang, D. Gao, Z. Cao, C. Zhang, D. Cheng, J. Liu, X. Shuai, Drug and gene co-delivery systems for cancer treatment, Biomaterials Science 3 (2015) 1035–1049.
[9] L. Jabr-Milane, L. van Vlerken, H. Devalapally, D. Shenoy, S. Komareddy, M. Bhavsar, M. Amiji, Multi-functional nanocarriers for targeted delivery of drugs and genes, J. Control. Release 130 (2008) 121–128.
[10] V.M. Gaspar, C. Gonçalves, D. de Melo-Diogo, E.C. Costa, J.A. Queiroz, C. Pichon, F. Sousa, I.J. Correia, Poly (2-ethyl-2-oxazoline)–PLA-g–PEI amphiphilic triblock micelles for co-delivery of minicircle DNA and chemotherapeutics, J. Control. Release 189 (2014) 90–104.
[11] A. Jhaveri, P. Deshpande, V. Torchilin, Stimuli-sensitive nanopreparations for combination cancer therapy, J. Control. Release 190 (2014) 352–370.
[12] T. Ishida, M. Harada, X.Y. Wang, M. Ichihara, K. Irimura, H. Kiwada, Accelerated blood clearance of PEGylated liposomes following preceding liposome injection: effects of lipid dose and PEG surface-density and chain length of the first-dose liposomes, J. Control. Release 105 (2005) 305–317.
[13] Z. Amoozgar, Y. Yeo, Recent advances in stealth coating of nanoparticle drug delivery systems, Wiley Interdiscip. Rev. Nanomed. Nanobiotechnol. 4 (2012) 219–233.
[14] K. Lava, B. Verbraeken, R. Hoogenboom, Poly (2-oxazoline) s and click chemistry: a versatile toolbox towards multi-functional polymers, Eur. Polym. J. 65 (2015) 98–111.
[15] V. Gaspar, D.d. Melo-Diogo, E. Costa, A. Moreira, J. Queiroz, C. Pichon, I. Correia, F. Sousa, Minicircle DNA vectors for gene therapy: advances and applications, Expert. Opin. Biol. Ther. 15 (2015) 1–27.
[16] D. Kobelt, M. Schleef, M. Schmeer, J. Aumann, P.M. Schlag, W. Walther, Performance of high quality minicircle DNA for in vitro and in vivo gene transfer, Mol. Biotechnol. 53 (2013) 80–89.
[17] G. Saravanakumar, W.J. Kim, Stimuli-responsive polymeric nanocarriers as promising drug and gene delivery systems, Intracellular Delivery II, Springer 2014, pp. 55–91.
[18] L. Brülisauer, M.A. Gauthier, J.-C. Leroux, Disulfide-containing parenteral delivery systems and their redox-biological fate, J. Control. Release 195 (2014) 147–154.
[19] G. Breuzard, M. Tertil, C. Goncalves, H. Cheradame, P. Geguan, C. Pichon, P. Midoux, Nuclear delivery of NFκB-assisted DNA/polymer complexes: plasmid DNA quantitation by confocal laser scanning microscopy and evidence of nuclear polyplexes by FRET imaging, Nucleic Acids Res. 36 (2008) e71–e71.
[20] Y.-X. Sun, X. Zeng, Q.-F. Meng, X.-Z. Zhang, S.-X. Cheng, R.-X. Zhuo, The influence of RGD addition on the gene transfer characteristics of disulfide-containing polyethyleneimine/DNA complexes, Biomaterials 29 (2008) 4356–4365.
[21] T.K. Endres, M. Beck-Broichsitter, O. Samsonova, T. Renette, T.H. Kissel, Self-assembled biodegradable amphiphilic PEG–PCL–lPEI triblock copolymers at the borderline between micelles and nanoparticles designed for drug and gene delivery, Biomaterials 32 (2011) 7721–7731.
[22] V.M. Gaspar, C.J. Maia, J.A. Queiroz, C. Pichon, I.J. Correia, F. Sousa, Improved minicircle DNA biosynthesis for gene therapy applications, Hum. Gene Ther. Methods 25 (2013) 93–105.
[23] I. Horcas, R. Fernández, J.M. Gómez-Rodríguez, J. Colchero, J. Gómez-Herrero, A.M. Baro, WSXM: a software for scanning probe microscopy and a tool for nanotechnology, Rev. Sci. Instrum. 78 (2007) 013705.
[24] V. Gaspar, J. Marques, F. Sousa, R. Louro, J. Queiroz, I. Correia, Biofunctionalized nanoparticles with pH-responsive and cell penetrating blocks for gene delivery, Nanotechnology 24 (2013) 275101.
[25] N. Shao, H. Wang, B. He, Y. Wang, J. Xiao, Y. Wang, Q. Zhang, Y. Li, Y. Cheng, Hydrogen-bonding dramatically modulates the gene transfection efficacy of surface-engineered dendrimers, Biomater. Sci. 3 (2015) 500–508.
[26] M.M. Jensen, J.T. Jørgensen, T. Binderup, A. Kjær, Tumor volume in subcutaneous mouse xenografts measured by microCT is more accurate and reproducible than determined by 18F-FDG-microPET or external caliper, BMC Med. Imaging 8 (2008) 16.
[27] X. Chen, R.J. Swanson, J.F. Kolb, R. Nuccitelli, K.H. Schoenbach, Histopathology of normal skin and melanomas after nanosecond pulsed electric field treatment, Melanoma Res. 19 (2009) 361.
[28] S.-J. Kim, H. Ise, E. Kim, M. Goto, T. Akaike, B.H. Chung, Imaging and therapy of liver fibrosis using bioreducible polyethylenimine/siRNA complexes conjugated with N-acetylglucosamine as a targeting moiety, Biomaterials 34 (2013) 6504–6514.
[29] V.M. Gaspar, I.J. Correia, Â. Sousa, F. Silva, C.M. Paquete, J.A. Queiroz, F. Sousa, Nanoparticle mediated delivery of pure P53 supercoiled plasmid DNA for gene therapy, J. Control. Release 156 (2011) 212–222.
[30] D.M. Klinman, S. Klaschik, D. Tross, H. Shirota, F. Steinhagen, FDA guidance on prophylactic DNA vaccines: analysis and recommendations, Vaccine 28 (2010) 2801–2805.
[31] F. Sousa, D. Prazeres, J. Queiroz, Improvement of transfection efficiency by using supercoiled plasmid DNA purified with arginine affinity chromatography, The Journal of Gene Medicine 11 (2009) 79–88.
[32] T. Bieber, W. Meissner, S. Kostin, A. Niemann, H.-P. Elsasser, Intracellular route and transcriptional competence of polyethylenimine–DNA complexes, J. Control. Release 82 (2002) 441–454.
[33] R.V. Benjaminsen, M.A. Mattebjerg, J.R. Henriksen, S.M. Moghimi, T.L. Andresen, The possible "proton sponge" effect of polyethylenimine (PEI) does not include change in lysosomal pH, Mol. Ther. 21 (2013) 149–157.
[34] C. Ganas, A. Weiß, M. Nazarenus, S. Rösler, T. Kissel, P. Rivera_Gil, W.J. Parak, Biodegradable capsules as non-viral vectors for in vitro delivery of PEI/siRNA polyplexes for efficient gene silencing, J. Control. Release 196 (2014) 132–138.

[35] R. Cheng, F. Feng, F. Meng, C. Deng, J. Feijen, Z. Zhong, Glutathione-responsive nanovehicles as a promising platform for targeted intracellular drug and gene delivery, J. Control. Release 152 (2011) 2–12.
[36] Y.L. Choi, J.H. Lee, J. Jaworski, J.H. Jung, Mesoporous silica nanoparticles functionalized with a thymidine derivative for controlled release, J. Mater. Chem. 22 (2012) 9455–9457.
[37] A. Akinc, R. Langer, Measuring the pH environment of DNA delivered using nonviral vectors: implications for lysosomal trafficking, Biotechnol. Bioeng. 78 (2002) 503–508.
[38] T. Nomoto, S. Fukushima, M. Kumagai, K. Machitani, Y. Matsumoto, M. Oba, K. Miyata, K. Osada, N. Nishiyama, K. Kataoka, Three-layered polyplex micelle as a multifunctional nanocarrier platform for light-induced systemic gene transfer, Nat. Commun. 5 (2014) 3545.
[39] G. Mehta, A.Y. Hsiao, M. Ingram, G.D. Luker, S. Takayama, Opportunities and challenges for use of tumor spheroids as models to test drug delivery and efficacy, Journal of Control Release 164 (2012) 192–204.
[40] S. Son, R. Namgung, J. Kim, K. Singha, W.J. Kim, Bioreducible polymers for gene silencing and delivery, Acc. Chem. Res. 45 (2012) 1100–1112.
[41] J.-G. Piao, S.-G. Ding, L. Yang, C.-Y. Hong, Y.-Z. You, Bioreducible cross-linked nanoshell enhances gene transfection of polycation/DNA polyplex in vivo, Biomacromolecules 15 (2014) 2907–2913.
[42] J. Ding, C. Xiao, C. He, M. Li, D. Li, X. Zhuang, X. Chen, Facile preparation of a cationic poly (amino acid) vesicle for potential drug and gene co-delivery, Nanotechnology 22 (2011) 494012.
[43] A.A. Khalil, M.J. Jameson, W.C. Broaddus, P.S. Lin, S.M. Dever, S.E. Golding, E. Rosenberg, K. Valerie, T.D. Chung, The influence of hypoxia and pH on bioluminescence imaging of luciferase-transfected tumor cells and xenografts, International journal of molecular imaging (2013) 287697.
[44] Y. Hashimoto, T. Shimizu, A.S. Abu Lila, T. Ishida, H. Kiwada, Relationship between the concentration of anti-polyethylene glycol (PEG) immunoglobulin M (IgM) and the intensity of the accelerated blood clearance (ABC) phenomenon against PEGylated liposomes in mice, Biol. Pharm. Bull. 38 (2015) 417–424.

Supplementary Information

Bioreducible Poly(2-ethyl-2-oxazoline)-PLA-PEI-SS triblock Copolymer Micelles for Co-delivery of DNA minicircles and Doxorubicin

Journal of Controlled Release, 2015
DOI: 10.1016/j.jconrel.2015.07.011

11.1. Materials and Methods

11.1.1. Materials

Chromatographic convective interaction media ethylenediamine monolithic disk column (CIM® EDA) was kindly provided by BIA Separations (Ajdovščina, Slovenia). Arginine-Arginine dipeptide was purchased from Genscript (GenScript Corporation (Piscataway, NJ, US). N-Hydroxysuccinimide (NHS), N-(3-Dimethylaminopropyl)-N-ethylcarbodiimide hydrochloride (EDC), DMEM-high glucose culture medium, Dextran sulfate, and γ-L-Glutamyl-L-cysteinyl-glycine (GSH) were obtained from Sigma-Aldrich (Sintra, Portugal). Fetal bovine serum (FBS) was purchased from Biochrom AG (Berlin, Germany). Cy3 Label IT® nucleic acid labelling kit was acquired from Mirus Bio LLC (Madison, WI, US). Cy5®-NHS ester was obtained from Lumiprobe GmbH (Hannover, Germany). Quant-IT PicoGreen® dsDNA assay was purchased from Invitrogen (Carlsbad, USA).

11.1.2. Methods

11.1.2.1. Bioreducible triblock copolymer characterization

Characterization of the synthesized bioreducible PEI (PEI-SS) and of triblock copolymers was performed by 1D ^{1}H NMR spectroscopy by using a Brüker Avance III 400 MHz spectrometer (Brüker Scientific Inc., N.Y., USA). Prior to NMR analysis, polymer samples (10 mg) were dissolved 1 mL of 9:1 (v/v) H_2O/D_2O. NMR spectra were acquired with or without p*re-saturation* for water suppression, at 298 K. The recorded spectra were then post-processed in MNova software (Mestrelab Research, SL, Santiago de Compostela, Spain).

High resolution electrospray ionization mass spectrometry (HR ESI-MS) analysis was performed by using a Brüker Maxis Impact LC-Q-TOF mass spectrometer (Brüker Scientific Inc., N.Y., USA) equipped with an automatic syringe pump and operated in positive-ion polarity mode. The spectrometer was operated at 4.0 kV and at a dissolvation temperature of 150 ºC. Samples were scanned in the range of 300-3000 m/z, and nitrogen was used as the drying gas (4.0 $L.min^{-1}$). Samples were injected in water and the precursor ion was Na^{2+}.

11.1.2.2. Affinity Chromatography

The recovery of mcDNA supercoiled isoform form a native mcDNA sample (open circular and supercoiled isoform) was carried out by affinity chromatography using a monolithic disk. Prior to chromatography runs, a CIM® EDA disk was modified with arginine-arginine (Arg-Arg) dipeptides (1 g) by using EDC/NHS coupling chemistry. Successful immobilization was confirmed by differences in the retention time of a model pDNA vector injected in the column. Chromatography mediated recovery of sc mcDNA was performed by using two buffers: (i) 10 mM Tris.HCl (pH 8.0), and (ii) 500 mM NaCl in 10 mM Tris.HCl (pH 8.0). All runs were performed at room temperature at a flow rate of 1 $mL.min^{-1}$, in an AKTA purifier chromatography system (GE Healthcare Biosciences, Uppsala, Sweden). Vivaspin® concentrators were used to remove

the salt from preparations by successive washes with 10 mM Tris.HCl buffer (pH 8.0). Recovered sample fractions were analyzed by agarose gel electrophoresis.

11.1.2.3. Characterization of redox-responsive properties

The stimuli-responsiveness of bioreducible micelleplexes was evaluated by agarose gel electrophoresis, by the Quant-IT PicoGreen® dsDNA assay, and by fluorescence resonance energy transfer (FRET). For electrophoresis experiments sc mcDNA-loaded micelleplexes were incubated during 4 h with 50 mM dithiothreitol (DTT) at 37 ºC, under horizontal stirring. Following incubation, samples were loaded in an agarose gel stained with Safe-green™ DNA gel stain.

For the Quant-IT PicoGreen® dsDNA assay bioreducible and non-bioreducible nanocarriers were dispersed in 50 mM of GSH, in PBS pH = 7.4, during 4 h, at 37 ºC, in a shacking water bath. After indicated incubation period, the micelles were pelleted by centrifugation and the supernatant was collected for quantification of release mcDNA by using the Quant-IT PicoGreen® dsDNA assay as recommended by the manufacturers. Fluorescence measurements were performed in a Spectramax Gemini XS spectrofluorometer (Molecular Devices LLC, USA) (λ_{ex}= 333 nm and λ_{ex}= 335 nm; λ_{em}= 390 nm). In the dextran sulfate competition assay micelleplexes were resuspended in 1 mL of Dextran solution (PBS, pH = 7.4) for 4 h at 37 ºC. A Dextran:mcDNA w/w ratio of 40:1 was used for these assays in a similar way as described in the literature [1]. Following the incubation period the nanocarriers were pelleted by centrifugation and the DNA in the supernatant was quantified by using the Quant-IT PicoGreen® dsDNA assay.

FRET experiments were performed with Cy3-Cy5 FRET pair. In brief, -SS polymers and PPP control polymers were labelled with Cy5-NHS ester (1:0.25 w/w ratio PPP-SS:Cy5-NHS) for 48 h, at RT. PPP non bioreducible Afterwards, the Cy5-labelled PPP-SS was dialyzed (MWCO 1000 Da) against water for 6 days in the dark to remove excess labelling reagent. The Cy5-polymer was acidified and then recovered by freeze drying. McDNA was labelled with Cy3 Label IT® nucleic acid labelling kit by following manufacturer's instructions (1:1 w/w ratio Cy3:mcDNA). This protocol is referred by the manufacture to yield one Cy3 molecule per 40 bp DNA. Cy3-mcDNA/Cy5-PPP-SS micelleplexes were then formulated as described in the main article. FRET experiments were performed by incubating fluorescent nanocarriers during 4 h in HeLa cells ($1x10^4$) cultured on µ-Slide 8-well flat bottom imaging plates (Ibidi GmbH, Germany), in DMEM-HG/10 % FBS medium. Imaging was performed in a Zeiss LSM 710 (Carl Zeiss SMT Inc., US) confocal microscope equipped with a 63x/1.4 oil DIC objective. Image acquisition was performed in multi-track mode by exciting the Cy3 donor at 543 nm (detected at 560-615 nm), by exciting the Cy5 acceptor at 633 nm (detected above 650 nm), and by exciting the FRET channel at 543 nm (detected above 650 nm). Donor quenching (E_d) was used to determine FRET efficiency [2] under optimized laser power/gain settings (E_d = 75.6 ± 6.7 %) by analyzing nanocarriers dispersed in aqueous solution in Ibidi 8-well imaging plates.

11.1.2.4. Characterization of Doxorubicin *in vitro* release profile

Drug release from the nanocarriers was performed by the dialysis bag method by using Spectra/Por® Foat-A-Lyzer ® G2 Dialysis Device, MWCO: 500-1000 Da (Spectra/Por, Laguna Hills, CA). For this purpose, micelles were resuspended in release medium (PBS, pH = 7.4) and transferred to the dialysis bag. Drug release was performed in a shaking water bath (45 rpm) at 37 ºC in the dark to maintain Dox fluorescence. Supernatant samples were collected at different time points and analyzed by UV-vis spectrophotometry at λ= 485 nm in a Shimadzu UV-1700 spectrophotometer (Shimadzu Inc., Japan).

In addition, a time course of Dox *in vitro* release in B16F10 cancer cells was qualitatively evaluated by confocal microscopy. Briefly, cancer cells (20 x 10^3 cells per well) were seeded in sterile cell culture treated µ-slide 8-well imaging plates (Ibidi GmbH, Germany). In the following day, PPP-SS-Dox-mcDNA micelleplexes were administered during 4 h. After this period the cells were washed with PBS and the medium replaced by fresh medium. Time course analysis of Dox *in vitro* release in cancer cells was performed by cell fixation (4 %, PFA, RT, 15 min) at given time points (4, 6, 12, 24, 48 h).

11.2. Results

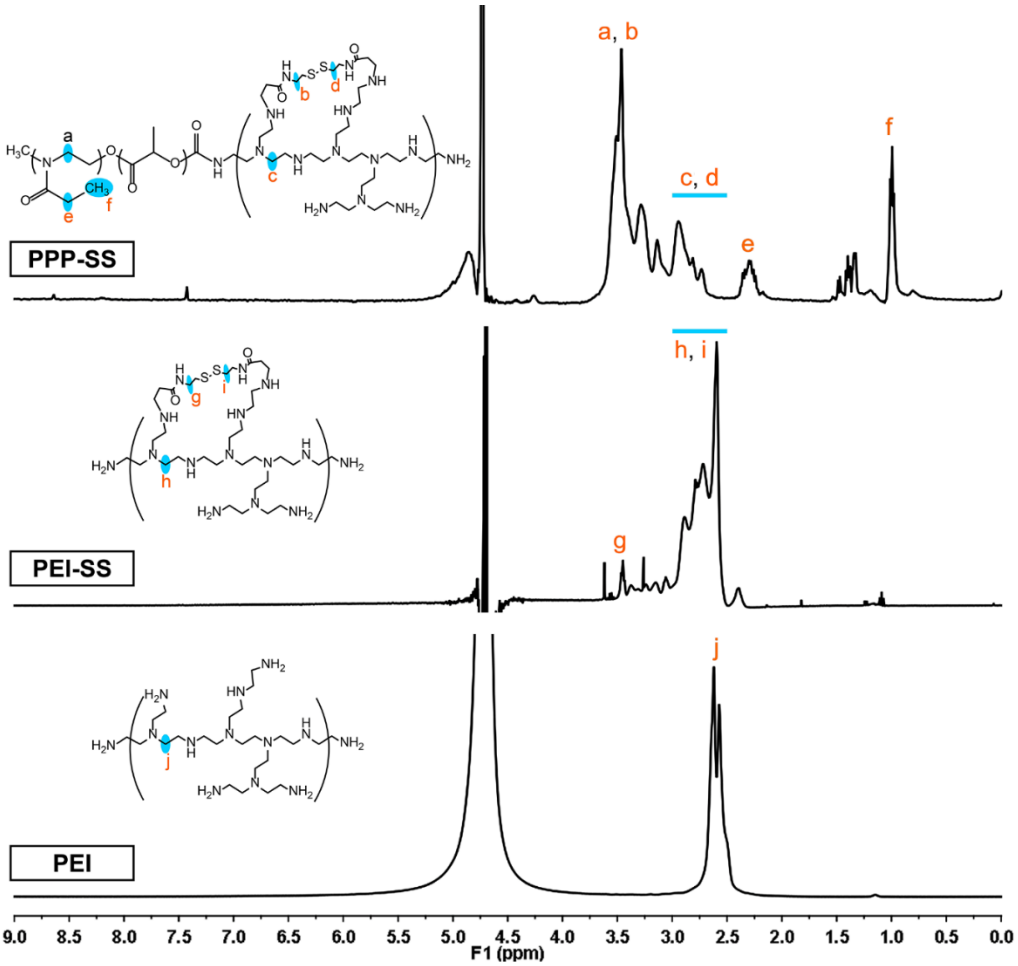

Figure S1. ^{1}H NMR spectroscopy analysis of bioreducible PEOz-PLA-g-PEI-SS triblock co-polymers. Modification of native PEI with disulfide containing CBA results in the formation of PEI-SS as evidenced by the characteristic methylene -C**H₂**-CH₂-S-S-CH₂-C**H₂**- and -CH₂-C**H₂**-S-S-C**H₂**- CH₂- peaks of cystamine bisacrylamide (CBA), δ ~ 3.45 ppm (g) and δ ~ 2.8 ppm (i) [3], respectively. Moreover, CBA acrylamide peaks are absent (δ ~ 6.5-5.8 ppm) suggest that all groups reacted with PEI amines. In PPP-SS spectra, the δ ~ 3.45 ppm peak was assigned to the methylene protons of PEOz (CH₂-; a) and CBA (-C**H₂**-CH₂-S-S-CH₂-C**H₂**-; b) [4]. The δ ~ 2.4-2.1 ppm and δ ~ 1.0 ppm peaks correspond to the methylene (-CH₂-CH₃; e) and methyl (-CH₃; f) protons of PEOz, respectively [4]. The c-d band is assigned to PEI and CBA (-CH₂-C**H₂**-S-S-C**H₂**- CH₂-) methylene proton peaks, respectively. These results confirm the successful synthesis of PPP-SS.

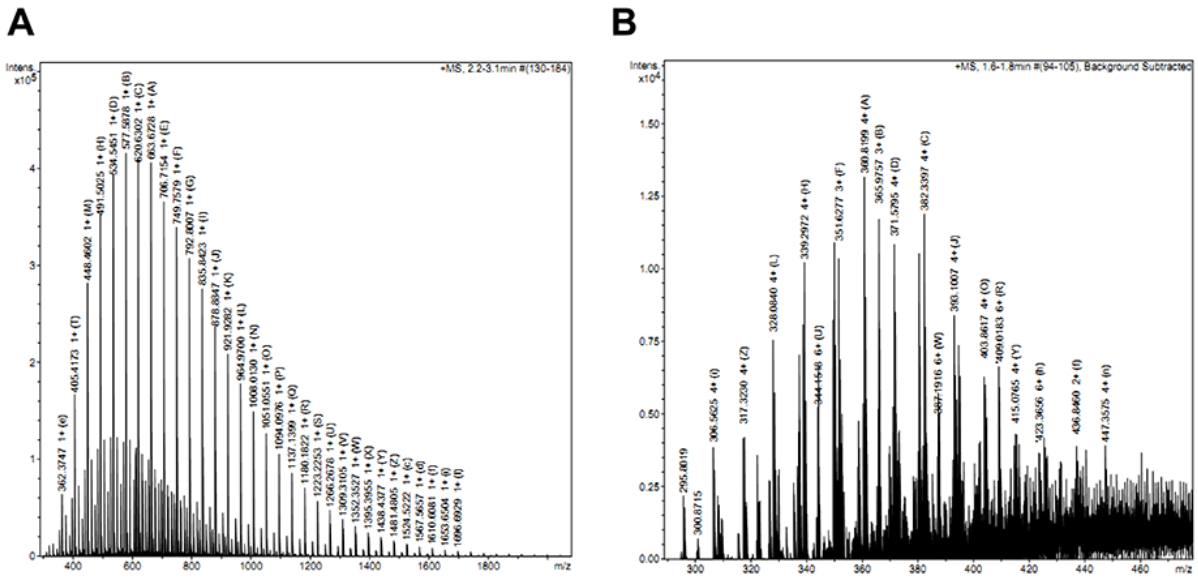

Figure S2. HR ESI-MS analysis of polyethylenimine (PEI). **A.**) Commercial PEI sample. (B) Synthesized PEI-SS disulfide crosslinked polymer.

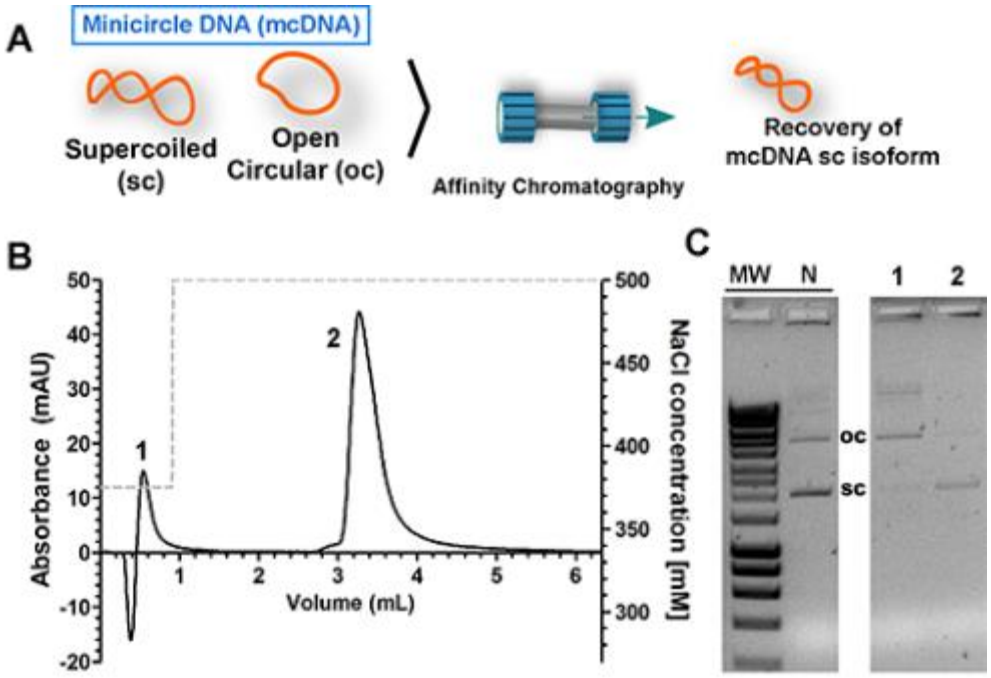

Figure S3. Recovery of supercoiled (sc) minicircle DNA (mcDNA) by affinity chromatography. (A) Schematics of sc mcDNA recovery by affinity chromatography by using a monolith disk modified with arginine-arginine dipeptides. (B) Chromatographic profile. Peak 1: oc mcDNA; Peak 2: sc mcDNA. (C) Representative agarose gel electrophoresis of chromatographic fractions. MW – DNA ladder. N – native sample containing both oc and sc mcDNA isoform.

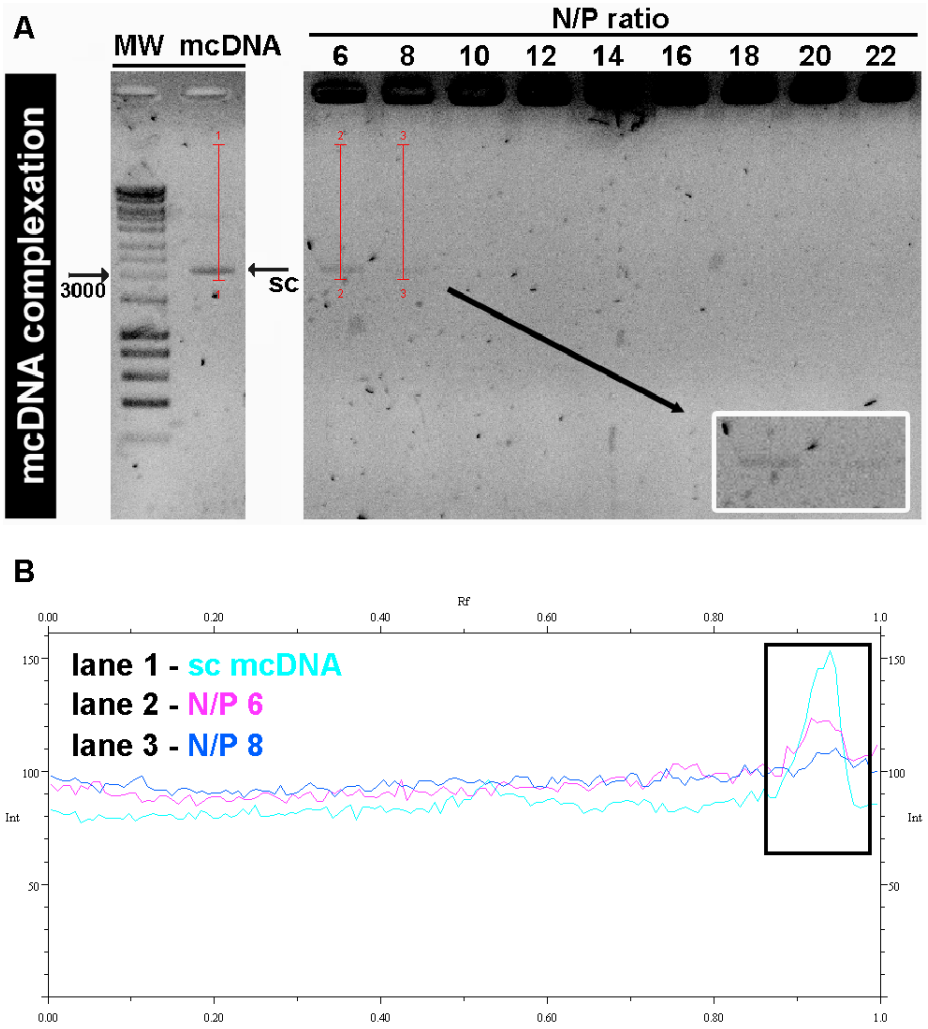

Figure S4. Analysis of mcDNA complexation. **(A)** Agarose gel electrophoresis of bioreducible mcDNA micelleplexes (PPP-SS) formulated at N/P ratios ranging from 20 to 24. MW – HyperLadder™ 1kb Plus, DNA marker (Bioline Ltd., London, UK). mcDNA lane - Non-complexed mcDNA; sc - supercoiled isoform. Red lines – markers used for lane density profile plotting. **(B)** Plotting of different lanes profile. Lane 1- sc mcDNA, Lane 2 – PPP-SS Micelleplexes formulated at N/P 6, Lane 3 – PPP-SS Micelleplexes formulated at N/P 8. Black box indicates the signal intensity of mcDNA bands in the agarose gel.

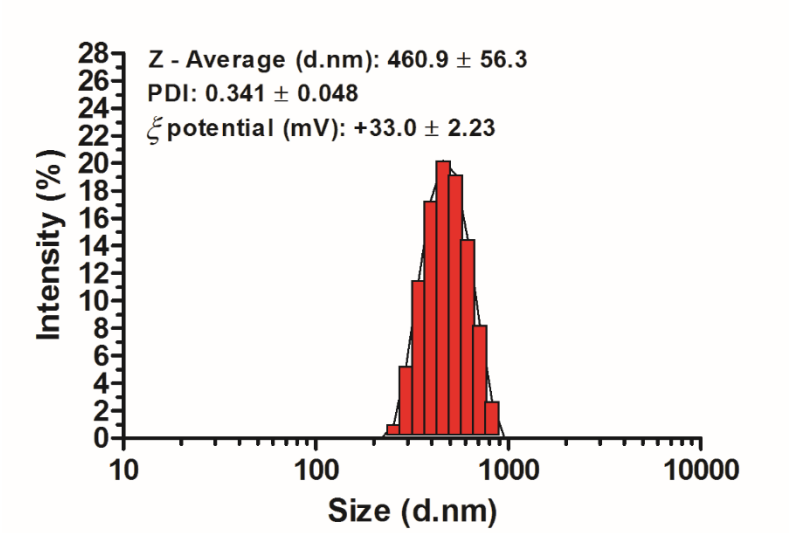

Figure S5. DLS characterization of PPP-SS blank micelles formulated by ultrasound mediated self-assembly. PDI – polydispersity index.

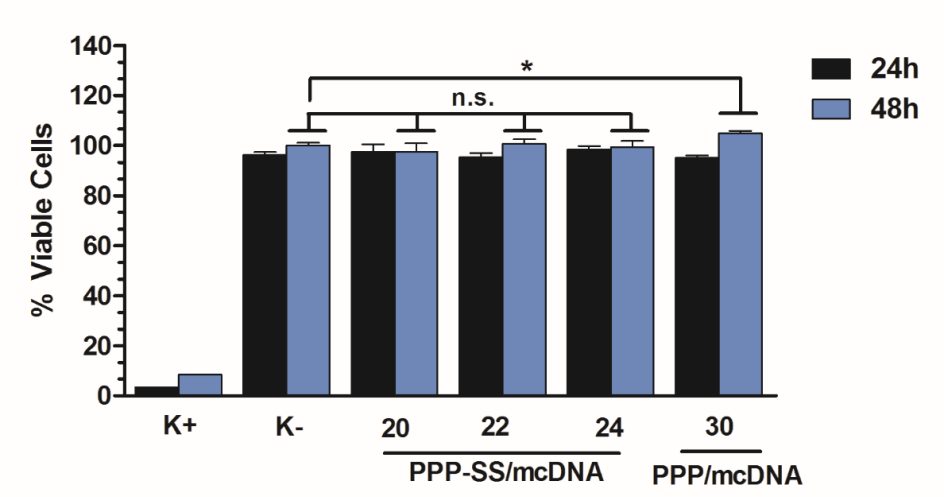

Figure S6. Characterization of micelleplexes biocompatibility profile in B16F10 cells following incubation with micelleplexes formulated at different N/P ratios, at 24 and 48 h. PPP-SS/mcDNA represent bioreducible micelleplexes formulated at N/P 20, 22 and 24. PPP/mcDNA represent non-bioreducible micelleplexes formulated at N/P 30. Data represents mean ± s.d., *n*=5. *p<0.05. n.s. – non significant.

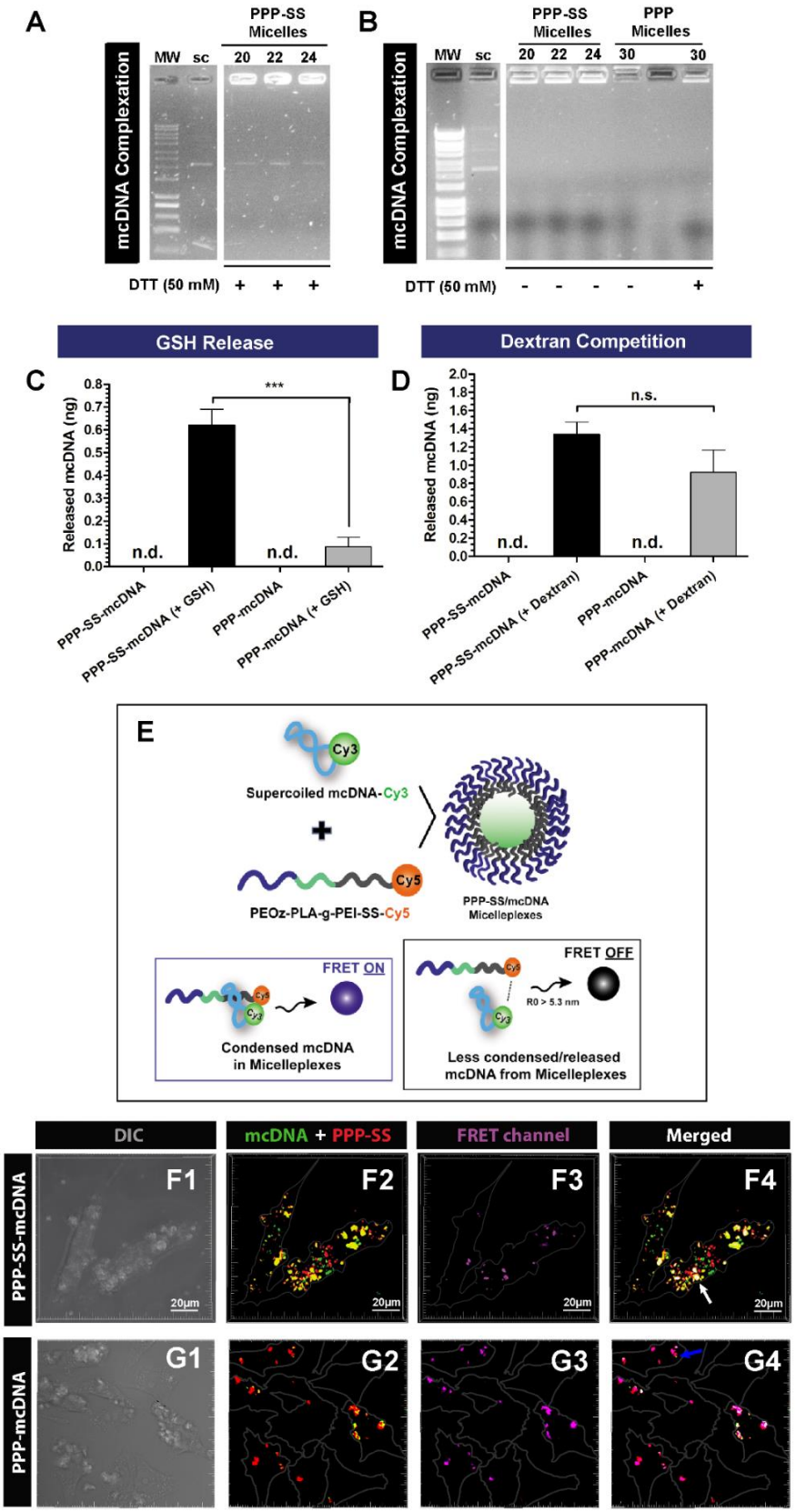

Figure S7. Analysis of PEI-SS bioreducible character. **(A and B)** Agarose gel electrophoresis of mcDNA-loaded PPP-SS micelleplexes and PPP control micelleplexes in reducing and non-reducing conditions at different ratios, respectively. MW – DNA ladder. Sc – Supercoiled mcDNA. PPP micelles – represent non-bioreducible controls. The absence of a band in PPP-mcDNA incubated under redox conditions is correlated with the limit of quantification of agarose gel electrophoresis. **(C)** Picogreen quantification of GSH-mediated mcDNA release from different micelleplexes formulations at 4 h of incubation. n.d. – non-detected signal. Data represents mean ± s.e.m., *n*=3. *p<0.05. n.s. – non significant. **(D)** Picogreen

quantification of Dextran sulfate-mediated mcDNA release from different micelleplexes (N/P 20), at 4 h of incubation. **(E)** Schematics of FRET experiments with mcDNA-cy3 and PPP-SS-Cy5 copolymer and interpretation of the FRET signal. **(F and G)** CLSM FRET imaging of bioreducible and non-bioreducibe micelleplexes delivered to HeLa cancer cells after 4 h, respectively. White arrows indicate FRET ON signals. Blue arrow indicates release/loosely complexed mcDNA.

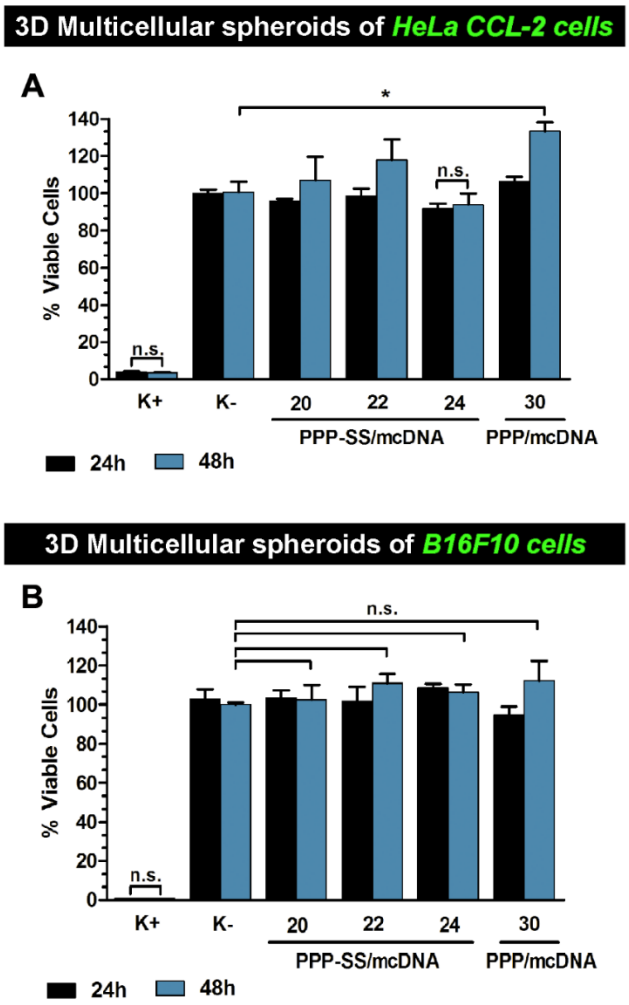

Figure S8. Characterization of micelleplexes biocompatibility in 3D multicellular tumor spheroids of B16F10 cells following incubation with micelleplexes produced at different N/P ratios, at 24 and 48 h. PPP-SS/mcDNA represent bioreducible micelleplexes formulated at N/P 20, 22 and 24. PPP/mcDNA represent non-bioreducible micelleplexes formulated at N/P 30 Data represents mean ± s.d., *n*=5. *p<0.05. n.s. – non significant.

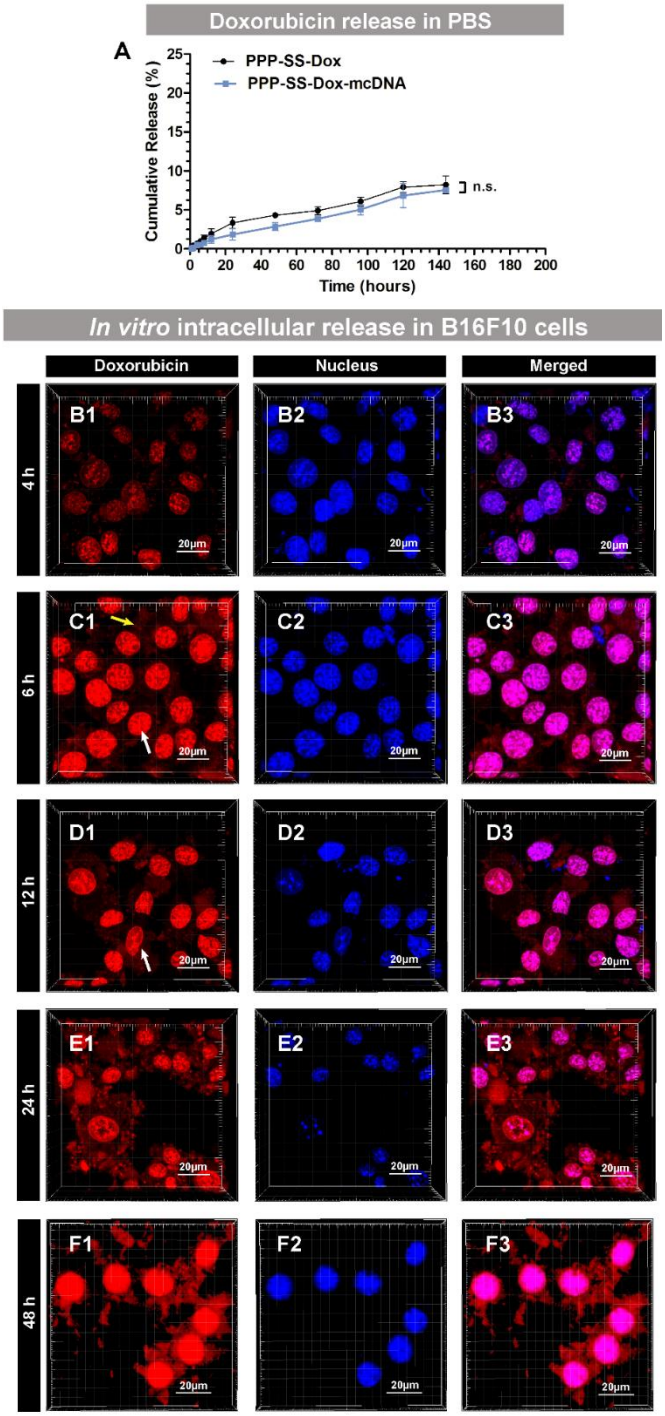

Figure S9. Assessment of Doxorubicin release from micellar carriers. **(A)** Cumulative release profile of Doxorubicin from PPP-SS-Dox-mcDNA and PPP-SS-Dox micelleplexes. Data represents mean ± s.e.m.; n.s. – non significant. **(B to F)** CLSM microscopy analysis of Dox *in vitro* release from PPP-SS-Dox-mcDNA micelleplexes in B16F10 cells. Red channel: Doxorubicin. Blue channel: Hoechst 33342® labeled nucleus. Merged: merged channels.

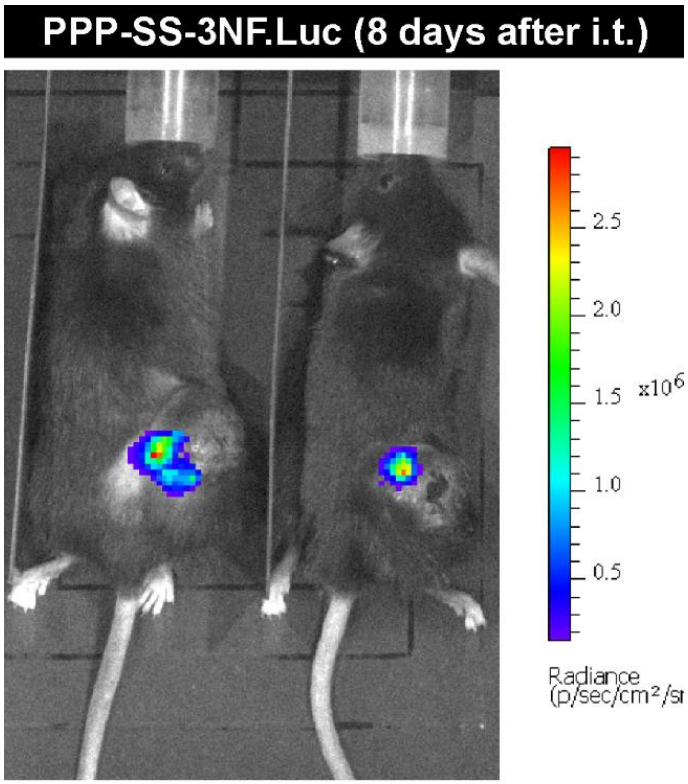

Figure S10. Bioluminescence imaging of luciferase gene expression at 8 days following administration of p3NF-Luc-3NF/ PPP-SS micelleplexes (15 µg DNA; N/P 20).

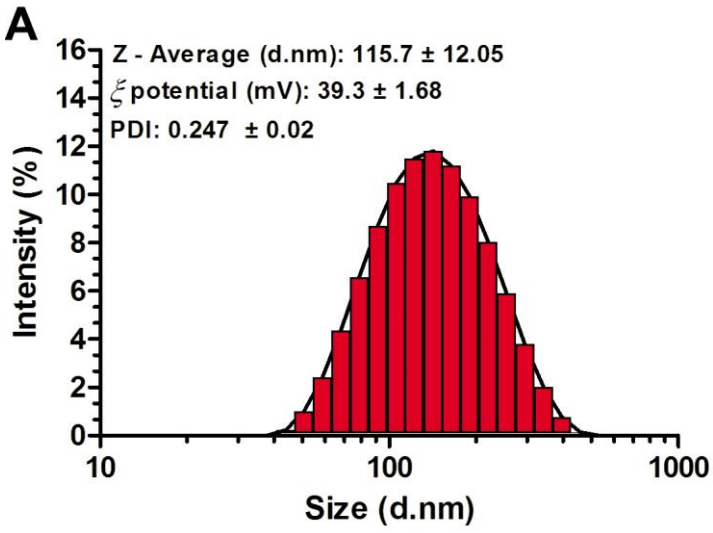

Figure S11. Characterization of Dox loaded micelleplexes. (A) DLS characterization of Dox-mcDNA loaded micelleplexes. PDI – polydispersity index.

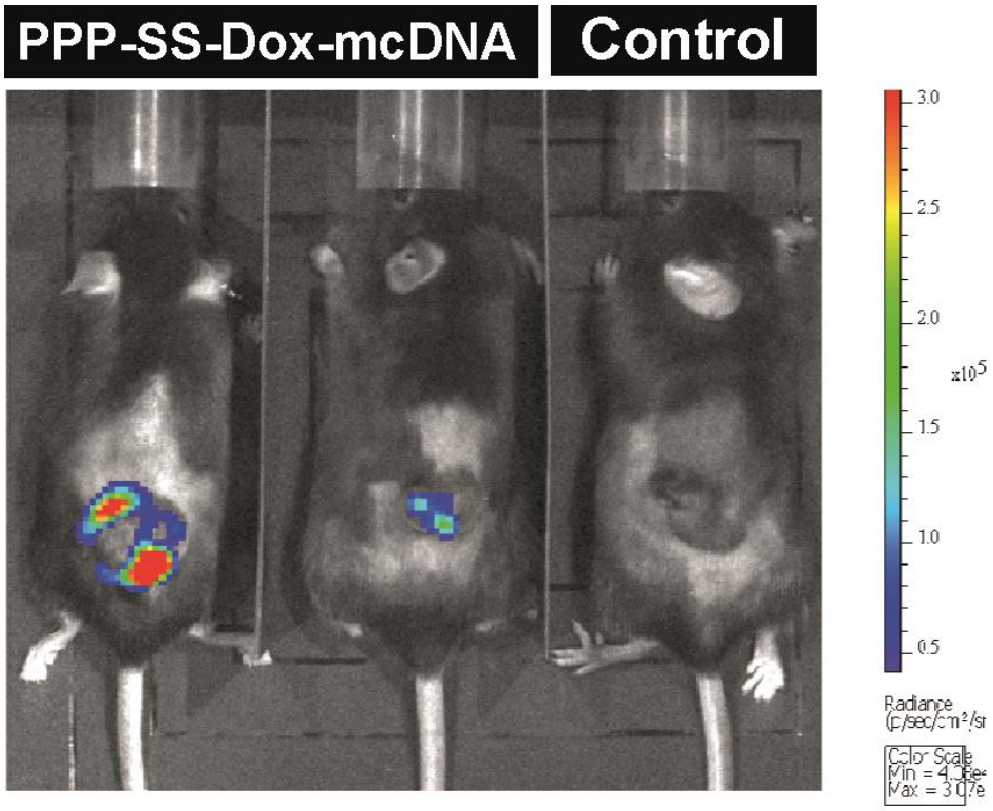

Figure S12. Bioluminescence imaging of luciferase gene expression following administration of p3NF-Luc-3NF and Dox loaded PPP-SS micelleplexes (formulated at N/P 20) to B16F10 tumor bearing mice. Images were acquired 48 h after dual-loaded nanocarriers administration.

11.3. References

1. Dai, Z., Gjetting, T., Mattebjerg, M.A., Wu, C., and Andresen, T.L., Andresen, *Elucidating the interplay between DNA-condensing and free polycations in gene transfection through a mechanistic study of linear and branched PEI*. Biomaterials, 2011. **32**(33): p. 8626-8634.
2. Schneider, S., Lenz, D., Holzer, M., Palme, K., and Süss, R., *Intracellular FRET analysis of lipid/DNA complexes using flow cytometry and fluorescence imaging techniques*. Journal of Controlled Release, 2010. **145**(3): p. 289-296.
3. Guo, Z., Tian, H., Xia, J., Chen, J., Lin, L., and Chen, X., *Bioreducible crosslinked low molecular weight branched PEI-PBLG as an efficient gene carrier*. Science China Chemistry, 2010. **53**(12): p. 2490-2496.
4. Kim, C., Lee, S.C., Shin, J.H., Yoon, J.-S., Kwon, I.C., and Jeong, S.Y., *Amphiphilic diblock copolymers based on poly (2-ethyl-2-oxazoline) and poly (1, 3-trimethylene carbonate): synthesis and micellar characteristics*. Macromolecules, 2000. **33**(20): p. 7448-7452.

Section IV

General Conclusions and Future Perspectives

CHAPTER 12

12. General Conclusions and Future Perspectives

12.1. General Conclusions

Minicircle DNA vectors are currently emerging as the next generation of gene expression cassettes for nonviral gene therapy due to their improved activity and therapeutic efficacy *in vivo*. To unravel the full potential of this technology and explore the use of mcDNA biopharmaceuticals for realistic therapeutic applications it is crucial to investigate different aspects related to their manufacture and mode of administration. To this end, the recent advent of nanotechnology and the possibility to manipulate materials at the nanoscale has provided the perfect momentum to combine nonviral minicircles with nano-sized carriers, and discover cutting-edge technologies with potential for human use. Interestingly, due to nanovehicles intrinsic versatility, combinatorial therapies based on the simultaneous administration of various bioactive molecules can also be explored. Among the different types of materials that can be used for nanocarriers assembly, biodegradable polymers are particularly advantageous since the repeating and terminal chemical groups can act as anchoring sites for modification of polymers intrinsic physicochemical properties, or for the attachment to other materials (e.g., polymers, small bioactive molecules, drugs). This is an advantageous property that can also be used to increase polymeric nanocarriers stability in biological fluids or improve their gene transfer efficacy. The study of these therapeutic approaches assumes a remarkable importance in light of the biosafety issues and limited efficacy of currently administered cancer treatments. Therefore, aiming to address such challenges, in this Doctoral work the biosynthesis, purification, nanocarrier-mediated delivery of mcDNA vectors, and co-delivery of mcDNA-Doxorubicin were exploited.

In a global analysis, initially, in chapter 5, the biosynthesis of mcDNA vectors was studied by manipulating the bacterial fermentation temperature and the parental-to-minicircles conversion process. With this manipulation, higher titers of parental plasmid (PP) vectors were obtained and optimal induction conditions were established (e.g., inductor concentration and time of induction). The in-line monitoring of the recombination process also proved to be useful for the discovery of important information regarding an optimal conversion time where mcDNA production achieves its highest yield and purity. The know-how obtained from this study provided valuable information regarding various parameters that must be addressed to achieve optimal mcDNA production, either at a laboratory or industrial scale.

In chapter 6, the possibility of using dipeptides as innovative ligands for mcDNA isolation and purification was explored. The obtained results demonstrated that from the tested ligands those comprised by arginine-arginine dipeptides were particularly effective in establishing interactions with mcDNA vectors. These preferential interactions were proven under precise temperature conditions and ionic strength as demonstrated by surface plasmon resonance data.

Particularly, the determination of dissociation constants (K_D) revealed that ligand-analyte interactions are favored at low ionic strength buffer, and reduced in high salt concentrations. Such findings proved the concept of exploring biologically relevant interactions to discover original materials for mcDNA vectors isolation. As such, the newly discovered ligands were subsequently used to create a monolithic chromatography column with arginine dipeptides for mcDNA recovery (Chapter 11).

In chapter 7 and 8 the possibility of using amino acids, hydrophilic PEG chains and cell targeting ligands to improve the biological efficacy of chitosan nanocarriers was investigated. As shown by NMR analysis the use of amine coupling chemistry allowed the grafting of different amino acids into chitosan polymeric backbone (CH-HR). With an additional strategy based on Michael type coupling chemistry, folic acid targeting ligands and PEG hydrophilic polymers were also successfully linked to chitosan (CM-PFA). The resulting biofunctionalized and targeted nanocarriers showed high selectivity towards cancer cells and negligible uptake in normal cells. Experiments performed in 3D tumor models revealed that the multifunctional CM-PFA carriers have improved gene transfer in serum-containing medium when compared to their non-targeted counterparts. Taken together, the results from these two studies corroborate the benefit of using amino acids to imprint novel physicochemical properties in chitosan, since both the biofunctional carriers presented in chapter 7, and the multifunctional targeted carriers presented in chapter 8, demonstrated an increased biological efficacy in comparison with unmodified chitosan nanoparticles. The biofunctional delivery systems proved to be a good platform for gene transfer to cancer cells *in vitro* under biologically relevant conditions. An up-front comparison of these two technologies reveals that the inclusion of PEG and small targeting moieties significantly improved cell selectivity and nucleic acids transfer efficiency even in *in vitro* 3D tumor models, letting uncover that in the future these systems have more potential for application in DNA delivery to cancer cells.

In chapter 9, triblock copolymer micellar carriers were developed to explore the emerging concept of combinatorial cancer therapy since it is recognized that this treatment modality encloses the potential to improve the treatment outcome. It is important to emphasize that for investigating drug-gene co-delivery through nanocarriers, the chitosan-based platforms developed in chapter 8 required complex chemical modifications in order to encapsulate the anticancer drug doxorubicin. Such chemical modifications would alter the biological performance of these carriers and limit the anchoring points where amino acids, PEG and folic acid could be attached. Hence, to overcome this limitation, PEOz-PLA-g-PEI micellar carriers were produced for co-delivery. This unique polymer combination provided the necessary chemical versatility to load drugs and condense mcDNA, as confirmed by carriers physicochemical characterization. In this work, micelles *in vitro* gene transfer efficacy and doxorubicin-mediated cytotoxicity in cancer cells also demonstrated the efficiency of this technology for combinatorial therapy applications. As an additional proof-of-concept, *in vivo*

administration of PEOz-PLA-g-PEI micelles via intratumoral injection confirmed successful gene expression, and no toxicity was detected in major organs.

Aiming to further explore the co-delivery of drug-mcDNA combinations, both technologies developed in the previous studies (CH-HR amino acid chitosan nanoparticles, and PEOz-PLA-g-PEI micellar nanocarriers), were used in two complementary approaches (Chapter 10 and 11). These different studies shared the underlying hypothesis that imprinting a stimuli-responsive character in drug-gene delivery systems could provide remarkable improvements in the control over the release of bioactive molecules, and possibly improve the overall effect. In chapter 10 mcDNA-loaded biofunctional amino acid carriers were encapsulated in gas-generating, pH-responsive, doxorubicin-loaded, biodegradable PLGA-TPGS microspheres. The resulting nano-in-micro hybrid systems, where found to react to acidic pH of intracellular compartments, and rapidly burst-release their payload in the intracellular compartment of cancer cells. Such control over carriers biological behavior under precise biological conditions proved to be beneficial in terms of the cytotoxic activity towards cancer cells, when compared to non-responsive PLGA microspheres. The concept of co-delivery was confirmed by successful GFP expression mediated by mcDNA-CH-HR carriers, thus indicating that this platform could be advantageous for combinatorial delivery. Although this system was evaluated through more fundamental *in vitro* studies these encouraging preliminary results demonstrate its potential to be used either as a stand-alone hybrid system or in conjugation with other platforms as hydrogels or nanofibers.

Complementarily, in chapter 11, the triblock micellar carriers were chemically modified to be responsive to the dynamic redox conditions found in the intracellular compartment. These carriers demonstrated mcDNA-doxorubicin loading and self-assembled into nanosized micelles. In comparison with the PEOz-PLA-g-PEI non-responsive systems the bioreducible micelles promoted a higher gene expression *in vitro* in 3D multicellular tumor spheroids of different types of cancer cells. These encouraging findings, corroborate the gain-of-function when disulfide linkages were imprinted in the cationic polymer backbone. *In vivo,* focal administration of drug-gene loaded micelles resulted in a reduction in tumor volume and malignant cells growth. Also, 8 days following gene transfer, positive signals were detected in tumor tissues suggesting that a prolonged transgene expression could be obtained.
These findings led to conclude that the biological performance demonstrated by PEOz-PLA-g-PEI-SS bioreducible micelles, the validation of their co-delivery and stimuli-responsive capacity *in vivo* reveals the tremendous potential of this particular delivery system to be used as a new tool for combinatorial therapies.

In an overall perspective, by using a hypothesis driven approach this Doctoral work led to beyond state-of-the-art advances in the various stages involving mcDNA-based gene therapy and fostered the discovery of novel delivery platforms which can positively impact combinatorial therapies in a foreseeable future.

12.2. Future Perspectives

On the topic of prospective directions in the field of mcDNA biopharmaceuticals it would be highly valuable to further explore the various stages of the process from production, to recovery and delivery/co-delivery to human hosts in the future. All together, these three phases are the main pillars that support minicircles applicability and improvements in each of them could increase the speed-to-clinic of this technology. Taking this into account and as a follow-up of this Doctoral work, it would be of noteworthy interest:

I. Production stage:

To explore the pilot scale or large scale production of mcDNA vectors under dynamic conditions that could lead to production of grams of minicircles. Moreover, it would be interesting to study the influence of new bioprocess related parameters such as the type of culture media, the effects of amino acid limitation, bacterial cultures genetic stability during growth, batch/fed-batch strategies. All of these are prospective directions and the results described in this thesis may provide the foundation for discovery of additional bioprocess improvements. Also, as investigated in this thesis such future studies could take advantage of the on-line monitoring of PP-to-mcDNA recombination process described herein, since it is of paramount importance to assure the quality control of the final preparation. Such strategy is envisioned to contribute for a cGMP compliant production of mcDNA vectors.

II. Purification/Recovery stage:

To further study the purification of mcDNA vectors from complex bacterial lysates by using monolithic chromatographic columns with dipeptide arginine ligands. The application of such technology would be advantageous since large scale mcDNA recovery by commercial purification kits that involve precipitation/centrifugation is unfeasible and too expensive. Along, with the fact that affinity chromatography with arginine dipeptide ligands could provide a cost-effective purification platform for large scale mcDNA purification, this technology could also be used to reduce the endotoxin levels of mcDNA preparations. For this purpose it will be of particular interest to explore different conditions for mcDNA isolation such as: (i) buffer type; (ii) temperature; (iii) ionic strength; (iv) presence of competing ligands. Moreover, to explore large scale purification it would be beneficial to investigate the dynamic binding capacity of arginine-arginine monolith disks and the final purity of the recovered fractions following the injection of milligrams/grams of mcDNA. Addressing this parameter in the future is crucial for obtaining pharmaceutical-grade mcDNA preparations. Alongside with these improvements different biomimetic ligands for mcDNA purification from complex lysates could also be investigated. In this context, currently ongoing studies are exploring protein-mcDNA or cationic ions (Mg^{2+}, Zn^{2+}) mcDNA biointeractions.

III. Nucleic acid delivery/mcDNA-drug co-delivery stage:

Nucleic acid *delivery:* To test in *in vivo* tumor models the focal/intravenous administration, cell selectivity, and therapeutic performance of the developed CM-PFA folic acid targeted nanocarriers, since these systems demonstrated promising results when administered to 3D multicellular tumor spheroids *in vitro*. With this validation the feasibility of using this delivery platform for mcDNA biopharmaceutics delivery in the future could be unraveled. It is also important to emphasize that despite this platform is not optimal for drug-gene co-delivery it could be used in for example in targeted co-delivery of mcDNA/mRNA combinations.

mcDNA-drug co-delivery: To investigate in *in vivo* tumor models the antitumoral efficacy of mcDNA-CH-HR/Doxorubicin loaded, pH responsive PLGA-TPGS microspheres. The study of different modes of administration including focal or intravenous delivery could also be of major interest to bring about the full potential of this cost-effective co-delivery platform. Moreover, *in vivo* analysis would also provide important insights in the pH-responsiveness of the microspheres in the acidic tumor microenvironment.

Regarding the specific case of PEOz-PLA-g-PEI-SS nanocarriers the investigation of their *in vivo* biological performance demonstrated encouraging results. In the follow-up of this research it would be of particular relevance to methodically study the pharmacokinetic/pharmacodynamic profile of mcDNA-Doxorubicin loaded bioreducible micelles following intravenous injection since this would reduce the invasiveness of the administration procedure. From a manufacture point of view this system presents various advantages including its cost-effectiveness and ease of purification/recovery, hence it would be highly valuable to explore parameters that could assure batch-to-batch reproducibility in large scale manufacture. Moreover, it could be particularly valuable to functionalize micelles surface with cancer cells targeting ligands and test their tumor selectivity. These ligands can be small-molecules, antibody fragments or new peptide ligands recognized to present both targeting capacity to tumor cells and their surrounding microenvironment, such could contribute for encouraging the translation of these carriers up to clinical trials testing. I do believe that the field of nanobiotechnology, and particularly, of combinatorial therapy will flourish in the near future and that its developments will have a profound impact in everyday patients lives, either those bearing cancer or other types of currently incurable diseases. The work presented in this thesis will surely contribute for the advanced of the state-of-the-art in the delivery systems and vectors used for cancer gene therapy.